

Inelastic local buckling of tubes for combined walls and pipelines

van Es, Sjors

DOI

[10.4233/uuid:48e61e69-a35f-43d5-a417-b393cbacaa98](https://doi.org/10.4233/uuid:48e61e69-a35f-43d5-a417-b393cbacaa98)

Publication date

2016

Document Version

Final published version

Citation (APA)

van Es, S. (2016). *Inelastic local buckling of tubes for combined walls and pipelines*. [Dissertation (TU Delft), Delft University of Technology]. <https://doi.org/10.4233/uuid:48e61e69-a35f-43d5-a417-b393cbacaa98>

Important note

To cite this publication, please use the final published version (if applicable). Please check the document version above.

Copyright

Other than for strictly personal use, it is not permitted to download, forward or distribute the text or part of it, without the consent of the author(s) and/or copyright holder(s), unless the work is under an open content license such as Creative Commons.

Takedown policy

Please contact us and provide details if you believe this document breaches copyrights. We will remove access to the work immediately and investigate your claim.

Inelastic local buckling of tubes for combined walls and pipelines

PROEFSCHRIFT

ter verkrijging van de graad van doctor
aan de Technische Universiteit Delft,
op gezag van de Rector Magnificus prof. ir. K.C.A.M. Luyben,
voorzitter van het College voor Promoties,
in het openbaar te verdedigen op
vrijdag 8 juli 2016 om 15:00 uur

door:

Sjors Harry Jan VAN ES

Civiel ingenieur
geboren te Amersfoort

Dit proefschrift is goedgekeurd door de
promotor: Prof. ir. F.S.K. Bijlaard
copromotor: Dr. M.H. Kolstein

Technische Universiteit Delft
Technische Universiteit Delft

Samenstelling promotiecommissie:

Rector Magnificus
Prof. ir. F.S.K. Bijlaard
Dr. M.H. Kolstein

voorzitter
Technische Universiteit Delft, promotor
Technische Universiteit Delft, copromotor

Onafhankelijke leden:

Prof. dr. S.A. Karamanos

Πανεπιστήμιο Θεσσαλίας (University of Thessaly),
Griekenland

Prof. dr.-ing. T. Ummenhofer

Karlsruher Institut für Technologie (Karlsruhe
Institute of Technology), Duitsland

Prof. dr. M. Veljkovic

Technische Universiteit Delft

Prof. dr. ir. J. Wardenier

Technische Universiteit Delft, National University of
Singapore, Singapore

Prof. dr. ir. M.A.N. Hendriks

Technische Universiteit Delft, Norges Teknisk-Natur-
vitenskapelige Universitet (Norwegian University of
Science and Technology), Noorwegen, reservelid

Overige leden:

Ir. A.M. Gresnigt

Technische Universiteit Delft

ISBN 978-94-6299-368-6

Printed by Ridderprint, The Netherlands

Cover design by Sjors van Es

© S.H.J. van Es. All right reserved. No part of this publication may be reproduced or utilized in any form or by any means, electronic or mechanical, including photocopying, recording, or by any information storage and retrieval system, without prior consent of the author.

Acknowledgements

After finishing my Master's programme in Civil Engineering at Delft University of Technology, I did not feel I was done with learning at an academic level. Furthermore, during the research I performed for my Master Thesis, I was offered the chance to do experimental research. I experienced that this is a part of research I very much enjoy. Therefore, when a position as a PhD-candidate became available that included work on two major experimental programmes, I did not hesitate to take this opportunity. I think this was the right choice.

To perform these experiments, I largely depended on the assistance of the laboratory technicians in the Stevin-laboratory. Many thanks are extended to Arjen van Rhijn, John Hermsen, Louis den Breejen, Ron van Leeuwen and especially Kees van Beek, who have helped me performing the experiments that are presented in this thesis. Without their help, ideas and hard work, it would have been impossible to achieve such high quality experiments. Further thanks go to Peter Meijnders, Martin van de Raad, Maikel Kammeron and Arnold van de Wollenberg, who provided valuable support in completing the experiments under considerable pressure.

I want to thank Nol Gresnigt, Frans Bijlaard and Henk Kolstein for supervising my progress. You were always willing to answer my questions. Also the support and comments of the research partners in RFCS projects COMBITUBE and GIPIPE were very valuable.

I would also like to thank my parents for supporting me in my choice to do a PhD and for always being there for me, even under difficult circumstances. Finally, I want to express my deepest gratitude to my wife, Greta, with whom I could share all ups and downs over the last four years. I would not have managed without you.

Samenvatting

In dit proefschrift wordt het gedrag van ronde buisprofielen beschouwd. Het proefschrift bestaat uit vier delen:

Part I: Literature study of the bending behaviour of tubular members

Part II: Spiral-welded tubes for application in combined walls

Part III: Deformation of buried pipelines crossing active strike-slip faults

Part IV: Closure

Part I bespreekt een literatuuronderzoek naar het buiggedrag van buizen. In Parts II en III worden twee meer toegespitste onderzoeksonderwerpen binnen dit brede onderzoeksveld besproken, gevolgd door een afsluitend vierde deel.

Part I: Literature study of the bending behaviour of tubular members

Het buiggedrag van buizen kan nauwkeurig worden beschreven met behulp van eindige-elementen analyses of door middel van analytische formulerings. In geval van buizen met een relatief slanke doorsnede treedt onder invloed van buiging instabiliteit van de gedrukte buiswand op. Deze vorm van instabiliteit wordt plooiën genoemd. Voor de buizen die in dit proefschrift zijn onderzocht is dit een belangrijk faalmechanisme.

In tegenstelling tot het pre-kritische buiggedrag van buizen, kan het faalmechanisme plooiën nog niet altijd voldoende nauwkeurig worden beschreven, doordat zeer veel parameters het plooiëgedrag van buizen beïnvloeden. Part I van dit onderzoek bevat een literatuurstudie naar dit fenomeen, resulterend in een database met meer dan 400 experimenten waarbij plooiën is opgetreden. Op basis van deze database is een nieuwe ontwerprichtlijn voor plooiën van buizen ontwikkeld.

Part II: Spiral-welded tubes for application in combined walls

Combiwanden zijn grondkerende constructies bestaande uit stalen buispalen waartussen standaard damwandprofielen zijn aangebracht. De buispalen fungeren als hoofddraagconstructie voor horizontale belastingen ten gevolge van grond- en waterdrukken. Om een maximale buigstijfheid en buigsterkte te verkrijgen bij een minimaal materiaalgebruik hebben deze buispalen doorgaans een grote diameter en relatief dunne wand. Door de hoge slankheid van de doorsnede is plooi doorgaans het maatgevend faalmechanisme voor dergelijke buispalen. Voor toepassing in combiwanden zijn spiraalgelaste buizen zeer geschikt omdat deze vervaardigingsmethode zeer economisch is voor dunwandige buizen met een grote diameter. Verder is deze techniek geschikt voor de productie van lange buispalen zonder dat hierbij rondlassen nodig zijn.

Naar het buig- en plooi gedrag van spiraalgelaste buizen is nog niet veel onderzoek gedaan. Daarnaast zijn de huidige normen waarin het ontwerp en de berekening van slanke buispalen is vastgelegd relatief conservatief. In een Europees onderzoeksproject genaamd COMBITUBE is onderzoek gedaan naar het buiggedrag van spiraalgelaste buizen met als doel om een nieuwe, meer economische, ontwerprichtlijn voor buispalen in combiwanden te ontwikkelen. Het onderzoek in Part II van dit proefschrift heeft bijgedragen aan dit project.

Om het buig- en plooi gedrag van spiraalgelaste buizen te bestuderen zijn dertien grootschalige vierpuntsbuigproeven uitgevoerd op dergelijke buizen. Daarnaast zijn ter vergelijking ook twee buigproeven uitgevoerd op langsgelaste buizen. Voordat de buigproeven zijn uitgevoerd, zijn van alle buizen de initiële geometrie, initiële imperfecties en materiaaleigenschappen nauwkeurig bepaald. De in het laboratorium gemeten imperfecties zijn vergeleken met imperfecties in een combiwand in de praktijk.

In de buigproeven zijn de buizen belast door een constant buigend moment over een bepaalde lengte. De proeven op buizen zonder verbindingslassen tussen buisdelen laten zien dat, ondanks dat het buigend moment constant is, de kromming varieert over deze lengte. Deze lokalisatie van vervormingen manifesteert zich ook nabij rondlassen en stuiklassen ten gevolge van het wisselen van een staalrol tijdens de vervaardiging van de buis. In die gevallen wordt deze lokalisatie van vervormingen veroorzaakt door de discontinuïteit in doorsnede-eigenschappen van de buis ter plaatse van de las. Dit fenomeen en de verdere effecten van de aanwezigheid van dergelijke lassen in de buis is uitgebreid bestudeerd. Na het plooiën behielden alle proefstukken een significant deel van de draagkracht. Daarom is een analyse van de nakritische momentweerstand van de buizen uitgevoerd.

De resultaten van de buigproeven zijn gebruikt door partners binnen het COMBITUBE project om numerieke en analytische modellen die het buig- en plooi gedrag van buizen beschrijven te testen en te ijken. Vanwege de geschiktheid voor gebruik in de ontwerp praktijk is het analytische model verder gevalideerd met behulp van de uitgevoerde proeven. Er worden economische en veilige ontwerpen verkregen bij het gebruik van de voorgestelde modellen.

Part III: Deformation of buried pipelines crossing active strike-slip faults

Ingegraven buisleidingen kunnen worden blootgesteld aan verplaatsingen van de grond die de buis omringt. Vooral verplaatsingsverschillen in de ondergrond kunnen leiden tot grote vervormingen van de buisleiding. Dergelijke verplaatsingsverschillen kunnen ontstaan door bijvoorbeeld aardverschuivingen, zettingsverschillen of actieve breuklijnen. Veel verschillende parameters hebben invloed op dergelijke situaties en de interactie tussen buis en grond is complex. Daardoor is vaak ook het ontwerp van een buisleiding voor dergelijke belastingen complex. In een Europees project genaamd GIPIPE is onderzoek uitgevoerd om meer inzicht te krijgen in het gedrag van ingegraven leidingen onder invloed van opgelegde verplaatsingen door de omliggende grond en om ontwerprichtlijnen te ontwikkelen voor dergelijke situaties.

Part III van dit proefschrift heeft een bijdrage geleverd aan dit project en focust op het effect van een actieve breuklijn op een ingegraven buisleiding. Door middel van grootschalige proeven is meer inzicht verkregen in het gedrag van buisleidingen in dergelijke situaties. Om het gedrag van de buis onder invloed van de opgelegde vervormingen te kunnen monitoren is het grondgedrag in de proeven gesimuleerd met behulp van niet-lineaire veren zodat de buis bloot kon liggen. In een programma van tien proeven is de invloed van verschillende parameters bestudeerd.

Met behulp van de uitgevoerde proeven is een eindige-elementen model ontwikkeld voor ingegraven buisleidingen onder invloed van opgelegde vervorming. Het model combineert een relatief simpele modellering van de interactie tussen pijp en grond door middel van niet-lineaire veren met een uitgebreide analyse van het vervormingsgedrag van de stalen buis. In het model is met name het faalmechanisme plooiën uitgebreid bestudeerd. Door de tien uitgevoerde proeven te simuleren is het model gevalideerd en geïjkt. Deze analyses laten zien dat het model in staat is om het gedrag van buizen ten gevolge van opgelegde grondverplaatsingen zeer nauwkeurig te voorspellen. Hoewel het model gevalideerd is met proeven die een actieve breuklijn simuleren, is het model toepasbaar voor opgelegde vervormingen van ingegraven buizen door verplaatsingen van de omringende grond in het algemeen. De relatief eenvoudige schematisatie van de pijp-grond interactie die is gebruikt voor de grondveren in de experimenten en de validatie van het model kan vervangen worden door een willekeurige andere, nauwkeurigere, schematisatie.

Summary

In this study, the bending behaviour of tubular members is investigated. The thesis consists of four parts:

Part I: Literature study of the bending behaviour of tubular members

Part II: Spiral-welded tubes for application in combined walls

Part III: Deformation of buried pipelines crossing active strike-slip faults

Part IV: Closure

In Part I, a literature study of the bending of tubular members is presented. In Parts II and III, two more specific topics within this broad field of research are discussed. In a final part of the thesis, an evaluation of the performed research is presented.

Part I: Literature study of the bending behaviour of tubular members

The bending behaviour of tubular members can accurately be described using FE-analyses or analytical formulations. For tubes with a relatively slender cross-section, the compressed wall of the tube becomes unstable at some point in the bending response, which is denoted as local buckling. For the elements considered in this study, this is an important failure mode.

In contrast with the pre-critical bending behaviour, the failure mode local buckling is difficult to describe accurately, due to the many parameters that are of influence on the phenomenon. In Part I of this study, over 400 local buckling experiments are collected, originating from studies performed in the last 50 years. Based on this database, a design guideline for local buckling of tubular members was developed.

Part II: Spiral-welded tubes for application in combined walls

Combined walls are soil retaining walls that consist of an alteration between tubular elements and standard sheet piling. The tubes act as primary structural elements that resist horizontal loads from soil and water. To achieve maximum bending stiffness and bending moment capacity at a minimum steel use, these combined walls are typically constructed using large-diameter thin-walled tubes. As a result, the dominating failure mechanism of these tubes is local buckling. Tubes for combined walls are typically manufactured using the spiral-welding manufacturing process, which allows the manufacturing of tubes of long lengths without the need for girth welds. Furthermore, this manufacturing process is most suitable to economically manufacture the large-diameter, thin-walled tubes that are typically applied in combined walls.

From literature, it appears that the bending and local buckling behaviour of spiral-welded tubes is not well understood. Furthermore, current design regulations for tubes in combined walls are concluded to result in uneconomical designs. Therefore, a European research project with acronym COMBITUBE was started in 2011, which aimed to study the bending and local buckling behaviour of spiral-welded tubes and develop safe and economical design guidelines for tubes in combined walls. The research in Part II of this study contributed to this project.

To study the bending behaviour of spiral-welded tubes, thirteen large-scale four-point bending tests were performed on such tubes, until failure in local buckling occurred. In addition, two comparison tests on longitudinal-welded tubes were performed. Before the bending tests, the initial geometry, geometrical imperfections and material properties of these tubes were carefully documented. The imperfection measurements in the laboratory were compared with observations at a construction site.

In the bending tests, it was observed that in a plain tube segment that is loaded by a constant bending moment, curvature is not always constant. This curvature localization also occurred at girth welds and coil connection welds, where discontinuities in cross-sectional properties occur. This effect and the effect of the presence of a girth weld or coil connection weld was thoroughly investigated. After local buckling failure, it was observed that significant bending moment capacity remained. Therefore, an analysis of the remaining post-buckling bending moment capacity was performed.

The results of the bending tests were used by partners within the research project to develop a numerical and an analytical model to predict the bending behaviour of these tubes. The analytical model is intended for use by designers and is validated in this thesis using the results of the four-point bending tests. Safe and economical designs are obtained when using this design procedure.

Part III: Deformation of buried pipelines crossing active strike-slip faults

Buried pipelines may be exposed to movement of the soil surrounding the pipeline. Especially differential movements may result in large deformation of the pipeline. Causes of such differential movements are for example landslides, uneven settlements or movements of active faults. Due to the many parameters involved and the complex interaction between pipe and soil, design for such imposed deformations is often complex. To investigate the behaviour of buried steel pipelines under imposed deformations and to develop guidance for designers, a European research project with acronym GIPIPE was started in 2011.

Part III of this study contributed to this project and focuses on the effect of an active strike-slip fault on buried pipelines. Ten full scale tests were performed which took into account many parameters that are of influence on the behaviour of these buried pipelines. To allow careful study of the deformation of the pipeline during the tests, the soil behaviour was simulated using elasto-plastic mechanical springs so that the pipe could remain bare during the experiments.

Using the results of the performed tests for validation and calibration purposes, an FE-model for buried pipelines under ground-induced deformation was developed. The model combines relatively simple non-linear soil springs with a rigorous analysis of the steel pipe.

Simulations of the ten laboratory experiments showed that the developed FE-model can accurately predict the effects of ground-induced deformations on a buried pipeline. Especially the failure mechanism of local buckling was thoroughly investigated. The validated model can not only be applied to predict the effects of strike-slip fault movements, but also to predict the effects of ground-induced deformations of buried pipelines in general, and allows for the implementation of new and alternative soil models in the non-linear soil springs.

Table of contents

Acknowledgements.....	iii
Samenvatting.....	v
Part I: Literature study of the bending behaviour of tubular members.....	v
Part II: Spiral-welded tubes for application in combined walls	vi
Part III: Deformation of buried pipelines crossing active strike-slip faults.....	vii
Summary.....	ix
Part I: Literature study of the bending behaviour of tubular members.....	ix
Part II: Spiral-welded tubes for application in combined walls	x
Part III: Deformation of buried pipelines crossing active strike-slip faults.....	xi
Table of contents.....	xiii
List of symbols.....	xix
Symbols relating to steel structures.....	xix
Symbols relating to soil mechanics	xxii
Subscripts	xxiii
List of abbreviations	xxv
Preface	1
Part I: Literature study of the bending behaviour of tubular members.....	3
Chapter 1 Moment-curvature behaviour of tubular members	5
1.1 Introduction.....	5
1.2 Prediction of the pre-buckling moment-curvature behaviour	6
1.3 Bifurcation buckling	7
1.4 Summary of Chapter 1	17
1.5 Recommendations for further research	17
Chapter 2 Design rule for local buckling of tubes.....	19

2.1	Introduction and methods	19
2.2	Plain specimens	19
2.3	Influence factors	20
2.4	Full model.....	30
2.5	Comparison with existing design guidelines	34
2.6	Comparison with Eurocode 3	36
2.7	Evaluation of assessment methods.....	37
2.8	Summary of Chapter 2.....	38
2.9	Recommendations for further research.....	38
Chapter 3	Summary of Part I and recommendations	41
3.1	Summary of Part I.....	41
3.2	Recommendations for further research.....	42
Part II: Spiral-welded tubes for application in combined walls.....		43
Chapter 4	Introduction to Part II.....	45
4.1	COMBITUBE research project.....	45
4.2	Spiral-welding manufacturing process	45
4.3	Combined walls	47
4.4	Literature review.....	48
4.5	Objective.....	49
4.6	Summary of Chapter 4.....	50
Chapter 5	Experimental study of spiral-welded tubes.....	51
5.1	Test programme	51
5.2	Measurement of initial geometry and imperfections	53
5.3	Material testing	79
5.4	Four-point bending tests	87
5.5	Results of four-point bending tests	92
5.6	Summary of Chapter 5.....	98
Chapter 6	Analysis and interpretation of bending test results.....	101
6.1	Definitions	101
6.2	Ultimate bending moment and deformation capacity	102
6.3	Buckling location.....	107
6.4	Influence of the presence of girth welds and coil connection welds.....	109

6.5	Numerical analysis of manufacturing process and four-point bending tests.....	112
6.6	Post-buckling behaviour	113
6.7	Influence of spiral-welding manufacturing process	115
6.8	Effect of a soil fill	121
6.9	Comparison of test results with strain-based prediction model	122
6.10	Application of results	127
6.11	Summary of Chapter 6	128
Chapter 7	Summary of Part II and recommendations	131
7.1	Summary of Part II	131
7.2	Recommendations for further research	132
Part III: Deformation of buried pipelines crossing active strike-slip faults		135
Chapter 8	Introduction to Part III.....	137
8.1	GIPIPE research project.....	137
8.2	Imposed deformation on pipelines due to soil movement.....	137
8.3	Literature review.....	138
8.4	Objective.....	142
8.5	Summary of Chapter 8	142
Chapter 9	Experimental study of buried pipelines crossing active strike-slip faults	145
9.1	Test programme	145
9.2	Measurement of initial geometry	155
9.3	Material testing	156
9.4	Test setup	158
9.5	Boundary conditions of individual tests.....	170
9.6	Results of large-scale testing.....	175
9.7	Summary of Chapter 9	189
Chapter 10	Analysis and interpretation of test results.....	191
10.1	Method of analysis	191
10.2	Influence of soil behaviour and pipe-soil interaction.....	191
10.3	Influence of the presence of a girth weld in a critical segment of the pipeline	192
10.4	Influence of fault angle and axial normal force	194
10.5	Rupture in test T5	195
10.6	Summary of Chapter 10	197

Chapter 11	Numerical analysis of buried pipelines crossing active strike-slip faults	199
11.1	Description of numerical model.....	199
11.2	Model calibration and validation	209
11.3	Summary of Chapter 11	218
Chapter 12	Summary of Part III and recommendations.....	221
12.1	Summary of Part III.....	221
12.2	Recommendations for further research.....	222
Part IV: Closure	225
Chapter 13	Concluding remarks	227
13.1	Evaluation of performed research.....	227
13.2	Recommendations for further research.....	228
References.....		231
Literature.....		231
Standards and design guidelines		239
Appendices	241
Appendix A:	Database of local buckling test results collected from literature	243
Appendix B:	Results of bending tests on tubes for combined walls	255
B.1	Summary of experimental results	256
B.2	Specimen layout	256
B.3	Moment-curvature diagrams	258
B.4	Ovalisation-curvature diagrams.....	263
Appendix C:	Comparison of design guidelines with tests on tubes for combined walls	269
Appendix D:	Results of tests on pipelines crossing active strike-slip faults	275
D.1	Summary of test results	276
D.2	Specimen layout	277
D.3	Ring-spring geometry.....	280
D.4	Ring-spring response.....	281
D.5	Results of strain measurements	291
D.6	Results of ovalisation measurements	312
Appendix E:	Results of calibration and validation of numerical model for buried pipelines.....	323
E.1	Comparison of ring-spring response.....	323
E.2	Comparison of strain	345

E.3 Comparison of ovalisation	386
Appendix F: Stress-strain diagrams	397
F.1 Stress-strain diagrams of tubes tested in Part II	397
F.2 Stress-strain diagrams of pipes tested in Part III.....	408
Appendix G: Probabilistic evaluation of test results	415
G.1 Local buckling of tubes	416
G.2 Remaining post-buckling bending moment capacity of tubes in combined walls.....	422
G.3 Critical strain of tubes in combined walls	431
G.4 Maximum bending moment capacity of tubes in combined walls	432
Curriculum Vitae	439

List of symbols

Symbols relating to steel structures

Greek

α	Influence factor on the critical compressive strain	[-]
α_{σ_y}	Influence of the yield strength on the critical compressive strain	[-]
α_{geo}	Influence of the geometrical imperfections on the critical compressive strain	[-]
α_{GW}	Influence of the presence of a girth weld on the critical compressive strain	[-]
α_P	Influence of the internal pressure on the critical compressive strain	[-]
α^*_P	Adjusted influence of the internal pressure on the critical compressive strain	[-]
α_{sand}	Influence of a sand fill on the critical compressive strain	[-]
α_{sh}	Influence of strain hardening on the critical compressive strain	[-]
β	Reliability index	[-]
γ	Partial safety factor	[-]
γ_M	Partial safety factor on resistance. Ratio between characteristic value of the calculated resistance and design value of the calculated resistance using mean values for the input parameters	[-]
γ^*_M	Partial safety factor on resistance. Ratio between mean value and design value of the calculated resistance using nominal values for the input parameters	[-]
δ	Measured distance	[mm]
δ_{imp}	Measured imperfection size	[mm]
ΔC	Change in circumference	[mm]
ΔD	Change in diameter, ovalisation parameter	[mm]
ΔK	Ratio between nominal and characteristic resistance	[-]
ΔK^*	Ratio between nominal and mean resistance	[-]
Δr	Change in radius	[mm]
ε	Strain or coefficient dependent on σ_y	[-]/[-]
ζ	Strength ratio	[-]

θ	Angle of spiral weld with respect to the tube axis	[-]
κ	Curvature	[mm ⁻¹]
$\kappa_{avg;U}$	Average curvature determined from measured displacements at the supports	[km ⁻¹]
$\kappa_{avg;b}$	Average curvature determined from a curvature bracket	[km ⁻¹]
κ_{buc}	Curvature at which local buckling occurs	[km ⁻¹]
κ_i	Local curvature determined from a curvature bracket, with $i=1,2,3$	[km ⁻¹]
κ_l	Curvature-like parameter	[km ⁻¹]
ν	Poisson factor	[-]
ρ	Pearson product-moment correlation coefficient	[-]
σ	Stress	[MPa]
$\sigma_{0.2\%}$	Proof stress at 0.2% plastic strain	[MPa]
$\sigma_{0.5\%}$	Proof stress at 0.5% total strain	[MPa]
σ_y	Yield stress	[MPa]
σ_u	Ultimate tensile stress	[MPa]

Latin

a_{imp}	Initial geometrical imperfection amplitude in FE-model for buried pipelines	[mm]
A	Area or coefficient in prediction model	[mm ²]/[-]
A_{steel}	Steel surface area	[mm ²]
$A_{internal}$	Internal cross-sectional surface area of a tube	[mm ²]
b	Width of the beam used to introduce loads into ring-springs	[mm]
B	Coefficient in prediction model	[-]
D	Outer diameter of a tube or pipe	[mm]
E	Modulus of elasticity	[MPa]
EI_{wall}	Bending stiffness of the wall of a ring-spring	[Nmm ²]
f	Ovalisation parameter	[-]
F	Force	[kN]
F_{ring}	Force in a ring-spring	[kN]
$F_{p;ring}$	Plastic resistance of a ring-spring	[kN]
L	Length	[mm]
L_e	Gauge length for determination of critical strain	[mm]
L_{el}	Element length	[mm]
L_{em}	Length over which imperfections in the form of an eigenmode are applied	[mm]
L_{hw}	Length of a half-wave in an eigenmode	[mm]
M	Bending moment	[kNm]
M_p	Full-plastic bending moment	[kNm]

$M_{p;wall}$	Full-plastic bending moment of the wall of a ring-spring	[kNm]
M_{pb}	Remaining post-buckling bending moment capacity	[kNm]
M_y	Bending moment at which the yield strength is reached in the outer fibre	[kNm]
N	Normal force	[kN]
N_β	Normal force in a buried pipe due to a fault angle	[kN]
N_P	Normal force in a buried pipe due to internal pressure	[kN]
$N_{P;spec}$	Normal force in a pipe specimen due to internal pressure	[kN]
N_S	Normal force in a buried pipe due to formation of an S-curve	[kN]
N_{test}	Normal force applied to the test specimen	[kN]
n	Number of data points	[-]
p	Performance of a model	[-]
P	Probability or pressure. Positive for internal pressure in a pipe, negative for external pressure acting on a pipe	[-]/[MPa]
P_b	Pressure containment resistance (burst pressure)	[MPa]
P_f	Probability of failure of a structure	[-]
P_y	Yield pressure. Pressure resulting in a hoop stress equal to the yield stress	[MPa]
P_{SMYS}	Specified yield pressure. Pressure resulting in a hoop stress equal to the specified minimum yield strength	[MPa]
r	Radius of a tube or pipe	[mm]
S	Skewness	[mm]
s	Standard deviation	[]
t	Wall thickness of a tube or pipe	[mm]
u	Displacement or deformation	[mm]
$u_{p;ring}$	Deformation of a ring-spring at which the plastic resistance $F_{p;ring}$ is reached	[mm]
V	Coefficient of variation	[-]
V_δ	Coefficient of variation of the resistance due to model inaccuracies	[-]
V_{σ_y}	Coefficient of variation of the yield stress	[-]
V_D	Coefficient of variation of the tube or pipe diameter	[-]
V_r	Coefficient of variation of the resistance	[-]
V_{rt}	Coefficient of variation of the resistance due to variation of the input parameters	[-]
V_t	Coefficient of variation of the wall thickness	[-]
$x_{ring;i}$	Distance of the location of a ring-spring to the fault centreline	[mm]
X	Input parameter in a model	[-]

Symbols relating to soil mechanics

Greek

α	Coefficient to account for the execution method of a buried pipeline	[-]
β	Fault angle	[-]
γ	Unit weight of soil	[kN/m ³]
δ'	Friction angle of the interface layer between a pipeline and surrounding soil	[-]
Δu_{fault}	Change in fault movement	[mm]
ν'	Poisson factor in drained conditions	[-]
ν_u	Poisson factor in undrained conditions	[-]
σ	Stress	[kPa]
σ'	Effective stress	[kPa]
φ	Angle of internal friction	[-]
φ'	Effective angle of internal friction in drained conditions	[-]
φ_u	Angle of internal friction in undrained conditions	[-]

Latin

a	Adhesion	[kPa]
A	Coefficient of non-linear behaviour	[-]
B	Coefficient of non-linear behaviour	[-]
c'	Effective cohesion in drained conditions	[kPa]
c_u	Cohesion in undrained conditions	[kPa]
E'	Modulus of elasticity in drained conditions	[MPa]
E_u	Modulus of elasticity in undrained conditions	[MPa]
K	Horizontal soil pressure coefficient	[-]
K_0	Horizontal soil pressure coefficient in case of neutral soil pressure	[-]
K_c	Load coefficient to account for the effect of cohesion in drained conditions	[-]
K_{cu}	Load coefficient to account for the effect of cohesion in undrained conditions	[-]
K_q	Load coefficient to account for the effect of the effective stress in the soil	[-]
$L_{stirred}$	Pipe length over which no soil pressures act due to soil stirring near the fault	[mm]
q_h	Lateral soil resistance	[kPa]
q_{he}	Ultimate lateral soil resistance	[kPa]
S	Saturation	[-]
u_{fault}	Fault movement	[mm]
w	Friction resistance	[kPa]

x	Axial displacement of a pipe through the soil	[mm]
x_{wmax}	Axial displacement of a pipe through the soil at which w_{max} is reached	[mm]
y	Lateral displacement of a pipe through the soil	[mm]
y_{30}	Transition between elastic and plastic soil resistance in the bilinear model	[mm]
y_{qhe}	Lateral displacement of the pipe through soil at which q_{he} is reached	[mm]
Z	Burial depth of the pipe centreline	[-]

Subscripts

acc	Most accurate result available
actuator i	Value of a parameter at actuator i
avg	Average value
axial	Direction of the longitudinal pipeline axis
bl	Parameter measured at the location where a local buckle occurred
cor	Corrected value
crit	Critical value
e	Value of a parameter resulting from experiments
d	Design value
hoop	Hoop direction (circumferential direction)
i	i -th parameter or parameter referring to i
incident	Value of a parameter at the occurrence of an incident
i^{th}	result of an i -th order calculation
j	j -th parameter or parameter referring to j
k	Characteristic value
lateral	Horizontal direction perpendicular to longitudinal pipe axis
left	Parameter on the left side
m	Mean value
max	Maximum value
min	Minimum value
n	Nominal value
norm	Normalized value
photo	Value of a parameter at the moment a photograph was taken
ref	Reference value
right	Parameter on the right side
shift	Value of a parameter at the occurrence of a strap shift

target	Target value
t	Value of a parameter resulting from a model
v	Vertical direction
X	Referring to parameter <i>X</i>

List of abbreviations

CCW	Coil connection weld
CLR	Curvature localization ratio
CSM	Centro Sviluppo Materiali
FE	Finite element
HDPE	High-density polyethylene
GW	Girth weld
HFW	High frequency welded
HSAW	Helical submerged arc welding
ID	Identification
LVDT	Linear variable differential transformer
NTUA	National Technical University of Athens
OCR	Over consolidation ratio
OV	Ovalisation measurement
PI	Plasticity index
PSL	Product specification level
PVC	Polyvinylchloride
RFCS	Research fund for coal and steel
SG	Strain gauge
TIG	Tungsten Inert Gas
UOE	Tube forming process. Forming a U, then an O, after which the pipe is expanded
Y/T-ratio	Ratio between yield stress and ultimate tensile stress

Preface

In this study, the bending behaviour of tubular members is investigated. Various applications of tubular members are discussed in this study. In agreement with common practice, tubular members in general or tubular members employed in structural applications are referred to as ‘tube’, while tubular members employed in fluid or gas transportation are referred to as ‘pipe’. The thesis consists of four parts:

Part I: Literature study of the bending behaviour of tubular members

Part II: Spiral-welded tubes for application in combined walls

Part III: Deformation of buried pipelines crossing active strike-slip faults

Part IV: Closure

In Part I, a literature study of the bending of tubular members is presented. In Parts II and III, two more specific topics within this broad field of research are discussed. In a final part of the thesis, an evaluation of the performed research is presented. For specific conclusions and recommendations regarding Parts I, II and III, the reader is referred to the final chapter of each part.

In Part I of this study, the current state of the art with respect to describing the bending behaviour of tubes is discussed in a general literature review. The local buckling behaviour of tubes is studied by collecting results of relevant experiments performed in recent decades. On the basis of these collected results, an alternative design guideline for local buckling of tubes is proposed.

Part II of this study investigates the bending behaviour of spiral-welded tubes in comparison with longitudinal-welded tubes. The research was performed within the framework of a European research project with acronym COMBITUBE that aimed to develop suitable guidelines for spiral-welded tubes in combined walls. In this part, an extensive, large-scale experimental programme is presented that investigated the material properties, geometrical imperfections and bending behaviour of spiral- and longitudinal-welded tubes. The influence of the presence of a girth weld or coil connection weld was also investigated. The presented research was continued by other research partners within the project, resulting in a complete overview of the bending behaviour of the tubes under consideration.

Part III of this study focuses on the behaviour of buried pipelines crossing active strike-slip faults. This research was performed within the framework of a European research project with acronym GIPIPE. The project aimed to develop design guidance for buried pipelines that are exposed to ground-induced deformations. In this thesis, the focus is on strike-slip faults. The

interaction between pipe and soil was investigated in an extensive experimental study that modelled a moving strike-slip fault. A numerical model to predict the response of a pipe to such an event was developed and was calibrated and validated using the results of the performed tests. It is shown that the model is able to accurately predict the response of the pipeline and strain demand in the pipeline.

Part IV provides general closure and provides evaluation of the performed research. Furthermore, this thesis contains various appendices providing additional information, graphs and extensive test results. When appropriate, reference to these appendices is made in the main text.

Part I:
Literature study of the bending
behaviour of tubular members

Chapter 1

Moment-curvature behaviour of tubular members

1.1 Introduction

For many applications, the bending behaviour of steel members such as I-sections can be described with sufficient accuracy using elastic Euler-Bernoulli beam theory. However, for many applications of tubular members, the effects of physical and geometrical non-linearity need to be taken into account to obtain an accurate description of the moment-curvature relation. In this chapter, an overview of the available tools to predict the moment-curvature relation of tubular members is presented. The overview is limited to the behaviour of straight tubes with a diameter to wall thickness ratio (D/t ratio) between approximately 15 and 150.

An important application of tubular members is pipelines. For such elements, instead of bending and shear strength, design is more focused on prevention of loss of containment. Therefore, significant plastic deformation of the structure is tolerated, meaning that a simple linear elastic analysis of the moment-curvature behaviour of the considered tubulars is insufficient. Instead, a physical non-linear analysis is necessary.

Besides the physical non-linearity due to plasticity of the material, geometric non-linearity can be of significance in case of thinner walled tubes. Longitudinal bending deformation of a tubular member induces ovalisation of the tube cross-section, a special feature of tube bending also known as the “Brazier effect” (1927). Ovalisation of the cross-section reduces the tubes bending stiffness because of flattening, increases the local radius of the cross-section at the compression side (intrados). Furthermore, it introduces a biaxial stress state, because of ring bending, leading to yielding at lower curvatures. As a result of the combined effects of ovalisation, in many cases a tubular member is unable to resist the theoretical full plastic moment of the initial cross-section.

Upon increasing bending deformation, structural instability of the compressed tube wall may occur in the form of a localized wavy pattern, in literature referred to as “local buckle”,

“wrinkle” or “kink”. The formation of a local buckle is associated with a bending moment drop in the moment-curvature equilibrium path of the tubular member. In many cases, the occurrence of such instabilities is regarded as failure of the member. In this study, local buckling failure is regarded as an important phenomenon. The formation and shape of a local buckle depends on the slenderness of the cross-section of the tube. Figure 1.1 presents a schematic overview of the behaviour of tubes of a moderate steel grade with cross-sections of various slenderness. For very thick-walled tubes, the Brazier effect results in a limit point instability and no bifurcation buckling occurs. Thick-walled tubes with a D/t ratio of between 30 and 50 gradually form a single kink. Intermediate tubes ($D/t=60-80$) form multiple wrinkles, but the formation remains relatively gradual. For slender tubes ($D/t>100$) wrinkle formation occurs very rapidly, leading to sudden collapse. In general, tubular elements with a higher D/t have a lower local buckling resistance. Because ovalisation effectively increases the D/t by increasing the local radius of the cross-section, it has a direct effect on the local buckling resistance of a tube.

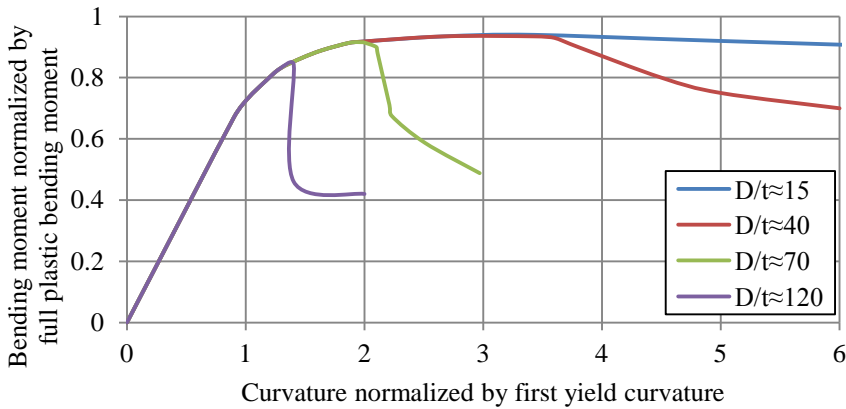


Figure 1.1 Moment-curvature behaviour and local buckling formation of tubes of moderate steel grade with various D/t ratios.

1.2 Prediction of the pre-buckling moment-curvature behaviour

The first analytical attempt to model the mechanical behaviour of straight tubes under bending loading was reported by Brazier (1927). In that study, the ovalisation of thin-walled tubes was predicted using ring theory and elastic material properties. The analysis of Brazier was expanded by Reissner and Weinitschke (1963). Their study shows that for many cases, the solution of Brazier suffices.

The physical non-linear nature of the problem was first analysed by Ades (1957), adopting numerical methods to solve developed algebraic equations. Further development of such methods was performed by Kyriakides and Shaw (1982) and Corona and Kyriakides (1988). In

these two publications, extensive validation of the developed models was performed, increasing confidence in the proposed prediction models.

A fully algebraic solution to the problem was developed by Gresnigt (1986), which uses an extensive set of equations that allows prediction of the moment-curvature relation of tubulars without numerical integration. Comparison with bending test results proved the model to be accurate.

Presently, the moment-curvature relation of a tubular member is easily obtained numerically, using modern FE-software, as was shown for example by Hilberink (2011). If an analytical analysis is preferred, in Europe and especially The Netherlands, the model as proposed by Gresnigt is most commonly used.

1.3 Bifurcation buckling

1.3.1 Prediction of bifurcation buckling

An analysis of the elastic buckling of cylinders under pure bending is presented in many well-known publications (Seide and Weingarten, 1961), (Timoshenko and Gere, 1961), (Axelrad, 1965), (Fabian, 1977). However, for tubes that are of interest to this study, local buckling generally occurs beyond the elastic range. An initial analysis of the plastic buckling behaviour of tubular members under bending was performed by Gellin (1980), which is an extension of the work performed by Ades (1957). Further work on the formation of local buckles in inelastic tubes was performed by Ju and Kyriakides (1992).

In more recent years, the progress in FE-modelling techniques has allowed researchers to fully model the formation of a local buckle (e.g. Karamanos and Tassoulas, 1996, Murray, 1997, Fonzo et al., 2012, Rotter et al., 2014, Vasilikis et al., 2016). These rigorous 3D models are able to accurately capture the phenomenon, but are demanding in terms of user and computational effort.

Typically, for thinner walled tubes, generally referred to as shells, the local buckling is predicted in terms of a maximum bearing capacity. For thicker walled tubes, which are for example employed as pipelines, a critical deformation in terms of strain or curvature is generally used. The boundary between the range of application of these two concepts is not very clearly defined. As discussed in section 1.1, this study considers tubular members with a D/t ratio between approximately 15 and 150. For these tubes, the strain-based approach is considered to be most applicable, which is therefore used from here on.

Algebraic models to predict the critical strain at which a local buckle forms exist, but are often empirical. Well known models were proposed by Murphey and Langner (1985), Gresnigt (1985), Mohareb et al. (1986) and Zimmerman et al. (1995). In European (EN 1993-4-3, 2009) and Dutch (NEN 3650-2, 2012) pipeline standards, the method proposed by Gresnigt is used. Furthermore, the model is also suggested in ALA guidelines (2001) and a variation of the model was adopted in Canadian standards (CSA, 2011). A second common model is the model stated in the DNV design guidelines (2010). Most of these models are empirical or contain empirical

components. This originates from the scatter that is found in test results. Apparently, many parameters are of influence on the local buckling behaviour of these elements, which is difficult to capture in algebraic equations.

1.3.2 Experimental investigations in literature

To gain more insight into the existing scatter in local buckling test results, a database of test results was compiled. In this database, test results from various sources were collected. The results originate from bending and axial loading tests reporting at least the specimen D/t ratio and critical strain at which local buckling occurred. Further relevant parameters such as geometry, material properties, presence of a girth weld (GW), internal pressure and tube manufacturing process have also been included in the database if the necessary data were available.

Besides the scatter that is caused by not considering relevant parameters such as for example steel grade, Y/T-ratio and residual stresses, additional scatter occurs if test results are not directly comparable. Because the database was compiled from test results collected from many studies, incomparability between test results is unavoidable. The parameters that are considered to constitute the main causes of this additional scatter are discussed in the following sections.

Test setup

The test results that are included in the database are the results of tubular specimens tested in pure axial, pure bending or combined axial and bending deformation. Although the influence of the axial force on the critical strain is assumed to be limited, the difference in strain distribution over the cross-section may influence the critical strain of the tube. A second influence originates from the type of load introduction that is used in the experiments. Because the ovalisation of a tube is considered to be an important influencing factor on the local buckling resistance (see section 1.1), the extent to which the test setup restricts or induces ovalisation may be of influence on the test result. Provided that the test specimen is sufficiently long, the effect of such influences on the ovalisation of the specimen may be significantly reduced at the location where local buckling occurs. Furthermore, for specimens with relatively low D/t ratio, the Brazier effect is relatively small.

Ideally, tests are performed in pure bending without any ovalisation influence of the test setup. In practice, such tests are impossible. The test methods used by Van Foecken and Grenigt (1998), Gresnigt (1977) and Vitali et al. (2005) are believed to closely approximate an ideal test. Unfortunately, such tests are rare, as they require relatively long test specimens.

Measurement and definitions

In this study, instability is defined as the point on the moment-curvature path where the maximum bending moment occurs. In load controlled situations, instability evidently occurs at this maximum of the resisted bending moment. In deformation controlled situations, thicker walled tubes may be able to retain a stable situation at higher curvatures and lower bending

moments until a sudden drop in the bending moment resistance of the specimen occurs. In practice, the occurrence of a maximum bending moment is mostly associated with rapid concentration of curvature and consequently local buckling.

The definition chosen in this study is not used by all investigators. Alternatively, for example a sudden drop in bending moment resistance or visual assessment of the development of wrinkles was defined as the moment of instability. Where possible, the critical strain at maximum bending moment was extracted from these publications, or else the values presented by the author were used. It should be noted that for tubes with D/t ratios above approximately 70, the various definitions of instability hardly influence the value of the critical strain, because they all occur nearly simultaneously.

In some experiments, local buckling did not occur or was accelerated by some cause. An example is the research by Wilhoit and Merwin (1973), where no decrease in bending moment capacity was observed. Another example is the investigation by Sherman (1976), who reported the exceedance of the full plastic bending moment (M_p) in some specimens. Upon reaching this bending moment, the tests were ended without the occurrence of local buckling. In these and similar other cases, only a lower bound of the critical strain is determined. They are therefore marked as such in the database and graphs.

In the database, a distinction is made between plain tubes and non-plain tubes. A tube is regarded as 'plain' when it is free of welds other than the welds strictly necessary for the manufacturing of that tube such as a longitudinal seam weld or spiral weld. An example of a non-plain tube is a tube that contains a girth weld.

Selected studies

In the recent decades, the bending response of metal tubes was investigated numerous times. In the early 1970s, the importance of critical strains instead of stresses became prevalent. An early study by Wilhoit and Merwin (1973) investigated local buckling by testing scaled models. More bending tests on small scale specimens were performed by Schroeder et al. (1974) and Tugcu and Schroeder (1979), whose research mainly includes tests on tube branches besides a few tests on plain tubes, and Reddy (1979), who tested tubing with D/t ratios up to 80 made of steel and aluminium. Testing on slender tubes ($D/t=81-102$) of intermediate scale was performed by Van Douwen et al. (1974), focusing on the application of pipelines in settlement areas. To validate these scaled tests, a single large-scale test was performed by Gresnigt (1977). The combination of the tests by Van Douwen and Gresnigt led to the development of a design guideline for the compressive strain limit (Gresnigt, 1985). Many small-scale specimens were tested using the test setup developed by Kyriakides and Shaw (1982). In this test setup, the response of scaled aluminium tubes to combined bending and external pressure was first investigated (Kyriakides and Shaw, 1982), (Conona and Kyriakides, 1988), followed by research into the bending response of such tubes under atmospheric pressure (Kyriakides and Ju, 1992). In the same test setup, Kyriakides and Shaw (1987) investigated the cyclic behaviour of aluminium and steel tubes using two static tests as reference. More recently, the test setup was used by Limam et al. (2008, 2010) to investigate the local buckling behaviour of stainless steel tubes under combined bending and internal pressure. Other small-scale bending tests were performed by Nomoto et al. (1986) on tubes made of steel and aluminium.

One of the first full scale studies which included measurement of the critical strain was performed by Sorenson (1970). Unfortunately, the original publication could not be made available. Instead, the summarized results as published by Stephens et al. (1991) were used. More full scale experiments were performed by Jirsa et al. (1972), who performed six bending tests on tubes up to 20 inch in diameter. Two of these tubular specimens were concrete coated and are not included in the database. The same results were published by Wilhoit et al. (1972). A large research programme funded by Shell was published by Murphey and Langner (1975) and resulted in a new design guideline for the compressive strain limit. Similar as for the results by Sorenson, the results by Murphey and Langner were taken from the report by Stephens et al. In preparation of the construction of the Trans-Alaska pipeline, eight tests were performed by Bouwkamp et al. (1973, 1974) to evaluate the behaviour of specimens of relatively high slenderness ($D/t=82-103$) under bending and internal pressure, while containing a girth weld. Shortly after, a study into the behaviour of tubular columns followed (Bouwkamp, 1975), which includes the results of two stub-columns that failed in local buckling. Further large-scale testing was performed by Sherman (1976). These tests were performed with an unusual set of boundary conditions, making only part of the research fit for this database. In similar fashion, Korol (1979) performed bending tests in four and seven point bending on eleven specimens with D/t ratios ranging from 29 to 80. A comparable D/t range was investigated by Kimura (1980) in a series of thirteen tests, of which unfortunately only four are sufficiently documented. More recent studies, focusing on the behaviour of plain tubes with lower D/t ratios, were performed by Tajika and Suzuki (2009) and Vitali et al. (2005).

Continuing the work of Bouwkamp, Sherman (1983, 1984) investigated the behaviour of fabricated steel tubes including girth welds. The data points of this study were taken from the work by Stephens et al. (1991), in which, apart from the summary of past work, also two new bending tests were presented. Also Prion and Birkemoe (1992) investigated the influence of girth welds on the local buckling behaviour of tubes, as did Zimmerman (1995). In the latter publication, a new design guideline for compressive strain limits is presented. A large-scale experimental evaluation of both plain and girth welded tubes was performed in the laboratories of the University of Alberta, documented in the work by Mohareb et al. (1994), Yoosef-Ghodsi et al. (1994), DelCol et al. (1998) and Dorey et al. (2000). Using more than 40 combined loading tests, a negative influence of girth welds on the local buckling resistance of tubulars was demonstrated. The study by Yoosef-Ghodsi et al. attributes this to a possible mismatch in bending moment capacity of the two connecting tubulars, a possible misalignment at the girth weld, and geometric imperfections and residual stresses that may occur due to weld shrinkage.

In the previously discussed tests performed by Bouwkamp (1975) and Sherman (1976), tubes originating from different manufacturing processes were already included in one testing programme. In both cases, however, this appears to be more a necessity due to the limitations in available cross-section geometry than an investigation into the effect of the manufacturing process of the tube on its bending behaviour. Such an investigation was performed by Fowler (1990), who compared seamless tubes with longitudinal-welded tubes. The work by Van Foeken and Gresnigt (1998) and Gresnigt and Van Foeken (2001) presents a study that compares the collapse and bending behaviour of UOE manufactured tube with seamless tubes. In more recent years, several studies were performed that investigate the bending and local buckling behaviour

of spiral-welded tubulars. In the work by Zimmerman et al. (2004), four spiral-welded tubes with D/t ratios between 48 and 82 were tested. Two of these specimens included internal pressure in the tube. A similar research programme of four spiral-welded tubes was performed by Zimmermann et al. (2013). However, neither of these studies make a direct comparison with tubes originating from other manufacturing processes. In a recent RFCS project with acronym COMTITUBE, more testing on spiral-welded tubes was performed (COMBITUBE Research Consortium, 2015). The motivation for these tests and a full description of the majority of these tests is given in Part II of this study. The tests that are discussed in Part II of this study are not included in the database, as they are discussed in great detail in Part II of this study. In collaboration with the COMBITUBE project, a similar study on the effect of sand-fill on the local buckling behaviour of longitudinal-welded and spiral-welded tubes was performed by SBRCURnet (2013).

Besides the focus on the manufacturing processes, recent research focused on high performance materials. Suzuki et al. (2007, 2008 and 2010) investigated the local buckling behaviour of X80 tubes. Similar research was performed by Kang et al. (2007) and Shitamoto et al. (2012) who also investigated the local buckling behaviour of X80 tubes. Tests studying the influence of the presence of a girth weld on the local buckling in X80 tubes resistance were performed by Tsuru and Agata (2012).

Research into the specific effect of post yield stiffness was performed by Suzuki (2001), who studied the effect of the strain hardening exponent on local buckling of X80 tubes. Carr et al. (2009) investigated the difference in local buckling behaviour between tubes exhibiting yielding with and without a Lüder plateau.

Further well known early experimental work on local buckling of tubular members was conducted by Moore and Clark (1952) on specimens machined from aluminium-alloy rolled rod with D/t ratios ranging from 2 to 150. Their scaled experiments include bending, compression and torsion testing. However, the research by Moore and Clark focuses on the bearing capacity of the specimens in terms of bending moment, axial force and torsion moment rather than on the deformation capacity. As a result, this research does not report a critical strain for the tubes making it incomparable with the other available research. Therefore, the results are not included in the database of the present study. Results of other well-known studies were not included in the database due to insufficient documentation. For example, the tests by Johns et al. (1975), were not included for this reason. Similarly, in some publications only part of the data was sufficiently documented and included in the database.

The results that are used in the database originate from more than 40 publications. As a consequence, exact comparability of the results cannot reasonably be expected. If such comparability would have been required, only very accurately documented tests could have been included in the database. In this scenario, only a very insignificant number of tests would have been suitable. For this reason, relatively tolerant selection criteria were adopted. The collected database of all results is presented in Appendix A.

1.3.3 Scatter in collected data

An overview of the selected test results on tubulars without internal pressure is presented in Figure 1.2. The experimental results are characterized by a critical strain, which is plotted against the D/t ratio of the specimen. It is clear that considerable scatter is present in the data. Similar observations were made in other studies (Gresnigt, 1985, Zimmerman et al., 1995). The observed scatter is attributed to a number of factors.

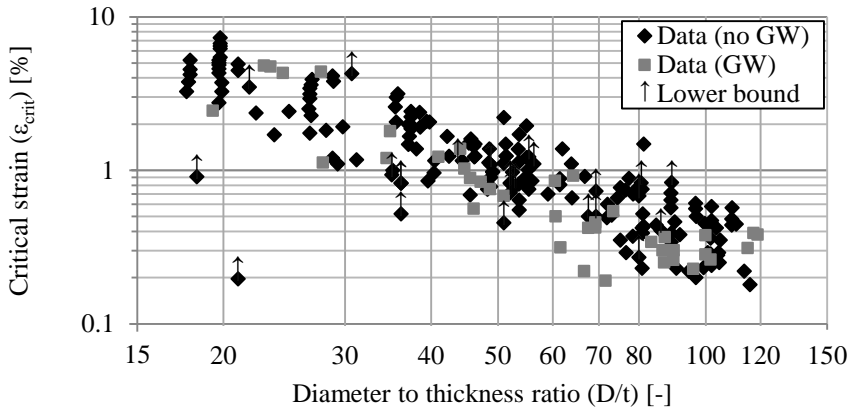


Figure 1.2 Overview of collected data.

Firstly, not all data points originate from similar test setups (see section 1.3.2). Differences in boundary conditions of the test specimens may to some extent have influenced their local buckling behaviour. Also the way of determining the critical strain may have influenced the experimental result. For example, the gauge length over which a critical strain or curvature is determined, or the definition of instability on the moment-curvature relation may be of influence on the reported experimental results.

Aside from the testing methods and boundary conditions, the comparability between the test specimens can be an important cause of the observed scatter. In Figure 1.2, the critical strain is plotted against the D/t ratio, as this is generally recognized as the most important parameter regarding local buckling. However, many more parameters are of influence.

An important influencing factor in local buckling is the initial geometry of the tube. Imperfections in this geometry may take the form of initial out-of-roundness, dimples, dents or misalignments at girth welds. Depending on the execution quality of a girth weld, the initial geometrical imperfection at the weld may be larger than in a plain section of a tubular. Furthermore, a mismatch in material properties in the two tube segments adjoining the girth weld may exist, resulting in concentration of deformation. These factors may result in earlier local buckling in these tubes. Therefore, in Figure 1.2, a distinction is made between plain and non-plain specimens.

The material mechanical properties of the steel may also influence the local buckling behaviour of a tubular. Aside from a possible influence of the yield strength of the steel, the shape of the

stress-strain diagram as well as the strain hardening properties may influence the local buckling behaviour. Also residual stresses in the tubular, either in a plain segment or near a girth weld, may have an effect.

The manufacturing method of a tubular may further influence its local buckling behaviour. Various manufacturing methods exist, resulting in different residual stress states and different levels of geometrical imperfections in the manufactured tubes.

Unfortunately, in many of the considered studies that describe experimental investigations into local buckling of tubulars, not all relevant influencing factors are documented with sufficient accuracy. As discussed in section 1.3.2, adopting a requirement of full comparability in terms of test boundary conditions and procedures between the data points would have resulted in a very insignificant number of tests in the database. Furthermore, the influence of differences between the test specimens in terms of geometry, material behaviour and manufacturing process could not be assessed satisfactorily in all cases. If available, the relevant information was included in the database (see Appendix A).

1.3.4 Comparison of standards with collected data

Safety level and load factors

In this section, the collected data points are compared with three commonly used pipeline design standards:

- Dutch pipeline standard NEN 3650-2 (2012)
- European pipeline standard Eurocode 3 Part 4-3 (EN 1993-4-3, 2009)
- DNV offshore standard DNV-OS-F101 (2010).

Within these three design standards, similar safety levels are defined. NEN 3650-2 aims for an annual failure probability of $5.3 \cdot 10^{-5}$, which corresponds to a reliability index β equal to 4.4 (Guijt et al., 2004, Vrouwenvelder et al., 2003). The standard assumes a design life of 30 years, resulting in a failure probability in the design life of the pipeline of $1.59 \cdot 10^{-4}$ ($\beta=3.6$).

With regard to the analysis of structural reliability, Eurocode 3 Part 4-3 refers to Eurocode 0 (EN 1990, 2002). In Eurocode 0, various structural reliability classes are defined. Structural reliability class 1 compares reasonably well with the safety level defined in NEN 3650-2. An annual failure probability of $9.7 \cdot 10^{-6}$ is defined ($\beta=4.2$). Eurocode 0 defines a 50 year design life of a structure, resulting in a failure probability in the design life of the pipeline of $4.83 \cdot 10^{-4}$ ($\beta=3.3$).

DNV guidelines define four safety classes. Safety class ‘high’ corresponds to an annual failure probability of $1.0 \cdot 10^{-5}$ ($\beta=4.3$). For a 30 year design life, this corresponds to a failure probability equal to $3.0 \cdot 10^{-4}$ ($\beta=3.43$).

The above failure probabilities are defined per pipeline, but actually related to the length of the pipeline (Vrouwenvelder et al. 2003). In the study by Vrouwenvelder, a reference length of 5 to 10 km was assumed to be representative of the Dutch situation for pipelines away from dike crossings. The analysis concludes that the value of the partial safety factor is insensitive to the

chosen reference length. The above reliability indices from the three different standards are therefore assumed to be comparable.

The load factors applied to most loads are similar between these three design standards. While NEN 3650-2 and DNV-OS-F101 define partial load factors within the standard, Eurocode 3 Part 4-3 refers to Eurocode 0 (2002) and Eurocode 7 Part 1 (EN 1997-1, 2012). An overview of most partial load factors relevant for local buckling is presented in Figure 1.3. The figure shows that with exception of a load case that considers only internal pressure, which generally is not the leading load case for local buckling, the partial load factors of these three design standards are similar.

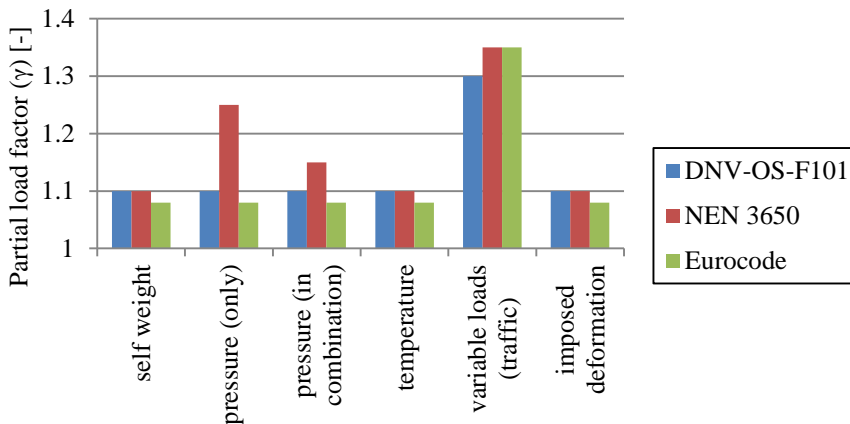


Figure 1.3 Comparison of partial load factors between three considered design standards.

In case of geotechnical loads, NEN 3650-1 gives clear guidance on the partial safety factors that are to be applied to soil parameters. In Eurocode 3-4-3 no guidance is given, but reference is made to Eurocode 7 Part 1. Clear guidance with respect to geotechnical load is lacking in the DNV F101, but in DNV recommended practice (DNV-RP-F110, 2007), guidelines are given. Due to the complexity of the effects of soil parameters on the deformation of the pipeline, a safety level comparison between these codes with regard to geotechnical loads can only be made on the basis of a design comparison. This was not performed in this study.

The characteristic loads to which the load factors are applied to are not equal between the three codes. Eurocode and NEN 3650-1 (2012) define a dominant characteristic load as a load which is expected to be exceeded once in the lifetime of the structure. In DNV guidelines, the dominant load is defined as a load with a 100 year return period. This results in additional safety of the DNV guidelines at the loading side, allowing a slightly more liberal calculation of the resistance. Despite the small difference in load factors and the loads they are applied to, a comparison between the compressive strain resistance models of these codes is considered to be acceptable. As mentioned before, a fully accurate comparison can only be made by comparing design cases. This was not done in this study.

Design formulas for the critical strain

The formulas to obtain the design value for the critical strain used in NEN 3650-2 and Eurocode 3 Part 4-3 are both derived from the work by Gresnigt (1986) (see equation (1.1)).

$$\begin{aligned} \text{for } \frac{t}{r} > \frac{1}{60}: \varepsilon_{crit} &= 0.25 \frac{t}{r} - 0.0025 + 3000 \left(\frac{Pr}{Et} \right)^2 \cdot \frac{|P|}{P} \\ \text{for } \frac{t}{r} < \frac{1}{60}: \varepsilon_{crit} &= 0.10 \frac{t}{r} + 3000 \left(\frac{Pr}{Et} \right)^2 \cdot \frac{|P|}{P} \end{aligned} \quad (1.1)$$

With:

P : Pressure. Positive for positive internal pressure, negative for positive external pressure.
Net pressure to be calculated according to $P = P_{internal} - P_{external}$

The critical strain according to the DNV guidelines is presented in equation (1.2). A design value for the critical strain, in line with the safety level discussed earlier, is found by applying a partial safety factor of 3.3.

$$\varepsilon_{crit} = 0.78 \cdot \left(\frac{t}{D} - 0.01 \right) \cdot \left(1 + 5.75 \cdot \frac{P}{P_b(t)} \right) \cdot \alpha_{sh}^{-1.5} \cdot \alpha_{GW} \quad (1.2)$$

Valid for: $D/t \leq 45$ or under condition of additional checks for $D/t \leq 60$. Only valid for net internal overpressure.

With:

P : Pressure. Positive for internal pressure, negative for external pressure. Net pressure to be calculated according to $P = P_{internal} - P_{external}$

P_b : Pressure containment resistance (burst pressure)

α_{sh} : Factor to take into account the strain hardening properties of the steel, expressed in the Y/T ratio

α_{GW} : Factor to take into account the effect of a girth weld

Comparison

A comparison between the three considered design guidelines and the available data points on tests without internal pressure (see section 1.3.2) is presented in Figure 1.4. The figure shows that none of the data points that are not marked as a lower bound fall below the DNV design rule, while a considerable number of data points fall below the design rules according to NEN 3650-2 and Eurocode Part 4-3.

In a test, loads are measured and therefore deterministic. In such a scenario, a higher failure probability applies than for stochastic loading. According to Eurocode 0 (EN 1990, 2002) and Vrouwenvelder et al. (2003), typically a reduction factor of 0.8 has to be applied to the safety index β to account for this effect. This results in a probability of failure of approximately 10^{-3} for

the considered design rules. It is therefore expected that approximately one in a thousand of the non-lower bound data points falls below the design guidelines, which for the given data corresponds to less than one data point. The DNV design guidelines meet this expectation: none of the non-lower bound data points fall below the design guideline. In contrast, many of the data points fall below the NEN 3650-2 and Eurocode 3 Part 4-3 design guidelines.

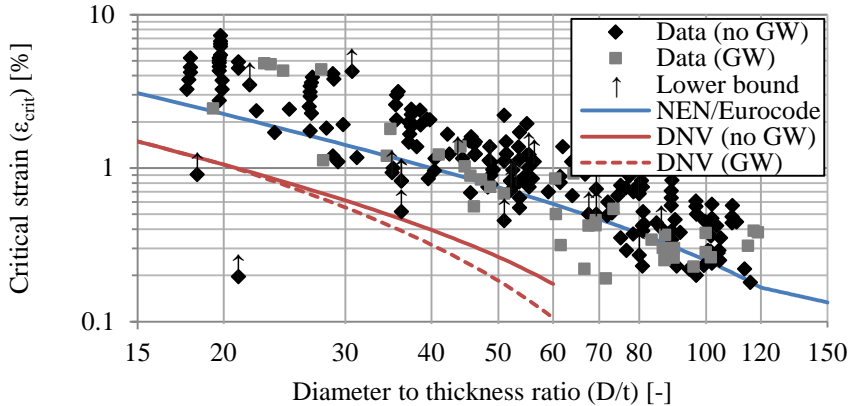


Figure 1.4 Comparison of test data (no internal pressure) and design guidelines.

The above observations may lead to the conclusion that the design rules as adopted in NEN 3650-2 and Eurocode 3 Part 4-3 are too liberal. However, as remarked in section 1.3.3, the significant scatter that is observed in the database may partly be caused by incomparability of the data points in terms of for example test procedures. Furthermore, not all specimens may meet the quality demands that are necessary for the application of the considered standards. Therefore, it is also possible that many of the data points falling below the NEN 3650-2 and Eurocode 3-4-3 design rule would have been rejected if more information had been available.

A statistical interpretation of the database is presented in Chapter 2 of this study. On the basis of the collected test data, a design guideline is determined. As a result of the considerable scatter in this data, this design rule is likely to be more conservative than the NEN 3650-2 and Eurocode 3-4-3 design rules.

In Part II of this study, the local buckling failure of relatively slender tubulars ($65 < D/t < 120$) for the application in combined walls is investigated within the framework of a European research project. Within this subspace of the D/t range considered in Figure 1.4, large-scale four-point bending tests were performed, supplemented by FE-analyses. The project aims to obtain better insight into the cause of the scatter that is visible in Figure 1.4. A modification of the formulation by Gresnigt (1986), which is used in the NEN 3650-2 and Eurocode 3 Part 4-3 design guidelines is shown to be adequate in a procedure to determine the critical curvature and maximum bending moment capacity of these tubulars in combined walls.

1.4 Summary of Chapter 1

In this chapter, the current state of the art with respect to the analysis of the bending behaviour of tubular members is discussed. The prediction of the pre-critical behaviour of such elements is discussed in section 1.2. The section concludes that the prediction of the moment-curvature behaviour of tubulars including geometric and physical non-linearities is very accessible using modern FE-software, provided that correctly validated models are used. Moreover, a very good approximation is easily obtained when using the analytical formulations proposed by Gresnigt.

Prediction of the local buckling behaviour of tubulars is more difficult and is discussed in section 1.3. Also for the analysis of this phenomenon, FE-analyses are popular. In addition, many experimental investigations were carried out. A collection of over 400 experimental results is discussed and presented. The critical compressive strain of the selected data is compared with existing design guidelines for pipelines.

The collected test results show considerable scatter. This scatter is attributed to the following factors:

- Not all data points originate from the same type of test setup.
- Measurement techniques differed between data points. Especially the gauge length for determining the critical curvature or critical compressive strain is of importance
- Not all data points result from experiments on comparable test specimens.

1.5 Recommendations for further research

It is recommended to take action to reduce the scatter in results of experiments investigating local buckling in tubes. To achieve this, the following issues need to be addressed:

- Comparability between the experimental procedures needs to be increased by testing in some standardized manner. Measurements, boundary conditions and test procedures need to be agreed upon. It is proposed that the procedures as described in Part II of this study are used.
- Comparability between the test specimens needs to be increased. Therefore, the material and geometric properties of each specimen need to be carefully determined. Furthermore, the test specimens need to be in agreement with some quality and execution requirements that are relevant to the considered application. This allows for more careful selection of test results for a database, and an appropriate division of the data in subsets.
- Documentation of tests needs to be accurate, extensive and accessible.

Chapter 2

Design rule for local buckling of tubes

2.1 Introduction and methods

The comparison between the data points found from literature and existing guidelines was not satisfactory (see section 1.3.4). To interpret the information that is contained within the database of test results, a design guideline was developed on the basis of the analysis of this database.

Many design guidelines for local buckling use a semi-empirical formula. To achieve an optimal fit with the test data, a fully empirical formula, obtained through curve-fitting, is used in this chapter. To determine a design guideline at a sufficient safety level, the methods for ‘design by testing’ as described in Eurocode 0 (EN 1990, 2002) and by Bijlaard et al. (1988) were used.

2.2 Plain specimens

Firstly, a prediction model was developed using only the data of carbon steel specimens in which no girth weld was present. Also experimental results of which the presence or absence of a girth weld is unknown were included in this data set. Spiral-welded specimens that contain a coil connection weld (see section 4.2) were excluded from the group of plain specimens, as the influence of such a weld was expected to be significant. Specimens loaded by internal or external pressure were also disregarded for this initial analysis.

The t/D ratio is regarded as a key parameter in local buckling of tubes (Timoshenko, 1961). Therefore, this parameter was also considered as main parameter for the prediction model for the critical strain. As discussed in section 2.1, the model was developed by curve fitting. For plain specimens, an exponential function with the t/D ratio of the tube as base resulted in the best fit in terms of the least square error. The test data and prediction model are presented in Figure 2.1. The prediction model for the mean value of the critical strain is presented in equation (2.1).

$$\varepsilon_{crit,m} = 3.8 \cdot \left(\frac{t}{D} \right)^{1.5} \quad (2.1)$$

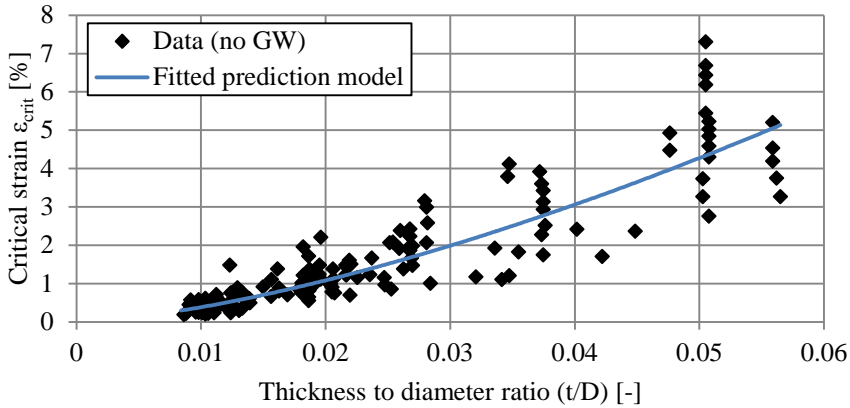


Figure 2.1 Data of specimens without a girth weld or internal pressure and the fitted prediction model.

2.3 Influence factors

Equation (2.1) is a relatively simple formula for the prediction of a complex limit state, because it only uses the D/t ratio of the tube as input for the calculation. As a result, a significant scatter occurs with respect to the proposed model. In this section, the influence of parameters other than the D/t ratio is investigated in an attempt to improve the predicting capabilities of the model.

The effect of these parameters on the critical strain is taken into account through influence factors (α_i). Although several of such influence factors are available in literature, the aim of this chapter is to solely interpret the available test data. Therefore these influence factors are, similarly as the basis of the model, determined through curve fitting. For simplicity, only linear relations were considered for the influence factors.

2.3.1 Girth weld

The negative influence of a girth weld on the local buckling resistance of pipes and tubes is discussed in various publications (e.g. Yoosef-Ghodsí et al., 1994, Tsuru and Agata 2012). Girth welds may be a source of geometrical imperfections and residual stresses, which may be detrimental to the local buckling resistance of especially more slender tubes.

Ideally, the influence factor for the presence of a girth weld is related to these effects. However, for the vast majority of the available test data no information was available on the execution quality of the girth weld. Therefore, only a generalized effect could be determined.

The imperfection sensitivity of a shell increases with increasing slenderness. It is therefore expected that the effect of the presence of a girth weld is more severe for more slender elements. Therefore, a D/t -dependent influence factor is proposed. To determine a suitable influence factor

for equation (2.1) that accounts for the influence of the presences of a girth weld, the predictions of equation (2.1) were compared with available data on girth welded tubes. The performance (p) of these available data points is defined according to equation (2.2). The performance of equation (2.1) with respect to the available data points including a girth weld, but excluding internal or external pressure is presented in Figure 2.2. Despite the very large scatter present in the data, it is clear that the majority of the girth-welded tubes fail in local buckling at a critical strain that is lower than the critical strain predicted by equation (2.1). Therefore, a girth weld influence factor for equation (2.1) was fitted to the data. The adjusted model is presented in equations (2.3) and (2.4).

$$p = \frac{\text{experimental result}}{\text{model result}} = \frac{\varepsilon_{crit,e}}{\varepsilon_{crit,t}} \quad (2.2)$$

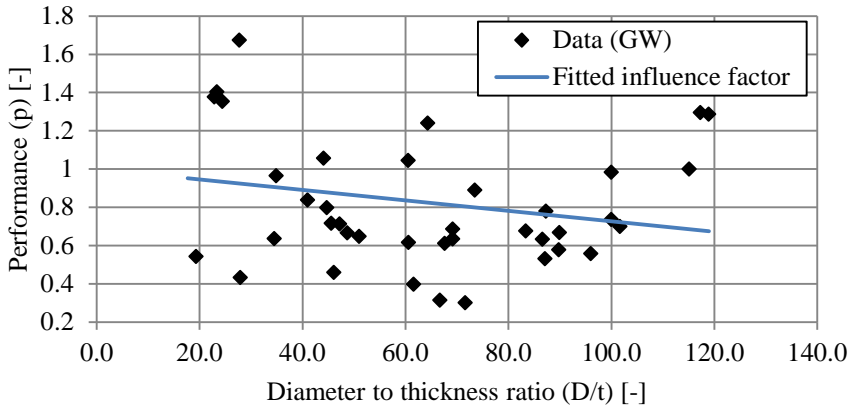


Figure 2.2 Performance of equation (2.1) with respect to available data points with a girth weld under atmospheric conditions.

$$\varepsilon_{crit,m} = 3.8 \cdot \left(\frac{t}{D}\right)^{1.5} \cdot \alpha_{GW} \quad (2.3)$$

With:

α_{GW} : Influence factor to account for the effect of the presence of a girth weld (see equation (2.4))

$$\begin{aligned} \alpha_{GW} &= 1 && \text{for tubes without girth weld} \\ \alpha_{GW} &= 1 - 2.7 \cdot 10^{-3} \frac{D}{t} && \text{for tubes with a girth weld} \end{aligned} \quad (2.4)$$

2.3.2 Yield stress

To study the effect of the yield stress of the specimens on their local buckling resistances, the predictions of equation (2.3) were compared with the data points of which the yield strength is available. Both plain and girth welded data points under atmospheric conditions were considered. The performance of equation (2.3) with respect to these selected data points is presented in Figure 2.3.

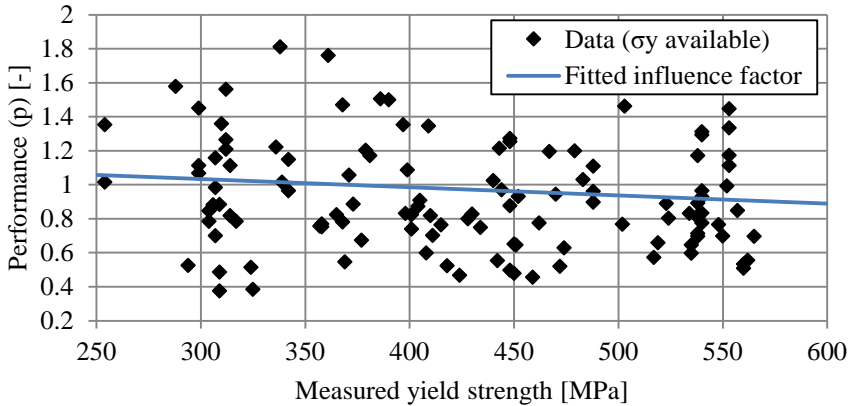


Figure 2.3 Performance of equation (2.3) with respect to available data points under atmospheric conditions of which the yield strength is available.

Despite the considerable scatter, an influence factor was fitted to the data, which predicts decreasing local buckling resistance for increasing yield strength. To obtain more insight into the validity of the determined influence factor, the data was binned as presented in Table 2.1. Within each bin, the average performance (see equation (2.2)) was determined, which is presented in Figure 2.4. Also in this figure, a higher yield strength appears to negatively influence the local buckling resistance of the specimen.

Table 2.1 Binning of data points with known yield stress with respect to yield stress.

Yield stress (σ_y)	No. of data points
$250 < \sigma_y < 350$	31
$350 < \sigma_y < 450$	42
$450 < \sigma_y < 550$	37
$\sigma_y > 550$	12

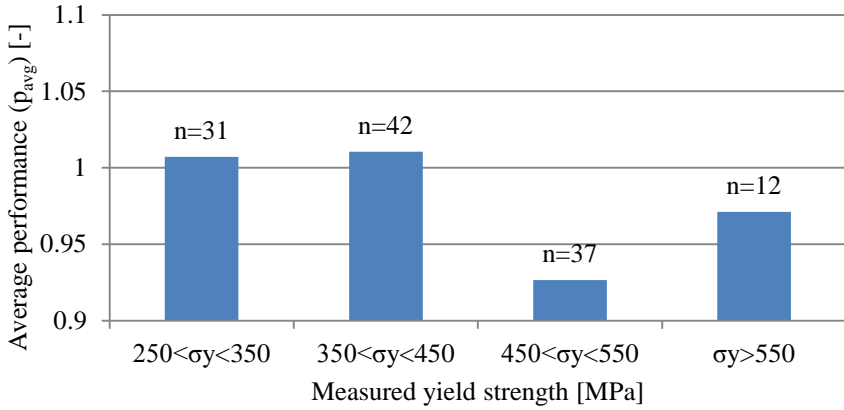


Figure 2.4 Performance of equations (2.3) and (2.4) with respect to available data points of which the yield strength is available under atmospheric conditions.

Based on the adjustment factor fitted to Figure 2.3, a possible model adjustment is presented in equations (2.5) and (2.6). However, within the range of steel grades commonly applied in practice (X60 – X80), a maximum change in α_{σ_y} of 7% is observed, which is very small compared to the scatter observed in the data. For simplicity, the influence factor is therefore not included in the full model in section 2.4.

$$\varepsilon_{crit;m} = 3.8 \cdot \left(\frac{t}{D} \right)^{1.5} \cdot \alpha_{GW} \cdot \alpha_{\sigma_y} \quad (2.5)$$

With:

α_{σ_y} : Influence factor to account for the effect yield strength (see equation (2.6))

$$\alpha_{\sigma_y} = -4.8 \cdot 10^{-4} \cdot \sigma_y + 1.2 \quad (2.6)$$

It must be noted that it is well known that for higher strength steels, the amount of strain hardening is generally reduced. Therefore, an increase in yield stress is mostly accompanied by an increase in the Y/T ratio. This parameter was investigated separately (see section 2.3.3).

2.3.3 Y/T ratio

To study the effect of the yield to tensile stress ratio (Y/T-ratio) of the test specimens on their local buckling resistances, the predictions of equation (2.3) were compared with the data points of which the Y/T ratio is available. Both plain and girth welded specimens under atmospheric conditions were considered. The performance of equation (2.3) with respect to these selected data points is presented in Figure 2.5.

A visual inspection of the graph results in the identification of two groups, circled in red and blue in Figure 2.5. The group circled in blue appears to be negatively influenced by an increasing Y/T-ratio of the material. This corresponds with the theory that a high Y/T-ratio correlates with a low post-yield stiffness and therefore lower local buckling resistance. The data point group circled in red exhibits behaviour conflicting with this theory, as the Y/T ratio and performance of equation (2.3) are positively correlated within this group.

No common properties or test parameters were found in the two identified groups. They are only distinguishable by visual inspection of Figure 2.5. Because sufficient justification for removal of the group of data points circled in red from the procedure of determining of an influence factor was not found, all available data points were used to determine a suitable influence factor. When an influence factor is fitted to all data (see Figure 2.6), hardly any influence of the Y/T ratio is found. Therefore, this influence factor is not included in the full model.

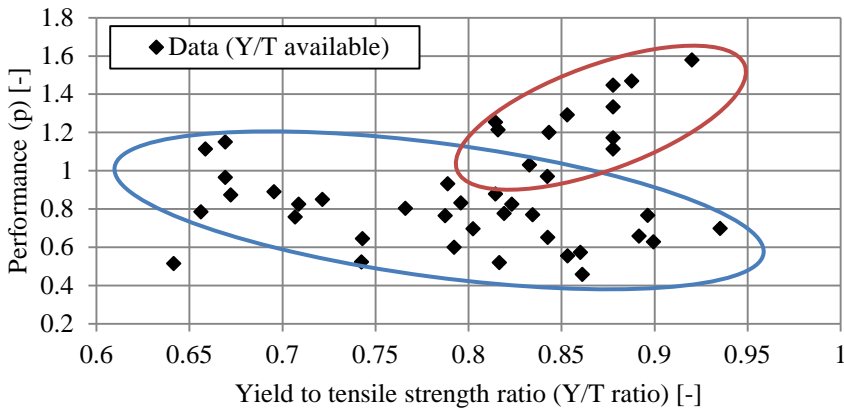


Figure 2.5 Performance of equation (2.3) with respect to available data points under atmospheric conditions of which the Y/T ratio is available.

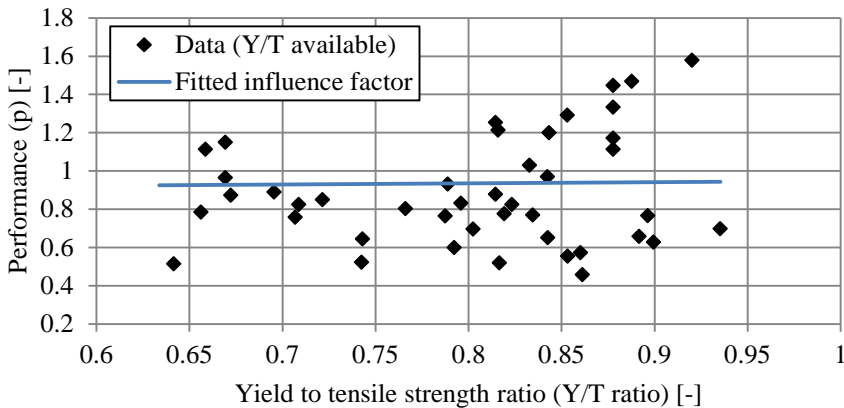


Figure 2.6 Fitted influence factor to Figure 2.5.

2.3.4 Manufacturing process

Because the manufacturing process of tubular members influences their geometrical imperfections and residual stress state, an influence of the manufacturing process on the local buckling resistance of tubes may be expected. To study the possible effect of the manufacturing process on the local buckling resistance of tubes, the predictions of equation (2.3) were compared with the available data points. Both plain and girth welded specimens under atmospheric conditions were considered. Unfortunately, many of the considered studies did not list the manufacturing process of the tested specimens. Furthermore, in case of specimens containing a longitudinal seam weld, most authors did not further specify the manufacturing process. As a result, only four groups of data points could be considered: longitudinal-welded tubes, seamless tubes, spiral-welded tubes and a large group of specimens with unknown manufacturing process. The performance of equation (2.3) with respect to these selected data points is presented in Figure 2.7.

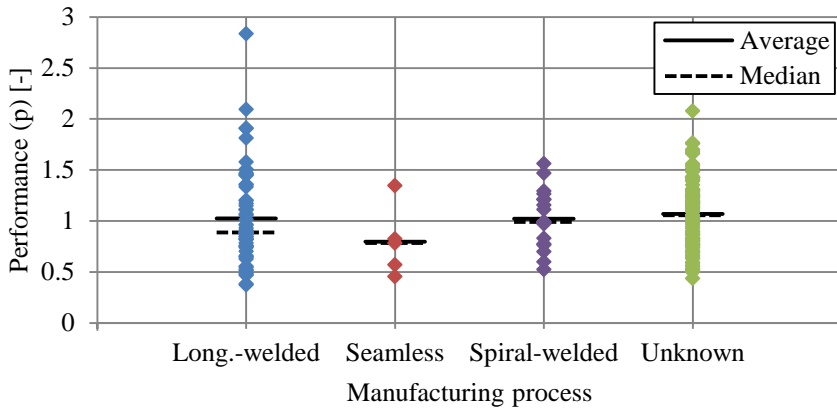


Figure 2.7 Performance of equation (2.3) with respect to data points under atmospheric conditions.

Similarly as for the material yield strength, a large scatter is present in the data. A comparison of the mean and median performance of each group is presented in Figure 2.8. Only the group of seamless specimens clearly appears to be influenced by its manufacturing process. However, due to the very low number of data points within this group, the significance of this observation is minor. Furthermore, some manufacturing techniques are typically only suitable for certain D/t ranges, which may also influence the results of this analysis. For these reasons, no influence factor for the manufacturing process is included in the full model in section 2.4.

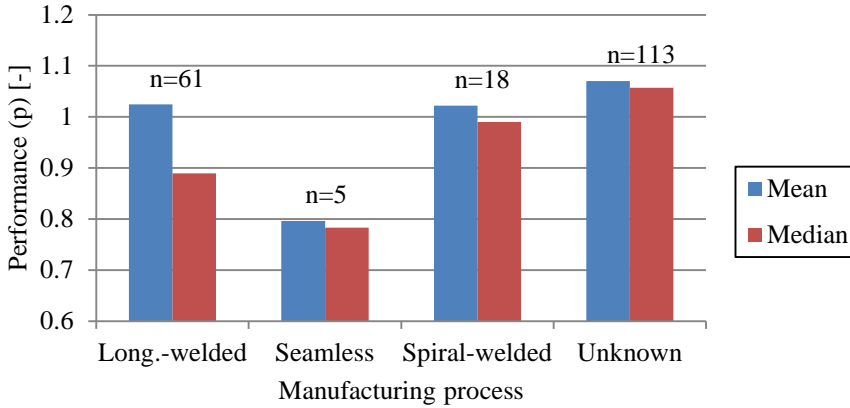


Figure 2.8 Mean and median performance of equation (2.3) with respect to data points under atmospheric conditions.

2.3.5 Internal and external pressure

Internal or external pressure acting on the pipeline is known to have a distinct influence on the local buckling behaviour of a tubular member (e.g. Van Douwen et al., 1974, Kyriakides and Shaw, 1982, Fowler 1990). First, the internal or external pressure limits or accelerates ovalisation due to bending. Furthermore, in case of sufficient internal pressure, the local buckling shape changes (see Figure 9.42). In case of external pressure, an interaction between local buckling and collapse of the tube may occur. To study the effect of pressure on the local buckling resistance of the considered data, the predictions of equation (2.3) were compared with the available data points that are under the influence of internal or external pressure. Both plain and girth welded specimens were considered. The performance of equation (2.3) is plotted versus the pressure ratio (see equation (2.7)) in Figure 2.9. As a consequence of using the pressure ratio as relevant parameter, only specimens of which the diameter, wall thickness and yield strength are known, were taken into account. If the source of the experimental data distinguished material properties in axial and hoop direction, the pressure ratio was calculated using the yield stress in hoop direction.

$$\text{Pressure ratio} = \frac{P}{P_y} = P \cdot \frac{(D - 2 \cdot t)}{2 \cdot t \cdot \sigma_y} \quad (2.7)$$

With:

P : Pressure. Positive for positive internal pressure, negative for positive external pressure.

In Figure 2.9, an overall trend can be observed. However, one extreme outlier is present. This concerns a specimen from the scaled test series performed by Van Douwen et al. (1974). Available photographs of the specimen at its maximum deformation reveal that even at the

reported critical strain no full local buckle had formed. Therefore, it was excluded from the procedure of determining the influence factor for internal pressure.

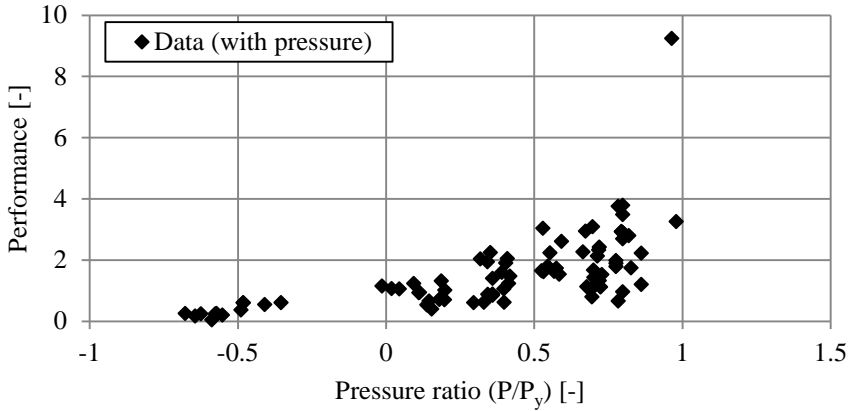


Figure 2.9 Performance of equation (2.3) with respect to available data points under non-atmospheric conditions of which the dimensions and yield strength are available.

After removal of the outlier, the influence of internal or external pressure on the local buckling resistance is much more clear, although a large scatter remains present (see Figure 2.10). For low internal pressure, hardly any beneficial effect of the internal pressure can be observed. For higher internal pressures, the expected beneficial effect of internal pressure is clearly visible. Up to a pressure ratio of 0.2, no influence of the internal pressure was assumed. For higher pressure ratios, a linear influence factor was fitted to the data. The adjusted model which also includes the effect of internal pressure is presented in equations (2.8), (2.9) and (2.10).

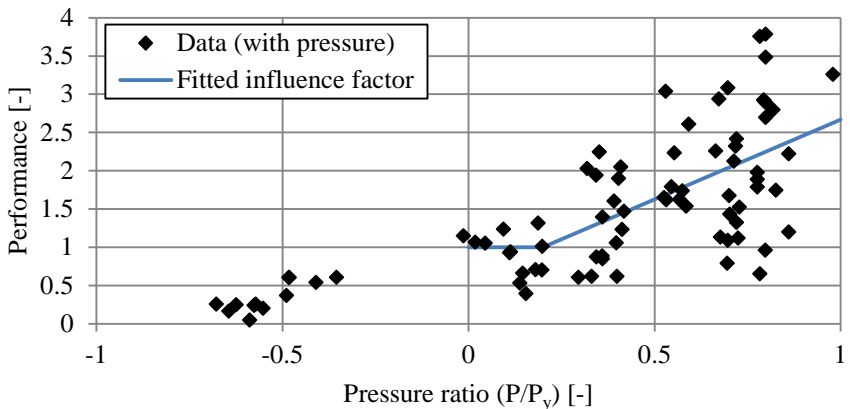


Figure 2.10 Performance of equation (2.3) with respect to available data points under non-atmospheric conditions of which the dimensions and yield strength are available.

$$\varepsilon_{crit,m} = 3.8 \cdot \left(\frac{t}{D} \right)^{1.5} \cdot \alpha_{GW} \cdot \alpha_p \quad (2.8)$$

With:

α_{GW} : Influence factor to account for the effect of the presence of a girth weld (see equation (2.9))

α_p : Influence factor to account for the effect of the presence of a positive internal pressure (see equation (2.10))

$$\begin{aligned} \alpha_{GW} &= 1 && \text{for pipes without girth weld} \\ \alpha_{GW} &= 1 - 2.7 \cdot 10^{-3} \frac{D}{t} && \text{for pipes with a girth weld} \end{aligned} \quad (2.9)$$

$$\begin{aligned} \alpha_p &= 1 && \text{for } 0 \leq \frac{P}{P_y} \leq 0.2 \\ \alpha_p &= 2.1 \cdot \frac{P}{P_y} + 0.58 && \text{for } 0.2 \leq \frac{P}{P_y} \leq 1.0 \end{aligned} \quad (2.10)$$

For negative pressure ratios, corresponding to external pressure acting on the tube, much less suitable data points are available. Furthermore, the data points that are available, concern specimens that were subjected to such a high external pressure that the occurring failure mode very likely was an interaction between collapse and local buckling. Because collapse is not considered in this study, and sufficient data with small more moderate external pressures were lacking, only the positive effect of internal pressure was considered in the calculation model.

One of the effects that contribute to the higher local buckling resistance of tubes with internal pressure is the ovalisation restraint that results from the internal pressure. Because more slender tubes are more susceptible to ovalisation, the beneficial effect of internal pressure may be depending on the D/t ratio. Therefore the available data were binned according to Table 2.2. The slope of α_p , which takes a value of 2.1 in equation (2.10), was calculated for each group of specimens. The results, as presented in Figure 2.11, show that no clear trend is visible. For the model, the beneficial effect of internal pressure is therefore assumed to be independent of the D/t ratio of the tube.

Table 2.2 Binning of data points with respect to D/t ratio.

D/t ratio	No. of data points
$15 < D/t < 30$	3
$30 < D/t < 50$	16
$50 < D/t < 70$	14
$70 < D/t < 90$	17
$90 < D/t < 120$	6

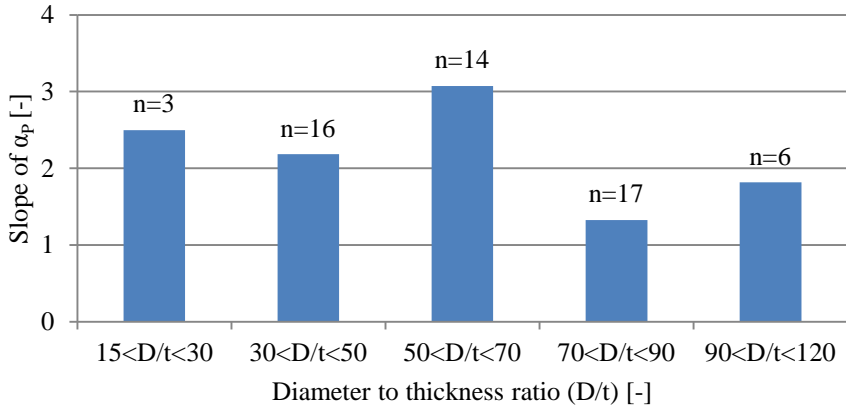


Figure 2.11 Performance of equation (2.3) with respect to available data points under non-atmospheric conditions of which the dimensions and yield strength are available.

2.3.6 Gauge length for determination of critical strain

For the D/t range under consideration, in most cases, local buckling occurs in the inelastic regime. Under influence of variations of for example material properties or wall thickness over the length of the tube, deformation may localize. When approaching the critical strain, deformation may localize further.

In many researches, the critical strain of a pipe was directly measured using strain gauges (Fowler, 1990, Korol, 1979, Nomoto et al., 1986, Schroeder et al., 1974, Sherman et al., 1976 and Wilhoit and Merwin, 1973). Alternatively, strain was measured using a strain measurement over some length, such as for example the experiments performed at the University of Alberta (Dorey et al. 2000). In these cases, the measured critical strain is the average strain over the measuring length. Other researchers determined the critical strain from a measured curvature. Generally, this curvature was determined over some length (L_c), also resulting in an averaged strain. Common curvature measurement lengths are 2-3·D (Bouwkamp et al., 1973, Van Foecken and Gresnigt, 1998, Suzuki et al., 2001, Suzuki et al., 2007, Suzuki et al., 2010, Zimmerman et al., 2004 and Zimmermann et al., 2013). Other researchers opted for other lengths, varying from 1·D (e.g. Tsuru and Agata, 2012) to 8·D (Shitamoto et al., 2012). In case of localization of deformation, the length over which the strain is averaged, influences the result. For shorter measurement lengths, higher critical strains will be obtained from the measurements.

The performance of equation (2.8) versus the lengths over which the critical strain was averaged is presented in Figure 2.12. As was the case for other influence factors, a large scatter is present. If an influence factor is fitted to the data, a rising trend is visible. This is striking, because mechanics predict a negative effect. Furthermore, the effect is relatively small compared to the effect of the two influence factors that are already considered in equation (2.8). For these two reasons, no influence of the strain averaging length is included in the model.

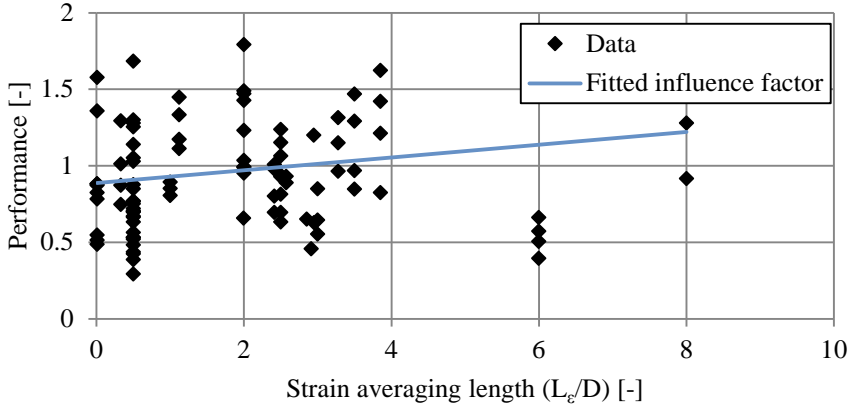


Figure 2.12 Performance of equation (2.8) with respect to available data points.

2.4 Full model

The developed model is presented in section 2.3.5 in equations (2.8), (2.9) and (2.10). The model is a prediction model on the basis of curve-fitting to the available test data. As a result, the model predicts the mean value of the data scatter band. By applying the procedures for ‘design by testing’ according to Eurocode 0 (2002) and Bijlaard et al. (1988), a prediction of the characteristic value of the critical strain and a safe design guideline was developed. More information on this procedure and assumptions made for the calculations can be found in Appendix G.1. The final model is presented in equations (2.11), (2.12) and (2.13). Partial safety factors for safety levels that correspond to existing guidelines are presented in Table 2.3. For the selected safety factors, the probability of failure of the element is presented, assuming that for the determination of the design load, appropriate probabilistic analyses are used. Due to the large scatter in the data points from literature, the values for γ_M^* are high. Further comments on the value of γ_M^* as well as a suitable model for the serviceability limit state are given in Appendix G.1. A comparison of the design guidelines with the database from which they were derived is presented in Figure 2.13 and Figure 2.14.

$$\varepsilon_{crit;d}(X_n) = \frac{\varepsilon_{crit;m}(X_n)}{\gamma_M^*} = \frac{3.8 \cdot \left(\frac{t_n}{D_n}\right)^{1.5} \cdot \alpha_{GW}(X_n) \cdot \alpha_p^*(X_n)}{\gamma_M^*} \quad (2.11)$$

Validated for carbon steel tubes with: $15 < D/t < 120$, $250 < \sigma_y < 650$ and $0 < P/P_y < 1$

With:

X_n : Nominal values of input parameters

α_{GW} : Correction factor to account for the effect of the presence of a girth weld (see equation (2.12))

α_p^* : Correction factor to account for the effect of the presence of a positive internal pressure (see equation (2.13))

$$\begin{aligned} \alpha_{GW}(X_n) &= 1 && \text{for tubes without girth weld} \\ \alpha_{GW}(X_n) &= 1 - 2.7 \cdot 10^{-3} \frac{D_n}{t_n} && \text{for tubes with a girth weld} \end{aligned} \quad (2.12)$$

$$\begin{aligned} \alpha_p^*(X_n) &= 1 && \text{for } 0 \leq \frac{P_d}{P_{y;n}} \leq 0.25 \\ \alpha_p^*(X_n) &= 1.9 \cdot \frac{P_d}{P_{y;n}} + 0.53 && \text{for } 0.25 \leq \frac{P_d}{P_{y;n}} \leq 1.0 \end{aligned} \quad (2.13)$$

With:

X_n : Nominal values of input parameters

P_d : Design value of minimum internal pressure

Table 2.3 Values for γ_M^* for use in equation (2.11).

P_f		γ_M^*
1 year (β)	30 years (β)	
$1.6 \cdot 10^{-5}$ (4.2)	$4.8 \cdot 10^{-4}$ (3.3)	3.1
$5.3 \cdot 10^{-6}$ (4.4)	$1.6 \cdot 10^{-4}$ (3.6)	3.4

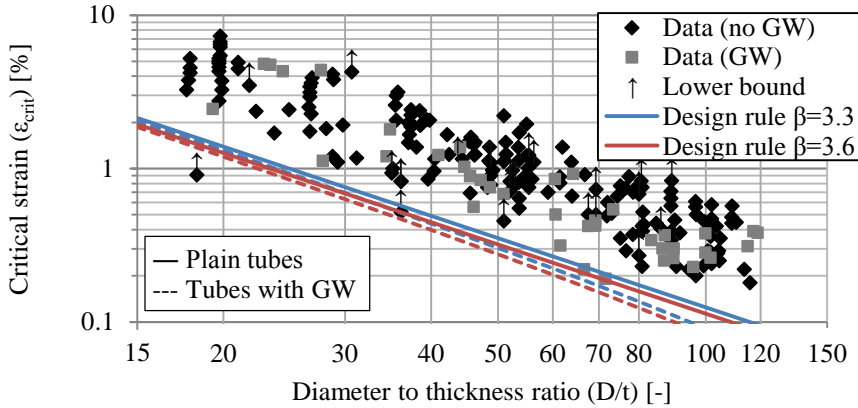


Figure 2.13 Comparison of the developed design rule with the available data points under atmospheric conditions.

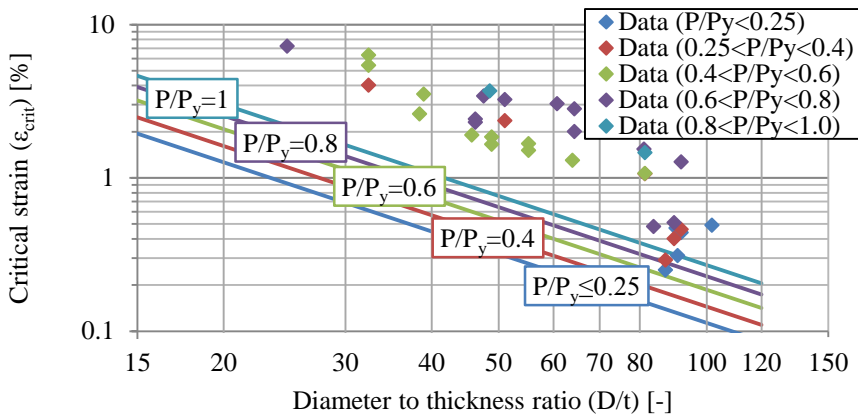


Figure 2.14 Comparison of the developed design rule ($\beta=3.6$) with the available data points under non-atmospheric conditions. Specimens including a girth weld are not considered in this graph.

2.4.1 Assessment of effect of influence factors

From the various influence factors that were considered (see section 2.3), two were selected for inclusion in the full model. In both cases, the influence factors were fitted to heavily scattered data (see Figure 2.2 and Figure 2.10). In this section, the benefit of inclusion of these two influence factors in the full model is assessed.

As an alternative to the chosen procedure of fitting a model to all available atmospheric plain specimens and subsequently fitting a girth weld influence factor, a model could have been fitted to all atmospheric data, regardless whether a girth weld is present. In such a model, the

calculated resistance for plain and girth welded tubes is regarded as equal. Implementing this simplification results in more scatter of the model with respect to the available data points, thereby resulting in an increased value of γ_M^* . However, this increase in the value of γ_M^* is less substantial than the predicted reduction in local buckling resistance for girth welded tubes according to equation (2.12). The considered simplification therefore results in higher calculated resistances for girth welded tubes, and lower calculated resistances for plain tubes.

The considered alternative procedure is compared with the model proposed in equation (2.11) in Figure 2.15. The figure shows that for plain tubes, higher strains are allowable when using a model that includes a girth weld influence factor. The calculated resistance of girth welded tubes is reduced if this factor is included. For a less scattered data set, both the calculated resistance for plain tubes and girth welded tubes would increase in case of an implementation of a girth weld influence factor.

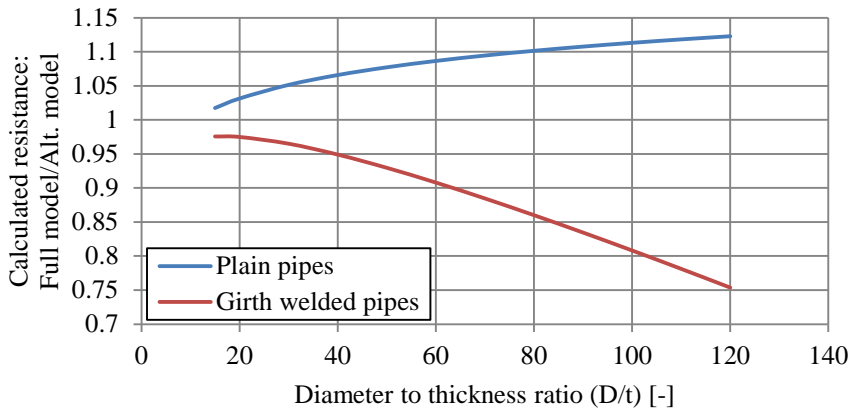


Figure 2.15 Comparison between design models for tubes under atmospheric conditions including and excluding a girth weld influence factor (α_{GW}). Comparison made for $\beta=3.6$.

Similarly, instead of including an influence factor for the presence of a girth weld (α_{GW}) and an influence factor for the presence of internal pressure (α_p), a single equation could have been fitted to all available data. In such a model, the calculated resistance for tubes with and without girth welds and with and without internal pressure is equal. The considered alternative procedure is compared with the model proposed in equation (2.11) in Figure 2.16. The inclusion of the beneficial effect of internal pressure in the design model naturally results in higher calculated resistances for high internal pressures, but also for internal pressures below the $0.25 \cdot P/P_y$ threshold (see equation (2.13)), up to 31% higher critical strains are calculated due to reduced scatter of the considered test results with respect to the model.

It can therefore be concluded that the inclusion of the influence factor for internal pressure is a valuable addition to the model. It allows designers to benefit from the positive effect of internal pressure in a tubular member at the moment of local buckling. Inclusion of the girth weld factor (α_{GW}) is debatable. Although it results in higher calculated critical strains for plain tubes, the calculated deformation capacity drops for girth welded tubes. This results from the fact that the effect of α_{GW} is quite severe with a reduction in critical strain of up to 33% (see equation (2.12)),

while a smaller reduction in partial safety factor results from the reduction in scatter that is associated with the inclusion of α_{GW} in the model. In this study, it was chosen to include α_{GW} in the model to allow a higher critical strain in plain tubes.

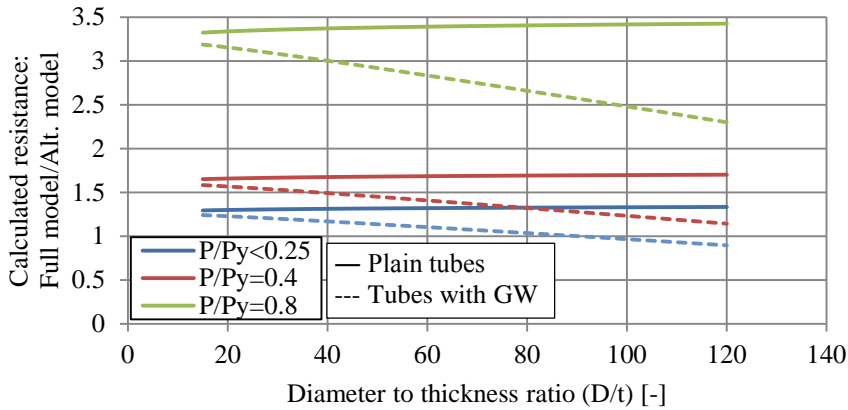


Figure 2.16 Comparison between design models including and excluding influence factors for pressure and the presence of a girth weld. Comparison made for $\beta=3.6$.

2.5 Comparison with existing design guidelines

In this section, the developed design rule is compared with existing design rules. For this comparison, the three design rules discussed in section 1.3.4 are used. The comparison between the three existing design rules and the newly developed design rule is presented in Figure 2.17.

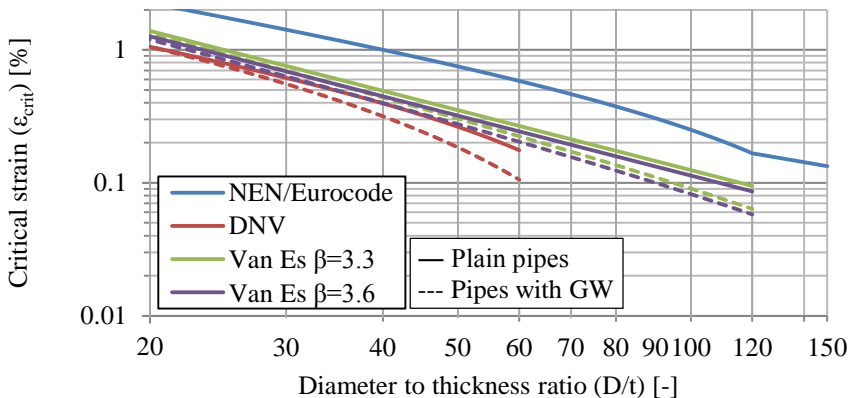


Figure 2.17 Comparison between proposed design rule and existing design rules.

As expected, the proposed design rule is more conservative than the design rules given in NEN 3650-2 (2012) and Eurocode 3 Part 4-3 (EN 1993-4-3, 2009). The proposed design rule is more

economical than the current DNV design rule and is applicable over a larger D/t range. As discussed earlier, this comparison may only be used as a general comparison of the design rules, for a fully accurate analysis of the differences between the design rules, a comparison of design cases is necessary.

2.5.1 Influence factors

Both the proposed design rule and the DNV design rule include an influence factor for the presence of a girth weld in a tube. In contrast, the design rules according to NEN 3650-2 and Eurocode 3 Part 4-3 predict the same critical strain for both a plain and girth welded tube. A comparison of the influence factors for the presence of a girth weld in a tubular member between the proposed design rule and the considered existing design rules is presented in Figure 2.18. Similar as for the overall behaviour, the proposed design rule is more conservative than the Eurocode/NEN design rule, but more economical than the DNV design rule.

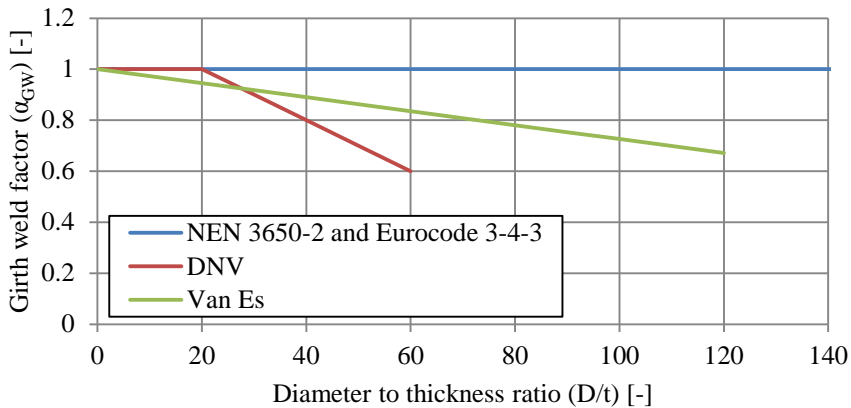


Figure 2.18 Influence of presence of a girth weld in proposed design rule and existing design rules.

A comparison of the influence factors for the presence of internal pressure in a tubular member between the considered existing design rules and the proposed design rule is presented in Figure 2.19. With respect to the beneficial effect of internal pressure, the proposed design rule is more conservative than the DNV design rule. This is a result of the high scatter in the observed beneficial effect due to internal pressure for data points with $D/t > 70$ (see Figure 2.14). The comparison between the proposed design rule and the rules according to NEN 3650-2 and Eurocode 3 Part 4-3 depends on the considered D/t ratio. For tubes with a D/t ratio of 60, the influence factor of the proposed design rule and design rules according to NEN 3650-2 and Eurocode 3 Part 4-3 is similar.

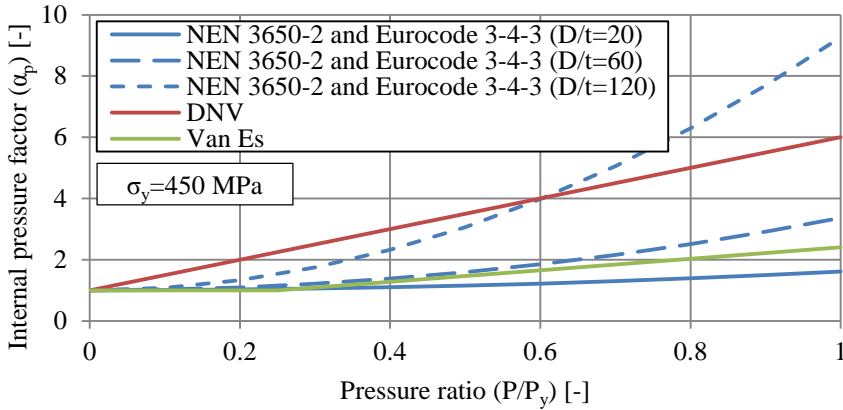


Figure 2.19 Influence of internal pressure in proposed design rule and existing design rules.

2.6 Comparison with Eurocode 3

Besides fluid and gas transportation, tubes may also be applied as structural elements. Within the European Union, Eurocode 3 Part 1-1 (EN 1993-1-1, 2006) applies for the design of such members. This design standard distinguishes cross-section classes ranging from 1 to 4. Cross-section classes 1 and 2 are able to attain a full plastic moment. Cross-section class 3 is only able to attain its first yield moment, while cross-sections in class 4 are unable to attain the first yield moment due to local instabilities. The model proposed in section 2.4 predicts critical strains below the first yield strain for high D/t ratios. This results from the calibration of a relatively simple curve-fitting model to scattered data points in a large D/t spectrum. The transition between critical strains above and below the first yield strain corresponds to the transition between cross-section classes 3 and 4 in EN 1993-1-1. In Table 2.4, a comparison is made between the transition between these cross-section classes according to EN 1993-1-1 and equation (2.11). The comparison is made for a safety level that is in agreement with EN 1993-1-1, which corresponds to $\beta=3.8$. The table shows that for commonly used steel grades, equation (2.11) predicts a transition between class 3 and class 4 cross-sections at a higher slenderness of the cross-section than is predicted by EN 1993-1-1.

The developed design model is safe to use up to a D/t ratio of 120. However, the model may predict very low critical strains at the upper end of this spectrum. Alternatively, for D/t ratios beyond the values stated in the fourth column of Table 2.4, designers are recommended to also investigate application of EN 1993-1-1, which refers to EN 1993-1-6 (2007) for tubular class 4 cross-sections. This may result in a more economical design.

Table 2.4 Class 3 cross-section limits in EN 1993-1-1 and equation (2.11) for plain tubes.

Steel grade	Class 3 boundary (EN 1993-1-1)		Class 3 boundary (eq. (2.11), $\beta=3.8$)	
	D/t	D/te^2	D/t	D/te^2
X52	59	90	73	112
X60	51	90	66	117
X65	47	90	63	120
X70	44	90	60	123

2.7 Evaluation of assessment methods

In section 1.3.4, a comparison between the collected test results and existing design standards is presented. This comparison demonstrates that many experimental results showed a critical strain below a commonly accepted European and Dutch design rule (see Figure 1.4). Therefore, in this chapter, the safe lower bound of the collected data was determined through analysis of the database.

Already in Chapter 1, the scatter in the found data was discussed extensively. In this chapter, an attempt is made to reduce this scatter by determining influence factors for various effects such as differences in yield strength, strain hardening properties and internal pressure. From section 2.3 can be concluded that the determination such influence factors on the basis of the database alone is difficult. Due to the nature of the database, the effect of individual parameters could not be isolated. As a result, the influence factors were determined from heavily scattered data (see for example Figure 2.2). Furthermore, not all relevant parameters could be taken into account, due to lack of sufficient experimental results that provide information on a certain effect. An important example is the effect of the presence of a girth weld in a tube. It is expected that this effect is related to the execution quality of the weld, which is generally not documented in the considered studies. A second example is the effect of the strain hardening of the steel. Instead of implementing the effect of the actual hardening modulus of the steel, the strain hardening properties of the material had to be approximated using the Y/T-ratio.

The result of this chapter therefore should be seen as further motivation for the recommendations made in section 1.5. In case of a test database that includes more information, unsuitable experiments may be excluded from the analysis and subsets within the dataset can be made on the basis of which influencing factors may be quantified better. Moreover, the analysis in this chapter consciously only considers the information contained within the database. A well validated and calibrated numerical or analytical model may be able to further enhance the understanding of the local buckling behaviour of tubes.

It is therefore clear that there are drawbacks to the analysis performed in this chapter. Nevertheless, the developed design guideline is not unsafe for the considered design spectrum. As a result of the applied mathematics, a safe design value of the critical strain was determined

on the basis of the available data. However, by implementing the improvements discussed above, it is expected that a significant improvement in economy may be gained.

An example of such an improvement is found in Part II of this study. Part II of this study investigates a specific application of tubes within the broader field of local buckling in tubes. Section 6.9 discusses a design rule for tubes in combined walls that was proposed by research partners of the basis of a combination of well executed and documented experiments and the results of advanced numerical modelling. Although more limited in its range of application than equation (2.11), it allows for significantly more economical designs.

2.8 Summary of Chapter 2

In this chapter, the development of a new design rule for the critical compressive strain of tubes is presented. On the basis of the test database that is discussed in Chapter 1, a new design rule was derived by analysing the test results that were collected in Chapter 1.

By fitting a model to only the results of specimens without girth welds that were loaded under atmospheric conditions, a basis of the model was derived. Inclusion of additional input variables for the model was considered. The influence of the presence of a girth weld, the yield stress and Y/T ratio, manufacturing process and acting internal pressure was analysed separately. The final model allows for the design of tubes with a D/t ratio between 15 and 120, with a yield strength between 250 and 650 MPa and takes the beneficial effect of internal pressure and the negative influence of the presence of a girth weld into account. External pressure acting on the tube is not considered in the model.

Using the procedures for ‘design by testing’ described in Eurocode 0 (EN 1990, 2002) and by Bijlaard et al. (1988), suitable partial safety factors were determined for the developed model. In comparison with the existing design model included in European and Dutch design standards, the developed model is more conservative. The proposed model allows for more economical design than the current DNV design rule. Furthermore, the model can be applied at a larger D/t range than the DNV model.

As a result of the applied assessment methods, the newly developed guideline is relatively conservative. It is shown that for higher D/t ratios (above approximately $D/t=110$), other, stress based, design guidelines may be more economical. Moreover, over the full range of considered D/t ratios, it is expected that improved economy of designs may be possible if the recommendations made in section 1.5 are followed. Furthermore, information from validated models may also be taken into account in determining a more economical design guideline.

2.9 Recommendations for further research

As a consequence of the applied mathematics, the developed design rule achieves the desired safety levels. However, due to the large scatter that is present in the collected test data, a fairly large safety margin is used in the proposed design rule. In line with the recommendations made

in section 1.5, it is therefore recommended to investigate the possibilities to reduce this scatter. Furthermore, a well validated and calibrated numerical or analytical model may be able to further quantify various influences.

It is also recommended to review the desired probability of occurrence of local buckling. Many design codes such as for example NEN 3650-2 (2012) and Eurocode 3 Part 4-3 (EN 1993-4-3, 2009) regard local buckling failure as an ultimate limit state. However, for example in case of pipeline applications, it could be argued that local buckling is a less harmful phenomenon than loss of containment. Therefore, the necessary safety level for this failure mode can possibly be reduced. In case that local buckling can even be regarded as a serviceability limit state, significant increases in economy of design may be expected. For example, for the formula developed in this chapter, a transition from an ultimate limit state to serviceability limit state may result in a 63% higher allowable critical compressive strain. In structural applications, such a relaxation of the safety level may not be possible.

Chapter 3

Summary of Part I and recommendations

3.1 Summary of Part I

Part I of this study consists of two chapters. In Chapter 1, the current state of the art with regard to the prediction of the bending behaviour of tubes is discussed. Especially the available research on local buckling of these tubes under bending is given considerable attention. It is found that modern FE-calculations are able to accurately describe this failure mode, but are demanding in terms of user and computational effort. Furthermore, such models require validation by experimental work. In addition to numerical investigations, many experimental investigations were performed. A database of more than 400 experimental results is presented and compared to existing guidelines. The collected test results show considerable scatter, which is attributed to the following factors:

- Not all data points originate from the same type of test setup.
- Measurement techniques differed between data points. Especially the gauge length for determining the critical curvature or critical compressive strain is of importance.
- Not all data points result from experiments on comparable test specimens.

A new design rule for the critical compressive strain of tubes was derived by analysing the database. The influence of various parameters such as the steel grade, internal pressure and presence of a girth weld was taken into account. Where appropriate, an influence factor for the effect of such parameters was included in the model. Using the procedures for design by testing (Bijlaard et al, 1988), suitable partial safety factors were determined for the developed model.

The newly developed guideline is relatively conservative. It is shown that for higher D/t ratios (above approximately $D/t=110$), other, stress based, design guidelines may result in more economical designs. Moreover, over the full range of considered D/t ratios, it is expected that improved economy of designs may be possible if the scatter in the database is reduced by more careful selection of test results and division of the data into subsets. If information from

validated models is taken into account in determining a design guideline, further improvement of the guideline is possible.

3.2 Recommendations for further research

It is recommended to take action to reduce the scatter in the results of experiments investigating local buckling in tubes. To achieve this, the following issues need to be addressed:

- Comparability between the experimental procedures needs to be increased by testing in a standardized manner. Measurements, boundary conditions and test procedures need to be agreed upon. It is proposed that the procedures as described in Part II of this study are used.
- Comparability between the test specimens needs to be increased. Therefore, the material and geometric properties of each specimen need to be carefully determined. Furthermore, the test specimens need to be in agreement with some quality and execution requirements that are relevant to the considered application. This allows for more careful selection of test results for a database, and an appropriate division of the data in subsets.
- Documentation of tests needs to be accurate, extensive and accessible.

Following these recommendations, as well as using the information from validated numerical and analytical models may result in more accurate quantification of various influences on the local buckling behaviour of tubes and as a consequence more economical design guidelines.

It is also recommended to review the required safety level for local buckling. In case that local buckling may be assigned a higher failure probability than more severe limit states, such as loss of containment in pipelines, design economy may improve considerably. In structural applications, such a relaxation of the safety level may not be possible.

Part II:

Spiral-welded tubes for application in combined walls

The chapters within Part II of this study form the basis of the publication:
Ultimate bending capacity of spiral-welded steel tubes – Part I: Experiments
(Van Es et al., 2016)

Chapter 4

Introduction to Part II

4.1 COMBITUBE research project

To develop economic and safe design guidance for tubes in combined walls, a multi-disciplinary European Research project with acronym COMBITUBE (COMBITUBE Research Consortium, 2015) was started in 2011. This research project explored the structural behaviour of tubes in combined walls. In particular the application of spiral-welded tubes was investigated.

The COMBITUBE research project was coordinated by Delft University of Technology and was carried out by European research partners from academia and industry:

- Delft University of Technology, The Netherlands (coordinator)
- ArcelorMittal, Luxemburg
- University of Edinburgh, United Kingdom
- Karlsruhe Institute of Technology, Germany
- University of Thessaly, Greece
- BAM Infraconsult B.V., The Netherlands

The research presented in Part II of this study is part of the COMBITUBE project and was funded by the Research Fund for Coal and Steel (RFCS) of the European Commission under Grant Agreement No. RFSR-CT-2011-00034.

4.2 Spiral-welding manufacturing process

An economical and efficient method to manufacture relatively thin-walled large-diameter steel tubes is offered by the spiral-welding (or helical-welding) manufacturing process (HSAW). This process consists of the spiral-welding of a steel plate from a hot-rolled steel coil, as shown schematically in Figure 4.1. First, the steel is de-coiled and flattened and prepared for welding by bevelling the edges and if necessary pre-heating. Using a three-roll forming process, the plate is continuously formed into a spiral which is welded together from both sides of the plate, forming an X-weld.

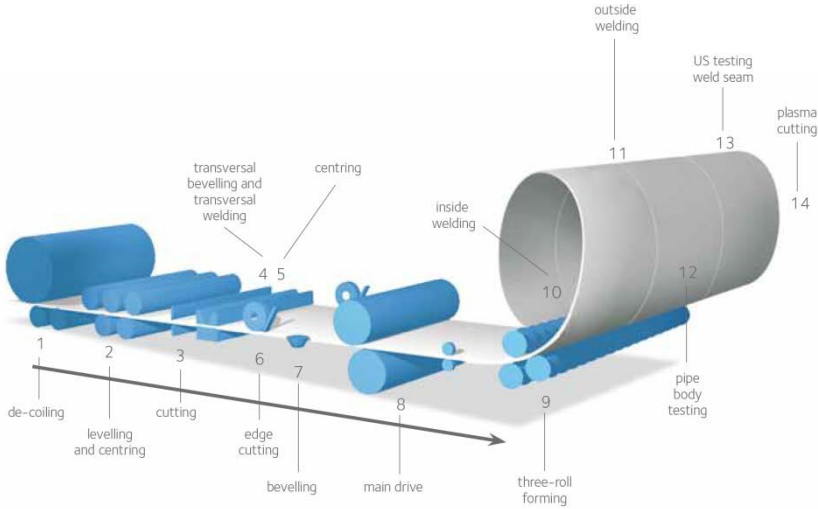


Figure 4.1 Schematic overview of HSAW manufacturing process (ArcelorMittal, 2010).

The manufacturing process of spiral-welded tubes is continuous. A steel coil that runs out is connected to a new coil by means of a butt weld without interruption of the spiral-welding process (see Figure 4.2 and Figure 4.3). This weld, running perpendicular between two spiral welds is denoted in this study as a coil connection weld (CCW). An advantage of the continuous production is that tubes of significant length can be manufactured, sufficient for tubular up to 53 m length without the need for a connection between two tubes (ArcelorMittal, 2010).



Figure 4.2 Coil connection weld in a spiral-welded tube applied in a combined wall.

In case of the need of a connection between two tube elements, a girth weld (GW) is made. This weld can be executed at the manufacturing plant, but also on site. A schematic overview of a spiral-welded tube with a girth weld and coil connection weld is presented in Figure 4.3.

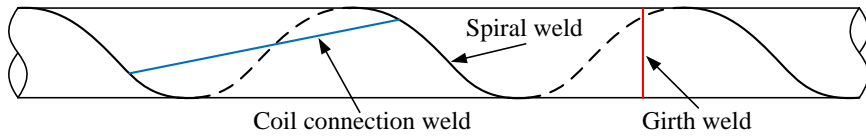


Figure 4.3 Schematic overview of spiral weld, coil connection weld and girth weld in a spiral-welded tube.

4.3 Combined walls

Large-diameter spiral-welded tubes are employed in many onshore pipeline applications, mainly for water transportation. Furthermore, spiral-welded tubes are used in many structural applications, for example for tubular piling, towers, masts and other large tubular structures. An important application of spiral-welded tubes is the use in combined walls as primary structural elements that resist horizontal loads from soil and water pressure and vertical loads in case of a combined wall in a quay wall. Those combined walls, often referred to as “combiwalls”, consist of a series of large diameter tubes connected by infill sheeting (see Figure 4.4). For their connection, standard sheet piling slots are welded to the tubes.



Figure 4.4 Example of a combined wall system under construction (ArcelorMittal, 2008).

Typically, tubular piles in combined walls are mainly loaded in bending. In addition, a compressive normal force can be present. To achieve maximum stiffness and bending moment capacity at minimum steel use, combined walls are commonly constructed using large-diameter tubes with relatively thin walls (de Gijt and Broeken, 2013). As a result, local buckling of the tube wall is the dominant failure mode for these elements.

Because large-diameter thin-walled steel tubes of long length are manufactured very economically with the spiral-welding manufacturing process, spiral-welded tubes are often used for combined walls. Typical diameters range up to 3000 mm, with a wall thickness up to 25 mm, specified minimum yield strength between 350 MPa and 480 MPa and length up to 50 meters, whereas typical values of the corresponding D/t ratio range from 65 to 120.

An advantage of using the continuous spiral-welding manufacturing process for tubes in this application is the capability of producing tubes of significant length, thereby minimizing the number of girth welds in the structure. However, girth welds do occur in combined walls made from spiral-welded tubes, since in some cases stock tubes are used or combined wall piles are re-used. In both cases the length of the available material needs to be adjusted to the required length of the tubular pile, either by cutting or by attaching another tube by a girth weld. Also in case of discontinuities in wall thickness within the tubes, a girth weld is present.

4.4 Literature review

4.4.1 Bending behaviour of spiral-welded tubes

Many investigations into the bending and local buckling behaviour of tubular members in general were performed. A summary of relevant publications is discussed in Chapter 1 and is not fully repeated here.

The bending and local buckling behaviour of spiral-welded tubes is less well understood. As discussed in section 1.3.2, only a limited number of publications present and discuss the bending behaviour of spiral-welded tubes. In the publications by Zimmerman (2004) and Zimmermann (2012), the focus lies on line pipe applications of spiral-welded tubes. As a result, these investigations focus on slightly thicker walled tubes than are commonly applied in combined walls. Furthermore, the effect of internal hydrostatic pressure on the local buckling behaviour of the tubes is extensively discussed, which is not relevant for application in combined walls. In another investigation aimed at application in pipelines, Fonzo et al. (2011) found spiral-welded tubes to be suitable for application of a limit strain design after performing bending experiments on both UOE formed and spiral-welded tubes. Research carried out at the Karlsruhe Institute of Technology, which was performed as part of the same research project as the present study (Reinke, 2014, COMBITUBE Research Consortium, 2015) investigated the structural applications of spiral-welded tubes, mainly focusing on the maximum bending moment capacity rather than deformation capacity. Research performed by CUR in close collaboration with the COMBITUBE project investigates the positive effect of a sand fill in tubes in combined walls on their local buckling behaviour (Royal HaskoningDHV, 2013). Its main objective is to investigate the effect of the sand fill. The testing programme featured a combination of both spiral-welded and longitudinal-welded tubes.

It can therefore be concluded that, at the start of the COMBITUBE project, the majority of the research into spiral-welded tubes was focused on the application in pipelines. The COMBITUBE project focused on structural applications of tubes with a relatively slender cross-section.

4.4.2 Current regulations regarding the design of combined walls

The design of combined walls is covered in Eurocode 3 Part 5 (EN 1993-5, 2006). For the verification of the tubular steel piles, EN 1993-5 refers to Eurocode 3 Part 1-1 (EN 1993-1-1, 2006). This document identifies cross-section classes which identify to what extent the resistance and rotation capacity of a structural member is limited by local buckling. Considering the slender design of combined walls, only two classes are relevant for these structures: class 3 and class 4. Class 3 cross-sections can reach the yield strength of the material in an elastic stress distribution without the formation of a local buckle. Class 4 cross-sections are not able to reach the yield strength of the material in an elastic stress distribution. Local buckling occurs before the yield strength is reached. Both cross-section classes are not able to deform plastically without local instability. The design values for the boundaries between the cross-section classes are expressed in Eurocode 3 Part 1-1 in terms of values of the cross-sectional slenderness, as defined by equation (4.1).

$$\text{cross-sectional slenderness} = \frac{D}{t \cdot \varepsilon^2} \quad (4.1)$$

With:

ε : Parameter to account for the influence of the yield strength of the material: $\varepsilon^2 = 235 / \sigma_y$

In case of a class 4 cross-section, Eurocode 3 Part 1-6 (EN 1993-1-6, 2007) provides design rules. Application of this standard shows that the verification calculations for local buckling may lead to very uneconomical designs. The main cause is the application of a local stress buckling criterion in EN 1993-1-6, which is very restrictive for tubes at the boundary between cross-section classes 3 and 4. Furthermore, the transition between the various cross-section classes is accompanied by large discontinuities in the bending moment capacity (van Es et al., 2013), (Gresnigt et al., 2011).

4.5 Objective

It is the objective of Part II of this study to provide more insight into the strength and deformation capacity of spiral-welded tubes for application in combined walls. For this purpose, a large-scale experimental programme was carried out, investigating the bending behaviour of spiral-welded tubes. For comparison, also two longitudinal-welded tubes were included in the testing programme.

This study contributed to the COMBITUBE research project, which aimed to develop economic and safe design guidance for tubes in combined walls, in particular for spiral-welded tubes.

4.6 Summary of Chapter 4

In this chapter, an introduction is given to the research that is presented in Part II of this study. Firstly, the COMBITUBE project is outlined, which aimed to develop economical and safe design guidelines for tubes in combined walls. Because spiral-welded tubes are very common in these structures, the development of these design guidelines requires further study of the bending behaviour of spiral-welded tubes.

The spiral-welding manufacturing technique is presented and its various aspects are explained. The resulting specific features in a tube (spiral weld and coil connection weld) are discussed. A typical application of these spiral-welded tubes is presented: the combined wall. An overview of common dimensions and steel grades is given, as well as the specific advantages of employing spiral-welded tubes in these structures.

The general literature study with respect to bending of tubular members (see Chapter 1) is supplemented with an overview of investigations into the behaviour of spiral-welded tubes. It is concluded that the behaviour of spiral-welded tubes in the D/t ratio range that is applicable for combined walls is not yet well understood. This lack of understanding, combined with relatively uneconomical European design regulations that are currently governing, led to the initiation of the COMBITUBE research project.

The objective of Part II of this study is to provide more insight into the strength and deformation capacity of spiral-welded tubes for application in combined walls in terms of local buckling failure. To this aim, a large-scale experimental programme was performed, which compared the behaviour of spiral-welded tubes with longitudinal-welded tubes.

Chapter 5

Experimental study of spiral-welded tubes

5.1 Test programme

The research presented in Part II of this study is centred around a series of large-scale four-point bending tests on thirteen spiral-welded tubes and two UOE longitudinal-welded tubes. To correctly understand the observed bending behaviour, the four-point bending tests were supplemented by a large programme investigating the geometric and material properties of the specimens. The programme included extensive measurements of the tubes' initial geometry and geometrical imperfections. Furthermore, the tensile and compressive material behaviour was investigated by performing tensile and compressive coupon tests.

The testing programme aimed to understand the bending behaviour of spiral-welded tubes for use in combined walls. Therefore, typical features that may occur in such structures, such as a girth weld and coil connection weld were included in the testing programme.

5.1.1 Test specimens

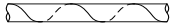
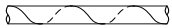

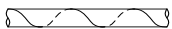
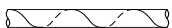


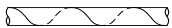
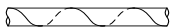




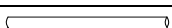
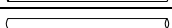
All specimens had a specified outer diameter of 1067 mm (42 inch), and a length of 16500 mm. The D/t ratios were varying between 65 and 120 with steel grades varying from X52 to X70. This range of D/t ratios and steel grades was determined to be representative for application in combined walls (COMBITUBE Research Consortium, 2015). The diameter of the specimens was chosen for reasons of availability of tube material.

As discussed in section 5.1, the testing programme also included tubes with girth welds and coil connection welds. Specimens that did not contain these features are denoted as 'plain' specimens. These specimens only included a longitudinal or spiral weld. Specimens that included a girth weld, coil connection weld or both are denoted by the abbreviation of these features. If a girth weld or coil connection weld was present in a specimen, such a specimen was

divided by that weld into two or more sections, each section having its own material and geometrical properties. These sections are referred to as ‘specimen parts’ and are identified by their position in the four-point bending test. They are denoted by adding the indicators ‘left’, ‘middle’ and ‘right’ to the specimen identification.

An overview of the experimental programme is depicted in Table 5.1. For detailed drawings of the specimen layout, reference is made to Appendix B.2. Considering the geometry of the four-point bending test setup, all investigations were focused at the central 8 meters of the specimen, the segment with constant bending moment in the bending test (see section 5.4.1).

Table 5.1 Overview of test specimens in Part II of this study. Presented geometric properties are measured values.

Spec.	Part	D [mm]	t [mm]	D/t [-]	Type	Layout	Steel grade
T1		1066	16.4	65.1	Spiral	Plain	 X70
T2		1067	9.0	118.3	Spiral	Plain	 X60
T3	Left	1067	8.8	121.3	Spiral	GW	
	Right	1070	9.2	116.3			
T4		1065	9.2	116.2	Spiral	Plain	 X60
T5		1070	9.0	118.3	Spiral	Plain	 X60
T6	Left	1067	16.1	66.4	Spiral	CCW	
	Right	1066	16.4	65.0			
T7	Left	1068	16.4	65.3	Spiral	GW/CCW	
	Middle	1067	16.3	65.4			
	Right	1069	16.3	65.6			
T8		1068	9.1	117.4	Spiral	Plain	 X60
T9		1069	16.3	65.4	Spiral	Plain	 X70
T10	Left	1071	13.3	80.6	Spiral	GW/CCW	
	Middle	1070	13.3	80.4			
	Right	1069	12.8	83.5			
T11		1068	12.9	82.8	Spiral	Plain	 X52
T12	Left	1069	9.1	117.5	Spiral	GW/CCW	
	Middle	1067	9.2	115.6			
	Right	1067	9.1	117.3			
T13	Left	1070	9.1	117.6	Spiral	GW	
	Right	1071	9.2	116.4			
T14		1068	9.8	108.8	UOE	Plain	 X60
T15		1070	14.8	72.3	UOE	Plain	 X70

On the basis of the results of the material tensile tests (see section 5.3), measured wall thickness and initial imperfections (see section 5.2) and visual observations, some specimens appeared to be very similar (e.g., all specimens with a wall thickness of about 9 mm). Furthermore, they

were acquired from the same provider at the same time. It is assumed that these specimens originate from the same manufacturer, possibly even from the same production batch.

5.2 Measurement of initial geometry and imperfections

5.2.1 Programme

Before performing the four-point bending tests, the initial geometry of all specimens was measured. The programme included measurements of the specimen diameter, initial ovalisation and geometrical imperfections. All the measurements were focused at the central 8 m of the specimen, as this is the section of the specimen that was loaded by a constant bending moment in the four-point bending test.

The aim of the programme was to gather data which can be used to:

- Describe geometrical imperfections that are present in the considered spiral-welded tubes.
- Evaluate the differences in geometrical imperfections between spiral-welded tubes and UOE-formed longitudinal-welded tubes.
- Allow geometrically accurate FE-models of the test specimens to be developed which are to be used for validation of a more general FE-model. Subsequently, this general FE-model can be used to perform parameter studies.

In this section, the measurement methods are discussed. Results of the measurements of initial geometry and imperfections are presented in sections 5.2.2 to 5.2.6. A full report of these results can be found in Van Es and Gresnigt (2016).

Measurement of specimen diameter and initial ovalisation

The diameter of the specimen was measured using two methods. Firstly, the external diameter of the tube was measured. For this, five cross-sections were defined on the specimen. In cases where a girth weld was present at the exact centre of the specimen, the middle cross-section was replaced by two cross-sections just next to the girth weld, resulting in a total of six cross-sections. A laser-equipped bracket was placed around the tube enabling measurement of the tube diameter. By rotating the tube in 45 degree increments, an estimate of the initial ovalisation of the specimens was obtained at each of the five designated cross-sections. The process is depicted schematically in Figure 5.1

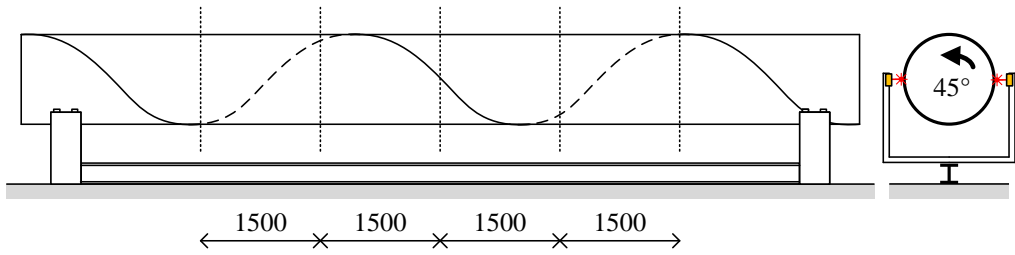


Figure 5.1 Overview of the measurements of the outer diameter at five cross-sections in 45 degree rotation increments (dimensions in mm).

Secondly, the initial internal diameter of the tube was measured using a robotic laser-equipped trolley driving on the inside surface of the tube. The trolley was designed for use during the tests, but was also used at the start of the test, providing information on the initial state of the specimen. The trolley featured a rotating laser, which was able to provide circumferential scans of the tube at certain intervals over the tube length. These scans provide much more information on the cross-section shape and initial ovalisation, but are less accurate due to the uneven driving surface of the trolley, imperfect laser reflection on the dirty inside surface of the tube and possible noise due to foreign objects inside the tube, such as dirt and pebbles. An overview of the measurement setup is presented in Figure 5.2, while detailed photographs of the trolley are presented in Figure 5.3.

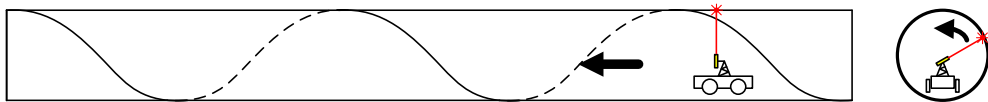
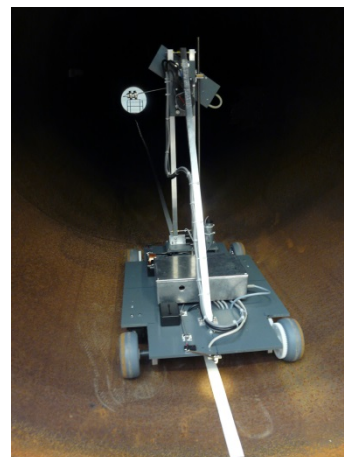


Figure 5.2 Overview of the measurements of the internal diameter with a laser-equipped trolley.



(a) Front of the trolley with rotating laser



(b) Trolley inside a tube

Figure 5.3 Laser-equipped trolley for internal scanning of the specimen.

The laser trolley delivered an output in the form of a series of approximately circular point clouds. Through these point clouds, a best fitting ellipse was constructed using an unweighted least squared error fit-estimation method. Although the assumption of an elliptical shape of the cross-section is not justified per se, in general the correspondence of the fitted ellipse with the measurement data was found to be satisfactory. A minimum and maximum diameter for each cross-section was found from the long axis and short axis of the fitted ellipse.

Measurement of specimen wall thickness

The wall thickness of each specimen was measured using an ultrasonic thickness measurement device. For a general overview of the wall thickness variation over the specimen, thickness measurements were performed at the cross-sections defined for the diameter measurements (see Figure 5.1). At each cross-section, eight measurements were carried out, evenly distributed over the circumference of the tube. Additionally, the variation of the wall thickness of the tube over the original width of the coiled plate was investigated by measuring the wall thickness along a line perpendicular to the spiral weld (see Figure 5.4). This was performed twice for each specimen. Finally, the variation of the wall thickness towards the end of a coiled plate was investigated by measuring the wall thickness close to a coil connection weld in a fine grid on both sides of the weld.



Figure 5.4 Measurement of wall thickness over original coil width.

Estimation of residual stresses

The cold forming of the spiral-welded tubes leads to a complex residual stress state in the finished tubular product. However, not only the forming process of the spiral-welded tube, but the full history of the steel is of influence on this residual stress state. A hot steel plate is coiled and cools unevenly on the coil. Depending on its location within the coil, a section of steel plate needs a certain amount of flattening before the spiral-welding manufacturing starts. The residual stress state in the final tube product depends on all these factors and is therefore difficult to predict.

To enable accurate numerical and analytical modelling, information on the distribution and magnitude of these residual stresses is required. Within the COMBITUBE project, various attempts were made to estimate the residual stresses in the tubes. Research partners at the

Karlsruhe Institute of Technology used the hole drilling method and partners at the University of Thessaly used numerical modelling (see section 6.5). Supplementary to these measurements, the ring-cutting method was used at Delft University of Technology.

From each spiral-welded specimen part, a short length of tube was made available by the supplier. By cutting the rings in longitudinal direction, the cold-formed steel experienced an elastic spring back. The opening or closing deformation of the ring was measured, which allows estimation of the magnitude of the residual stresses once a distribution of these stresses is assumed.

Measurement of geometrical imperfections in the laboratory

In the analysis of thin-walled shells with large values of the D/t ratio, initial geometrical imperfections are considered a paramount factor in determining the resistance against local buckling (Timoshenko and Gere, 1961). Although the tubes considered in this research have significantly lower values of the D/t ratio than the shells considered in shell buckling analysis, initial imperfections are expected to have an influence on the buckling location, the critical strain and the bending moment capacity of the specimens.

The outer profile of all tubular specimens was scanned using a laser trolley driving on rails below the specimen. An overview of the test setup is depicted in Figure 5.5. Of each tube, sixteen scans were made, evenly distributed over the circumference of the tube, with the exception of the first two specimens, where eight scans were made.

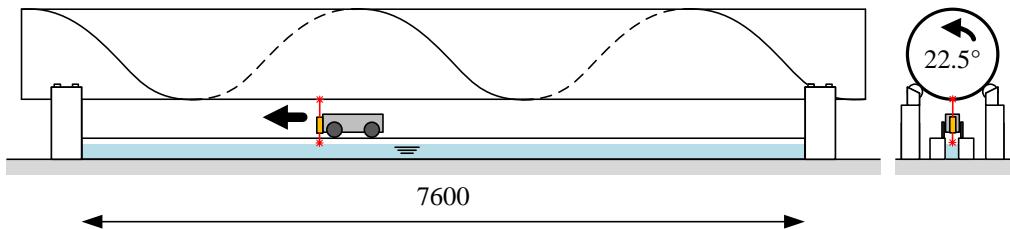


Figure 5.5 Overview of laser measurements of geometrical imperfections (dimensions in mm).

As the geometrical imperfections were expected to be very small and the scans took place over a significant length, any influence of geometrical imperfections of the laser trolley's rails on the measurement result needed to be prevented. By scanning a fluid surface, the imperfections of the rails were documented and could be subtracted from the measured imperfections of the specimens. Further corrections of the geometry measurements for unevenness of the tube's supports and sag of the tube under its self-weight were also carried out.

Measurement of geometrical imperfections at a building site

The imperfections measured in the laboratory may or may not be representative of what can be expected in realistic situations. The quality of tubes that are used in combined walls may suffer from for example transportation, handling, pile driving and excavation on one side of the wall. In case of temporary combined walls, tubes may be re-used, which means that the

mentioned influences may be repeated and the deconstruction of the structure may result in additional influences. To investigate to what extent the laboratory conditions were representative of a tube in a combined wall, geometric imperfections were also measured on tubes already in use in a combined wall.

The investigation took place on a construction site at the A4 motorway between Delft and Amsterdam in The Netherlands. At the time of this research, the motorway was being reconstructed as a sunken motorway in a roofless tunnel near the city of Leiden (see Figure 5.6a). In the usage phase of the new motorway, the combined walls are hidden from sight and access. However, during construction, the lower parts of the combined walls were accessible for measurements (see Figure 5.6b).



(a) Overview (Rijkswaterstaat, 2015)

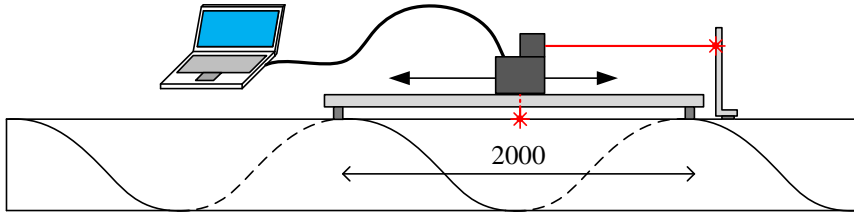


(b) Exposed combined walls in building pit

Figure 5.6 Construction site near Leiden where field measurements took place.

Since the tubes were already in place, the horizontal measurement setup as used in the laboratory (see Figure 5.5) could not be used. Instead, a handheld measuring device with similar capabilities was developed. An overview of the measurement setup is presented in Figure 5.7. The measurement setup consists of an aluminium rail and a handheld laser unit equipped with two lasers. One laser measures the distance from the unit to the tube, the second laser measures the distance of the unit to a reflector placed at the end of the rails. Firstly, the rails were attached to the tube by magnets at each end (see Figure 5.7c). Secondly, two intermediate supports were placed, to limit the deformation of the rail during measurement operations (see Figure 5.7d).

The relative simplicity of the setup resulted in high sensitivity to the smoothness of operation. Therefore, each scan was performed several times, so that during post-processing, a more accurate result could be obtained using a trimmed mean over the various scans at each location. Further inaccuracy is caused by flexure of the aluminium rail. As a result, the field scans are only useful for investigation of local imperfections, which was sufficient for the purpose of these measurements on site.



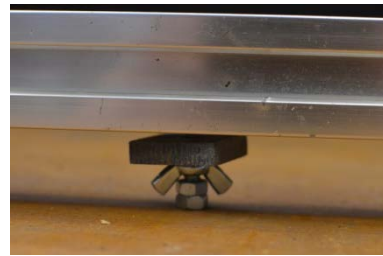
(a) Schematic overview of setup for field measurements.



(b) Measurement setup in operation



(c) Magnetic support and rail cross-section



(d) Adjustable intermediate support

Figure 5.7 Overview of setup for field measurements (dimensions in mm).

In total, nineteen scans were performed on nine tubes. All tubes had a specified outer diameter of 1220 mm and steel grade X56. Five tubes had a specified wall thickness of 12.7 mm ($D/t=96.1$), the remaining four tubes had a specified wall thickness of 11.2 mm ($D/t=104.3$). Neither the diameter nor wall thickness was verified. It was assumed that they were close to the specified values. Scans were made of plain tube sections including one or more spiral welds and of tube sections including a coil connection weld, girth weld, dent or scratch.

5.2.2 Results of the measurements of specimen diameter and initial ovalisation

The average measured diameter as listed in Table 5.1 was determined on the basis of the measurements with the laser-equipped bracket (see Figure 5.1) as these measurements were assumed to be most accurate. Besides the average diameter, the initial ovalisation (initial out-of-roundness) of the tube is recognized as a relevant parameter. The ovalisation parameter f is defined as $(D_{max}-D_{min})/D_{avg}$. Given the measurement procedure with the laser-equipped bracket

(see section 5.2.1), the minimum and maximum diameter were not necessarily measured, resulting in a lower bound estimate for parameter f . Alternatively, the initial ovalisation of the tubes can be obtained from the internal laser scan, albeit with possible lesser accuracy due to causes discussed in section 5.2.1.

In Figure 5.8, the average ovalisation resulting from both the laser-equipped bracket and internal laser measurements is presented. In addition, a 95% confidence interval of the initial ovalisation per specimen part is presented. This confidence interval was calculated by using the sample mean and standard deviation as best estimate for the population mean and standard deviation.

Because the outer diameter of the tube was measured at only five cross-sections with the laser-equipped bracket, the result maximum sample size for parameter f per specimen part was five. The internal laser measurement was performed at much more closely spaced cross-sections, leading to a sample size per specimen part of up to 35. Therefore, the 95% confidence interval was only calculated on the basis of the internal laser measurements. Unfortunately, the internal laser measurements could not be split into data sets for the separate specimen parts. Instead, only the results for the full specimens could be obtained. As a result, the average initial ovalisation and 95% confidence interval resulting from the internal laser measurements are presented per full specimen in Figure 5.8.

From Figure 5.8 it can be concluded that the initial ovalisation of all specimens is small as it generally remains smaller than 1% on average. This value may for example be compared with EN 10219-2 (2006), which specifies the tolerances for the tubes under consideration. This standard specifies a maximum of 0.02 for f , provided that $D/t < 100$. For more slender tubes, the standard states that the maximum out of roundness must be agreed upon. Eurocode 3 Part 1-6 (EN 1993-1-6, 2007) specifies a maximum value of 0.0087 for f to classify tubes of the considered diameter in the highest possible fabrication tolerance quality class (class A), while a maximum value for f of 0.0124 is allowed for the second highest fabrication tolerance quality class. All of the considered specimens show an initial ovalisation below the maximum out of roundness allowed in EN 10219-2. Furthermore, most specimens would be classified in the highest fabrication tolerance quality class with regard to initial ovalisation according to EN 1993-1-6.

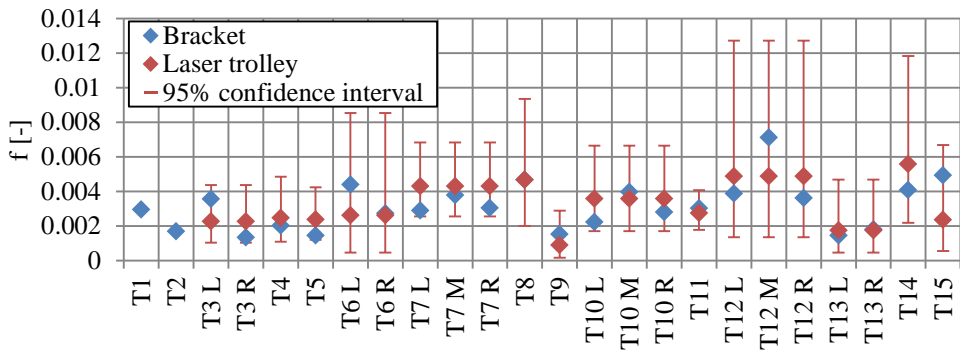


Figure 5.8 Average initial ovalisation (f) of each specimen part and 95% confidence interval. No internal laser measurements were available for specimens T1 and T2.

5.2.3 Results of the measurements of specimen wall thickness

The average wall thickness of each specimen part is listed in Table 5.1. Using the sample mean value of the wall thickness as best estimate for the population mean and the sample standard deviation of the wall thickness as best estimate for the population’s standard deviation, a 95% confidence interval of the tube wall thickness was determined for each specimen part under assumption of a normally distributed population. An overview of these confidence intervals is presented in Figure 5.9. The figure shows that within each specimen part, very little variation of the wall thickness exists.

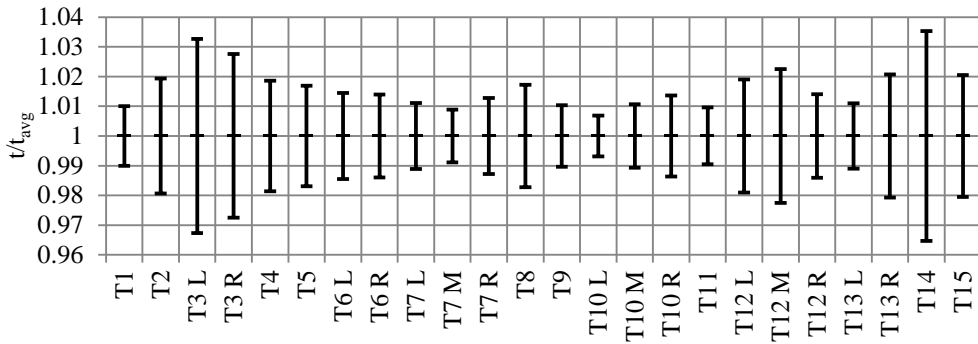


Figure 5.9 95% confidence intervals of wall thicknesses in each specimen part.

To investigate the variation of the plate thickness across the width of the coiled steel plate of which the tubular specimens were manufactured, thickness measurements were performed along a line perpendicular to the spiral welds. Because the width of the original coiled steel plate varied between the tubular specimens, these measurements were performed at locations relative to the coil width. To allow comparison between the specimens, the data were normalized by the average wall thickness of the considered specimen part. By considering the normalized data at each measuring station as a sample of the population at that location, a 95% confidence interval was calculated at each measuring station with similar methods used for Figure 5.9. The results of this procedure are presented in Figure 5.10, which shows that the wall thickness slightly decreases close to the spiral welds. In the specimens considered in this study, the average decrease was found to be 1.2%.

The thickness measurements that were performed close to the coil connection welds did not show any noticeable reduction of wall thickness. During manufacturing, a small length of coiled steel is removed from the start and end of each coil to avoid using imperfect material in the tubes. The results from the measurements show that this measure is effective in eliminating variation of tube wall thickness near the coil connection weld (Van Es and Gresnigt, 2016).

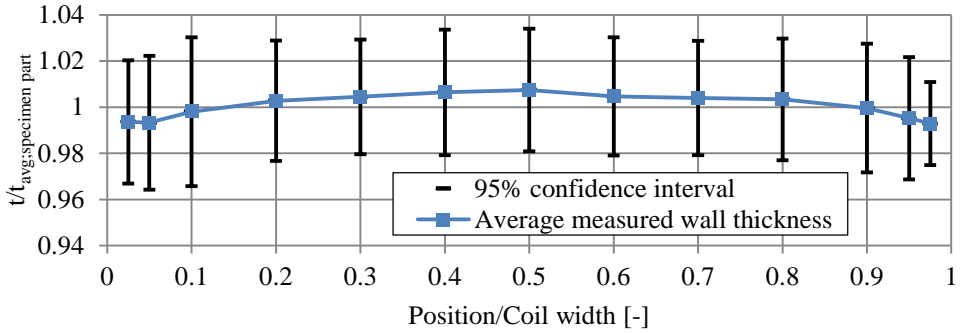


Figure 5.10 Development of wall thickness over width of coiled plate.

5.2.4 Results of the estimation of residual stresses

For each available ring, the following measurements were performed (see Figure 5.11):

- Ring opening or closing in tangential direction (change in circumference): ΔC
- Ring opening or closing in radial direction (change in radius): Δr
- Skewness of the opening: S

An overview of the results is shown in Table 5.2. The change in radius could not be measured in all cases, especially when the ring deformation in tangential direction was large.

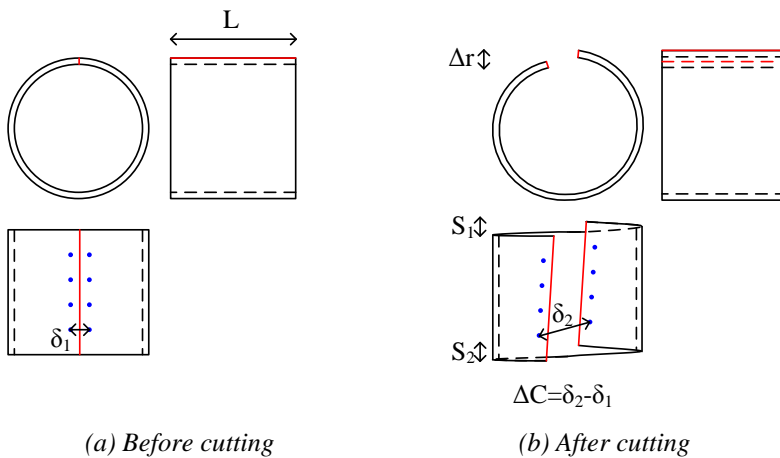


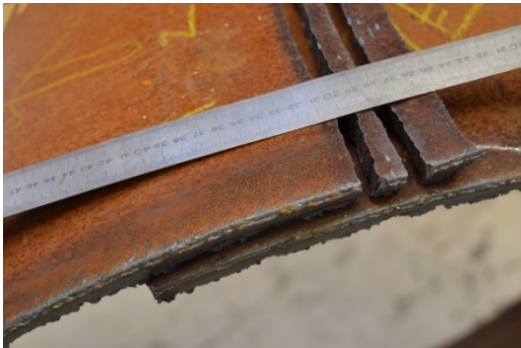
Figure 5.11 Schematic overview of ring-cutting measurements

It is clear that the results presented in the table show a very large variation. In case of the specimens with a specified wall thickness of 15.9 mm, some rings were observed to have a tendency to close after cutting (T1, T6Right), while others opened (T7Left, T7Right and T9). For the specimens with intermediate wall thickness, the rings opened a small amount. In case of the specimens with a specified wall thickness of 9 mm, results varied from an opening of 436

mm to 856 mm. The thinner walled rings also showed to be prone to opening very askew. Two examples of deformed rings are presented in Figure 5.12.

Table 5.2 Overview of ring-cutting measurements results.

Specimen part	Dimensions ($D \times t \times L$) [mm ³]	ΔC_{avg} [mm]	Δr_{avg} [mm]	S_{avg} [mm]
T1	1066×16.4×500	-154	-	<10
T2	1067×9.0×395	503	-	30
T3Left	1067×8.8×260	466	-	11
T3Right	1070×9.2×1000	856	-	106
T4	1065×9.2×400	475	-	101
T6Right	1066×16.4×320	-156	-	0
T7Left	1068×16.4×400	340	-	77
T7Right	1069×16.3×473	276	62	30
T9	1069×16.3×413	214	50	15
T10Right	1066×12.8×515	60	-	27
T11	1068×12.9×548	7	15	22
T13Left	1070×9.1×500	436	-	47
T13Right	1071×9.2×1000	626	-	48



(a) Closing of ring T6Right before further material removal to allow free deformation



(b) Opening of ring T13Right

Figure 5.12 Examples of ring deformation after cutting.

The large variation that was observed in the results of the ring-cutting tests may have various origins. Spiral-welded tubes are manufactured from coiled steel plate. The position of a plate section on the coil can influence its residual stress state in the final manufactured tube. This position determines the radius of curvature of the plate while it is on the coil and therefore the amount of straightening that is necessary to achieve a straight plate that is used as input in the spiral-welding manufacturing process (see Figure 4.1). Furthermore, differences in residual stresses can arise when the straightening of the plate is not performed with sufficient accuracy.

When an incorrectly straightened plate is fed into the bending process that forms the tube, the resulting residual stresses may significantly differ from a perfectly straight plate. Similarly, insufficient accuracy in this bending process may also generate differences in residual stresses. Other differences in residual stresses between tubes or within a tube may occur due to the differences in temperature history of the plate sections, used coiling methods and specific features of a spiral-welding manufacturing plant.

Unfortunately, these parameters were not documented and as a result cannot be used to clarify the results of the observations in the ring-cutting experiments. Considering this, and the similarly erratic results found in the measurements performed at the Karlsruhe Institute of Technology (COMBITUBE Research Consortium, 2015), the estimation of the residual stresses was discontinued. A more thorough study is required to obtain sufficiently useful results.

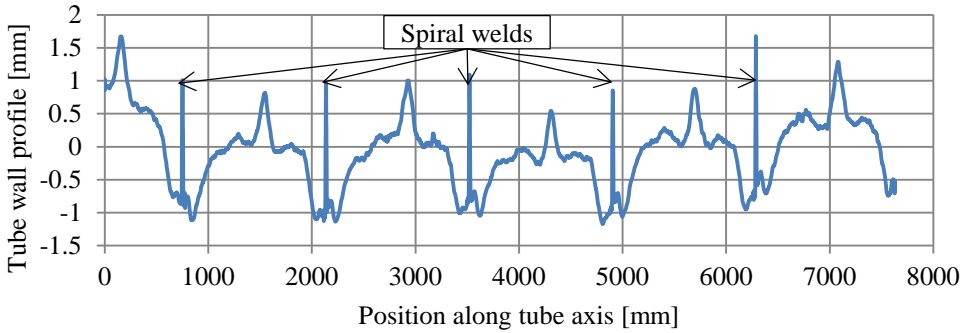
5.2.5 Results of laboratory measurements of geometrical imperfections

Considering the large amount of data, not all results are presented in this section or in the appendices to this thesis. Instead, a summary of the data is presented that sufficiently illustrates the conclusions that were drawn on the basis of the full data set. More results can be found in Van Es and Gresnigt (2016).

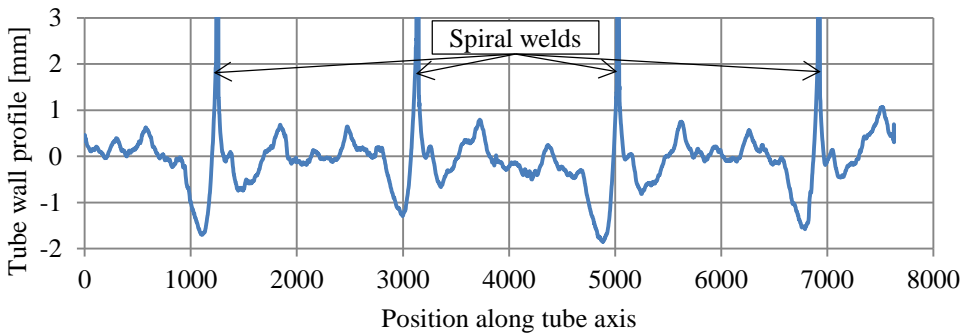
Plain spiral-welded tubes

The surface scans of the spiral-welded tubes show several notable characteristics. In a segment between two spiral welds, the tube wall surface is not flat, but shows a series of local “hills” and “valleys”. Two examples of a laser scan of the initial tube wall profile are depicted in Figure 5.13 for specimens T2 and T9. The graphs represent a laser scan of the outer surface of the tube. The area above the graph line represents space outside the tube, the area beneath the graph line represents the tube wall or space inside the tube. Since wall thickness variations were very small (see Figure 5.10), the scanned outer surface of the tube wall is assumed to represent the geometry of the middle surface of the shell. At the location of the spiral weld, the scan includes the weld bead, meaning that, at these locations, the scanned surface does not represent the middle surface. This discrepancy results in the sharp peaks at the location of the spiral welds, which for the analysis of geometrical imperfections can be disregarded.

It appears that in between the spiral welds, a quasi-repeating tube wall profile pattern is present. This is attributed to the fact that the wavy imperfections may be the result of the manufacturing process. As described in section 4.2 and modelled by Vasilikis et al. (2016), spiral-welded tubes are cold-formed by means of a three-roller system that bends the steel coil. If these rollers are not continuous but discrete, a series of discrete geometrical imperfections may be the result. These imperfections then repeat themselves between each pair of spiral welds, as seen in Figure 5.13. After forming the coiled plate into a tube, the tube is supported on several smaller, but certainly discrete, rollers. These rollers might also have an influence on the observed initial imperfections profile.



(a) Specimen T2 at orientation 0° .



(b) Specimen T9 at orientation 0° .

Figure 5.13 Examples of geometrical imperfections in spiral-welded specimens. The sharp spikes mark the presence of a spiral weld.

Upon closer inspection it appears that some of the tubes feature visible marks of rollers on the outside of the wall, running in parallel with the spiral welds (see Figure 5.14). When these marks are lined up with a measurement of initial imperfections, it can be concluded that the imperfections are indeed caused by the rollers in the manufacturing process (see Figure 5.15). Over time, the visible markings of the rollers disappear due to wear of the tube's surface or light surface corrosion, but the corresponding geometrical imperfections remain. As a result, not every specimen showed the roller markings to match the measured initial geometrical imperfections. Furthermore, when roller markings were visible on the specimen, most of them were very vague and, although the number of marks between two spiral welds theoretically should remain constant within one specimen part due to the nature of the manufacturing process, the number of observed marks fluctuated (see Figure 5.15a). It is therefore possible that, although not every imperfection peak matches with a roller mark, these rollers have a significant influence on the observed quasi-repeating imperfections. In this study, it is assumed that all the observed quasi-repeating geometrical imperfections are caused by the cold-forming process.

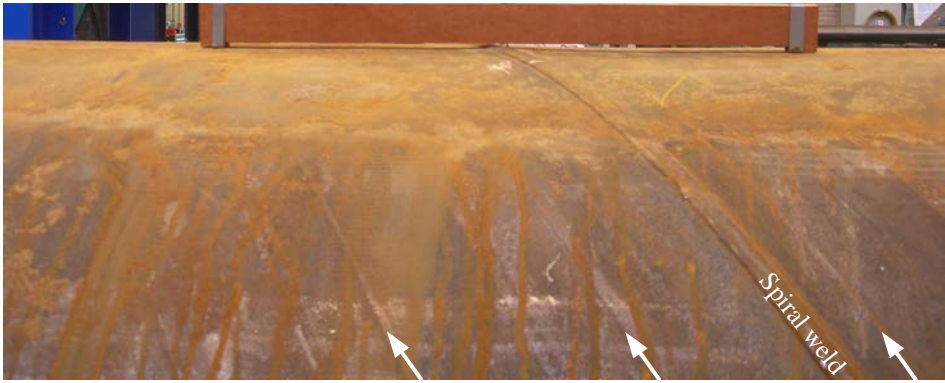
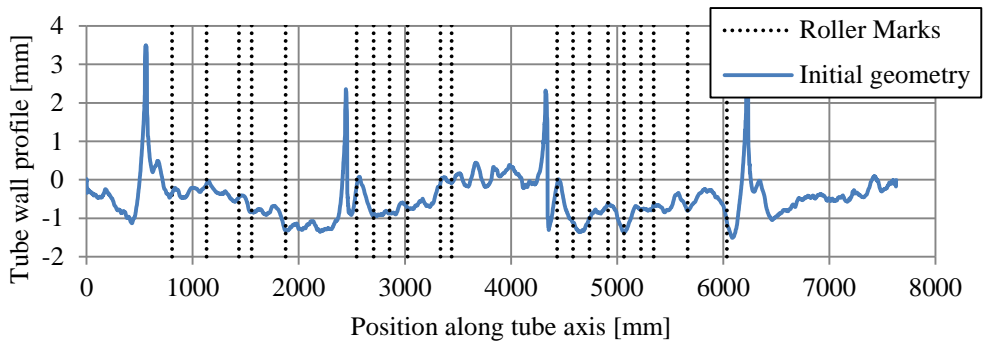
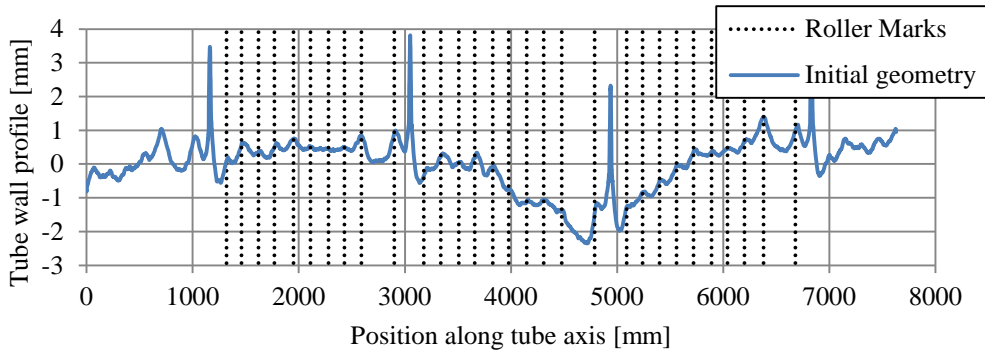


Figure 5.14 Photo of specimen T1 featuring roller marks. The visible marks are indicated by arrows.



(a) Specimen T1 at orientation 0°



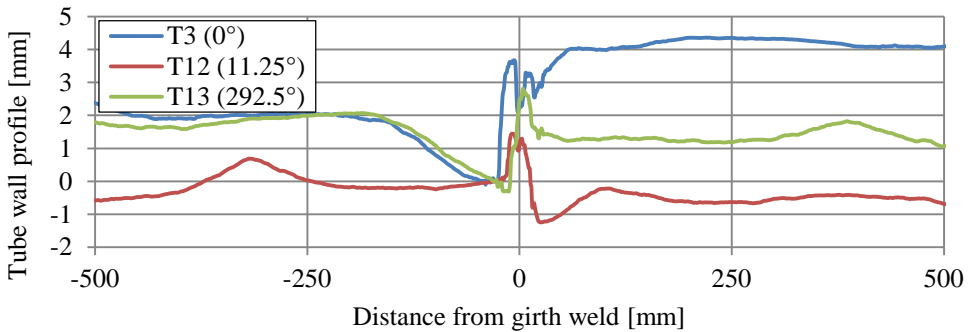
(b) Specimen T11 at orientation 22.5°

Figure 5.15 Initial imperfect geometry of tubular specimens with roller mark overlay.

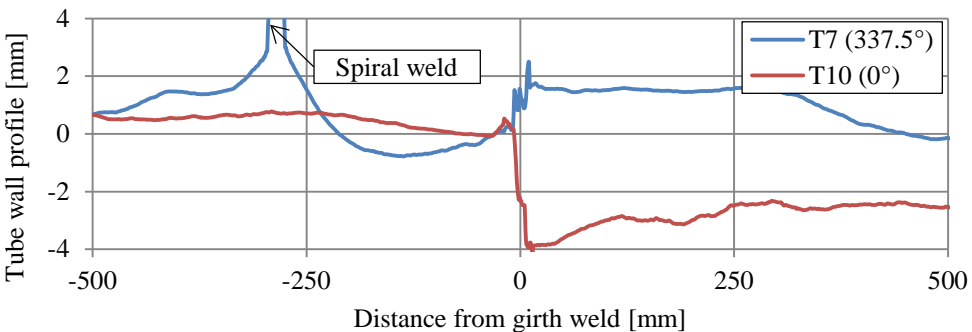
Tubes with girth or coil connection welds or both

The presence of girth or coil connection welds introduces additional imperfections which, if exceeding certain sizes, may result in local buckling at these welds instead of in the adjacent plain tube sections. In pipeline applications, tubes connected by girth welds are usually aligned with internal clamps and welded fully automatically. However, in many structural applications, the use of advanced clamping equipment to minimize misalignments of the tube wall is not as common. Furthermore, manual welding may take place on site. Therefore, misalignments at the girth weld are expected to occur. On the other hand, welding of the coil connection weld is performed in a controlled environment in the spiral mill, so that significant misalignments are far less likely to occur. For both welds, the formation of geometrical imperfections due to weld shrinkage is possible.

A comparison of examples of initial imperfections at girth welds is presented in Figure 5.16. Similarly as in the geometry profile diagrams of plain tubes, the lines can be assumed to represent the middle surface of the shell, with the exception of weld caps. The figures show that in many cases a misalignment of the two adjoining tube walls occurs. In addition, an inward geometrical imperfection may be present, probably caused by weld shrinkage.



(a) Scans of specimens T3, T12 and T13, all with a wall thickness of 9 mm

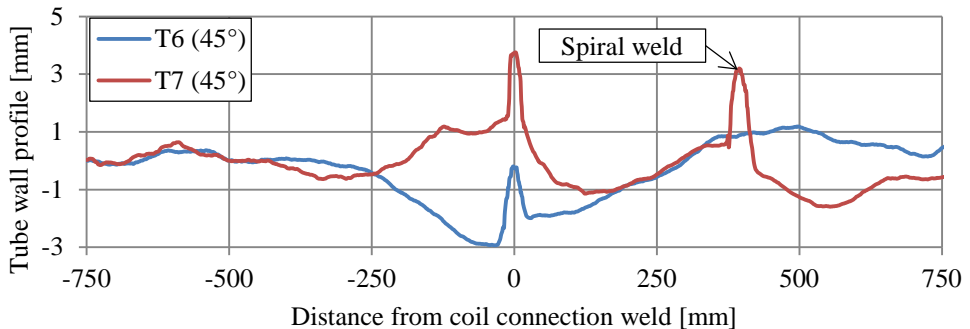


(b) Scans of specimens T7 ($t=16$ mm) and T10 ($t=13$ mm)

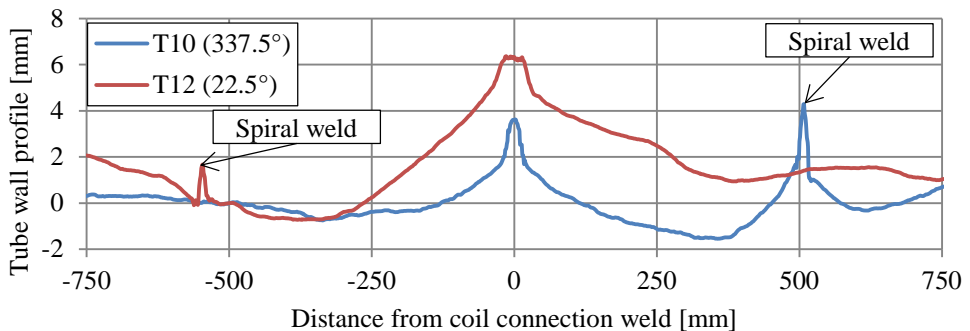
Figure 5.16 Examples of geometrical imperfections in the vicinity of a girth weld.

The tube wall profile of specimen T3 (see Figure 5.16a) shows a misalignment of about 3 mm directly at the girth weld, which is 33% of the wall thickness for that particular specimen. If the misalignment is determined at a distance of 250 mm from the girth weld, the misalignment is reduced by 30% to about 2 mm. In fact, the observed imperfection shape can be interpreted as a combination of a misalignment and an additional imperfection, possibly caused by weld shrinkage. A similar effect can be observed in the imperfection scans of T12, T13 (see Figure 5.16a) and T7 (see Figure 5.16b).

In Figure 5.17, examples of the initial geometrical imperfections near coil connection welds are presented. Apparently, the coil connection welds tend to bulge outwards of the tube. The imperfections near these welds appear to be equal in size or larger than the geometrical imperfections caused by the spiral welding. For example, Figure 5.17a includes a scan of a spiral weld in the scan of specimen T7, and Figure 5.17b includes a spiral weld in both example scans. An exception to this general trend is found in specimen T6, where the coil connection weld does not bulge outwards, but shows a tube wall profile bending inwards (see Figure 5.17a). Considering that the top of the weld bead coincides exactly with the surrounding plate material, it is likely that this weld was forced inwards during manufacturing, transportation or storage. In addition, this specimen also shows a misalignment at the coil connection weld.



(a) Specimens T6 and T7, both with a wall thickness of 16 mm



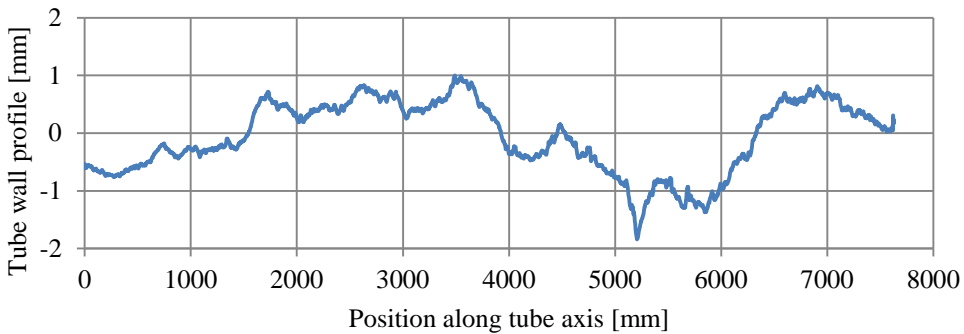
(b) Specimens T10 ($t=13$ mm) and T12 ($t=9$ mm)

Figure 5.17 Examples of geometrical imperfections in the vicinity of a coil connection weld.

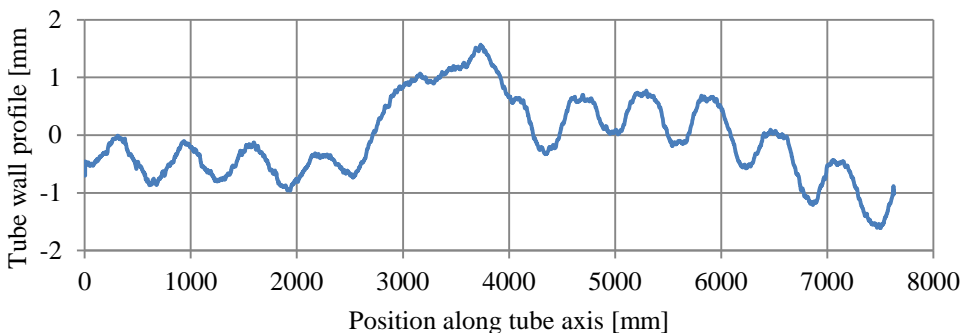
The tube wall profiles shown in Figure 5.16 and Figure 5.17 are a selection of the available data that are most fit to visualize the overall behaviour. The figures do not necessarily depict the wall profiles that were present at the compression side of the cross-section in the bending test.

Longitudinal-welded UOE tubes

The tube wall profiles measured on the two available UOE tubes have a different appearance than the results obtained from the spiral-welded tubes. Naturally, the spiral welds are absent. Furthermore, also the regular repeating pattern of geometrical imperfections related to the spiral-welding process is not observed, because the specific features that cause these imperfections are absent in the UOE manufacturing process. Two examples of an initial tube wall profile are depicted in Figure 5.18. The graphs clearly show a different tube wall profile than was observed in the results of measurements on the spiral-welded tubes. The tube wall profile of specimen T14 appears irregular and features a small dent at position 5200 mm (see Figure 5.18a). The tube wall profile of specimen T15 features a very regular wave shape, which is interrupted for about 1.5 meters in the centre of the specimen. Likely, the explanation for this regular shape can be found in the manufacturing process of the tubes as was also the case for the spiral-welded tubes.



(a) Specimen T14 at orientation 157.5°



(b) Specimen T15 at orientation 315°

Figure 5.18 Examples of geometrical imperfections in longitudinal-welded UOE tubes.

Dents

In a few specimens, a dent was observed. There are many possible causes for such dents. Identifying the cause for a particular dent is not straightforward, since the history of the tubes is not known. It is assumed that they are the result of handling and transportation.

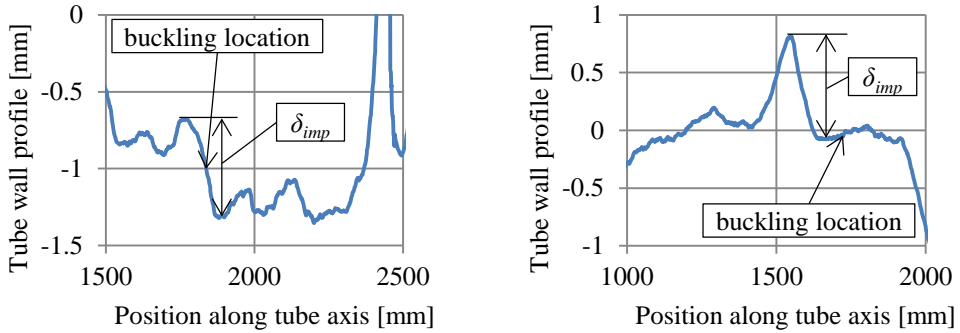
The research that was performed within the COMBITUBE project mainly focuses on the behaviour of spiral-welded tubes. Because only limited experimental investigation was performed relating to this type of tubes (see section 1.3.2), the more general influence of dents on the local buckling resistance of tubes is not included in the present experimental study. To achieve this, only minor dents were accepted in the specimens and the dents that were present were not placed at the intrados of the specimen, where compressive bending stresses occur. Dents are not analysed further in this study, but are included in the numerical parameter study performed by research partners at the University of Thessaly (see section 6.5).

Quite a large number of dents was observed during the imperfection measurements at the construction site. In section 5.2.6, the dents that were found in the laboratory specimens are compared with the dents found at the construction site.

Quantification of imperfection sizes

The data resulting from the initial geometrical imperfection measurements on the test specimens, together with similar measurements performed by research partners at the Karlsruhe Institute of Technology, were carefully analysed using a combination of single and double Fourier series to assess the dominant imperfections modes and the corresponding amplitudes (Sadowski et al., 2014). For the full results of that study, the reader is referred to the original article.

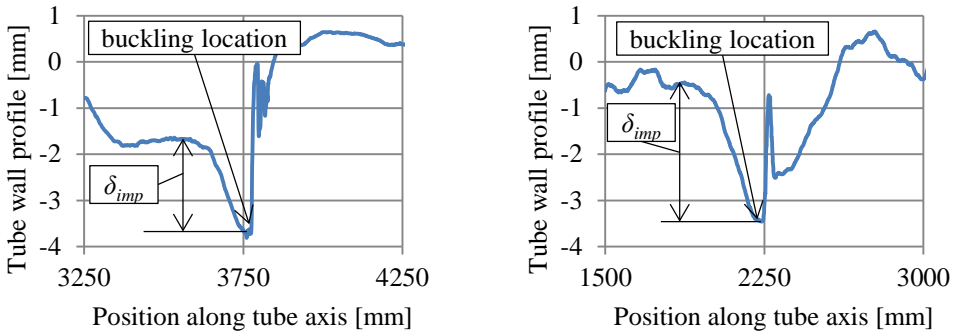
In this study, the geometrical imperfection sizes were quantified in a more simple manner. This allows direct comparison of the observed imperfections with more simple imperfections such as for example dents. Furthermore, because this simple quantification method used only one parameter, the results of the analysis are easily used in a finite element analysis (see section 6.5). For each specimen, the geometrical imperfections were quantified by a single value δ_{imp} . For plain specimens, this was determined as the vertical distance between a high-point and a low-point in the tube wall profile close to the buckling location. Examples of this procedure are presented in Figure 5.19.



(a) Measurement of value of δ_{imp} for tube T1. For full tube wall profile see Figure 5.15a
 (b) Measurement of value of δ_{imp} for tube T2. For full tube wall profile see Figure 5.13a

Figure 5.19 Examples of determination of imperfection size at buckling location.

The quantification of the geometrical imperfections at girth welds and coil connection welds is somewhat more complicated due to the previously discussed possible combination of a misalignment with an additional geometrical imperfection. For these tubes, the values of the imperfection size δ_{imp} were chosen such that they sufficiently capture the overall geometrical imperfections. Two examples of the procedure to determine the value of δ_{imp} at a girth weld and coil connection weld are presented in Figure 5.20.



(a) Measurement of value of δ_{imp} for tube T3. For tube wall profile also see Figure 5.16a
 (b) Measurement of value of δ_{imp} for tube T6. For tube wall profile also see Figure 5.17a

Figure 5.20 Examples of determination of imperfection size at buckling location.

An overview of all measured values for δ_{imp} is presented in Table 5.3. The average value of δ_{imp} measured at geometrical imperfections relevant for local buckles that formed in a plain tube section is 8.4% of the tube wall thickness, while the average value of δ_{imp} measured at geometrical imperfections relevant for local buckles that formed at a coil connection weld or girth weld is 22.9% of the tube wall thickness. Note that two specimens did include a coil connection weld or girth weld, but failed in local buckling away from these details (T7 and T12).

The measured value of δ_{imp} at the buckling location, which was in a plain tube section, is much higher than the average for plain tube sections.

Although the appearance of the initial geometrical imperfections in the longitudinal-welded tubes was quite different from what was seen in the measurements on spiral-welded tubes, the measured values of δ_{imp} correspond quite well. The average value of δ_{imp} for plain spiral-welded tubes is 8.5% of the tube wall thickness, while the average value if δ_{imp} for the two longitudinal tubes is 7.9% of the tube wall thickness. In the analysis of the measured initial imperfections by Sadowski et al. (2014), it is similarly concluded that although there are distinct differences in geometrical imperfections between spiral-welded and longitudinal-welded tubes, the overall wave-length and amplitude of the imperfections in both tube types are comparable.

Table 5.3 Overview of determined values of δ_{imp} near the local buckling location.

Specimen	Type	Layout	Buckling location	D/t [-]	δ_{imp} [mm]	δ_{imp}/t [%]
T1	Spiral	Plain	Plain	65.1	0.6	3.6
T2	Spiral	Plain	Plain	118.3	0.8	9.0
T3	Spiral	GW	GW	118.8	1.8	20.0
T4	Spiral	Plain	Plain	116.2	0.55	6.0
T5	Spiral	Plain	Plain	118.3	0.65	7.2
T6	Spiral	CCW	CCW	65.7	3.0	18.6
T7	Spiral	GW/CCW	Plain	65.5	1.8	11.0
T8	Spiral	Plain	Plain	117.4	1.05	11.6
T9	Spiral	Plain	Plain	65.4	1.5	9.2
T10	Spiral	GW/CCW	GW	81.5	3.6	27.4
T11	Spiral	Plain	Plain	83	0.8	6.2
T12	Spiral	GW/CCW	Plain	116.8	1.15	12.7
T13	Spiral	GW	GW	117	2.35	25.5
T14	UOE	Plain	Plain	108.8	1.0	10.0
T15	UOE	Plain	Plain	72.3	0.85	5.7

5.2.6 Results of measurements of geometrical imperfections at a building site

A typical result of a scan of a plain section of a tube is presented in Figure 5.21. The figure shows that for this particular scan, four passes were made. The result of pass 1 is slightly different than the others, which is a result of the relatively sensitive equipment (see section 5.2.1). A suitable filtered result is obtained by selecting the trimmed mean over the four passes at each position along the horizontal axis.

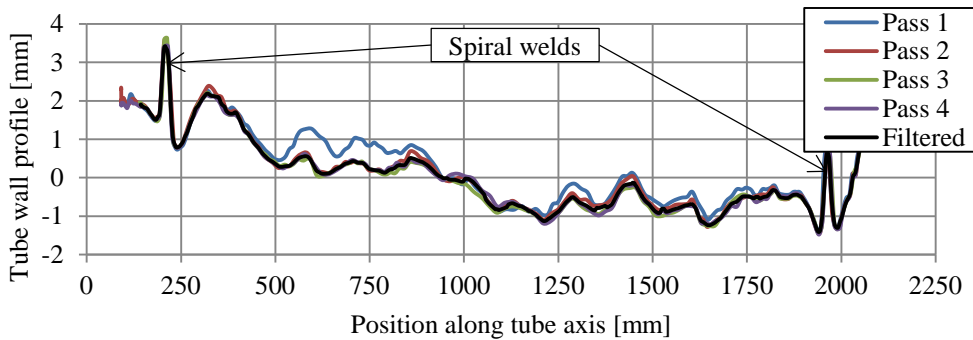


Figure 5.21 Scan of a $1220 \times 11.2 \text{ mm}^2$ tube featuring two spiral welds.

Discussion of observed conditions of tubes in practical use

The tubes that were used for experimental work in the laboratory were for the greater part undamaged and unaltered. As discussed in section 5.2.1, uncertainty exists about whether the tubes that were tested in the laboratory are representative of tubes in structures. Before the measurements of geometrical imperfections performed in the laboratory and at the construction site are compared, firstly the overall condition of the tubes at the construction site is discussed.

During selection of suitable tubes to measure at the construction site, it was noted that the number of tubes showing some kind of damage was higher than expected on the basis of the tubes available in the laboratory. Observed damages include dents, scratches or a combination of both. Some examples of these damages are presented in Figure 5.22.

Especially the combination of a dent and a scratch is interesting, because this was not observed in the laboratory. It is assumed that these damages occurred during excavation of the building pit, which was done by hydraulic excavators in this particular case. If this assumption is justified, these damages will not influence the local buckling resistance of the tubes in case of an anchored combined wall, because they then in principle only occur on the tensile side of the cross-section (see Figure 5.23). If the damages are the result of some other cause, such as rough handling, or if the tubes are re-used, the damages may occur at any location in the tube, which may have consequences for the local buckling resistance of the tube. These effects were not studied by the four-point bending experimental programme (see section 5.4.1) but are included in a parameter study performed by research partners at the University of Thessaly (see section 6.5).

It must be noted that only one construction site was visited. Therefore, the observed conditions of the tubes in practical use are not necessarily typical for all combined walls. In other structures, more strict quality procedures may result in considerably improved conditions of the tubes.

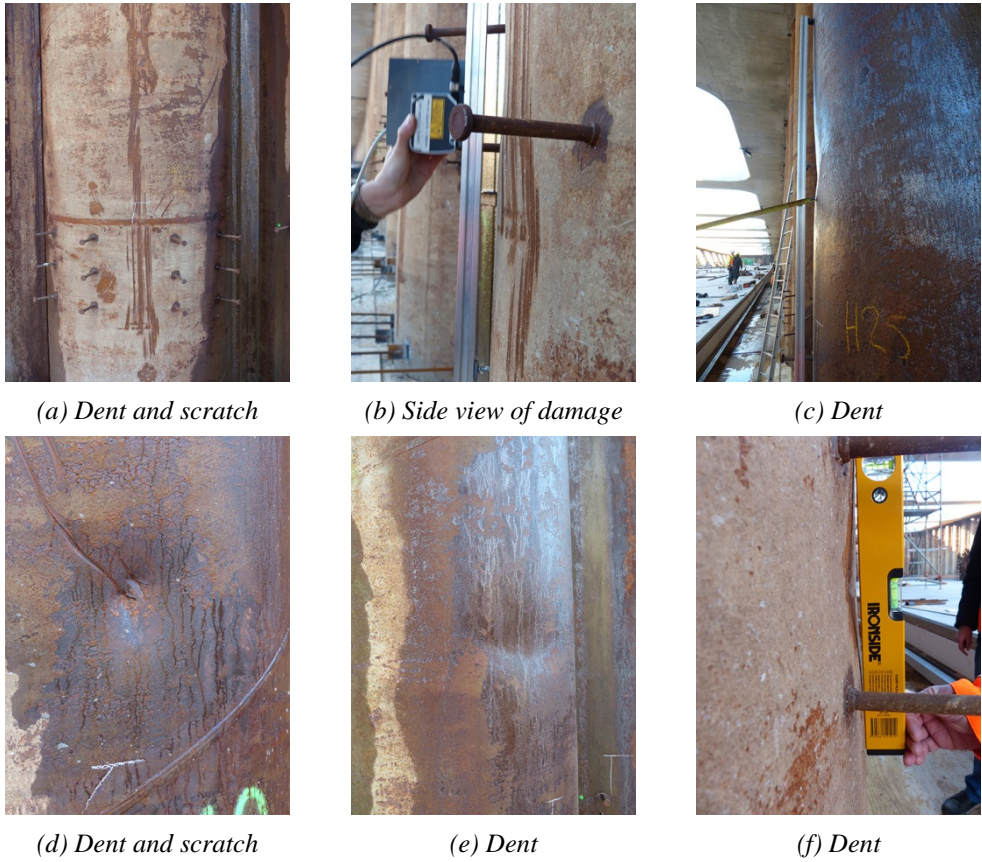


Figure 5.22 Overview of observed damages in tubes found at construction site.

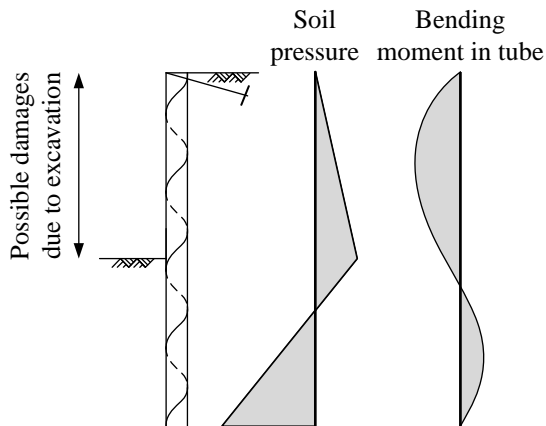


Figure 5.23 Sketch of typical soil pressures against a combined wall and the resulting bending moments in the tube compared with the area in which damages due to excavation may occur.

Another feature of the tubes that was observed in practice, which is not included in the laboratory tests or even the numerical parametric study of Vasilikis et al. (2016), is that welded attachments are present. During inspection of the construction site, a wide range of welded attachments to the tubes was observed. These attachments range from structural necessities, such as steel studs to aid shear force transfer between the tube and the concrete wall that will be placed in front and attachment of reinforcement bars to ad-hoc solutions to problems encountered by the construction crew, such as for example a temporary step. Examples of found welded attachments are presented in Figure 5.24.

The influence of the welded attachment was not part of the COMBITUBE research, and therefore any influence on the local buckling resistance of the tubes is unknown. In case a negative effect of welded attachments is expected, these attachments can simply be omitted at the compressive side of the cross-section in areas where the tube is loaded in high bending moments. Furthermore, the ad-hoc solutions, such as the crew step as shown in Figure 5.24c, can only be expected in certain areas and usually not at the compression side of the cross-sections. Similarly as for the excavation damages, once tubes are re-used, no areas of the tube can be guaranteed to be free from any influence without inspection.

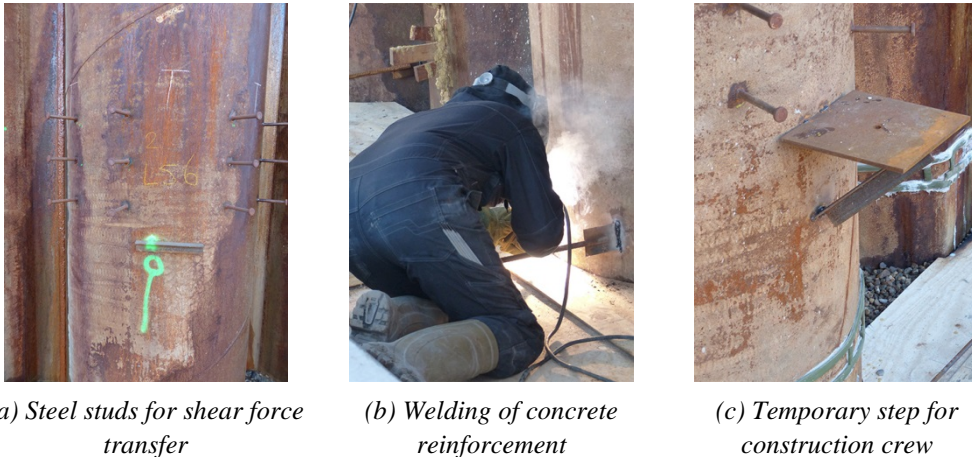


Figure 5.24 Overview of welded attachments observed at the construction site.

Plain spiral-welded tubes: results and comparison with laboratory measurements

Similarly as observed in the laboratory specimens, a repeating pattern of geometrical imperfections in between the spiral welds was found in the scans made at the construction site. To illustrate this, two scans of the same tube at different locations are compared in Figure 5.25. Although the match is not exact, the similarities between the two tube wall profiles are evident.

Due to the applied measuring methods (see section 5.2.1), only relatively short scans of the tube geometry were available. Furthermore, a relatively low number of geometry scans was available per tube. For these two reasons, the analysis method applied by Sadowski et al. (2014) could not be applied to these results. Instead, by visual comparison it was determined whether tubular specimens in the laboratory were a good representation of tubes in practical applications. For this, the field measurements were overlaid with three measurements from the laboratory

covering the full spectrum of considered D/t ratios. Two examples of such a comparison are presented in Figure 5.26. In these comparisons, no notable differences between the laboratory and field measurements were noted in terms of imperfection wave-length or amplitude.

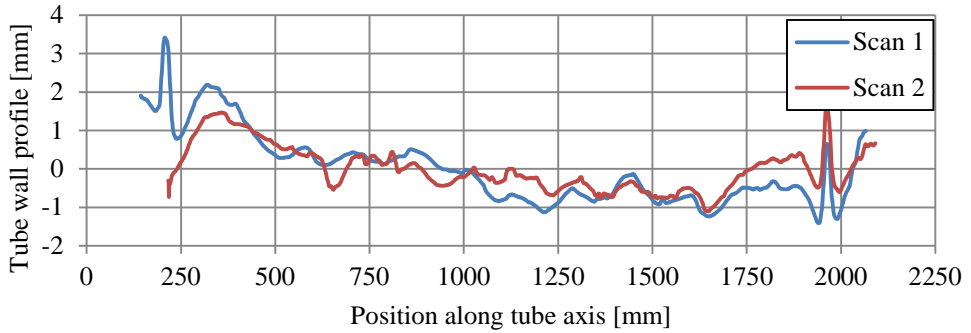
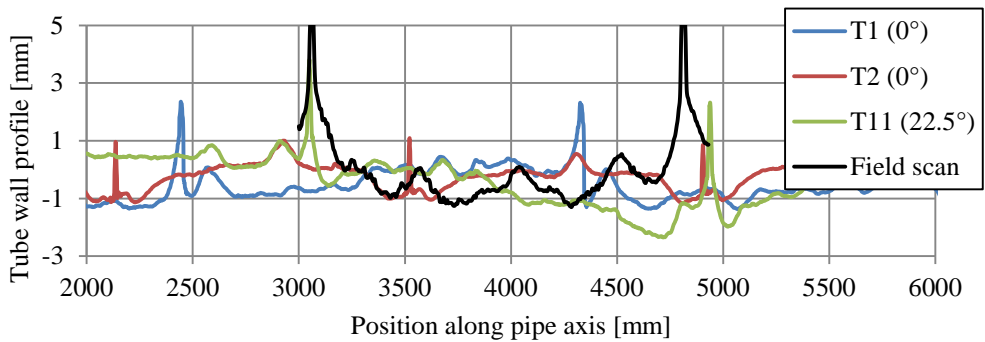
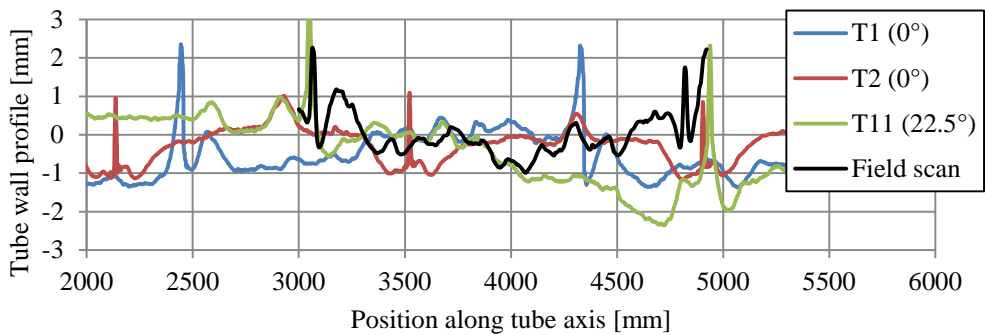


Figure 5.25 Overlay of two scans of the same tube at different locations. Tube dimensions: $1220 \times 11.2 \text{ mm}^2$.



(a) Comparison with field measurement of a tube with dimensions $1220 \times 12.7 \text{ mm}^2$

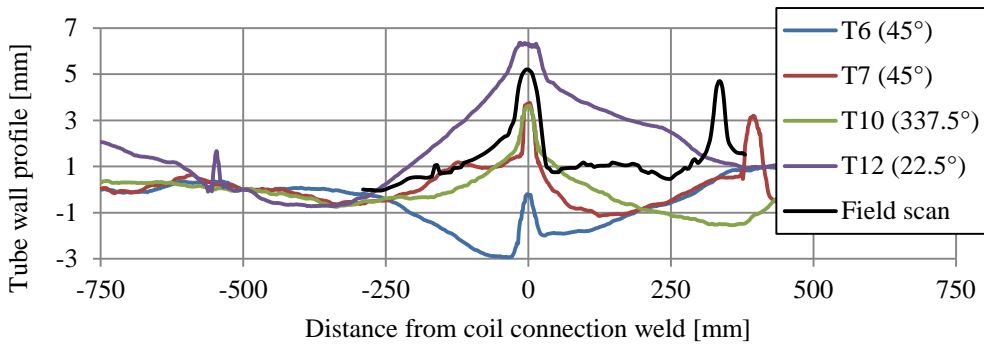


(b) Comparison with field measurement of a tube with dimensions $1220 \times 11.2 \text{ mm}^2$

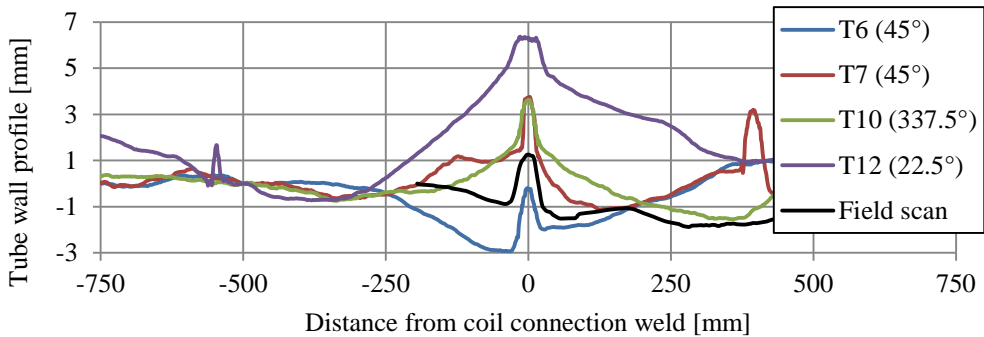
Figure 5.26 Visual comparison between laboratory measurements and field measurements.

Tubes with girth or coil connection welds: results and comparison with laboratory measurements

To make a comparison of the geometry of the tube wall near a coil connection weld between tubes at the construction site and tubes in the laboratory, overlay images were used, similarly as was done for the plain tubes. This method does not yield quantifiable results, but allows a visual comparison of the measured tube wall profiles. The two scans made of one coil connection weld at the construction side are compared with the laboratory measurements in Figure 5.27. The geometry of the tube wall as measured at the construction site does not seem to differ significantly from the geometries as measured in the laboratory.



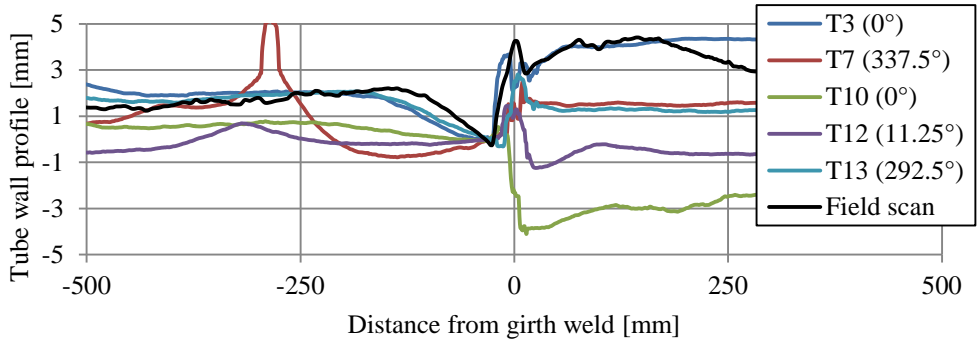
(a) Comparison with first field measurement of tube



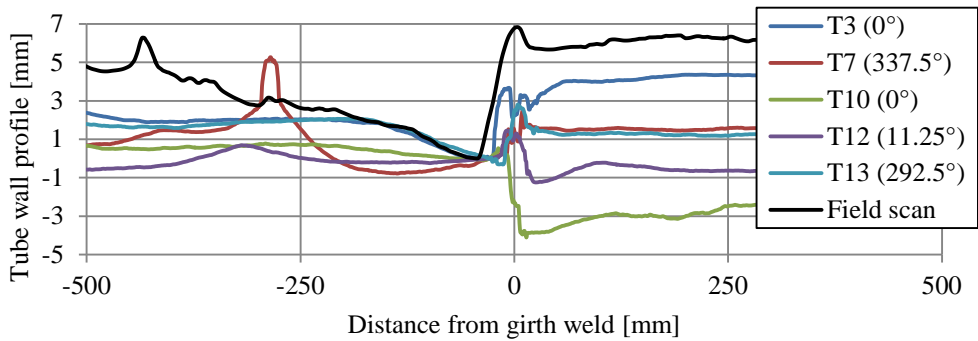
(b) Comparison of second field measurement of tube

Figure 5.27 Visual comparison between laboratory measurements and two field measurements of a tube with dimensions $1220 \times 11.2 \text{ mm}^2$ containing a coil connection weld.

In a similar way, the tube wall profile near girth welds as measured at the construction site was compared to the laboratory measurements. Two examples of such a comparison are presented in Figure 5.28. In general, the geometry of the tube wall near a girth weld does not appear to be very different at the construction site than in the laboratory. Figure 5.28 shows a larger misalignment in case of the tube at the construction site, but such relatively small differences are easily dealt with in a parametric study using a validated model.



(a) Comparison with field measurement of first tube

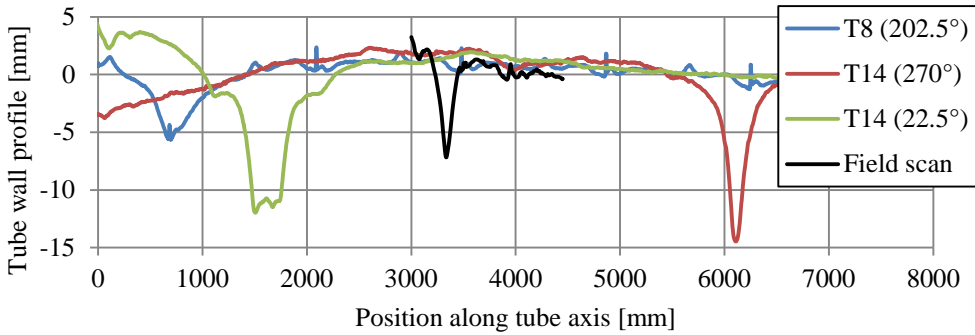


(b) Comparison with field measurement of second tube

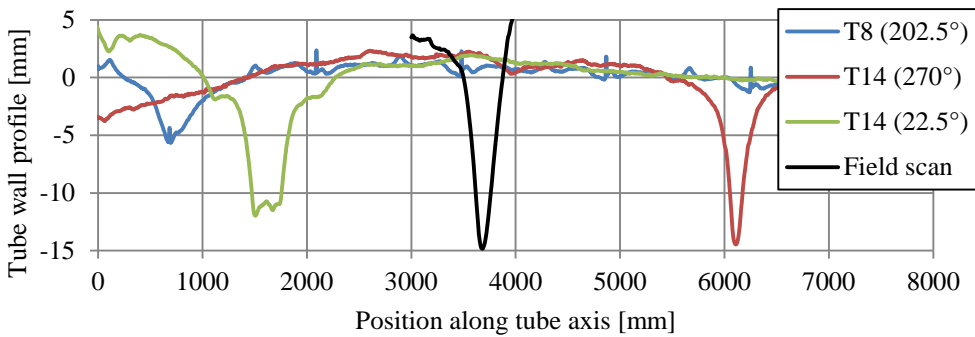
Figure 5.28 Visual comparison between laboratory measurements and field measurements of two tubes with dimensions $1220 \times 12.7 \text{ mm}^2$ containing a girth weld.

Dented tubes: results and comparison with laboratory measurements

As noted earlier, the number of dents that were spotted at the construction site was larger than expected on the basis of observations on the laboratory specimens. One spiral-welded laboratory specimen and one longitudinal-welded specimen showed a dent. Because the observed dents are assumed to be independent of the tube manufacturing process, a direct comparison between spiral-welded and longitudinal-welded specimens is possible. Two examples of a comparison between the dents observed at the construction site and the dents observed in the laboratory specimens are presented in Figure 5.29. The dents at the construction site appear to be similar to the dents in the laboratory. Especially the dent in the laboratory specimen T14 at orientation 270° appears to be very similar to the dents observed at the construction site.



(a) Comparison between laboratory measurements and field measurement of first tube



(b) Comparison between laboratory measurements and field measurement of second tube

Figure 5.29 Visual comparison between laboratory measurements and field measurements of two tubes with dimensions $1220 \times 11.2 \text{ mm}^2$ containing a dent.

Conclusion

The measurements that were performed at the construction site near the A4 motorway show that the tubes that were tested in the laboratory appear to be representative of practical applications with the exceptions of dents, scratches and welded attachments.

The dents and scratches that were observed at the construction site, likely caused by excavation, will generally occur at the tensile side of the cross-section and therefore are not expected to have a significant influence on the local buckling resistance of the tubes. However, in case of re-use of tubes or dents resulting from other causes, these imperfections may occur at any location within the tube.

At the investigated construction site, welded attachments only occurred at the tensile side of the cross-section. It is expected that welded attachments are removed in case of re-use of the tubes. However, it is not certain whether this fully neutralizes the possible negative effects of the welded attachments. The removal of the attachment may result in new imperfections due to for example grinding and residual stresses caused by welding may remain present in the tube.

Therefore, in case of re-use, such welded attachments may influence the local buckling resistance of the tubes.

To what extent the presence of dents, scratches and present or removed welded attachments at the compression side of the cross-section significantly influences the local buckling resistance of the tubes may be subject of further research.

5.3 Material testing

5.3.1 Programme

From each specimen, the material mechanical behaviour was thoroughly investigated. The investigation included tensile tests on all specimen parts, supplemented by compression tests on material from a selection of tubes. The aim of the programme was to gather information on:

- The material mechanical behaviour of the tested specimens to aid correct modelling
- Certain aspects of the material behaviour of spiral-welded tubes such as e.g.: anisotropy, Y/T ratio, etc.
- The behaviour of the tube material under compression, specifically the presence of a Bauschinger effect.

Tensile testing

For each tubular specimen, tensile tests were performed in the longitudinal direction of the tube axis and in the circumferential (hoop) direction, from both the inside and outside of the tube wall. These specimens had a thickness of 3 mm and were machined from the tube wall, so that flattening of the reduced section of the tensile coupons was not necessary (see Figure 5.30). Plate material for these specimens was taken out of the tubular specimens in each specimen part at the neutral line after the four-point bending test. Material close to the buckle was taken out at sufficient distance to eliminate influence of the large plastic deformations that were present in the buckling area (see Figure 5.31).

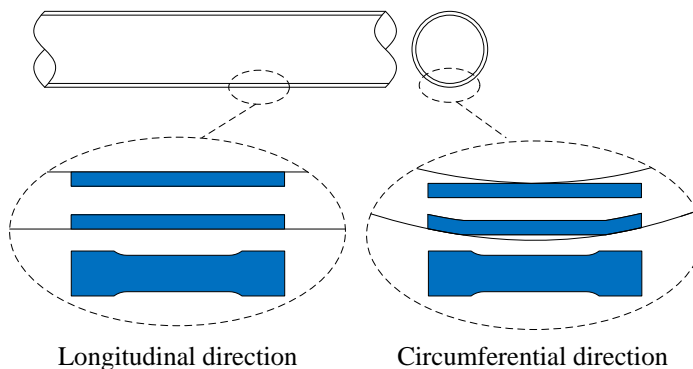


Figure 5.30 Extraction of tensile coupons on the inside and outside of the tube wall.

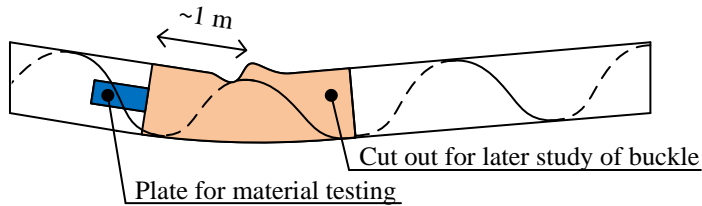


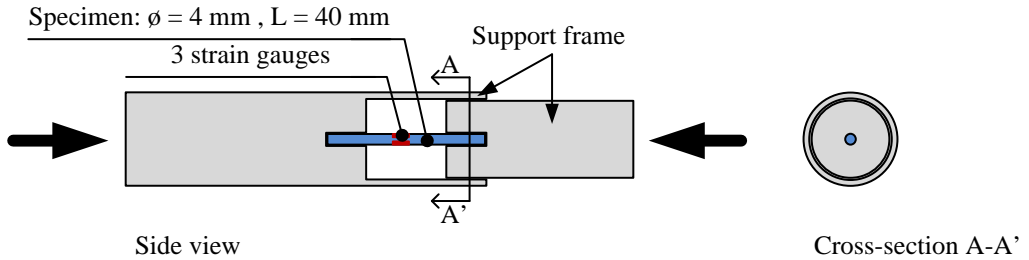
Figure 5.31 Extraction of material for material testing near local buckle.

In addition, from several specimens, tensile coupons with a thickness equal to the tube wall thickness were extracted from the rings that were used for the estimation of residual stresses (see section 5.2.1). These full thickness specimens were oriented in both longitudinal and hoop direction. Additional full thickness specimens were taken in the direction axial and perpendicular with respect to the original coil. In the tube, these specimens were oriented parallel and perpendicular to the spiral welds. Finally, tensile testing of small specimens extracted from the spiral welds was also conducted. All tensile tests were performed in accordance with ISO 6892-1 (2009).

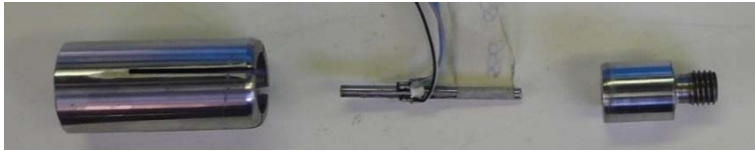
Compressive testing

Compression material tests were performed on several tubes, to examine whether the tension and compression behaviour of the material is symmetrical. To perform compression tests, small cylinders were machined from the tube wall, and compressed while being supported against rotation on either end. An overview of the compressive test setup is presented in Figure 5.32. To measure the deformation of the specimen, three strain gauges were applied. The reported strain is the average of the three applied strain gauges. Even though the compression specimens were supported against buckling, instability is unavoidable upon approaching or reaching the yield strength of the material, due to the extreme reduction in bending stiffness of the specimens in that situation. Because the specimens could not be observed during the test, the exact moment of buckling of the specimens could not be determined. However, bending in the specimen is detected by the three strain gauges. When one strain gauge starts deviating significantly from the other two, the specimen exhibits bending. In the results, this point is marked in the graphs. After this marker, the specimen may have been laterally unstable to some extent.

From each set of tubular specimens which were deemed to be similar (see section 5.1.1), one tubular specimen was selected for compression tests. From these selected tubes, compression specimens were machined in longitudinal and hoop direction, at the inside and outside of the tube wall.



(a) Schematic overview of compression test setup



(b) Photo of specimen with support frame

Figure 5.32 Overview of compression test setup with a cylindrical specimen fitted with strain gauges.

5.3.2 Results and analysis

Results and analysis of tensile tests

An overview of the results of the tensile tests on machined partial-thickness coupon specimens is presented in Table 5.4 in terms of tensile yield stress corresponding to 0.2% plastic strain. More tensile tests results are presented in Appendix F.1. The results show that, on average, the axial yield strength is 6.7% higher than the yield strength in hoop direction. Furthermore, the yield strength on the inside of the tube wall is about 3.7% lower than on the outside of the tube wall. These values differ among the tubular specimens, but show similarities among tubes which were deemed to originate from the same production batch (see section 5.1.1). These differences are of such limited magnitude, that in practice the tubes can be assumed to be isotropic. Furthermore, no clear differences were observed between spiral-welded tubes and longitudinal-welded tubes.

As discussed in section 5.3.1, tensile tests were performed on strip coupon specimens extracted in the axial direction and hoop direction, as well as on the inside and the outside of the tube wall. Because the main loading during the tests is in longitudinal direction, the reference yield strength ($\sigma_{y,ref}$) of a specimen or specimen part is defined as the average yield strength ($\sigma_{0.2\%}$) of the machined specimens in the axial direction. This reference yield strength is used for normalization purposes later in this study.

Table 5.4 Overview of measured tensile yield stress ($\sigma_{0.2\%}$) in MPa from machined partial-thickness specimens.

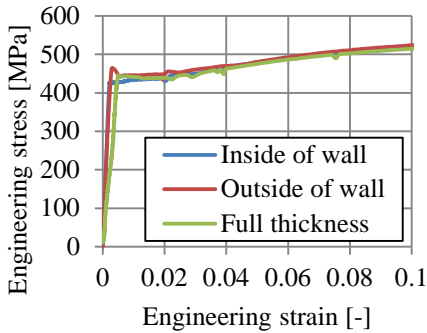
Specimen	Specimen part	Type	Layout	Inside of wall		Outside of wall	
				Axial	Hoop	Axial	Hoop
T1		Spiral	Plain	510	508	555	584
T2		Spiral	Plain	401	379	412	374
T3	Left	Spiral	GW	381	326	403	392
	Right			431	374	436	393
T4		Spiral	Plain	427	389	455	408
T5		Spiral	Plain	419	411	379	400
T6	Left	Spiral	CCW	550	508	505	534
	Right			520	519	573	576
T7	Left	Spiral	GW/CCW	605	497	622	585
	Middle			614	452	594	573
	Right			623	529	592	550
T8		Spiral	Plain	448	421	457	413
T9		Spiral	Plain	609	510	617	555
	Left			527	476	559	538
	Middle			521	450	489	486
T10	Right	Spiral	GW/CCW	329	304	336	340
T11		Spiral	Plain	343	326	357	334
T12	Left	Spiral	GW/CCW	453	416	441	421
	Middle			499	472	516	467
	Right			436	414	462	423
T13	Left	Spiral	GW	440	403	446	412
	Right			461	423	464	434
T14		UOE	Plain	506	533	507	562
T15		UOE	Plain	530	521	541	550

The comparison between the results obtained from the machined specimens and the full thickness specimens is good. Some examples of this comparison are presented in Figure 5.33. In case a relatively large difference was found between the tensile tests on machined specimens from the inside and outside of the tube wall, the results from the corresponding full thickness specimen mostly lie in between. Because the full thickness specimens in hoop direction needed to be flattened before testing, in many cases the sharp transition between the elastic behaviour and the yield plateau disappeared, as shown in Figure 5.33d.

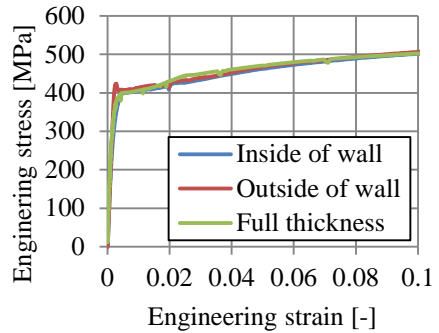
Considering the relatively small difference in material properties between the hoop direction and the longitudinal direction (see Table 5.4), it is not surprising that the differences between the results of the full thickness specimens in the direction parallel and perpendicular to the spiral weld and the principal directions of the tube are rather small. Some influence of the flattening of

the full thickness specimens in directions other than parallel to the tube axis creates some apparent additional anisotropy.

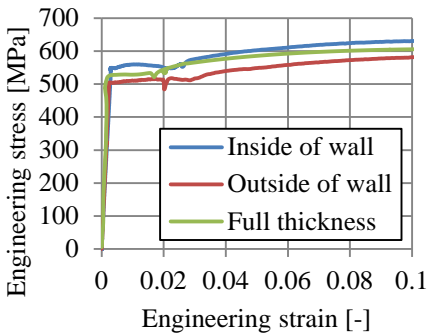
All specimens containing a girth weld or a coil connection weld consisted of two or more specimen parts. The material behaviour of these parts was not equal, leading to a strong and weak side of the weld. In most cases, the differences were small. An exception is specimen T10, which consists of two specimen parts with a measured yield strength over 500 MPa and one weaker part with a measured yield strength of 333 MPa (see Figure 5.34). This large difference was not expected beforehand.



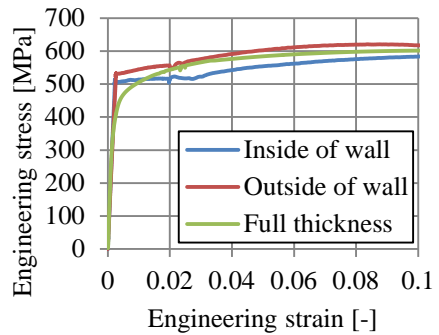
(a) Specimen T4 in axial direction



(b) Specimen T4 in hoop direction



(c) Specimen T6 in axial direction



(d) Specimen T6 in hoop direction

Figure 5.33 Comparison of tensile tests from machined specimens with full thickness specimens.

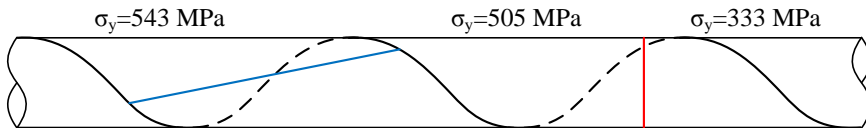


Figure 5.34 Sketch of specimen T10 featuring a girth weld connection two specimen parts of significant different measured yield strength.

The strength of the weld material was also measured. An example of the comparison of the spiral weld material behaviour and the surrounding tube wall is depicted in Figure 5.35. Over all three conducted tensile tests, the average overmatch of the spiral weld was found to be 20% on yield strength and 19% on tensile strength. Ductility of the weld material was found to be satisfactory with ultimate strain values ranging from 17% to 29%.

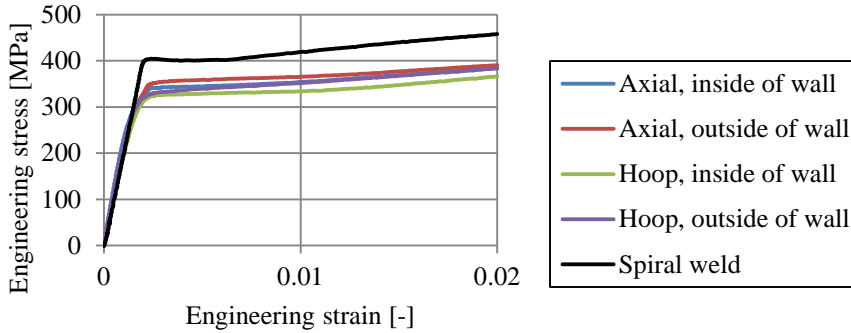


Figure 5.35 Comparison of properties of weld material and tube wall material for tube T11.

Results and analysis of compressive tests

The compressive tests were performed to verify whether the material behaviour found in the tensile tests is representative of the compressive behaviour of the steel. The latter is of interest for the research, as local buckling occurs in the area of the cross-section loaded in compression.

To make a direct comparison, the compressive coupon orientations and locations were chosen such that all specimens have a corresponding tensile test, so that a direct comparison could be made between the tensile and compressive material behaviour of the material. One example of the full results of a compression test and its corresponding tensile test is presented in Figure 5.36. The figure shows that upon reaching the yield plateau, bending occurred in the compressive specimen, meaning that buckling occurred or was imminent. Furthermore, the figure shows an excellent comparison between the pair of tensile and compressive tests.

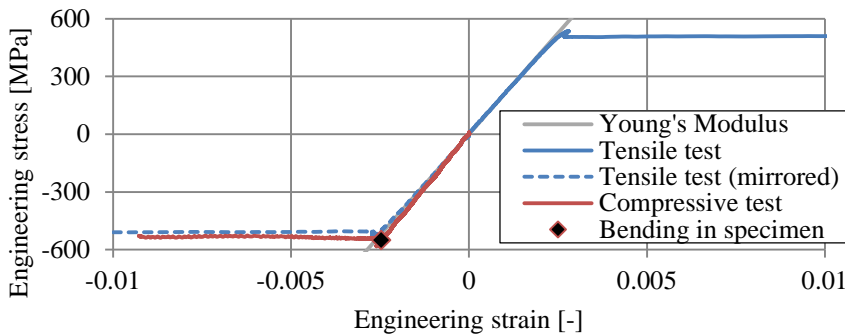


Figure 5.36 Results of compressive and tensile tests on coupons taken from specimen T1 in hoop direction on the inside of the tube wall.

Further compression tests on specimens taken from spiral-welded tubes are summarized in Figure 5.37. Results for specimens taken from longitudinal-welded tubes are presented in Figure 5.38. To enable a comparison between corresponding pairs of tensile and compressive tests, the tensile test results are depicted in the compression domain.

The results from the compressive tests on specimens taken from the spiral-welded tubes are quite similar to their tensile counterparts. Some compressive coupons exhibited premature buckling, such as T1_{axial;inside} and possibly T11_{axial;outside} (see Figure 5.37a and Figure 5.37e). A few specimens show a Bauschinger effect due to the straining of the tube wall during manufacturing of the tube. This behaviour is most notable on the outside of the tube wall, which is where the largest tensile strain occurred during manufacturing. In general it can be concluded that in the longitudinal direction of the tubes, the compressive stress-strain behaviour of the material can be assumed to be identical to the tensile stress-strain behaviour.

Similarly as for the specimens taken from the spiral-welded tubes, the results of the compressive tests on specimens taken in axial direction from the longitudinal-welded tubes appear to be quite similar to their tensile counterparts. It is possible, but not certain, that premature buckling occurred in specimen T15_{axial;outside}. In hoop direction, the results of the compressive tests performed on specimens taken from specimen T15 appear to show a strong Bauschinger effect. However, it must be noted that these tests were performed last in the series. Due to wear, the clamping effect of the support frame may have been reduced (see Figure 5.32). Furthermore, in case of specimen T15_{hoop,inside}, one strain gauge failed at the start of the test, decreasing reliability of the strain measurements.

Overall it can be concluded that in comparison with the spiral-welded tubes, the compressive behaviour of the longitudinal-welded UOE tubes in axial direction is similar. For both tube types, the compressive material behaviour closely matches the tensile behaviour. In hoop direction, for both tube types, some specimens show a Bauschinger effect. This appears to be more pronounced in the longitudinal-welded tubes than in the spiral-welded specimens. However, the significance of this observation is uncertain, for reasons stated above. Since the observed Bauschinger effect in the fifteen specimens is mostly minor and only observed in hoop direction, the influence of the Bauschinger effect on local buckling is assumed to be small.

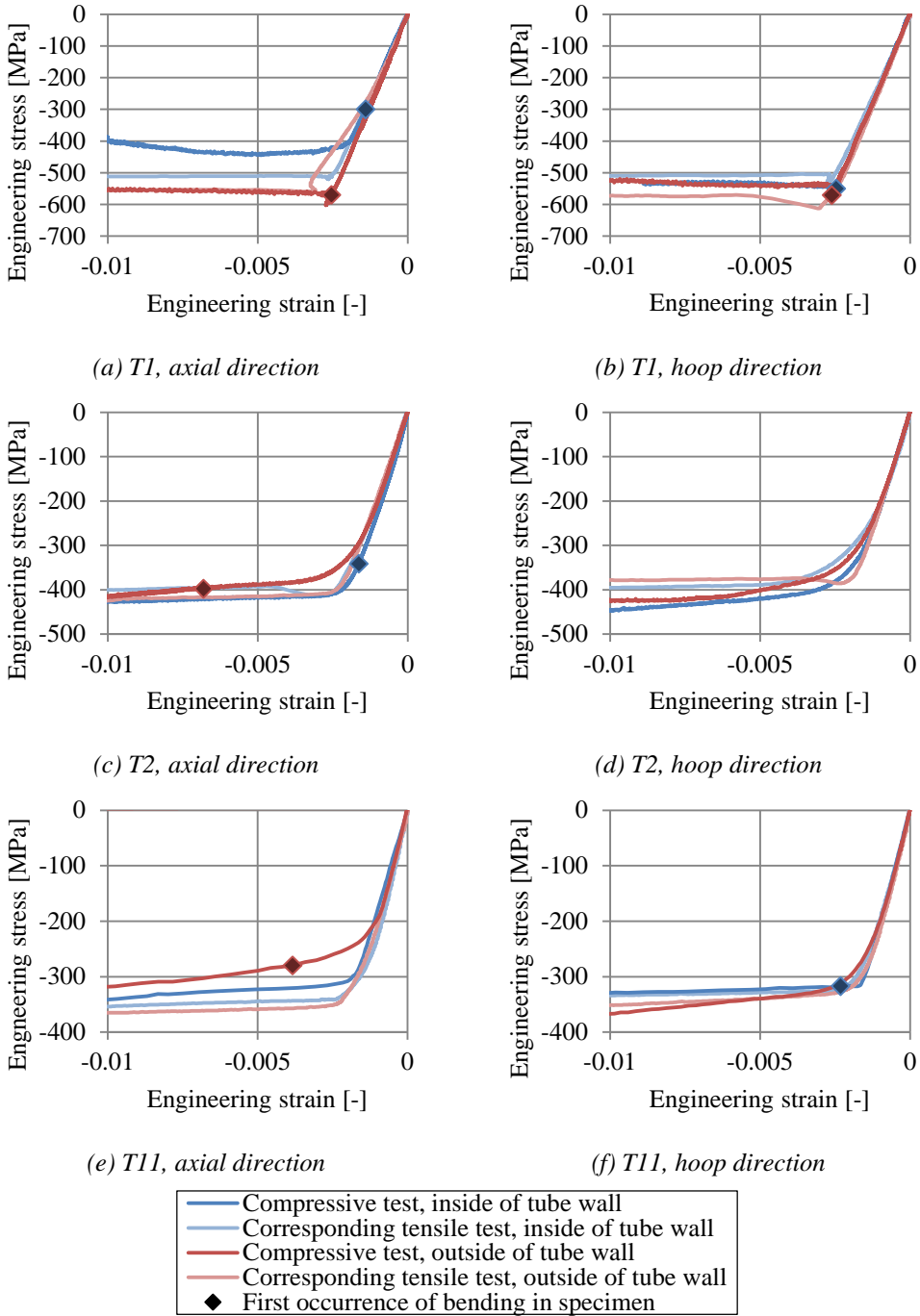


Figure 5.37 Results of compressive tests on specimens taken from spiral-welded tubes compared with results of corresponding tensile tests.

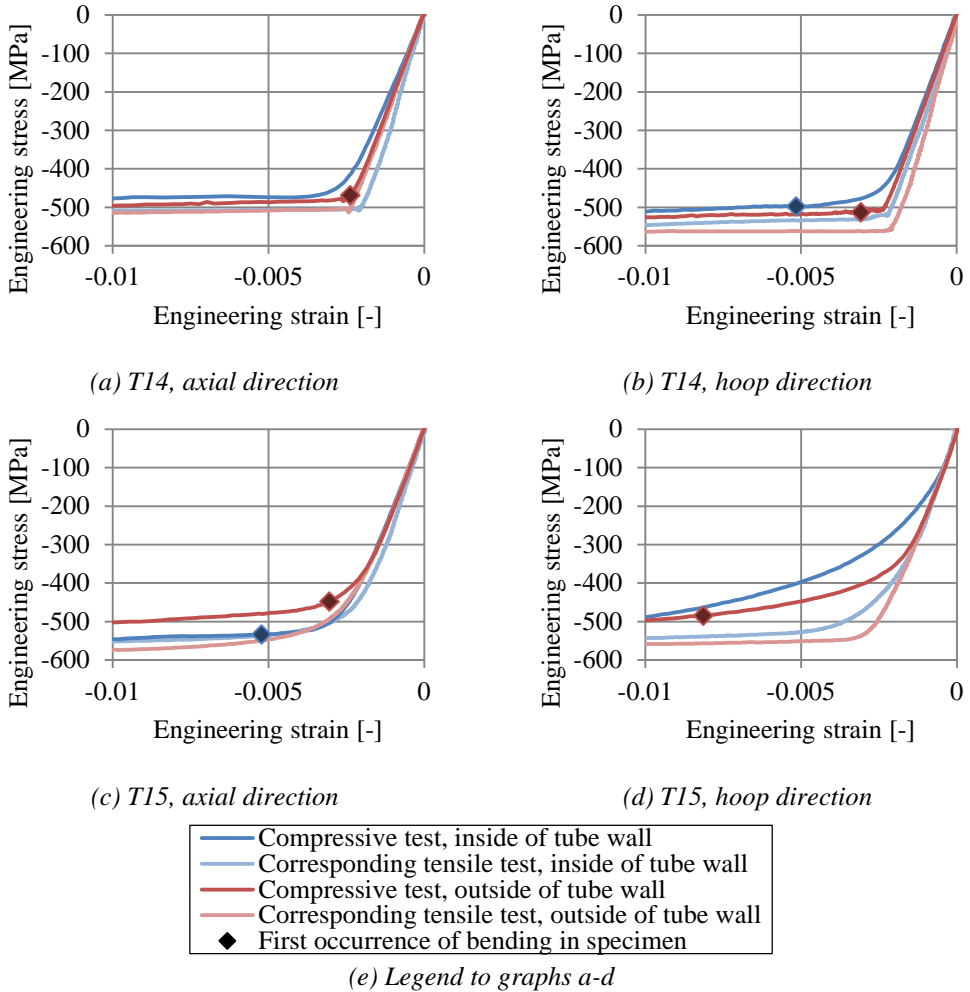


Figure 5.38 Results of compressive tests on specimens taken from longitudinal-welded UOE tubes compared with results of corresponding tensile tests.

5.4 Four-point bending tests

5.4.1 Test setup

To investigate the bending behaviour of the tubular specimens, the tubes were loaded in four-point bending until failure due to local buckling occurred. Considering the large diameter of the tubes, the forces involved in the test setup are of significant scale. The test setup was designed to deliver a maximum of 3500 kN at each support of the four-point bending setup, with a stroke of 350 mm. Because of these requirements and the limited availability of high capacity hydraulic

actuators, different actuators were used on each side of the test setup. Despite this difference, the loading on the specimen itself is symmetric. An overview of the test setup is shown in Figure 5.39, while photographs of the setup are presented in Figure 5.40.

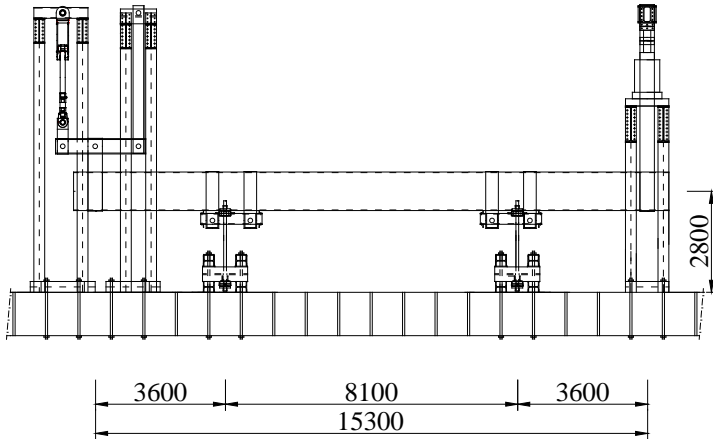


Figure 5.39 Schematic overview of four-point bending test setup (dimensions in mm).

To minimize the influence of the introduction of the loads into the specimen on the local buckling failure, the loads were applied through thin, flexible steel straps. Furthermore, at the middle support, the load was spread over two straps at each support, to further reduce any local effects due to the load introduction. A more detailed description of the test setup is found in Van Es and Gresnigt (2016a).

The bending tests were all performed in a displacement-controlled scheme. The displacements of the specimen ends were increased in small steps. After the formation of a local buckle, the loading was continued until the end of the actuators stroke was reached or until a stage were further development of the local buckle would cause damage to the measurement equipment.



(a) Overview of test set-up with specimen T5



(b) Local buckle in specimen T11 ($D/t=83$)

Figure 5.40 Photos of the four-point bending test set-up.

During the test, the specimen was oriented such that the intrados coincided with one of the scanned tube wall profiles. Based on the initial geometry measurements (see section 5.2), the most detrimental orientation of the tube was chosen for testing. The most detrimental orientation was estimated based on the measured imperfection amplitudes in plain tubes or the measured misalignments and imperfection amplitudes at the welds in case of specimens containing a girth weld or coil connection weld. The initial geometry of the intrados of each tube is documented in Van Es and Gresnigt (2016a). Major accidental damage, such as dents, was intentionally kept out of the zone of maximum compression. The influence of such accidental damage is studied in the numerical analyses described in section 6.5.

5.4.2 Measurements

During the bending tests, two types of measurements were performed: continuous measurements and measurements that could only be performed while the specimen was stationary. The latter measurements were performed in between the deformation steps that are described in section 5.4.1.

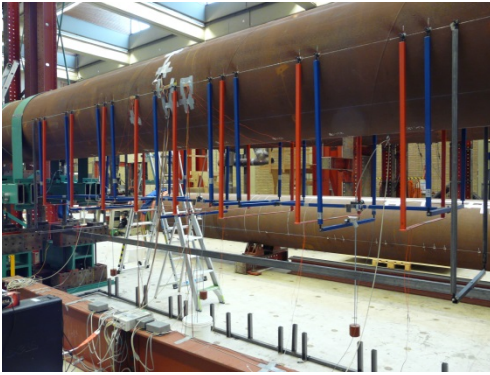
Continuous measurements

Most measurements could be performed continuously. Naturally, the applied force and displacements at all four load application points were monitored. In addition to this, strains at the compressive side of the specimen (intrados) and tensile side of the specimen (extrados), horizontal ovalisation at eight locations and curvatures were measured. Curvature was measured using curvature brackets (see Figure 5.41 and Figure 5.42a). For each curvature measurement, three brackets were attached to the neutral axis of the specimen with ball hinges. The outer two of these brackets were coupled by a horizontal coupler bar. The measured distance δ between the middle bracket and the coupler bar with length L was used to calculate the bending curvature using equation (5.1).

$$\kappa = 8 \frac{\delta}{L^2} \quad (5.1)$$

Three brackets (κ_1 , κ_2 and κ_3) were used to measure the curvature over a length of 1500 mm, which is approximately 1.4 times the specimen's diameter. One additional larger curvature measurement ($\kappa_{avg;b}$) was added after test T3 and measured the average curvature over a much longer length (5400 mm) within the constant bending moment part of the bent tube. In addition to these measurements, the average curvature was also calculated from the measured displacements at the four load applications points of the tube ($\kappa_{avg;U}$). The rotation of the mid-supports was calculated from these displacements and an elasto-plastic analysis of the two outer "loading arms" of the specimen. Then, the bending curvature was easily determined from these rotations, assuming a constant curvature over the middle part of the tube. In the results of the bending tests, typically only one average curvature is displayed ($\kappa_{avg;b}$). In case of tests T1 and T2, for which this bracket was not yet available, the value $\kappa_{avg;U}$ is shown.

The horizontal ovalisation of the tubes was measured by attaching brackets with flexible horizontal strips to the neutral line of the specimens. By measuring the strain in the bending horizontal strips with strain gauges, the horizontal ovalisation of the tube was determined (see Figure 5.42b).



(a) Brackets for measurements of ovalisation and curvature



(b) Attachment of the measurement brackets to neutral line with a ball hinge

Figure 5.41 Photographs of brackets for measurement of curvature and ovalisation.

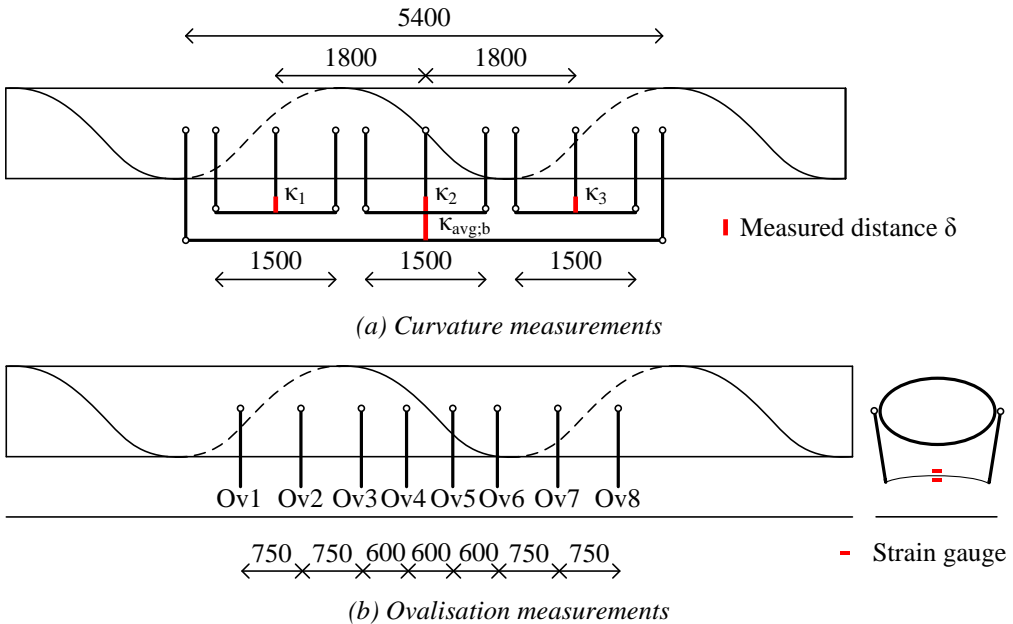


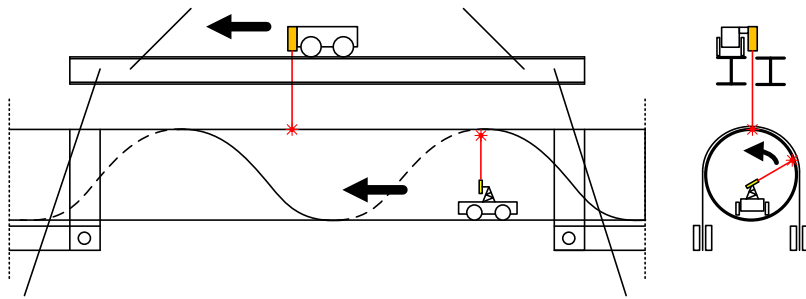
Figure 5.42 Overview of curvature and ovalisation measurements during the bending tests (dimensions in mm).

Discrete measurements of the tube geometry

During the tests, a trolley, running on rails suspended above the specimen, monitored the development of geometrical imperfections into a local buckle by laser scanning a line profile of the specimen intrados. The trolley performed very precise measurements, but the measurements had to be corrected to account for the curvature of the specimen, as the rails did not curve with the specimen.

An additional trolley on the inside of the specimen performed line scans similar to the external trolley (see Figure 5.3). As this trolley moved inside the bent tube, no correction to account for the bending curvature was necessary. In addition to the longitudinal line scans, the internal trolley was also capable of performing circumferential scans of the tube, which give information on the actual shape of the cross-section. These scans provide much more information on the cross-section shape and ovalisation, but are less accurate due to the uneven driving surface of the trolley, imperfect laser reflection and possible noise in the data (see section 5.2.1).

Using very closely spaced circumferential laser scans, 3D images of the buckled section could also be obtained. As these internal and external scans required the specimen to be stationary, they were performed in between deformation steps. A sketch of the two laser equipped trolleys and a photograph of the external trolley are presented in Figure 5.43.



(a) Schematic overview of laser scanning during test



(b) Suspended rails for external laser equipped trolley

Figure 5.43 Overview of laser scanning during bending tests.

5.5 Results of four-point bending tests

As a result of the exerted bending loads, all tubular specimens failed in the form of local buckling. The specimens with a D/t ratio equal to 120 failed suddenly and violently. In contrast, the transition between a stable and unstable tube wall was much more gradual for the thick-walled specimens. Especially thick-walled specimens with large initial geometrical imperfections, such as specimen T6 (see Figure 5.17a) had a very smooth transition between the pre-buckling stage and post-buckling stage. Some of the sudden failures of the thin-walled specimens resulted in failure of some of the more sensitive measurement equipment. In these cases, the post-buckling stage of the bending response was removed from the corresponding diagrams. In this section, the results of the bending tests are summarized. More extensive reporting on each separate test is found in Appendix B and in Van Es and Gresnigt (2016a).

In most cases, the local buckle configuration consisted of one main buckle with two adjacent secondary buckles which formed after little further deformation of the specimen. Some examples of local buckling shapes are presented in Figure 5.40b and Figure 5.44 to Figure 5.46. Using the data of the internal laser equipped trolley (see Figure 5.3), 3D images of the buckles tube segment were created, which further clarify the shape of the local buckles.

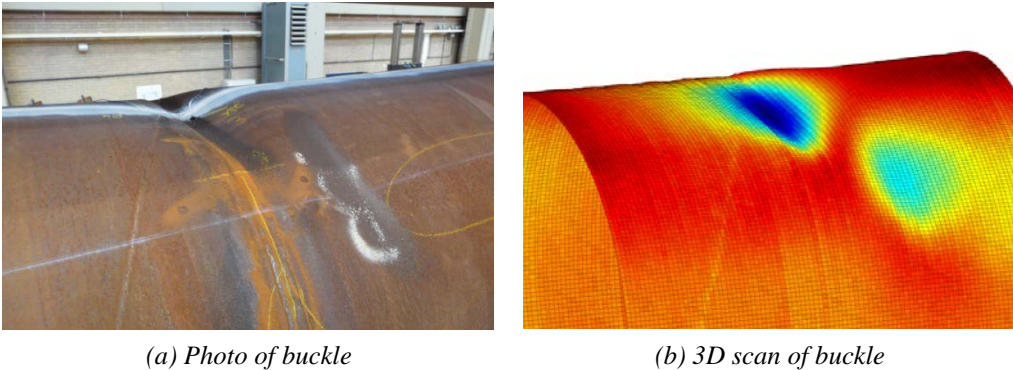


Figure 5.44 Local buckle in specimen T3 ($D/t=118$) at the girth weld, directly after formation.

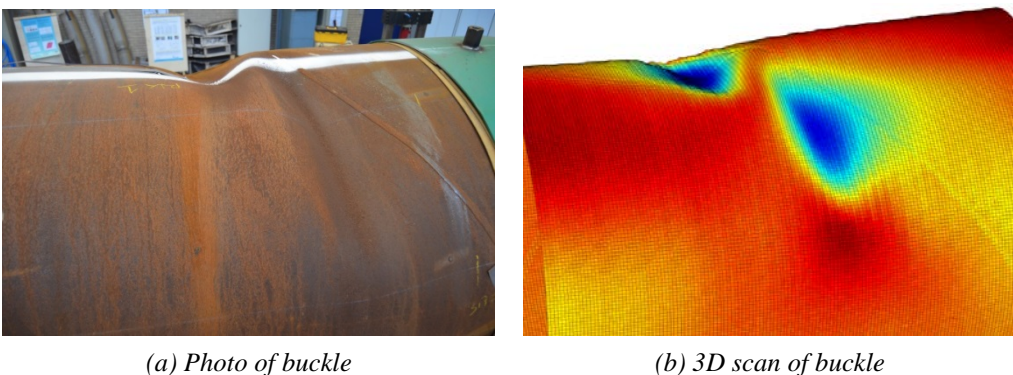


Figure 5.45 Local buckle in specimen T7 ($D/t=65.4$), directly after formation.

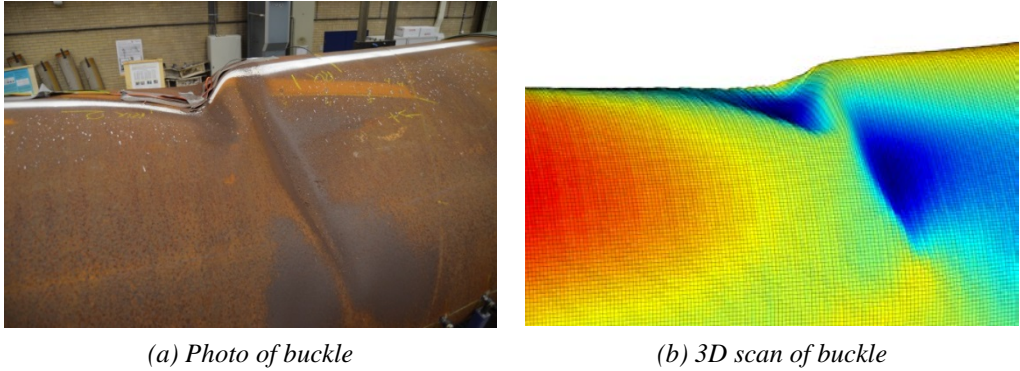


Figure 5.46 Local buckle in specimen T12 ($D/t=117$) at final deformation stage of the specimen.

5.5.1 Moment-curvature diagrams

Two typical moment-curvature diagrams resulting from the bending tests on spiral-welded tubes are shown in Figure 5.47. As discussed earlier, some of the sudden failures of the thin-walled specimens resulted in failure of the curvature measurement equipment. In Figure 5.47a, the first data point after the failure is still included in the graphs as a visual aid to the reader.

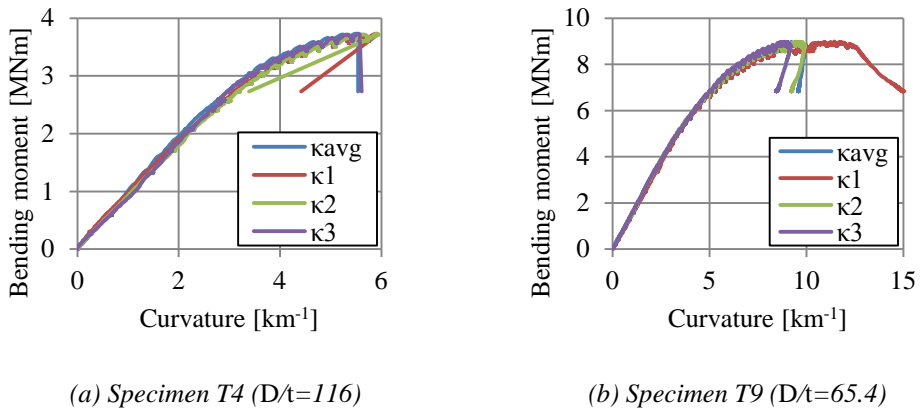
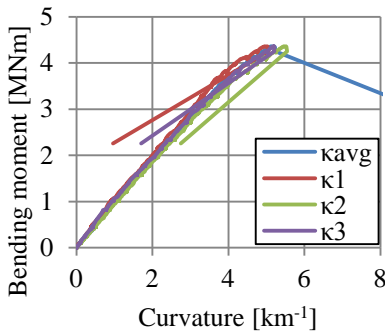


Figure 5.47 Examples of moment-curvature diagrams for two typical spiral-welded plain specimens. Local buckling took place within curvature bracket κ_1 in both tests.

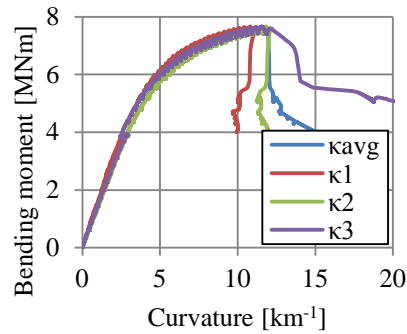
The curvatures shown in the diagrams in Figure 5.47 directly follow from the measurements (see section 5.4.2). The displayed bending moment is the bending moment at the location of the local buckle, which was calculated from the applied forces. The diagrams present the bending moment in relation to the local and average curvature measurements (see section 5.4.2). The diagrams show that the thicker specimens ($D/t \approx 65$) have a much more pronounced deformation capacity than the thinner specimens ($D/t \approx 115-120$). Furthermore, this plastic deformation is not evenly distributed over the tube segment with constant moment. Clearly, the curvature measured

by bracket κ_i is higher than the average other local curvatures in Figure 5.47b. This not only occurs close to the formation of a local buckle, but is already visible well before the maximum bending moment is reached or a local buckle forms. In case of thinner specimens, differences between the curvature measurements are smaller, but still present. It can therefore be concluded that the bending moment capacity of these tubes is varying over their length.

The moment-curvature diagrams resulting from the bending tests on the longitudinal-welded specimens are shown in Figure 5.48. The large differences in plastic deformation that can be observed in the results of the bending tests on spiral-welded specimens seem to be absent in the results of the bending tests on longitudinal-welded tubes. Naturally, Figure 5.48b shows a larger curvature in the bracket where the local buckle formed (κ_3) after instability occurred, but during the stable moment-curvature equilibrium path, the differences between the three local curvature measurements are relatively small.



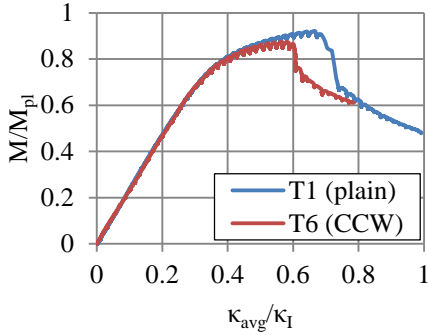
(a) Specimen T14 ($D/t=109$)



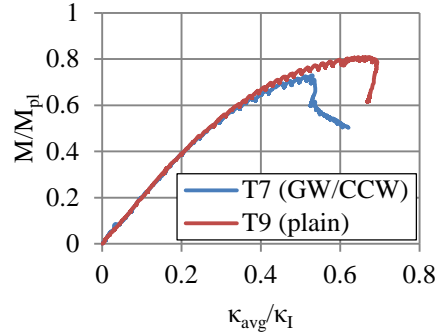
(b) Specimen T15 ($D/t=72.3$)

Figure 5.48 Examples of moment-curvature diagrams for the two longitudinal-welded plain specimen. Local buckling took place within curvature bracket κ_3 in both tests.

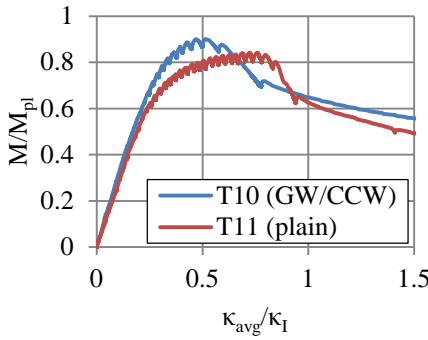
The bending behaviour of all spiral-welded tubes is collected in graphs presenting the moment-curvature diagrams of specimens of similar wall thickness and material properties using the average curvature (see Figure 5.49). In case of the specimens with a wall thickness of 9 mm, the specimens are grouped with specimens of similar behaviour. The horizontal axes of the diagrams are normalized by curvature-like parameter κ_i , defined as $\kappa_i=t/D^2$. The vertical axes are normalized by the initial plastic bending moment capacity of the cross-section. For both normalizations, the specimen properties at the location of the local buckle are used. A collection of all moment-curvature diagrams in terms of the average and the three local curvature measurements as well as a table containing numerical values of characteristic points in these graphs can be found in Appendix B.



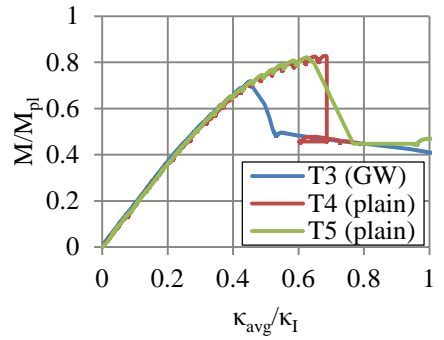
(a) Tubes with $t \approx 16$ mm and $\sigma_{y,ref} \approx 530$ MPa



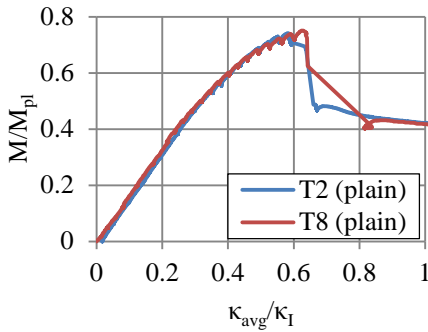
(b) Tubes with $t \approx 16$ mm and $\sigma_{y,ref} \approx 610$ MPa



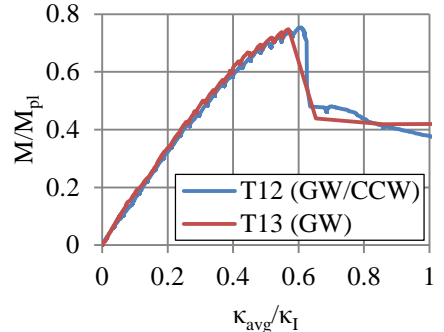
(c) Tubes with $t \approx 13$ mm and $\sigma_{y,ref} \approx 340$ MPa



(d) Tubes with $t \approx 9.0$ mm and $\sigma_{y,ref} = 390-450$ MPa



(e) Tubes with $t \approx 9.0$ mm and $\sigma_{y,ref} = 410-450$ MPa



(f) Tubes with $t \approx 9.0$ mm and $\sigma_{y,ref} \approx 340$ MPa

Figure 5.49 Normalized moment-curvature diagrams of the spiral-welded specimens using average curvature.

The results show that specimens containing a girth weld or coil connection weld generally appear to perform less than their plain counterparts, both in terms of maximum bending moment capacity and critical curvature. Only Figure 5.49e and Figure 5.49f indicate that plain specimens may have a structural response similar to the specimens containing an additional weld. Summarizing, the additional welds appear to penalize the structural strength and deformation capacity. Possible causes for this are discussed in section 6.4.

An exception to the above general observation is specimen T10. As discussed in section 5.3.2, this specimen featured a specimen part that was significantly weaker than the attached other two. Because local buckling took place in the weaker part very close to the girth weld where it was connected to a stronger part, a significant supporting effect of the attached stronger specimen part is to be expected. This support results in higher resistance against buckle formation due to a thicker wall and higher yield strength of the adjacent part, but also a higher resistance against ovalisation. A cross-section with less ovalisation is less prone to local buckling, due to the smaller radius of the tube wall. Furthermore, the average curvature of the specimen is strongly influenced by the thicker specimen parts away from the buckle. The difference in curvature between the stronger and weaker part is clearly visible in Figure B.11. These two effects result in a relatively low critical average curvature in combination with a high maximum bending moment in Figure 5.49c.

5.5.2 Results of ovalisation measurements

The ovalisation measurements also provide useful information on the behaviour of the specimens under consideration. Typical results of these measurements are presented in Figure 5.51 to Figure 5.53 in terms of the change in horizontal diameter (ΔD).

The graphs in Figure 5.51a to Figure 5.53a present the overall development of the horizontal ovalisation of the specimen with respect to curvature. In all tests, the formation of a local buckle led to a sudden increase of horizontal ovalisation near the buckling location. Further away, the horizontal ovalisation slightly decreased after local buckle formation, corresponding to the reduced curvature in these areas due to the decreased bending moment. In many cases, also before bifurcation, the ovalisation of the tube is larger around the location of the local buckle than in other parts of the tube. This feature is not only clearly visible in Figure 5.51a and Figure 5.52a, but in almost all tests.

The graphs in Figure 5.51b to Figure 5.53b present a profile of horizontal ovalisation over the length of the test specimen at a curvature close to the critical curvature. The graphs provide a comparison between the measured ovalisation with external brackets (see Figure 5.42) and the measurements performed by the internal laser scans (see Figure 5.2). The figures show that there is good agreement between these two measurement methods. The profiles of all three tubes show that the specimen ovalisation is slightly reduced toward the middle supports. This may be the result of a supporting effect of the two outer 'loading arms' of the specimens. These tube segments are curved less and therefore have a lower ovalisation. Since the ovalisation of the tube over its length must be continuous, this decreases ovalisation in the middle section of the tube near the middle supports. In addition, a supporting effect of the load application straps at the

middle supports may occur. The initially parallel steel straps are deformed by the ovalising tube, leading to a restriction of ovalisation (see Figure 5.50).

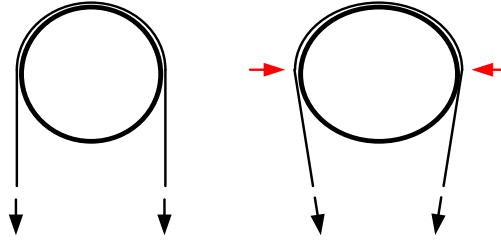
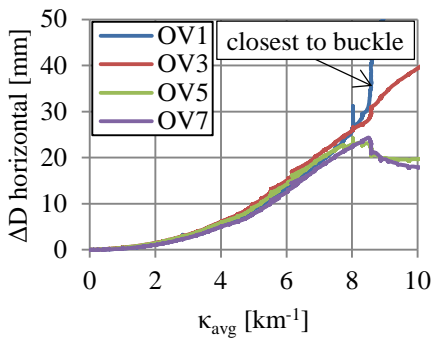
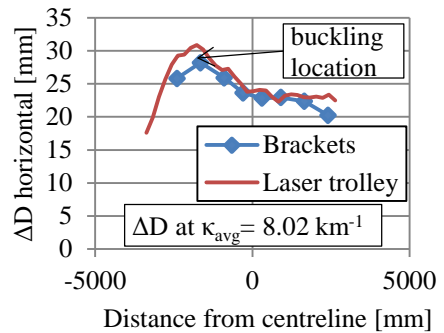


Figure 5.50 Restriction of ovalisation by middle supports.

Figure 5.51b and Figure 5.52b show that ovalisation is clearly higher at the location where local buckling would occur later during the bending test. This may be the result of a locally larger bending curvature at these locations due to variation in bending moment capacity over the length of the tube. In case of specimen T14, local buckling did not occur at a maximum in the ovalisation distribution (see Figure 5.53b). Also in this specimen a maximum in ovalisation is found, but local buckling occurred elsewhere. A likely cause for this is a geometrical imperfection at the buckling location in the form of a small dent (see Figure 5.18a). Apparently, this imperfection triggered local buckling for this particular specimen. Apart from such cases, tube ovalisation appears to be a good predictor of the buckling location.

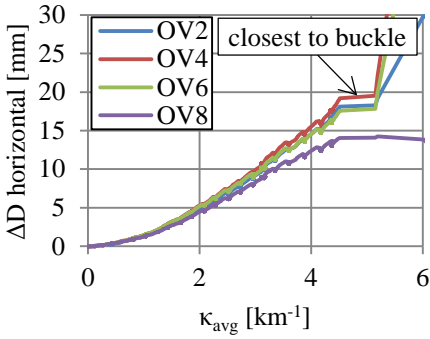


(a) Measured ovalisation with brackets.
Selection of bracket results displayed

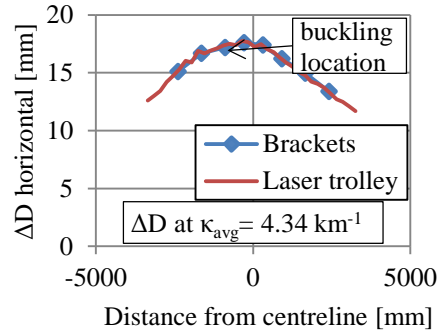


(b) Comparison between the measurements
from brackets and internal laser trolley

Figure 5.51 Ovalisation measurements of test T6.

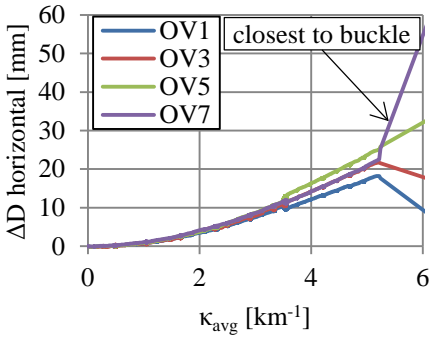


(a) Measured ovalisation with brackets. Selection of bracket results displayed

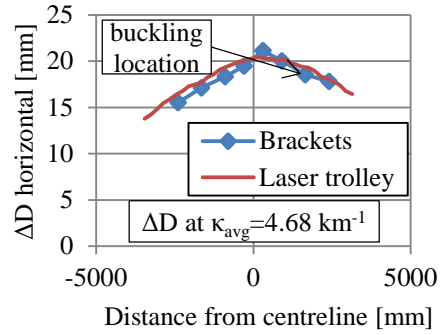


(b) Comparison between the measurements from brackets and internal laser trolley

Figure 5.52 Ovalisation measurements of test T13.



(a) Measured ovalisation with brackets. Selection of bracket results displayed



(b) Comparison between the measurements from brackets and internal laser trolley

Figure 5.53 Ovalisation measurements of test T14.

5.6 Summary of Chapter 5

This chapter presents a summary of the results obtained from fifteen full-scale four-point bending tests. Before the bending test until failure in local buckling, the initial state of the tubular specimens was carefully documented.

Of the fifteen tubular specimens, thirteen were manufactured using the spiral-welding manufacturing process. Two specimens were manufactured using the UOE manufacturing process and therefore contained a longitudinal weld. The thirteen spiral-welded specimens included plain specimens and specimens with a girth weld, coil connection weld or both.

The measurements of the initial geometry showed a very low variation of the diameter and wall thickness over the tube length. For the spiral-welded tubes, a small decrease in wall thickness

was observed close to the spiral welds. Attempts to determine the residual stresses in the tubes resulted in a large scatter. Possible causes for this scatter were identified.

The initial profile of the tube wall was measured extensively. The measurement results show a pattern of regular imperfections in the plain spiral-welded tubes. By overlaying visual markings on the tubes with the measurements, it is demonstrated that, for the tested tubes, these initial geometrical imperfections were caused by rollers used in the spiral-welding manufacturing process. Accordingly, these specific patterns were not present in the longitudinal-welded UOE tubes. Geometrical imperfections near girth welds and coil connection welds were generally larger in amplitude than imperfections in plain tubes.

Measurements of initial geometrical imperfections in combined walls at a construction site show similar results as the measurements performed in the laboratory. As a result, the typical geometrical imperfections that were present in the four-point bending tests can be assumed to be realistic. A noteworthy exception is the presence of dents. The tubes at the visited construction site showed a larger number of dents than was expected on the basis of the observations made in the laboratory. It must be noted that since only one construction site was visited, this observation cannot be regarded as typical for all combined walls. In the investigated case, the dents were likely caused by excavation after installation of the tubes. As a result, they only occur in the tensile zone of the cross-section and will therefore have negligible influence on the formation of a local buckle. In case of re-use of the tubes, or in case of accidental imperfections due to other causes, they may also occur in the compression zone of the cross-section. The effect of such accidental imperfections in the compression zone was not studied experimentally, but is included in a parameter study performed by research partners at the University of Thessaly (see section 6.5).

Extensive material tests were performed on the tubular specimens on tension and compression coupons. The results from the tensile tests showed that for practical purposes, the material of the tubes can be assumed to be isotropic. Furthermore, the material behaviour in the compression domain was generally found to be similar to the behaviour in the tension domain. In some cases a small Bauschinger effect was observed, mainly in the hoop direction of the tubes. No clear differences were observed between spiral-welded tubes and longitudinal-welded tubes.

The four-point bending tests that were performed on the tubular specimens all resulted in failure in local buckling. Depending on the slenderness of the cross-section of the specimens, a local buckle formed suddenly and violently or more gradually. Within the tube section loaded in constant bending moment, curvature was found to far less constant in case of the spiral-welded tubes than in case of the longitudinal-welded tubes.

The critical curvature and maximum bending moment capacity were observed to be influenced for specimens containing a girth weld or coil connection weld, which showed worse, or at most equal, performance to similar plain specimens.

Ovalisation measurements were found to be indicative of the location where buckling would occur, as the ovalisation distribution over the tube length generally showed a maximum at the buckling location before the local buckle formed.

Chapter 6

Analysis and interpretation of bending test results

6.1 Definitions

For the analysis of the four-point bending tests, numerical values for parameters such as the maximum resisted bending moment and critical curvature were determined from the moment-curvature diagrams. The critical strain of the tubes can directly be calculated from the latter parameter (see section 6.2.2). Two key points on the diagram are recognised (see Figure 6.1). The point where the maximum bending moment is resisted was used to determine the ‘critical curvature’ (κ_{crit}). Simultaneously or somewhat later on the moment-curvature path, a sudden drop in resisted bending moment can be observed. This point was used to determine the ‘buckling curvature’ (κ_{buc}). In this study, instability (ϵ_{crit} , κ_{crit}) is defined on the moment-curvature path at the point where the maximum bending moment occurs. The reasoning for this definition is discussed in section 1.3.2. Directly after the formation of the local buckle, some remaining post-buckling bending moment capacity (M_{pb}) is present.

All measured moment-curvature diagrams results show a mildly oscillating line. After slowly applying a deformation step, the test setup was stationary for several minutes to allow the discrete measurements with laser equipped trolleys to be completed. During this period, the resisted bending moment slightly decreased. The line that represents the ‘true’ moment-curvature relation of a specimen can either be assumed to follow the local maxima or local minima of the measured diagram. For thinner walled tubes, the local minimum of the resisted bending moment at the critical curvature could only be found through extrapolation due to the sudden failure in a rising branch of the moment-curvature relation of these tubes, resulting in an uncertain determination of the maximum resisted bending moment. Therefore, the maximum resisted bending moment was defined as the actually measured maximum bending moment for these tubes. To allow a fair comparison of all test specimens, this procedure was also followed for the thicker walled tubes (see Figure 6.1). The difference between the local maxima and local minima of the resisted bending moment typically does not exceed 5%.

In the following sections, many diagrams feature parameters that follow from the tube diameter, wall thickness and yield stress. In all cases, these parameters were determined on the basis of the diameter, wall thickness and yield stress of the specimen part in which the local buckle occurred. In all cases where local buckling occurred close to a girth weld or coil connection weld, the origin of the buckle was located at one side of the weld. The diameter, wall thickness and yield stress of that specimen part were used to determine the necessary parameters.

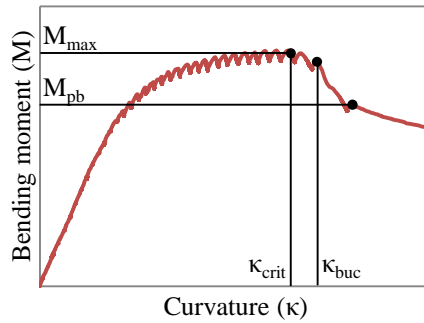


Figure 6.1 Definition of characteristic values of a moment-curvature diagram.

6.2 Ultimate bending moment and deformation capacity

6.2.1 Ultimate bending moment

An overview of the bending moment capacities of the tested tubes is depicted in Figure 6.2. The cross-sectional slenderness of the tubes is defined using both the diameter to thickness ratio (D/t) and the specimen's yield strength, as is common in structural analysis (EN 1993-1-1, 2006) (AISC, 2005). More specifically, the definition according to EN 1993-1-1 was used (see equation (4.1)).

The figure shows a decreasing bending moment resistance for increasing cross-sectional slenderness. Furthermore, the maximum bending moment capacity of tubular specimens containing a girth weld or coil connection weld is, generally, equal to or lower than their plain counterparts, with the exception of specimen T10 due to the strong discontinuity of cross-sectional properties (see Figure 5.34). The results of the longitudinal-welded UOE specimens appear to be in line with the spiral-welded specimens.

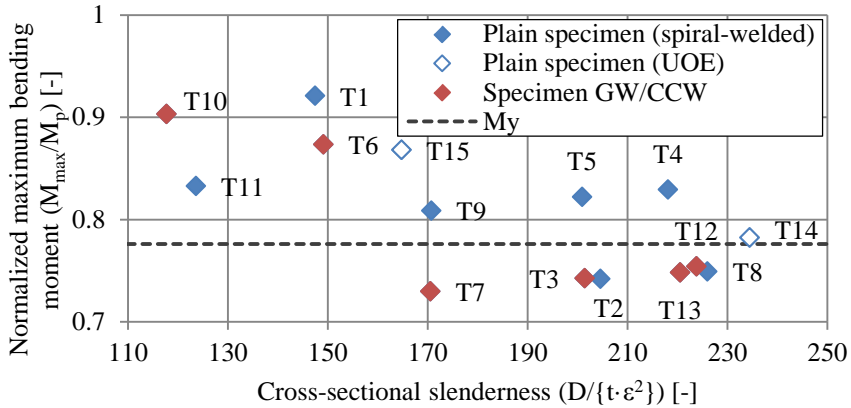


Figure 6.2 Bending moment capacity of tubular specimens. M_y is defined as the bending moment of first yielding of the outer fibre of a non-ovalising tube.

6.2.2 Critical strain

An overview of the critical strains at maximum bending moment is depicted in Figure 6.3. To avoid including the effects of local wall bending and very local variations curvature in the results, the reported strains are calculated from measured curvatures and diameters measured before the bending test, instead of strain gauges. The figure shows the critical strain calculated from curvature measurement κ_{avg} , which averages the curvature over almost the full tube section with constant bending moment (see Figure 5.42). Considering the common practice in pipeline engineering to relate the critical strain to D/t as cross-sectional slenderness parameter (e.g. DNV-OS-F101, 2010, Gresnigt, 1985), this approach was also used for Figure 6.3.

Similarly as for the bending moment capacity, Figure 6.3 shows that the critical strain of the tubes decreases when the slenderness of the cross-section of the tube is increased. Also for the critical strains, there seems to be a negative influence of the presence of a girth weld or coil connection weld. From Figure 6.2 and Figure 6.3 it can be concluded that many specimens featuring a girth weld or coil connection weld have a lower bending moment and deformation capacity than comparable plain specimens. The latter in this case refers to average curvatures.

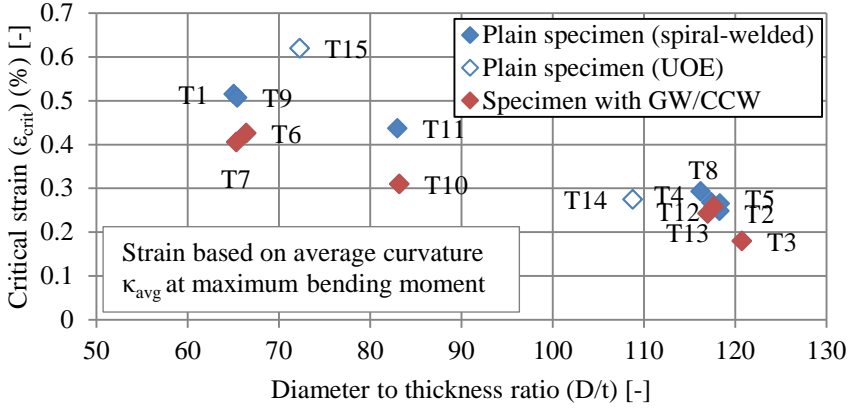


Figure 6.3 Critical strains based on average curvature at the maximum bending moment.

Local curvature versus average curvature

As shown in Figure 5.47, even before the maximum bending moment is reached, differences between locally measured curvatures and measured average curvatures arise. The curvature localization ratio (CLR) is defined as the ratio between local and average curvature at the buckling location ($\kappa_{i:bl}/\kappa_{avg}$). The calculated values of the CLR, determined at the critical curvature (κ_{crit}), are presented in Figure 6.4. The figure shows that the local curvature is significantly higher than the average curvature in almost all cases.

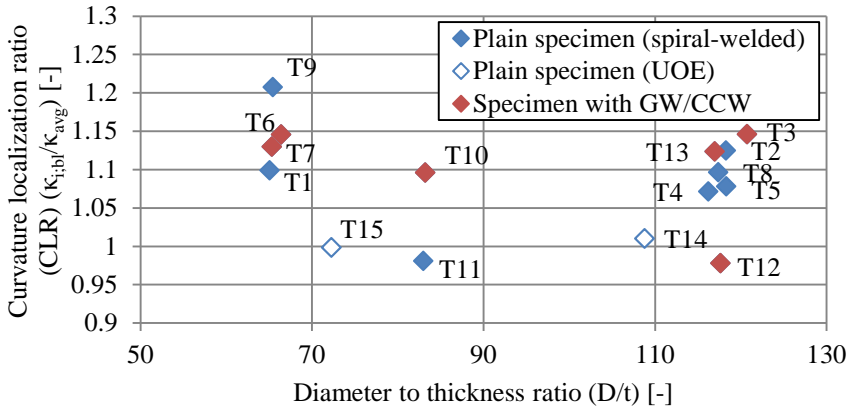


Figure 6.4 Curvature localization ratio at the buckling location at maximum bending moment.

Exceptions are the two specimens originating from the UOE manufacturing process. Further exceptions are specimens T11 and T12. In these specimens, curvature localized away from the buckling location. If instead of the local curvature at the buckling location ($\kappa_{i:bl}$), the maximum local curvature ($\kappa_{i:max}$) is used to determine the curvature localization ratio, the CLR of T11 and T12 is in line with the other results from spiral-welded tubes (see Figure 6.5). The CLR of

specimen T3 increases dramatically when the maximum local curvature is used. This is caused by the wall thickness differences at the girth weld. The CLR of the two longitudinal-welded tubes also increases, but remains lower than the other data points. Apparently, localization of curvature over a tube section with constant bending moment is typical for spiral-welded tubes.

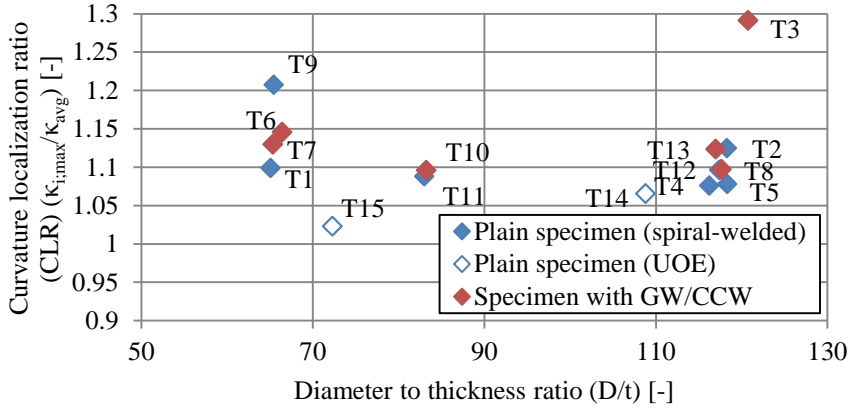


Figure 6.5 Curvature localization ratio at the location of maximum curvature at maximum bending moment.

Specimens containing a girth weld or coil connection weld generally appear to show more curvature localization than plain specimens. Firstly, this may be caused by differences in yield strength on both sides of the weld. In case of such a difference, curvature concentrates on the weaker side of the weld. Further explanation for this higher localization can be found in the misalignments, residual stresses and geometrical imperfections that are present at these welds (see section 5.2.5). These features cause a locally reduced bending stiffness of the tube, resulting in a larger localization of curvature.

An overview of the average curvature localization ratios is presented in Table 6.1. The table shows that longitudinal-welded tubes hardly show localization of curvature, while for spiral-welded specimens a curvature localization of about 10-12% was observed. Furthermore, the curvature localization ratio was indeed found to be slightly higher for specimens containing a girth weld or coil connection weld.

Table 6.1 Curvature localization ratios at the maximum bending moment using local curvature at the buckling location ($\kappa_{i,bl}$) and maximum local curvature ($\kappa_{i,max}$).

Specimens		CLR at M_{max}	
		$\kappa_{i,bl}$	$\kappa_{i,max}$
All		1.086	1.116
Spiral-welded	All	1.098	1.127
	Plain	1.094	1.110
	GW/CCW	1.103	1.147
Longitudinal-welded		1.004	1.044

In literature, various authors have recognized the importance of the length of curvature measurements (also see section 1.3.2). Zimmerman (1995, 2004) defines a gauge length of 1 or 2 times the tube diameter as practical. Other authors have followed this definition in their research (e.g. Tajika and Suzuki, 2009). In the research by Carr et al. (2009), bending tests were performed on seamless pipes with a D/t ratio of 19 with and without internal pressure, using various gauge lengths to determine the critical strain. Similarly, Suzuki et al. (2008) used various gauge lengths in two bending tests on pressurized tubes with a D/t ratio of 49. In the work by Shitamoto et al. (2012), only a gauge length of 8 times the tube diameter was used during the performed bending tests, but various gauge lengths were used in FE-analyses. Also this study focuses on thick-walled tubes ($D/t=38$). In these three studies, values of the curvature localization ratio up to 2 were found, which is significantly higher than was found in the present study.

It can thus be concluded that the concept of curvature localization is recognized in literature. Furthermore, while in the present study, hardly any curvature localization was found for longitudinal-welded tubes, various authors found significant curvature localization in such tubes. However, studies on tubes with comparable D/t ratio as in the present study that comment on localization of curvature were not found. Since only two longitudinal-welded tubes were tested in the present testing programme, further research needs to be performed to provide additional information on the curvature localization behaviour of slender tubes originating from various manufacturing processes.

Critical curvature versus buckling curvature

In all previous analyses, the critical values of each specimen were defined at the moment where the maximum bending moment resistance was reached. Alternatively, the occurrence of buckling can be defined at the curvature where the resisted bending moment suddenly drops (κ_{buc}). It may be expected that, for specimens with a high D/t ratio, these two definitions provide the same result, while for specimens with a low D/t ratio, there may be a certain difference. Figure 6.6 presents the ratio of curvatures at the maximum bending moment and the moment the bending resistance drops. This ratio is recognized as a measure of ductility of the tube and is therefore denoted as ductility ratio. Figure 6.6a presents ductility ratios that were calculated using average curvatures (κ_{avg}), while Figure 6.6b presents ductility ratios that were calculated using the local curvatures at the buckling location ($\kappa_{i,bl}$).

Using the diameter to thickness ratio of the specimens (D/t), hardly any correlation between ductility ratio and slenderness is found (Van Es et al., 2016). If the cross-sectional slenderness parameter $D/(te^2)$ is used, the graphs show that a more slender cross-section results in a lower ductility ratio. It should be noted that beyond a certain value, further increase of the slenderness does not lead to further decrease of the ductility ratio. Naturally, a ductility ratio of unity is the minimum, which implies that the maximum bending moment and the sudden drop in bending moment resistance occur simultaneously. Finally, Figure 6.6 shows that specimens containing a girth weld or coil connection weld show a slight tendency to have a lower ductility ratio than comparable plain specimens; especially when average curvatures are used to calculate the ductility ratio.

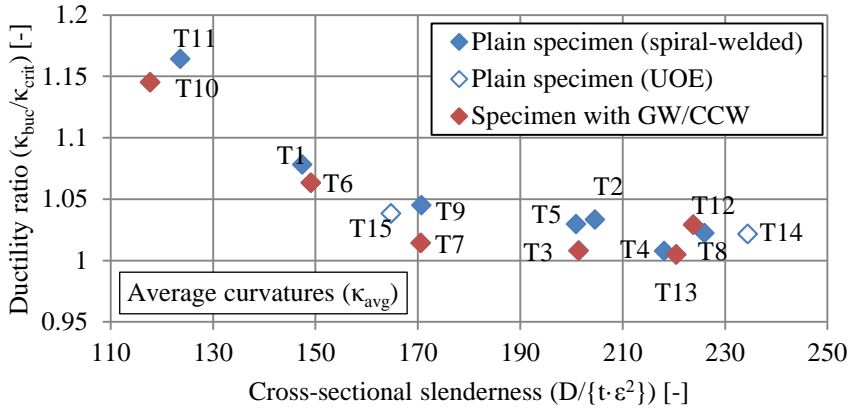
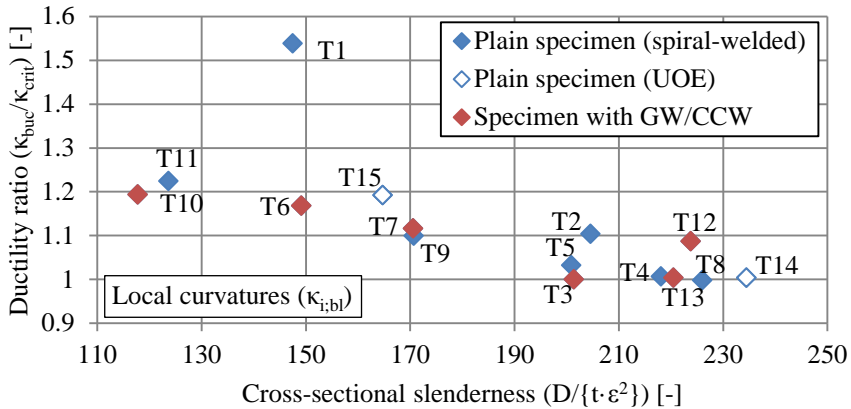
(a) Ductility ratio calculated from average curvatures (κ_{avg})(b) Ductility ratio calculated from local curvatures at the buckling location ($\kappa_{i,bl}$)

Figure 6.6 Ductility ratio of tubular specimens.

6.3 Buckling location

From each specimen, the initial geometric profile of the intrados is known, because the intrados aligns with one of the initial imperfection scans. Therefore, the location of the local buckle can be related to the initial geometry. This allows examination of the influence of the initial geometric imperfections on the formation of a local buckle.

The development of a local buckle can be recognized in the measurements of the geometry of the intrados of the specimen during the test (see Figure 5.43). The compression side geometry before testing and at the onset of buckling is presented for two specimens in Figure 6.7. Note that in both graphs, the local buckle forms at a geometric imperfection. The results plotted in

Figure 6.7b are particularly interesting: local buckling occurred at an initial geometric imperfection, which is certainly caused by the cold-forming process, since it aligns with a roller mark. As discussed in section 5.2.5, all regular geometric imperfections are assumed to be caused by the cold-forming process. Because these imperfections are apparently leading in forming a weak link in the tube, the cold-forming manufacturing process may have a direct influence on the local buckling behaviour of these tubes.

It is worth noticing that in all but one specimen, local buckling occurred away from the spiral weld, although in many cases significant imperfections were visible in that region. Apparently, the influence of other factors may result in the formation of a local buckle away from that weld. Strengthening effects from the overmatched weld material and stiffening and strengthening effects from the weld cap may constitute such factors.

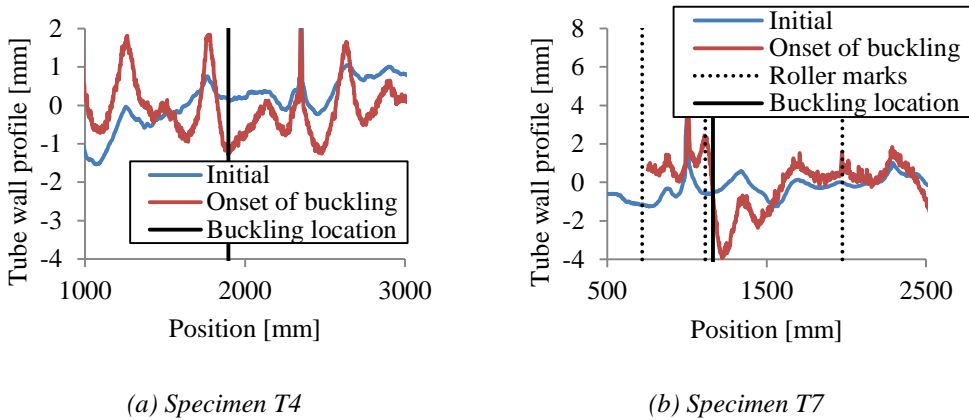


Figure 6.7 Buckling location for specimens T4 and T7.

In case of specimens containing a girth weld or coil connection weld, the geometrical imperfections near that weld are generally larger than the imperfections in the plain tube specimen (compare the values for plain and non-plain specimens in Table 5.3). Considering that in plain tubes the geometrical imperfections cause a ‘weak link’, it is expected that in case of these welds with larger geometrical imperfections, local buckling occurs in the weld area. In four out of the six specimens containing such a weld, local buckling actually did occur in the immediate vicinity of the weld. In these four specimens, the local buckle formed at a maximum distance from the weld of 10% of the tube diameter (see Figure 6.8). In the other two cases, local buckling occurred significantly further away from those welds ($>1 \cdot D$). Possible explanations for this are discussed in section 6.4. The exact position of the girth welds, coil connection welds and local buckles in all specimens can be found in Figure B.1 in Appendix B.



(a) Specimen T3



(b) Specimen T6



(c) Specimen T10



(d) Specimen T13

Figure 6.8 Local buckles in the vicinity of girth welds and coil connection welds.

6.4 Influence of the presence of girth welds and coil connection welds

The presence of girth welds and coil connection welds may have a severe influence on the bending behaviour of the tube. Firstly, the welding itself has influences due to heat input and added weld material. Secondly, the weld may be associated with severe geometrical imperfections. Finally, these welds act as a boundary between two specimen parts, which may have different cross-sectional properties.

Welding itself has two implications. Firstly, welds are thicker than the surrounding plate material and have a higher yield strength (overmatched welds). Therefore, the weld has a stiffening and strengthening effect that increases the local buckling resistance. Because many local buckles occurred at these welds and the presence of such a weld was found to penalize the local buckling resistance of the considered tubes, this stiffening effect is assumed to be minor compared to other effects. Secondly, all welding results in residual stresses. These residual

stresses due to welding may have an influence on local buckling, but have not been investigated in the present study. In the numerical parametric study that was performed within the COMBITUBE project (see section 6.5), residual stresses resulting from the spiral-welding manufacturing process were found to have a favourable effect on the critical curvature (Vasilikis et al. 2016). Whether the residual stresses resulting from a girth weld or coil connection weld have a similar effect may be subject of further research.

The geometrical imperfections that are created by the girth welds and coil connection welds can be in the form of misalignments or of similar shape as the “hills” and “valleys” observed in plain spiral-welded tube sections. As shown in section 5.2.5, the initial imperfections near the welds are significant, and because many of the local buckles occur at this location, they may have a negative effect on the buckling resistance of the tubes. These imperfections might result in a locally slightly larger curvature of the tube. Experimental observations show that, very locally, the tube undergoes a rotation around the “hinge” that is formed by the imperfection. This effect is visible in Figure 6.9b, where the curvature measured over the girth weld (κ_2) is significantly larger than the curvature measured away from the girth weld during almost the complete test.

Even in the case of a girth welded connection between two tubes that are identical by specification, the diameter, wall thickness and especially material behaviour will differ to some extent. This implies a strong and a weak side of the weld. In this analysis, the product of wall thickness and yield strength is used as a measure of strength of either side of the weld. When this strength parameter is normalized by the strength parameter that is measured at the buckling location, the strength ratio ζ is found:

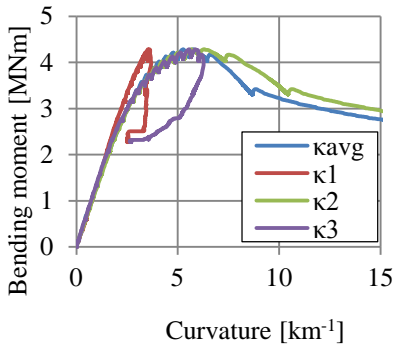
$$\zeta_i = \frac{t_i \cdot \sigma_{y:i}}{t_{bl} \cdot \sigma_{y:bl}} \text{ with } i = \text{Left, Middle, Right} \quad (6.1)$$

A strength ratio ζ larger than 1 indicates that local buckling occurred in the weakest specimen part of the tube. A strength ratio smaller than 1 indicates that the local buckle occurred at another location within the specimen. An overview of all strength ratios found in the specimens that contain a girth weld or coil connection weld is presented in Table 6.2. A strength difference of more than 2% always resulted in a local buckle in the specimen part with the weakest cross-section.

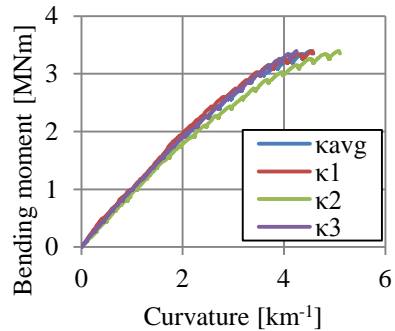
Table 6.2 Strength ratios (ζ) for specimens containing a girth weld or coil connection weld.

Specimen I.D.	ζ_i			Buckled specimen part	Buckling location
	Left	Middle	Right		
T3	1.00	-	1.16	Left	At GW
T6	1.00	-	1.06	Left	At CCW
T7	1.00	0.98	0.99	Left	In plain part
T10	1.69	1.58	1.00	Right	At GW
T12	1.00	1.15	0.99	Left	In plain part
T13	1.00	-	1.06	Left	At GW

A second implication of the difference in bending resistance between the two sides of the weld is that the curvature concentrates on the weaker side of the weld. During elastic deformation, only the wall thickness difference is of influence, but during plastic deformation, the combined effect of the wall thickness and yield strength difference can be significant. This is an unfavourable situation, because a concentration of curvature at one location within a tube may lead to earlier failure of the tube as a whole. For example, in the experiments, the localization of curvature is clearly visible in the results of specimen T10 (see Figure 6.9a).



(a) Specimen T10



(b) Specimen T13

Figure 6.9 Effects of girth welds and coil connection welds on the moment-curvature behaviour.

There are two effects of a strength ratio factor unequal to 1. Firstly, a stronger specimen part attached to a weaker tube part may support the weaker tube part, delaying local buckling failure and possibly resulting in higher bending moment resistance of this weaker part (see specimen T10 in Figure 6.2). Secondly, the presence of a stronger part may result in localization of curvature in a deformation controlled situation, which leads to earlier local buckling of the tube as a whole.

In the tests, curvature was measured at the same locations in each tube (see Figure 5.42). In all tests on tubes that included a girth weld or coil connection weld, these welds were included in one of the local curvature measurements. In case of a connection between a stronger and a weaker specimen part at this weld, curvature localized on one side of the weld. In the measurements, the larger curvature of the weaker specimen was averaged over the full length of the local curvature measurement. As a result, curvatures for such specimens may be underestimated to some extent, depending on the strength difference ζ and the location of the weld within the curvature measurement. This must be considered when interpreting the test results.

In the bending experiments, six specimens were tested that included a girth weld or coil connection weld. As discussed in section 6.3, in four of these specimens, local buckling took place in the immediate vicinity of the girth or coil connection weld (see Figure 6.8). In all four cases, local buckling occurred at the weaker side of the weld. In the remaining two specimens, local buckling took place in a plain part of the tube, away from the welds. Apparently, other factors were dominant in determining the buckling location for these specimens.

One of these factors may be the size of the geometrical imperfections at the weld in relation to the size of the geometrical imperfections in a plain tube segment. As discussed in section 5.2.5, imperfections near a girth weld are generally larger than in a plain tube segment (see Table 5.3). However, in the case of specimen T7, the misalignment and other geometrical imperfections that are measured at the girth weld are not so severe. Furthermore, due to its stockiness, specimen T7 is expected to be less sensitive to geometrical imperfections, which allows other factors to be decisive in the formation of a local buckle. In specimen T12, geometrical imperfections at the girth weld also were relatively small, but the initial imperfection at the coil connection weld was quite large. The specimen consisted of three parts, where the middle part had a strength ratio of 1.15. As a result, this stronger part may have been able to support the attached weaker parts close to their welded connection. This support may have prevented the formation of a local buckle, and may have reduced cross-sectional ovalisation due to bending. Further away from the welds (GW and CCW), the plain, weaker specimen parts apparently were more vulnerable to buckling. It should be noted that the aforementioned support effect could also be expected to prevent local buckling at the girth weld in specimen T10, where an even larger difference in strength between the joined parts exists. In that case, however, local buckling took place at the girth weld, very likely triggered by the very large initial geometrical imperfection at that location (see Table 5.3).

Overall, it can be concluded that the critical curvature (deformation capacity) of specimens containing a girth weld or coil connection weld is generally observed to be lower than in plain specimens (see Figure 6.3). The maximum resisted bending moment is equal or lower than similar plain specimens (see Figure 6.2). In tubes containing a girth weld or coil connection weld, the curvature tended to localize more than in plain specimens (see Table 6.1), especially when local buckling took place at these welds. Because of this difference in curvature localization, a comparison of critical strains based on local curvature instead of average curvature results in less discrepancy between plain specimens and specimens containing a girth weld or coil connection weld. However, even when the local curvatures are used, tubes containing a girth weld or coil connection weld are on the lower end of the scatter band in terms of the measured critical strain. It must be noted that the averaging of curvatures over a certain length may have contributed to this observation in case of a strength mismatch at a girth weld or coil connection weld within the curvature measurement. Finally, the difference between reaching the maximum bending moment and load drop-off (ductility ratio) is lower for specimens containing a girth weld or coil connection weld. This effect is visible for the four specimens that have failed at the weld for both global and local curvatures (see Figure 6.6).

6.5 Numerical analysis of manufacturing process and four-point bending tests

As part of the COMBITUBE project, research partners at the University of Thessaly developed a numerical model to simulate the behaviour of spiral-welded steel tubes under bending, focusing on the D/t range that is relevant for combined walls (Vasilikis et al., 2016). To validate this

model, the four-point bending tests on spiral-welded tubes that were performed at Delft University of Technology were simulated.

For a correct simulation of the bending behaviour of the considered tubes, information with regard to the present residual stresses in the spiral-welded tubes was required. Considering the erratic results that were found in measurements of residual stresses on the spiral-welded tubes (see section 5.2.1), a numerical model was developed, aimed at predicting the residual stresses that are developed during manufacturing of the tube.

For the simulation of the bending behaviour of the spiral-welded tubes, use was made of the FE-software package ABAQUS (2010). In the model, the tube is considered initially imperfect, with a wavy-type (wrinkling) geometric imperfection, in the form of the first buckling mode, obtained through a standard eigenvalue analysis of the tube under pure bending. The amplitude of these modelled imperfections was chosen such that it matched the actual geometrical imperfections in the considered specimen (see section 5.2.5). Using the residual stresses of the numerical simulation of the spiral-welding manufacturing process, the geometrical imperfections measured on the test specimens and the actual material properties from the material tests (see section 5.3.2), a very good comparison was found between the numerical results and the experimental data reported in this research. The comparison is good in terms of maximum resisted bending moment, critical curvature and the deformed buckle shape. Using this validated model, an extensive parametric study was performed, which further increases the understanding of the bending behaviour of the tubes under consideration.

More information on the modelling by the research partners from the University of Thessaly such as the used modelling techniques, comparison with the experiments and the results of the parametric study can be found in Vasilikis et al. (2016).

6.6 Post-buckling behaviour

A noticeable feature of all tests (see Figure 5.49 and Appendix B.3) is that considerable strength remained after local buckling ‘failure’ occurred. Directly after formation of a local buckle, the bending moment resistance of the tested tubes was significantly reduced, but a considerable part of the pre-buckling resistance remained.

In certain structures, local buckling and the accompanying large deformations may lead to significant reduction of the load. For example, a reduction in soil load may be expected on a buckled tube in a combined wall, due to the large deformations associated with local buckling of the tube. Depending on the conditions during its service life, this may be a considerable reduction in soil pressure. Additional reduction may be expected due to arch formation in the soil, leading to load transfer to neighbouring tubes. In a parallel structural system, such as a combined wall, the formation of a buckle in one element may therefore not lead to total failure if considerable bending moment capacity remains after the formation of a local buckle.

An overview of the bending moment capacity of all specimens directly after buckling (M_{pb}) is presented in Figure 6.10. Since the post-buckling bending moment capacity clearly is correlated

to the cross-sectional slenderness, a calculation model for the remaining bending moment capacity was developed on the basis of linear regression of the test data.

Using probabilistic design procedures as described in annex D of Eurocode 0 (EN 1990, 2002) and Bijlaard et al. (1988), a safe design guideline on the basis of this calculation model was developed. Further elaboration on this process and the necessary assumptions for the calculation can be found in Appendix G.2.

In Figure 6.10, the result of test T9 appears to be an outlier. Re-examination of that particular test result concluded that a considerable strength drop within a short time-frame cannot be identified. Instead, the strength of the specimen gradually decreased for increasing curvatures. Therefore, the result of test T9 was not taken into account in the analysis of the proposed calculation model.

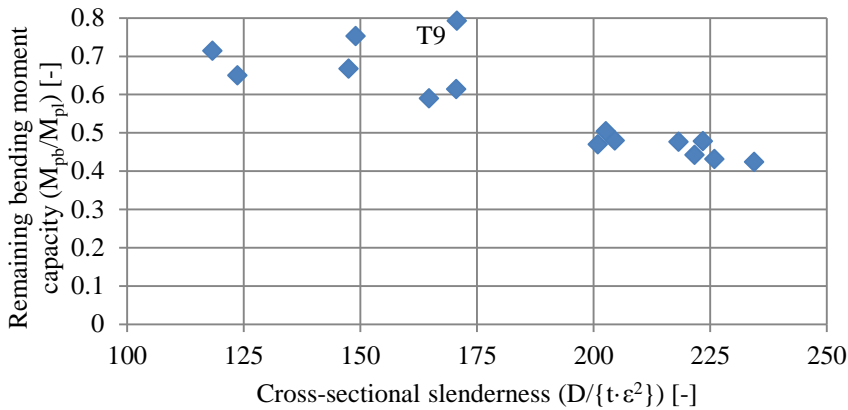


Figure 6.10 Overview of the remaining post-buckling bending moment capacity of the tested specimens.

The remaining post-buckling bending moment capacity of tubular members can be predicted with equation (6.2) for a safety level of $\beta=3.8$ assuming appropriate probabilistic determination of the design loads. For a deterministic load, use of equation (6.2) results in a failure probability $P_f=10^{-3}$ at 75% prediction probability using nominal values for all input parameters. Calculation models for the mean, characteristic and design strengths using mean values of the input variables are given in Appendix G.2. A comparison of the design model and the test results is presented in Figure 6.11.

For the analysis, the remaining post-buckling bending moment capacity was analysed directly after formation of a local buckle. As can be seen in the moment-curvature diagrams resulting from the tests (see Appendix B.3), further deformation of the tubes results in further reduction of the bending moment capacity. In all but one of the tests, 40% of the maximum bending moment capacity remained available under considerable post-buckling deformation. Additional analyses are necessary to quantify this effect.

$$M_{pb;d}(X_n) = \frac{M_{pb;m}(X_n)}{\gamma_M^*} = \frac{\left(A \cdot \frac{D_n}{t_n \cdot \varepsilon_n^2} + B \right) \cdot (D_n - t_n)^2 \cdot t_n \cdot \sigma_{y;n}}{\gamma_M^*} \quad (6.2)$$

Validated for the parameter range:

$$115 \leq \frac{D}{t \cdot \varepsilon^2} \leq 235, \quad 65 \leq \frac{D}{t} \leq 125 \text{ and } 330 \leq \sigma_y \leq 620$$

With:

ε : Cross-sectional slenderness. $\varepsilon^2=235/\sigma_y$.

A : Dimensionless coefficient. $A=-2.65 \cdot 10^{-3}$.

B : Dimensionless coefficient. $B=1.04 \cdot 10^0$.

X_n : Nominal value of an input parameter

γ_M^* : Model factor. For equation (6.2): $\gamma_M^*=1.28$ (for discussion, see Appendix G.2)

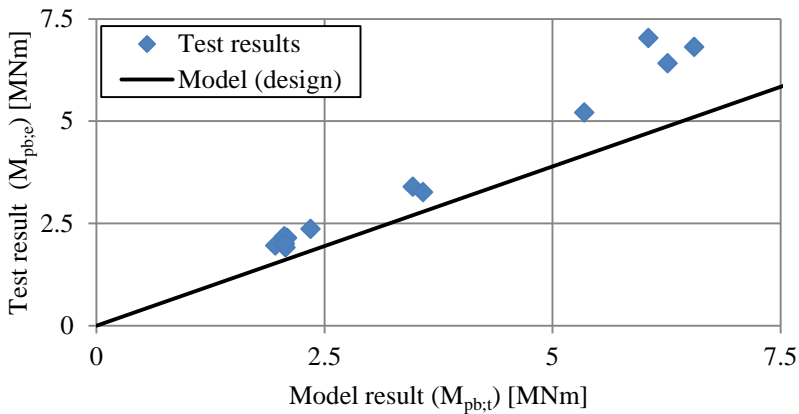


Figure 6.11 Comparison of design model (see equation (6.2)) with test results.

6.7 Influence of spiral-welding manufacturing process

6.7.1 Observed differences in behaviour between spiral-welded and longitudinal-welded tubes

The maximum bending moment capacity of the tested spiral-welded and longitudinal-welded tubes was found to be similar (see Figure 6.2). Naturally, for a more thorough analysis more than two longitudinal-welded tubes should be taken into account. A comparison of the test

results with pure bending test results found in literature (see Chapter 1) is presented in Figure 6.12. Tests that include an axial force in the tube are not considered. Besides the test results of the current research, the figure features test results of spiral-welded tubes originating from the SBRCURnet research (Royal HaskoningDHV, 2013) which was performed in close collaboration with the COMBITUBE research project. The other data points represent tests on tubes manufactured using other techniques than spiral-welding. Furthermore, it is noticeable that for a considerable amount of the results from literature the theoretical full plastic moment is exceeded. This may be caused by incorrect documentation or assessment of the yield stress of that specific test result, or the absence of a yield plateau and significant strength increase directly after reaching $\sigma_{0.2\%}$.

When comparing the test results with the test results found in literature, the tested spiral-welded tubes appear to have a bending moment capacity that is similar to that of tubes manufactured using other techniques.

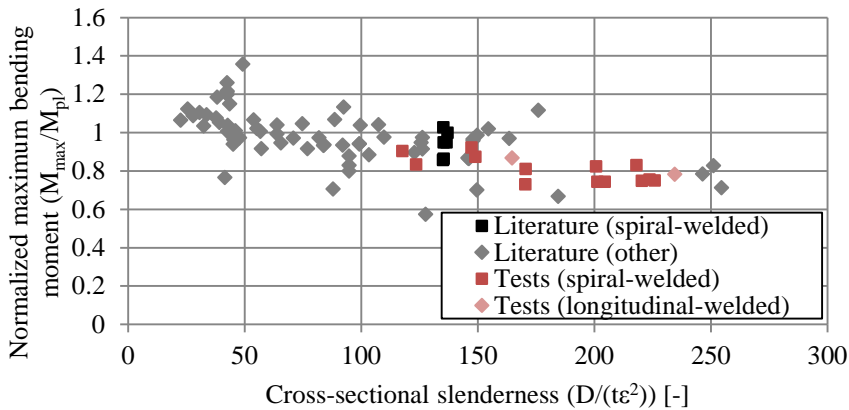
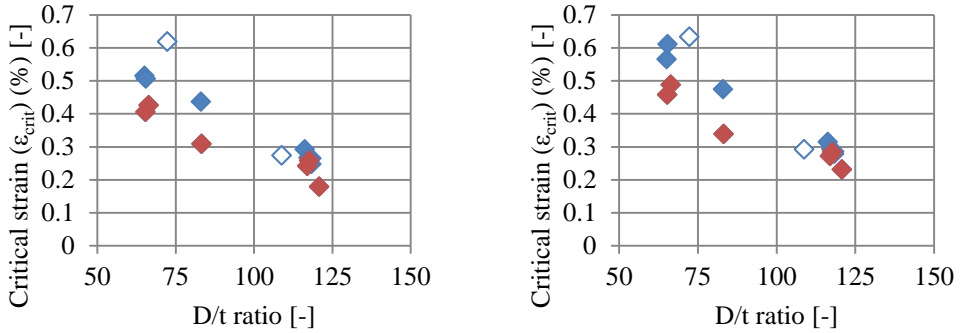


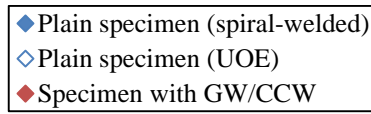
Figure 6.12 Comparison of test results with results found in literature (see section 1.3.2).

As discussed in section 6.2, in the tested spiral-welded tubes, curvatures localized before a local buckle formed. In contrast, in the tested longitudinal-welded tubes, the curvature remained approximately uniform over the section loaded in constant bending moment. A comparison of critical curvature between the spiral-welded tubes and longitudinal-welded tubes therefore depends on the definition of curvature. An overview of the test results using both average and local curvature is presented in Figure 6.13. Figure 6.13a shows that specimen T15 has a higher average critical curvature than comparable spiral-welded specimens, while Figure 6.13b shows that locally, the behaviour of the spiral-welded and longitudinal-welded specimens is similar.

A comparison of the test results of the present study with test results found in literature is presented in Figure 6.14. In this figure, the locally measured curvature is used as basis for the critical strains obtained from the results of the experiments performed in this study. Similarly as observed in Chapter 1, considerable scatter is visible. The test results of the current research fit well within the results found in literature. There is no indication that the spiral-welded specimens performed significantly better or worse than longitudinal-welded tubes.



(a) Average curvature (same as Figure 6.3) (b) Local curvature at buckling location



(c) Legend to both graphs

Figure 6.13 Comparison of critical strains between longitudinal and spiral-welded tubes determined from average curvatures and local curvatures.

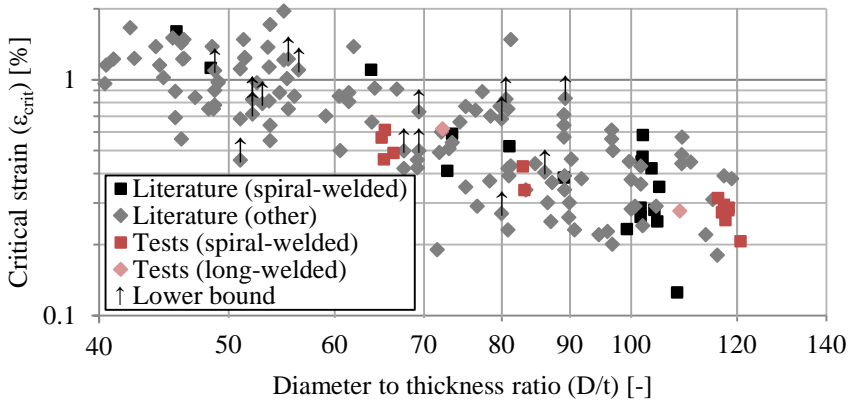


Figure 6.14 Comparison of test results with results found in literature (see section 1.3.2).

Although the two main parameters of the bending tests (M_{max} and ϵ_{crit}) seem to be unaffected by the manufacturing technique, an important difference in behaviour between spiral-welded and longitudinal-welded tubes is found in the curvature localization ratio (CLR, see Figure 6.5). The teste spiral-welded tubes showed an average CLR of 10-12%, while the tested longitudinal-welded tubes showed hardly any localization of curvature. It should be noted that a CLR of such magnitude is small compared to the scatter that is found in test results (see Figure 6.14).

6.7.2 Possible causes of differences in curvature localization ratio

A localization of curvature can occur when the cross-sectional properties of a tube are not constant over its length. Therefore, the differences in curvature localization behaviour between spiral-welded and longitudinal-welded tubes are likely caused by differences in variation of cross-sectional properties over the length of the tube. The main cross-sectional properties that are of influence are the geometric properties of the tube cross-section (e.g. D , t and f) and the mechanical material properties of the tube cross-section (e.g. E and σ_y).

Variations in geometry

Measurements of initial geometry (see section 5.2) have shown that the variation of wall thickness and diameter is very small within one specimen part. While of the diameter variation only a global overview per specimen part is available, the wall thickness measurements have also been performed on a line perpendicular between two spiral welds. The results of these measurements show a decrease of wall thickness towards the spiral welds of on average 1.2% (see Figure 5.10). Due to the helical nature of the tube, this small stiffness reduction is present in the neutral line at some locations while at other locations it is present in the outer fibres of the cross-section. However, the change in wall thickness is so small, that the effect on the bending stiffness is also very small. Nonetheless, during the elastic trajectory, such a local reduction of the cross-sectional bending moment capacity results in a proportional increase in strain, and thus curvature. In the elasto-plastic part of the moment-curvature trajectory, such a small difference may lead to larger differences in deformation.

Variations in mechanical properties

Many tensile tests were performed on the tubular specimens. However, local variations of the material properties within one specimen part were not quantified. This section offers possible causes of variations in material mechanical properties in spiral-welded tubes that are not present in longitudinal-welded tubes.

The variation of material properties in a manufactured tube originates from variations of material properties in the steel plate or coiled steel that was used to manufacture the tube. Four possible variations in material properties are recognized (see Figure 6.15):

1. Systematic variation of material properties along the length of a coil or plate
2. Systematic variation of material properties over the width of a coil or plate
3. Systematic variation of material properties near the start and end of a coil
4. Random variations in material properties in a coil or plate

Variations 1, 2 and 4 can occur both in a steel plate or coiled steel. To what extent these two products exhibit similar variations is not known.

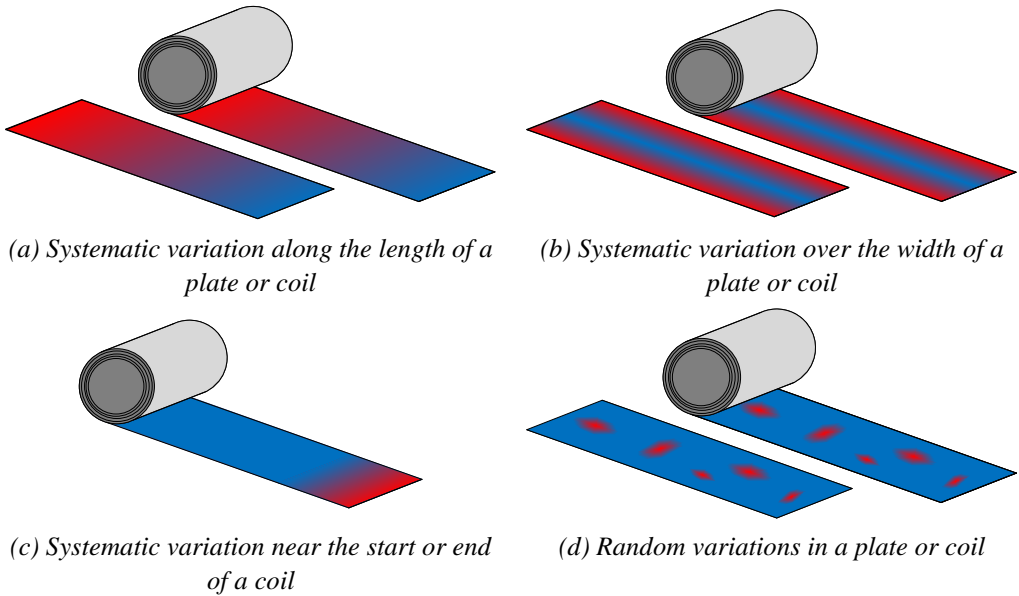


Figure 6.15 Recognized variations in material properties in flat plate or coiled steel.

The random variations of material properties (see Figure 6.15d) in a steel plate or coil will result in random variations of material properties in a tube manufactured from that parent material. In case of a similar amount of random variation of material properties in steel plate and coiled steel plate, these random variations are assumed to affect tubes of all manufacturing process equally. Therefore, the influence of random variations of material properties is not taken into account in this analysis.

The effect of a systematic variation of material properties over the length of a coiled plate or flat plate (see Figure 6.15a) on the variation of material properties along the length of a spiral-welded or longitudinal-welded tubular is presented in graphical form in Figure 6.16. In both a spiral-welded and a longitudinal-welded tube, a systematic variation of material properties of the parent material leads to a systematic variation of material properties of the tube in longitudinal direction. In a spiral-welded tube, the systematic variation is amplified by a factor $\cos(\theta)^{-1}$, with θ being the spiral welding angle, due to the spiral forming of the coiled steel (see Figure 6.16a). Considering the observed forming angles within this research, the amplification factor is limited to 1.22. The effect of this amplification on the CLR is deemed to be minor.

Apart from the aforementioned amplification of material properties variations, the variation of material properties in a spiral-welded tube is less smooth than in a longitudinal-welded tube (compare Figure 6.16a and b). Assuming that the material properties vary continuously and smoothly in the steel plate or coil, a similarly smooth variation is to be expected in the longitudinal-welded tube. In the case of a spiral-welded tube, small steps in material properties are present at the spiral weld when the material properties are inspected along a longitudinal line along the tube surface.

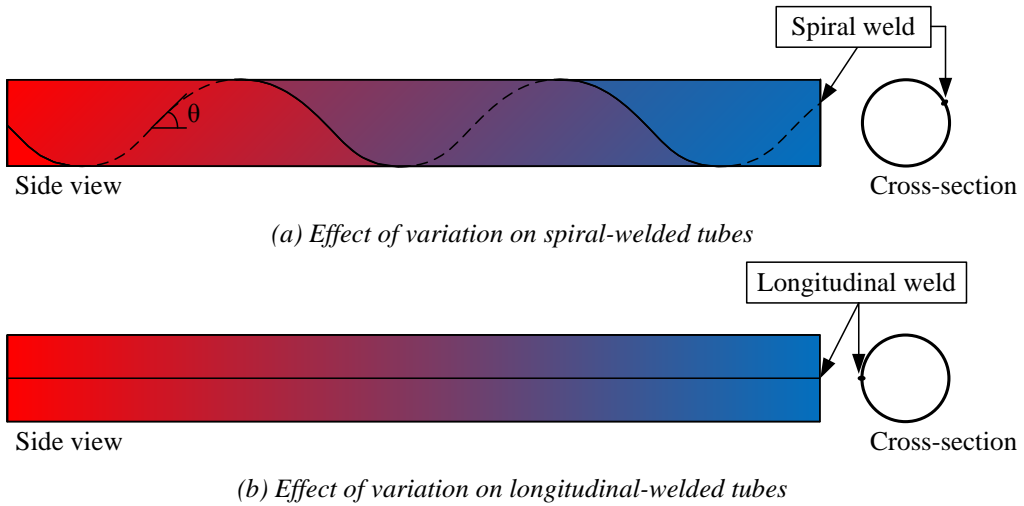


Figure 6.16 Effect of a variation of material properties along the length of a plate or coil.

The effect of a systematic variation of material properties over the width of a coil or plate (see Figure 6.15b) on the variation of material properties along the length of a spiral-welded or longitudinal-welded tubular is presented in graphical form in Figure 6.17. In case of longitudinal-welded tubes, the variation in material properties of the parent material results in a weak area of the cross-section. This area is present in the same orientation along the tube length, i.e., the distance to the seam weld does not vary over the length of the tubular (see Figure 6.17b). In case of spiral-welded tubes, the weak area of the cross-section spirals as a result of the spiral-welding manufacturing process. Therefore, when the material properties are inspected along a longitudinal line along the tube surface, maxima and minima are observed. The spiralling weak portion of the cross-section may result in cross-sections that are stronger or weaker in bending, depending on the orientation of the weak portion and the direction of bending.

The risk of not meeting requirements in terms of thickness, flatness and material properties near the end of a coiled plate is well understood by manufacturers. Furthermore, for a good execution of the coil connection weld, a straight edge of the coil is necessary. For these reasons, the starts and ends of a coil are not used in tubes. A certain length of coil material is removed so that the material that remains meets demands in terms of thickness and minimum yield strength. Whether, despite this removal of material, a variation of material mechanical properties is present towards the coil start and end is not known. If this is the case, this will translate into a variation of bending capacity of the tube near the coil connection weld.

In the previous discussion, the possible differences in variation of material properties within a product have not yet been addressed. If the variation of material properties within coiled steel and a flat plate differ significantly, this will also affect the tubes that are manufactured from these products.

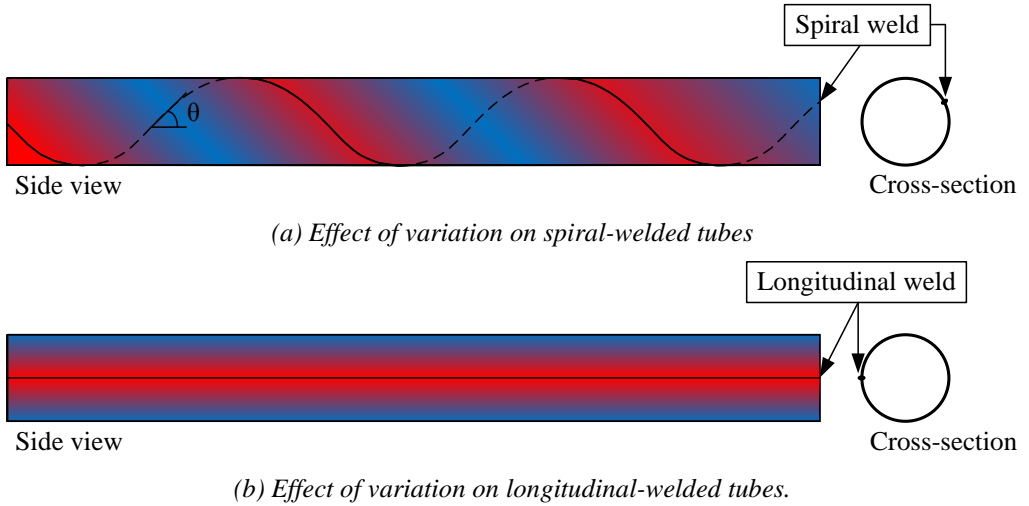


Figure 6.17 Effect of a variation of material properties over the width of a plate or coil.

It can be concluded that spiral-welded and longitudinal-welded tubes may have very different responses to variations in geometry and material properties of the parent flat or coiled steel plate. These responses may constitute a cause for the differences in curvature localization that were observed in section 6.2.2. However, with currently available experimental data, this hypothesis cannot be verified. Tensile tests on coupons taken at various locations within plate, coil and tube material in combination with bending tests on these tubes may provide further understanding of the mechanism behind the observed curvature localization.

6.8 Effect of a soil fill

In a combined wall, the tubular elements are typically fully or partially filled with soil. This is the soil that was present before placement of the element and is forced into the tube during installation. The typical local buckling shape of an empty tube without internal pressure shows one or more inward wave shapes (see Figure 5.46). The soil present inside the tube may resist the formation of these waves. A consequence can be that the local buckle is forced outwards (see Figure 9.42c and Figure 9.42d). Furthermore, the presence of soil inside the tube may limit the ovalisation of a tube due to bending and soil pressures. The outwards local buckling shape and reduced ovalisation are two effects that are also present in pressurized tubes and in that case contribute to a higher local buckling resistance. Apart from delaying local buckling failure, the soil may contribute to the resisted bending moment through compressive stresses. The steel tubular then acts as part of a composite cross-section.

The possible positive effect of soil that is present inside tubes in combined walls was investigated by SBRCURnet (Royal HaskoningDHV, 2013) in a project running parallel to the COMBITUBE research project. Within this project, 24 spiral-welded and longitudinal-welded tubes with D/t ratios between 72 and 119 and steel grades between S235 and X65 were tested in

four-point bending. Of these 24 tubes, 12 were filled with sand. The effect of other soil types was not investigated.

The testing programme showed that the typical outward buckling shape is the dominant mode for sand-filled tubes. Ovalisation was found to be restrained by the sand and local buckling delayed. Furthermore, after local buckling, only a small reduction in bending moment capacity was found. While in the COMBITUBE bending tests the bending moment capacity drop was found to be at least 25% (see section 6.6), the sand-filled tubes were reported to exhibit a drop in bending moment capacity of only 15% to 25%.

The SBRCURnet report recommends use of the ENV 1993-5 (1998) for empty tubes and presents a modification to the calculation models in this standard to deal with the beneficial effect of a sand fill.

6.9 Comparison of test results with strain-based prediction model

Within the framework of the COMBITUBE project, new strain based design guidelines were developed by research partners on the basis of the work by Gresnigt (1986). A summary of the design guidelines is presented in Gresnigt et al. (2016), while a more comprehensive description of the guidelines can be found in the final report of the research project (COMBITUBE Research Consortium, 2015). The guidelines include an analytical description of the moment-curvature behaviour of the tubes and a separate prediction formula for the critical strain.

6.9.1 Moment-curvature diagram

The model that describes the moment-curvature behaviour of the tubes requires three input parameters: tube diameter, wall thickness and yield stress. For comparison of the model with the test results, the measured tube diameter and wall thickness of each specimen part were used as input for the model. Because relatively little variation in diameter and wall thickness was observed over the length of a specimen part (see section 5.2), the measured properties were assumed to be representative for the full specimen parts under consideration.

More variation was found in the measured yield strength of the tubes. As shown in section 5.3.2, different yield strengths were measured on the inside and outside of the tube wall. Further differences were found when comparing the yield strength in axial and hoop direction of the tube. Some of the material tests showed a sharp transition between elastic deformation and yielding, while in other cases a gradual transition was observed. In the model, these complex, anisotropic material properties are simplified to an elastic-perfectly-plastic material model, with equal yield strength in axial and hoop direction. It was found that using the average yield strength measured in hoop and axial direction on the inside and outside of the tube wall results in accurate predictions for tubes with a material behaviour that shows a sharp transition between elastic deformation and yielding. In case of a more gradual transition, the elastic-perfectly-

plastic material model that is incorporated in the prediction model results in a slight over prediction. It was found that for the tested specimens, applying a reduction of 5% to the measured yield stress ($\sigma_{0.2\%}$) resulted in an optimal comparison between model and test result.

Using these input parameters, a good comparison is found between the prediction model and test results as is shown in Figure 6.18 for two examples. The comparison between the model and all test results is presented in Appendix C.

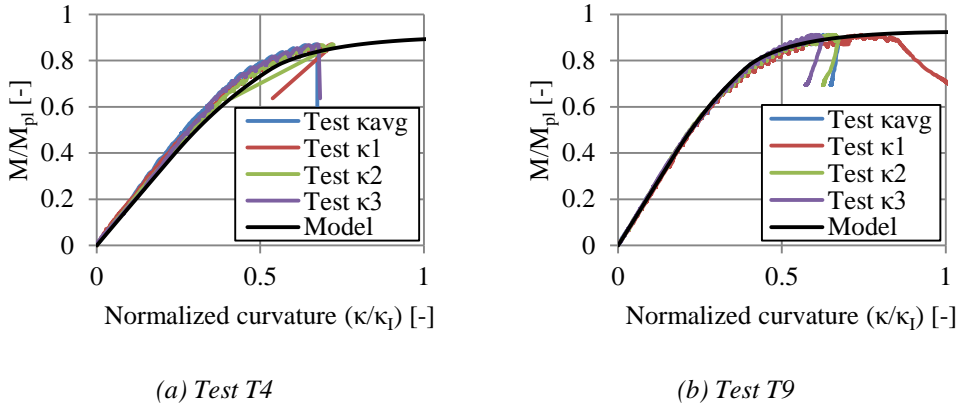


Figure 6.18 Two examples of a comparison between the prediction model and the test results.

The developed model does not consider anisotropic material properties. Yielding in axial and hoop direction is taken into account through one yield stress. The model may be improved by implementing such an anisotropy.

The effect of a gradual transition between elastic deformation and yielding of the tube material was taken into account in the above analysis through a constant reduction factor on the yield strength. However, this reduction factor will certainly be dependent on the exact shape of the stress-strain diagram, the D/t ratio of the tube and the curvature of the tube. It is recommended that this is further studied, for example by comparing a parametric study using an FE-model with the analytical model.

6.9.2 Critical strain

The new prediction model for the critical strain is based on the model proposed by Gresnigt (1986). The influence of geometrical imperfections, strain hardening of the material and the possible presence of a sand fill is taken into account through a series of correction factors (see equations (6.3) and (6.4)). These correction factors were based on the numerical work by Vasilikis et al. (2016) and SBRCURnet (2013). For the prediction of the test results, the measured values of the geometrical imperfections and strain hardening properties were taken into account.

A comparison between the calculated critical strain using the prediction model and the results of the fifteen experiments performed at Delft University of Technology is presented in Figure 6.19. For the experimental results, local curvatures were used. The critical strains shown in Figure

6.19 thus differ from the results shown in Figure 6.3 by a factor equal to the CLR (see section 6.2.2). The figure shows that the prediction model is conservative for all test results except test T10.

$$\text{for } \frac{t}{r} > \frac{1}{60}: \varepsilon_{crit} = 0.25 \frac{t}{r} - 0.0025 + 3000 \left(\frac{Pr}{Et} \right)^2 \cdot \frac{|P|}{P} \quad (6.3)$$

$$\text{for } \frac{t}{r} < \frac{1}{60}: \varepsilon_{crit} = 0.10 \frac{t}{r} + 3000 \left(\frac{Pr}{Et} \right)^2 \cdot \frac{|P|}{P}$$

$$\varepsilon_{crit}^* = \varepsilon_{crit} \cdot \alpha_{geo} \cdot \alpha_{sh} \cdot \alpha_{sand} \quad (6.4)$$

With:

ε_{crit}^* : Critical strain including the influence of imperfections, strain hardening and sand fill

α_{geo} : Effect of geometrical imperfections on critical strain.

α_{sh} : Effect of strain hardening on critical strain.

α_{sand} : Effect of sand fill on critical strain.

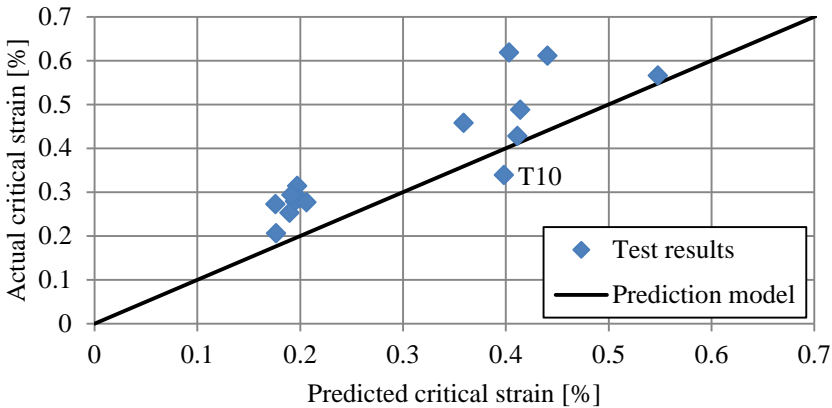


Figure 6.19 Comparison between prediction model and experimental results.

As discussed earlier, specimen T10 featured considerable discontinuities in bending moment capacity of the cross-section (see Figure 5.34). The local curvature measurement that contains the local buckle partly contains the thinner walled specimen part with lower yield strength and partly contains the adjacent thicker walled specimen part with higher yield strength (see Figure 6.20). Due to the considerable discontinuities in cross-sectional properties, it may be assumed that the curvature in the stronger specimen part was very small. This assumption is confirmed by the very low curvature that is measured by local curvature measurement κ_l in comparison with the two other local curvature measurements (see Figure B.11). The larger curvature of the weaker specimen part is averaged over the full length of the local curvature measurement (see section 6.4). As a result, the actual critical curvature is higher than displayed in Figure 6.19. The data point therefore was removed from the analysis.

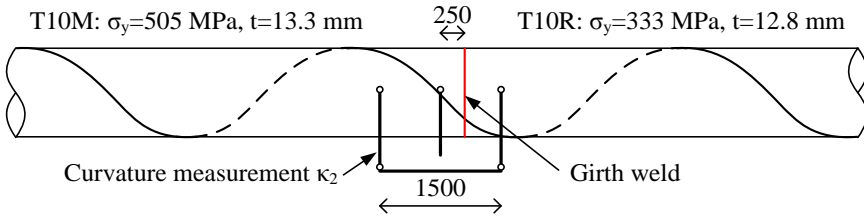


Figure 6.20 Considerable discontinuity in cross-sectional properties within local curvature measurement κ_2 in specimen T10 (dimensions in mm).

Using the methods proposed in annex D of Eurocode 0 (EN 1990, 2002) and Bijlaard et al. (1988), the prediction model as proposed by Gresnigt et al. (2016) was compared with the results of the performed four-point bending tests. As is shown in Figure 6.21, the model by Gresnigt et al. (2016) can be shown to approximately correspond with a characteristic model, or 5% lower bound. The assumptions made for this calculation are presented in Appendix G.3. Based on the considerations stated above, specimen T10 was removed from this analysis. The difference between the prediction model and the calculated characteristic value of the prediction model is approximately 1.5%, which is a negligible difference considering the scatter in the test results.

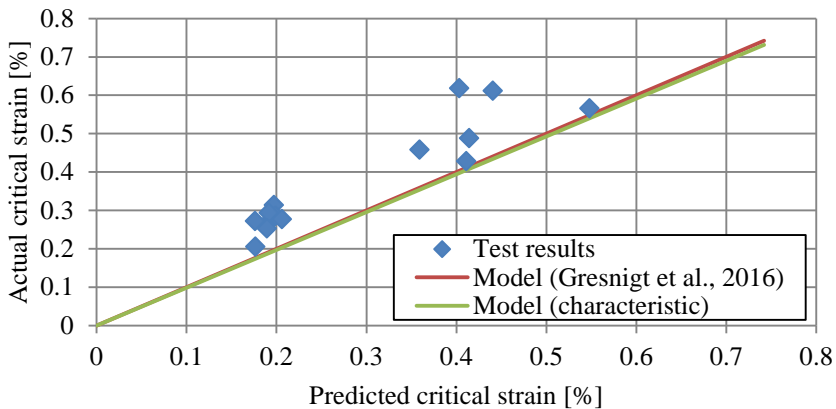


Figure 6.21 Comparison between test results, prediction model and calculated characteristic value of prediction model.

It should be noted that this analysis presents a totally different safety level of equations (6.3) and (6.4) than the analysis presented in Part I of this thesis, where a similar comparison was made. Various explanations are available for this. Firstly, in Part I of this thesis, the modification factors for the critical strain as presented in equation (6.4) were not considered. More importantly, as discussed in Chapter 1, accuracy of the experiments and comparability between the data points that are used for validation of the safety level of a design formula may greatly influence the result of such an analysis. The test results that were used to determine the safety level of equations (6.3) and (6.4) were all comparable and well documented.

6.9.3 Maximum bending moment capacity.

After determining the moment-curvature behaviour of a tube and its critical strain and critical curvature, the maximum bending moment capacity can be determined. This procedure is given in Figure 6.22.

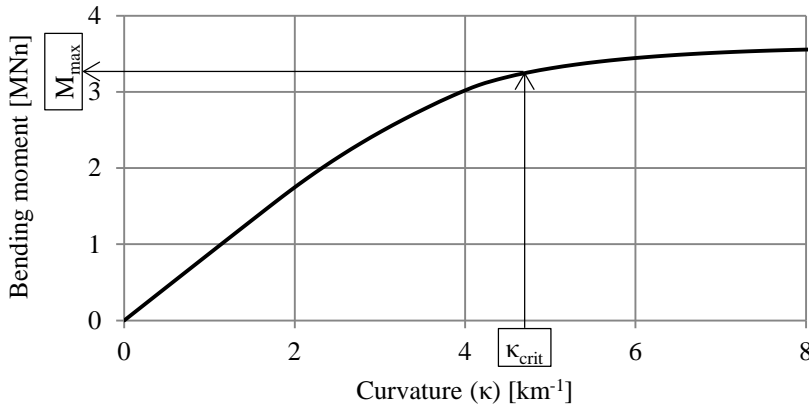


Figure 6.22 Procedure to determine maximum bending moment capacity using strain-based design guidelines.

Using the methods proposed in annex D of Eurocode 0 (2002) and Bijlaard et al. (1988), a safe design value of the maximum bending moment capacity was determined. This analysis is presented in Appendix G.4. To obtain a design value that is conservative in practical application, no correction to the yield stress was applied in case of a gradual transition between elastic deformation and yielding (see section 6.9.1). The analysis shows that for a large part of the cross-sectional slenderness ($D/\{t\varepsilon^2\}$) spectrum, the formula proposed by Gresnigt et al. (2016) corresponds to a characteristic value.

A comparison between the method using the models proposed by Gresnigt et al. (2016), a conservative design line and the test results is presented in Figure 6.23. To obtain a safe design value of the maximum bending moment capacity of a tube, the moment-curvature relation and critical curvature are to be determined using the models as proposed by Gresnigt et al. (2016). Only to the calculated maximum bending moment capacity a partial safety factor (γ_M^*) of 1.15 is applied. This partial safety factor was determined under the assumption that each tube is designed to a probability of failure corresponding to $\beta=3.8$. Perhaps a lower safety level may be acceptable, considering that:

- Local buckling of a tube results in loss of part of the bending moment capacity, but not the full bending moment capacity (see section 6.6)
- Local buckling of a single tube in a long combined wall does not necessarily result in total failure of the structure because the structure consists of a series of tubes.
- Local buckling of a tube results in significant deformation of a combined wall, thereby reducing the horizontal soil pressure acting on the combined wall (see section 6.6).

A more elaborate safety analysis may therefore result in reduction of the value of γ_M^* . However, such an analysis may be strictly bound to applications in combined walls.

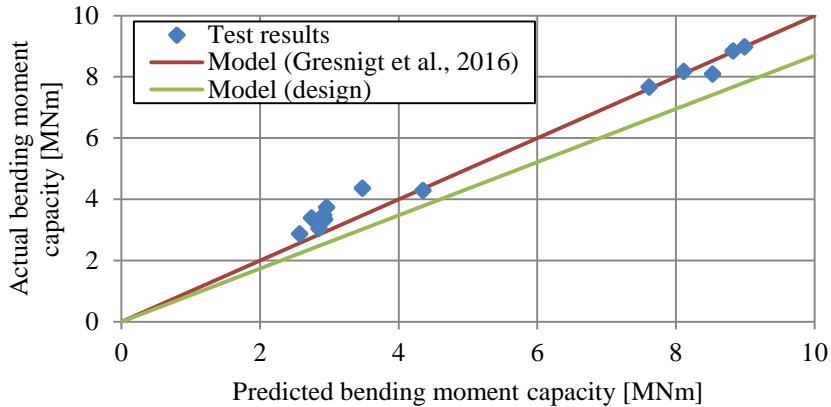


Figure 6.23 Procedure to determine maximum bending moment capacity using strain-based design guidelines.

6.10 Application of results

6.10.1 Application of results to combined walls

The experiments presented in this study have aided development of accurate numerical models (see section 6.5). The results of this numerical work, in combination with the test results presented in this study contributed to the development of calculation models for the moment-curvature behaviour of tubes in combined walls (see section 6.9), and their remaining post-buckling bending moment capacity (see section 6.6).

Additional research into the bending behaviour of combined walls was performed by SBRCURnet (see section 6.8). The results of this work were used by Gresnigt et al. (2016) to include the beneficial effect of a sand fill in tubes on their bending behaviour in their models.

All failure analyses were performed assuming that failure of a single tube results in failure of the total structure. As discussed in sections 6.6 and 6.9, this may not be the case for several reasons:

- Local buckling of a tube results in loss of part of the bending moment capacity, but not the full bending moment capacity (see section 6.6)
- Local buckling of a single tube in a long combined wall does not necessarily result in total failure of the structure because the structure consists of a series of tubes.
- Local buckling of a tube results in significant deformation of the combined wall, thereby reducing the horizontal soil pressure acting on the combined wall (see section 6.6).

For these reasons, a more elaborate safety analysis and possibly additional experimental testing (see Appendix G.4.3) may result in a lower required safety and therefore increased economy of the design. Analysis that takes into account the latter two of the above effects is strictly bound to application in combined walls.

6.10.2 Other applications

The bending behaviour of spiral-welded tubes is not only relevant for the design of combined walls. As discussed in section 4.3, large-diameter spiral-welded tubes may also be applied in pipeline or structural applications other than combined walls, such as towers and masts. The results of these tests as well as the developed guidelines may also be of use for the design of these structures.

Especially for pipeline applications, the newly developed strain-based design guidelines by Gresnigt et al. (2016) may be of interest. These design guidelines originate from earlier design guidelines for pipelines (Gresnigt, 1986) and were improved using the results of the experiments, numerical work performed within the COMBITUBE project and research from other sources.

6.11 Summary of Chapter 6

This chapter deals with the analysis of the results of the tests performed on spiral- and longitudinal-welded tubes. In the performed tests and comparisons with literature, no clear effect of the spiral-welding manufacturing technique on the maximum bending moment capacity of the tubes was found.

The deformation behaviour of the tested spiral-welded tubes was found to be different from that of the tested longitudinal-welded tubes. Before a local buckle formed, curvature localized in a tube section with constant bending moment. As a result, the critical curvature that was found in an experiment also depended on the length over which the curvature was measured. In the tested spiral-welded tubes, the local curvature was found to be 10-12% higher than the average curvature at the point of maximum bending moment resistance, while for the two longitudinal-welded tubes that were tested, this difference was found to be 0-4%.

In general, the presence of girth welds and coil connection welds penalized the critical curvature of the tested tubes. In many tests, the maximum bending moment capacity of such tubes was also somewhat lower than similar plain tubes. This effect is partially caused by additional imperfections near the weld. A second factor is localization of curvature on one side of the weld, due to differences in cross-sectional bending moment resistance of the specimen parts adjoining the weld. Under inelastic deformation, a small difference in bending moment capacity may lead to a considerable difference in deformation under constant bending moment loading.

In cases where local buckling did not take place at a girth weld or coil connection weld, all buckles occurred at a geometrical imperfection which could clearly be identified in the pre-test

laser scans. In the case of the spiral-welded tubes, local buckling occurred at the geometrical imperfections that were attributed to the spiral-welding manufacturing process.

After reaching their maximum bending moment capacity, some tubes were able to resist bending moments close to the maximum bending moment under considerable extra deformation, especially the stockier specimens. Furthermore, after the formation of a local buckle, a considerable part of the bending moment capacity remained available. For increasing post-buckling deformation, the bending moment capacity was further reduced, but in all but one test at least 40% of the maximum bending moment capacity remained available under considerable rotation of the hinge formed by the local buckle. In parallel systems such as combined walls, this property can possibly be used to prevent local failures to govern failure of the full structure. A design formula for this remaining bending moment capacity was developed on the basis of the test results.

Reference is made to a study that investigates the influence of a soil fill inside the tube on the bending and local buckling behaviour. Such a soil fill may reduce the ovalisation of a tube due to bending and soil pressures. Furthermore, the formation of a local buckle was shown to be delayed and the post-buckling resistance of the tubes to be improved. These effects have not been studied within the COMBITUBE project.

Further reference is made to a study presenting numerical analyses performed by research partners. An FE-model was validated using the bending tests described in Chapter 5 of this study, followed by an extensive parametric study.

Strain-based design guidelines that were developed within the COMBITUBE project, using the results of the bending tests described in this study, were validated. Safe and economical designs are possible using these design guidelines.

Chapter 7

Summary of Part II and recommendations

7.1 Summary of Part II

Part II of this study consists of three chapters. In Chapter 4, an introduction to the spiral-welding manufacturing process and unique features of spiral-welded tubes is presented. The combined wall soil retaining structure in which spiral-welded tubes are often used is introduced.

In a literature overview it is shown that the behaviour of spiral-welded tubes with a relatively slender cross-section is not yet well understood. This lack of understanding, combined with relatively uneconomical European design regulations that govern the design of tubes in combined walls led to the start of a European research project with acronym COMBITUBE. The aim of this research project was to develop economical and safe design guidelines for spiral-welded tubes in combined walls. To that aim, the strength and deformation capacity of spiral-welded tubes under bending loading was investigated and is presented in Part II of this thesis.

To investigate the bending behaviour of spiral-welded tubes, a large-scale experimental programme was carried out. The programme consisted of careful investigation of the initial geometrical imperfections and material properties and subsequent bending tests on thirteen spiral-welded tubes and two longitudinal-welded tubes. The programme and its results are described in Chapter 5, while the test results are analysed and interpreted in Chapter 6.

Measurements of the initial geometry of the tubes showed a very consistent diameter and wall thickness of the tubes. For the spiral-welded tubes, a small decrease in wall thickness close to the spiral welds was observed. Measurements of the initial geometrical imperfections show that the manufacturing process of spiral-welded tubes directly influences the imperfection shapes. As a result, the initial imperfections in spiral-welded tubes are very different from the imperfections observed in longitudinal-welded tubes. The imperfections that were measured on the fifteen laboratory specimens were compared with imperfections measured in tubes in a combined wall at a construction site. It is shown that the imperfections observed in the laboratory are similar to

the imperfections that are present in undamaged tubes used in practice. Attempts to determine the residual stress state of the tubes resulted in a large scatter. Possible causes for this scatter were identified.

Extensive material testing on the fifteen tubular specimens was conducted, showing almost isotropic behaviour. Furthermore, a comparison between compressive and tensile coupon tests showed an almost symmetrical tensile-compressive material mechanical behaviour. In some cases a Bauschinger effect was observed, mainly in hoop direction of the tubes. No clear differences were observed between spiral-welded tubes and longitudinal-welded tubes.

Four-point bending tests were performed on the tubes, resulting in failure in the form of local buckling in all cases. Depending on the slenderness of the cross-section of the specimens, a local buckle formed suddenly and violently or more gradually. Within the tube segment loaded in constant bending moment, curvature was shown to be much less constant in case of the spiral-welded tubes than in case of the longitudinal-welded tubes. Tubes containing a girth weld or coil connection weld were observed to be penalized in terms of bending moment resistance and deformation capacity and showed more localization of deformation. In some cases, such tubes reached comparable performance as plain tubes. This negative effect of the girth and coil connection welds is partially caused by additional imperfections near the weld. A second factor is localization of curvature on one side of the weld, due to differences in cross-section bending moment capacity of the specimen parts adjoining the weld.

In cases where local buckling did not take place near a girth or coil connection weld, all local buckles formed at geometrical imperfections that could clearly be identified in the pre-test laser scans. In the case of spiral-welded tubes, local buckling occurred at the geometrical imperfections that were caused by the spiral-welding manufacturing process.

After local buckling failure of the tubes, a considerable part of the bending moment capacity remained available. For increasing post-buckling deformation, the bending moment capacity was further reduced but remained substantial. A design formula to predict the bending moment capacity that remains available directly after the formation of a local buckle is proposed.

A numerical model was developed by the University of Thessaly, a research partner within the COMBITUBE project, which was validated using the bending tests and geometrical imperfection measurements presented in this study. Using the validated numerical model, an extensive parameter study was performed. Further reference is made to a study investigating the effect of internal soil on the strength and deformation capacity of tubes in combined walls.

Strain-based design guidelines that were developed within the COMBITUBE project, using the results of the bending tests described in this study were validated. Safe and economical designs are possible using these design guidelines.

7.2 Recommendations for further research

The initial geometrical imperfections were found to differ between the investigated spiral-welded tubes and longitudinal-welded tubes. More specifically, in this study, the longitudinal-welded tubes originated from the UOE manufacturing process. Because differences were found

between the spiral-welded tubes and UOE-tubes, tubes originating from other manufacturing processes that are relevant for the geometrical range that is applied in combined walls, require a similar investigation. Moreover, the influence of manufacturing processes on local buckling of tubes in general may require attention.

This study and also the COMBITUBE research consortium did not sufficiently succeed in determining the residual stresses in spiral-welded tubes. It is therefore recommended to evaluate the influence of various patterns and levels of residual stresses on the local buckling behaviour of the considered tubes. In case of a substantial effect, further investigation into the general residual stresses resulting from the spiral-welding manufacturing process, as well as the residual stresses that develop near a coil connection weld or girth weld may require additional study.

In the bending tests, curvature was found to localize in the thirteen spiral-welded tubes, while much less localization of deformation was observed in the longitudinal-welded tubes. Considering the small sample size of especially the longitudinal-welded tubes, further investigations are necessary to confirm this behaviour. A possible explanation for the localization of curvature is given in section 6.7.2, which needs verification.

The more pronounced localization of deformation in tubes containing a girth weld or coil connection weld may result from imperfections near the weld or from a strength mismatch in the tubes adjoining the weld. In a further study, this effect may be quantified, and maximum differences may be proposed. In general it is recommended to minimize differences in bending moment capacity between adjacent tubes, except in case of design choices such as changes in wall thickness.

Measurements of imperfections on tubes in a combined wall at a construction site showed a larger number of dents, scratches and welded attachments than was expected on the basis of the observations made in the laboratory. These flaws were not investigated in the laboratory. However, by the nature of their origin, these flaws typically only occur at the extrados of the tubes in the use phase of the combined wall. In case of re-use however, they may be present in the intrados where they may influence the local buckling behaviour of the tubes. The influence of these flaws requires further investigation.

In this study and the COMBITUBE project, failure of a single tube is considered a failure of the total structure. However, for various reasons this may not be the case. Because a combined wall consists of a large number of tubes in a parallel structure and considerable bending moment capacity remains after formation of a local buckle, failure of a single tube may not result in failure of the total structure. Additional safety analyses may therefore show that a lower safety level is justified.

In this study, the remaining post-buckling bending moment capacity was determined directly after formation of a local buckle. As can be seen in the moment-curvature diagrams resulting from the tests (see Appendix B.3), further deformation of the tubes resulted in further reduction of the bending moment capacity. Additional analyses are necessary to quantify this effect.

The experiments that were performed within this study and within the COMBITUBE project focus on the pure bending behaviour of steel tubes for application in combined walls. However, in a combined wall, many influencing factors may exist which have not all been explicitly investigated. Such factors may be the presence of discontinuities in the tubes, such as changes in

tube wall thickness, concrete plugs, welded attachments or damages and dents. Furthermore, the sheet piling in between the tubes (see Figure 4.4) may exert loads on the tubes resulting in ovalisations of the tubes, while sand that is present in the tube may resist ovalisation and delay local buckle formation. It is recommended to include the effect of such factors in the formulations discussed in section 6.9, using research that is currently available or by performing analytical or numerical modelling, possibly supplemented by appropriate experimental work.

Part III:
Deformation of buried pipelines
crossing active strike-slip faults

Chapter 8

Introduction to Part III

8.1 GIPIPE research project

To investigate the behaviour of steel pipelines under severe permanent ground-induced deformations, a multi-disciplinary European Research project with acronym GIPIPE was started in 2011. The project involved investigation of the interaction between pipeline and soil and behaviour of the pipeline as a consequence of this interaction and movement of the surrounding soil. The aim of the project was to develop safe and usable design guidelines which extend the current design practice under these demanding conditions (GIPIPE Research Consortium, 2015).

The GIPIPE research project was coordinated by the University of Thessaly and was carried out by European research partners from academia and industry:

- University of Thessaly, Greece (coordinator)
- Centro Sviluppo Materiali, Italy
- Delft University of Technology, The Netherlands
- National Technical University of Athens, Greece
- Corinth Pipeworks, Greece
- Tebodin B.V., The Netherlands

The research presented in Part III of this study is part of the GIPIPE project and was funded by the Research Fund for Coal and Steel (RFCS) of the European Commission under Grant Agreement No. RFSR-CT-2011-00027.

8.2 Imposed deformation on pipelines due to soil movement

Buried pipelines may be exposed to imposed deformations due to movement of the soil surrounding the pipeline. Especially differential movements may result in deformation of the pipeline. Causes of these differential movements are, for example, uneven settlements,

landslides and fault movements (see Figure 8.1). In this study, the effect of a strike-slip fault movement on a buried pipeline is studied.

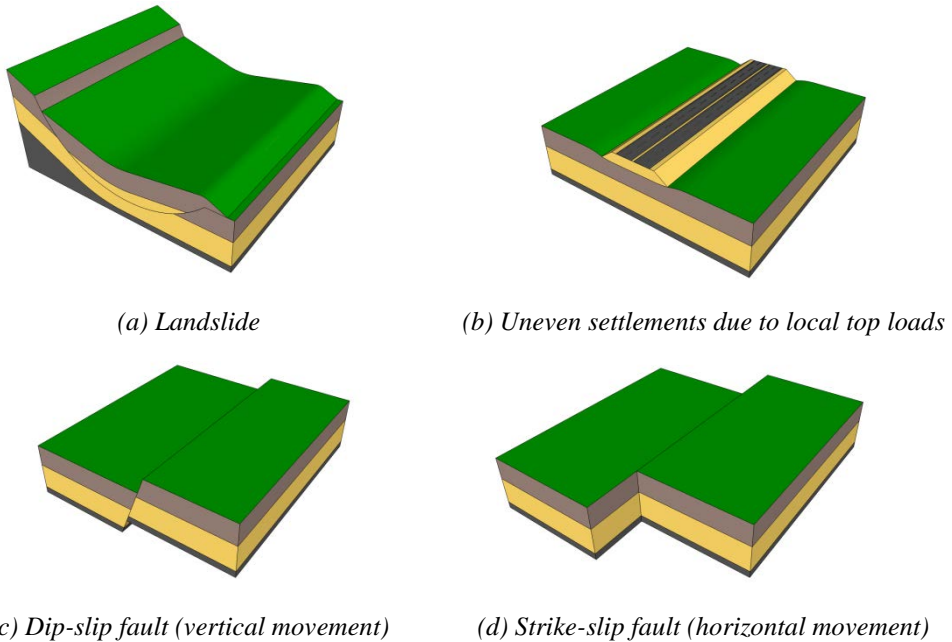


Figure 8.1 Possible causes of imposed pipeline deformations due to soil movement.

Typically, ground-induced deformations are applied to the pipeline in a quasi-static manner. Because the soil movements may be of considerable magnitude, significant stresses and strains can arise in the pipeline. As a result of these actions, failure of the pipeline may occur. Failure is recognized in the form of loss of containment through tearing of the pipeline wall due to high tensile stresses or strains. In case of high compression stresses or strains, local buckling of the pipeline wall may occur which impairs pipeline serviceability. Furthermore, the folding of the pipeline wall that is associated with local buckling may, in case of extreme deformations, also result in loss of containment. In general, neither of these failure mechanisms is tolerated in pipelines.

8.3 Literature review

8.3.1 Buried pipelines crossing strike-slip faults

The bending behaviour and local buckling behaviour of pipes is described extensively in Chapter 1 of this study, and requires no further discussion. However, in case of ground-induced deformations, both the pipe and soil behaviour influence the effect of the imposed deformation on the pipeline.

Early work investigating the interaction between a buried pipeline and its surrounding soil in case of lateral movement was performed by Brinch-Hansen (1961) and Audibert and Nyman (1975, 1977). Well-known studies that compared these formulations with experimental investigations were performed by Trautmann and O'Rourke (1985) and Trautmann et al. (1985). In their work, alternative pipe-soil interaction models are also considered (e.g. Ovesen, 1964).

Such analytical formulations of the soil response to pipe displacement have been used for many years. Typically, these formulations are applied in horizontal and vertical soil springs, which were used to analyse the behaviour of buried pipelines. The formulations by Brinch-Hansen and Audibert and Nyman were re-examined by Korff and Hergarden (2002). Using their experiments, the proposed relations were calibrated to Dutch soil conditions. Further re-evaluation of the formulations of soil springs was performed within the GIPIPE project by research partner CSM (GIPIPE Research Consortium, 2015).

Analytical methods to calculate the pipeline response to severe ground-induced deformations were developed by Newmark and Hall (1975), Kennedy et al. (1977) and Wang and Yeh (1985). The latter model is employed in a parameter study by Wang and Wang (1995), in which global buckling of the pipeline is also considered. An extension of the Kennedy model was offered by Takada et al. (2001), who proposed a new method to evaluate the strain of pipes crossing a moving fault. By means of a set of FE-calculations using a shell model for the pipeline, a relation was found between the pipeline deformation determined according to the Kennedy model and the maximum strain in the pipeline.

Further improvement of the analytical models by Wang and Yeh was proposed by Karamitros et al. (2007) and Trifonov and Cherniy (2010, 2012). This model accounts for inelastic deformation of the pipe using a bilinear stress-strain diagram, while local buckling failure of the pipe wall is disregarded. The models regard soil as elastic-perfectly-plastic, which for example allows the implementation of the soil models by Brinch-Hansen (1961) and a simplification of the model by Audibert and Nyman (1977). The model by Trifonov and Cherniy is shown to correspond well to FE-calculations in case of a pipeline crossing a strike slip fault.

The work by Karamitros et al. and Trifonov and Cherniy was validated by performing analyses with an FE-model that employs shell elements for the analysis of the pipeline and non-linear soil springs to account for the effect of pipe-soil interaction. Comparable models are presented in the work by Liu et al. (2008), Gu and Zhang (2009) and Shitamoto et al. (2010), that use either shell elements or beam elements to model the pipeline. In some cases, modified beam elements were used to model the pipeline, which incorporate the influence of hoop stresses on longitudinal bending behaviour as well as the stiffness reduction due to ovalisation of the pipe. A common factor in these studies is the lack of experimental verification of the models. Furthermore, local buckling failure of the pipe wall is not discussed.

More recently, the interaction between pipe and soil was studied using a 3D model of the soil surrounding the pipe that allows for elastic and plastic deformation of the soil. In the work by Daiyan et al. (2010), the pipe remains non-deformable, while the work by Odina and Tan (2009) and Varouras et al. (2010, 2012) presents full 3D modelling of both the pipe and the surrounding soil. The latter model allows for the analysis of pipeline failure due to high tensile strains as well as local buckling of the pipe wall. A drawback of this type of analysis is the large computational

effort that is required. Furthermore, experimental verification of the model calculations is often not performed.

Only a limited number of results of full scale experimental studies of pipes under ground-induced deformation is available. Full scale tests on steel and HDPE pipes subjected to strike-slip fault movements are published by O'Rourke et al. (2008, 2009). Tests on pipes including elbows subjected to strike-slip faults were presented by Yoshizaki et al. (2000, 2003). Within the framework of the GIPIPE research project, full scale tests were performed by research partner CSM (GIPIPE Research Consortium, 2015).

More testing within the GIPIPE project was performed at NTUA, in the form of scaled tests (GIPIPE Research Consortium, 2015). Further scaled experiments are more readily available than full-scale experiments, such as for example the work by O'Rourke (2005), who investigated the effect of a strike slip fault on buried pipelines. In this study, FE-models using soil springs in accordance with ASCE guidelines (ASCE 1984) and beam elements for the pipeline, show good agreement with the experiments. Similar experiments were performed by Ha et al. (2008) which were compared with the Kennedy model. In a subsequent publication by Ha et al. (2009), favourable comparison is found between scaled experimental results and a case history. Further scaled tests are published by Abdoun et al. (2009).

Overall, it can be concluded that various modelling techniques are available for pipes crossing active strike-slip faults. However, most of them do not take local buckling failure into account and the few that do, are not validated experimentally. Experimental research is available, but soil pressures acting on the pipe as well as strain and ovalisation of the pipe are not easily obtained from the experiments. This limits the insight into deformational behaviour of the steel during such an event and hinders validation of the models.

8.3.2 Design codes and guidelines

Besides scientific literature, various standards and guiding documents are available that are applicable to the design of buried pipelines. Some of these standards may be relevant for all pipelines, while others are limited to pipelines for specific applications, such as gas, hydrocarbon or water transportation. The documents that were found to be relevant for this study are:

- ALA Guidelines for the Design of Buried Steel Pipe (ALA, 2001)
- ALA Seismic Guidelines for Water Pipelines (ALA, 2005)
- ASCE Guidelines for the Seismic Design of Oil and Gas Pipeline Systems (ASCE, 1984)
- ASME B31.4 Pipeline Transportation Systems for Liquid Hydrocarbons and Other Liquids (ASME, 2009)
- AWWA M11 Steel Water Pipe: A Guide for Design and Installation (AWWA, 2004)
- DNV-OS-F101 Offshore Standard OS-F101, Submarine Pipelines (DNV, 2010)
- EN 805 Water supply – Requirements for systems and components outside buildings (EN 805, 2000)

- EN 1594 Gas infrastructure – Pipelines for maximum operating pressure over 16 bar – Functional requirements (EN 1594, 2013)
- EN 1993-4-3 Design of steel structures – Part 4-3: Pipelines (EN 1993-4-3, 2009)
- EN 1998-4 Design of structures for earthquake resistance – Part 4: Silos, tanks and pipelines (EN 1998-4, 2007)
- EN 14161 Petroleum and natural gas industries – Pipeline transportation systems (EN 14161, 2011)
- NEN 3650-2 Eisen voor buisleidingsystemen – Deel 2: Aanvullende eisen voor leidingen van staal (NEN 3650-2, 2012).

Overall, two design strategies are recognized: a limit stress and a limit strain design. In a limit stress design, all actions on the pipeline are translated to stresses in the pipeline. Commonly, the stress state of the pipe is translated into a single resultant stress, using an appropriate yield criterion (e.g. Von Mises). This resultant stress is then compared to a limit stress. In limit strain design, the equivalent strain rather than equivalent stress is considered to be governing. Especially in deformation controlled loading of the pipeline, large differences can occur between the two methods. The majority of the considered documents recognize a limit strain design as most efficient in case of displacement controlled loading.

Methods for estimating strain demand in case of ground-induced deformations are proposed in various documents. Most commonly, an FE-analysis is proposed that employs elastic-perfectly plastic springs similar to a Winkler foundation to model the pipe-soil interaction. Most documents refer to the work by Brinch-Hansen (1961) and Audibert and Nyman (1977) or the work by Trautmann and O'Rourke (1985) for methods to determine the properties of the soil springs. Also NEN 3650-1 (2012) uses the work by Brinch-Hansen, but uses the adjustments that were proposed by Korff and Hergarden (2002), to better suit typical Dutch soil conditions. For modelling the pipeline, most documents either recommend a full 3D model or a model using (modified) beam elements. A graphical overview of this modelling method is presented in Figure 8.2.

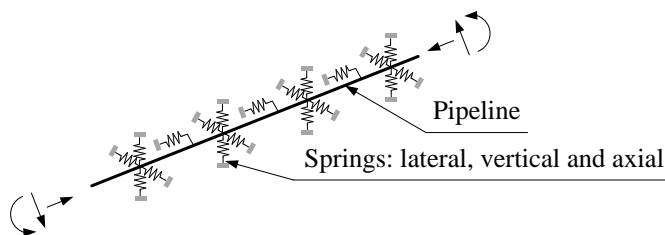


Figure 8.2 Modelling of pipeline and pipe-soil interaction using an FE-analysis.

The allowable tensile strain in the pipeline that is proposed in the various codes greatly varies. While Dutch pipeline standard NEN 3650-2 (2012) only allows a maximum strain of 0.5% or 0.7% for common steel grades, other standards such as EN 1998-4 allow a tensile strain up to 3%. It should be noted that the former document also recognizes that higher limit strains may be allowable. It is left to the designer to demonstrate that this higher limit strain can be allowed for a specific material in combination with specific requirements regarding the welding and welding process.

Many other documents leave the determination of the limit strain to the designer, either by proposing experimental research (ALA, 2001) or by providing more general guidance as to which parameters are to be considered when determining the allowable strain (ASCE, 1984, ASME, 2009, EN 14161, 2011).

Some of the considered standards also provide guidance with respect to the critical compressive strain of the pipeline (DNV, 2010, EN 1993-4-3, 2009, EN 1998-4, 2007, NEN 3650-2, 2012). Other codes specifically mention local buckling as a failure mode, but do not provide formulations to determine the critical compressive strain (ASME, 2009).

8.4 Objective

It is the objective of Part III of this study to provide more insight into the deformational behaviour of steel pipelines crossing an active strike-slip fault. To this aim, large-scale experiments were performed on bare pipes, allowing boundary conditions and response of the pipeline to be documented accurately.

Subsequently, a numerical model that employs shell elements for the pipeline and non-linear soil springs was developed, which is also suitable to model local buckling failure of the pipe. The extensive data set that is available from the experimental work allows careful calibration and validation of the numerical model.

This study contributed to the GIPIPE research project, which aimed to develop safe design guidelines covering the design of buried pipelines under ground-induced deformations of significant magnitude.

8.5 Summary of Chapter 8

In this chapter, an introduction is presented to the research carried out in Part III of this study. The GIPIPE research project is outlined, which aimed to develop safe and usable design guidelines which extend the current design practice for pipelines subjected to ground-induced deformation.

Various examples of ground-induced deformations on a pipeline and the possible resulting failure mechanisms are discussed. One specific design situation is selected as topic for the present research, which is the effect of an active strike-slip fault on buried pipelines.

In addition to the general literature review with regard to bending and local buckling behaviour of pipes (see Chapter 1), an additional literature review was carried out which is more focused on buried pipelines under imposed deformations. It was found that various analytical models exist to predict the interaction between pipe and soil in case of imposed displacement of a buried pipe through the soil. These analytical models have found application in an analysis of the pipeline that employs springs to model the soil behaviour. More recently, more complex models have become available, which feature a 3D model of pipe and soil.

Besides scientific literature, also a review of applicable design guidelines is given. This review of the current state of the art shows that, although many models exist to calculate the behaviour of buried pipelines crossing moving faults, various aspects remain unclear. For example, experimental verification is often lacking, as is the inclusion of local buckling failure of the pipeline in the model.

It is the objective of Part III of this study to provide more insight into the deformational behaviour of steel pipelines crossing active strike-slip faults. To this aim, large-scale experiments were performed. Furthermore, a numerical model was developed which was calibrated and validated using the results of these tests.

Chapter 9

Experimental study of buried pipelines crossing active strike-slip faults

9.1 Test programme

The deformation of a pipeline under ground-induced deformations is the result of interaction between the pipeline and the surrounding soil. Therefore, a model considering only the pipeline or soil is unable to capture the behaviour of the system. To enhance understanding of the pipeline deformational behaviour under these conditions, as well as to aid validation of analytical and numerical models, a series of ten full scale tests was performed. To be able to accurately monitor the behaviour of the steel pipeline, actual burial of the pipeline was avoided by replacing the soil with appropriate non-linear springs that simulate the soil behaviour.

9.1.1 Situation modelled by experiments

Imposed deformation of buried pipelines can be caused by many mechanisms (see Figure 8.1). Despite many differences, common factors between the various mechanisms exist. In most cases, the pipeline crosses a boundary between soil bodies which experience relative motion with respect to each other (see Figure 9.1). When the effects of the pipeline self-weight as well as static vertical loading at the soil surface on the pipeline behaviour are considered to be negligible, it is of secondary importance for whether the movement in this diagram is in vertical direction (Figure 8.1b and c), in horizontal direction (Figure 8.1d) or a combination (Figure 8.1a), as this direction only dictates the pipe-soil interaction. In the experiments, only one situation is modelled for reasons of simplicity: a horizontal strike-slip fault movement. However, results are applicable to many other comparable scenarios as a consequence of the similarities between various ground-induced deformation design situations.

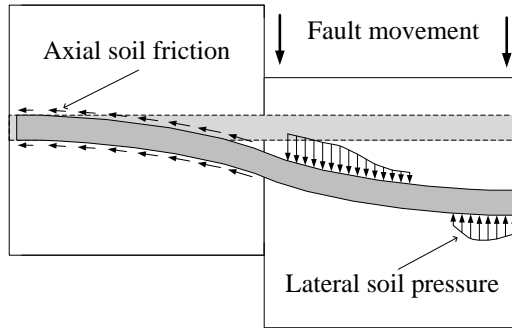
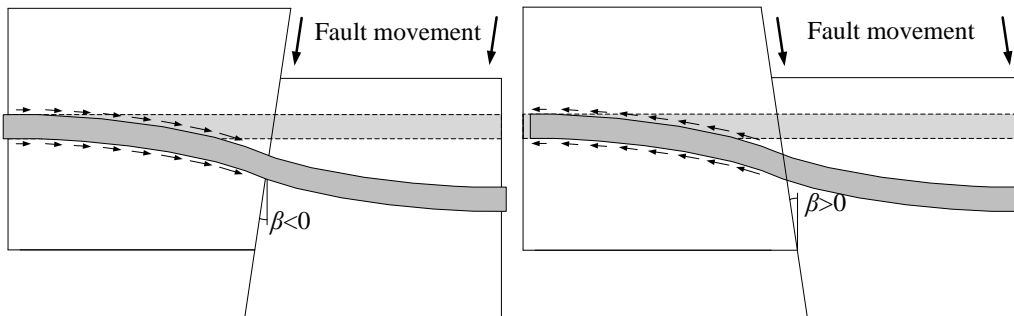


Figure 9.1 General case of pipeline crossing two soil bodies undergoing a horizontal differential displacement. Soil friction due to pipeline deformation drawn on the left, lateral soil pressures drawn on the right.

At the interface of the two soil bodies, here under denoted as ‘fault’, a displacement discontinuity exists, which cannot be followed by the pipeline. As a result, the pipeline moves laterally through the soil resulting in lateral soil pressures against the pipeline. The deformed pipeline follows an S-curve of longer arc length than the original straight pipeline. Consequently, the pipe displaces in axial direction, resulting in soil friction against the pipeline. In case of infinite pipeline length, the soil friction decreases with increasing distance to the fault, until, at large distance from the fault, the pipeline cross-section no longer displaces in axial direction, thus reducing the axial soil friction to zero. In both cases a tensile normal force in the pipeline results from the axial soil friction. This normal force, denoted as N_s , increases with increasing fault movement.

In Figure 9.1, the direction of the fault movement is exactly perpendicular to the pipeline axis, which is denoted as a fault angle (β) of 0° . For other directions of the fault movement ($\beta \neq 0$), the component of the fault movement in the direction of the pipeline axis results in additional soil friction against the pipeline (see Figure 9.2). The additional normal force that is generated by this additional friction is denoted as N_β . For $\beta < 0$, N_β is a compressive normal force, while for $\beta > 0$, N_β is a tensile normal force.



(a) Negative fault angle: $N_\beta < 0$

(b) Positive fault angle: $N_\beta > 0$

Figure 9.2 Soil friction against pipeline due to a non-zero fault angle.

A third component of the total normal force in the pipeline is caused by actions independent from the ground-induced deformation. Temperature and internal pressure are examples of such actions. In this experimental study, only the normal force resulting from internal pressure (N_p) is taken into account. In case of internal pressure, hoop stresses and strains occur. In a straight, infinitely long pipeline, the lateral contraction in axial direction resulting from these hoop stresses is constrained by the soil surrounding the pipe, resulting in an axial force. Besides resulting in a normal force in the pipe, internal pressure may influence the bending behaviour of the pipe as a consequence of the hoop stresses that result from this internal pressure.

9.1.2 Soil properties

Naturally, the properties of the soil surrounding the pipeline are of great influence on the behaviour of the pipeline in case of a ground-induced deformation. To obtain uniform research efforts, four soil types were defined within the GIPIPE research project, two of which are used in the experiments: a non-cohesive soil and a cohesive soil. The assumed properties of these two soils for a soil element at vertical stress $\sigma_v=50$ kPa are listed in Table 9.1. For both soil types, a thin loose sand layer with friction angle δ' is assumed at the interface between the pipeline and the surrounding soil. The actions on the pipeline are considered to be quasi static (see section 8.2). However, the behaviour of cohesive soils is assumed to be undrained, because in case that drained conditions apply, the timescale of the event is so large that measures to relieve the pipeline deformation can be undertaken during the event.

Table 9.1 Assumed soil properties.

<i>(a) Non-cohesive soil (sand)</i>			<i>(b) Cohesive soil (clay)</i>		
Parameter		Value	Parameter		Value
φ'	Friction angle	32°	c_u	Cohesion	50 kPa
E'	Modulus of elasticity	8 MPa	φ_u'	Friction angle	0°
ν'	Poisson factor	0.3	E_u	Modulus of elasticity	5 MPa
γ	Unit weight	18 kN/m ³	ν_u	Poisson factor	0.5
δ'	Interface friction angle	16°	γ	Unit weight	17 kN/m ³
			OCR	Over consolidation ratio	6.6
			PI	Plasticity index	30%
			S	Saturation	100%
			δ'	Interface friction angle	16°

In all tests, the pipeline is assumed to be buried in a uniform soil body with a burial depth of the pipeline centreline of 2.5 m ($Z=2.5$ m). Near the fault, the soil surrounding the pipeline will have significantly reduced stiffness and strength due to soil stirring as a result of the fault movement. To take this into account, a zone between 500 and 700 mm length is assumed to be completely without soil resistance in the experiments.

9.1.3 Assumed pipe-soil interaction

As a result of the imposed deformation on the soil surrounding the pipe, and the resistance of the pipe to this movement, the pipeline will move through the soil. The form and magnitude of the resistance of the soil to this movement depends on various pipe and soil parameters and is summarized by the term pipe-soil interaction. In the experimental investigation of this study, the pipeline was not buried, requiring a substitute for the pipe-soil interaction. As discussed in section 8.3.2, in many design models and standards it is proposed to account for pipe-soil interaction using uncoupled linear or non-linear springs in three directions (see Figure 8.2). This way of modelling the pipe-soil interaction was also adopted in the experiments. Because the experimental investigation was limited to strike-slip faults and the effects of other loads were considered to be negligible, only the pipe-soil interaction in lateral and axial direction needed to be taken into account. In this section, the chosen models of these interactions are discussed. The interactions were modelled according to the recommendations of NEN 3650-1 (2012). These models are generally based on the theory by Brinch-Hansen and Audibert and Nyman (see section 8.3).

Lateral pipe-soil interaction model

A theoretical model for the maximum soil resistance against lateral movement was proposed by Brinch-Hansen (1961). The relation between pipe displacement (y) and soil resistance (q_h) was described by Audibert and Nyman (1977). The used soil model (NEN 3650-1, 2012), is a modification of these models. According to NEN 3650-1, the lateral soil springs simulating the pipe-soil interaction behave as presented in Figure 9.3. The ultimate horizontal soil pressure q_{he} is described by equation (9.1) for non-cohesive soils and by equation (9.2) for cohesive soils. The full non-linear soil behaviour is described by equations (9.3) and (9.4). A simplification of the non-linear soil model is allowed in the form of a bilinear diagram. In this simplification, the soil stiffness is defined as the secant modulus of the non-linear behaviour at $0.3 \cdot q_{he}$. The displacement y_{30} at which the transition between elastic and plastic soil response occurs in the simplified model is found with equation (9.5)

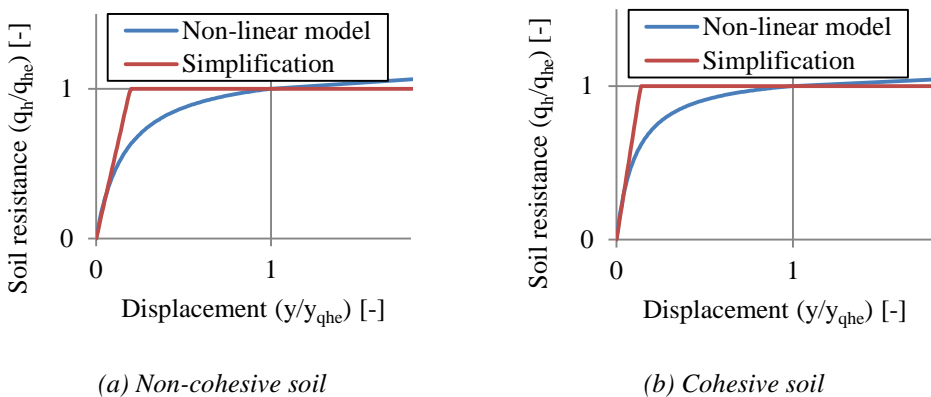


Figure 9.3 Behaviour of lateral horizontal soil spring.

$$q_{he} = K_q \cdot \sigma' + 0.7 \cdot \alpha \cdot K_c \cdot c' \quad (9.1)$$

With:

K_q : Load coefficient according to Brinch-Hansen. $K_q = f(\varphi, Z, D)$, see NEN 3650-1 (2012)

α : Coefficient for execution. $\alpha=0.6$ for open excavation, $\alpha=1.0$ for jacking methods

K_c : Load coefficient according to Brinch-Hansen. $K_c = f(\varphi, Z, D)$, see NEN 3650-1 (2012)

Remark: the value 0.7 is related to a systematic deviation, demonstrated when the result of the formula is compared with the average of the results of experiments.

$$q_{he} = 0.7 \cdot \alpha \cdot K_{cu} \cdot c' \quad (9.2)$$

With:

α : Coefficient for execution. $\alpha=0.6$ for open excavation, $\alpha=1.0$ for jacking methods (trenchless installation)

K_{cu} : Load coefficient according to Brinch-Hansen. $K_{cu} = f(\varphi, Z, D)$, see NEN 3650-1 (2012)

Remark: the value 0.7 is related to a systematic deviation, demonstrated by comparing the formula result with the average of the results of experiments.

$$y_{max} = D \cdot [0.05 + 0.03 \cdot (Z/D + 0.05)] \quad (9.3)$$

$$\frac{q_h}{q_{he}} = \frac{y / y_{max}}{A + B \cdot y / y_{max}} \quad (9.4)$$

With:

A : Coefficient of non-linear behaviour. $A=0.145$ for non-cohesive soil and $A=0.1$ for undrained cohesive soil.

B : Coefficient for non-linear behaviour. $B=1-A$.

$$y_{30} = \frac{0.3 \cdot A \cdot y_{max}}{1 - 0.3 \cdot B} \quad (9.5)$$

Validation of lateral pipe-soil interaction model

Validation for the adopted model for lateral pipe-soil interaction is available in literature. Further validation is performed by testing as part of the GIPIPE project. The NEN 3650-1 (2012) model, as outlined in the previous section, is an adjustment of the models that were originally proposed by Brinch-Hansen (1961) and Audibert and Nyman (1977). The adjustment consists of an adjustment factor in the contribution of cohesion to the maximum lateral soil resistance q_{he} and slight adjustments of the factors A and B in equation (9.4) on the basis of pipe-soil interaction experiments that were performed in The Netherlands and FE-calculations (Korff and Hergarden, 2002). The work of Trautmann et al. (1985) shows similar experimental results as in the work by

Korff and Hergarden and finds the Brinch-Hansen model, without the adjustments by Korff and Hergarden, to overestimate the test results. Further testing of the lateral pipe-soil interaction was performed by Paulin et al. (1998). In that study, tests were performed with loose and dense sand and stiff and soft clay. The tests were compared with ASCE guidelines (ASCE, 1984), which recommend a soil model in accordance with the work by Ovesen (1964). It was found that the guidelines generally overestimate the soil resistance that is measured in experiments.

Within the GIPIPE project, further pipe-soil interaction tests were performed by research partner CSM (GIPIPE Research Consortium, 2015). In three tests, a 2900 mm pipe section with a diameter of 219 mm was drawn through a sandy soil in lateral direction (see Figure 9.4). The forces applied to the pipe, as well as the soil pressures against the pipe were measured. Test 1 and 2 were performed with a bare pipe, while Test 3 was performed with a coated pipe. The compaction level of the sand was low for Tests 2 and 3, while a higher compaction level was used for Test 1 (GIPIPE Research Consortium, 2015). For both compaction levels, a similar friction angle of the sand was determined in a separate direct shear test.

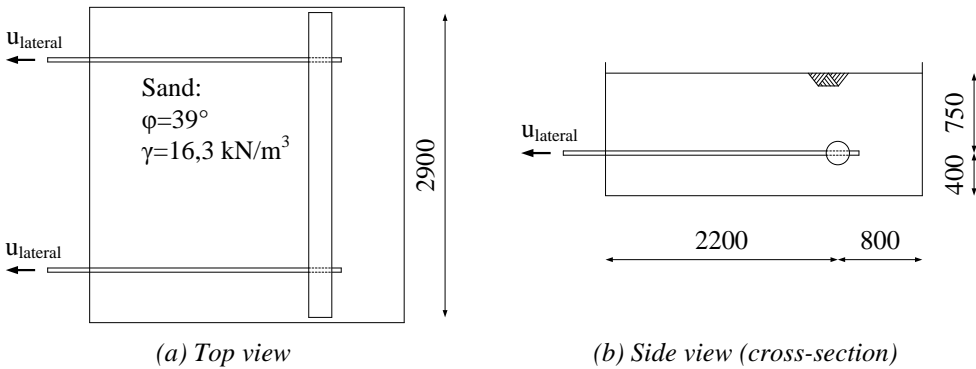


Figure 9.4 Schematic overview of transversal pulling tests performed by CSM (dimensions in mm).

A comparison between these tests and the used pipe-soil interaction models is presented in Figure 9.5. The results show similar behaviour in all three tests. Apparently, the coating or compaction of the soil have a limited effect on the measured soil resistance, especially for larger displacements. Some discrepancy between the horizontal forces measured by the load cells and the pressure sensor that was placed on the pipe is visible in the graphs. This difference may be explained by friction between the pipe and its guiding rails, where sand may collect, or by possible inaccuracies in the calculation methods used to translate the measured soil pressures in a lateral soil resistance. Furthermore, for larger displacements the pipe displaced upwards through the soil, resulting in a tested pipe-soil behaviour that is not taken into account in the model. Overall, the comparison between the models and test results is considered to be satisfactory.

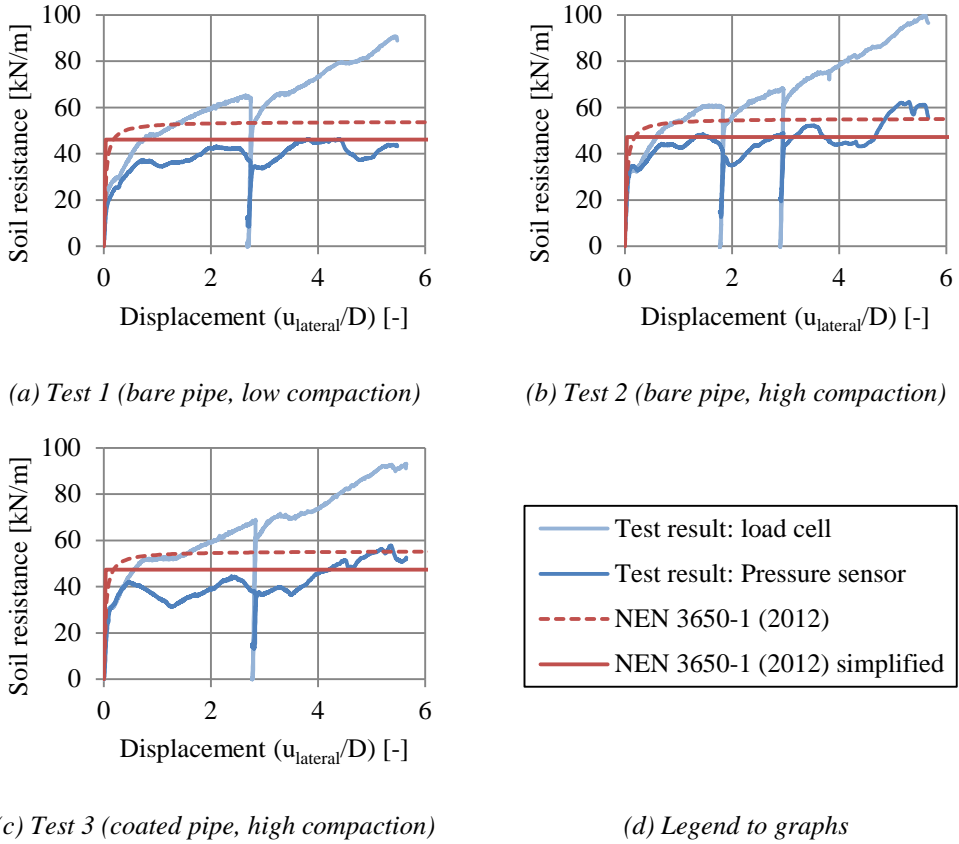


Figure 9.5 Comparison of lateral soil resistance models with test results.

Axial pipe-soil interaction

The axial soil springs that are defined in NEN 3650-1 (2012) have properties as shown in Figure 9.6. The ultimate friction resistance per unit of pipe surface area w_{max} is described by equation (9.6) and is attained at a displacement (x_{wmax}) of 5 and 6 mm for cohesive and non-cohesive soil respectively.

$$w = \frac{1+K}{2} \cdot \sigma' \cdot \tan(\delta') + 0.6 \cdot a \quad (9.6)$$

With:

- K : A relation between horizontal and vertical intergranular pressure. For neutral pressure: $K=K_0 \approx 1 - \sin(\varphi)$
- σ' : Effective soil stress
- δ' : Angle of friction of boundary layer between pipe and soil
- a : Adhesion of cohesive soils. As discussed in section 9.1.2, adhesion is not considered for friction ($a=0$)

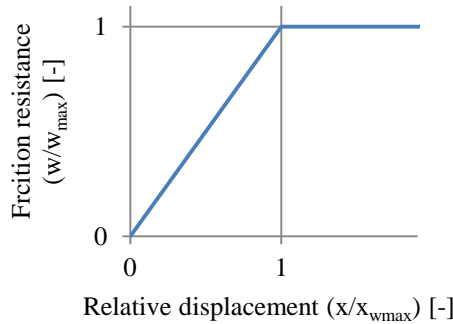


Figure 9.6 Behaviour of axial horizontal soil spring.

Validation of axial pipe-soil interaction model

Similar to the lateral pipe-soil interaction model, validation for the adopted axial pipe-soil interaction model is available. However, as discussed in section 9.4, the normal force in the pipeline is very sensitive to variables other than the axial soil spring resistance. Therefore, the validation of the axial pipe-soil interaction model is considered to be secondary to the validation of the lateral pipe-soil interaction model.

Korff and Hergarden (2002) found a δ'/ϕ ratio of 2/3 applicable to all sandy soils in combination with all pipe materials, which was adopted by NEN 3650-1 (2012). The presence of a strength peak, as is observed in for example direct shear tests, is denied. Research by Wijewickreme et al. (2009) observed a small strength peak for dense sands, but an almost bilinear behaviour for loose sands. In the study by Wijewickreme, equation (9.6) was found to underestimate the axial soil friction.

In a similar test setup as the experiments that were used for validation of the lateral pipe-soil interaction model, research partner CSM performed three axial pulling tests (see Figure 9.7). Tests 1 and 2 were performed with a bare pipe, while Test 3 was performed with a coated pipe. A high soil compaction was used in Tests 1 and 3, while a lower soil compaction was used in Test 2 (GIPIPE Research Consortium, 2015).

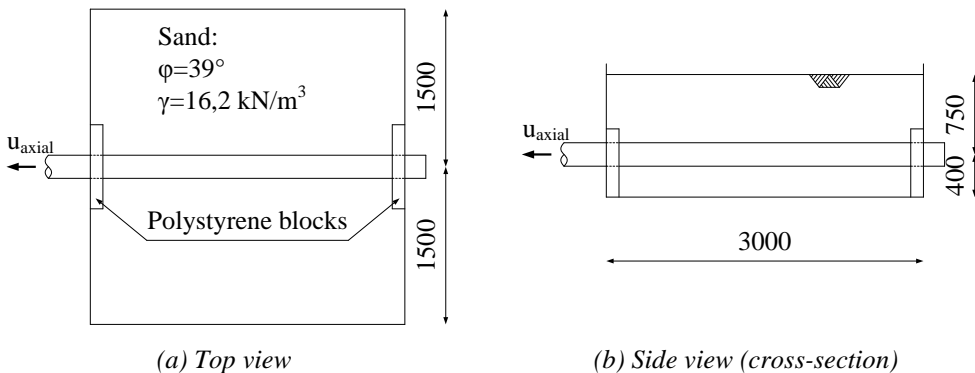
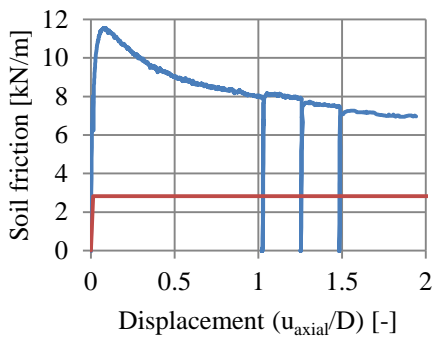
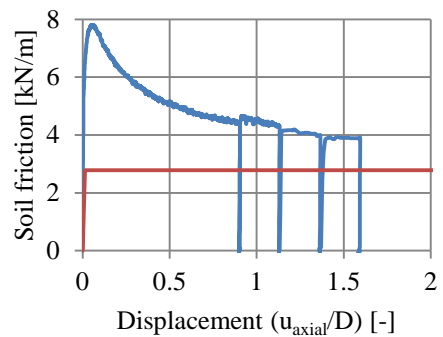


Figure 9.7 Schematic overview of axial pulling tests performed by CSM (dimensions in mm).

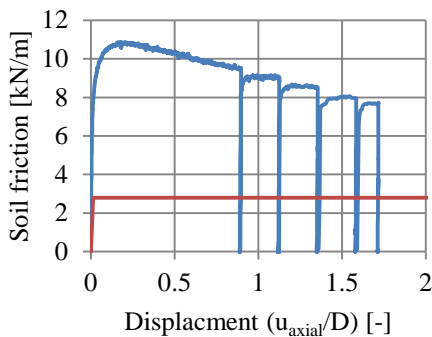
A comparison between the axial pulling tests and the used pipe-soil interaction model is shown in Figure 9.8. It is clear that the model in NEN 3650-1 underestimates the actual behaviour in the tests by a considerable margin, similar to the observations made by Wijewickreme et al. (2009). Rather than a bilinear behaviour, the test results show a peak in the friction resistance. The post-peak behaviour is similar for both bare pipe tests, but the resistance drop is much less sharp for the coated pipe. Furthermore there is a clear effect of the grade of compaction of the soil surrounding the pipe, which is not included in the NEN 3650-1 model. It must be noted that this model was calibrated to Dutch soils (Korff and Hergarden, 2002), while the studies within the GIPIPE project and by Wijewickreme were focused at soil in general. This may partly explain the observed differences. The differences between the model and test observations may be further explained by an incorrect estimate of the friction angle δ' , or the horizontal soil pressure coefficient K_0 . Additional development or improvement of soil models is considered to be out of the scope of this study. Due the lesser importance of the axial soil springs relative to the lateral soil springs, the selected model is considered to be acceptable.



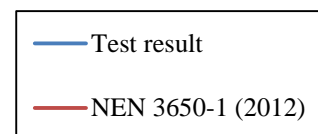
(a) Test 1 (bare pipe, high compaction)



(b) Test 2 (bare pipe, low compaction)



(c) Test 3 (coated pipe, high compaction)



(d) Legend to graphs

Figure 9.8 Comparison of axial soil resistance models with test results.

9.1.4 Test programme overview

For the experimental study, two types of HFW pipe were available (see Table 9.2), manufactured by Corinth Pipe Works in Thisvi, Greece. The two pipe types differ in D/t ratio and steel grade. A further difference between the experiments with the two pipe diameters results from the fixed pipe depth of 2.5 m (see section 9.1.2) leading to a different Z/D ratio for the two pipe types, which influences the lateral soil resistance q_{he} .

Table 9.2 Overview of available pipe material for experiments in Part III of this study.

D [mm]	t [mm]	D/t [-]	Steel grade	No. of pipes	Total pipe length [m]
219.1	5.59	39.2	X65	9	71.6
406.4	7.30	54.9	X60	8	68.2

To investigate the behaviour of pipes under high and low tensile forces, fault angles other than 0° were considered in the testing programme. Further parameters that were varied in the testing programme are internal pressure in the pipeline and the presence of a girth weld in a pipe segment that is expected to experience high longitudinal strains. This segment is denoted as the critical segment. When a girth weld was placed in the critical segment on one side of the fault, the critical segment on the opposite side of the fault was kept free of welds so that a direct comparison between a girth welded pipe and a plain pipe under similar conditions was available. By selecting appropriate combinations of parameters for the ten tests, a comprehensive testing programme was compiled, which is presented in Table 9.3.

Table 9.3 Overview of tests in Part III of this study.

Test	Pipe type [mm ²]	Soil type	Fault angle [-]	GW in critical segment	Internal pressure [MPa]	P/P_{SMYS} [-]
T1	219×5.6	Sand	0°	No	0	0
T2	406×7.3	Sand	0°	No	0	0
T3	219×5.6	Clay	-3.25°	Yes (right)	0	0
T4	219×5.6	Sand	-1.5°	No	0	0
T5	219×5.6	Sand	-2.25°	Yes (left)	6.3	0.26
T6	219×5.6	Sand	0°	No	12.3	0.51
T7	406×7.3	Clay	0°	Yes (left)	7.9	0.51
T8	406×7.3	Sand	0°	Yes (right)	0	0
T9	406×7.3	Clay	-2°	No	0	0
T10	406×7.3	Sand	-2°	No	3.9	0.25

Test specimens

All test specimens were assembled from the two available pipe types (see Table 9.2). Because the test specimens were longer than the available pipe lengths, all specimens contained girth welds. As shown in Table 9.3, in some cases these girth welds were purposely placed in a highly strained section of the test specimen. The pipe sections between the girth welds are identified as specimen parts and were preferably aligned such that the longitudinal seam weld of the pipe was placed away from the compressive side of the specimen (intrados) and tensile side of the specimen (extrados). In some cases, sections of the specimen that remained straight during the tests were re-used in other tests.

The pipe sections were TIG-welded using an alloyed TIG rod (LNT NiMo1) suitable for welding high strength steels (LincolnElectric, 2015). The pipes were preheated to 50°C and the interpass temperature was limited to 200° C.

9.2 Measurement of initial geometry

9.2.1 Programme

After assembly of the test specimens from the available pipe material, the diameter and wall thickness of the specimens were measured at cross-sections with 1000 mm spacing. At each cross-section, the wall thickness was measured at the intrados and extrados of the pipe, using an ultrasonic thickness measurement device. The diameter of the pipe was measured in the direction of and perpendicular to the neutral line using a large-diameter micrometre. These orientations correspond to the horizontal and vertical direction respectively in the test setup. The position of the longitudinal seam weld of the specimen part was noted for later reference.

The purpose of these measurements was to document the geometrical properties of the specimen so that modelling of the test results could be performed accurately. A full analysis of the initial geometrical state of the pipes, including geometrical imperfections and variations of wall thickness and diameter is considered to be of lesser importance for the application under consideration and is out of scope of this study.

9.2.2 Results

In general, the measured diameter of the specimens was found to be very close to the nominal diameter. The largest deviation was found in specimen T4, where the measured diameter was found to be 0.6% larger than specified. On average, the measured diameter of the specimens was 0.3% larger than specified. Using the measured diameter of the cross-sections in horizontal and vertical direction, the initial ovalisation of the cross-section in its principal direction was calculated. The average initial ovalisation in this direction was found to be 0.3%, which is considered to be excellent. For comparison, API 5L pipeline specifications (2009) give out-of-roundness tolerances for the considered pipes of 1.5%.

The wall thickness of the pipe material was found to be in agreement with specification. On average, the $219.1 \times 5.59 \text{ mm}^2$ pipes had a wall thickness of 5.53 mm, while the $406.4 \times 7.3 \text{ mm}^2$ pipes had an average wall thickness of 7.6 mm. The coefficient of variation of the wall thickness, assuming the sample parameters to be representative for the full population, was found to be 1.4% for the smaller diameter specimens, and 0.8% for the larger diameter specimens. It should be noted that the maximum measurement accuracy of 0.1 mm may have prevented sufficiently accurate determination of small variations in wall thickness.

9.3 Material testing

9.3.1 Programme

The set of pipes that was available for testing is listed in Table 9.4. From each available pipe, four tensile coupons were taken out with a thickness equal to the pipe wall thickness. Two coupons were taken out in axial direction and two coupons in hoop direction of the pipe. In case of the axial coupons, the ends of the coupon were flattened to allow adequate clamping in the test setup. The coupons taken in hoop direction of the pipe were flattened over their full length.

The tensile tests were performed in accordance with ISO 6892-1 (2009). Since all test specimens were some assembly of the available pipe material, by testing all available pipes and assuming constant material properties over the length of these pipes, the material mechanical properties are known for each specimen part. These properties are vital to accurately model the experiments (see Chapter 11).

9.3.2 Results and analysis

An overview of the results of the tensile coupon tests is presented in Table 9.4. The results are presented in terms of the stress at 0.2% plastic strain, the stress at 0.5% total strain and the ultimate stress. The presented values are the average of the two tests available for each position. The reference yield stress ($\sigma_{y,ref}$) and the reference ultimate stress ($\sigma_{u,ref}$) are defined as the average of the measured values of $\sigma_{0.2\%}$ and σ_u in axial direction of the pipe material. These reference values were for example used for comparison of material properties between pipes.

All tensile test results lacked a clear yield plateau. Examples of typical results of the tensile coupon tests for two pipes are presented in Figure 9.9. The transition between elastic and plastic behaviour was generally observed to be sharper in axial direction than in hoop direction, possibly caused by the necessary flattening of the tensile coupons taken out in hoop direction. The full results of the tensile tests are presented in Appendix F.2.

Table 9.4 Overview of tensile test results.

Pipe ID	$D \times t$ [mm ²]	Axial			Hoop		
		$\sigma_{0.2\%}$	$\sigma_{0.5\%}$	σ_u	$\sigma_{0.2\%}$	$\sigma_{0.5\%}$	σ_u
H60410114	406.4×7.3	562	577	630	521	534	635
H60414405	406.4×7.3	553	558	595	498	513	598
H60415422	406.4×7.3	485	496	563	458	473	564
H60415859	406.4×7.3	552	556	597	436	463	591
H60416153	406.4×7.3	502	517	577	480	488	571
H60416313	406.4×7.3	506	518	594	491	502	590
H60423631	406.4×7.3	559	569	629	545	551	641
H60423640	406.4×7.3	545	552	609	509	518	619
H60423730	406.4×7.3	535	543	591	494	506	592
H86916024	219.1×5.6	571	578	611	508	523	598
H8696270B	219.1×5.6	594	604	653	525	545	644
H86916288	219.1×5.6	587	596	644	531	538	647
H86916288B	219.1×5.6	598	605	650	509	527	643
H86916314	219.1×5.6	581	590	636	508	525	620
H86916331B	219.1×5.6	591	595	646	544	556	643
H86916400B	219.1×5.6	567	569	606	532	536	612
H87016408	219.1×5.6	548	561	608	521	531	611

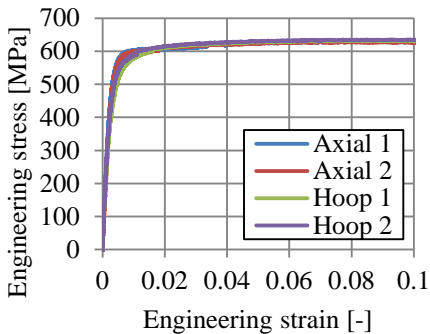
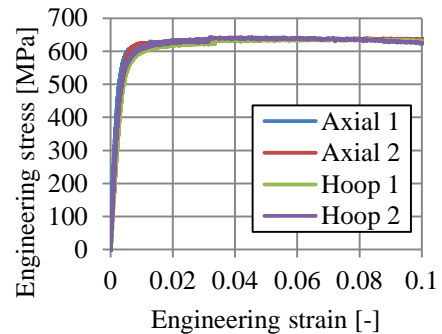
(a) 406.4×7.3 mm² pipe(b) 219x5.6 mm² pipe

Figure 9.9 Examples of typical results of tensile tests on pipe material.

In applications with high strain demand, sufficient strain hardening of the pipeline steel is necessary to prevent concentration of deformations. Therefore, a parameter indicating the fitness of a pipe for applications with high strain demand is the yield to tensile strength ratio (Y/T ratio) (NEN 3650-2, 2012). Various standards apply limits to the Y/T ratio of pipelines. DNV offshore standard F101 (2010) allows a Y/T ratio of 0.93 for normal (C-Mn) steel line pipe. Furthermore, in a supplementary requirement which applies when strains larger than 1% occur, the maximum

Y/T ratio is limited to 0.90. In the DNV offshore standard, the Y/T ratio is defined as $\sigma_{0.5\%}/\sigma_u$. Using the same definition, API 5L pipeline specifications (2009) and ISO 3183 (2012) specify two product specification levels (PSL). For PSL 1 pipes, no Y/T ratio limit is stated, while for PSL 2 pipes, a maximum Y/T ratio of 0.93 is allowed for pipes with a diameter larger than 12.75 inch and steel grades up to X80. Dutch pipeline code NEN 3650-2 (2012) prescribes that pipes must not exceed a Y/T ratio of 0.90. Further guidance can be found in EN 1594 (2009) which applies to high pressure gas pipelines. In this standard, a maximum Y/T ratio of 0.85 is recommended for design cases where strains higher than 0.5% may occur.

In agreement with API specifications and DNV guidelines, the Y/T ratio is defined as the ratio between $\sigma_{0.5\%}$ and σ_u in this study. During the investigation of the data, the Y/T ratio of the available pipes was found to be correlated to $\sigma_{0.5\%}$. An overview of the values found for the Y/T ratio in the performed tensile coupon tests, is presented in Figure 9.10. In many tensile tests, Y/T ratios were found that are higher than the aforementioned limits. It should be noted that the 219.1 mm-diameter pipes strictly do not have to comply with the limits stated in ISO 3183 due to their smaller diameter. However, it is clear that the Y/T ratio of the used pipes is very high.

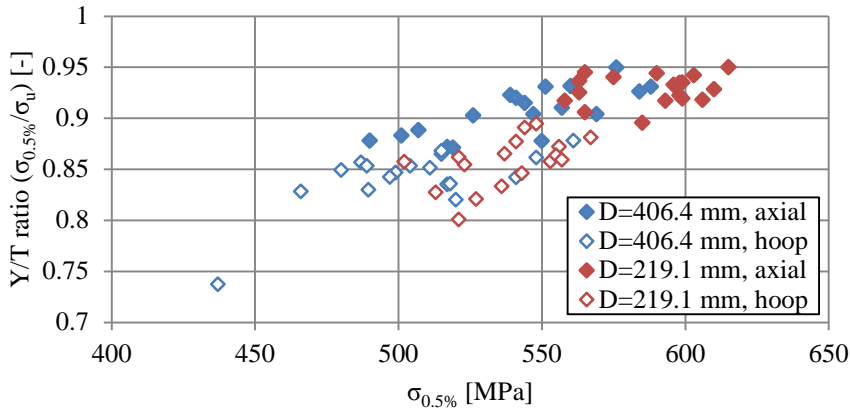


Figure 9.10 Y/T ratios found in tensile coupon tests on pipe material.

9.4 Test setup

The aim of the test setup was to simulate the behaviour of a pipeline crossing an active strike-slip fault. In reality, soil pressures act on the pipeline as a result of the fault movement. The adopted modelling of the pipe-soil interaction, as well as the resulting loads on the pipeline was discussed in section 9.1.

A conceptual overview of the test setup is presented in Figure 9.11. When this conceptual overview is compared with the general case of a pipeline crossing an active strike-slip fault (see Figure 9.1), it is clear that several characteristics were approximated. Firstly, the axial soil friction was replaced by a normal force at the end of the test specimen. Furthermore, the continuous lateral interaction between pipe and soil was modelled by discrete springs. An

important similarity between the concept and the general case is found in the application of the fault movement. In both cases, the fault movement is applied not directly to the pipe. Instead, this movement is applied to a soil body, or the base of the discrete soil springs. In the following sections, the various aspects of the test setup are further explained.

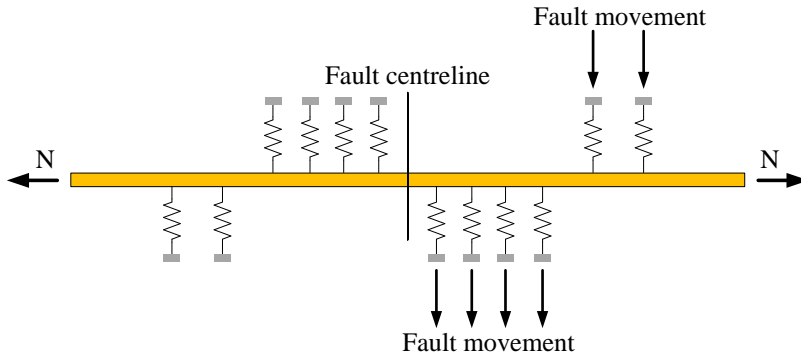


Figure 9.11 Conceptual overview of test setup.

9.4.1 Specimen length and application of normal force

To estimate the required geometry of the test setup, a preliminary study was performed by GIPIPE research partner Tebodin (Huinen, 2013). Four test scenarios were investigated (see Table 9.5), using FE-software specifically aimed at the design of buried pipelines (PLE4WIN, 2015). This software package uses modified beam elements for the pipeline and pipe-soil interaction according to NEN 3650-1 (2012), resulting in a model setup similar to as what is displayed in Figure 8.2. In the analysis, a 300 m long buried pipeline was simulated which was loaded by a strike-slip fault. The analyses were performed up to a fault movement of 1500 mm, as this is the stroke of the hydraulic actuators that were available for use in the test. Material properties for the pipe were assumed on the basis of the steel grade. The modelling of the soil was performed as described in section 9.1.3, using the soil properties presented in Table 9.1.

Table 9.5 Overview of preliminary analysis by Tebodin.

Analysis	Pipe type [mm ²]	Soil type	Fault angle [-]	Internal pressure	
				[MPa]	P/P_{SMYS} [-]
1	219×5.6	Sand	0°	0	0
2	219×5.6	Clay	0°	0	0
3	406×7.3	Sand	0°	0	0
4	406×7.3	Clay	0°	0	0

An overview of the deformed pipeline axis at maximum fault movement for the four analyses is presented in Figure 9.12. The figure shows that nearly all deformation of the pipeline occurs within 10 m from the fault. This distance is denoted as the influence length of the fault movement. The figure further shows that the ratio between pipeline stiffness and soil stiffness

influences the magnitude of the pipeline curvature and thus the influence length of the fault movement. The lateral soil pressures acting on the pipeline, corresponding to the deformed states plotted in Figure 9.12 are presented in Figure 9.13. Also in this figure, influence of the ratio between pipeline stiffness and soil stiffness on the influence length of the fault movement is visible. Considering the observations made in Figure 9.12 and Figure 9.13, the available pipeline material, laboratory space and costs associated with test setup size, a specimen length of 20 m was selected. This length is sufficient for most pipe-soil combinations, but introduces a small error for a 16-inch-diameter pipeline in clay, because in this scenario the influence length of the fault slightly exceeds 10 m (see Figure 9.13). This error is assumed to be negligible.

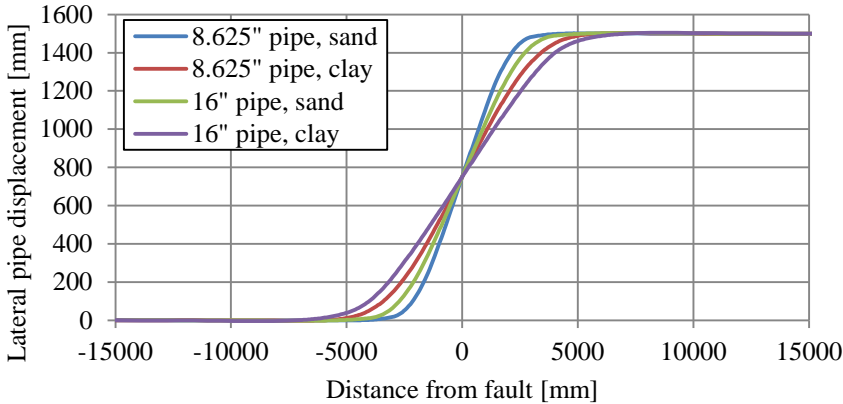


Figure 9.12 Results of preliminary analyses: deformed pipeline axis at $u_{\text{fault}}=1500$ mm.

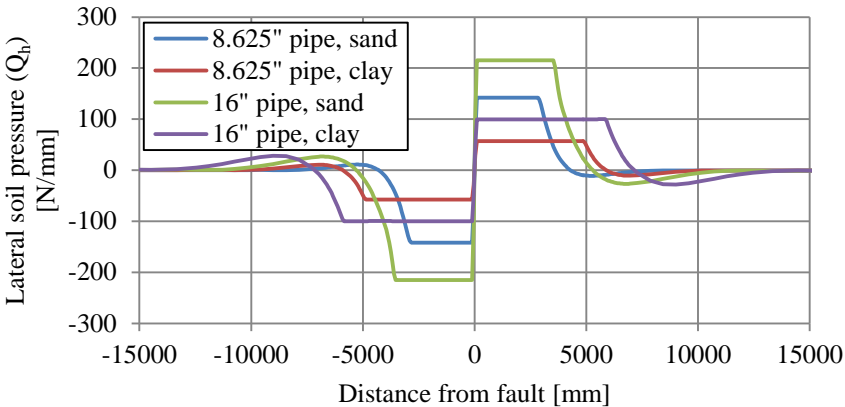


Figure 9.13 Results of preliminary analyses: lateral soil pressures against the pipeline at $u_{\text{fault}}=1500$ mm.

An overview of the normal forces developing in the pipeline at maximum fault movement is presented in Figure 9.14. The figure demonstrates that the large majority of axial soil friction occurs at a large distance from the fault, because only a small change in axial force is observed

within 15 m from the fault. In the test setup, the normal force was applied at the pipeline ends and therefore was constant along the specimen. Based on the results shown in Figure 9.14, this simplification is deemed to be acceptable. The maximum error in the acting normal force in a cross-section lies in the order of 5%.

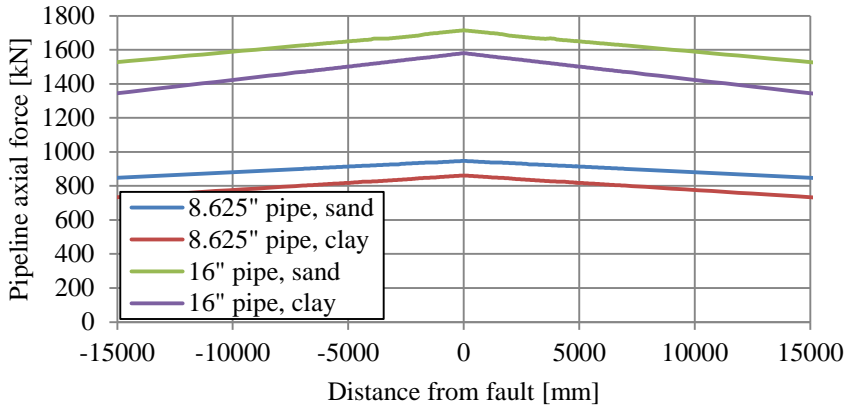


Figure 9.14 Results of preliminary analyses: axial forces in the pipeline at $u_{\text{fault}}=1500$ mm.

9.4.2 Modelling of pipe-soil interaction

As discussed in section 9.1.3, the test setup employed a non-linear pipe-soil interaction in accordance with NEN 3650-1 (2012). The springs that are depicted in Figure 9.11 therefore require a non-linear force-deformation relation. Furthermore, a large stroke is necessary, especially for springs near the fault. Due to these two requirements, standard coil or disc springs were not suitable for use in the test setup. Instead, the non-linear pipe-soil interaction was modelled mechanically using inelastically deforming steel rings (see Figure 9.15), in this study named ‘ring-springs’. In a preliminary experimental program, the behaviour of these rings was examined. Furthermore, a model was developed which was used for designing ring-springs for the large-scale tests.

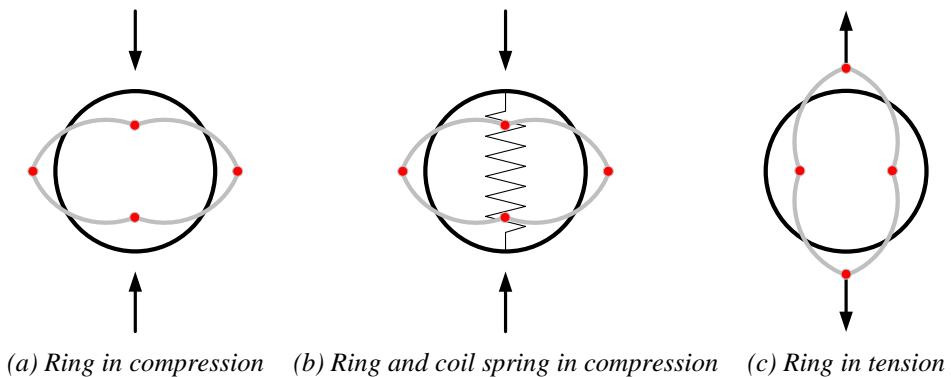


Figure 9.15 Non-linear springs in the form of ring-springs.

Preliminary testing of ring-springs and validation of mechanical model

To understand the behaviour of the three mechanical models of a non-linear spring (see Figure 9.15), three preliminary tests were performed on 157x2.7 mm² steel rings:

- Ring in compression without a coil spring (see Figure 9.15a and Figure 9.16a)
- Ring in compressing with a coil spring (see Figure 9.15b and Figure 9.16a)
- Ring in tension (see Figure 9.15c and Figure 9.16b)

Additionally, tensile tests were performed on the ring material and the spring coefficient k of the coil spring used in the second test was determined.

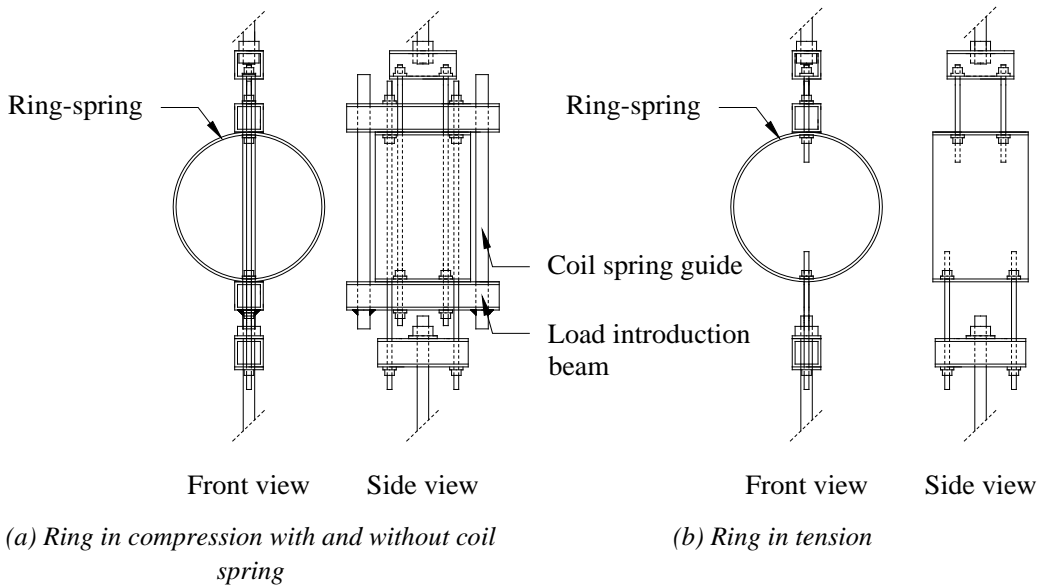


Figure 9.16 Preliminary ring-spring tests on 159x2.7 mm² steel rings.

To design suitable ring-springs for the full scale fault movement test, an analytical model of the ring-spring was developed, which was validated using the results of the three preliminary ring-spring tests. The analytical model assumes elastic-perfect-plastic material behaviour and a bilinear response of the ring-spring (see Figure 9.17). The ring is assumed to collapse due to formation of four or six plastic hinges (see Figure 9.17). The plastic resistance of the ring-spring $F_{p;ring}$ can be calculated with equation (9.7). For large deformations, the arm of the plastic bending moment, present in the denominator of equation (9.7), increases, thereby reducing $F_{p;ring}$. On the other hand, $F_{p;ring}$ is increased due to strain hardening of the material and plate bending effects. Comparisons with the preliminary tests show that these effects approximately cancel out and do not have to be taken into account to obtain a satisfactory estimate of the behaviour of the ring-spring. In case of the second test, which combines a ring-spring with a coil spring, superposition was applied to obtain the total resistance of the spring system.

$$F_{p;ring} = \frac{4 \cdot M_{p;wall}}{r} \text{ for rings without load introduction beam} \quad (9.7)$$

$$F_{p;ring} = \frac{4 \cdot M_{p;wall}}{r - \frac{1}{2}b} \text{ for rings with load introduction beam}$$

With:

$M_{p;wall}$: Plastic moment capacity of the ring wall: $M_{p;wall} = 0.25 \cdot L \cdot t^2 \cdot \sigma_y$, with L being the ring length

r : Radius of the ring-spring

b : Width of the load introduction beam

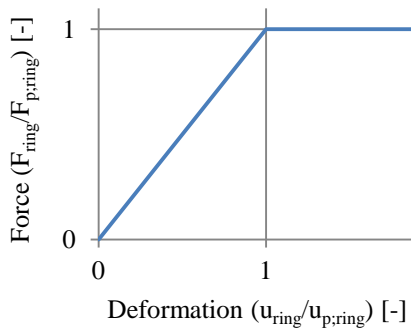


Figure 9.17 Idealized behaviour of ring-spring

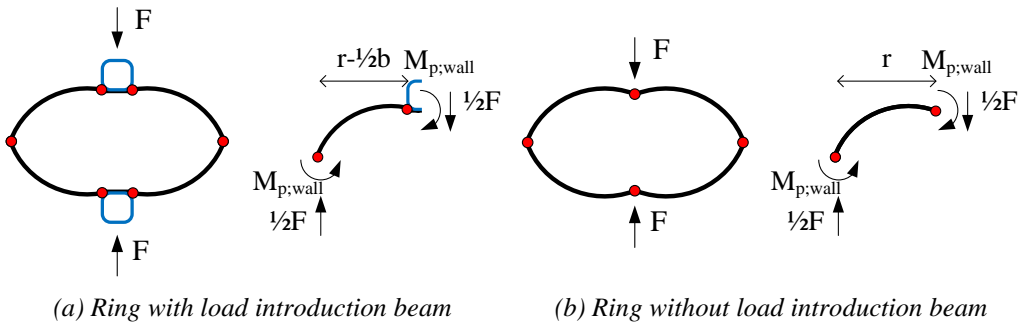


Figure 9.18 Analytical model to predict ring-spring behaviour.

The deformation $u_{p;ring}$ at which the plastic resistance $F_{p;ring}$ is reached can be calculated using equation (9.8). The geometric non-linearity of the force-deformation behaviour can be taken into account through a second order calculation using equation (9.9), assuming an ovalisation of the ring of half the vertical deformation.

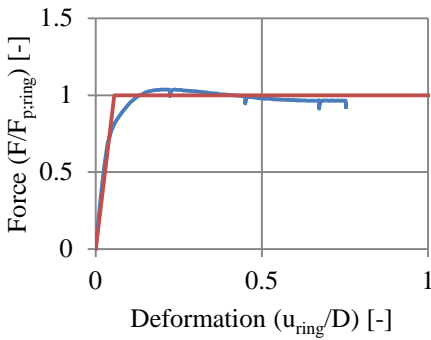
$$u_{p;ring} = \frac{F_{p;ring} \cdot r^3}{EI_{wall}} \cdot \frac{\pi - \frac{8}{\pi}}{4} \tag{9.8}$$

With:

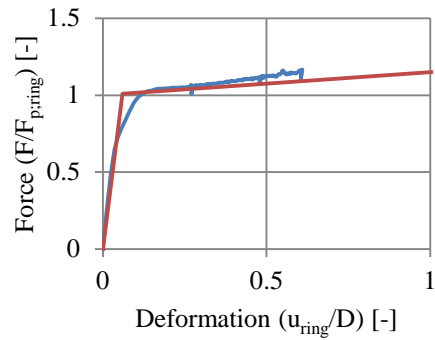
EI_{wall} : Bending stiffness of the ring wall.

$$u_{p;ring;2^{nd}} = u_{p;ring;1^{st}} \cdot \left(\frac{r + \frac{1}{2}u_{p;ring;1^{st}}}{r} \right)^3 \tag{9.9}$$

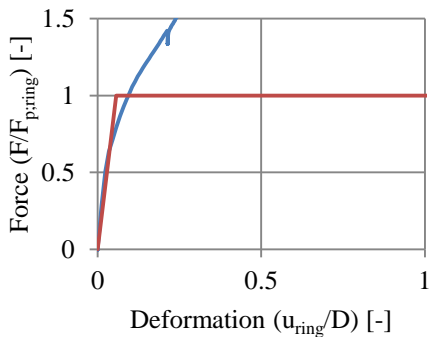
The results of the preliminary ring tests and comparisons with the analytical model are presented in Figure 9.19. The two rings that were loaded in compression (Figure 9.19a and b) performed well and the comparison with the analytical model is good. Both ring-spring designs are suitable for use in the full scale fault movement test. The combination of a ring-spring in compression with a coil spring offers more flexibility in terms of calibration to a specific soil behaviour. However, the coil springs require complicated support structures, resulting in high costs.



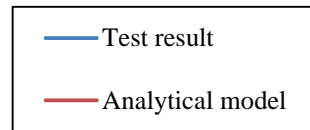
(a) Ring in compression without coil spring



(b) Ring in compression with coil spring



(c) Ring in tension



(d) Legend to graphs

Figure 9.19 Results of preliminary ring tests and comparisons with analytical model.

Figure 9.19c shows that the ring loaded in tension very quickly starts developing membrane action and therefore lacks a clear plateau in its force-deformation response. As a result, this ring-spring type is only able to model the elastic behaviour of the soil. To unify the ring-spring design across the test setup, all ring-springs in the full-scale fault movement experiments were designed as compression rings without the addition of a coil spring (see Figure 9.15a).

Design of ring-springs for tests on buried pipelines

The comparison presented in Figure 9.19a confirms correct prediction of the ring-spring force-deformation behaviour by the developed model. Equations (9.7), (9.8) and (9.9) show a relation between a ring-springs diameter, wall thickness and yield strength and its response under compression. These three equations establish the proportion between the elastic stiffness and plastic plateau of the ring-springs force-deformation relation. However, small adjustments to this proportion are possible by adjusting the width of the load introduction beam (see Figure 9.18a). Because of this nearly fixed relation between elastic stiffness and plastic plateau, a specific combination of pipe and soil requires a specific combination of diameter, wall thickness and steel grade for a ring-spring. Further parameters requiring consideration are the stroke of the ring-spring, which is approximately 90% of its diameter, and the overstrength of the steel with respect to the specified minimum yield strength. The majority of the pipe material of which ring-springs were made was generously provided by Salzgitter Mannesmann Forschung GmbH.

9.4.3 Test setup overview

Using the preliminary analyses performed by Tebodin and the results of the preliminary ring-spring tests, a test setup was designed that is capable of performing all ten tests as proposed in Table 9.3. The test setup contained a 20 m long pipeline specimen, allowed for the use of twelve ring-springs at flexible locations and was able to apply a maximum axial tensile force to the test specimen of 2000 kN. A maximum fault movement of approximately 1480 mm could be applied, which was dictated by the stroke of actuators 2 and 3. The setup consisted of two rigid steel frames, one of which was movable to simulate the fault movement. The ring-springs connected the rigid frames and the test specimen. At its two ends, the test specimen was fixed to the frames in lateral direction, but free to move in axial direction.

Because the movement direction of the movable steel frame was fixed, no other fault angles than 0° could be simulated with the test setup. In practice, at some distance from the fault, the lateral and axial soil pressure against the pipeline is not influenced by the fault angle in case of isotropic soil. Furthermore, for small fault angles, the pipe-soil interaction close to the fault may also be assumed to be similar to pipe-soil interaction in case of a 0° fault angle. As a result of this approximation, the fault angles that are listed in Table 9.3 could be taken into account by only taking into account the additional normal force N_β . Moreover, the fault angles are so small, that the actuator displacement may be assumed equal to the fault displacement (see equation (9.10)).

$$u_{\text{fault}} = \frac{u_{\text{actuator 2;3}}}{\cos \beta} \stackrel{\text{for small } \beta}{\approx} \frac{u_{\text{actuator 2;3}}}{1} \quad (9.10)$$

An overview of the test setup without ring-springs is presented in Figure 9.20. Figure 9.21a shows an overview photograph of the setup at the end of a test. A detail photograph of the ring-springs is presented in Figure 9.21b, while the load introduction into the specimen is shown in more detail in Figure 9.21c.

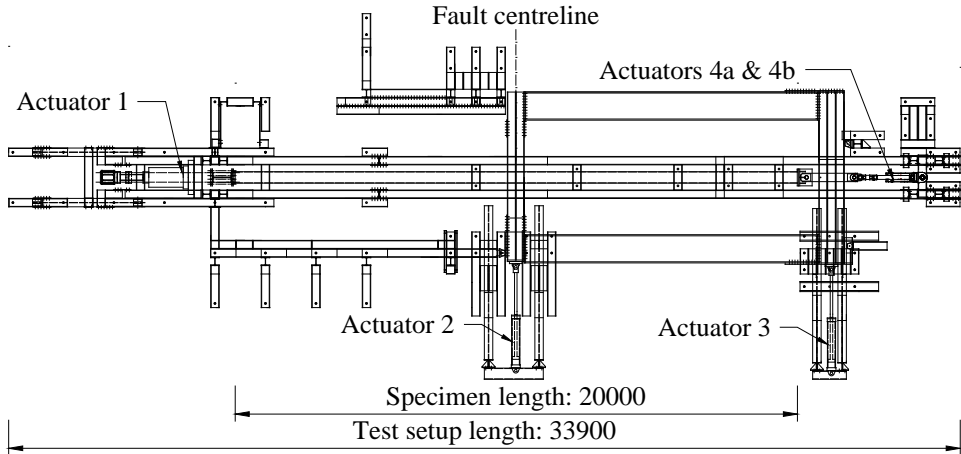
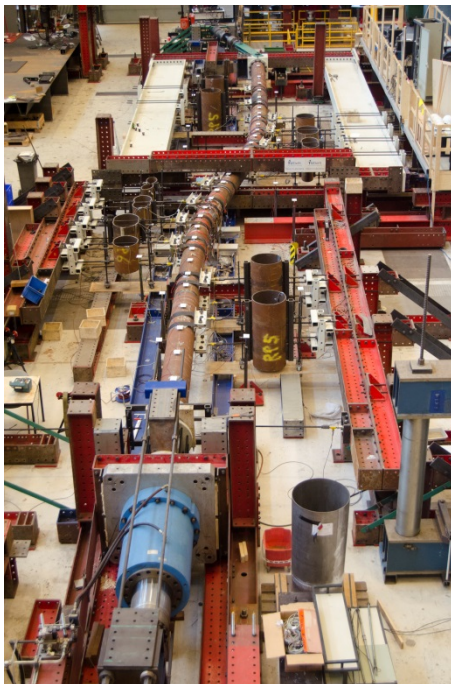


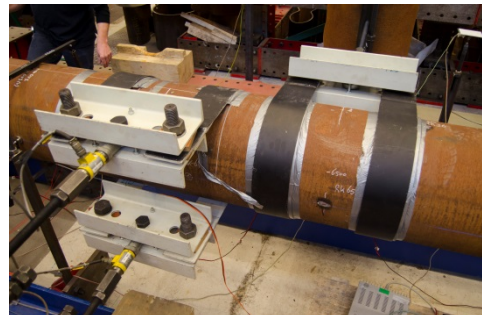
Figure 9.20 Schematic overview of fault movement tests (dimensions in mm).



(a) Overview of test setup (test 8)



(b) Pipe-soil interaction by ring-springs (test 8)



(c) Load introduction into the pipe (test 7)

Figure 9.21 Photographs of test setup.

Test procedures

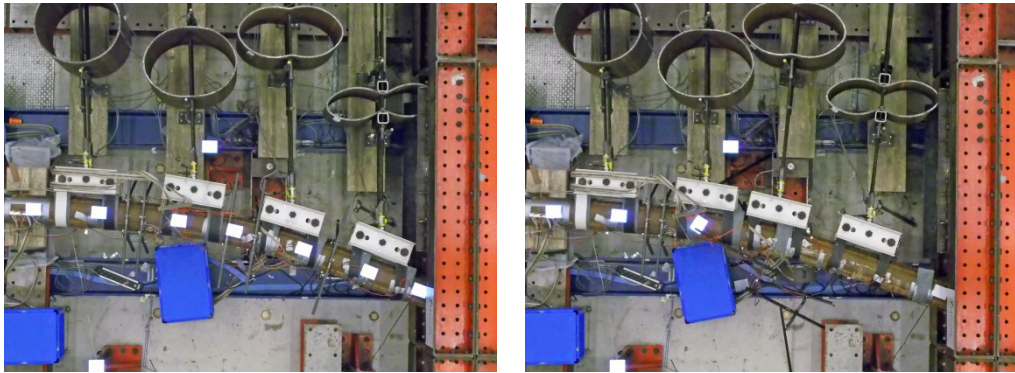
Before the test, the initial axial force was applied to the test specimen by actuators 1, 4a and 4b (see Figure 9.20). In case that no initial axial force was prescribed, a small force of approximately 10 kN was applied to activate test control systems and keep the test specimen in place. If applicable, internal pressure was applied, using water and a water pump. Subsequently, all ring-springs were pre-tensioned to a force of approximately 5 kN to ensure immediate activation of all ring-springs at the start of the fault movement. As a result of this pre-tensioning, longitudinal stresses occurred in the test specimen before starting the test. For the larger diameter specimens, these longitudinal stresses typically do not exceed 25 MPa, while in the smaller diameter specimens stresses up to 50 MPa were observed at the location of maximum stress. Because the tests result in strains far beyond the elastic range, these relatively low stresses at the start of the test are considered to be acceptable. However, they were not neglected. Measurements of the strain were started before pre-tensioning of the rings. Therefore, also the strains in the test specimen due to this pre-tensioning operation are included in the test results.

During the tests, the fault movement was increased in steps of 10 mm until the maximum possible fault movement of 1480 mm was reached. The fault movement was applied to the moving frame by actuators 2 and 3 (see Figure 9.20). Although at the specimen ends the test specimen was connected to the moving and stationary frames, the lateral movement of the test specimen in principle was only determined by the pipe-soil interaction which is simulated with the ring-springs. In axial direction, the centre of the 20 m long test specimen is maintained at the centreline of the fault, while actuators 1 and 4 (see Figure 9.21) apply the necessary axial force to the test specimen.

Load application

The tests simulated a situation where forces are continuously applied to the pipeline, while in the test these continuous loads were approximated by discrete forces, which were applied to the specimen by twelve ring-springs. To apply these discrete forces to the specimen as gradually as possible, two flexible steel straps per ring-spring were used (see Figure 9.21c). The forces were divided evenly between these two straps by using a spreader beam with a width of 240 mm or 350 mm. Provided that the ring-spring spacing was sufficient, the larger spreader beam was always used to achieve maximum spread of the load.

Due to the large displacements that were imposed, large rotations of the pipe occurred in the horizontal plane, especially near the fault. As a result, in many tests on the smaller diameter pipes, the load application straps shifted, sometimes suddenly and violently (see Figure 9.22). As a result of this shift, ring-springs relaxed and forces on the test specimen were relieved to some extent. In none of the tests did this shift occur before a local buckle formed or longitudinal tensile strains of significant magnitude ($>2\%$) were attained. Therefore, these shifts did not influence the failure mechanisms observed in the tests. The fault movement at which such a shift of straps occurred ($u_{fault;shift}$) is listed in Table D.1 in Appendix D.



(a) Before shift of straps

(b) After shift of straps

Figure 9.22 Shift of load application straps at large deformation over $\Delta u_{\text{fault}} = 10 \text{ mm}$.

9.4.4 Measurements

The fault was used as reference for all other test setup features. For example, the 20 m long pipeline specimen spanned from -10 m to +10 m from the fault, referred to as ‘left’ and ‘right’ of the fault. The ring-springs were symmetrical with respect to the fault centreline and were numbered starting from this centreline, with the addition of an indication of ‘left’ or ‘right’. Since both sides of the test specimen featured an intrados and extrados, a ‘front side’ and ‘back side’ of the test specimen were defined. The above definitions are presented in Figure 9.23.

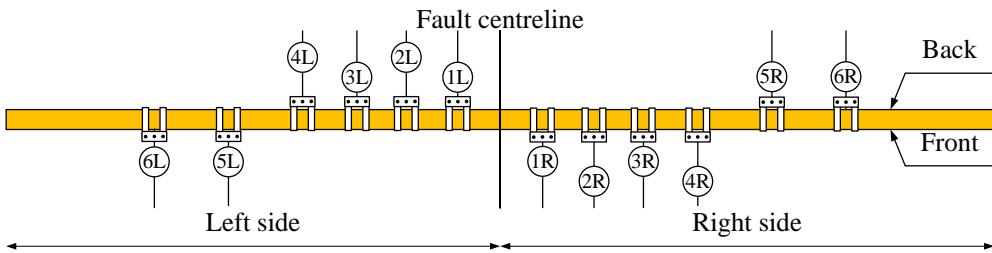


Figure 9.23 Definitions in the full scale fault movement test setup.

The applied forces and displacement at each of the four actuators were measured continuously, as well as the deformation of each ring-spring and the forces that acted on the test specimen. The latter was monitored by two load cells attached directly to the spreader beams, so that the resulting measurements ignore friction losses within the ring-springs and exactly indicate the forces that were applied to the test specimen. As described in section 9.4.3, the pipe ends were fixed to the stationary and moving frames in lateral direction. The forces necessary to achieve this were also monitored.

Deformation of the pipe itself was measured using 66 strain gauges. In case of specimens with atmospheric internal pressure, all strain gauges were placed at the intrados and extrados in longitudinal direction of the pipe, distributed evenly over the four quadrants of the test

specimen, and concentrated in expected areas of high strain. In case of pressurized specimens, a small portion of the strain gauges was placed in hoop direction. Different strain gauge positioning was used for each test, to suit the unique expected deformation of each test specimen. To allow for the application of strain gauges underneath the load application straps, 4 mm thick flexible PVC strips were placed underneath the steel straps with cut-outs at the location of the strain gauges.

Two methods were available for measuring the ovalisation of the pipe. For tests with atmospheric pressure, two holes were drilled in the pipe wall through which a small rod was installed, attached to a LVDT (see Figure 9.24a). For small ovalisations, the horizontal and vertical ovalisation may be assumed equal and opposite in an unpressurized pipe (Gresnigt, 1986). Therefore, in tests with atmospheric internal pressure, only the vertical ovalisation was measured. Because the ovalisation measurements using an LVDT breached the pipe wall, they were not suitable for pressurized pipes. Furthermore, for pressurized pipes, the total ovalisation is the result of the effects of bending and internal pressure. Therefore, in these tests, the ovalisation was measured in two directions by attaching brackets with flexible steel strips to the specimen. By measuring the strain in the bending strips using strain gauges, the ovalisation of the pipe was determined (see Figure 9.24b and Figure 9.24c). Photographs of both measurement methods are presented in Figure 9.25.

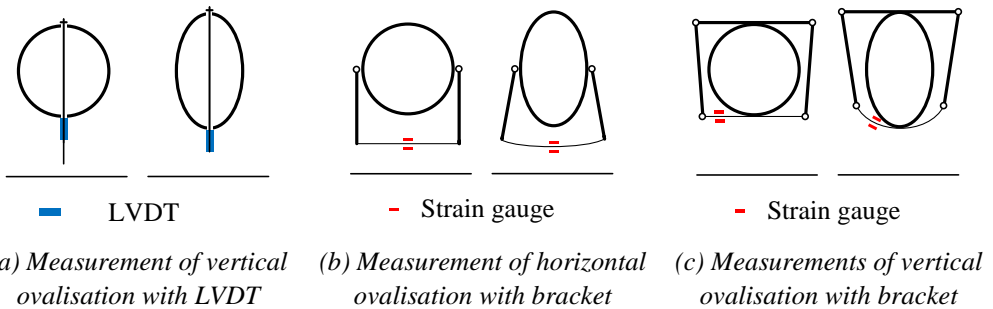
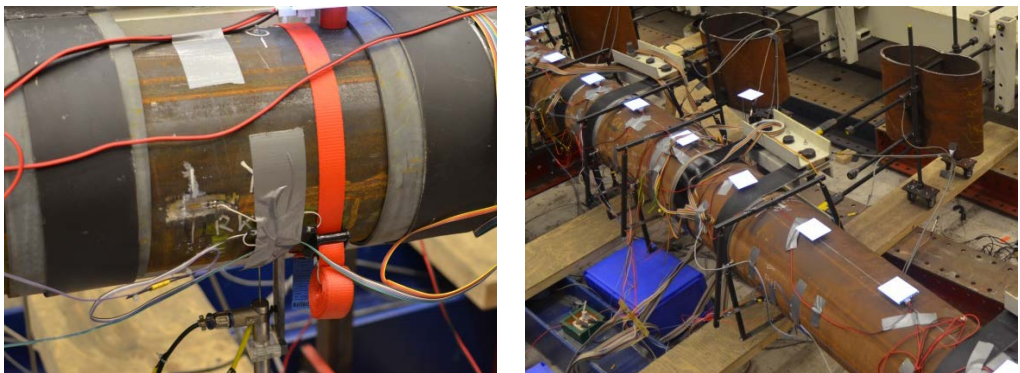


Figure 9.24 Three methods of measuring ovalisation during fault movement tests.



(a) Measurement using LVDT

(b) Measurements using brackets

Figure 9.25 Photographs of ovalisation measurement methods.

9.5 Boundary conditions of individual tests

The different parameters that were selected for every test (see Table 9.3) required different boundary conditions. For each test, an appropriate axial force and ring-spring configuration was determined. The following sections present a summary of the applied procedures. A more elaborate description of the design of each test can be found in Van Es and Gresnigt (2016b).

9.5.1 Axial force

The axial force acting in the pipeline during a fault movement can be split into three components (see section 9.1.1):

- N_s : Normal force due to formation of an S-curve
- N_β : Normal force due to a non-zero fault angle
- N_p : Normal force due to restrained lateral contraction as a result of internal pressure

For small fault angles, these three forces are assumed to be independent from each other. The total axial force in the pipeline was found by superposition of the three components.

Procedure to determine N_s

The axial force due to the formation of an S-curve was taken from the preliminary analyses by Tebodin (see section 9.4.1). The model that is used in these analyses is a simplification as it does not include local buckling. Furthermore, assumptions were made for the pipeline properties. As a result, the value of N_s used in the tests is an approximation of a realistic value for N_s . Due to the close approximation of pipeline properties in the model used by Tebodin, the approximation is expected to be accurate up to the moment local buckling occurs. Since the aim of the experiments is to increase understanding of the pipeline behaviour and validation of numerical models, a good estimate of the normal force N_s up till the moment of local buckling is sufficient.

Procedure to determine N_β

The axial force due to a non-zero fault movement was determined using a method similar to the proposal by Vazouras et al. (2012). The axial displacement of the pipe through the two soil bodies adjoining the fault as a result of a non-zero fault angle is given by equation (9.11) using the assumption for small angles made in equation (9.10). Using a pull-out test of the pipe-soil combination under consideration, a relation between u_{axial} and N_β was obtained. In this study, a relatively simple FE-analysis was performed to obtain this relation, which is not further described here. An example of the influence of the fault angle on the normal force in the pipeline is presented in Figure 9.26. The figure shows that already for small fault angles, a significant change in the axial force in the pipeline occurs. For further increasing or decreasing fault angle, the additional change in axial force is less severe.

$$u_{axial} = \frac{u_{lateral} \cdot \sin \beta}{2} = \frac{u_{fault} \cdot \sin \beta}{2 \cdot \cos \beta} \stackrel{\text{for small } \beta}{\approx} \frac{u_{fault} \cdot \sin \beta}{2} \quad (9.11)$$

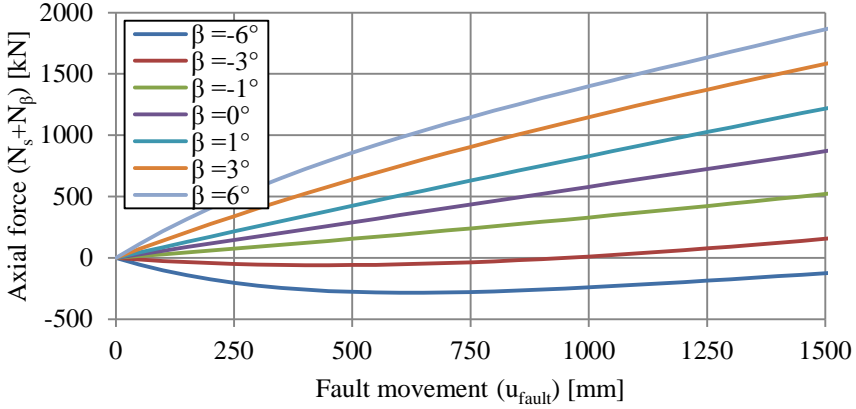


Figure 9.26 Example of influence of the fault angle on the axial force in the pipeline: 219x5.6 mm² pipe in clay.

Procedure to determine N_p

The tests are assumed to simulate an infinitely long, straight and fully constrained pipeline. In such a case, the normal force due to internal pressure N_p arises due to restrained lateral contraction of the pipeline material. The internal pressure P causes tensile hoop strains, resulting in contraction of the pipeline in axial direction. The resulting normal force N_p was calculated with equation (9.12).

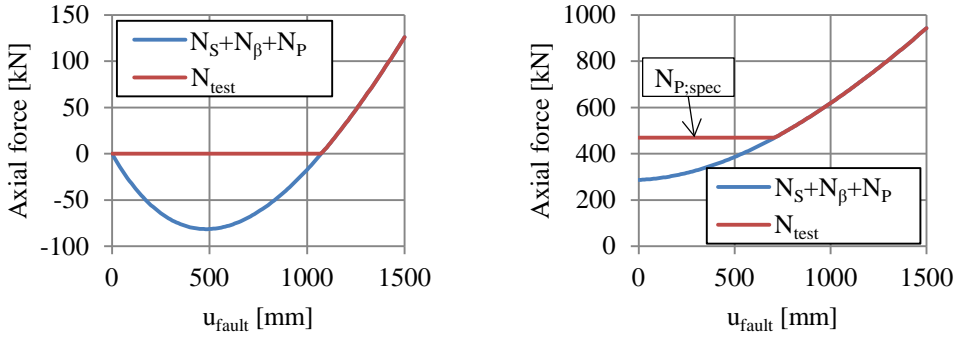
$$N_p = A_{steel} \cdot \nu \cdot \sigma_{hoop} = \frac{\pi \cdot \nu \cdot P}{2} \cdot (D - t) \cdot (D - 2 \cdot t) \quad (9.12)$$

Procedure to determine the total axial force in the test specimen

The total normal force that needed to be applied during the test was calculated as the sum of contributions N_s , N_β and N_p . The selected non-zero fault angles for the test programme were all negative, resulting in a compressive axial force N_β . In case of a pressurized test, a tensile normal force ($N_{p,spec}$) occurs in the specimen due to the capped end conditions of the pipe, which can be calculated with equation (9.13) and is always larger than N_p . The axial force that was applied to the specimen was corrected for this difference.

$$N_{p,spec} = A_{internal} \cdot P = \frac{\pi \cdot P}{4} \cdot (D - 2 \cdot t)^2 \quad (9.13)$$

For reasons of stability of the specimen and economics of the test setup steel structure, the test setup was designed to only apply a tensile force to the pipeline. In cases where the axial force that needed to be applied to the specimen was calculated to be in compression, an axial force of 0 kN was applied (see Figure 9.27). As a result, in some tests, the axial force was incorrect during an initial phase of the test. By designing the tests in such a manner that pipeline failure did not occur during this phase of the test, the influence of this approximation was minimized.



(a) Approximation of compressive axial force (b) Approximation of normal force in case of pressurized test specimen

Figure 9.27 Approximation of the axial force in the test specimen.

9.5.2 Ring-spring configuration

The selected test setup utilizes twelve ring-springs and two end supports to transfer lateral soil loads to the pipeline, while in reality, soil loads are continuously transferred to the pipeline. To approximate realistic conditions as closely as possible, the layout and dimensions of the twelve ring-springs were designed thoroughly. To perform this design, FE-models were used.

Numerical models for individual test design

To check the accuracy of the ring-spring configuration, an FE-model was used. The model features a full 3D analysis of the steel pipeline using shell elements. The pipe-soil interaction is modelled using soil springs with appropriate parameters, distributed along the pipeline. A full description of the general numerical model used for analysis of buried pipelines can be found in Chapter 11. For the design of the ring-spring configuration, two variants of the model were used: the “semi-continuous model” and the “discrete model”.

Both model identifications refer to the placement of soil springs in the model. In the semi-continuous model, soil springs are closely spaced. For the purpose of test design, it is assumed that the semi-continuous model generates results equal to a model featuring continuous soil springs. In the discrete model, the pipeline is coupled to the surrounding soil by only a limited number of soil springs. In this study, twelve ring-springs were used in the experiments, and therefore also twelve soil springs are employed in the discrete model. The link between the semi-continuous model, discrete model and test setup is presented in Figure 9.28. By comparing the output of the two models in terms of strain in the pipeline, the accuracy of the ring-spring configuration was determined. In an ideal match, the strains in the pipeline are equal in both models. However, due to the much more concentrated introduction of soil loads in the discrete model in comparison with the semi-continuous model, an exact match was not possible.

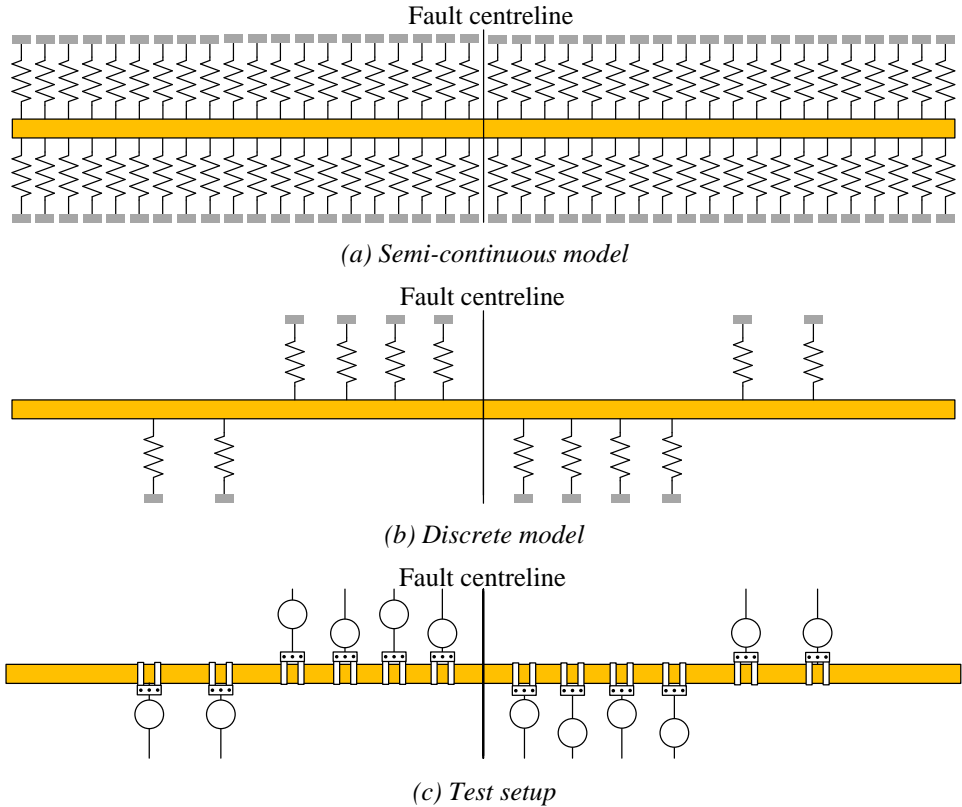


Figure 9.28 Comparison of two models for test setup design and test configuration.

Design procedure

To design the test layout, the expected test result was calculated using the semi-continuous model. The input parameters for the model were based on the known test parameters (see Table 9.3), while for unknowns such as the exact material behaviour and pipe geometry, assumptions were made. The output of the semi-continuous model in terms of pipeline strain and measured soil reaction forces was used as target for the final design of the test setup using ring-springs.

An initial estimate of the ring-spring positioning was made. Subsequently, the target ring-spring properties $u_{p;ring;target}$ and $F_{p;ring;target}$ were determined by concentrating the continuous soil pressures at the estimated ring-spring locations using equations (9.14) to (9.16). The method is presented graphically in Figure 9.29.

$$u_{p;ring;target} = y_{30} \quad (9.14)$$

$$F_{p;ring;target} = q_{he} \cdot L_{ref} \quad (9.15)$$

With:

L_{ref} : Length of continuous soil pressure that a ring-spring represents (see equation (9.16)).

$$L_{ref} = \begin{cases} \text{Ring 1} & \frac{x_{ring:1} - L_{stirred}}{2} + \frac{x_{ring:2} - x_{ring:1}}{2} \\ \text{Ring 2-5} & \frac{x_{ring:i} - x_{ring:i-1}}{2} + \frac{x_{ring:i+1} - x_{ring:i}}{2} \text{ with } i = 2, 3, 4, 5 \\ \text{Ring 6} & x_{ring:6} - x_{ring:5} \end{cases} \quad (9.16)$$

With:

$L_{stirred}$: Length over which no soil pressures act on the pipeline due to stirring of soil near the fault. Typical values used during the tests are 500 and 700 mm.

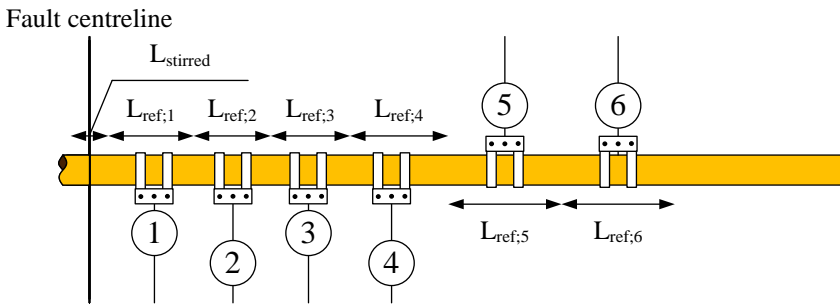


Figure 9.29 Method of determining reference length for each ring-spring.

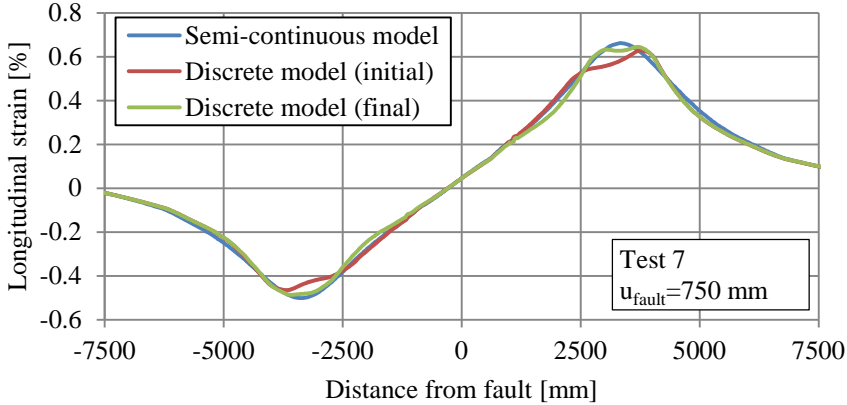
The initial parameters and positions of the test ring-springs were then used as input in the discrete model. By comparing the output of this model with the target strain distribution resulting from the semi-continuous model, the fitness of the chosen ring-spring configuration was evaluated. This fitness was primarily determined in the area of maximum deformation on either side of the fault, where failure is expected to occur.

In case of insufficient agreement, the ring-spring configuration was adjusted. New ring-spring target properties were obtained using equations (9.14) to (9.16) and a new comparison between the two models was made. Typically, a satisfactory agreement between the discrete and continuous model could be obtained in two to four iterations of this process. In some cases, further improvement was necessary in terms of slight adjustments of the reference lengths as defined in Figure 9.29 to reduce peak stresses and strains in the discrete model that were not present in the semi-continuous model. An example of a comparison of the semi-continuous model and two discrete models is presented in Figure 9.30.

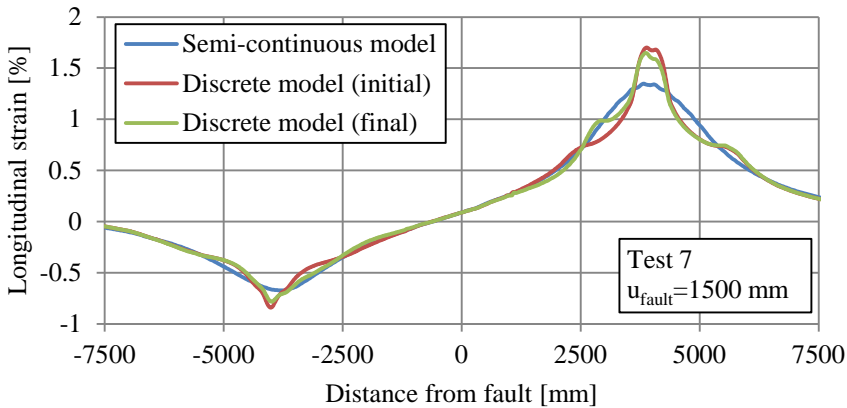
The figure shows that by adjustment of the ring-spring properties and placement, improvements in the comparison between the discrete model and semi-continuous model are possible. However, due to the discrete introduction of forces in the discrete model, strain peaks always occur in this model which are less pronounced in the semi-continuous model. Therefore, the test setup, which used discrete ring-springs, could not simulate reality fully accurately, although the deviation was relatively small (see Figure 9.30). The discrepancy between realistic, continuous soil and the discrete ring-springs in the test setup resulted in an approximation of the real

behaviour of the pipe. Because for validation of the numerical model (see Chapter 11) the actual properties of the test were used, this discrepancy did not influence the validation procedure.

Once a ring-spring configuration was determined, the ring-springs were designed using the procedures described in section 9.4.2 to match the target behaviour as closely as possible.



(a) Results for a fault movement of 750 mm



(b) Results for a fault movement of 1500 mm

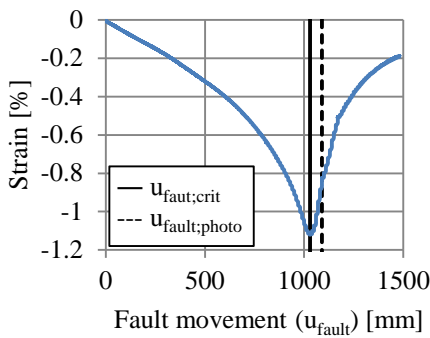
Figure 9.30 Comparison between semi-continuous model and the initial and final iterations of the discrete model in terms of resulting pipe strains.

9.6 Results of large-scale testing

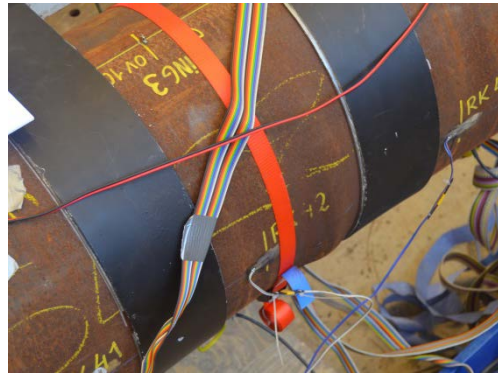
In this section, the main results of the tests are presented. For each test, the distribution of strains over the length of the specimen at different levels of applied fault movement is presented. Furthermore, the fault movement at which local buckling occurred or at which tensile strains of

0.5%, 1%, 2% and 3% were reached during the test are presented in summarizing section 9.6.11. Further results, such as the response of the ring-springs, the relation between measured strains and the applied fault movement and ovalisation of the test specimen, are presented in Appendix D and Van Es and Gresnigt (2016b). The tests are analysed in Chapter 10.

In seven out of ten tests, local buckling of the pipe wall occurred. These local buckles formed gradually, meaning that the critical fault movement at which the buckle formed ($u_{fault;crit}$) was difficult to determine. The critical fault movement was defined at a minimum in a u_{fault} -strain relation of a strain gauge close to the buckling location (see Figure 9.31a). An example photograph, taken at a fault movement 60 mm larger than the critical fault movement, is presented in Figure 9.31b. From the two figures in Figure 9.31 it can be concluded that the chosen definition of the critical fault movement approximately corresponds to the earliest possible visual identification of a local buckle.



(a) Definition of critical fault movement on the basis of strain gauge results



(b) Photo at a fault movement 60 mm past $u_{fault;crit}$ (see figure a) showing the initial stages of a local buckle

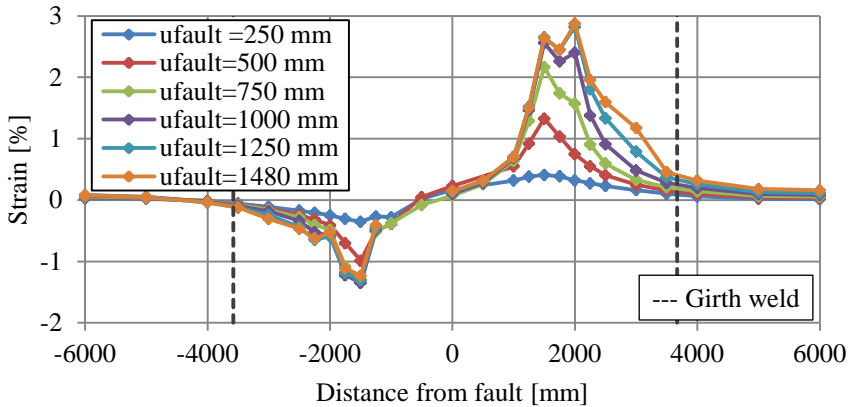
Figure 9.31 Definition of the critical fault movement (example: test T9).

For various reasons, one or more strain gauges did not provide reliable data during a part of the tests. In these cases, the results were removed from graphs when appropriate. For example, in the graphs presented in sections 9.6.1 to 9.6.10, this results in discontinuous lines. Causes for these failures may be: clipping of the output signal of the strain gauge in case of very high strains that were out of range of the measuring equipment, damage to the gauge or cables due to shifting of the load application straps (see Figure 9.22), or detachment of cables as a result of the large displacements involved with the tests. Furthermore, due to folding of the pipe wall near a local buckle, measured compressive strains in this area are meaningless with regard to the overall pipe behaviour after local buckling failure.

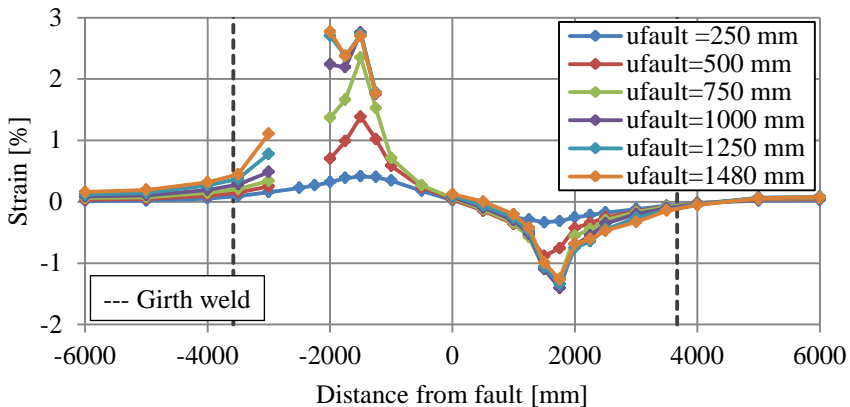
On each side of the fault, a pipe segment exists where deformation is most severe, resulting in high longitudinal strains, large ovalisation and possibly local buckling. This area is denoted as the critical segment of the test specimen. Within this segment, one single cross-section is subjected to the maximum strain. This cross-section is denoted as the critical cross-section.

9.6.1 Test T1

Test T1 simulates a 219 mm-diameter non-pressurized pipe buried in sandy soil. The test simulates a fault movement perpendicular to the pipe axis ($\beta=0^\circ$). At the maximum fault movement of 1480 mm, no local buckles had formed. An overview of the longitudinal strains in the test specimen measured during the test is presented in Figure 9.32. The figure shows symmetrical behaviour of the test specimen, which is confirmed by the results shown in Appendix D. Furthermore, it appears that the tensile strains are no longer increasing for increasing fault movement after some threshold value was reached. Instead, deformation spreads out over a longer length of the specimen.



(a) Strains at front side of the specimen



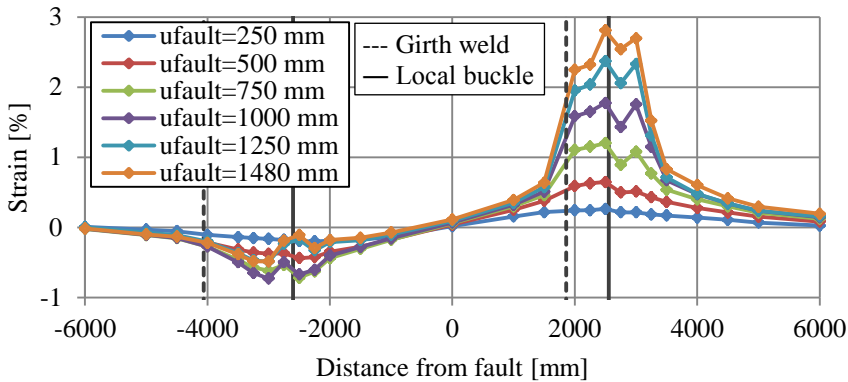
(b) Strains at the back side of the specimen

Figure 9.32 Longitudinal strains measured during test T1.

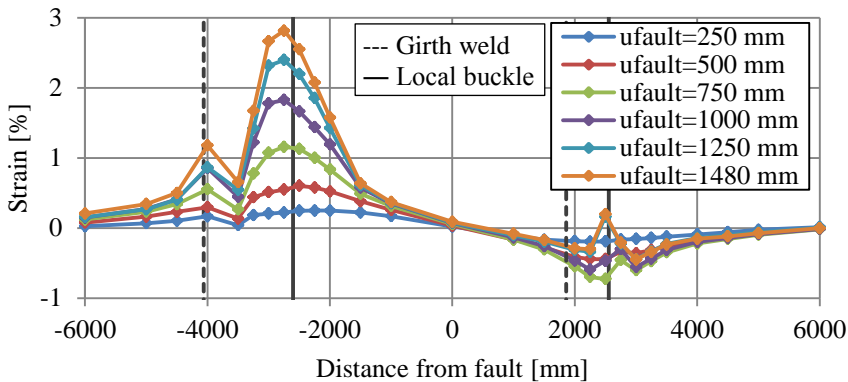
9.6.2 Test T2

Test T2 simulates a 406 mm-diameter non-pressurized pipe buried in sandy soil subjected to. The test simulates a fault movement perpendicular to the pipe axis ($\beta=0^\circ$). Local buckles formed at fault movements of 840 mm and 910 mm on the right and left side of the fault respectively. At $u_{fault}=250$ mm, a failure occurred in multiple load application straps. After replacement of the damaged components, the ring-springs were reloaded and the test was continued. Despite careful reloading of the ring-springs, a small discontinuity is visible in the results (see Appendix D).

An overview of the longitudinal strains measured during the test is presented in Figure 9.33. Due to the formation of local buckles, strains at the tensile side keep increasing with increasing fault movement, in contrast to what was observed in test T1. At the back side of the specimen, a clear influence of the girth weld at a distance of -4030 mm from the fault is visible in the form of a strain offset. Strains concentrate on the left of this girth weld, which corresponds with the slightly lower yield and ultimate strength of that specimen part (see Appendix D.2).



(a) Strains at the front side of the specimen



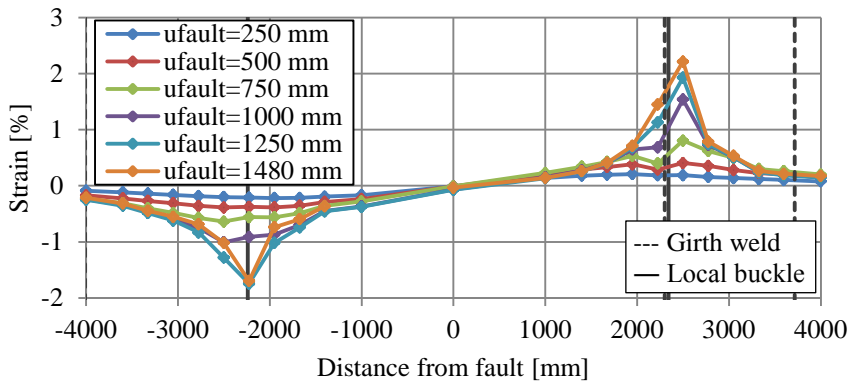
(b) Strains at the back side of the specimen

Figure 9.33 Longitudinal strains measured during test T2.

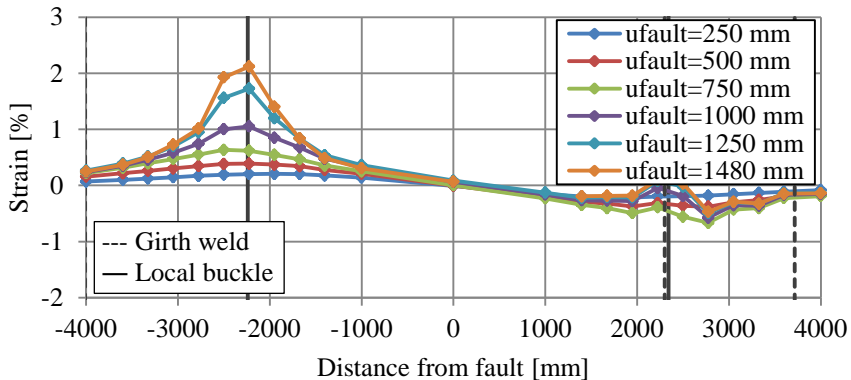
9.6.3 Test T3

Test T3 simulates a 219 mm-diameter non-pressurized pipe buried in clayey soil. The test simulates a fault movement with an angle of -3.25° to the pipe axis ($\beta = -3.25^\circ$). Local buckles formed at fault movements of 810 mm and 1201 mm on the right and left side of the fault respectively. On the right side of the fault, local buckling occurred at a girth weld in the critical segment of the pipe. The relatively large difference between $u_{fault;crit;left}$ and $u_{fault;crit;right}$ indicates a negative effect of the presence of a girth weld in the critical segment.

An overview of the longitudinal strains measured during the test is presented in Figure 9.34. The influence of the presence of a girth weld is visible at relatively low fault movements, especially at the tensile side (see Figure 9.34a). Strains concentrate on one side of the girth weld, which is in line with the material properties of pipes adjoining the girth weld (see Appendix D.2).



(a) Strains at the front side of the specimen

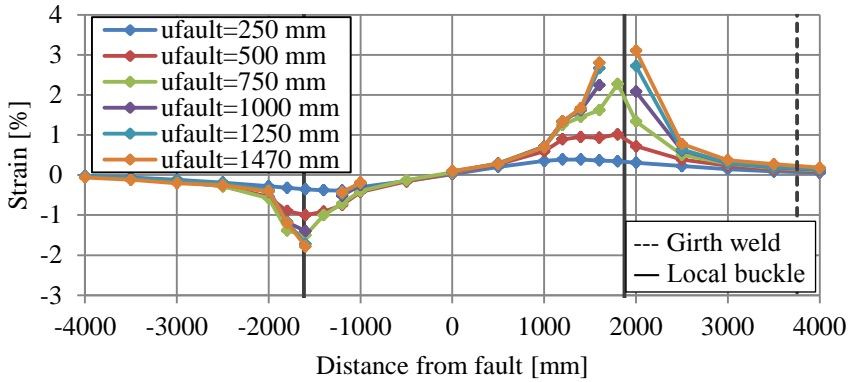


(b) Strains at the back side of the specimen

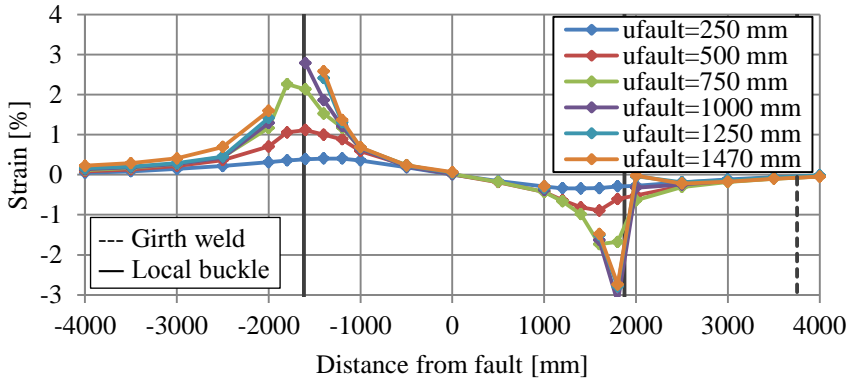
Figure 9.34 Longitudinal strains measured during test T3.

9.6.4 Test T4

Test T4 simulates a 219 mm-diameter non-pressurized pipe buried in sandy soil. The test simulates a fault movement with an angle of -1.5° to the pipe axis ($\beta = -1.5^\circ$). Local buckles formed at fault movements of 689 mm and 771 mm on the left and right side of the fault respectively. An overview of the longitudinal strains measured during the test is presented in Figure 9.35.



(a) Strains at the front side of the pipeline specimen

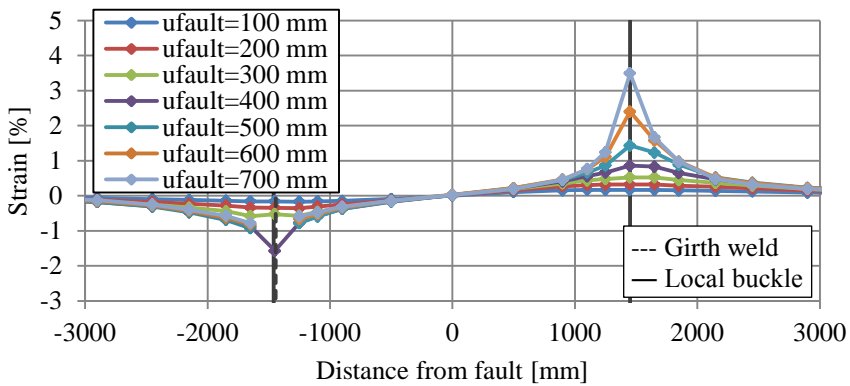


(b) Strains at the back side of the pipeline specimen

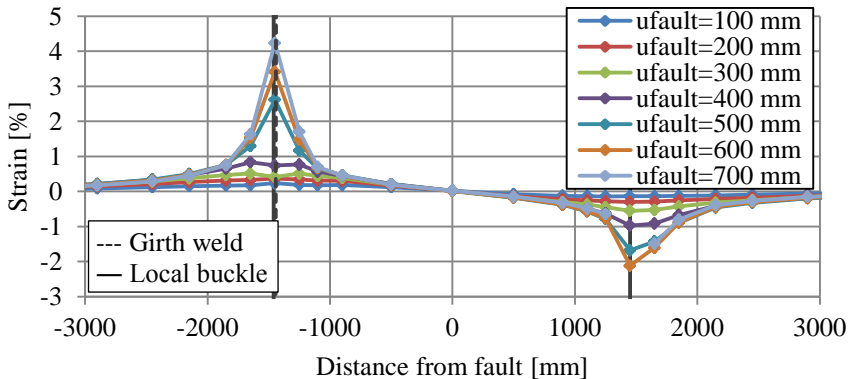
Figure 9.35 Longitudinal strains measured during test T4.

9.6.5 Test T5

Test T5 simulates a 219 mm-diameter pressurized pipe buried in sandy soil. The test simulates a fault movement with an angle of -2.25° to the pipe axis ($\beta = -2.25^\circ$). An internal pressure was applied, resulting in a hoop stress of approximately 25% of the specified minimum yield strength. Local buckles formed at fault movements of 460 mm and 569 mm on the left and right side of the fault respectively. The local buckle on the left side of the fault occurred near a girth weld that was purposely placed in the critical segment of the specimen. At a fault movement of 710 mm, a rupture occurred on the opposite side of the local buckle on the left side of the fault, resulting in loss of containment. The test was stopped immediately after this event. Possible causes for the occurrence of this rupture are discussed in section 10.5. An overview of the longitudinal strains measured during the test is presented in Figure 9.36.



(a) Strains at the front side of the pipeline specimen



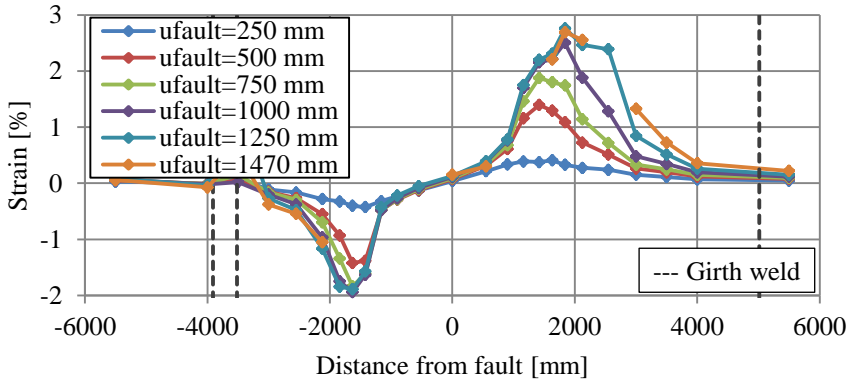
(b) Strains at the back side of the pipeline specimen

Figure 9.36 Longitudinal strains measured during test T5.

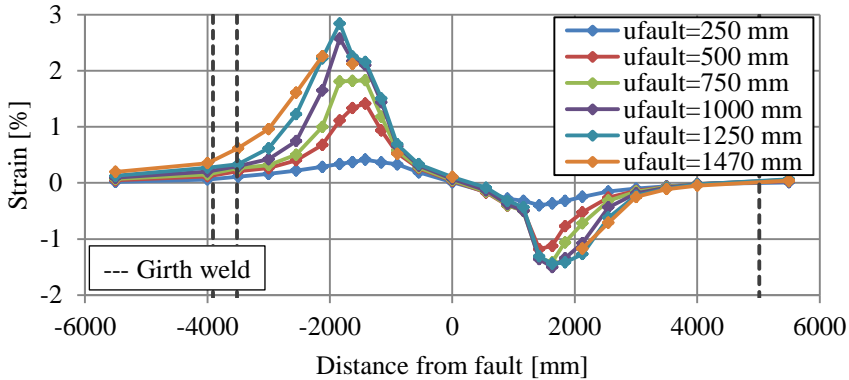
9.6.6 Test T6

Test T6 simulates a 219 mm-diameter pressurized pipe buried in sandy soil. The test simulates a fault movement perpendicular to the pipe axis ($\beta=0^\circ$). An internal pressure was applied, resulting in a hoop stress of approximately 50% of the specified minimum yield strength. At the maximum fault movement of 1470 mm, no local buckles had formed.

An overview of the longitudinal strains measured during the test is presented in Figure 9.37. The girth weld 3910 mm left of the fault apparently includes some geometrical imperfection, leading to wall bending, which is measured by a nearby strain gauge. As noted earlier, these measurements are not relevant for the overall behaviour of the specimen.



(a) Strains at the front side of the pipeline specimen



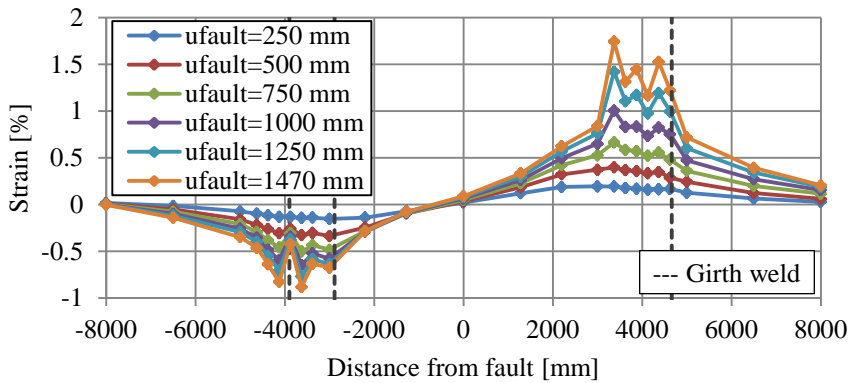
(b) Strains at the back side of the pipeline specimen

Figure 9.37 Longitudinal strains measured during test T6.

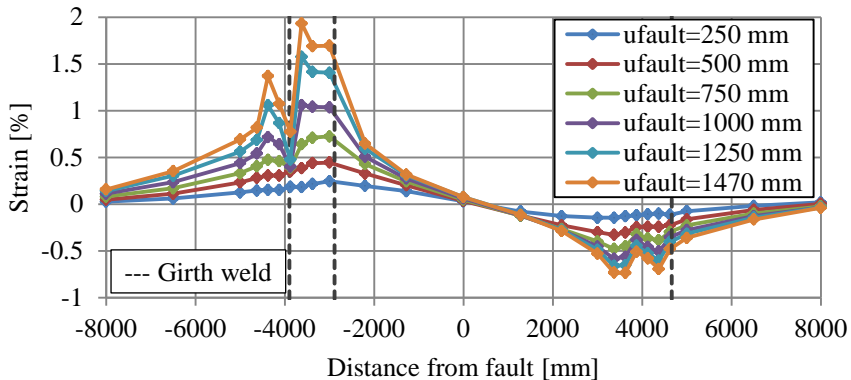
9.6.7 Test T7

Test T7 simulates a 406 mm-diameter pressurized pipe buried in sandy soil. The test simulates a fault movement perpendicular to the pipe axis ($\beta=0^\circ$). An internal pressure was applied, resulting in a hoop stress of approximately 50% of the specified minimum yield strength. At the maximum fault movement of 1470 mm, no local buckles had formed.

An overview of the longitudinal strains measured during the test is presented in Figure 9.38. Similarly as in earlier tests, the presence of a girth weld 3900 mm left of the fault can be clearly recognized in the measured longitudinal strains. It is unclear whether this is the result of a concentration of strains on one side of the girth weld (similarly as in e.g. test T2) or if the measurements by the strain gauges close to the girth weld include bending of the pipe wall due to geometrical imperfection present near the girth weld.



(a) Strains at the front side of the pipeline specimen



(b) Strains at the back side of the pipeline specimen

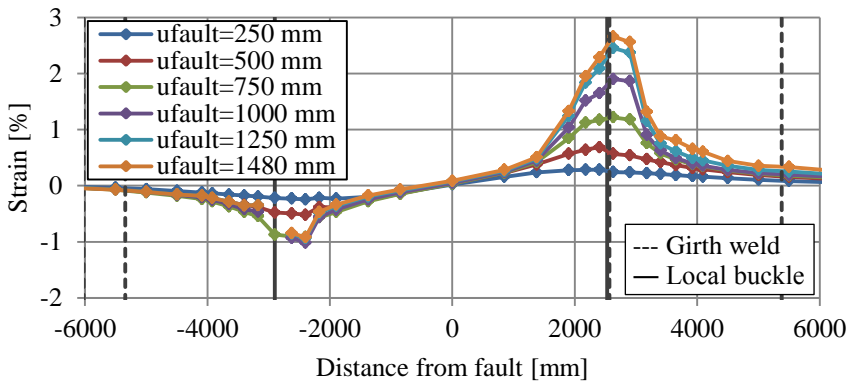
Figure 9.38 Longitudinal strains measured during test T7.

9.6.8 Test T8

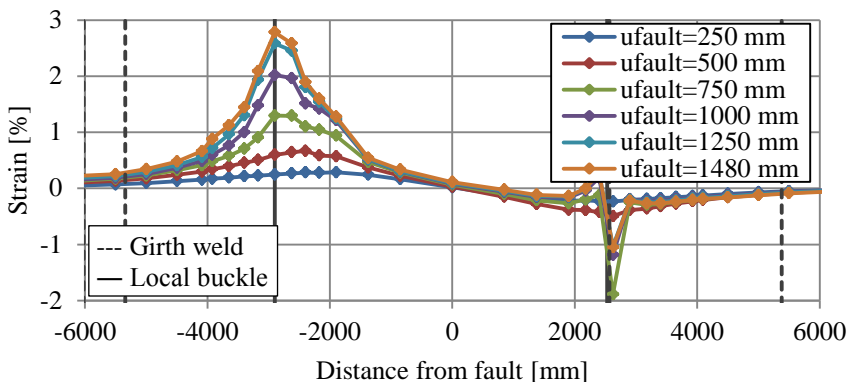
Test T8 simulates a 406 mm-diameter non-pressurized pipe buried in sandy soil. The test simulates a fault movement perpendicular to the pipe axis ($\beta=0^\circ$). Local buckles formed at fault movements of 590 mm and 891 mm on the right and left of the fault respectively. The local buckle on the right side occurred at a girth weld purposely placed in a highly strained section of the test specimen.

The test parameters of tests T2 and T8 are identical, with the exception of a girth weld in a critical segment in test T8. However, availability of ring-spring material dictated some small differences between the two tests in terms of ring-spring properties.

An overview of the longitudinal strains measured during the test are presented in Figure 9.39. Already early in the test, strains concentrated on one side of the girth weld present 2565 mm right of the fault.



(a) Strains at the front side of the pipeline specimen

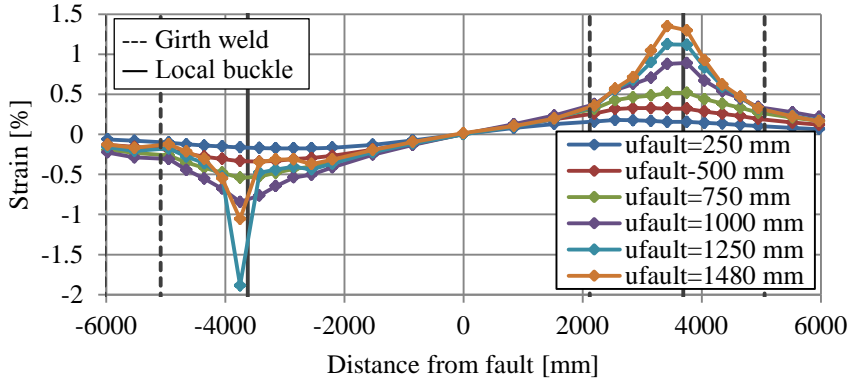


(b) Strains at the back side of the pipeline specimen

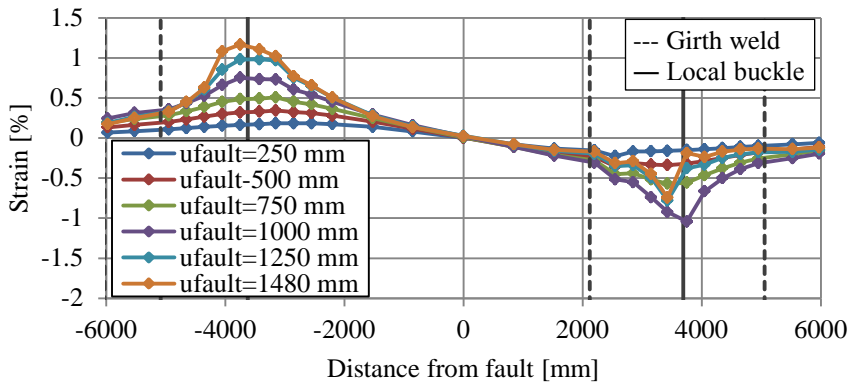
Figure 9.39 Longitudinal strains measured during test T8.

9.6.9 Test T9

Test T9 simulates a 406 mm-diameter non-pressurized pipe buried in clayey soil. The test simulates a fault movement with an angle of -2° to the pipe axis ($\beta=-2^\circ$). Local buckles formed at fault movements of 1030 mm and 1120 mm on the right and left of the fault respectively. An overview of the longitudinal strains measured during the test is presented in Figure 9.40.



(a) Strains at the front side of the pipeline specimen



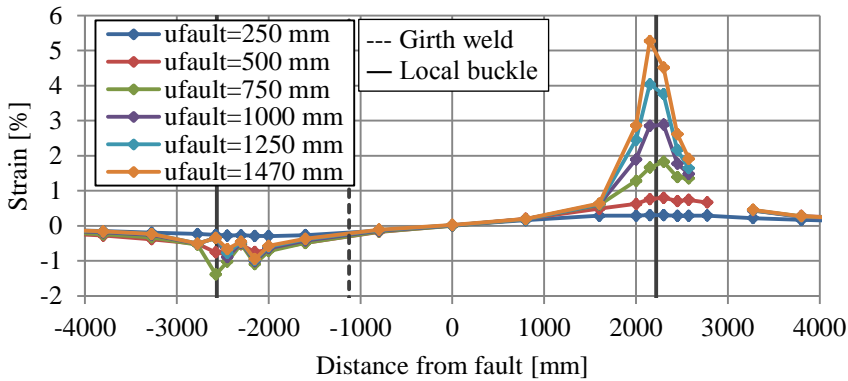
(b) Strains at the back side of the pipeline specimen

Figure 9.40 Longitudinal strains measured during test T9.

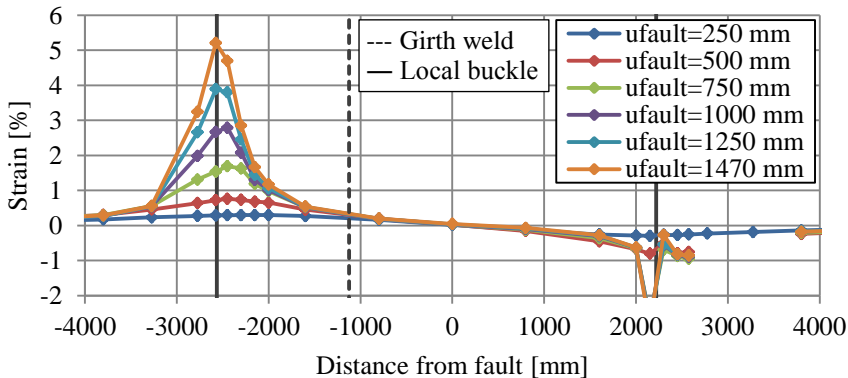
9.6.10 Test T10

Test T10 simulates a 406 mm-diameter pressured pipe buried in sandy soil. The test simulates a fault movement with an angle of -2° to the pipe axis ($\beta = -2^\circ$). An internal pressure was applied, resulting in a hoop stress of approximately 25% of the specified minimum yield strength. Local buckles formed at fault movements of 641 mm and 650 mm on the right and left side of the fault respectively.

An overview of the longitudinal strains measured during the test is presented in Figure 9.41. The very high tensile strains on the opposite side of the local buckles are noteworthy. The magnitude of these strains is unmatched in any other test. Even in test T8, during which a local buckle formed very early, allowing for significant concentration of deformation at the buckling location, the maximum measured strains were lower.



(a) Strains at the front side of the pipeline specimen



(b) Strains at the back side of the pipeline specimen

Figure 9.41 Longitudinal strains measured during test T10.

9.6.11 Summary of test results

An overview of the test results is presented in Table 9.6. For each specimen on each side of the fault, the table lists the critical fault movement as well as the first occurrence of tensile strains of magnitude 0.5%, 1%, 2% and 3% on the extrados of the specimen. Naturally, these strains may have occurred earlier in the pipe segments in-between the strain gauges where no data were available.

After formation of a local buckle on either side of the fault, strains and deformations may rapidly increase due to the local loss of stiffness of the pipeline. Moreover, the formation of a local buckle is recognized as failure of the pipeline (see section 8.2). Events in Table 9.6 that occurred after this failure on either side of the fault are displayed in italics.

Table 9.6 Overview of measurement results in critical segments on either side of the fault. Values presented in italics occurred after a local buckling failure.

Test	Side	GW	$u_{fault,crit}$ [mm]	u_{fault} [mm] of occurrence of tensile strain value:			
				0.5%	1%	2%	3%
T1	Left	No	-	286	421	660	-
	Right	No	-	288	430	692	-
T2	Left	No	910	444	690	<i>1084</i>	-
	Right	No	840	425	660	<i>1100</i>	-
T3	Left	No	1201	631	986	<i>1420</i>	-
	Right	Yes	810	580	<i>820</i>	<i>1341</i>	-
T4	Left	No	689	300	471	<i>701</i>	<i>911</i>
	Right	No	771	310	501	<i>701</i>	<i>642</i>
T5	Left	Yes	460	296	410	<i>440</i>	<i>549</i>
	Right	No	569	290	430	<i>570</i>	<i>651</i>
T6	Left	No	-	287	451	798	-
	Right	No	-	289	477	804	-
T7	Left	Yes	-	552	971	-	-
	Right	No	-	601	1001	-	-
T8	Left	No	891	405	<i>652</i>	<i>997</i>	-
	Right	Yes	590	471	<i>645</i>	<i>1033</i>	-
T9	Left	No	1120	740	<i>1285</i>	-	-
	Right	No	1030	730	<i>1062</i>	-	-
T10	Left	No	650	391	576	821	<i>1051</i>
	Right	No	641	380	559	791	<i>1031</i>

All unpressurized specimens that failed in local buckling during the tests featured one or multiple inward folds of the pipe wall (see Figure 9.42a and b). In the cases of local buckling in specimens with internal pressure, the pipe wall buckled outward (see Figure 9.42c and d). As can be observed in the results of tests T5 and T10, tensile strains at the extrados opposite to a local buckle in a pressurized pipe may be very high, considerably higher than in case of an unpressurized pipe.



(a) Unpressurized specimen T8 (right side of the fault)



(b) Unpressurized specimen T9 (right side of the fault)



(c) Pressurized specimen T5 (right side of the fault)



(d) Pressurized specimen T10 (right side of the fault)

Figure 9.42 Examples of local buckling shapes.

The placement of a girth weld in a critical segment of the test specimen clearly influenced the strain distribution over the pipeline specimen. In many cases, deformation localizes on one side of the girth weld due to yield strength differences between the two adjoining specimen parts (see e.g. Figure 9.34a). A girth weld in a highly strained section of the test specimen was always combined with a plain pipe section in the critical segment on the opposite side of the fault. If local buckling occurred in such tests, the side that included the girth weld always buckled first. Apparently, the presence of a girth weld makes the pipeline more susceptible to local buckling, either by concentration of curvature, imperfections at the girth weld or a combination of both effects.

9.7 Summary of Chapter 9

This chapter presents the design and results of a full-scale testing programme, simulating the behaviour of buried pipes under fault movement. A collection of the exact design of each test and a more comprehensive presentation of the test results can be found in Appendix D.

Instead of testing a buried pipeline specimen, the pipe-soil interaction was simulated using ring-springs. The properties of these ring-springs were determined in accordance with NEN 3650-1 (2012), which follows the theory by Brinch-Hansen (1961) and Audibert and Nyman (1977). Similar pipe-soil interaction models are recommended in many other relevant standards. Using initial analyses by research partner Tebodin, appropriate dimensions and capacities were selected for the test setup. The individual design of each test was based on FE-analyses.

During the tests, extensive measurements were taken of the deformation of the pipeline specimen and the soil pressures that were simulated by the ring-springs. As a result, the response of the pipelines to the imposed deformation of the fault movement is very well documented.

In the ten tests that were performed, all specimens reached at least a longitudinal tensile strain of 1%, while the vast majority of the specimens also reached a longitudinal tensile strain of 2%. Local buckling occurred in seven out of ten tests. In test T5, very high longitudinal tensile strains resulted in a rupture in the pipe. Critical pipe segments that included a girth weld were more susceptible to local buckling. Furthermore, a local buckle in a pressurized pipe was found to lead to very high tensile strains in the extrados opposite to the local buckle.

Chapter 10

Analysis and interpretation of test results

10.1 Method of analysis

The aim of the experiments was stated to be twofold. Firstly, the experiments aimed to enhance understanding of the deformation of a buried pipeline under ground-induced deformations. Secondly, the experiments were performed to validate a numerical model. The development, validation and calibration of this model is presented in Chapter 11.

For the purpose of validation of the numerical model, the ten tests that were performed cover a wide range of design parameters (see Table 9.3). The conclusions that were drawn on the basis of the preparation, execution and analysis of the tests are presented in this chapter.

10.2 Influence of soil behaviour and pipe-soil interaction

In the tests, four pipe-soil combinations were taken into account. Naturally, a combination of a stiff pipeline in soft soil results in relatively low deformations in the pipelines, while a more flexible pipeline in stiff soils reaches a limit state at much smaller fault movements.

It was also observed that the inelastic response of both the pipeline and soil results in the movement of the critical cross-section in the pipeline. For increasing fault movement, the distance between the critical cross-section and the fault centreline was observed to increase. This behaviour is illustrated in Figure 10.1. This effect, in combination with the uncertainty in the exact location where ground-induced deformation of a pipeline may occur, results in a critical cross-section location that is difficult to predict with accuracy.

A further conclusion was drawn on the basis of the results of tests T1 and T6. The strain measurements show that for larger fault movements no further strain increase is measured. Instead, strains spread out over a longer section of pipeline. It is assumed that this is caused by

two factors. Firstly, strain hardening of the steel prevents very local deformation. Secondly, with increasing fault movement, the loading on the pipeline changes in size but also in shape due to the plastic behaviour of the ring-springs. Additional studies may further quantify this effect.

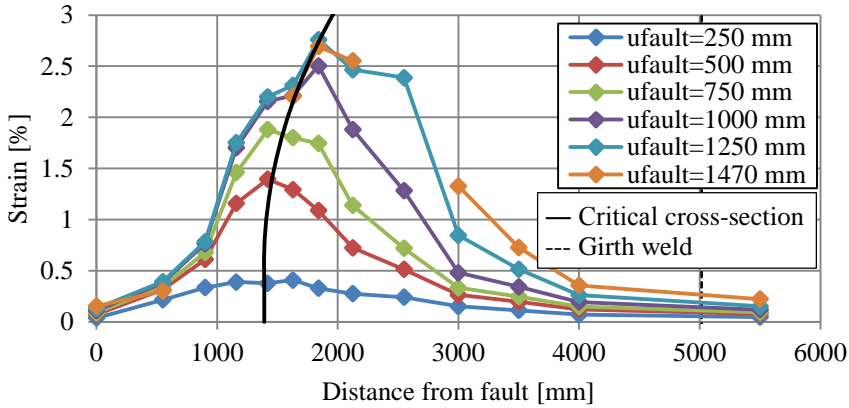


Figure 10.1 Example of movement of critical cross-section for increasing fault movement.

10.3 Influence of the presence of a girth weld in a critical segment of the pipeline

In four out of ten tests, a girth weld was placed in a critical segment of the pipeline, while on the opposite side of the fault, the critical segment of the pipeline was kept free of girth welds. In one of these tests (T7), no local buckling failure occurred. In the remaining three of these tests, failure in the form of local buckling occurred first at the side of the fault where the girth weld was placed in the critical segment. These local buckles all formed in the immediate vicinity of the girth weld. Furthermore, when the test results of the four tests that include a girth weld in the critical segment are compared with comparable tests on pipeline specimens that lack this feature, local buckling is observed to occur earlier in specimens with a girth weld in the critical segment.

On average, the critical fault movement of girth welded pipe segments was found to be 72% of the critical fault movement of the plain pipe segment on the opposite side of the fault. It should be noted that in this plain segment, local buckling failure was influenced by the stiffness loss caused by the formation of a local buckle at the girth weld. A more fair comparison is made by examining the results of tests T2 and T8, which feature approximately the same boundary conditions (see Table 9.3 and section 9.6.8). In test T8, which featured a girth weld in the critical segment of the pipe, local buckling occurred at a fault movement of 590 mm. In test T2, which only features plain pipe in the critical segments, the first local buckling failure did not occur until a fault movement of 840 mm. For this specific case, the critical fault movement of the girth welded critical segment was 70% of the critical fault movement of the plain critical segment.

Two causes are recognized for the observed lower local buckling resistance of the critical sections that include a girth weld. Firstly, a mismatch in bending moment capacity of the two

pipes adjoining the girth weld may result in concentration of deformation on one side of the girth weld. Under a constant bending moment, a small difference in bending moment capacity of the two connected pipes may result in a significant concentration of deformation, especially during inelastic deformation. It must be noted that in the tests, this effect was not very pronounced. Only tests T2, T3 and T7 do exhibit this behaviour to some extent (see section 9.6). Likely, the strong variation of the acting bending moment over the specimen length limits the concentration of deformation due to a strength mismatch at a girth weld. Secondly, geometrical imperfections that may be associated with a girth weld can also reduce the local buckling resistance of a pipe.

It is likely that a larger strength difference between two connected pipe segments results in more concentration of deformation. This may result in a reduction of the critical fault movement for pipes containing a girth weld in the critical segment. To further explore this effect, the strength mismatch in the three specimens that contained a girth weld in the critical segment was quantified using the strength ratio ζ , as defined in section 6.4. The effect of the strength mismatch on the critical fault movement was quantified by comparing the critical fault movement of the critical segment including the girth weld with the critical fault movement of the critical segment on the opposite side of the fault. The ratio between these fault movements, denoted as critical fault movement ratio, was used for comparison purposes. In Figure 10.2, the relation between the strength ratio (ζ) and the critical fault movement ratio is shown. It indeed appears that a larger difference in bending moment capacity between the two pipes adjoining the girth weld results in a greater reduction of the critical fault movement.

Specimens without a girth weld in the critical segment had an average difference between the two critical fault movements of 7% (see Table 9.6). In specimen T5, where no strength mismatch was present, a critical fault movement ratio of 0.81 was measured. Besides a strength difference, there apparently are other causes for the reduced local buckling resistance of girth welded pipes. The earlier mentioned imperfections at the girth weld may be such a cause.

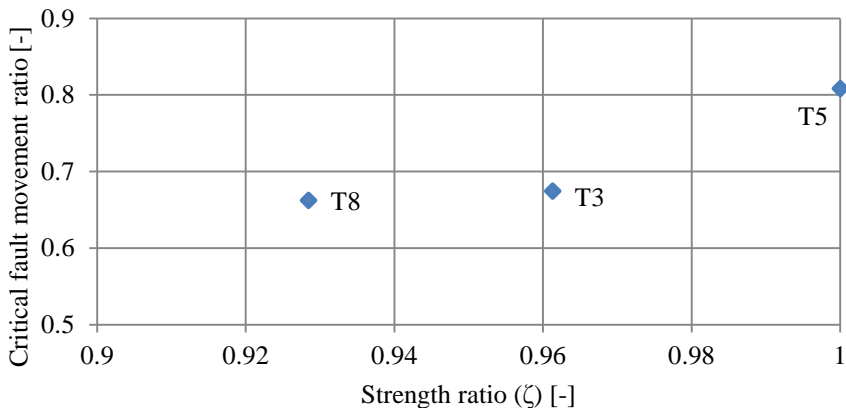


Figure 10.2 Relation between the strength ratio (ζ) and critical fault movement ratio.

Avoidance of a girth weld in a pipeline section subjected to high strains may very well be unattainable because of the movement of the critical cross-section (see section 10.2) and the uncertainty of the exact location of the fault and direction of the applied soil movement.

It can therefore be concluded that the presence of a girth weld in the critical segment of a pipeline negatively affects the ability of a pipeline to remain intact in case of severe ground-induced deformations. To limit this effect, it is important to limit the strength mismatch at girth welds. Furthermore, execution quality of the weld is assumed to be an important factor. The possible negative effects of the girth weld itself, and the geometrical imperfections that may be associated with a girth weld were already discussed in Part I and Part II of this study.

10.4 Influence of fault angle and axial normal force

During the initial analyses and design of the individual test boundary conditions, it became clear that very small fault angles result in significant variations of the axial force in the pipeline (see Figure 9.26). Since the exact location or orientation of a ground-induced deformation may be uncertain, such variations can be expected to occur in practice.

An example of the effect of the fault angle is found when tests T1 and T4 are compared (see Table 9.3 and Table 9.6). With respect to test T1, in test T4 a 40% reduction of axial force was applied (see Figure 10.3). While in test T1 no local buckling occurred until the maximum fault movement of 1480 mm, local buckling occurred in test T4 at a fault movement of 689 mm. The measured tensile strain in specimen T1 was slightly higher than in test T4. However, it must be taken into account that such small differences in measured longitudinal strain may also result from differences in placement of strain gauges, as discussed in section 9.6.11.

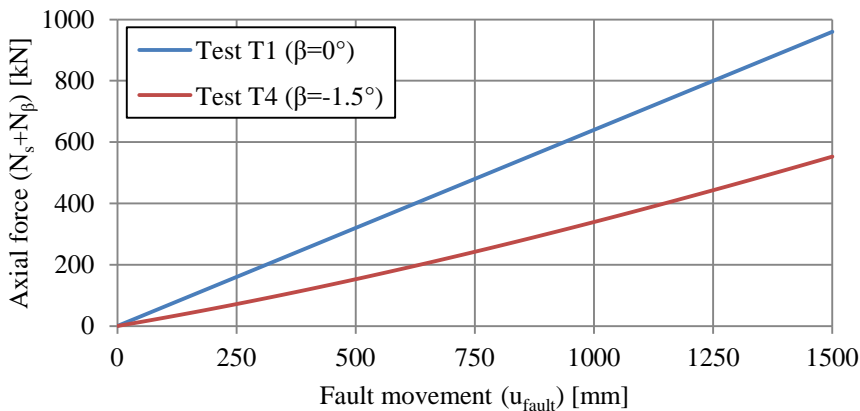


Figure 10.3 Applied axial force in tests T1 and T4.

The influence of the axial force is complex. Firstly, to resist the axial force, additional normal stresses will develop in the pipe. Furthermore, the axial force influences the amount of bending deformation that results from the applied fault movement. For example, an increase in tensile axial force results in a decrease of curvature of the pipeline. An exact quantification of the influence of the axial force on the resulting stresses, strains and bending deformation in the pipeline may be subject of further study.

10.5 Rupture in test T5

In test T5, a girth weld was deliberately placed in a critical segment of the pipeline specimen. During the test, local buckling occurred at this girth weld. Similarly as in other tests, critical segment containing a girth weld demonstrated a lower local buckling resistance by buckling earlier than the plain pipe in the critical segment at the opposite side of the fault. No yield strength difference over the girth weld was present, as the girth weld was executed by cutting a section of pipe and re-joining the two resulting sections with a girth weld. Therefore, the location of the local buckle was assumed to not have been influenced by deformation concentration due to a yield strength difference in the two pipes adjoining the girth weld.

During further increase of the fault movement after the initial formation of a local buckle, a rupture occurred at a fault movement of 710 mm. The rupture occurred in the extrados opposite to the local buckle near the girth weld (see Figure 10.4). Before the rupture occurred, very large strains were measured close to the rupture location. Furthermore, observations of the rupture surface confirm that a ductile fracture occurred, directly next to the weld.



(a) Overview of buckled and ruptured pipe



(b) Close-up of rupture surface near weld



(c) Close-up of rupture surface near weld



(d) Close-up of rupture surface (piece 2)

Figure 10.4 Photographs of rupture in specimen T5.

The measured longitudinal strains closest to the rupture are presented in Figure 10.5. The figure shows that the measured longitudinal strain reached 4.5% at a distance of 15 mm of the rupture. The location of this specific strain gauge is visible in Figure 10.4d. Because the rupture occurred at some distance from this measuring location, it is assumed that the strain at the rupture location was even higher.

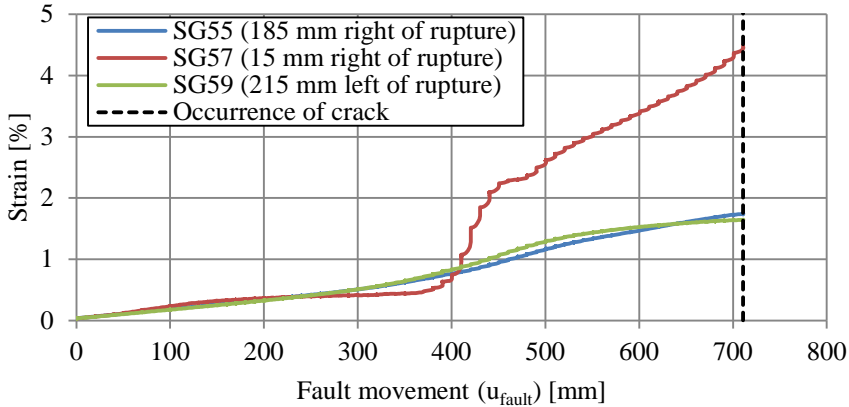


Figure 10.5 Strains measured in the vicinity of the rupture in test T5.

When the material behaviour of the used pipe is studied, the very high Y/T ratio is striking (see Appendix F.2 and Figure 9.10). In the specific pipe that was used in the experiment, Y/T ratios of 0.95 and 0.91 were found in longitudinal direction. As discussed in section 9.3.2, in many standards, the Y/T ratio is limited to values between 0.85 and 0.93. It can thus be concluded that the Y/T ratio of the used pipeline material was too high for the high strain demand application it was employed in. As discussed in section 10.2, a sufficiently low Y/T ratio prevents concentration of high tensile strains. The high Y/T ratio of the considered test specimen may have allowed high localization of strains resulting in the formation of a rupture. Steel with a more moderate Y/T ratio would not likely have ruptured so early in the test, if at all.

Besides the Y/T ratio, the occurrence of the rupture very close to the girth weld requires further investigation. As is clear from the results of tests T5 and T10 (see section 9.6), tensile strains opposite to a local buckle in a pressurized pipe can be very large. Assuming a correctly overmatched weld, the parent material adjacent to the weld is strained even further, increasing the risk of a rupture. Also imperfections caused by the welding, such as undercuts or notches, may have resulted in strain concentrations. Furthermore, the heat input by the welding process may have influenced the material properties of the parent material close to the weld, possibly resulting in a reduced yield stress or reduced ductility. No further material analysis was undertaken to support this hypothesis.

It can therefore be concluded that the following causes may have contributed to the formation of a rupture in test specimen T5:

1. The very high Y/T ratio of the pipeline material allows for concentration of strains
2. The occurrence of a local buckle results in high tensile strains on the opposite side of this buckle. The presence of an overmatched weld results in extra strain concentration in the adjacent parent material.
3. Welding imperfections may have resulted in additional strain concentration.
4. Heat input during welding may have influenced the material mechanical properties of the parent material, possibly resulting in a reduced yield stress or reduced ductility.

In practice, additional strain concentration at girth welds may occur due to yield strength differences and wall thickness differences on either side of the girth weld. The application of a sufficiently low Y/T ratio is therefore very important to prevent excessive localization of strains. Furthermore, variations in bending moment capacity due to for example variation of geometrical properties or material properties of the pipe need to be sufficiently small.

10.6 Summary of Chapter 10

This chapter discusses the large-scale tests simulating the effect of a strike-slip fault on buried pipelines. The conclusions were drawn on the basis of preparation, execution and analysis of the tests discussed in Chapter 9.

The ratio between pipe and soil stiffness is found to greatly influence the resulting pipeline deformation in case of ground-induced deformation. For increasing pipeline stiffness with respect to the soil stiffness, deformation of the pipeline decreases. Furthermore, the location of the critical cross-section was found to move away from the fault for increasing fault movement.

The presence of a girth weld was shown to have a negative effect on the local buckling resistance of a pipe. This is attributed to a strength mismatch between the two pipes adjoining the girth weld, which resulted in concentration of deformation. Furthermore, imperfections associated with the girth weld may also have had a negative influence on local buckling.

A change in the fault angle was found to have a significant effect on the axial force in the pipeline, especially for small fault angles. The magnitude of the axial force greatly influences the deformation of the pipeline. As a result, the axial force is a main parameter to consider when determining the dominant failure mode of the pipeline and the fault movement at which this limit state is reached. An exact quantification of the influence of the axial force on the resulting stress, strain and bending deformation in the pipeline may be subject of further study.

The high Y/T ratio of the pipes used in the performed tests is not suitable for applications with high strain demand. The high Y/T ratio allowed concentration of strains, which was possibly further accelerated by the presence of a strength mismatch at girth welds. In specimen T5, this contributed to the formation of a rupture, after the failure mode local buckling was reached earlier in the test. Possibly, weld influences may have further accelerated the occurrence of this rupture.

Chapter 11

Numerical analysis of buried pipelines crossing active strike-slip faults

11.1 Description of numerical model

11.1.1 Introduction

To verify the effects of a large, ground-induced deformation on a pipeline, various modelling options are currently available, denoted as Level 1, 2 and 3 analyses:

Level 1: Analytical analysis of pipeline and soil behaviour

Level 2a: Numerical analysis of pipeline and soil behaviour using soil springs and (modified) beam elements for the pipeline

Level 2b: Numerical analysis of pipeline and soil behaviour using soil springs and 3D analysis of the pipeline

Level 3: Numerical analysis of pipeline and soil behaviour using a rigorous 3D analysis of pipeline and soil

Inclusion of non-linearity of the material behaviour of soil and steel is possible at any of the complexity levels, although most Level 1 analyses only allow for elastic-perfectly-plastic non-linear material behaviour. Geometric non-linearity in the form of stiffness reduction of the pipe due to ovalisation can be included for complexity levels 2a and higher. The differences between the complexity levels further lie in the required computational effort and accuracy of the solution. Furthermore, not all complexity levels account for local buckling failure.

As the effects of the ground-induced deformation on the pipeline are complex and determined by many parameters (see Chapter 9), a Level 1 analytical formulation requires many approximations. Furthermore, a local buckling failure criterion has not yet been successfully implemented in such methods. Examples of available analytical models for pipelines crossing moving faults are presented in section 8.3.1.

More complex analytical models for the bending behaviour of the pipe, such as the model by Gresnigt (1986), include ovalisation of the pipeline due to bending and soil pressures. Furthermore, a local buckling criterion is included. However, the complexity of such models generally calls for numerical solving techniques. Therefore, they are considered to be beyond a Level 1 analysis.

A numerical analysis using soil springs with beam elements for the pipeline (Level 2) is a method that is currently used in many design situations. An example of a Level 2a analysis is the software package PLE4WIN (PLE4WIN, 2015), which utilizes soil springs according to NEN 3650-1 (2012) and a modified beam element for the pipeline. The modified beam element includes reduction of stiffness due to ovalisation of the pipeline cross-section as a result of bending. However, because the pipe elements are relatively simple, more complex behaviour, such as the exact distribution of strains of the pipeline cross-section or the formation of a local buckle, is difficult to model. For example, for the latter, PLE4WIN issues a warning when an analytically determined critical strain is exceeded, but the stiffness of the beam element is not reduced as a result of this buckle. Furthermore, such analytical formulas to determine the occurrence of local buckling failure may not correctly account for the positive or negative effect of very high axial forces in the pipe.

Examples of Level 2b methods are found in the work by Karamitros et al. (2007) and Liu et al. (2008). The advantage of a Level 2b complexity over a Level 2a complexity is the more accurate modelling of the pipeline behaviour. Such an analysis may be able to include the effects of hoop stresses, ovalisation due to bending and possibly local buckling failures. In both a Level 2a and Level 2b calculation, any type of soil spring may be used. In practice, most soil springs are modelled as bilinear or trilinear. Many times a simple elastic-perfectly-plastic pipe-soil interaction is assumed.

Level 3 analyses, using a full numerical analysis of both the soil and pipeline, theoretically are able to capture all relevant failure mechanisms of the pipeline, while including realistic pipe-soil interaction. However, such analyses are complex and therefore costly. Currently, this type of analysis is mainly seen as fit for academic study of the phenomenon instead of a design tool. Examples of this type of analysis can be found in the work by Vazouras et al. (2010, 2012).

This chapter presents the development of a Level 2b numerical model that allows a rigorous analysis of the pipeline behaviour, including local instabilities. Using a Level 2b analysis, complex analysis techniques that are required for a full 3D analysis of both pipe and soil are avoided. To demonstrate the validity of the model, extensive comparisons are presented between the model and the test results of the tests simulating the effect of an active strike-slip fault on a buried pipeline (see Chapter 9).

11.1.2 Description of general numerical model

Overview

The new numerical model was developed using software package ABAQUS (2010) and consists of a pipeline modelled with shell elements and non-linear springs that simulate pipe-soil interaction. An overview of the FE-model, configured for validation by modelling a test result

(see section 11.2) is presented in Figure 11.1. The pipeline is modelled using four-node reduced integration shell elements (S4R) and is given elasto-plastic material properties using a Von Mises plasticity model with isotropic hardening. The soil springs are modelled using axial elasto-plastic connectors with appropriate properties to model the interaction between the pipeline and surrounding soil. In this study, it is proposed to use standardized soil behaviour, such as presented in NEN 3650-1 (2012). However, the model allows for other soil behaviour to be implemented. In the model configuration presented in Figure 11.1, only a limited number of axial and lateral soil springs is present. However, in other configurations (see section 11.1.4), the number of soil springs may be increased and also vertical soil springs may be added.

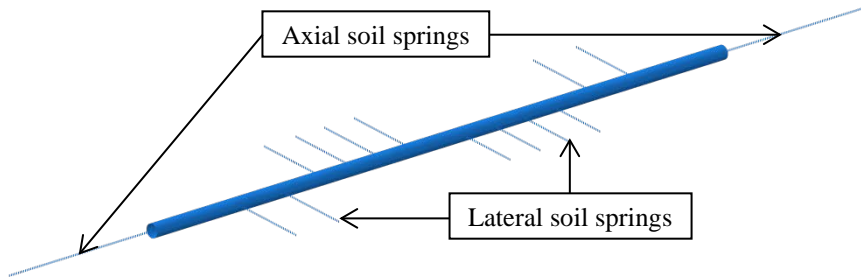


Figure 11.1 Overview of numerical model in configuration for model validation.

The soil springs are coupled to the pipeline in an appropriate manner. In case of closely spaced soil springs, forces may be introduced at one node only, preferably at the pipe centreline, where bending stresses are low. In model configurations with springs at larger intervals, as for instance in the validation models (see section 11.2), a more complex connection between pipeline and soil spring may be necessary to allow a smooth force transition from the spring to the pipeline.

In the model, actions due to ground-induced deformations are not directly applied to the pipeline, but to the base of the soil springs that are connected to the pipeline. Other actions, such as internal pressure or an axial force due to temperature differences, may be applied directly to the pipeline itself.

The model has to be of sufficient length to allow full development of all soil stresses that act on the pipeline. However, for full development of axial soil stresses, very long pipeline lengths may be required, which greatly impacts the computational effort. Alternatively, a two-step approach can be used, where the pipeline is given only sufficient length to develop all lateral and vertical soil stresses (similar as in Figure 9.13), and an axial spring is applied at the pipeline end to correctly model the development of a normal force in the pipe (similar as in Figure 11.1). The properties of this axial spring are determined by means of a pull-out analysis using another configuration of the same model.

The actions are applied to the pipeline in steps. Actions other than the ground-induced deformation such as axial force due to temperature effects or internal pressure are applied first. In a second step, the ground-induced deformation is applied. An arc-length algorithm is employed in this step to allow the analysis to trace the load displacement path including instabilities of the pipe wall and post-buckling behaviour.

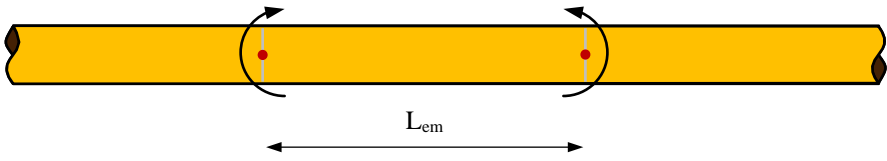
Imperfections

An important failure mode that was observed during the tests is local buckling. Additional modelling efforts are necessary to allow accurate modelling of this failure mode. A common method to achieve satisfactory results is the introduction of geometrical imperfections in the numerical model.

The pipes used in practice are assumed to be initially imperfect in the form of for example geometrical imperfections, residual stresses, wall thickness and material property variations. These imperfections influence the local buckling resistance of the pipeline. In the numerical model, the combined effect of these imperfections is taken into account through a geometrical imperfection in the shape of the first buckling eigenmode of a segment of the pipeline under pure bending. In the validation analyses, the desired location of the initial imperfections is known, as the position of the local buckle in the tests is known. In practical application, a preliminary analysis with Level 1 or Level 2a complexity may be used to determine the critical segments of the pipeline. In the subsequent Level 2b analysis, initial imperfections are to be applied in these critical segments.

To obtain the buckling eigenmode shape, two equal and opposite bending moments are applied to two cross-sections at a spacing of L_{em} (see Figure 11.2). At the location where these rotations are applied, cross-sectional distortion (ovalisation) is restrained. Using a linear buckling analysis, the first eigenmode shape is then calculated. An example of the resulting imperfection shape is presented in Figure 11.3. The obtained imperfection shape amplitude is scaled appropriately to a maximum imperfection amplitude a_{imp} and applied to the intrados of the pipeline. In case of a pipeline crossing a fault, this procedure is applied to the critical segments of the pipeline on both sides of the fault (see Figure 11.4).

The applied initial imperfections initiate local buckling in the numerical model. Provided that an appropriate amplitude is selected for the applied initial imperfection, the model yields accurate results. As is clear from Figure 11.4, the amplitude of the buckling eigenmode varies over the length L_{em} . To retain a relation between the local buckling behaviour of the model and the chosen initial geometrical imperfection, local buckling needs to occur at the maximum imperfection, exactly halfway length L_{em} . However, because the amplitude of the initial geometrical imperfection develops approximately sinusoidal over the length L_{em} , formation of a local buckle approximately halfway length L_{em} likely results in acceptable accuracy of the model, provided that L_{em} is chosen sufficiently long. The desire for a long length L_{em} is opposed by the necessary mesh refinement in this region (see Figure 11.4). To accurately obtain a buckling eigenmode with accuracy, a fine, regular mesh is required. In other regions of the pipeline, where strains may be lower and local buckling does not occur, a much coarser mesh is sufficient. As a result, a balance needs to be sought between model accuracy and computational effort.



(a) Applying loading to a section of the pipeline specimen with length L_{em}



(b) Corresponding loading scheme of the selected pipe section

Figure 11.2 Loading conditions to obtain buckling eigenmode.

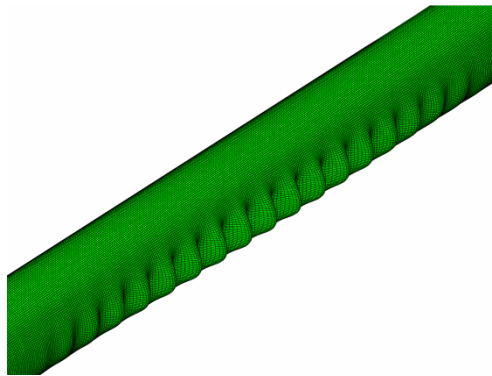


Figure 11.3 Shape of first buckling eigenmode. Amplitude magnified for visualisation purposes.

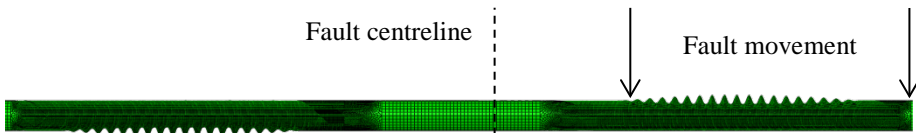


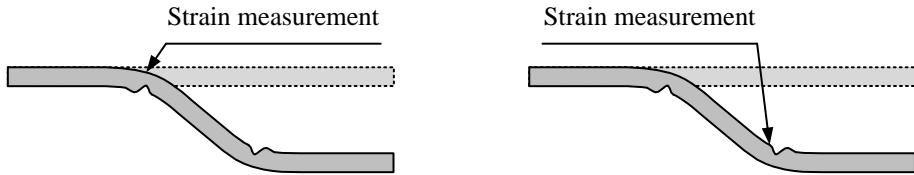
Figure 11.4 Geometrical imperfection in the form of a buckling eigenmode in the critical segments of a pipeline. Imperfection amplitude magnified for visualisation purposes.

Apart from the initiation of a local buckle, the presence of the initial geometrical imperfection influences the stiffness of the pipeline. Through this mechanism, the length of L_{em} may influence the behaviour of the modelled pipeline. To investigate the magnitude of this effect, the model in configuration for the analysis of test T2 was employed with a value of L_{em} of 1000 mm and 2500 mm. At a reasonable initial imperfection amplitude of 0.05 mm (see section 11.2), the comparison between the two models is very good. A comparison between tensile strains opposite to the local buckles that formed in the two models is presented in Figure 11.5a. Local buckling occurs at slightly different locations in the two models. This is caused by the fact that the two buckling eigenmodes that are applied in the two models have amplitudes at slightly different locations, resulting in a shift of the local buckling location of approximately 100 mm. As a result of this shift, the comparison of compression strains at a fixed distance from the fault

centreline is only valid until local buckling occurs (see Figure 11.5b). The critical fault movement, determined according to the definition presented in section 9.6, is found to differ by 3,5%, which is attributed to the combined effect of:

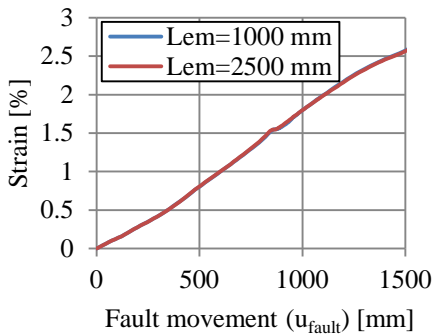
- Curvature localization differences due to a different length of L_{em} and the resulting pipeline stiffness differences
- Relocation of the local buckle and thus different stress and strain conditions at the buckling location at $u_{fault;crit}$
- Effects of the more quickly diminishing amplitude of the initial imperfection waves in case $L_{em}=1000$ mm.

On the basis of the observations made in Figure 11.5 and the analysis of the difference in critical fault movement between the two model configurations it can be concluded that there is a slight sensitivity to the value of L_{em} with regard to $u_{fault;crit}$. Therefore, all analyses should be preferably undertaken in a model configuration with a fixed value for L_{em} . However, the sensitivity is low, and the maximum tensile strains appear to be unaffected. Therefore, small adjustments of L_{em} will have negligible effects on the outcome of an analysis in practical usage of the model.

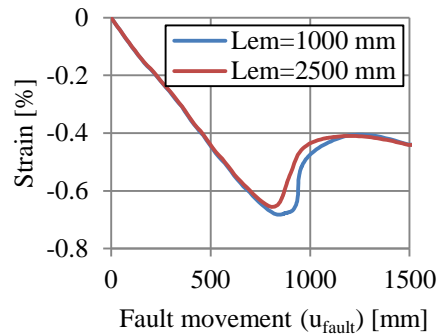


(a) Measurement location for Figure 11.5(c)

(b) Measurement location for Figure 11.5d



(c) Tensile strain at highly strained cross-section



(d) Compressive strain at on average 500 mm from the local buckling position

Figure 11.5 Comparison of longitudinal strains at equal distances from the fault for model configurations with $L_{em}=1000$ mm and $L_{em}=2500$ mm.

Mesh convergence study

In the critical segment of the pipeline, a fine mesh is necessary to successfully capture the behaviour of the pipeline. However, because in many cases the model requires significant length to accurately model the pipe-soil interaction, a coarser mesh in pipeline segments undergoing

less deformation is necessary to reduce the required computational effort. In this study, the maximum element length L_{el} in the coarse mesh was chosen as 10% of the pipeline diameter. In cases of extremely long pipelines, a transition from shell elements to beam elements may be considered to further reduce the problem size.

The mesh in a critical segment of the pipeline must be sufficiently fine to allow the FE-software to capture the deformational and possibly local buckling behaviour of the pipeline. Furthermore, a regular mesh is required to allow correct calculation of the buckling eigenmode which is used as initial imperfection. The distance between soil springs and other boundary conditions must therefore be divisible by L_{el} . Using the validation models for tests T1 and T2, a mesh convergence study was performed. The accuracy over the first 1500 mm of fault movement of the various mesh sizes is compared with the most accurate result available, using the relative error, which is defined in equation (11.1).

$$\text{relative error} = \frac{|result_i - result_{acc}|}{result_{acc}} \quad (11.1)$$

For a pipe not failing in local buckling, the relative error of the calculated tensile strain at the extrados of a critical segment is plotted versus the element size in Figure 11.6. It appears that for such models, a mesh size up to 8% of the pipeline diameter yields results with an error less than 1%.

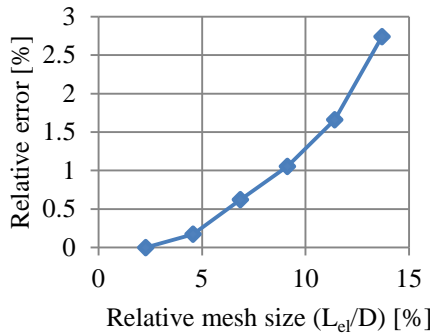


Figure 11.6 Influence of mesh size on tensile strain at the extrados of the critical cross-section.

In case of the formation of local buckling failure, deformations localize, which may require a finer mesh. To investigate the required mesh refinement, the validation model for test T2 was studied, using an initial imperfection amplitude (a_{imp}) of 0.05 mm. Figure 11.7 shows the influence of the mesh size on the calculated critical fault movement. However, it should be noted that the presented influence is not only caused by a change in computational accuracy as a result of a change in element size. Due to the change in element size, a slightly different initial imperfection shape and local buckling position results from the analyses, which also may influence the critical fault movement. Despite this, the general trend of the sensitivity of the model to the element size can be observed in Figure 11.7. As a balance between computational effort and accuracy, in this study, the mesh size was limited to approximately 2.5% of the pipe diameter. Generally, a value of L_{el} of 5 mm for the small diameter pipe (2.3% of D) or 10 mm

for the large diameter pipe (2.5% of D) was chosen to obtain a regular mesh that corresponds well with the introduction locations of the forces of the soil springs. In comparable studies, similar mesh sizes led to accurate results (Vasilikis et al., 2016, Vazouras et al., 2010).

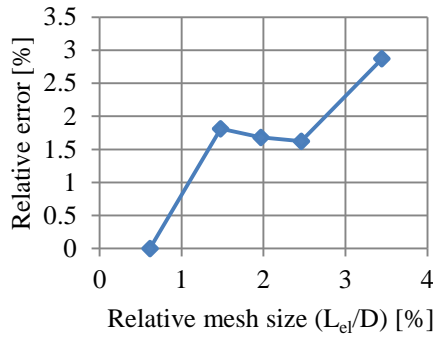


Figure 11.7 Influence of mesh size on critical fault movement.

Apart from the element size, the number of thickness integrations points in a shell element influences the computational effort and accuracy of the solution. In this study, Simpson’s rule for integration through the shell thickness was used, so that stresses and strains were calculated directly at the surface of the pipe. Using the validation models for tests T1 and T2, the influence of the number of thickness integration points was investigated, using the relative error (see equation (11.1)) as unit of measurement. The influence of the number of thickness integration points for pipes that do not fail in local buckling was found to be very low (see Figure 11.8).

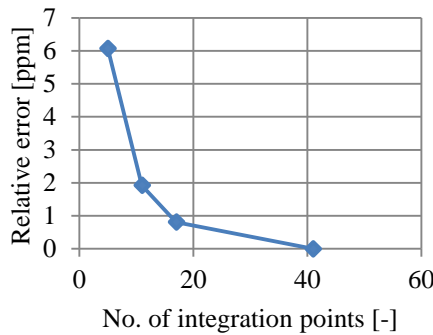
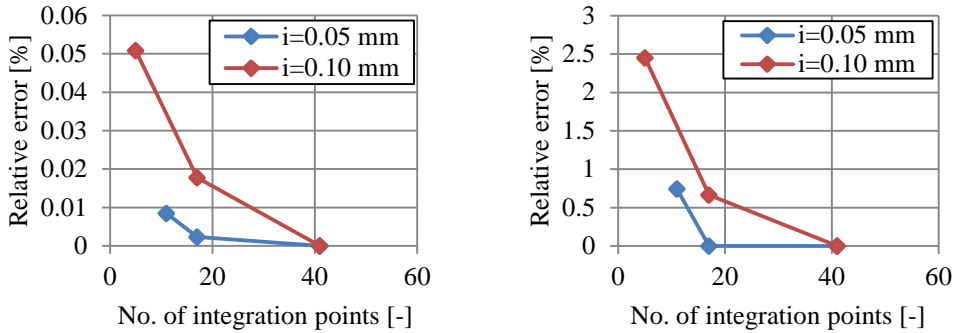


Figure 11.8 Influence of number of integration points on tensile strain in critical cross-section. For measurement location, see Figure 11.5a.

The number of thickness integration points becomes more relevant if local buckling occurs, since in that case bending stresses develop in the pipe wall, which are more accurately modelled when more integration points are used. To investigate the required number of thickness integration points, the validation model for test T2 was employed, using an initial imperfection amplitude (a_{imp}) of 0.05 mm and 0.10 mm. Figure 11.9 shows that, although the tensile strains are hardly affected, a significant effect of the number of integration points on the critical fault

movement can be observed. Based on this observation, a minimum of seventeen thickness integration points was used in the analyses of this study.



(a) Tensile strain opposite to local buckle.

(b) Critical fault movement ($u_{\text{fault;crit}}$)

For measurement location, see Figure 11.5a

Figure 11.9 Influence of number of integration points on pipeline deformational behaviour.

11.1.3 Description of numerical model for validation

To validate the numerical model, the ten full scale bending tests that were performed were modelled using the measured properties of the pipeline as input. A constant diameter was chosen for the full length of the specimen, because variations in diameter were small, but changes in material properties and pipe wall thickness were implemented in the model as they were measured in the test specimens.

Similar as in the test, the modelled pipe specimen was connected to its surroundings by means of twelve soil springs. The measured ring-spring non-linear force-deformation response ($F_{\text{ring}}-u_{\text{ring}}$) was assigned. The movement of the fault was applied to the base of the soil springs. An axial movement restraint was placed in the centre of the pipeline specimen, while the ends of the pipeline were laterally constrained to match the deformation of the fault. The axial force that was applied during the test is applied directly to the end of the pipeline, as well as the axial force that is generated in the test specimen due to internal pressure against the end caps. An overview of all applied boundary conditions is presented in Figure 11.10.

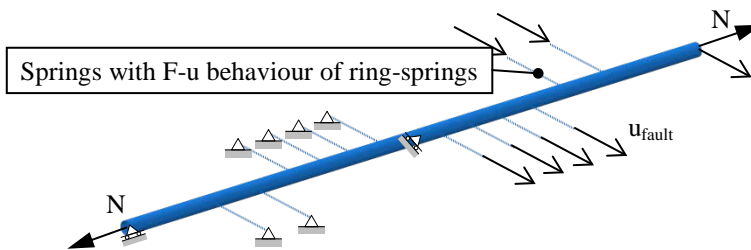


Figure 11.10 Overview of numerical model for validation.

In the test, the forces from the simulated soil are applied through only twelve soil springs, resulting in high forces in each soil spring. Applying forces of such magnitude to a single node of the mesh may lead to inaccurate solutions or convergence difficulties. Application of forces to the pipeline through straps, as was the case during the tests, was deemed impractical, although technically possible. To approximate the test boundary conditions in the validation model, the forces of each ring-spring were divided, and applied to the pipeline at a distance corresponding to the spreader beam that was used during that specific test (see Figure 9.21c). The forces were applied to the pipeline at the neutral line over a length corresponding to the width of the strap that was used in the test. The forces are divided over this length in an ‘average sense’ by using the ‘Continuum distributing’ coupling in ABAQUS (2010), thereby allowing rotation of the strap with respect to the spreader beam. An overview of the application of soil loads to the pipe is presented in Figure 11.11. The sudden shift of straps that occurred in some of the tests (see Figure 9.22) was not included in the model. For these tests, validation of the model can only be performed for the part of the test before shifting of the straps.

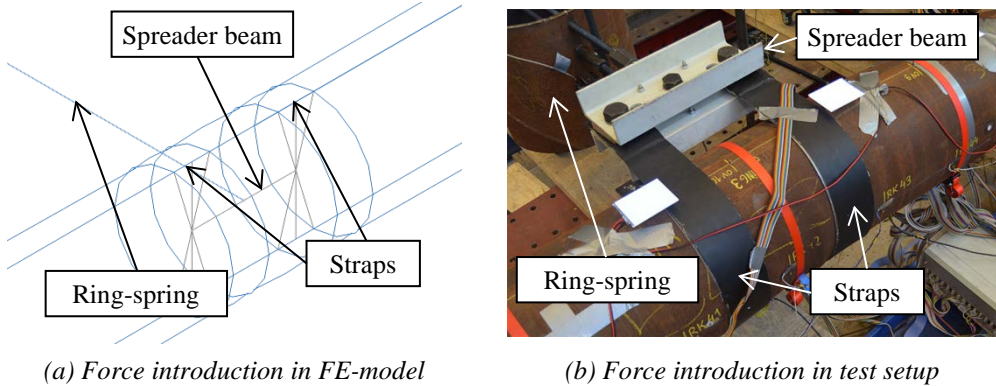


Figure 11.11 Comparison of the introduction of the ring-spring force in the pipeline between the FE-model and the test setup.

Imperfections

The actual imperfections of the pipeline were not measured, and could therefore not be used to select an appropriate scale factor a_{imp} for the geometrical imperfections in the model. Furthermore, the geometrical imperfection in the model not only represents the geometrical imperfection in the actual pipeline, but also effects due to e.g. residual stresses. The correct imperfection scale factor therefore was determined by calibration.

The imperfection length L_{em} was chosen such that approximately 20 imperfection waves formed within L_{em} , rounded to the nearest 10 mm. The length of the imperfection half-waves (L_{hw}) was estimated using equation (11.2) (Timoshenko, 1961). The applied initial geometrical imperfections were centred around the location of the critical cross-section in the bending tests.

$$L_{hw} \approx 1.72 \cdot \sqrt{\frac{(D-t)}{2}} \cdot t \quad (11.2)$$

As discussed in section 11.1, the calculation of the buckling eigenmodes requires a regular mesh. Furthermore, constant material and geometry parameters over the length of the pipeline result in a much higher quality of the calculated buckling eigenmode. Therefore, only during the eigenmode calculation, the wall thickness and material properties were assumed to be constant over the length of the pipeline. Because differences in wall thickness and material properties were relatively small and the actual properties were used in the final analysis of the tests, the influence of this approximation is assumed to be negligible.

11.1.4 Practical application of numerical model

The modelling procedure as described in section 11.1.2 can be applied to many design situations. The model is developed for analysis of buried pipelines under ground-induced deformations. For this type of analysis, a model very similar to the validation model (see section 11.1.3) may be used, but with a much finer grid of soil springs in lateral direction and the addition of soil springs in axial and vertical direction.

The model allows for the implementation of more elaborate and complex soil models. This may range from using a trilinear instead of the bilinear behaviour according to NEN 3650-1 (2012) to using the output of complex FEA models or test results as soil spring behaviour. Further improvement of the soil behaviour is possible by providing a shear coupling between the lateral soil springs, using appropriate modelling techniques.

Due to the 3D modelling of the pipeline, the user has better insight into the cross-sectional behaviour and local instabilities than when using a Level 2a analysis, while the technical expertise that is necessary for a Level 3 analysis is not required. However, since the developed model still requires a considerable modelling effort, the developed Level 2b analysis is typically valuable in assessment of existing structures, where the geometrical parameters of the pipeline, position of girth welds and material properties in many cases can be determined accurately. By means of the validation calculations performed in section 11.2, the capabilities and performance of the developed model is demonstrated. It is shown that also in case of large plastic strains and local buckling failures, the model performs well.

In the current investigation, all modelling took place in software package ABAQUS (2010). However, the modelling techniques that were described may also be implemented in any other 3D finite element package. Revalidation of the model may then be necessary.

11.2 Model calibration and validation

The numerical model was validated by modelling the ten full scale bending tests that were performed. As discussed in section 11.1.3, the correct value for the imperfection amplitude scale factor a_{imp} needed to be determined by calibration. Therefore, all tests were modelled using a number of values for a_{imp} . By comparing the test results with model results for the selected values of a_{imp} , the most suitable scale factor was obtained. After analysing all ten tests, a generic conclusion with regard to a suitable imperfection amplitude scale factor was drawn.

The FE-model was compared with the full scale tests on the basis of three parameters: the ring-spring response with respect to the fault movement, the longitudinal strains at the outer face of the pipe wall and ovalisation of the pipeline (see Appendix E). In comparison to the test results, it appeared that the modelled pipeline and ring-springs respond with higher forces at smaller fault movements. An example of this behaviour is presented in Figure 11.12. This effect is attributed to some elastic deformation and free movement in the test setup, which causes a relatively late response of the ring-springs and pipeline to the applied fault movement, while in the FE-model, the response is immediate. The effect is observed to be slightly stronger in case of the larger diameter pipeline specimens, most likely as a consequence of their higher stiffness with respect to the test setup. To allow for a fairer comparison between test results and FE-model results, the corrected fault movement $u_{fault,cor}$ was defined according to equation (11.3).

$$u_{fault,cor} = u_{fault} - \Delta u_{fault} \tag{11.3}$$

The value of Δu_{fault} was determined on the basis of the ring-spring response with respect to the fault movement of the rings nearest to the fault. An example of the determination of Δu_{fault} is presented in Figure 11.12. In comparisons between the model and test results, both the corrected and uncorrected data are displayed as the applied correction is not exact.

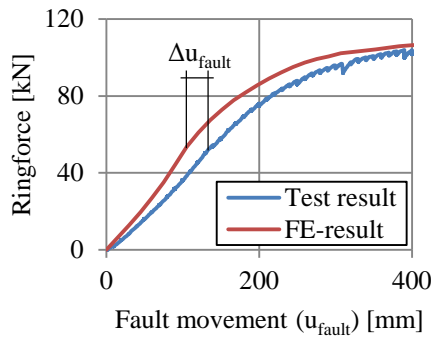


Figure 11.12 Example of determination of Δu_{fault} .

When comparing the test result with strain gauge results, it must be taken into account that the location of a local buckle may differ between the test result and the model result. This may affect the accuracy of the comparison of longitudinal strains. Longitudinal strains can be compared between the test result and model result at equal positions along the pipeline axis (i.e. at the location of the strain gauges) or at equal distances from the local buckling location. While the first comparison is expected to be more accurate at fault movements smaller than $u_{fault,crit}$, the second comparison is expected to yield more accurate results at fault movements larger than $u_{fault,crit}$, especially near the location of a local buckle. In this study, the comparison of strains is made at equal positions along the pipeline axis, as this is expected to result in the most accurate comparison between test and model before failure of the pipeline.

For validation purposes, the ten performed tests were divided into four categories, as presented in Table 11.1. The test results were categorized on the basis of whether local buckling occurred in the test and whether a girth weld was placed in a critical segment of the specimen.

Table 11.1 Categorizing of tests on the basis of pipeline specimen behaviour during the test.

Category	Local buckling	Girth weld in critical segment	Tests
1	Yes	No	2,4,9,10
2	Yes	Yes	3,5,8
3	No	No	1,6
4	No	Yes	7

In the following sections, the calibration procedure of each test category is briefly discussed. In addition, a summary of the comparison between test and FE-model results is presented. The full comparison between the model and test result can be found in Appendix E.

11.2.1 Category 1 tests

To calibrate the FE-model to tests in Category 1, a series of analyses was performed with the model for each test. Within this series, the imperfection scale factor a_{imp} was varied until a satisfactory match with the experimental results was obtained in terms of $u_{fault,crit}$. The comparison was made using both u_{fault} and $u_{fault,cor}$ from the test result. Because the pipes in the critical segments on both sides of the fault had approximately equal geometry and material properties and originate from the same manufacturer, it is assumed that for Category 1 tests, the calibration can be performed with an equal imperfection scale factor on either side of the fault.

In Figure 11.13, the results of this comparison are presented for the four tests in Category 1. For the comparison, use is made of the model performance, which is defined in equation (11.4).

$$p = \frac{\text{experimental result}}{\text{model result}} = \frac{u_{fault,crit,e}}{u_{fault,crit,t}} \quad (11.4)$$

Within these four tests, both pipe geometries, both soil types and atmospheric and high internal pressure are covered. Both pipe geometries are considered to be relatively insensitive to the initial imperfection scale factor, because for both pipe types a 50% change in imperfection amplitude roughly corresponds to a 10% change in critical fault movement.

A remarkable feature is visible in Figure 11.13a. The model performance on the left side of the fault is observed to decrease for an increase in applied imperfection amplitude from $a_{imp}/t=0.4\%$ to $a_{imp}/t=0.7\%$. This is counterintuitive, since for increasing imperfection amplitudes, the critical fault movement in the model is expected to decrease, resulting in increased model performance. More careful examination of the model result shows that the increase in imperfection amplitude from $a_{imp}/t=0.4\%$ to $a_{imp}/t=0.7\%$ resulted in a change of the buckling location. Due to the increase in imperfection amplitude, the local buckle ‘jumps’ to the next wave in the initial imperfection pattern, which causes an increase in critical fault movement. Below $a_{imp}/t=0.4\%$, for decreasing imperfection amplitude, the model performance is expected to decrease further.

The optimum imperfection scale factor is defined to be the factor for which the best match between test and FE-model result is obtained. Naturally, the value of this optimum imperfection scale factor differs between the tests. However, due to the relative insensitivity of the calculated

critical fault movement to initial imperfections of the pipe, choosing an imperfection scale factor close to the optimum also yields results with satisfactory reliability. From the modelling results presented in Figure 11.13 it can be concluded that, for plain pipes, using an imperfection scale factor of 0.5% of the wall thickness of the pipe results in a calculated critical fault movement with a maximum error of about 10%. This corresponds to a performance p between 0.9 and 1.1.

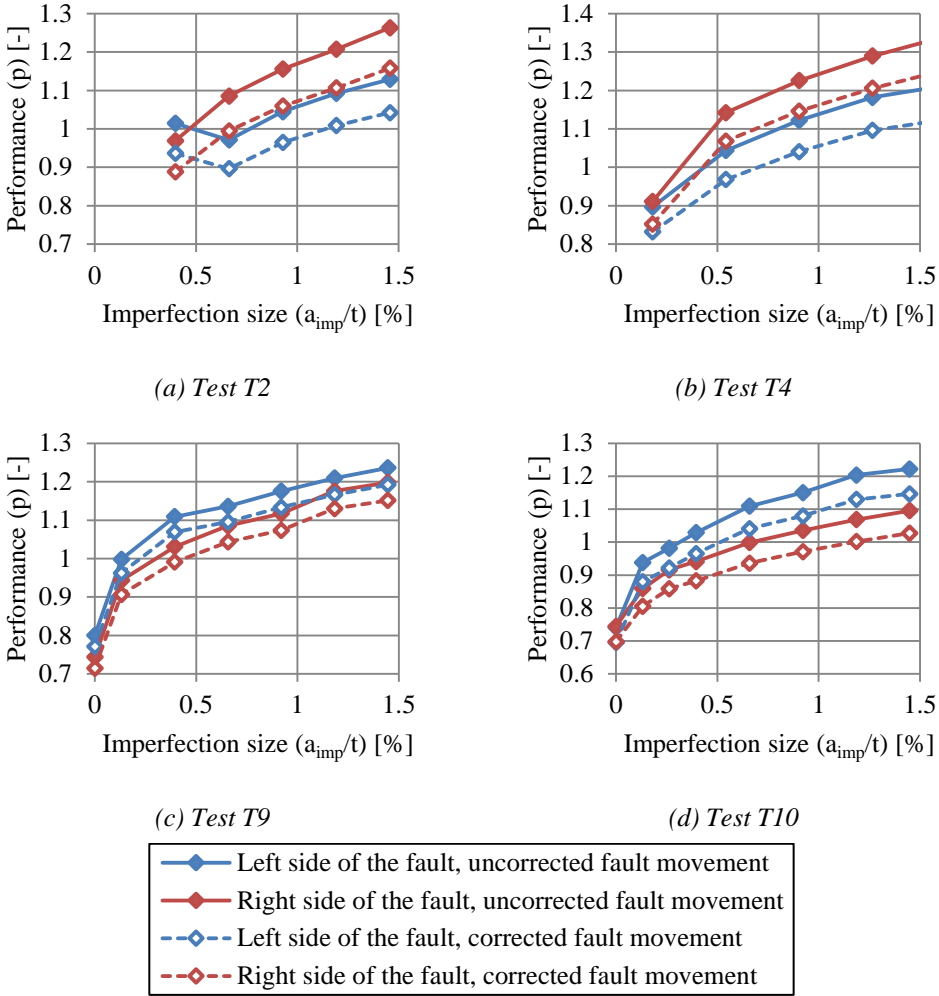


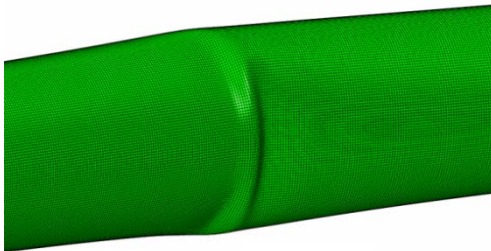
Figure 11.13 Comparison of test and FE-model results of Category 1 tests on the basis of $u_{\text{fault,crit}}$.

A comparison between the test and FE-model results is presented in Appendix E. A comparison between the ring-spring response and strain gauge measurements with respect to the fault movement is presented in Appendices E.1 and E.2. The influence of the imperfection size is clearly visible in these graphs. A comparison of the distributions of longitudinal strain and

ovalisation over the length of the pipeline is presented in Appendices E.2 and E.3. For these comparisons, only the optimum imperfection scale factor was used in the model.

The comparison between the test and the FE-model result on the basis of individual strain gauge results is not always accurate. This is mainly caused by differences in the position of the local buckle between the test and the model. Before local buckling occurs, such a direct comparison of strain results is generally good, especially at the extrados of the pipeline. The comparison of strain distributions over the pipe length between test and FE-model results is very good, but also in these comparisons, the difference in position of the local buckle in some cases leads to inaccuracies in the post-buckling trajectory of the test. The comparison of ovalisation distributions between test and FE-model results is less good than for the strain distributions, but the differences between the test and model are acceptable. The differences were assumed to be caused by the ovalisation restraint that is provided by the load application straps in the test (see Figure 5.50), which is absent in the FE-model (see Figure 11.11). As discussed in section 11.1.3, the shift of the load application straps that occurred in some of the tests is not included in the model. As a result, the results of the model are less reliable after such a shift occurred.

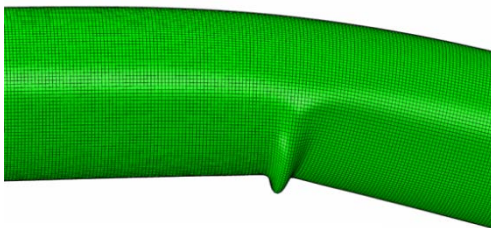
The local buckles that form in the FE-model correspond well with the observed buckles in the tests (see Figure 11.14). However, due to the applied imperfection shape, not all buckles in the model occur at exactly the same position as in the test, but rather at the location of an amplitude in the imperfection shape. With one exception, all local buckles occurred in the model at a maximum distance of $1 \cdot D$ of the location of the local buckle in the test.



(a) Test T9 Left, model result



(b) Test T9 Left, test result



(c) Test T10 Left, model result



(d) Test T10 Left, test result

Figure 11.14 Comparison of local buckling shape between FE-model and test.

11.2.2 Category 2 tests

All Category 2 tests included a girth weld in the critical segment of the pipe on one side of the fault, while on the symmetrical location on the other side of the fault, this segment consisted of plain pipe. On the basis of the results presented in section 11.2.1, an initial imperfection scale factor of 0.5% of the pipe wall thickness was assumed to be suitable for the critical segment consisting of plain pipe. For the girth welded critical segment, imperfections were varied to determine the optimum imperfection scale factor, similarly as in the procedure that was described in section 11.2.1.

Figure 11.15 shows the comparison between tests and FE-model results with regard to the critical fault movement of the critical pipeline segment containing a girth weld. Similarly as for the Category 1 tests, a single suitable imperfection size was found, despite the differences in test parameters (see Table 9.3). For critical pipe segments that include a girth weld, an applied initial imperfection amplitude of 4% of the pipe wall thickness results in a maximum error in the calculated value for $u_{fault,crit}$ of about 5%. This corresponds to a performance p between 0.95 and 1.05.

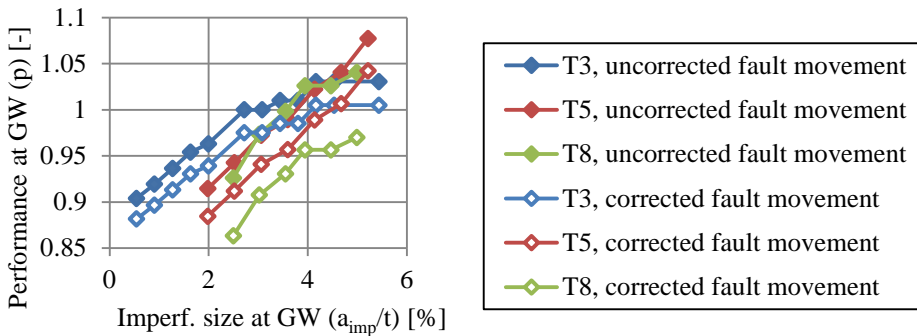


Figure 11.15 Comparison of test and FE-model results of Category 2 tests on the basis of $u_{fault,crit}$ at the girth weld.

Due to formation of a local buckle at the girth weld, the stiffness of the pipeline is reduced. This stiffness reduction is expected to accelerate failure in the form of local buckling on the opposite side of the fault where a plain pipe is placed in the critical segment. Therefore, an influence of the imperfection size at the girth weld on the critical fault movement of the plain pipe section on the opposite side of the fault is expected. The extent of this influence is presented in Figure 11.16 for tests T3 and T5. The results confirm this influence, but the influence is relatively small. Furthermore, choosing an imperfection scale factor of 0.5% of the pipe wall thickness for plain pipes and 4% of the pipe wall thickness for girth welded pipes resulted in a calculated critical fault movement with a maximum error of 8%, which is in line with the conclusions drawn in section 11.2.1.

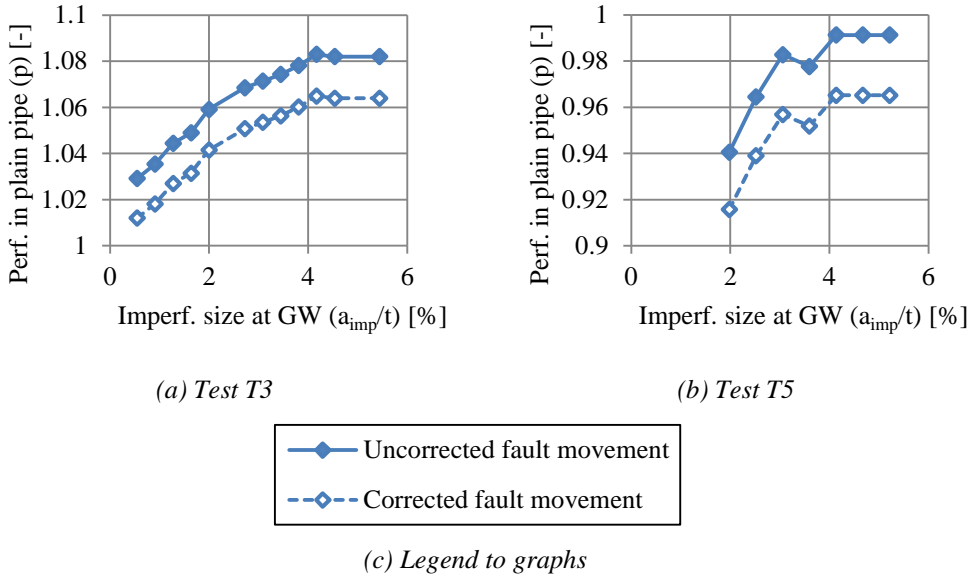
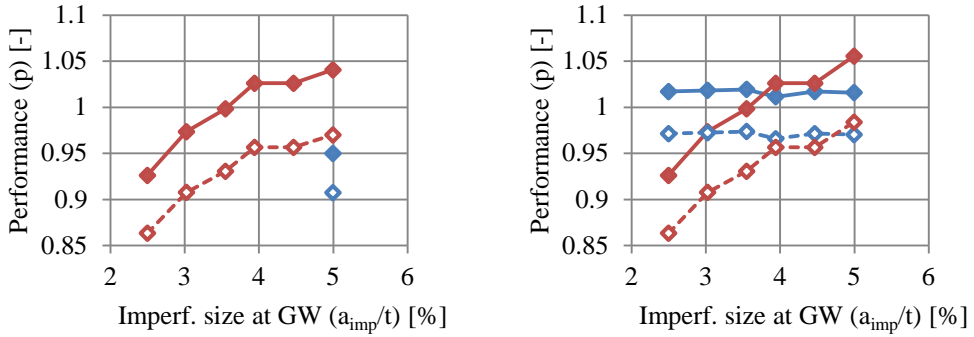


Figure 11.16 Comparison of test and FE-model results of tests T3 and T5. Influence of the imperfection scale factor at the girth weld on $u_{fault;crit}$ on opposite side of the fault. In plain pipe segment: $a_{imp}/t=0.50\%$.

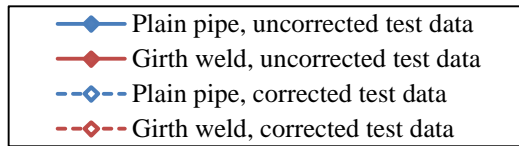
In case of test T8, using an imperfection scale factor of 0.5% of the pipe wall thickness for plain pipes and 4.0% of the pipe wall thickness for girth welded pipes did not result in a satisfactory comparison between the calculated result and test result. For an imperfection scale factor at the girth weld lower than 5.0%, no local buckling failure occurred in the plain pipe section. Doubling the initial imperfection size in the plain pipe section to 1.0% of the pipe wall thickness improved results (see Figure 11.17).

Further analyses on test T8 were performed using an imperfection scale factor $a_{imp}/t=4\%$ at the girth weld and a varying imperfection scale factor in the plain specimen (see Figure 11.18). These analyses show that using an imperfection scale factor of $a_{imp}/t=0.66\%$ results in a sufficiently accurate calculation of $u_{fault;crit}$ in the plain pipe section. Furthermore, the figure shows that the critical fault movement of the pipe section including a girth weld is not influenced by the imperfection scale factor of the plain pipe section.

A comparison between the test and FE-model results for all Category 2 tests is presented in Appendix E, using the optimum imperfection scale factors for that specific test. Similarly as for the Category 1 tests, the comparison is good. However, the increased imperfection sizes at the girth weld have a visible influence on the compressive strains in that region, especially in pressurized specimen T5. Because in all tests and most likely in all practical applications either local buckling or tensile strains dominate the failure of the pipeline, this observed influence of the imperfections at the intrados of the pipeline is not seen as problematic.



(a) Plain pipe imperfection size: $a_{imp}/t=0.5\%$ (b) Plain pipe imperfection size: $a_{imp}/t=1\%$



(c) Legend to graphs

Figure 11.17 Comparison of test and FE-model results of test T8. Influence of imperfection scale factor at girth weld on $u_{fault,crit}$ for two imperfection sizes in the plain pipe section.

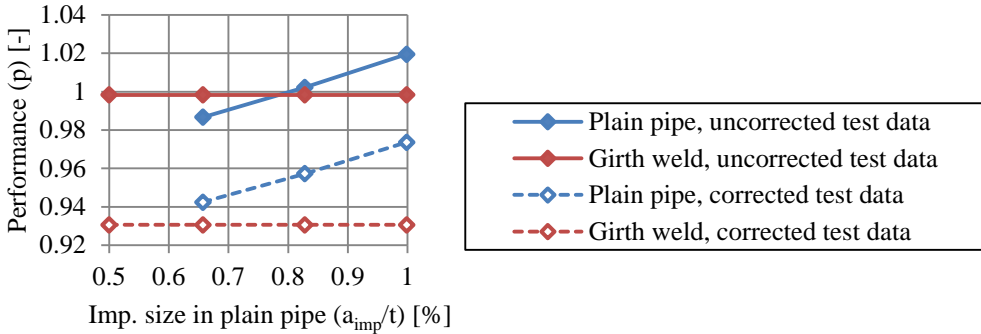


Figure 11.18 Comparison of test and FE-model results of test T8. Influence of imperfection scale factor at plain pipe section on $u_{fault,crit}$ on both sides of the fault. In girth welded pipe segment: $a_{imp}/t=4\%$

11.2.3 Category 3 tests

Since in Category 3 tests local buckling did not occur, applying a geometrical imperfection in the FE-model is not strictly necessary. However, to verify the imperfection scale factors proposed in sections 11.2.1 and 11.2.2, calculations were performed with the models for tests T1 and T6 using a variety of relatively large imperfections to determine the minimum necessary

imperfection to force local buckling failure in the FE-analysis of these tests. Because the applied imperfection scale factors were varied using large step sizes, the exact minimum imperfection size is unknown. Alternatively, the largest used imperfection that did not result in local buckling failure and the smallest used imperfection that did result in local buckling failure in the model are compared with the imperfection scale factors that were proposed on the basis of analysis of the Category 1 and 2 tests. This comparison is presented in Table 11.2. The table shows that for all available tests, the formation of a local buckle could only be forced by applying much larger imperfections than proposed in section 11.2.1. Local buckling failure did not occur while applying an imperfection 3 times as large as used in the analysis of Category 1 and 2 tests.

Table 11.2 Required imperfection size to force local buckling in Category 3 tests.

Test	Side	Proposed a_{imp}/t according to section 11.2.1 & 11.2.2	Highest a_{imp}/t without local buckle	Lowest a_{imp}/t with local buckle
1	Left	0.5%	1.4%	4.1%
	Right		1.4%	4.1%
6	Left		1.8%	5.5%
	Right		5.5%	9.1%

A comparison between the test and FE-model results is presented in Appendix E, using no geometrical imperfections. Similarly as for Category 1 and 2 tests, the comparison is good.

11.2.4 Category 4 tests

Similarly as for the Category 3 tests, no local buckling occurred in the only Category 4 test: T7. Also for this test, a variety of imperfection amplitudes was applied to the model to verify the imperfection scale factor of 4% for girth welded pipes that was proposed in section 11.2.2. The plain pipe section on the other side of the fault was not studied.

Increasing the imperfection scale factor did not lead to a fully developed local buckle, even for a very large imperfection size of $a_{imp}/t=26.4\%$. For this large imperfection size, stresses and strains started concentrating at one specific wave in the applied initial imperfection shape, but a local buckle did not fully form. Apparently, the high internal pressure and high tensile normal force in the pipe create a loading condition where local buckling failure of the pipe is almost impossible.

A comparison between the test and FE-model results, using no geometrical imperfections, is presented in Appendix E. The comparison between test and FE-model results is not as good as in the other nine tests. Especially in the small pipe section between the girth welds placed 2900 mm and 3900 mm left of the fault, large differences occur between the test and FE-model results.

It is possible that the material properties of this specimen part or an adjacent part were not modelled with sufficient accuracy. The material properties of each specimen part were assumed to be equal to the material properties obtained from tensile tests on coupons taken from the same pipe. However, some variation of material properties over the length of the available pipes may have been present. Furthermore, in this particular pipe specimen, differences in wall thickness

and material properties between the various specimen parts were small. Therefore, a relatively small error in the material properties of any of the specimen parts may result in a major change of response of the pipe to the fault movement, especially because such a short pipe section is present in the critical segment of the pipe. It is assumed that such an error caused the differences that are observed in the comparison between the model and test results for this specific test (see Appendix E).

11.2.5 Conclusion of model calibration and validation

The developed FE-model is able to accurately model the behaviour of the test specimens. In case significant differences between the model and test result occur, clear explanations are available such as for example a load application strap shift.

The analysis of Category 1 tests demonstrated that an imperfection size of 0.5% of the pipe wall thickness results in a calculated critical fault movement of satisfactory accuracy. Similar results were obtained for Category 2 tests, where an imperfection size of 4% of the pipe wall thickness was found to result in an accurate calculation of $u_{fault;crit}$. To obtain conservative results, a safety factor may be applied to the applied imperfection size. For example, the applied imperfection sizes may be increased by 50-100%. Such an increase yields conservative results for almost all comparisons with the performed tests. Alternatively, a safety factor may be applied to the calculated critical fault movement. A full analysis of the required partial safety factor that is necessary to reach a certain safety level was not performed.

The results of the Category 3 and 4 tests were used to verify the proposed imperfection amplitudes. It is shown that for imperfections three times the proposed size of 0.5% and 4.0% of the pipe wall thickness, local buckling could not be forced in the models of tests. It can thus be concluded that applying the proposed imperfection in all analyses results in accurate results in comparison with the ten tests.

It should be noted that the calibration of the model took place using only the ten tests that were performed at Delft University of Technology with the test parameters as described in Table 9.3. Further calibration of the model may be necessary, especially with respect to the validity of the proposed imperfection sizes for pipes with different D/t ratios, or originating from different manufacturers or manufacturing processes.

11.3 Summary of Chapter 11

In this chapter, the development and validation of a numerical model for the purpose of the analysis of buried pipelines under ground-induced deformations is presented. A 3D pipeline, composed of shell elements, is combined with soil springs in lateral, vertical and axial directions. In this manner, a detailed analysis of the steel pipeline behaviour is possible with a relatively low complexity of the model compared to analyses that include modelling soil bodies in full 3D.

The soil springs can be assigned any property. For the validation of the model, the measured characteristics of the ring-springs that were applied in the tests (see section 9.4.2) were used as input for the soil springs, but in practical application, the input can range from standardized soil behaviour to results of FE-analyses or experiments. Accuracy and complexity of the model can be adjusted by choosing the soil spring types, properties and spacing.

To allow correct modelling of local instabilities in the pipeline, imperfections in the form of an eigenmode are applied to the pipeline in the critical segments. In the performed validation analyses, the position of the critical segments was derived from the test results. In practical application, the location of the critical segments may need to be determined by a simplified preliminary analysis.

By modelling the ten tests that were performed (see Chapter 9), the model was validated. Using these analyses it was shown that for all pipes, a similar initial imperfection size generated results of sufficient accuracy. Using this standardized imperfection size, a good match between the FE-model results and test results was obtained, proving the validity of the numerical model.

Chapter 12

Summary of Part III and recommendations

12.1 Summary of Part III

Part III of this study discusses the effect of an active strike-slip fault on buried pipelines. In Chapter 8, an introduction to Part III of this study is presented and the GIPIPE research project is briefly outlined. The aim of this project was to develop safe and practical design guidelines which improve the current design practice with regard to ground-induced deformations acting on buried pipelines. The current research specifically focuses on the effect of moving strike-slip faults on buried pipelines, but results are applicable to a wider range of ground-induced deformations such as for example differential settlements.

In a review of the current state-of-the art with respect to the analysis of buried pipelines crossing strike-slip faults it is shown that, although many models exist to calculate the behaviour of buried pipelines crossing moving strike-slip faults, various aspects remain unclear. For example, experimental verification of these models is often lacking, as well as the correct modelling of local buckling of the pipe wall.

In Chapter 9, the development and results of a full-scale experimental programme are presented and discussed. In the developed test setup, a buried pipeline which crosses a strike-slip fault is simulated, leaving the pipe bare during the experiments. For this simulation, non-linear mechanical springs were used. In a total of ten tests, longitudinal tensile strains up to 3% were regularly reached, while in one extreme case a tensile strain of 5% was reached, resulting in rupture of the pipe. Apart from high tensile strains, high compressive strains resulted in local buckling of the compressed pipe wall in eight out of ten tests.

Chapter 10 presents the analysis of the test results. The ratio between pipe and soil stiffness is found to greatly influence the resulting pipeline deformation in case of ground-induced deformations. Furthermore, the location of the highest measured strain was found to move away from the fault for increasing fault movement.

It is shown that in case a girth weld was present in the segment of the pipeline that underwent the largest deformations, local buckling occurred in the direct vicinity of this girth weld. Furthermore, it was shown that local buckling occurs earlier when a girth weld is present in the pipe than in plain pipes. This is attributed to the presence of imperfections near the girth weld and a possible discontinuity in pipe properties between the two pipes adjoining the girth weld which results in concentration of deformation. In case of internal pressure, local buckling was observed to result in very high tensile strains opposite to the local buckle.

A change in fault angle β was found to have a significant effect on the axial force in the pipeline, especially at small fault angles. The magnitude of the axial force greatly influences the deformation of the pipeline and therefore is a main parameter to consider in design situations.

Prevention of concentration of deformation was found to be important in case of these situations with high strain demand. The specimens that did not fail in local buckling, showed redistribution of strains, likely as a result of strain hardening of the material. However, the tested pipes had a relatively high Y/T ratio. This increases the risk of strain concentrations and contributed to a rupture in one of the specimens.

Due to the many parameters involved in the ten tests that were performed, a full understanding of the effect of every individual parameter is not feasible on the basis of the test results alone. Therefore, the test results were used to calibrate and validate a model. This model is presented in Chapter 11. The model features a 3D pipeline, modelled in shell elements, combined with soil springs in lateral, vertical and axial direction. In this manner, a detailed analysis of the steel pipeline behaviour is performed, while, in comparison to full 3D soil analyses, relatively limited user and computational effort is necessary. To allow correct modelling of local instabilities in the pipeline, appropriate imperfections are applied to the pipe in the areas of the pipeline that are subjected to the most severe deformations.

By modelling the ten full-scale tests that were performed, the model was validated. A suitable initial imperfection amplitude was found, expressed as a fraction of the pipe wall thickness. Good agreement between the test results and calculation results was obtained for all ten tests.

12.2 Recommendations for further research

The ten tests that were performed provide information on the behaviour of buried pipelines crossing a strike-slip fault. However, due to the large number of parameters that is involved in such an event, the results of the testing programme only provide a global overview of this behaviour. The newly developed numerical model may provide additional insight. Specifically, the following topics require further investigation:

- During the tests, it was found that the location of the highest measured strain moves away from the fault for increasing fault movement. Because this maximum strain dominates the design, this effect may need further quantification.
- Strains were observed to increase with increasing fault movement. However, during the tests that did not fail in local buckling, after some threshold fault movement, strains started spreading over a longer pipe segment without increase of the maximum strain. It

is expected that this behaviour results from strain hardening of the steel, but further research may confirm and quantify this.

- Ductility of the total pipeline is important in high strain-demand design situations. During the tests, concentration of strain due to a strength mismatch at the girth welds was observed, contributing to a rupture in one test. The acceptable strength mismatch at such girth welds needs to be determined. Furthermore, appropriate guidance for designers needs to be established.

Besides these specific topics, a general parameter study using the new numerical model is recommended. A very extensive parameter study may even result in a set of design graphs, which allow a designer or pipeline owner to quickly assess the effects of ground-induced deformation on a pipeline.

After calibration, the developed numerical model was shown to compare very well with test results. However, this calibration only took place for two pipe geometries originating from one supplier. In a future study, the model may be further calibrated so that abilities of the model are also confirmed for other pipes.

Furthermore, the geometrical imperfections that were applied in the model were not related to actual measurements on the pipe. By performing measurements of geometrical imperfections on the pipe, the necessary initial imperfections in the model may be linked directly to the pipe geometry. However, it should be noted that, currently, the imperfections in the model represent both geometrical imperfections as well as other imperfections such as residual stresses. In case of a direct relation between the measured pipe geometry and the modelled geometrical imperfections, other imperfections may have to be accounted for in an alternative manner.

Part IV: Closure

Chapter 13

Concluding remarks

13.1 Evaluation of performed research

This section contains an overall evaluation of the performed research, for more detailed conclusions, the reader is referred to the summarizing chapter of each part.

The research that is presented in Part II and Part III of this study heavily relied on experimental work. Compared to analytical and FE-models, experimental work is much more expensive, especially at large scale. The process of development and validation of the numerical and analytical models that followed these experiments showed that experiments provide important information which otherwise would not be discovered. Examples are the localization of curvature due to a variation of bending moment resistance over a length of tube of pipe, and the effects of a strength mismatch at a girth weld. It can therefore be concluded that experimental work is very valuable, even now that very advanced modelling options are available.

On various occasions within this research, the discrepancy between a theoretical ‘perfect’ element and reality influenced the structural behaviour of the studied elements. Examples are:

- The specific manufacturing process of a tubular member may result in a complex residual stress state (see section 5.2.4) and initial geometrical imperfections (see section 5.2.5), which directly influence local buckling.
- Handling, installation and other activities during construction may influence the state of a tube (see section 5.2.6), possibly negatively influencing the local buckling behaviour.
- Differences in bending moment capacity between connected tubes may result in severe concentration of deformations (see sections 6.2.2 and 9.6.11).

It can therefore be concluded that it is very important to relate developed prediction models, analytical or numerical to actual structures instead of theoretical perfect elements.

The experimental work presented in this thesis was used to develop numerical and analytical models (see sections 6.5 and 6.9 and Chapter 11). For all these models, validation procedures were performed, greatly increasing confidence in the developed models. If possible, the model input in terms of geometry, material properties and imperfections was based on actual measured data in these validations.

In the conducted test programmes, it was shown that a variation of cross-sectional resistance over the length of a structure is important. Within spiral-welded tubes, a variation of bending moment resistance was observed over the length of plain tubes, while both in tubes and pipelines the influence of a strength mismatch at a girth weld was observed to be significant. Strong variations in bending moment resistance within a structure may result in concentration of deformations. Using steel with sufficient strain hardening may prevent these concentrations of becoming excessive.

Aside from the effects of a strength mismatch, the presence of a girth weld in a pipe or tube was found to negatively influence the strength and deformation capacity of that element. This is mainly attributed to geometrical imperfections near these welds. The quality of execution of welds is therefore very important.

13.2 Recommendations for further research

The research presented in this thesis contributes to a better understanding of the topics considered in the three separate parts of this study. Further improvement is possible by performing additional investigations. Specific recommendations regarding the topics in Parts I, II and III of this thesis are presented in the concluding chapters of these parts and are not repeated here. In this section, more general recommendations are presented.

In this study, several investigations were undertaken to determine the actual initial state of the tested specimens. Examples are the study of initial geometrical imperfections in spiral-welded tubes (see section 5.2) and the extensive measurement of material properties of all tested specimens (see sections 5.3 and 9.3). However, further study on this subject is necessary. In contrast to the tubes discussed in Part II of this study, measurements of geometrical imperfections of the pipes considered in Part III of this study were not taken, resulting in assumptions in the modelling phase. Assumptions with regard to the residual stresses due to manufacturing were made in both Part II and Part III of this study. A third example of the necessity of additional research is found in the variation of cross-sectional properties over the length of the spiral-welded tubes examined in Part II of this study. In this case, additional material testing would likely have provided a better insight into the behaviour of the tubes. In all these examples, additional input for the calculation models may result in even further improvement of the predictions. For the most accurate modelling results, knowledge of the actual state of a structure is of paramount importance.

Once a model is developed and validated, theoretically an engineering problem is solved. However, in cases of complex models, such as the models presented in section 6.5 and Chapter 11, further simplification of the model may be necessary. For this, parametric studies are suitable. With regard to the bending behaviour of tubes in combined walls, such a parametric study was performed by Vasilikis et al. (2016), supporting the development of the analytical model that is presented in section 6.9. The numerical model that predicts the behaviour of buried pipelines under ground-induced deformations is outlined and validated in this thesis, but no parametric study has been performed yet with this model. It is recommended to use the model presented in Part III of this study in a parametric study to fully utilize its potential. A similar

model, which was also developed within the framework of the GIPIPE project by Vazouras et al. (2010, 2012) was already employed for such a study. The results of such parametric studies may be used to generate design graphs, which help designers to quickly assess a structure without complex modelling.

References

Literature

- ABAQUS (2010). *Abaqus Version 6.10 Documentation*, Dassault Systèmes Simulia Corp.
- Adboun, T.H., Ha, D., O'Rourke, M.J., Symans, M.D., O'Rourke, T.D., Palmer, M.C. and Stewart, H.E. (2009). Factors influencing the behaviour of buried pipelines subjected to earthquake faulting. *Soil Dynamics and Earthquake Engineering* 29, 415-427.
- Ades C.S. (1957). Bending Strength of Tubing in the Plastic Range. *Journal of the Aeronautical Sciences* 24. 605-610.
- Alpsten, G.A. (1972). Variations in mechanical and cross-sectional properties of steel – State of Art Report. In *Proceedings of the International Conference on the Planning and Design of Tall Buildings*, Bethlehem, Pennsylvania, USA.
- ArcelorMittal (2008). Cuxhaven – Greener Energy – thanks to ArcelorMittal sheet piles (Online) Available: <http://sheetpiling.arcelormittal.com/projects/display/title/cuxhaven> (Accessed 02-06-2015).
- ArcelorMittal (2010). Spirally welded steel pipes, Advertisement Publication.
- Audibert, J.M.E. and K.J. Nyman (1975). Coefficients of subgrade reaction for the design of buried piping. In *Proceedings of the 2nd ASCE Specialty Conference on Structural Design of Nuclear Plant Facilities*, New Orleans, Louisiana, USA.
- Audibert, J.M.E. and K.J. Nyman (1977). Soil Restraint against Horizontal Motion of Pipes. *ASCE, Journal of the Geotechnical Division* 103 (10), 1119-1142.
- Aksel'rad (Axelrad) E.L. (1965). Refinement of buckling-load analysis for tube flexure by way of considering precritical deformation. *Izvestiya Akademii Nauk SSSR, Otdelenie Tekhnicheskikh Nauk, Mekhanika i Mashinostroenie* 4, 133-139. (in Russian).
- Bijlaard, F.S.K., G. Sedlacek and J.W.B. Stark (1988). Procedure for the determination of design resistance from tests – Background report to Eurocode 3 “Common unified rules for Steelstructures”. TNO-IBBC report BI-87-112.
- Bouwkamp, J.G., and R.M. Stephen (1973). Large Diameter Pipe Under Combined Loading. *ASCE, Journal of the Transportation Division* 99 (3), 521-536.

- Bouwkamp, J.G., and R.M. Stephen (1974). Full-scale studies on the structural behaviour of large diameter pipes under combined loading. University of California report to Alyeska Pipeline Service Company.
- Bouwkamp, J.G. (1975). Buckling and Post-Buckling Strength of Circular Tubular Sections. In *Offshore Technology Conference*, Houston, Texas, USA.
- Brazier, L.G. (1927). On the Flexure of Thin Cylindrical Shells and Other Thin Sections. In *Proceedings of the Royal Society of London. Series A, Containing Papers of a Mathematical and Physical Character*, Vol 116 (773), 104-14.
- Brinch-Hansen, J. (1961). The Ultimate Resistance of Rigid Piles Against Transversal Forces. *Geoteknisk Institut Bulletin 12*, 5-9.
- Carr, M., I. MacRae and D. Bruton (2009). Local buckling of pressurised seamless linepipe: results of the SAFEBUCK JIP. In *Pipeline Technology Conference*, Ostend, Belgium.
- COMBITUBE Research Consortium (2015). Bending resistance of steel tubes in CombiWalls. Final report of COMBITUBE RFCS project.
- Corona, E. and S. Kyriakides. (1988). On the collapse of inelastic tubes under combined bending and pressure. *Int. J. Solids Structures 24* (5), 505-535.
- Daiyan, N., S. Kenny, R. Phillips and R. Popescu (2010). Numerical investigation of oblique pipeline/soil interaction in sand. In *Proceedings of the 8th International Pipeline Conference*, Calgary, Alberta, Canada.
- DelCol, P.R., G.Y. Grondin, R.J.J. Cheng and D.W. Murray. (1998). Behaviour of Large Diameter Line Pipe Under Combined Loads. Structural Engineering Report No. 224, University of Alberta, Department of Civil Engineering.
- Dorey, A.B, D.W. Murray and J.J.R. Cheng (2000). An experimental evaluation of critical buckling strain criteria. In *Proceedings of the 3rd International Pipeline Conference*, Calgary, Alberta, Canada.
- van Douwen, A.A., A.M. Gresnigt and J.W.B. Stark (1974). Plastic design of buried steel pipelines for transport of oil, gas or water, verified by tests on scale models. TNO-IBBC report BI-74-67.
- van Es, S.H.J. and A.M. Gresnigt (2016). Measurements of imperfections in spiral-welded tubes. Stevin Report 6-16-2, Delft University of Technology.
- van Es, S.H.J. and A.M. Gresnigt (2016a). Four point bending tests on spiral-welded tubes. Stevin Report 6-16-3, Delft University of Technology.
- van Es, S.H.J. and A.M. Gresnigt (2016b). Design and results of fault movement tests on buried pipelines (RFCS GIPIPE), Stevin Report 6-16-4, Delft University of Technology.
- van Es, S.H.J., A.M. Gresnigt, M.H. Kolstein and F.S.K. Bijlaard (2013). Local Buckling of Spirally Welded Tubes – Analysis of Imperfections and Physical Testing. In *Proceedings of the 23rd (2013) International Offshore and Polar Engineering*, Anchorage, Alaska, USA.
- van Es, S.H.J., D. Vasilikis, A.M. Gresnigt and S.A. Karamanos (2016). Ultimate Bending Capacity of Spiral-Welded Steel Tubes – Part I: Experiments. *Thin-Walled Structures 102*, 286-304.

- Fabian, O. (1977). Collapse of cylindrical, elastic tubes under combined bending, pressure and axial loads. *Int. J. Solids Structures* 13, 1257-1270.
- van Foeken, R.J. and A.M. Gresnigt (1998). Buckling and Collapse of UOE manufactured steel pipes. TNO report 96-CON-R0500 for the Offshore and Onshore Design Applications Supervisory Committee of the Pipeline Research Committee of the American Gas Association.
- Fonzo, A., J. Ferino and C.M. Spinelli (2012). Pipeline Strain-Based Design Approach: FEM through Full-Scale Bending Tests. In *Proceedings of the 22nd (2012) International Offshore and Polar Engineering*, Rhodes, Greece.
- Fonzo, A., A. Lucci, J. Ferino, M. Di Biagio, C.M. Spinelli, V. Flaxa, S. Zimmermann, C. Kalwa and F.M. Knoop (2001). Full scale investigation on strain capacity of high grade large diameter pipes. In *18th Joint Technical Meeting on Pipeline Research*, San Francisco, California, USA.
- Fowler, J.R. (1990). Large scale collapse testing. Stress Engineering Services Inc. report for The Offshore Supervisory Committee of the Pipeline Research Committee of the American Gas Association.
- Gellin, S. (1980). The plastic buckling of long cylindrical shells under pure bending. *Int. J. Solids Structures* 16, 397-407.
- de Gijt, J.G. and M.L. Broeken (2013). *Quay Walls – Second edition*. CRC Press.
- Guijt, W., Vrouwenvelder, T., Gresnigt A.M. and G. Dijkstra (2004). Safety Concept in The New Dutch Pipeline Standard NEN 3650. In *Proceedings of the 14th International Offshore and Polar Engineering Conference*, Toulon, France.
- GIPIPE Research Consortium (2015). Safety of buried steel pipelines under ground-induced deformations. Final report of GIPIPE RFCS project.
- Gresnigt, A.M. (1977). Rapportage van de resultaten van de op ware grootte buizen ($\emptyset 24''-0,25''$) uitgevoerde proeven. TNO-IBBC report OPL 77-134. (in Dutch).
- Gresnigt, A.M. (1985). Kritieke stuik en kritieke rotatie in verband met plooiën van stalen transportleidingen. TNO-IBBC report BI-86-116 / OPL 85-343. (in Dutch).
- Gresnigt, A.M. (1986). Plastic design of buried steel pipelines in settlement areas. *Heron* 31 (4), 3-113.
- Gresnigt, A.M., S.H.J. van Es, D. Vasilikis and S.A. Karamanos (2016). Strain-based design procedures for spiral-welded steel tubes in combined walls. In *Proceedings of the International Colloquium of Stability and Ductility of Steel Structures*, Timisoara, Romania.
- Gresnigt, A.M. and R.J. van Foeken (2001). Local Buckling of UOE and Seamless Steel Pipes. In *Proceedings of the 11th International Offshore and Polar Engineering Conference*, Stavanger, Norway.
- Gresnigt, A.M., C.H. Jo and S.A. Karamanos (2011). Local buckling of tubular sections in structural applications. In *The 2011 World Congress on Advances in Structural Engineering and Mechanics (ASEM'11⁺)*, Seoul, Korea.

- Gu, X., and H. Zhang (2009). Research on aseismatic measures of gas pipeline crossing a fault for strain-based design. In *Proceedings of the ASME 2009 Pressure Vessels and Piping Division Conference*, Prague, Czech Republic.
- Gulvanessian, H., J.-A. Calgaro and M. Holický (2012). *Designers' guide to Eurocode: Basis of structural design EN 1990*. ICE Publishing.
- Ha, D., T.H. Abdoun, M.J. O'Rourke, M.D. Symans, T.D. O'Rourke, M.C. Palmer and H.E. Stewart (2008). Centrifuge Modeling of Earthquake Effects on Buried High-Density Polyethylene (HDPE) Pipelines Crossing Fault Zones. *Journal Of Geotechnical and Geoenvironmental Engineering* 134 (10), 1501-1515.
- Ha, D., T.H. Abdoun, M.J. O'Rourke, M.D. Symans, T.D. O'Rourke, M.C. Palmer and H.E. Stewart (2009). Earthquake Faulting Effects on Buried Pipelines – Case History and Centrifuge Study. *Journal of Earthquake Engineering* 14, 646-669.
- Hilberink A. (2011). Mechanical Behaviour of Lined Pipe. PhD thesis, Delft University of Technology.
- Huinen, W.L.J. (2013). Loading patterns for Delft GIPIPE test setup from PLE4Win. External memo 191204, Rev A.
- Jirsa, J.O., F.-H. Lee, J.C. Wilhoit and J.E. Merwin (1972). Ovaling of Pipeline Under Pure Bending. In *Offshore Technology Conference*, Houston, Texas, USA.
- Johns, T.G., R.E. Mesloh, R. Winegardner and J.E. Sorenson (1975). Inelastic Buckling of Pipelines under Combined Loads. In *Offshore Technology Conference*, Houston, Texas, USA.
- Ju, G.T. and S. Kyriakides (1992). Bifurcation and localization instabilities in cylindrical shells under bending-II: Predictions. *Int. J. Solids Structures* 29 (9), 1143-1171.
- Kang K.-B., J.-Y. Yoo, S.-S. Ahn, W. Y. Cho and T.-Y. Yoon (2007). Buckling behaviour of API-X80 Linepipe. In *Proceedings of the 17th International Offshore and Polar Engineering Conference*, Lisbon, Portugal.
- Karamanos, S.A. and J. L. Tassoulas (1996). Tubular Members. II: Local Buckling and Experimental Verification. *J. Eng. Mech* 122 (1), 72-78.
- Karamitros, D.K., G.D. Bouckovalas and G.P. Kouretzis (2007). Stress analysis of buried steel pipelines at strike-slip fault crossings. *Soil Dynamics and Earthquake Engineering* 27, 200-211.
- Kennedy, R.P., A.W. Chow and R.A. Williamson (1977). Fault Movement Effects on Buried Oil Pipeline. *Journal of the Transportation Engineering Division of ASCE* 103 (TE5), 617-633.
- Kimura, T., S. Idogai and K. Takada (1980). Experimental and analytical studies of the elastoplastic behaviour of offshore pipelines during laying. In *Offshore Technology Conference*, Houston, Texas, USA.
- Korff, M. and H.J.A.M. Hergarden (2002). Integraal ontwerp leidingen en riolen – Grondmechanische randvoorwaarden. Final report of research project “Integraal ontwerp leidingen en riolen”

- Korol, R.M. (1979). Critical buckling strains of round tubes in flexure. *Int. J. Mech Sci.* 21, 719-730.
- Kyriakides, S. and P.K. Shaw (1982). Response and stability of elastoplastic circular pipes under combined bending and external pressure. *Int. J. Solids Structures* 18 (11), 957-973.
- Kyriakides, S., and P.K. Shaw (1987). Inelastic Buckling of Tubes Under Cyclic Bending. *Journal of Pressure Vessel Technology* 109 (2), 169-178.
- Kyriakides, S. and G.T. Ju (1992). Bifurcation and localization instabilities in cylindrical shells under bending –I. Experiments. *Int. J. Solids Structures* 29 (9), 1117-1142.
- Limam, A., L.-H. Lee, E. Corona and S. Kyriakides (2008). Plastic buckling and collapse of tubes under bending and internal pressure. In *Proceedings of the 27th International Conference on Offshore Mechanics and Arctic Engineering*, Estoril, Portugal.
- Limam, A., L.-H. Lee, E. Corona and S. Kyriakides (2010). Inelastic wrinkling and collapse of tubes under combined bending and internal pressure. *International Journal of Mechanical Sciences* 52, 637-647.
- LincolnElectric (2015). LNT NiMo-1 (Online) Available: http://www.lincolnelectric.com/nl-nl/Consumables/Pages/product.aspx?product=Products_ConsumableEU_TIGWires-LNT-LNTNiMo1%28LincolnElectric_EU_Base%29 (Accessed 25-11-2015).
- Liu, M., Y.-Y. Wang and Z. Yu (2008). Response of Pipelines under Fault Crossing. In *Proceedings of the 18th International Offshore and Polar Engineering Conference*, Vancouver, British Columbia, Canada.
- Mohareb, M.E., A.E. Elwi, G.L. Kulak and D.W. Murray (1994). Deformational Behaviour of Line Pipe. Structural Engineering Report No. 202, University of Alberta, Department of Civil Engineering.
- Moore, R.L and J.W. Clark (1952). Torsion, compression and bending tests of tubular sections machined from 75S-T6 rolled round rod. Report of Aluminum Company of America to The National Advisory Committee for Aeronautics.
- Murphey, C.E. and C.G. Langner (1985). Ultimate Pipe Strength Under Bending, Collapse and Fatigue. In *Proceedings of the 4th International Offshore Mechanics and Arctic Engineering Symposium*, Dallas, Texas, USA.
- Murray, D.W. (1997). Local buckling, strain localization, wrinkling and postbuckling response of line pipe. *Engineering Structures* 19 (5), 360-371.
- Newmark, N.M. and W.J. Hall (1975). Pipeline Design to Resist Large Fault Displacement. In *Proceedings of the U.S. National Conference on Earthquake Engineering*, Ann Arbor, Michigan, USA.
- Nomoto, T., M. Enosawa and Y. Fujita. (1986) Simplified method of analysis for collapse strength of submarine pipelines under combined bending, external pressure and axial tension. In *Proceedings of the 5th International Offshore Mechanics and Arctic Engineering Symposium*, Tokyo, Japan.
- Odina, L. and R. Tan (2009). Seismic fault displacement of buried pipelines using continuum finite element methods. *Proceedings of the 28th International Conference on Ocean, Offshore and Arctic Engineering*, Honolulu, Hawaii, USA.

- O'Rourke, M., V. Gadicherla and T. Abdoun (2005). Centrifuge modelling of PGD response of buried pipe. *Earthquake Engineering and Engineering Vibration* 4 (1), 69-73.
- O'Rourke, T., M. Jezerski, N. Olson, A. Bonneau, M. Palmer, P. Stewart, M. O'Rourke and T. Abdoun (2008). Geotechnics of pipeline systems response to earthquakes. In *Proceedings of Geotechnical Earthquake Engineering and Soil Dynamics IV*, Sacramento, California, USA.
- O'Rourke, T.D., M.C. Palmer, H.E. Stewart and N.A. Olson (2009). Large-Scale Testing of Fault Rupture Effects. Cornell University Final Report for the San Francisco Public Utilities Commission.
- Ovesen, N.K. (1964). Anchor Slab, Calculation Methods and Model Tests. *Geoteknisk Institut Bulletin* 16.
- Paulin, M.J., R. Phillips and J.I. Clark (1998). A Full-Scale Investigation into Pipeline/Soil Interaction. In *Proceedings of the 2nd International Pipeline Conference*, Calgary, Alberta, Canada.
- PLE4WIN (2015). *PLE4WIN Version 4.3.1 User manual*, Expert Design Systems.
- Prion, H.G.L. and P.C. Birkemoe (1992). Beam-Column Behavior of Fabricated Steel Tubular Members. *Journal of Structural Engineering* 188 (5), 1213-1232.
- Reddy, B.D. (1979). An experimental study of the plastic buckling of circular cylinders in pure bending. *Int. J. of Solids Structures* 15, 669-685.
- Reinke, T., A.J. Sadowski, T. Ummenhofer and J.M. Rotter (2014). Large scale bending tests on spiral welded steel tubes. In *Eurosteel 2014*, Naples, Italy.
- Reissner, E. and H.J. Weinitschke (1963). Finite Pure Bending of Circular Cylindrical Tubes. *Quarterly of Applied Mathematics* 20 (4), 305-319.
- Rotter, J.M., A.J. Sadowski and L. Chen (2014). Nonlinear stability of thin elastic cylinders of different length under global bending. *Int. J. of Solids Structures* 51, 2826-2839.
- Royal HaskoningDHV (2013). Local Buckling tests on Tubular Pipes – Evaluation Report. Final report of SBRCURnet research.
- Rijkswaterstaat (2015). Beeldbank Rijkswaterstaat / Joop van Houdt (Online) Available: <https://beeldbank.rws.nl/MediaObject/Details/421926> (Accessed 19-01-2016).
- Sadowski, A.J., S.H.J. van Es, T. Reinke, J.M. Rotter, A.M. Gresnigt and Thomas Ummenhofer (2014). Harmonic analysis of measured initial geometric imperfections in large spiral welded carbon steel tubes. *Engineering Structures* 85, 234-248.
- SBRCURnet (2013) Local Buckling tests on Tubular Piles Evaluation Report. Final report 9W4231.
- Schroeder, J., K.R. Srinivasaiah and P. Graham (1974). Analysis of Test Data on Branch-Pipe Connections Exposed to Internal Pressure and/or External Couples *WRC Bulletin* 200.
- Seide, P. and V.I. Weingarten (1961). On the Buckling of Circular Cylindrical Shells Under Pure Bending. *J. Appl. Mech (ASME)* 28, 112-116.
- Sherman D.R. (1976). Tests of Circular Steel Tubes in Bending. *Journal of the Structural Division of ASCE* 102 (11), 2181-2195.

- Sherman, D.R. (1983). Bending Capacity of Fabricated Pipes. University of Wisconsin-Milwaukee Report.
- Sherman, D.R. (1984). Bending Capacity of Fabricated Pipes. Supplement to University of Wisconsin-Milwaukee Report.
- Shitamoto, H., M. Hamada, S. Okaguchi, N. Takahashi, I. Takeuchi and S. Fujita (2010). Evaluation of Compressive Strain Limit of X80 SAW Pipes for Resistance to Ground Movement. In *Proceedings of the 20th International Offshore and Polar Engineering Conference*, Beijing, China.
- Shitamoto, H., M. Hamada, N. Takahashi and Y. Nishi (2012). Effect of Full Scale Pipe Bending Test Method on Deformability Results of SAW Pipes. In *Proceedings of the 22nd International Offshore and Polar Engineering Conference*, Rhodes, Greece.
- Sorenson, J.E., R. E. Mesloh, E. Rybicki, A.T. Hopper and T.J. Atterbury. (1970). Buckling strength of offshore pipelines. Battelle report to The Offshore Pipeline Group.
- Stephens, D.R., R.J. Olson and M.J. Rosenfeld (1991). Topical report on Pipeline monitoring – Limit state criteria. Battelle report to Line Pipe Research Supervisory Committee of the Pipeline Research Committee of the American Gas Association.
- Suzuki, N., S. Endo, M. Yoshikawa and M. Toyoda (2001). Effects of a strain hardening exponent on inelastic local buckling strength and mechanical properties of line pipes. In *Proceedings of the 20th International Conference on Offshore Mechanics and Arctic Engineering*, Rio de Janeiro, Brazil.
- Suzuki, N. and I. Satoshi (2007). Compressive Strain Limits of X80 High-Strain Line Pipes. In *Proceedings of the 17th International Offshore and Polar Engineering Conference*, Lisbon, Portugal.
- Suzuki, N., J. Kondo and J. Simamura (2008). Strain Capacity of High-Strength Line Pipes. JFE Technical Report No. 12.
- Suzuki, N., H. Tajika, I. Satoshi, M. Okatsu, J. Kondo and T. Arakawa (2010). Local buckling behaviour of 48", X80 high-strain line pipes. In *Proceedings of the 8th International Pipeline Conference*, Calgary, Alberta, Canada.
- Tajika, H. and N. Suzuki (2009). Bending Capacity and Seismic Integrity of X65 ERW Line Pipe. In *Proceedings of the 19th International Offshore and Polar Engineering Conference*, Osaka, Japan.
- Takada, S., N. Hassani and K. Fukuda (2001). A new proposal for simplified design of buried steel pipelines crossing active faults. *Earthquake Engineering and Structural Dynamics* 30, 1243-1257.
- Timoshenko, S.P. and J.M. Gere (1961). *Theory of Elastic Stability* (Second edition ed.). Dover Publications.
- Trautmann C.H. and T.D. O'Rourke (1985). Lateral Force-Displacement Response of Buried Pipe. *Journal of Geotechnical Engineering* 111 (9), 1077-1092.
- Trautmann, C.H., T.D. O'Rourke and F.H. Kulhawy (1985). Uplift Force-Displacement Response of Buried Pipe. *Journal of Geotechnical Engineering* 111 (9), 1061-1076.

- Trifonov, O.V. and V.P. Cherniy (2010). A semi-analytical approach to a nonlinear stress-strain analysis of buried steel pipelines crossing active faults. *Soil Dynamics and Earthquake Engineering* 30, 1298-1308.
- Trifonov, O.V. and V.P. Cherniy (2012). Elastoplastic stress-strain analysis of buried steel pipelines subjected to fault displacements with account for service loads. *Soil Dynamics and Earthquake Engineering* 33, 54-62.
- Tsuru, E. and J. Agata (2012). Buckling Resistance of Line Pipes with Girth Weld Evaluated by New Computational Simulation and Experimental Technology for Full-Scale Pipes. *International Journal of Offshore and Polar Engineering* 22 (1), 76-82.
- Tugcu, P. and J. Schroeder (1979). Plastic deformation and stability of pipes exposed to external couples. *Int. J. Solids Structures* 15, 643-658.
- Vasilikis, D., S.H.J. van Es, S.A. Karamanos and A.M. Gresnigt (2016). Ultimate Bending Capacity of Spiral-Welded Steel Tubes – Part II: Predictions. *Thin-Walled Structures* 102, 305-316.
- Vazouras, P., S.A. Karamanos and P. Dakoulas (2010). Finite element analysis of buried steel pipelines under strike-slip fault displacements. *Soil Dynamics and Earthquake Engineering* 30, 1361-1376.
- Vazouras, P., S.A. Karamanos and P. Dakoulas (2012). Mechanical behaviour of buried steel pipes crossing active strike-slip faults. *Soil Dynamics and Earthquake Engineering* 41, 164-180.
- Vitali, L., L. Bartolini, D. Askheim, R. Peek and E. Levold (2005).. Hotpipe II Project Experimental test and FE-analyses. In *Proceedings of the 24th International Conference on Offshore Mechanics and Arctic Engineering*, Halkidiki, Greece.
- Vrouwenvelder, A.C.W.M., Guijt, W., Dijkstra, G.J. and A.M. Gresnigt (2003). Herziening rekenfactoren en spanningscorrectiefactoren in NEN 3650. TNO rapport 2003-CI-R0031 (in Dutch).
- Wang, L-J. and L.R.L. Wang (1995). Buried pipelines in large fault movements. In *Proceedings of the 4th US conference on Lifeline Earthquake Engineering*, San Francisco, California, USA.
- Wang, L.R.L, and Y. Yeh (1985). A refined seismic analysis and design of buried pipeline for fault movement. *Earthquake Engineering and Structural Dynamics* 13 (1), 75-96.
- Wijewickreme, D., H. Karimian and D. Honegger (2009). Response of buried steel pipelines subject to relative axial soil movement. *Canadian Geotechnical Journal* 46 (7), 735-752.
- Wilhoit, J.C., J.E. Merwin and J.O. (1972). Critical Plastic Buckling Parameters for Pipe in Pure Bending. ASME Paper 72-Pet29.
- Wilhoit, J.C. and J.E. Merwin (1973). Critical Plastic Buckling Parameters for Tubing in Bending Under Axial Tension. In *Offshore Technology Conference*, Houston, Texas, USA.
- Yoosef-Ghods, N., G.L. Kulak and D.W. Murray (1994). Behavior of Girth-Welded Line Pipe. Structural Engineering Report No. 203, University of Alberta, Department of Civil Engineering.

- Yoshizaki, K., T.D. O'Rourke, T. Bond, J. Mason and M. Hamada (2000). Large Scale Experiments of Permanent Ground Deformation Effects on Steel Pipelines. *MCEER Bulletin* 3, 21-28.
- Yoshizaki, K., T.D. O'Rourke and M. Hamada (2003). Large scale experiments of buried steel pipelines with elbows subjected to permanent ground deformation. *Structural Eng./Earthquake Eng., JSCE* 20 (1), 1-11.
- Zimmerman, T.J.E., M.J. Stephens, D.D. DeGeer, Q. Chen (1995). Compressive strain limits for buried pipelines. In *Proceedings of the 14th Offshore Mechanics and Arctic Engineering Conference*, Copenhagen, Denmark.
- Zimmerman, T., C. Timms, J. Xie and J. Asante (2004). Buckling resistance of large diameter spiral welded linepipe. In *Proceedings of 5th the International Pipeline Conference*, Calgary, Alberta, Canada.
- Zimmermann, S., H. Karbasian and F.M. Knoop (2013). Helical Submerged Arc Welded Line Pipe Engineering For Strain Based Design. In *Proceedings of the 23rd International Offshore and Polar Engineering Conference*, Anchorage, Alaska, USA.

Standards and design guidelines

- AISC (2010). Specification for Structural Steel Buildings.
- ALA (2001) Guidelines for the Design of Buried Steel Pipe.
- ALA (2005) Seismic Guidelines for Water Pipelines.
- API (2008). Specification 5L. Specification for Line Pipe.
- ASCE (1984). Guidelines for the Seismic Design of Oil and Gas Pipeline Systems.
- ASME B31.4 (1979). Liquid Petroleum Transportation Piping Systems.
- ASME B31.4 (2009). ASME Code for Pressure Piping B31 – Pipeline Transportation Systems for Liquid Hydrocarbons and Other Liquids.
- AWWA M11 (2004). Manual of Water Supply Practices M11 – Steel Water Pipe: A Guide for Design and Installation.
- BS7910 (2013). Guide to methods for assessing the acceptability of flaws in metallic structures.
- CSA Z662-11 (2011). Canadian Standards Association - Oil and Gas Pipeline Systems.
- DNV-OS-F101 (2010). Offshore Standard DNV-OS-F101 – Submarine Pipeline Systems.
- DNV-RP-F110 (2007) Recommended Practice DNV-RP-F110 – Global Buckling of Submarine Pipelines.
- EN 805 (2000). Water supply – Requirements for systems and components outside buildings.
- EN 1594 (2013). Gas infrastructure – Pipelines for maximum operating pressure over 16 bar – Functional requirements.
- EN 1990 (2002). Eurocode 0: Basis of structural design.

- EN 1993-1-1 (2006). Eurocode 3: Design of steel structures – Part 1-1: General rules for buildings.
- EN 1993-1-6 (2007). Eurocode 3: Design of steel structures – Part 1-6: General – Strength and Stability of Shell Structures.
- EN 1993-4-3 (2009). Eurocode 3: Design of steel structures – Part 4-3: Pipelines.
- EN 1993-5 (2006). Eurocode 3: Design of steel structures – Part 5: Piling.
- EN 1997-1 (2012). Eurocode 7: Geotechnical design – Part 1: General rules.
- EN 1998-4 (2007). Eurocode 8: Design of structures for earthquake resistance – Part 4: Silos, tanks and pipelines.
- NEN 3650-1 (2012). Eisen voor buisleidingsystemen – Deel 1: Algemene eisen.
- NEN 3650-2 (2012). Eisen voor buisleidingsystemen – Deel 2: Aanvullende eisen voor leidingen van staal.
- EN 10219-2 (2006). Cold formed welded structural hollow sections of non-alloy and fine grain steels – Part 2: Tolerances, dimensions and sectional properties.
- EN 14161 (2011). Petroleum and natural gas industries – Pipeline transportation systems.
- ENV 1993-5 (1998). Eurocode 3: Design of steel structures – Part 5: Piling (Prestandard).
- ISO 16708 (2006). Petroleum and natural gas industries - Pipeline transportation systems - Reliability-based limit state methods.
- ISO 3183 (2012). Petroleum and natural gas industries – Steel pipe for pipeline transportation systems.
- ISO 6892-1 (2009). Metallic materials – Tensile testing – Part 1: Method of test at room temperature.
- JCSS (2000). Probabilistic Model Code – Part 3: Material Properties.

Appendices

Appendix A: Database of local buckling test results collected from literature

This appendix presents an overview of the local buckling test results that were collected for the studies in Part I of this study. If available, for all variables the actual values as opposed to nominal values were used in the table.

The tables on the following pages contain fifteen columns:

ID	Specimen identification. Serial number referring to the source document combined with the identification from the original publication
Reference	Source of data point. For specimens marked with an asterisk the data were taken from Stephens et al. (1991)
D	Outer diameter of the specimen
t	Wall thickness of the specimen
D/t	Diameter to wall thickness ratio of the specimen
ϵ_{crit}	Critical strain. Lower bound values are marked with \uparrow
σ_y	Yield stress. In case of distinction between material properties in axial and hoop direction, the yield stress in axial direction is given in the table
σ_u	Ultimate tensile strength in axial direction of the specimen. In case of distinction between material properties in axial and hoop direction, the tensile strength in axial direction is given in the table
P	Pressure. Positive for positive internal pressure, negative for positive external pressure
GW	Girth weld present in the test specimen
GW buc.	Local buckling failure occurred in the immediate vicinity of the girth weld
Manuf.	Manufacturing process of the specimen
Material	Material of the specimen
Loading	Loading conditions of the specimen: bending, axial or combined
L_c/D	Gauge length for critical strain determination normalized by the tube diameter

ID	References	D [mm]	t [mm]	D/t [mm]	ϵ_{crit} [%]	σ_s [MPa]	σ_u [MPa]	P [MPa]	GW	GW Inc.	Manuf.	Material	Loading	L_e/D [mm]
1-1	Bouwkamp et al. (1973, 1974)	1219	12.6	97.0	0.42	438	562	6.49	yes	yes	long. w.	steel	comb.	2.50
1-2	Bouwkamp et al. (1973, 1974)	1219	12.3	99.0	0.47	438	562	6.32	yes	yes	long. w.	steel	comb.	2.50
1-3	Bouwkamp et al. (1973, 1974)	1219	12.4	98.0	0.31	438	562	0.17	yes	yes	long. w.	steel	comb.	2.50
1-4	Bouwkamp et al. (1973, 1974)	1219	12.4	98.6	0.69	438	562	6.55	yes	yes	long. w.	steel	comb.	2.50
1-5	Bouwkamp et al. (1973, 1974)	1219	12.4	98.6	0.27	438	562	1.03	yes	yes	long. w.	steel	comb.	2.50
1-5a	Bouwkamp et al. (1973, 1974)	1219	12.4	98.6	0.38	438	562	6.55	yes	yes	long. w.	steel	comb.	2.50
1-6	Bouwkamp et al. (1973, 1974)	1219	14.9	82.1	0.49	438	562	1.03	yes	yes	long. w.	steel	comb.	2.50
1-7	Bouwkamp et al. (1973, 1974)	1219	11.9	102.8	0.25	468	562	1.03	yes	yes	long. w.	steel	comb.	2.50
2-8	Bouwkamp (1975)	219.1	5.6	39.4	2.08	409	unkn.	0	no	N/A	seamless	steel	axial	unkn.
2-9	Bouwkamp (1975)	323.9	6.4	51.0	1.11	371	unkn.	0	no	N/A	long. w.	steel	axial	unkn.
3-1	Carr et al. (2009)	152.4	7.9	19.3	2.44	517	601	0	yes	yes	seamless	steel	bending	6.00
3-2	Carr et al. (2009)	152.4	7.9	19.3	2.82	517	601	8.6	yes	yes	seamless	steel	bending	6.00
3-3	Carr et al. (2009)	152.4	7.9	19.3	1.68	517	601	9.1	yes	yes	seamless	steel	bending	6.00
3-4	Carr et al. (2009)	152.4	7.9	19.3	2.59	517	601	17.4	yes	yes	seamless	steel	bending	6.00
4-1	Corona and Kyriakides (1988)	31.7	0.9	35.0	2.21	257	unkn.	0	no	N/A	seamless	stainl. st.	bending	unkn.
4-2	Corona and Kyriakides (1988)	31.7	1.2	25.7	0.42	342	unkn.	-17.4	no	N/A	seamless	stainl. st.	bending	unkn.
4-3	Corona and Kyriakides (1988)	31.7	1.2	25.7	0.70	342	unkn.	-13.7	no	N/A	seamless	stainl. st.	bending	unkn.
4-4	Corona and Kyriakides (1988)	31.7	1.2	25.7	1.08	342	unkn.	-8.8	no	N/A	seamless	stainl. st.	bending	unkn.
4-5	Corona and Kyriakides (1988)	31.7	1.2	25.7	1.42	342	unkn.	-5.1	no	N/A	seamless	stainl. st.	bending	unkn.
4-6	Corona and Kyriakides (1988)	31.7	1.2	25.7	1.60	342	unkn.	-2.6	no	N/A	seamless	stainl. st.	bending	unkn.
5-C45P00	DelCol et al. (1998)	762	8.3	91.8	0.38	404	601	0	no	N/A	long. w.	steel	comb.	0.33
5-C45P20	DelCol et al. (1998)	762	8.3	91.8	0.44	404	601	1.8	no	N/A	long. w.	steel	comb.	0.33
5-C45P40	DelCol et al. (1998)	762	8.3	91.8	0.46	404	601	3.6	no	N/A	long. w.	steel	comb.	0.33
5-C45P80	DelCol et al. (1998)	762	8.3	91.8	1.27	404	601	7.2	no	N/A	long. w.	steel	comb.	0.33
6-CP0N	Doney et al. (2000)	762	8.4	90.7	0.23	472	578	0	no	N/A	unkn.	steel	comb.	0.50
6-CP20N-1	Doney et al. (2000)	762	8.4	90.7	0.31	472	578	2.1	no	N/A	unkn.	steel	comb.	0.50
6-CP20N-2	Doney et al. (2000)	762	8.8	87.1	0.25	550	588	1.8	no	N/A	unkn.	steel	comb.	0.50
6-CP40N-2	Doney et al. (2000)	762	8.8	87.1	0.29	550	588	4.3	no	N/A	unkn.	steel	comb.	0.50
6-CP80N-2	Doney et al. (2000)	762	8.5	89.6	0.51	524	593	8.1	no	N/A	unkn.	steel	comb.	0.50
6-T20P40N	Doney et al. (2000)	762	8.5	89.6	0.40	524	593	4.3	no	N/A	unkn.	steel	comb.	0.50
6-KD/t=48	Doney et al. (2000)	610	12.8	47.5	3.42	483	580	16.8	no	N/A	unkn.	steel	comb.	0.50
6-KD/t=92-1	Doney et al. (2000)	610	6.8	90.2	0.47	483	580	0.5	no	N/A	unkn.	steel	comb.	0.50
6-KD/t=92-2	Doney et al. (2000)	610	6.8	90.2	0.46	483	580	0	no	N/A	unkn.	steel	comb.	0.50
6-L178P80BP-4	Doney et al. (2000)	508	8.4	60.7	3.04	448	550	12	no	N/A	unkn.	steel	comb.	0.50
6-L178P80BP-8	Doney et al. (2000)	508	6.1	83.7	0.48	448	550	8.8	no	N/A	unkn.	steel	comb.	0.50
6-CP0W-2	Doney et al. (2000)	762	8.8	87.1	0.25	550	588	0	yes	yes	unkn.	steel	comb.	0.50
6-CP20W	Doney et al. (2000)	762	8.7	87.6	0.25	523	569	2.2	yes	yes	unkn.	steel	comb.	0.50

ID	References	D [mm]	t [mm]	D/t [mm]	ϵ_{crit} [%]	σ_y [MPa]	σ_u [MPa]	P [MPa]	GW	GW h.c.	Manuf.	Material	Loading	L_x/D [mm]
6-CP40W	Dorey et al. (2000)	762	8.7	87.6	0.31	523	569	4.2	yes	yes	unkn.	steel	comb.	0.50
6-CP80W	Dorey et al. (2000)	762	8.7	87.6	0.54	523	569	8.9	yes	yes	unkn.	steel	comb.	0.50
6-T20P40W	Dorey et al. (2000)	762	8.7	87.6	0.30	523	569	4.4	yes	yes	unkn.	steel	comb.	0.50
6-T20P80W	Dorey et al. (2000)	762	8.7	87.6	0.28	523	569	8.5	yes	yes	unkn.	steel	comb.	0.50
6-Sp=0	Dorey et al. (2000)	333	6.8	48.7	0.75	358	429	0	yes	yes	unkn.	steel	comb.	0.50
6-Sp=40	Dorey et al. (2000)	333	6.8	48.7	1.20	358	429	6.3	yes	yes	unkn.	steel	comb.	0.50
6-Sp=80	Dorey et al. (2000)	333	6.8	48.7	1.70	358	429	12.6	yes	yes	unkn.	steel	comb.	0.50
6-CP05	Dorey et al. (2000)	762	8.5	89.8	0.26	502	560	0	yes	yes	unkn.	steel	comb.	0.50
6-CP80S	Dorey et al. (2000)	762	8.5	89.8	0.38	502	560	8.3	yes	yes	unkn.	steel	comb.	0.50
6-L178P80BW-1	Dorey et al. (2000)	508	8.4	60.7	0.44	448	550	12	yes	yes	unkn.	steel	comb.	0.50
6-L178P80BW-2	Dorey et al. (2000)	508	8.4	60.7	1.08	448	550	6	yes	yes	unkn.	steel	comb.	0.50
6-L178P80BW-3	Dorey et al. (2000)	508	8.4	60.5	0.85	448	550	0	yes	yes	unkn.	steel	comb.	0.50
6-L178P80BW-5	Dorey et al. (2000)	508	6.1	83.1	1.13	448	550	8.8	yes	yes	unkn.	steel	comb.	0.50
6-L178P80BW-6	Dorey et al. (2000)	508	6.1	83.4	0.24	448	550	4.4	yes	yes	unkn.	steel	comb.	0.50
6-L178P80BW-7	Dorey et al. (2000)	508	6.1	83.4	0.34	448	550	0	yes	yes	unkn.	steel	comb.	0.50
7-25	Van Douwen et al. (1974)	152.5	1.5	101.7	0.36	342	511	0	no	N/A	long. w.	steel	bending	3.28
7-26	Van Douwen et al. (1974)	152.5	1.5	101.7	0.43	342	511	0	no	N/A	long. w.	steel	bending	3.28
7-24	Van Douwen et al. (1974)	152.5	1.5	101.7	0.49	342	511	1.37	no	N/A	long. w.	steel	bending	3.28
7-28	Van Douwen et al. (1974)	152.5	1.5	101.7	3.45	342	511	7.06	no	N/A	long. w.	steel	bending	3.28
7-27	Van Douwen et al. (1974)	152.5	1.5	101.7	0.43	342	511	-0.1	no	N/A	long. w.	steel	bending	3.28
7-25b	Van Douwen et al. (1974)	122	1.5	81.3	1.48	365	515	0	no	N/A	long. w.	steel	bending	3.85
7-25c	Van Douwen et al. (1974)	122	1.5	81.3	0.43	365	515	0	no	N/A	long. w.	steel	bending	3.85
7-29	Van Douwen et al. (1974)	122	1.5	81.3	1.06	365	515	2.75	no	N/A	long. w.	steel	bending	3.85
7-21c	Van Douwen et al. (1974)	122	1.5	81.3	1.07	365	515	3.53	no	N/A	long. w.	steel	bending	3.85
7-23c	Van Douwen et al. (1974)	122	1.5	81.3	1.46	365	515	7.06	no	N/A	long. w.	steel	bending	3.85
8-F-2	Fowler (1990)	168.1	6.3	26.8	2.27	401	487	0	no	N/A	seamless	steel	comb.	0.01
8-G-4	Fowler (1990)	169.1	7.1	23.7	1.70	324	505	0	no	N/A	long. w.	steel	comb.	0.01
8-I-6	Fowler (1990)	168.7	7	24.1	0.15	308	486	-19.8	no	N/A	seamless	steel	comb.	0.01
8-J-7	Fowler (1990)	168.6	7.2	23.3	0.83	320	490	-20	no	N/A	seamless	steel	comb.	0.01
8-J-8	Fowler (1990)	168.6	7.1	23.7	2.00	320	490	-15.2	no	N/A	seamless	steel	comb.	0.01
8-J-9	Fowler (1990)	168.6	7.1	23.6	2.00	320	490	-15.2	no	N/A	seamless	steel	comb.	0.01
8-K-10	Fowler (1990)	168.7	6.9	24.4	0.64	317	483	-17.6	no	N/A	seamless	steel	comb.	0.01
8-K-11	Fowler (1990)	168.8	6.6	25.6	0.70	317	483	-17.5	no	N/A	seamless	steel	comb.	0.01
8-K-12	Fowler (1990)	168.9	6.8	24.9	2.41	317	483	0	no	N/A	seamless	steel	comb.	0.01
8-L-13	Fowler (1990)	168.8	6.9	24.5	1.70	329	481	-13.2	no	N/A	seamless	steel	comb.	0.01
8-L-14	Fowler (1990)	168.8	7	24.2	1.94	329	481	-11.6	no	N/A	seamless	steel	comb.	0.01
8-L-15	Fowler (1990)	168.8	7	24.1	0.82	329	481	-18.7	no	N/A	seamless	steel	comb.	0.01

ID	References	D [mm]	t [mm]	D/t [mm]	ϵ_{crit} [%]	σ_y [MPa]	σ_u [MPa]	P [MPa]	GW	GW Inc.	Manuf.	Material	Loading	L_e/D [mm]
8-M-16	Fowler (1990)	168.4	7	23.9	1.20	320	501	-16.1	no	N/A	seamless	steel	comb.	0.01
8-M-17	Fowler (1990)	168.5	7.1	23.7	0.54	320	501	-21.5	no	N/A	seamless	steel	comb.	0.01
8-M-18	Fowler (1990)	168.4	7.2	23.6	0.85	320	501	-23	no	N/A	seamless	steel	comb.	0.01
9-B1	Van Foeken and Cressnigt (1998)	509	11.2	45.4	1.50	479	568	0	no	N/A	long. w.	steel	bending	2.95
9-B2	Van Foeken and Cressnigt (1998)	514.7	17.5	29.3	1.10	459	533	0	no	N/A	seamless	steel	bending	2.91
9-B3	Van Foeken and Cressnigt (1998)	507.9	19	26.7	1.74	474	527	0	no	N/A	long. w.	steel	bending	2.95
9-B4	Van Foeken and Cressnigt (1998)	525.6	23.6	22.3	2.36	450	534	0	no	N/A	long. w.	steel	bending	2.85
10-1	Cressnigt (1977)	609.6	6.35	96.0	0.23	357	505	0	yes	no	long. w.	steel	bending	unkn.
11-10a	Jirsa et al. (1972)	273.1	5.9	46.1	1.43	381	unkn.	0	no	N/A	unkn.	steel	bending	unkn.
11-10b	Jirsa et al. (1972)	273.1	8.9	30.7	4.25†	334	unkn.	0	no	N/A	unkn.	steel	bending	unkn.
11-16a	Jirsa et al. (1972)	406.4	6.6	61.5	0.81	339	unkn.	0	no	N/A	unkn.	steel	bending	unkn.
11-20a	Jirsa et al. (1972)	508	6.5	78.4	0.37	377	unkn.	0	no	N/A	unkn.	steel	bending	unkn.
12-K1	COMBITUBE Research Consortium (2015)	820	11	73.5	0.59	443	543	0	no	N/A	spiral w.	steel	comb.	unkn.
12-K2	COMBITUBE Research Consortium (2015)	820	11.1	72.9	0.41	398	500	0	no	N/A	spiral w.	steel	comb.	unkn.
12-K3	COMBITUBE Research Consortium (2015)	820	9.1	89.1	0.38	299	454	0	no	N/A	spiral w.	steel	comb.	unkn.
12-K4	COMBITUBE Research Consortium (2015)	820	7.8	104.1	0.28	462	564	0	no	N/A	spiral w.	steel	comb.	unkn.
12-K5	COMBITUBE Research Consortium (2015)	820	7.5	108.3	0.12	418	563	0	no	N/A	spiral w.	steel	comb.	unkn.
12-K6	COMBITUBE Research Consortium (2015)	863	8.4	101.7	0.29	415	527	0	no	N/A	spiral w.	steel	comb.	unkn.
12-K7	COMBITUBE Research Consortium (2015)	863	8.4	101.7	0.26	444	527	0	yes	no	spiral w.	steel	comb.	unkn.
12-K8	COMBITUBE Research Consortium (2015)	863	8.6	99.3	0.23	408	515	0	no	N/A	spiral w.	steel	comb.	unkn.
13-A1	Kang et al. (2007)	711	19	37.4	2.42	553	630	0	no	N/A	long. w.	steel	bending	1.13
13-A2	Kang et al. (2007)	711	19	37.4	2.23	553	630	0	no	N/A	long. w.	steel	bending	1.13
13-B1	Kang et al. (2007)	711	19	37.4	1.96	553	630	0	no	N/A	long. w.	steel	axial	1.13
13-B2	Kang et al. (2007)	711	19	37.4	1.86	553	630	0	no	N/A	long. w.	steel	axial	1.13
14-1	Kimura et al. (1980)	355.6	16.3	21.8	3.48†	448	unkn.	0	no	N/A	unkn.	steel	bending	unkn.
14-2	Kimura et al. (1980)	355.6	6.3	56.4	1.10†	448	unkn.	0	no	N/A	unkn.	steel	bending	unkn.
14-3	Kimura et al. (1980)	609.6	7.8	78.5	0.70	448	unkn.	0	no	N/A	unkn.	steel	bending	unkn.
14-4	Kimura et al. (1980)	609.6	6.3	96.8	0.20	448	unkn.	0	no	N/A	unkn.	steel	bending	unkn.
15-3	Korol (1979)	168.3	4.8	35.2	1.00	369	unkn.	0	no	N/A	long. w.	steel	bending	0.01
15-4	Korol (1979)	508	6.4	80.0	0.27†	375	unkn.	0	no	N/A	long. w.	steel	bending	0.01
15-5	Korol (1979)	273.1	5.6	49.1	0.97	306	unkn.	0	no	N/A	long. w.	steel	bending	0.01
15-8	Korol (1979)	406.4	6.4	64.0	0.66	309	unkn.	0	no	N/A	long. w.	steel	bending	0.01
15-9	Korol (1979)	114.3	4	28.8	1.20	309	unkn.	0	no	N/A	long. w.	steel	bending	0.01
15-10	Korol (1979)	273.1	5.6	49.1	0.98	306	unkn.	0	no	N/A	long. w.	steel	bending	0.01
15-11	Korol (1979)	508	6.4	80.0	0.68†	361	unkn.	0	no	N/A	long. w.	steel	bending	0.01
16-1	Kyriakides and Ju (1992)	31.8	0.53	60.5	0.79	299	unkn.	0	no	N/A	seamless aluminium	bending	unkn.	
16-2	Kyriakides and Ju (1992)	38.1	0.72	52.6	0.95	299	unkn.	0	no	N/A	seamless aluminium	bending	unkn.	

ID	References	D [mm]	t [mm]	D/t [mm]	ϵ_{crit} [%]	σ_y [MPa]	σ_u [MPa]	P [MPa]	GW	hac.	Manuf.	Material	Loading	L_x/D [mm]
16-3	Kyriakides and Ju (1992)	25.4	0.51	50.0	1.01	308	unkn.	0	no	N/A	seamless aluminium	bending	unkn.	
16-4	Kyriakides and Ju (1992)	31.8	0.72	44.0	1.26	303	unkn.	0	no	N/A	seamless aluminium	bending	unkn.	
16-5	Kyriakides and Ju (1992)	35	0.91	38.5	1.32	285	unkn.	0	no	N/A	seamless aluminium	bending	unkn.	
16-6	Kyriakides and Ju (1992)	31.8	0.89	35.7	1.49	282	unkn.	0	no	N/A	seamless aluminium	bending	unkn.	
16-7	Kyriakides and Ju (1992)	28.6	0.89	32.2	1.58	286	unkn.	0	no	N/A	seamless aluminium	bending	unkn.	
16-8	Kyriakides and Ju (1992)	25.3	0.9	28.2	1.72	303	unkn.	0	no	N/A	seamless aluminium	bending	unkn.	
16-9	Kyriakides and Ju (1992)	31.8	1.26	25.3	2.03	285	unkn.	0	no	N/A	seamless aluminium	bending	unkn.	
16-10	Kyriakides and Ju (1992)	31.8	1.5	21.2	2.55	284	unkn.	0	no	N/A	seamless aluminium	bending	unkn.	
16-11	Kyriakides and Ju (1992)	31.8	1.63	19.5	2.79	309	unkn.	0	no	N/A	seamless aluminium	bending	unkn.	
17-2	Kyriakides and Shaw (1982)	31.8	0.9	35.7	0.15	unkn.	unkn.	-3.15	no	N/A	seamless aluminium	bending	unkn.	
17-3	Kyriakides and Shaw (1982)	31.8	0.9	35.7	0.23	unkn.	unkn.	-2.97	no	N/A	seamless aluminium	bending	unkn.	
17-4	Kyriakides and Shaw (1982)	31.8	0.9	35.7	0.34	unkn.	unkn.	-2.84	no	N/A	seamless aluminium	bending	unkn.	
17-5	Kyriakides and Shaw (1982)	31.8	0.9	35.7	0.47	unkn.	unkn.	-2.55	no	N/A	seamless aluminium	bending	unkn.	
17-6	Kyriakides and Shaw (1982)	31.8	0.9	35.7	0.49	unkn.	unkn.	-2.21	no	N/A	seamless aluminium	bending	unkn.	
17-7	Kyriakides and Shaw (1982)	31.8	0.9	35.7	0.63	unkn.	unkn.	-2.05	no	N/A	seamless aluminium	bending	unkn.	
17-8	Kyriakides and Shaw (1982)	31.8	0.9	35.7	0.65	unkn.	unkn.	-1.91	no	N/A	seamless aluminium	bending	unkn.	
17-9	Kyriakides and Shaw (1982)	31.8	0.9	35.7	0.75	unkn.	unkn.	-1.72	no	N/A	seamless aluminium	bending	unkn.	
17-10	Kyriakides and Shaw (1982)	31.8	0.9	35.7	0.67	unkn.	unkn.	-1.57	no	N/A	seamless aluminium	bending	unkn.	
17-11	Kyriakides and Shaw (1982)	31.8	0.9	35.7	0.79	unkn.	unkn.	-1.47	no	N/A	seamless aluminium	bending	unkn.	
17-12	Kyriakides and Shaw (1982)	31.8	0.9	35.7	0.75	unkn.	unkn.	-1.33	no	N/A	seamless aluminium	bending	unkn.	
17-13	Kyriakides and Shaw (1982)	31.8	0.9	35.7	0.84	unkn.	unkn.	-1.29	no	N/A	seamless aluminium	bending	unkn.	
17-14	Kyriakides and Shaw (1982)	31.8	0.9	35.7	0.86	unkn.	unkn.	-1.17	no	N/A	seamless aluminium	bending	unkn.	
17-15	Kyriakides and Shaw (1982)	31.8	0.9	35.7	0.86	unkn.	unkn.	-1.08	no	N/A	seamless aluminium	bending	unkn.	
17-16	Kyriakides and Shaw (1982)	31.8	0.9	35.7	0.89	unkn.	unkn.	-1.01	no	N/A	seamless aluminium	bending	unkn.	
17-17	Kyriakides and Shaw (1982)	31.8	0.9	35.7	0.98	unkn.	unkn.	-0.96	no	N/A	seamless aluminium	bending	unkn.	
17-18	Kyriakides and Shaw (1982)	31.8	0.9	35.7	1.06	unkn.	unkn.	-1.17	no	N/A	seamless aluminium	bending	unkn.	
17-19	Kyriakides and Shaw (1982)	31.8	0.9	35.7	1.01	unkn.	unkn.	-0.83	no	N/A	seamless aluminium	bending	unkn.	
17-20	Kyriakides and Shaw (1982)	31.8	0.9	35.7	0.97	unkn.	unkn.	-0.71	no	N/A	seamless aluminium	bending	unkn.	
17-21	Kyriakides and Shaw (1982)	31.8	0.9	35.7	1.09	unkn.	unkn.	-0.65	no	N/A	seamless aluminium	bending	unkn.	
17-22	Kyriakides and Shaw (1982)	31.8	0.9	35.7	1.03	unkn.	unkn.	-0.51	no	N/A	seamless aluminium	bending	unkn.	
17-23	Kyriakides and Shaw (1982)	31.8	0.9	35.7	1.25	unkn.	unkn.	0	no	N/A	seamless aluminium	bending	unkn.	
17-24	Kyriakides and Shaw (1982)	31.8	0.9	35.7	1.47	unkn.	unkn.	0	no	N/A	seamless aluminium	bending	unkn.	
18-1	Kyriakides and Shaw (1987)	31.8	0.9	35.7	1.42	297	unkn.	0	no	N/A	seamless aluminium	bending	unkn.	
18-2	Kyriakides and Shaw (1987)	38.1	0.9	35.7	1.89	579	unkn.	0	no	N/A	seamless stamI. st.	bending	unkn.	
19-15	Limamet al. (2008, 2010)	38.2	0.7	51.6	1.27	224	unkn.	0	no	N/A	seamless stamI. st.	bending	unkn.	
19-27	Limamet al. (2008, 2010)	38.2	0.7	51.8	2.47	220	unkn.	1.4	no	N/A	seamless stamI. st.	bending	unkn.	
19-17	Limamet al. (2008, 2010)	38.2	0.7	51.6	3.30	224	unkn.	2.1	no	N/A	seamless stamI. st.	bending	unkn.	

ID	References	D [mm]	t [mm]	D/t [mm]	ϵ_{crit} [%]	σ_y [MPa]	σ_u [MPa]	P [MPa]	GW	GW Inc.	Manuf.	Material	Loading	L_e/D [mm]
19-20	Linaмет et al. (2008, 2010)	38.1	0.7	52.0	4.12	220	unkn.	3.1	no	N/A	seamless	staml. st.	bending	unkn.
19-16	Linaмет et al. (2008, 2010)	38.2	0.7	51.6	4.48	224	unkn.	4.1	no	N/A	seamless	staml. st.	bending	unkn.
19-25	Linaмет et al. (2008, 2010)	38.2	0.7	51.8	5.22	229	unkn.	4.8	no	N/A	seamless	staml. st.	bending	unkn.
19-45	Linaмет et al. (2008, 2010)	38.2	0.8	50.6	5.86	240	unkn.	5.2	no	N/A	seamless	staml. st.	bending	unkn.
19-46	Linaмет et al. (2008, 2010)	38.2	0.8	50.6	6.97	240	unkn.	5.9	no	N/A	seamless	staml. st.	bending	unkn.
19-23	Linaмет et al. (2008, 2010)	38.2	0.7	51.7	7.03	229	unkn.	6.2	no	N/A	seamless	staml. st.	bending	unkn.
19-26	Linaмет et al. (2008, 2010)	38.2	0.7	51.6	7.54	229	unkn.	6.9	no	N/A	seamless	staml. st.	bending	unkn.
19-28	Linaмет et al. (2008, 2010)	38.2	0.7	52.0	7.64	220	unkn.	7.6	no	N/A	seamless	staml. st.	bending	unkn.
20-DGA.508	Mohareb et al. (1994)	508	7.9	64.3	2.81	386	unkn.	9.9	no	N/A	long. w.	steel	comb.	unkn.
20-DLR508	Mohareb et al. (1994)	508	7.9	64.3	2.00	386	unkn.	9.9	no	N/A	long. w.	steel	comb.	unkn.
20-UGA.324	Mohareb et al. (1994)	324	6.4	51.0	2.20	359	unkn.	0	no	N/A	long. w.	steel	comb.	unkn.
20-HGA.324	Mohareb et al. (1994)	324	6.4	51.0	2.36	359	unkn.	5.2	no	N/A	long. w.	steel	comb.	unkn.
20-DGA.324	Mohareb et al. (1994)	324	6.4	51.0	3.24	359	unkn.	10.3	no	N/A	long. w.	steel	comb.	unkn.
21-1	Murphey and Langner (1975)*	0	0	17.7	3.26	unkn.	unkn.	0	no	N/A	unkn.	steel	unkn.	unkn.
21-2	Murphey and Langner (1975)*	0	0	17.8	3.75	unkn.	unkn.	0	no	N/A	unkn.	steel	unkn.	unkn.
21-3	Murphey and Langner (1975)*	0	0	17.9	4.19	unkn.	unkn.	0	no	N/A	unkn.	steel	unkn.	unkn.
21-4	Murphey and Langner (1975)*	0	0	17.9	4.53	unkn.	unkn.	0	no	N/A	unkn.	steel	unkn.	unkn.
21-5	Murphey and Langner (1975)*	0	0	17.9	5.20	unkn.	unkn.	0	no	N/A	unkn.	steel	unkn.	unkn.
21-6	Murphey and Langner (1975)*	0	0	26.6	2.51	unkn.	unkn.	0	no	N/A	unkn.	steel	unkn.	unkn.
21-7	Murphey and Langner (1975)*	0	0	26.7	2.93	unkn.	unkn.	0	no	N/A	unkn.	steel	unkn.	unkn.
21-8	Murphey and Langner (1975)*	0	0	26.7	3.13	unkn.	unkn.	0	no	N/A	unkn.	steel	unkn.	unkn.
21-9	Murphey and Langner (1975)*	0	0	26.7	3.42	unkn.	unkn.	0	no	N/A	unkn.	steel	unkn.	unkn.
21-10	Murphey and Langner (1975)*	0	0	26.8	3.60	unkn.	unkn.	0	no	N/A	unkn.	steel	unkn.	unkn.
21-11	Murphey and Langner (1975)*	0	0	26.9	3.91	unkn.	unkn.	0	no	N/A	unkn.	steel	unkn.	unkn.
21-12	Murphey and Langner (1975)*	0	0	53.7	0.55	unkn.	unkn.	0	no	N/A	unkn.	steel	unkn.	unkn.
21-13	Murphey and Langner (1975)*	0	0	53.7	0.64	unkn.	unkn.	0	no	N/A	unkn.	steel	unkn.	unkn.
21-14	Murphey and Langner (1975)*	0	0	53.6	0.81	unkn.	unkn.	0	no	N/A	unkn.	steel	unkn.	unkn.
21-15	Murphey and Langner (1975)*	0	0	53.6	1.13	unkn.	unkn.	0	no	N/A	unkn.	steel	unkn.	unkn.
21-16	Murphey and Langner (1975)*	0	0	53.5	1.37	unkn.	unkn.	0	no	N/A	unkn.	steel	unkn.	unkn.
21-17	Murphey and Langner (1975)*	0	0	53.7	1.71	unkn.	unkn.	0	no	N/A	unkn.	steel	unkn.	unkn.
21-18	Murphey and Langner (1975)*	0	0	19.7	2.75	unkn.	unkn.	0	no	N/A	unkn.	steel	unkn.	unkn.
21-19	Murphey and Langner (1975)*	0	0	19.9	3.26	unkn.	unkn.	0	no	N/A	unkn.	steel	unkn.	unkn.
21-20	Murphey and Langner (1975)*	0	0	19.9	3.73	unkn.	unkn.	0	no	N/A	unkn.	steel	unkn.	unkn.
21-21	Murphey and Langner (1975)*	0	0	19.7	4.30	unkn.	unkn.	0	no	N/A	unkn.	steel	unkn.	unkn.
21-22	Murphey and Langner (1975)*	0	0	19.7	4.58	unkn.	unkn.	0	no	N/A	unkn.	steel	unkn.	unkn.
21-23	Murphey and Langner (1975)*	0	0	19.7	4.84	unkn.	unkn.	0	no	N/A	unkn.	steel	unkn.	unkn.
21-24	Murphey and Langner (1975)*	0	0	19.7	5.02	unkn.	unkn.	0	no	N/A	unkn.	steel	unkn.	unkn.

ID	References	D [mm]	t [mm]	D/t [mm]	ε_{crit} [%]	σ_y [MPa]	σ_u [MPa]	P [MPa]	GW	hac.	Manuf.	Material	Loading	L_e/D [mm]
21-25	Murphey and Langner (1975)*	0	0	19.7	5.22	unkn.	unkn.	0	no	N/A	unkn.	steel	unkn.	unkn.
21-26	Murphey and Langner (1975)*	0	0	19.8	5.44	unkn.	unkn.	0	no	N/A	unkn.	steel	unkn.	unkn.
21-27	Murphey and Langner (1975)*	0	0	19.8	6.18	unkn.	unkn.	0	no	N/A	unkn.	steel	unkn.	unkn.
21-28	Murphey and Langner (1975)*	0	0	19.8	6.43	unkn.	unkn.	0	no	N/A	unkn.	steel	unkn.	unkn.
21-29	Murphey and Langner (1975)*	0	0	19.8	6.68	unkn.	unkn.	0	no	N/A	unkn.	steel	unkn.	unkn.
21-30	Murphey and Langner (1975)*	0	0	19.8	7.30	unkn.	unkn.	0	no	N/A	unkn.	steel	unkn.	unkn.
21-31	Murphey and Langner (1975)*	0	0	21.0	4.47	unkn.	unkn.	0	no	N/A	unkn.	steel	unkn.	unkn.
21-32	Murphey and Langner (1975)*	0	0	21.0	4.92	unkn.	unkn.	0	no	N/A	unkn.	steel	unkn.	unkn.
21-33	Murphey and Langner (1975)*	0	0	28.9	3.79	unkn.	unkn.	0	no	N/A	unkn.	steel	unkn.	unkn.
21-34	Murphey and Langner (1975)*	0	0	28.8	4.11	unkn.	unkn.	0	no	N/A	unkn.	steel	unkn.	unkn.
21-35	Murphey and Langner (1975)*	0	0	35.6	2.06	unkn.	unkn.	0	no	N/A	unkn.	steel	unkn.	unkn.
21-36	Murphey and Langner (1975)*	0	0	35.5	2.88	unkn.	unkn.	0	no	N/A	unkn.	steel	unkn.	unkn.
21-37	Murphey and Langner (1975)*	0	0	35.6	2.99	unkn.	unkn.	0	no	N/A	unkn.	steel	unkn.	unkn.
21-38	Murphey and Langner (1975)*	0	0	35.8	3.15	unkn.	unkn.	0	no	N/A	unkn.	steel	unkn.	unkn.
21-39	Murphey and Langner (1975)*	0	0	37.1	1.47	unkn.	unkn.	0	no	N/A	unkn.	steel	unkn.	unkn.
21-40	Murphey and Langner (1975)*	0	0	37.2	1.66	unkn.	unkn.	0	no	N/A	unkn.	steel	unkn.	unkn.
21-41	Murphey and Langner (1975)*	0	0	37.1	1.98	unkn.	unkn.	0	no	N/A	unkn.	steel	unkn.	unkn.
21-42	Murphey and Langner (1975)*	0	0	38.6	1.91	unkn.	unkn.	0	no	N/A	unkn.	steel	unkn.	unkn.
21-43	Murphey and Langner (1975)*	0	0	38.5	2.38	unkn.	unkn.	0	no	N/A	unkn.	steel	unkn.	unkn.
21-44	Murphey and Langner (1975)*	0	0	55.0	1.21	unkn.	unkn.	0	no	N/A	unkn.	steel	unkn.	unkn.
21-45	Murphey and Langner (1975)*	0	0	55.0	1.95	unkn.	unkn.	0	no	N/A	unkn.	steel	unkn.	unkn.
21-46	Murphey and Langner (1975)*	0	0	80.9	0.23	unkn.	unkn.	0	no	N/A	unkn.	steel	unkn.	unkn.
21-47	Murphey and Langner (1975)*	0	0	81.0	0.39	unkn.	unkn.	0	no	N/A	unkn.	steel	unkn.	unkn.
21-48	Murphey and Langner (1975)*	0	0	80.9	0.75	unkn.	unkn.	0	no	N/A	unkn.	steel	unkn.	unkn.
21-49	Murphey and Langner (1975)*	0	0	89.2	0.34	unkn.	unkn.	0	no	N/A	unkn.	steel	unkn.	unkn.
21-50	Murphey and Langner (1975)*	0	0	89.2	0.39	unkn.	unkn.	0	no	N/A	unkn.	steel	unkn.	unkn.
21-51	Murphey and Langner (1975)*	0	0	89.1	0.57	unkn.	unkn.	0	no	N/A	unkn.	steel	unkn.	unkn.
21-52	Murphey and Langner (1975)*	0	0	89.1	0.64	unkn.	unkn.	0	no	N/A	unkn.	steel	unkn.	unkn.
21-53	Murphey and Langner (1975)*	0	0	89.1	0.71	unkn.	unkn.	0	no	N/A	unkn.	steel	unkn.	unkn.
21-54	Murphey and Langner (1975)*	0	0	96.9	0.50	unkn.	unkn.	0	no	N/A	unkn.	steel	unkn.	unkn.
21-55	Murphey and Langner (1975)*	0	0	96.7	0.56	unkn.	unkn.	0	no	N/A	unkn.	steel	unkn.	unkn.
21-56	Murphey and Langner (1975)*	0	0	96.7	0.61	unkn.	unkn.	0	no	N/A	unkn.	steel	unkn.	unkn.
21-57	Murphey and Langner (1975)*	0	0	109.1	0.44	unkn.	unkn.	0	no	N/A	unkn.	steel	unkn.	unkn.
21-58	Murphey and Langner (1975)*	0	0	109.1	0.48	unkn.	unkn.	0	no	N/A	unkn.	steel	unkn.	unkn.
21-59	Murphey and Langner (1975)*	0	0	109.2	0.57	unkn.	unkn.	0	no	N/A	unkn.	steel	unkn.	unkn.
22-1	Nomoto et al. (1986)	98.3	2.3	43.7	1.15†	150	unkn.	0	no	N/A	unkn.	aluminium bending	0.01	
22-2	Nomoto et al. (1986)	126.9	3.1	41.5	1.39	184	unkn.	0	no	N/A	unkn.	aluminium bending	0.01	

ID	References	D [mm]	t [mm]	D/t [mm]	ϵ_{crit} [%]	σ_y [MPa]	σ_u [MPa]	P [MPa]	GW	GW Inc.	Manuf.	Material	Loading	L_e/D [mm]
22-3	Nomoto et al. (1986)	112	2.1	52.3	1.54	207	unkn.	0	no	N/A	unkn.	stainl. st.	bending	0.01
22-4	Nomoto et al. (1986)	98.6	2.9	33.5	1.83	237	unkn.	0	no	N/A	unkn.	stainl. st.	bending	0.01
23-ST01	Prion and Birkmoe (1992)	450	6.5	69.2	0.46	304	unkn.	0	yes	yes	long. w.	steel	axial	unkn.
23-ST02	Prion and Birkmoe (1992)	450	6.5	69.2	0.42	304	unkn.	0	yes	yes	long. w.	steel	axial	unkn.
23-ST07	Prion and Birkmoe (1992)	450	4.5	100.0	0.28	254	unkn.	0	yes	no	long. w.	steel	axial	unkn.
23-ST08	Prion and Birkmoe (1992)	450	4.5	100.0	0.38	254	unkn.	0	yes	no	long. w.	steel	axial	unkn.
23-ST13	Prion and Birkmoe (1992)	450	7.3	61.6	0.31	450	unkn.	0	yes	no	long. w.	steel	axial	unkn.
24-1	Reddy (1979)	0	0	76.5	0.74	unkn.	unkn.	0	no	N/A	unkn.	steel	bending	unkn.
24-2	Reddy (1979)	0	0	79.8	0.77	unkn.	unkn.	0	no	N/A	unkn.	steel	bending	unkn.
24-3	Reddy (1979)	0	0	66.8	0.91	unkn.	unkn.	0	no	N/A	unkn.	steel	bending	unkn.
24-4	Reddy (1979)	0	0	61.5	0.88	unkn.	unkn.	0	no	N/A	unkn.	steel	bending	unkn.
24-5	Reddy (1979)	0	0	51.3	1.48	unkn.	unkn.	0	no	N/A	unkn.	steel	bending	unkn.
24-6	Reddy (1979)	0	0	51.4	1.23	unkn.	unkn.	0	no	N/A	unkn.	steel	bending	unkn.
24-7	Reddy (1979)	0	0	46.2	1.22	unkn.	unkn.	0	no	N/A	unkn.	steel	bending	unkn.
24-8	Reddy (1979)	0	0	46.3	1.23	unkn.	unkn.	0	no	N/A	unkn.	steel	bending	unkn.
24-9	Reddy (1979)	0	0	46.3	1.48	unkn.	unkn.	0	no	N/A	unkn.	steel	bending	unkn.
24-10	Reddy (1979)	0	0	42.2	1.66	unkn.	unkn.	0	no	N/A	unkn.	steel	bending	unkn.
24-A1	Reddy (1979)	0	0	55.4	0.75	unkn.	unkn.	0	no	N/A	unkn.	steel	bending	unkn.
24-A2	Reddy (1979)	0	0	57.1	0.68	unkn.	unkn.	0	no	N/A	unkn.	aluminium	bending	unkn.
24-A3	Reddy (1979)	0	0	45.9	1.00	unkn.	unkn.	0	no	N/A	unkn.	aluminium	bending	unkn.
24-A4	Reddy (1979)	0	0	46.1	1.07	unkn.	unkn.	0	no	N/A	unkn.	aluminium	bending	unkn.
24-A5	Reddy (1979)	0	0	36.9	1.96	unkn.	unkn.	0	no	N/A	unkn.	aluminium	bending	unkn.
24-A6	Reddy (1979)	0	0	36.9	1.24	unkn.	unkn.	0	no	N/A	unkn.	aluminium	bending	unkn.
24-A7	Reddy (1979)	0	0	34.7	1.41	unkn.	unkn.	0	no	N/A	unkn.	aluminium	bending	unkn.
24-A8	Reddy (1979)	0	0	34.7	1.30	unkn.	unkn.	0	no	N/A	unkn.	aluminium	bending	unkn.
24-A9	Reddy (1979)	0	0	34.7	1.04	unkn.	unkn.	0	no	N/A	unkn.	aluminium	bending	unkn.
25-A3	SBRCURnet (2013)	509.6	4.87	104.6	0.25	307	unkn.	0	no	N/A	spiral w.	steel	bending	unkn.
25-A4	SBRCURnet (2013)	508.8	4.91	103.6	0.42	307	unkn.	0	no	N/A	spiral w.	steel	bending	unkn.
25-A6	SBRCURnet (2013)	509.2	4.85	105.0	0.35	307	unkn.	0	no	N/A	spiral w.	steel	bending	unkn.
25-B2	SBRCURnet (2013)	515.6	7.15	72.1	0.60	488	unkn.	0	no	N/A	long. w.	steel	bending	unkn.
25-B5	SBRCURnet (2013)	514.6	6.91	74.5	0.66	488	unkn.	0	no	N/A	long. w.	steel	bending	unkn.
25-B6	SBRCURnet (2013)	507.8	5.99	84.8	0.44	488	unkn.	0	no	N/A	long. w.	steel	bending	unkn.
25-C2	SBRCURnet (2013)	614.1	6.03	101.8	0.45	312	unkn.	0	no	N/A	spiral w.	steel	bending	unkn.
25-C3	SBRCURnet (2013)	613.1	6.01	102.0	0.47	312	unkn.	0	no	N/A	spiral w.	steel	bending	unkn.
25-C6	SBRCURnet (2013)	612.3	6	102.1	0.58	312	unkn.	0	no	N/A	spiral w.	steel	bending	unkn.
25-D1	SBRCURnet (2013)	706.3	6.02	117.3	0.39	503	unkn.	0	yes	no	long. w.	steel	bending	unkn.
25-D2	SBRCURnet (2013)	706.4	5.94	118.9	0.38	503	unkn.	0	yes	no	long. w.	steel	bending	unkn.

ID	References	D [mm]	t [mm]	D/t [mm]	ϵ_{crit} [%]	σ_y [MPa]	σ_u [MPa]	P [MPa]	GW	GW bac.	Manuf.	Material	Loading	L_x/D [mm]
25-D3	SBRCUrnet (2013)	708.1	6.15	115.1	0.31	503	unkn.	0	yes	no	long. w.	steel	bending	unkn.
26-P1	Schroeder et al. (1974)	0	0	21.0	0.20†	198	unkn.	0	no	N/A	seamless	steel	bending	0.01
26-P3	Schroeder et al. (1974)	0	0	41.0	0.43†	194	unkn.	5.17	no	N/A	seamless	steel	bending	0.01
26-P4	Schroeder et al. (1974)	0	0	51.0	0.46†	191	unkn.	0	no	N/A	seamless	steel	bending	0.01
27-1	Sherman (1976)	272.2	14.86	18.3	0.91†	290	unkn.	0	no	N/A	seamless	steel	bending	0.01
27-4	Sherman (1976)	273.9	7.8	35.1	0.93†	304	unkn.	0	no	N/A	seamless	steel	bending	0.01
27-7	Sherman (1976)	273.9	5.61	48.8	1.09†	404	479	0	no	N/A	long. w.	steel	bending	0.01
27-10	Sherman (1976)	273.1	4.93	55.4	1.22†	421	unkn.	0	no	N/A	long. w.	steel	bending	0.01
27-13	Sherman (1976)	273.1	3.53	77.4	0.89	288	313	0	no	N/A	long. w.	steel	bending	0.01
27-17	Sherman (1976)	272.9	2.46	110.8	0.45	310	unkn.	0	no	N/A	long. w.	steel	bending	0.01
28-A2	Sherman (1983, 1984)*	456.9	18.7	24.4	4.29	299	unkn.	0	yes	unkn.	long. w.	steel	unkn.	unkn.
28-A3	Sherman (1983, 1984)*	458.5	16.5	27.7	4.39	338	unkn.	0	yes	unkn.	long. w.	steel	unkn.	unkn.
28-A4	Sherman (1983, 1984)*	458	13.1	34.9	1.79	299	unkn.	0	yes	unkn.	long. w.	steel	unkn.	unkn.
28-A5	Sherman (1983, 1984)*	457.7	9.9	46.1	0.56	294	unkn.	0	yes	unkn.	long. w.	steel	unkn.	unkn.
28-A6	Sherman (1983, 1984)*	457.7	6.9	66.7	0.22	325	unkn.	0	yes	unkn.	long. w.	steel	unkn.	unkn.
28-A6R	Sherman (1983, 1984)*	455.7	6.2	73.5	0.54	314	unkn.	0	yes	unkn.	long. w.	steel	unkn.	unkn.
28-A6L	Sherman (1983, 1984)*	456.2	6.4	71.6	0.19	309	unkn.	0	yes	unkn.	long. w.	steel	unkn.	unkn.
28-A7	Sherman (1983, 1984)*	609.9	12.9	47.2	0.84	314	unkn.	0	yes	unkn.	long. w.	steel	unkn.	unkn.
28-A8	Sherman (1983, 1984)*	609.6	6.8	89.9	0.30	373	unkn.	0	yes	unkn.	long. w.	steel	unkn.	unkn.
28-B2	Sherman (1983, 1984)*	458	19.6	23.4	4.74	390	unkn.	0	yes	unkn.	long. w.	steel	unkn.	unkn.
28-B2R	Sherman (1983, 1984)*	455.4	19.9	22.9	4.80	368	unkn.	0	yes	unkn.	long. w.	steel	unkn.	unkn.
28-B3	Sherman (1983, 1984)*	457.7	16.4	27.9	1.12	424	unkn.	0	yes	unkn.	long. w.	steel	unkn.	unkn.
28-B4	Sherman (1983, 1984)*	458	13.3	34.5	1.20	411	unkn.	0	yes	unkn.	long. w.	steel	unkn.	unkn.
28-B5	Sherman (1983, 1984)*	458	10	45.6	0.89	410	unkn.	0	yes	unkn.	long. w.	steel	unkn.	unkn.
28-B6	Sherman (1983, 1984)*	458.5	6.8	67.6	0.42	434	unkn.	0	yes	unkn.	long. w.	steel	unkn.	unkn.
28-B7	Sherman (1983, 1984)*	610.1	13.6	44.7	1.02	405	unkn.	0	yes	unkn.	long. w.	steel	unkn.	unkn.
28-B7R	Sherman (1983, 1984)*	607.8	13.8	44.1	1.38	379	unkn.	0	yes	unkn.	long. w.	steel	unkn.	unkn.
28-B8	Sherman (1983, 1984)*	609.1	7	86.6	0.30	430	unkn.	0	yes	unkn.	long. w.	steel	unkn.	unkn.
28-B9	Sherman (1983, 1984)*	607.6	10	60.6	0.50	401	unkn.	0	yes	unkn.	long. w.	steel	unkn.	unkn.
29-A	Shitamato et al. (2012)	610	15.9	38.4	2.61	556	729	20.3	no	N/A	long. W.	steel	comb.	8.00
29-B	Shitamato et al. (2012)	611	15.7	38.9	3.52	590	743	20.3	no	N/A	long. W.	steel	comb.	8.00
30-1	Sorenson (1970)*	507.5	6.3	80.9	0.42	428	unkn.	0	no	N/A	unkn.	unkn.	unkn.	unkn.
30-3	Sorenson (1970)*	507.5	7.1	71.9	0.49	368	unkn.	0	no	N/A	unkn.	unkn.	unkn.	unkn.
30-5	Sorenson (1970)*	508.6	8.2	62.0	1.38	361	unkn.	0	no	N/A	unkn.	unkn.	unkn.	unkn.
30-8	Sorenson (1970)*	509.6	9.2	55.3	1.01	369	unkn.	0	no	N/A	unkn.	unkn.	unkn.	unkn.
30-9	Sorenson (1970)*	508.1	9.9	51.4	1.24	467	unkn.	0	no	N/A	unkn.	unkn.	unkn.	unkn.
30-11	Sorenson (1970)*	508.5	10.5	48.6	1.38	336	unkn.	0	no	N/A	unkn.	unkn.	unkn.	unkn.

ID	References	D [mm]	t [mm]	D/t [mm]	ϵ_{crit} [%]	σ_y [MPa]	σ_u [MPa]	P [MPa]	GW	GW Inc.	Manuf.	Material	Loading	L_e/D [mm]
30-12	Sorenson (1970)*	508.1	12.8	39.8	2.06	397	unkn.	0	no	N/A	unkn.	unkn.	unkn.	unkn.
30-4	Sorenson (1970)*	34.2	1.2	28.2	1.82	538	unkn.	0	no	N/A	unkn.	unkn.	unkn.	unkn.
30-5	Sorenson (1970)*	34.1	1.1	29.8	1.92	538	unkn.	0	no	N/A	unkn.	unkn.	unkn.	unkn.
30-6	Sorenson (1970)*	33.4	0.8	40.5	1.15	540	unkn.	0	no	N/A	unkn.	unkn.	unkn.	unkn.
30-7	Sorenson (1970)*	33.4	0.8	42.5	1.23	538	unkn.	0	no	N/A	unkn.	unkn.	unkn.	unkn.
30-8	Sorenson (1970)*	33	0.6	54.6	0.88	540	unkn.	0	no	N/A	unkn.	unkn.	unkn.	unkn.
30-9	Sorenson (1970)*	33.1	0.6	52.5	0.97	540	unkn.	0	no	N/A	unkn.	unkn.	unkn.	unkn.
30-10A	Sorenson (1970)*	32.9	0.6	59.1	0.70	534	unkn.	0	no	N/A	unkn.	unkn.	unkn.	unkn.
30-11	Sorenson (1970)*	32.7	0.5	73.1	0.51	540	unkn.	0	no	N/A	unkn.	unkn.	unkn.	unkn.
30-12	Sorenson (1970)*	32.7	0.4	75.2	0.77	540	unkn.	0	no	N/A	unkn.	unkn.	unkn.	unkn.
30-12B	Sorenson (1970)*	32.6	0.4	75.2	0.35	535	unkn.	0	no	N/A	unkn.	unkn.	unkn.	unkn.
30-13	Sorenson (1970)*	32.5	0.4	94.6	0.22	unkn.	unkn.	0	no	N/A	unkn.	unkn.	unkn.	unkn.
30-15	Sorenson (1970)*	32.5	0.3	99.7	0.45	538	unkn.	0	no	N/A	unkn.	unkn.	unkn.	unkn.
30-16	Sorenson (1970)*	32.4	0.3	102.0	0.24	535	unkn.	0	no	N/A	unkn.	unkn.	unkn.	unkn.
30-16A	Sorenson (1970)*	32.3	0.3	116.0	0.18	unkn.	unkn.	0	no	N/A	unkn.	unkn.	unkn.	unkn.
30-17	Sorenson (1970)*	32.4	0.3	113.7	0.22	538	unkn.	0	no	N/A	unkn.	unkn.	unkn.	unkn.
30-18	Sorenson (1970)*	32.3	0.3	104.4	0.29	538	unkn.	0	no	N/A	unkn.	unkn.	unkn.	unkn.
30-A14	Sorenson (1970)*	33.9	1.1	31.2	1.17	560	unkn.	0	no	N/A	unkn.	unkn.	unkn.	unkn.
30-A252	Sorenson (1970)*	33.2	0.7	45.6	0.69	562	unkn.	0	no	N/A	unkn.	unkn.	unkn.	unkn.
30-A33	Sorenson (1970)*	32.7	0.4	76.7	0.29	560	unkn.	0	no	N/A	unkn.	unkn.	unkn.	unkn.
30-A41	Sorenson (1970)*	32.5	0.3	100.7	0.29	548	unkn.	0	no	N/A	unkn.	unkn.	unkn.	unkn.
30-1	Stephens et al. (1991)	168.3	3.2	53.0	2.03†	458	564	11.3	no	N/A	unkn.	steel	bending	unkn.
30-2	Stephens et al. (1991)	168.3	3.2	53.0	0.79†	442	550	0	no	N/A	unkn.	steel	bending	unkn.
31-1E1	Suzuki et al. (2001)	917	19	48.3	0.75	519	582	0	no	N/A	long. W.	steel	axial	2.00
31-LN1	Suzuki et al. (2001)	610	15.4	39.6	0.85	442	518	0	no	N/A	long. W.	steel	axial	3.00
31-LN2	Suzuki et al. (2001)	610	15.1	40.4	0.96	451	607	0	no	N/A	long. W.	steel	axial	3.00
31-HN1	Suzuki et al. (2001)	711	12.7	56.0	0.85	452	573	0	no	N/A	long. W.	steel	axial	2.57
31-HN2	Suzuki et al. (2001)	711	16	44.4	1.15	523	752	0	no	N/A	long. W.	steel	axial	2.57
31-HN3	Suzuki et al. (2001)	610	16	38.1	1.38	557	772	0	no	N/A	long. W.	steel	axial	3.00
32-C-1	Suzuki et al. (2007, 2008)	762	15.6	48.8	0.90	524	684	0	no	N/A	unkn.	steel	axial	2.41
32-C-2	Suzuki et al. (2007, 2008)	762	15.6	48.8	0.78	565	704	0	no	N/A	unkn.	steel	axial	2.41
32-B-1	Suzuki et al. (2007, 2008)	762	15.6	48.8	1.85	535	696	12	no	N/A	unkn.	steel	bending	2.41
32-B-2	Suzuki et al. (2007, 2008)	762	15.6	48.8	1.65	672	782	12	no	N/A	unkn.	steel	bending	2.41
33-1	Suzuki et al. (2010)	1219	22.1	55.2	1.67	585	701	12	no	N/A	unkn.	steel	comb.	2.00
33-2	Suzuki et al. (2010)	1219	22.1	55.2	1.51	600	725	12	no	N/A	unkn.	steel	comb.	2.00
34-A	Tajika and Suzuki (2009)	508	15.7	32.4	5.41	487	552	19	no	N/A	long. w.	steel	comb.	2.00
34-B	Tajika and Suzuki (2009)	508	15.7	32.4	4.02	487	552	11	no	N/A	long. w.	steel	comb.	2.00

ID	References	D [mm]	t [mm]	D/t [mm]	ϵ_{crit} [%]	σ_y [MPa]	σ_u [MPa]	P [MPa]	GW	hac.	Manuf.	Material	Loading	L_x/D [mm]
34-C	Tajika and Suzuki (2009)	508	15.7	32.4	6.30	487	552	17	no	N/A	long. w.	steel	comb.	2.00
35-1	Tsuru and Agata (2012)	914	19.8	46.2	2.30	650	unkn.	23.9	no	N/A	long. w.	steel	bending	1.00
35-2	Tsuru and Agata (2012)	914	19.8	46.2	2.41	650	unkn.	23.9	no	N/A	long. w.	steel	bending	1.00
35-3	Tsuru and Agata (2012)	914	19.8	46.2	1.90	650	unkn.	23.9	yes	yes	long. w.	steel	bending	1.00
36-3	Vitali et al. (2005)	406.7	16.5	24.7	7.23	475	573	30.3	no	N/A	seamless	steel	bending	unkn.
36-4	Vitali et al. (2005)	406.4	16.5	24.6	6.60	478	569	30.3	yes	unkn.	seamless	steel	bending	unkn.
37-69-0	Wilhoit and Merwin (1973)	63.5	1.75	36.2	0.82†	311	unkn.	0	no	N/A	long. w.	steel	comb.	0.01
37-69-1/4	Wilhoit and Merwin (1973)	63.5	1.75	36.2	0.82†	311	unkn.	0	no	N/A	long. w.	steel	comb.	0.01
37-69-1/2	Wilhoit and Merwin (1973)	63.5	1.75	36.2	0.52†	311	unkn.	0	no	N/A	long. w.	steel	comb.	0.01
37-48-0	Wilhoit and Merwin (1973)	63.5	1.22	52.1	0.71†	320	unkn.	0	no	N/A	long. w.	steel	comb.	0.01
37-48-1/4	Wilhoit and Merwin (1973)	63.5	1.22	52.1	0.82†	320	unkn.	0	no	N/A	long. w.	steel	comb.	0.01
37-48-1/2	Wilhoit and Merwin (1973)	63.5	1.22	52.1	0.82†	320	unkn.	0	no	N/A	long. w.	steel	comb.	0.01
37-36-0	Wilhoit and Merwin (1973)	63.5	0.94	67.6	0.50†	320	unkn.	0	no	N/A	long. w.	steel	comb.	0.01
37-36-1/4	Wilhoit and Merwin (1973)	63.5	0.91	69.4	0.50†	320	unkn.	0	no	N/A	long. w.	steel	comb.	0.01
37-36-1/2	Wilhoit and Merwin (1973)	63.5	0.91	69.4	0.73†	320	unkn.	0	no	N/A	long. w.	steel	comb.	0.01
37-29-0	Wilhoit and Merwin (1973)	63.5	0.79	80.6	0.83†	320	unkn.	0	no	N/A	long. w.	steel	comb.	0.01
37-29-1/4	Wilhoit and Merwin (1973)	63.5	0.74	86.2	0.40†	320	unkn.	0	no	N/A	long. w.	steel	comb.	0.01
37-29-1/2	Wilhoit and Merwin (1973)	63.5	0.71	89.3	0.83†	320	unkn.	0	no	N/A	long. w.	steel	comb.	0.01
38-UGA 20W-2	Yoosief-Choodsiet al. (1994)	508	7.9	64.3	0.92	386	unkn.	0	yes	yes	long. w.	steel	comb.	unkn.
38-HGA 20W	Yoosief-Choodsiet al. (1994)	508	7.9	64.3	1.16	386	unkn.	5	yes	yes	long. w.	steel	comb.	unkn.
38-DGA 20W	Yoosief-Choodsiet al. (1994)	508	7.9	64.3	2.13	386	unkn.	9.9	yes	no	long. w.	steel	comb.	unkn.
38-UGA 12W	Yoosief-Choodsiet al. (1994)	324	6.4	51.0	0.68	358	unkn.	0	yes	yes	long. w.	steel	comb.	unkn.
38-HGA 12W	Yoosief-Choodsiet al. (1994)	324	6.4	51.0	1.26	358	unkn.	5.3	yes	yes	long. w.	steel	comb.	unkn.
38-DGA 12W	Yoosief-Choodsiet al. (1994)	324	6.4	51.0	1.92	358	unkn.	10.5	yes	yes	long. w.	steel	comb.	unkn.
39-B1	Zimmerman et al. (1995)	610	7	87.3	0.43	440	unkn.	8.9	yes	no	unkn.	steel	comb.	unkn.
39-B2	Zimmerman et al. (1995)	610	7	87.3	0.37	440	unkn.	0	yes	no	unkn.	steel	comb.	unkn.
39-B3	Zimmerman et al. (1995)	610	7	87.3	0.79	440	unkn.	8.9	yes	no	unkn.	steel	comb.	unkn.
39-B4	Zimmerman et al. (1995)	611	14.9	41.0	1.41	470	unkn.	16.8	yes	no	unkn.	steel	comb.	unkn.
39-B5	Zimmerman et al. (1995)	611	14.9	41.0	1.22	470	unkn.	0	yes	no	unkn.	steel	comb.	unkn.
40-1	Zimmerman et al. (2004)	762	9.4	81.1	0.52	552	unkn.	0	no	N/A	spiral w.	steel	bending	2.00
40-2	Zimmerman et al. (2004)	762	9.4	81.1	1.54	552	unkn.	9.4	no	N/A	spiral w.	steel	bending	2.00
40-3	Zimmerman et al. (2004)	762	15.7	48.5	3.69	620	unkn.	26.1	no	N/A	spiral w.	steel	bending	2.00
40-4	Zimmerman et al. (2004)	762	15.7	48.5	1.12	620	unkn.	0	no	N/A	spiral w.	steel	bending	2.00
41-2-1	Zimmermann et al. (2013)	914	20	45.7	1.60	540	633	0	no	N/A	spiral w.	steel	bending	3.50
41-2-2	Zimmermann et al. (2013)	914	14.3	63.9	1.10	641	722	0	no	N/A	spiral w.	steel	bending	3.50
41-2-3	Zimmermann et al. (2013)	914	20	45.7	1.90	540	633	14	no	N/A	spiral w.	steel	bending	3.50
41-2-4	Zimmermann et al. (2013)	914	14.3	63.9	1.30	641	722	11.5	no	N/A	spiral w.	steel	bending	3.50

Appendix B: Results of bending tests on tubes for combined walls

This appendix presents detailed information on the bending experiments presented in Part II of the main text of this thesis. Appendix B.1 presents a tabular summary of the experimental results. In Appendix B.2, the layout and orientation of all tubular specimens is presented, including the location of any girth welds or coil connection welds as well as the location of the local buckle. Appendices B.3 and B.4 present the results of the bending tests in the form of moment-curvature diagrams and ovalisation-curvature diagrams respectively.

B.1 Summary of experimental results

Table B.1 Overview of test results of four-point bending tests. Bold figures concern measurements in curvature brackets which span a local buckle.

Spec.	M_{max} [kNm]	M_{max}/M_p [-]	$\kappa_{crit;avg}$ [km ⁻¹]	$\kappa_{crit;1}$ [km ⁻¹]	$\kappa_{crit;2}$ [km ⁻¹]	$\kappa_{crit;3}$ [km ⁻¹]	$\kappa_{buc;avg}$ [km ⁻¹]	$\kappa_{buc;1}$ [km ⁻¹]	$\kappa_{buc;2}$ [km ⁻¹]	$\kappa_{buc;3}$ [km ⁻¹]
T1	8840	0.921	9.66	10.62	9.89	8.45	10.41	16.33	9.67	8.08
T2	3047	0.742	4.65	5.23	4.79	4.21	4.80	5.77	4.88	4.07
T3	2869	0.742	3.36	4.33	3.85	3.56	3.38	4.40	3.84	3.60
T4	3731	0.829	5.50	5.89	5.92	5.54	5.54	5.93	5.95	5.57
T5	3338	0.822	4.95	4.41	5.34	4.77	5.10	4.59	5.51	4.71
T6	8174	0.873	7.99	9.15	8.02	7.93	8.49	10.69	8.31	8.63
T7	8096	0.730	7.59	8.58	7.75	7.03	7.70	9.57	7.70	7.03
T8	3469	0.749	5.01	5.50	5.31	5.12	5.12	5.48	5.45	5.25
T9	8979	0.809	9.47	11.44	9.64	8.90	9.90	12.57	9.91	9.17
T10	4286	0.903	5.78	3.61	6.33	5.88	6.62	3.64	7.55	6.19
T11	4221	0.832	8.17	8.02	8.89	7.90	9.51	9.81	10.16	8.46
T12	3446	0.754	4.84	4.73	5.31	4.65	4.98	5.14	5.35	4.60
T13	3393	0.748	4.53	4.56	5.09	4.25	4.55	4.58	5.11	4.26
T14	4360	0.782	5.13	4.96	5.47	5.19	5.24	5.06	5.54	5.21
T15	7666	0.868	11.57	10.82	11.83	11.56	12.01	10.81	11.92	13.78

B.2 Specimen layout

A schematic overview of each tubular specimen in Part II of this study is presented in Figure B.1. The drawings feature a side view which shows the location of the local buckle and, if applicable, the location of the girth weld and coil connection weld. Furthermore, a cross-sectional view in which the orientation of the specimen during the bending test is shown. This allows the initial imperfection scans to be related to the intrados of the specimens.

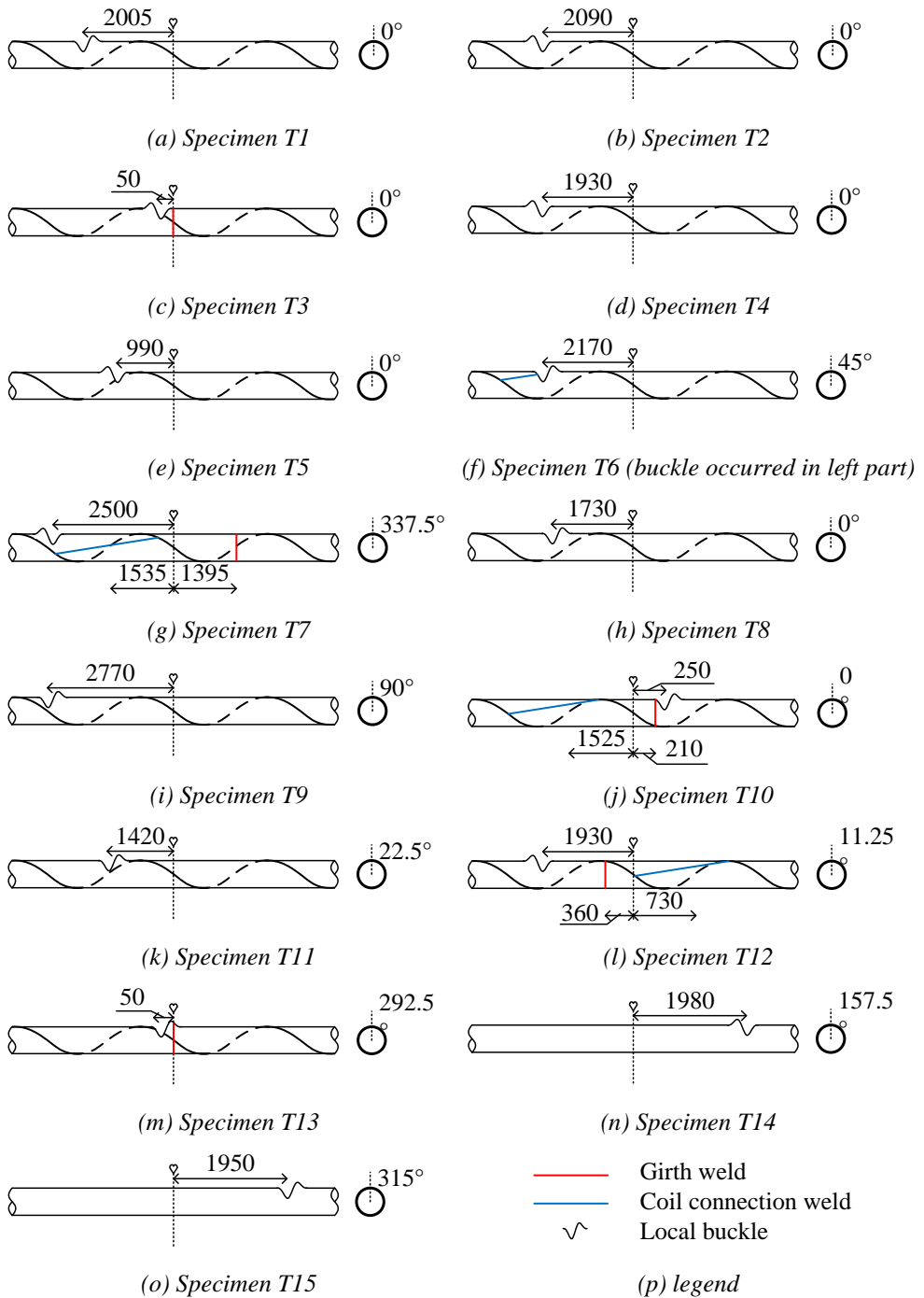


Figure B.1 Layout and orientation of specimens in Part II of this study (dimensions in mm).

B.3 Moment-curvature diagrams

The moment-curvature diagrams of all bending tests that were performed in Part II of this study are presented in Figure B.2 to Figure B.16. For each tube, four curvature measurements are available (see section 5.4.2 of the main text of this thesis). The local curvature measurement within which the local buckle formed is marked in the graph legend. Next to the figures, the main properties of the tube at the location of the buckle are given.

As discussed in section 5.5 of the main text of this thesis, some of the sudden failures of the thin-walled specimens resulted in failure of the curvature measurement equipment. Especially the local curvature measurement equipment was sensitive. Therefore, in some cases in the graphs below, the lines of the curvature measurements are cut off directly after local buckling occurred. The first data point after the equipment failure is still included in the graphs as a visual aid to the reader, even though the displayed curvature is unreliable.

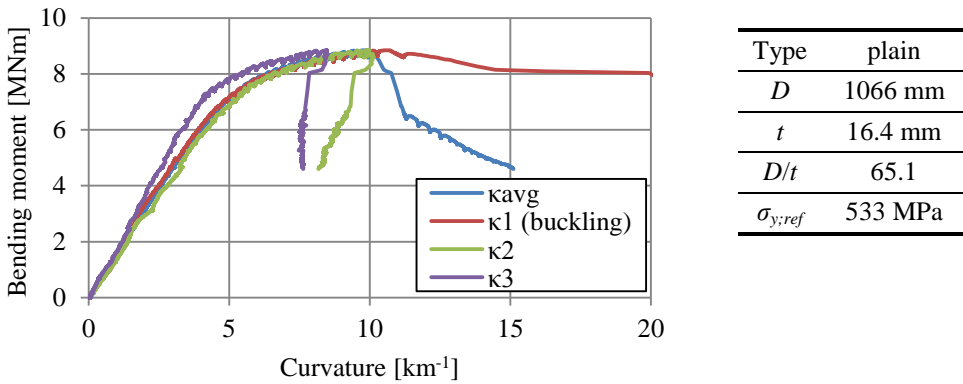


Figure B.2 Moment-curvature diagrams of specimen T1.

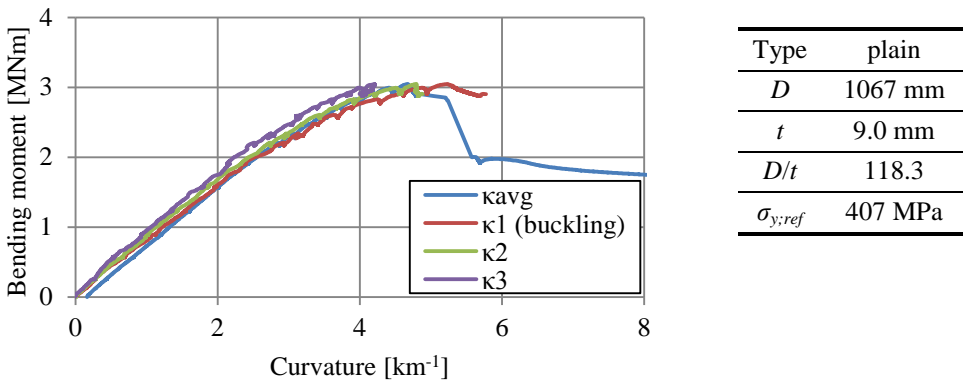
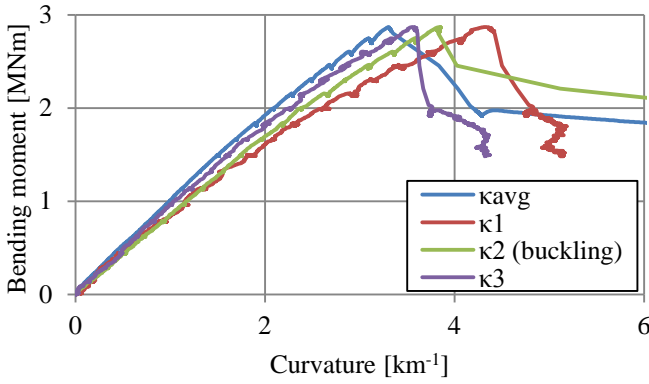
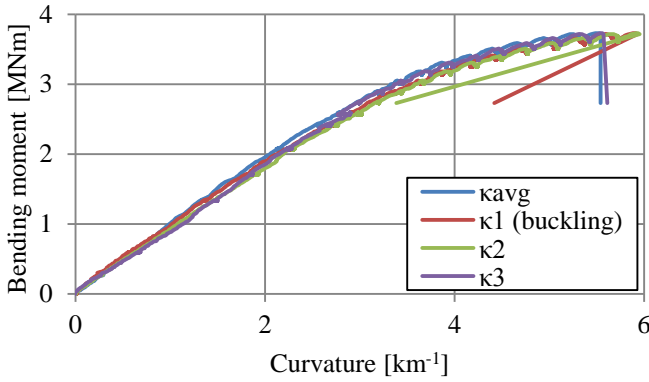


Figure B.3 Moment-curvature diagrams of specimen T2.



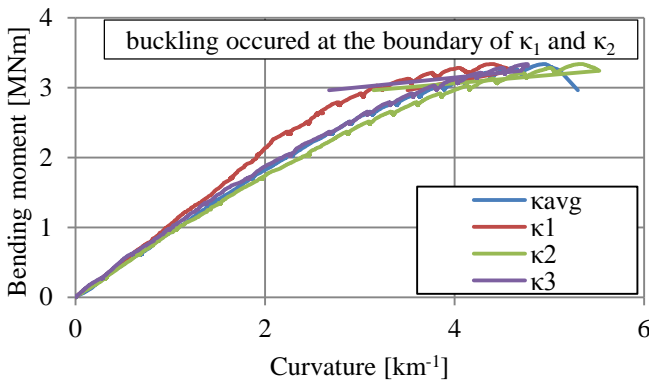
Type	GW
D	1067 mm
t	8.8 mm
D/t	121.3
$\sigma_{y,ref}$	392 MPa

Figure B.4 Moment-curvature diagrams of specimen T3.



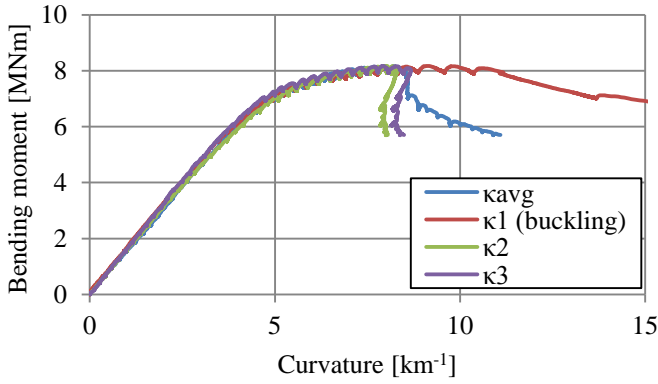
Type	plain
D	1065 mm
t	9.2 mm
D/t	116.2
$\sigma_{y,ref}$	441 MPa

Figure B.5 Moment-curvature diagrams of specimen T4.



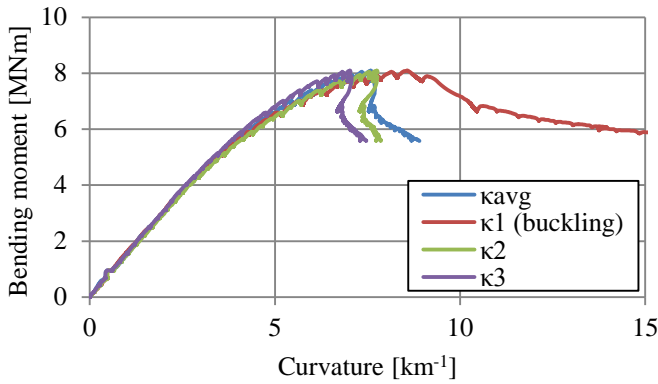
Type	plain
D	1070 mm
t	9.0 mm
D/t	118.3
$\sigma_{y,ref}$	399 MPa

Figure B.6 Moment-curvature diagrams of specimen T5.



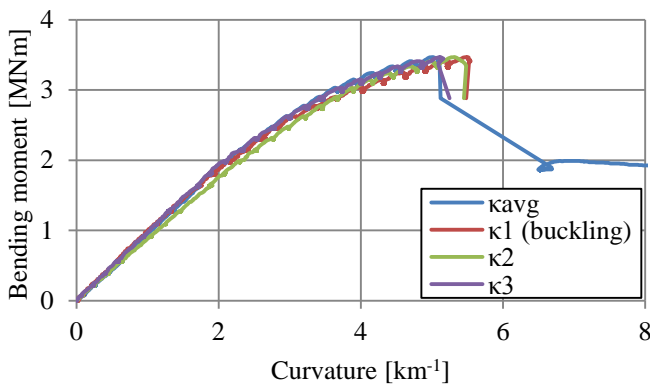
Type	CCW
D	1067 mm
t	16.1 mm
D/t	66.4
$\sigma_{y;ref}$	528 MPa

Figure B.7 Moment-curvature diagrams of specimen T6.



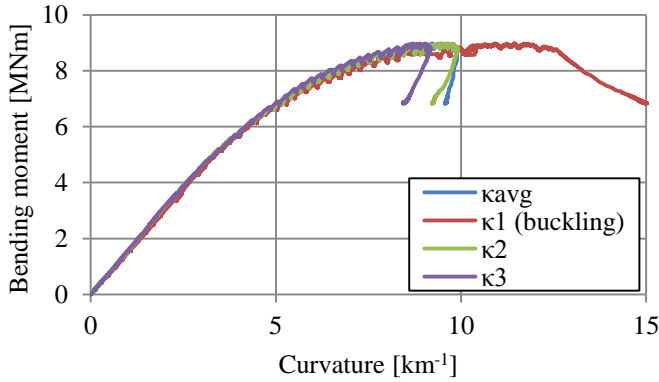
Type	GW/CCW
D	1068 mm
t	16.4 mm
D/t	65.3
$\sigma_{y;ref}$	614 MPa

Figure B.8 Moment-curvature diagrams of specimen T7.



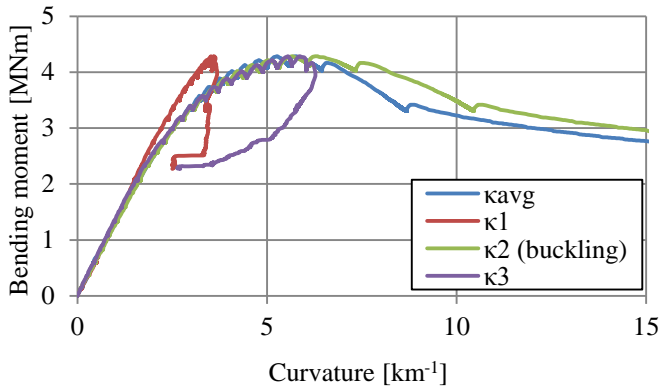
Type	plain
D	1068 mm
t	9.1 mm
D/t	117.4
$\sigma_{y;ref}$	453 MPa

Figure B.9 Moment-curvature diagrams of specimen T8.



Type	plain
D	1069 mm
t	16.3 mm
D/t	65.4
$\sigma_{y,ref}$	613 MPa

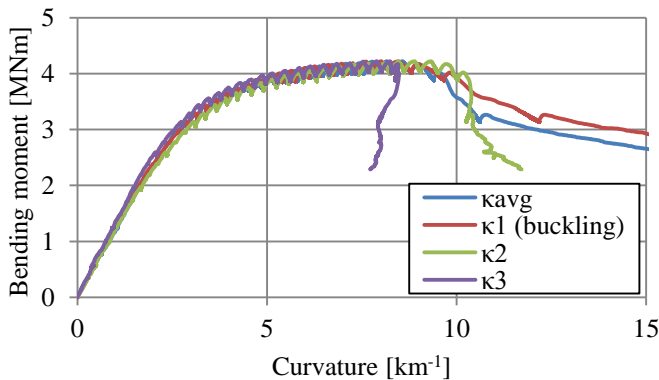
Figure B.10 Moment-curvature diagrams of specimen T9.



Type	GW/CCW
D	1069 mm
t	12.8 mm
D/t	83.5
$\sigma_{y,ref}$	333 MPa*

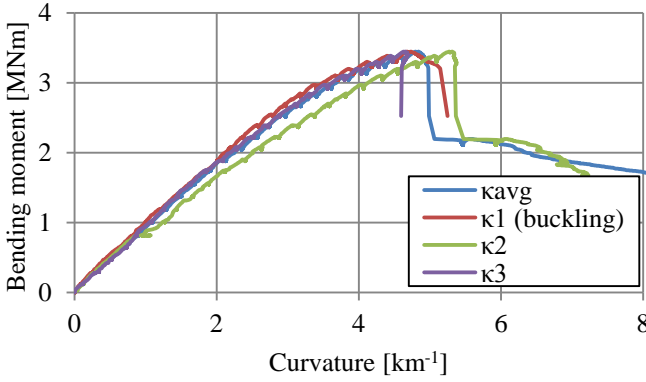
*large difference in σ_y within tube (see Figure 5.34)

Figure B.11 Moment-curvature diagrams of specimen T10.



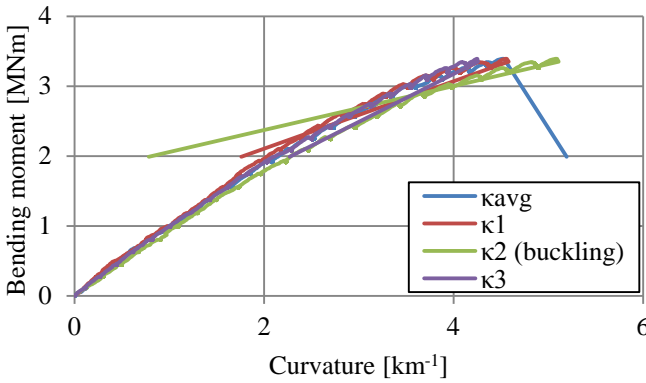
Type	plain
D	1068 mm
t	12.9 mm
D/t	82.8
$\sigma_{y,ref}$	350 MPa

Figure B.12 Moment-curvature diagrams of specimen T11.



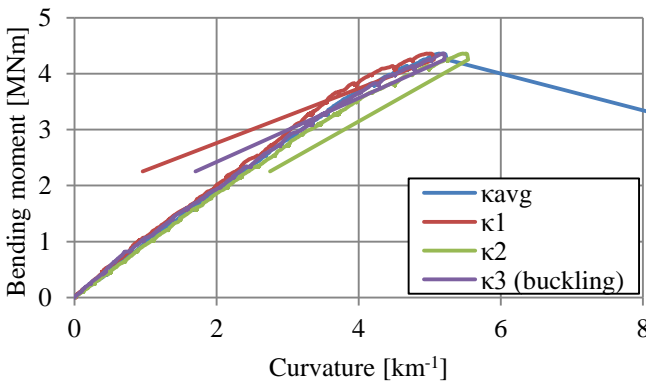
Type	GW/CCW
D	1069 mm
t	9.1 mm
D/t	117.5
$\sigma_{y;ref}$	447 MPa

Figure B.13 Moment-curvature diagrams of specimen T12.



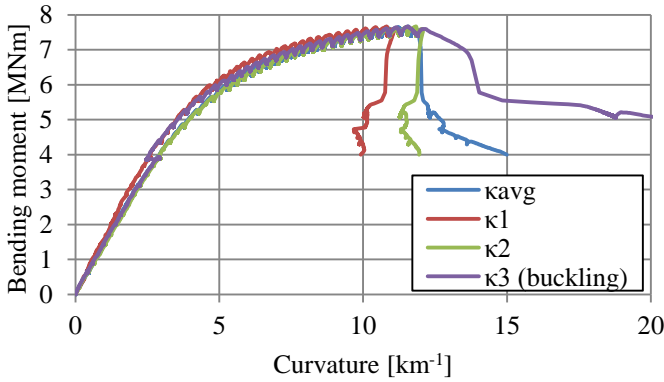
Type	GW
D	1070 mm
t	9.1 mm
D/t	117.6
$\sigma_{y;ref}$	443 MPa

Figure B.14 Moment-curvature diagrams of specimen T13.



Type	plain
D	1068 mm
t	9.8 mm
D/t	108.8
$\sigma_{y;ref}$	507 MPa

Figure B.15 Moment-curvature diagrams of specimen T14.



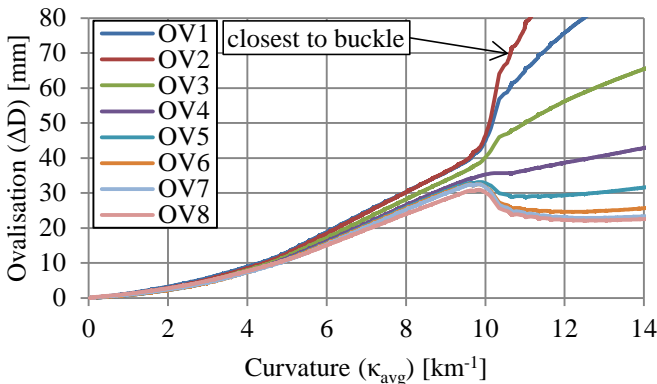
Type	plain
D	1070 mm
t	14.8 mm
D/t	72.3
$\sigma_{y,ref}$	536 MPa

Figure B.16 Moment-curvature diagrams of specimen T15.

B.4 Ovalisation-curvature diagrams

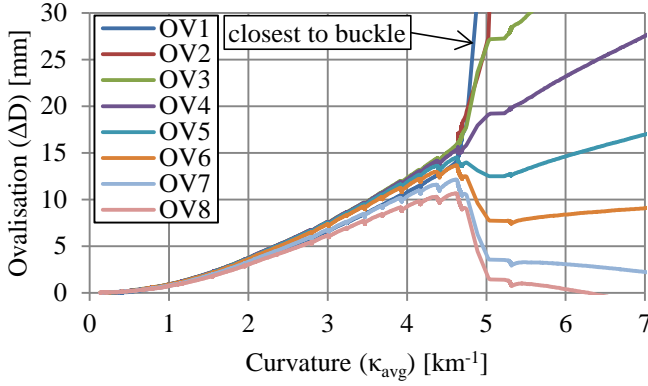
The development of ovalisation in all bending tests that were performed in Part II of this study are presented in Figure B.17 to Figure B.31. For each tube, eight ovalisation measurements are available (see Figure 5.42). The ovalisation measurement closest to the local buckle is identified in each graph. Next to the figures, the main properties of the tube at the location of the buckle are given.

The graphs show the development of the horizontal tube ovalisation in terms of the change in horizontal diameter (ΔD) over the full pre-buckling trajectory. After the formation of a local buckle, ovalisation measurements close to the local buckle show a strong increase. The graphs are focused on the pre-critical behaviour and therefore exclude parts of the post-critical behaviour.



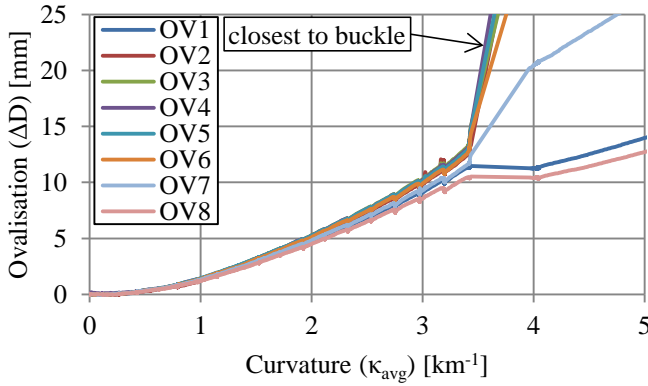
Type	plain
D	1066 mm
t	16.4 mm
D/t	65.1
$\sigma_{y,ref}$	533 MPa

Figure B.17 Development of ovalisation of specimen T1.



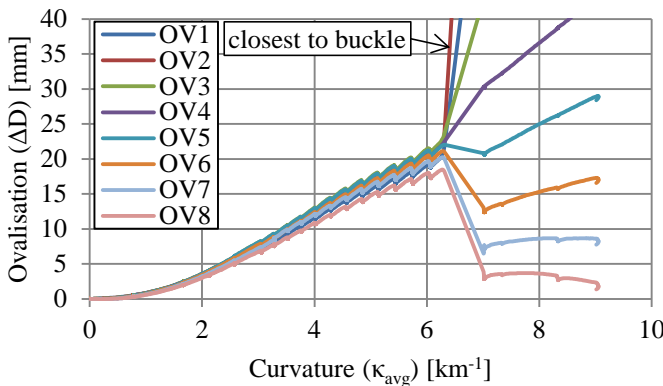
Type	plain
D	1067 mm
t	9.0 mm
D/t	118.3
$\sigma_{y;ref}$	407 MPa

Figure B.18 Development of ovalisation of specimen T2.



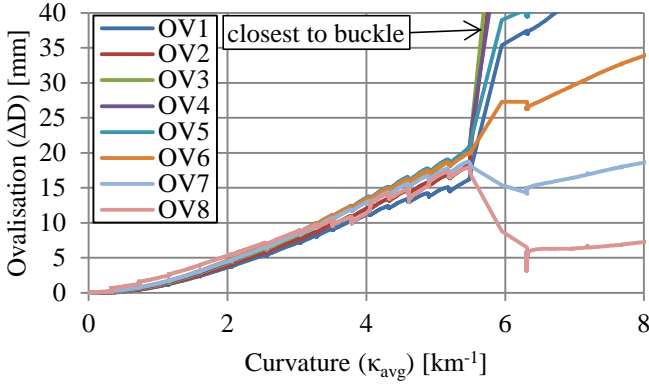
Type	GW
D	1067 mm
t	8.8 mm
D/t	121.3
$\sigma_{y;ref}$	392 MPa

Figure B.19 Development of ovalisation of specimen T3.



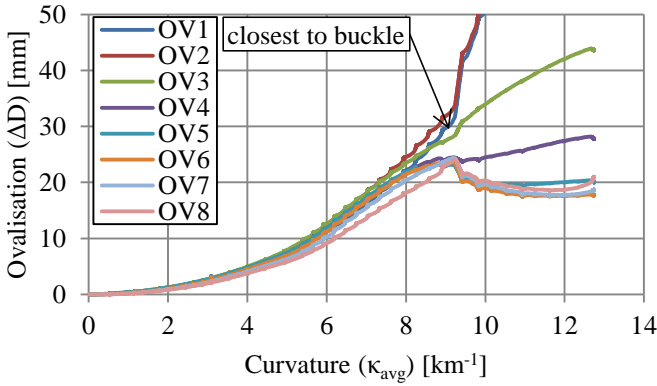
Type	plain
D	1065 mm
t	9.2 mm
D/t	116.2
$\sigma_{y;ref}$	441 MPa

Figure B.20 Development of ovalisation of specimen T4.



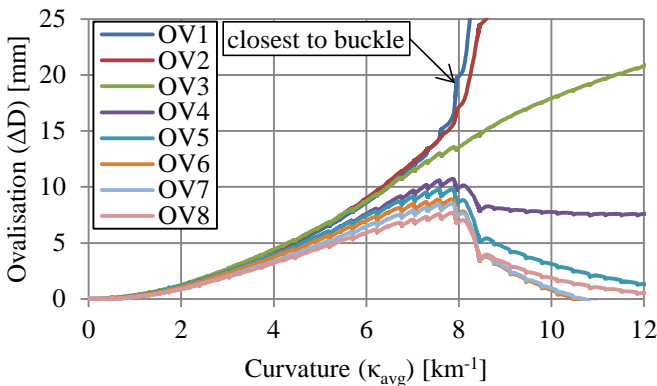
Type	plain
D	1070 mm
t	9.0 mm
D/t	118.3
$\sigma_{y:ref}$	399 MPa

Figure B.21 Development of ovalisation of specimen T5.



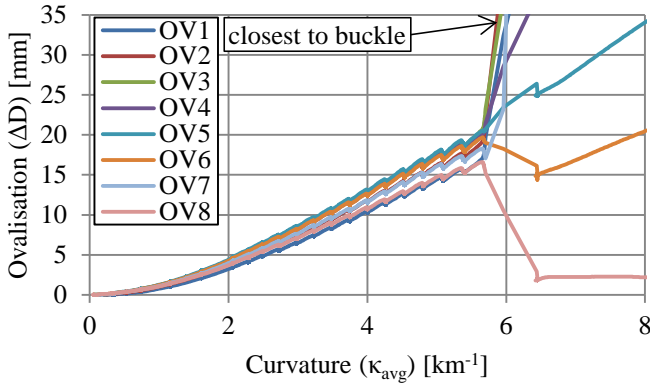
Type	CCW
D	1067 mm
t	16.1 mm
D/t	66.4
$\sigma_{y:ref}$	528 MPa

Figure B.22 Development of ovalisation of specimen T6.



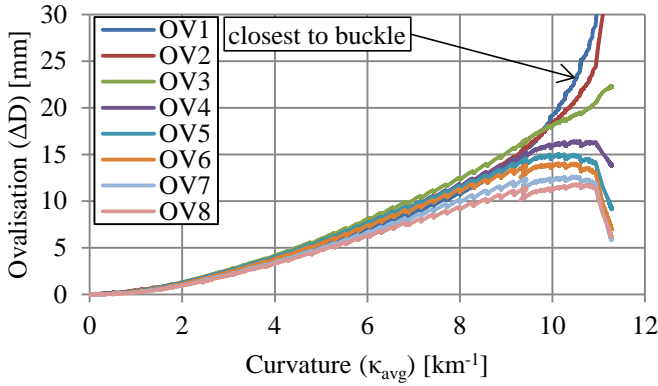
Type	GW/CCW
D	1068 mm
t	16.4 mm
D/t	65.3
$\sigma_{y:ref}$	614 MPa

Figure B.23 Development of ovalisation of specimen T7.



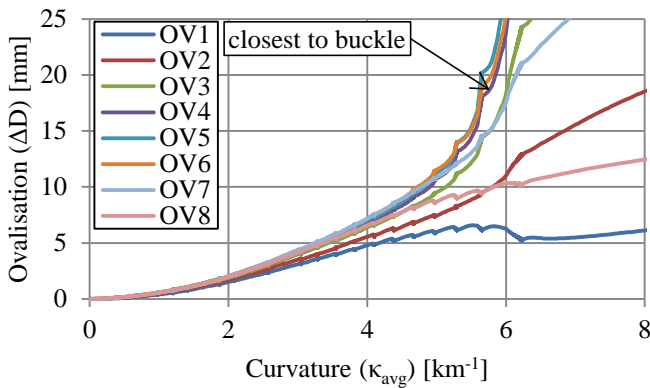
Type	plain
D	1068 mm
t	9.1 mm
D/t	117.4
$\sigma_{y;ref}$	453 MPa

Figure B.24 Development of ovalisation of specimen T8.



Type	plain
D	1069 mm
t	16.3 mm
D/t	65.4
$\sigma_{y;ref}$	613 MPa

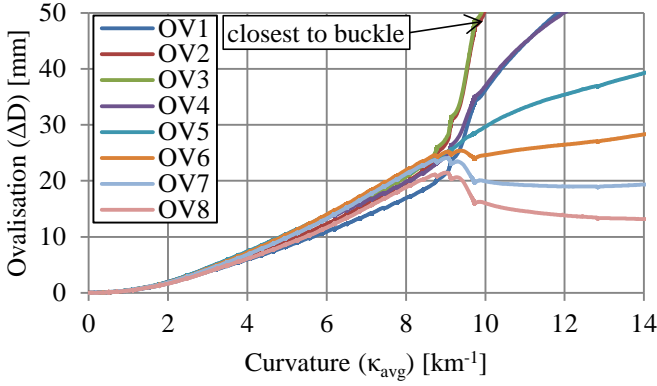
Figure B.25 Development of ovalisation of specimen T9.



Type	GW/CCW
D	1069 mm
t	12.8 mm
D/t	83.5
$\sigma_{y;ref}$	333 MPa*

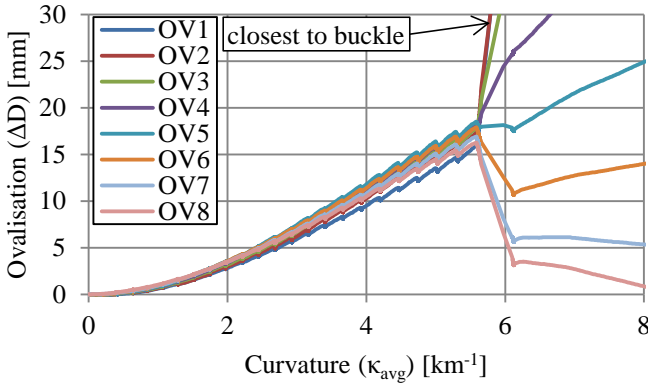
*large difference in σ_y within tube (see Figure 5.34)

Figure B.26 Development of ovalisation of specimen T10.



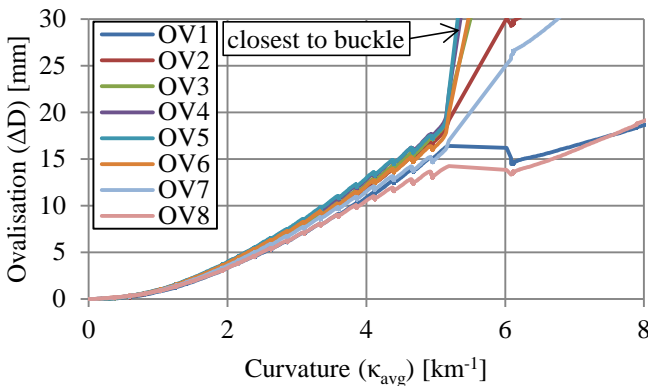
Type	plain
D	1068 mm
t	12.9 mm
D/t	82.8
$\sigma_{y:ref}$	350 MPa

Figure B.27 Development of ovalisation of specimen T11.



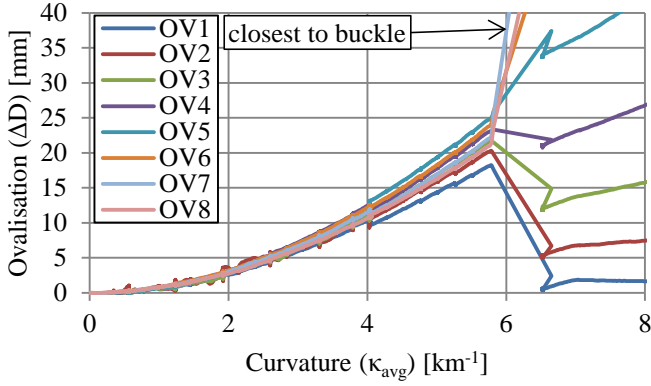
Type	GW/CCW
D	1069 mm
t	9.1 mm
D/t	117.5
$\sigma_{y:ref}$	447 MPa

Figure B.28 Development of ovalisation of specimen T12.



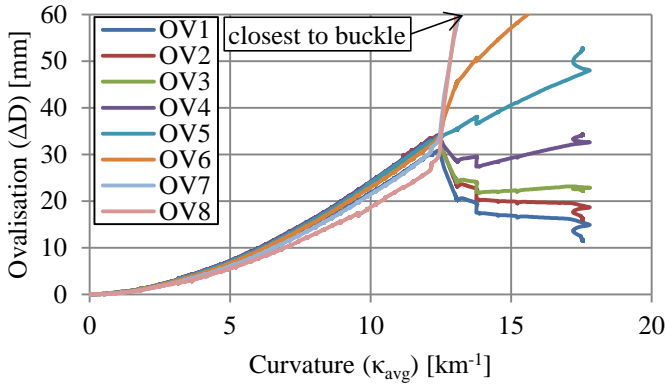
Type	GW
D	1070 mm
t	9.1 mm
D/t	117.6
$\sigma_{y:ref}$	443 MPa

Figure B.29 Development of ovalisation of specimen T13.



Type	plain
D	1068 mm
t	9.8 mm
D/t	108.8
$\sigma_{y;ref}$	507 MPa

Figure B.30 Development of ovalisation of specimen T14.



Type	plain
D	1070 mm
t	14.8 mm
D/t	72.3
$\sigma_{y;ref}$	536 MPa

Figure B.31 Development of ovalisation of specimen T15.

Appendix C: Comparison of design guidelines with tests on tubes for combined walls

This appendix presents a comparison between the moment-curvature behaviour that is predicted using the analytical model that was developed within the COMBITUBE project and the tests presented in Part II of this study. An overview of the used model input is presented in Table C.1. Note that the input for the yield stress differs from the reference yield stress (see sections 5.3.2 and 6.9 of the main text of this thesis). The input parameters of the model and the critical strain that the model predicts are further discussed in section 6.9 of the main text of this thesis.

Table C.1 Overview of used input parameters in analytical model for graphs in this appendix.

Spec.	D [mm]	t [mm]	σ_y [MPa]
T1	1066	16.4	539
T2	1067	9.02	392
T3	1067	8.80	376
T4	1065	9.16	420
T5	1070	9.04	382
T6	1067	16.1	524
T7	1068	16.4	548
T8	1068	9.10	435
T9	1069	16.3	544
T10	1070	12.8	311
T11	1068	12.9	340
T12	1069	9.10	433
T13	1070	9.10	425
T14	1068	9.82	527
T15	1070	14.8	509

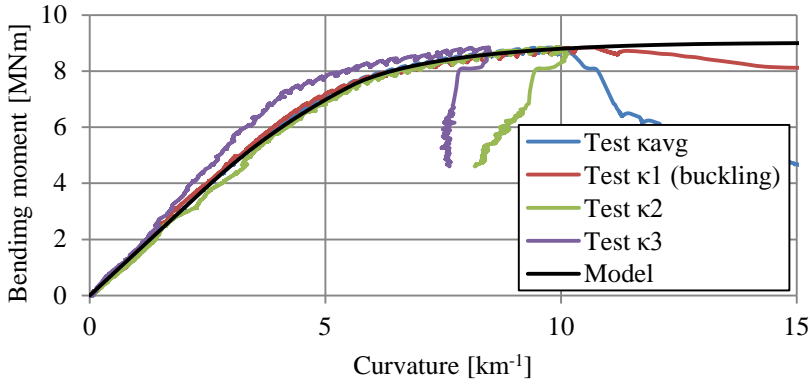


Figure C.1 Comparison between model and test results for test T1.

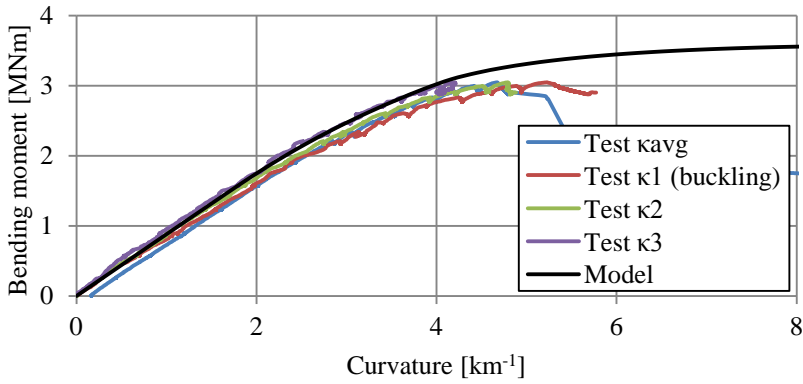


Figure C.2 Comparison between model and test results for test T2.

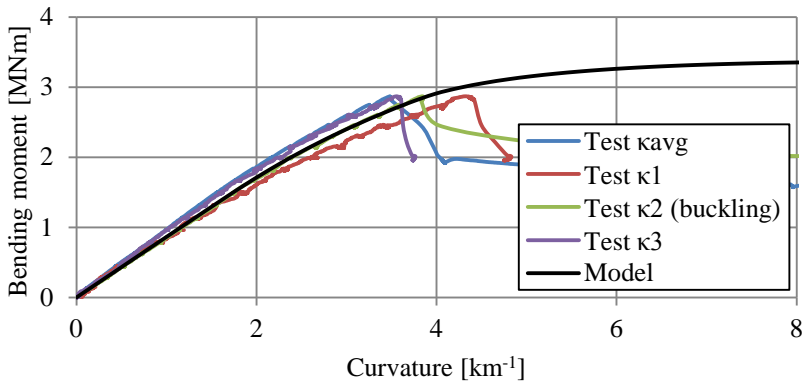


Figure C.3 Comparison between model and test results for test T3.

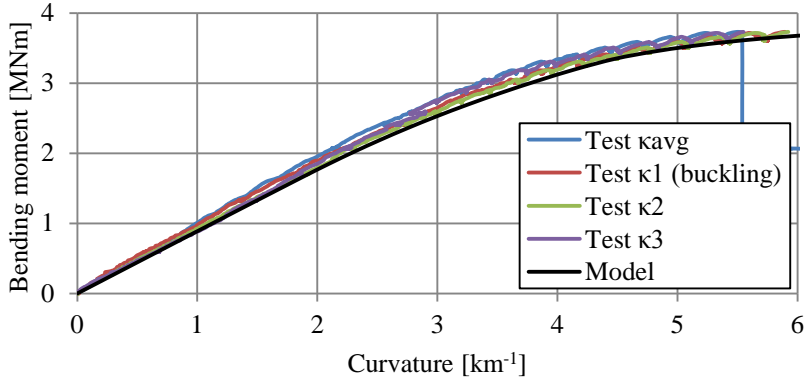


Figure C.4 Comparison between model and test results for test T4.

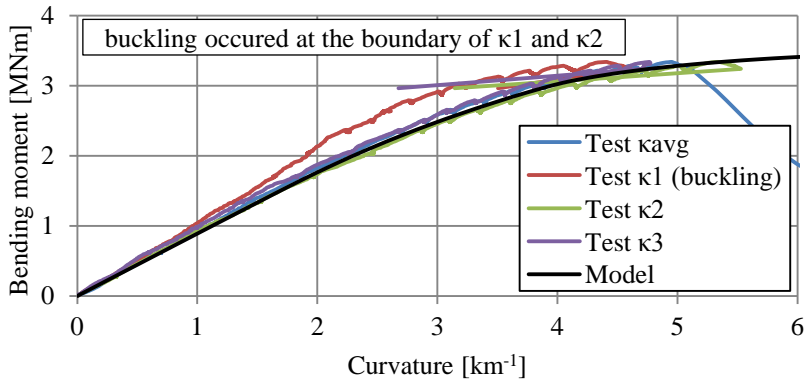


Figure C.5 Comparison between model and test results for test T5.

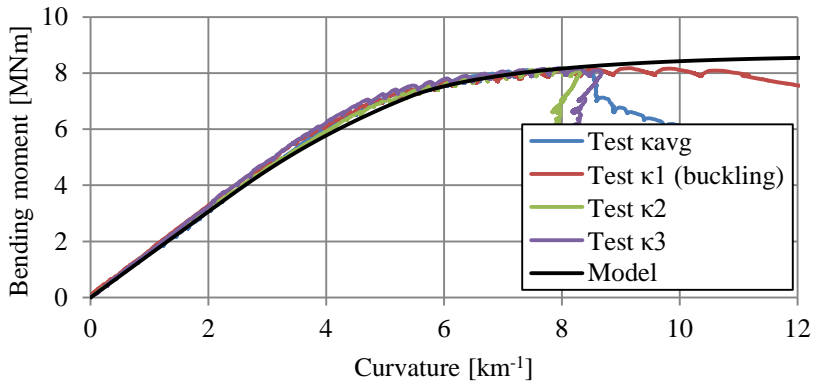


Figure C.6 Comparison between model and test results for test T6.

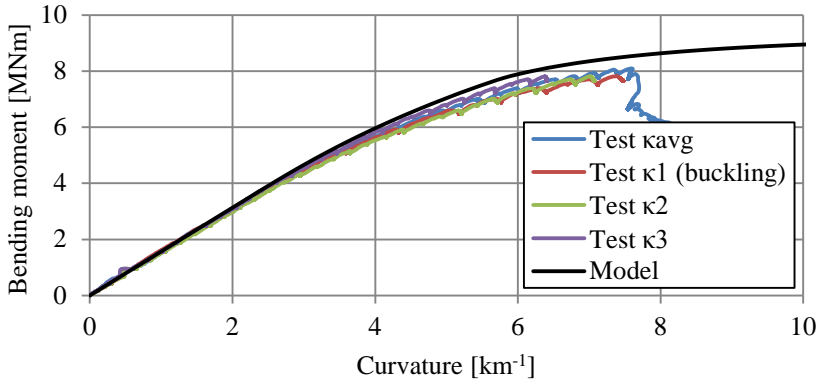


Figure C.7 Comparison between model and test results for test T7.

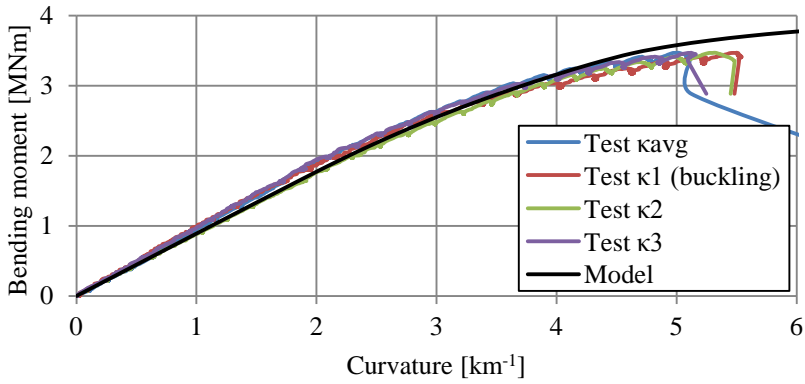


Figure C.8 Comparison between model and test results for test T8.

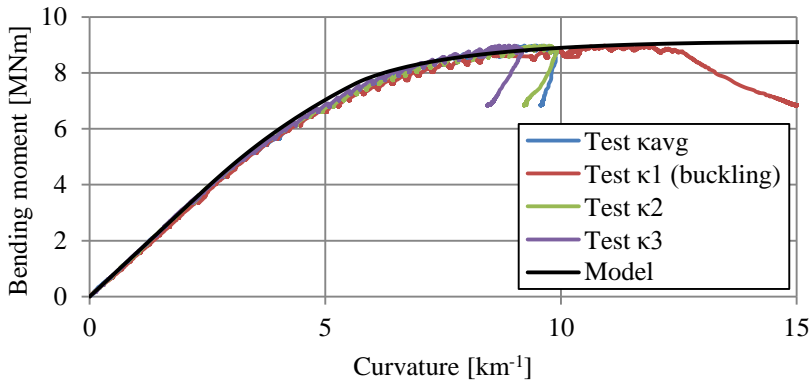


Figure C.9 Comparison between model and test results for test T9.

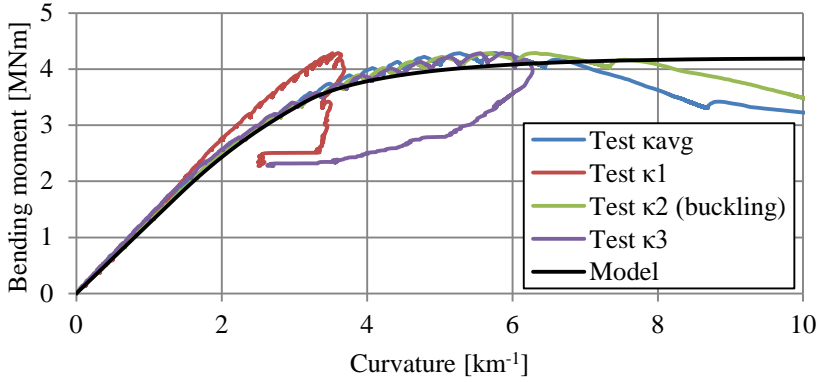


Figure C.10 Comparison between model and test results for test T10.

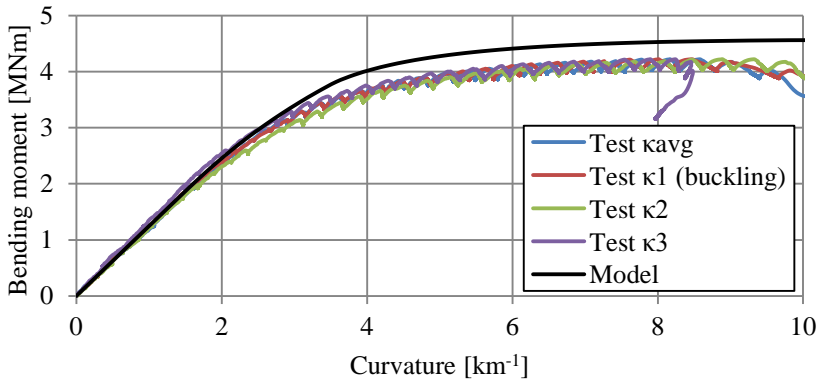


Figure C.11 Comparison between model and test results for test T11.

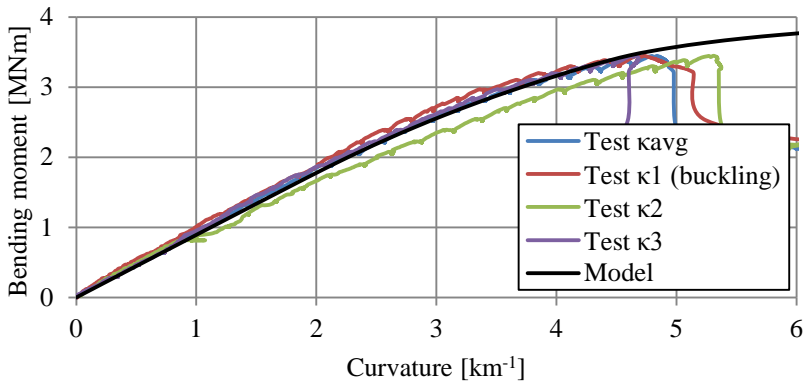


Figure C.12 Comparison between model and test results for test T12.

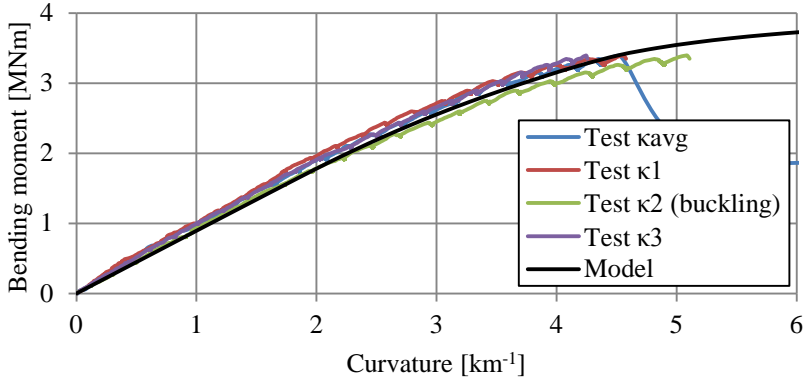


Figure C.13 Comparison between model and test results for test T13.

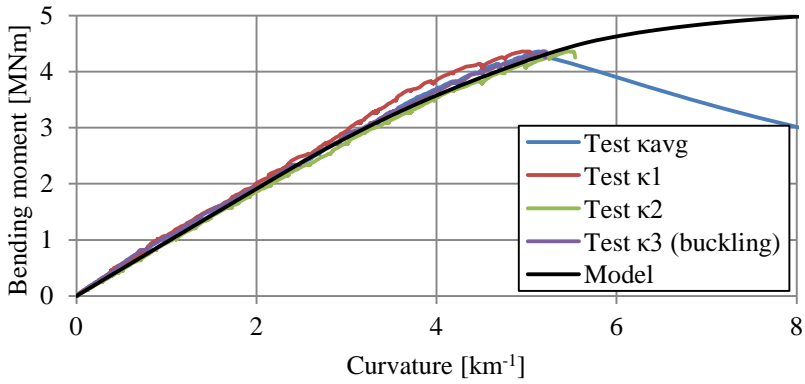


Figure C.14 Comparison between model and test results for test T14.

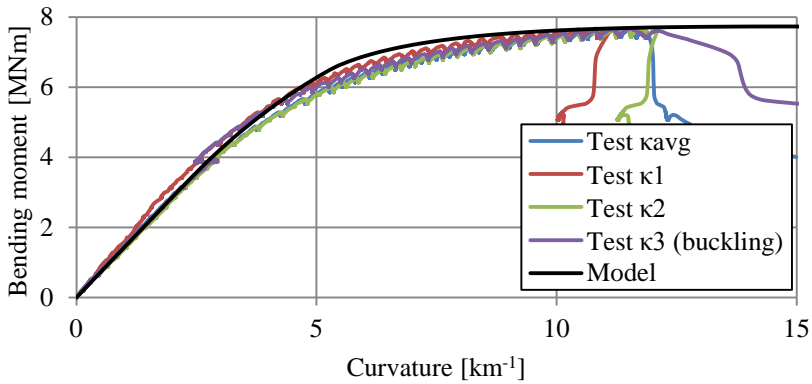


Figure C.15 Comparison between model and test results for test T15.

Appendix D: Results of tests on pipelines crossing active strike-slip faults

This appendix presents detailed information on the experiments presented in Part III of this study. Appendix D.1 presents a tabular summary of the experimental results. In Appendix D.2, the layout of all pipeline specimens is presented, as well as the identification numbers of the pipes used for the specimens. The ring-spring configuration of each separate test is presented in Appendix D.3. The results of the tests are presented in Appendices D.4, D.5 and D.6. Appendix D.4 presents the response of the ring-springs during the test. Appendix D.5 presents a selection of the results of the strain measurements. Ovalisation measurements are presented in Appendix D.6.

D.1 Summary of test results

An overview of the results of the bending tests performed in Part III of this study is presented in Table 9.6. An addendum to this table, with more information on the tests, is presented in Table D.1. For each specimen on each side of the fault, the table lists fault movements at which noteworthy events occurred. After local buckling failure on one side of the fault, deformations rapidly increased due to the local loss of stiffness of the pipeline. Events that occurred after local buckling failure on either side of the fault are displayed in italics in Table D.1.

Table D.1 Summary of results of tests on buried pipelines (addendum to Table 9.6).

Test	Side	GW	Distance of local buckle to fault [mm]	$u_{fault;shift}$ [mm]	$u_{fault;incident}$ [mm]
T1	Left	No	-	-	-
	Right	No	-		
T2	Left	No	2600	-	249 (see section 9.6.2)
	Right	No	2555		
T3	Left	No	2240	<i>1271</i>	-
	Right	Yes	2340		
T4	Left	No	1615	837	-
	Right	No	1875		
T5	Left	Yes	1445	-	710 (see section 9.6.5)
	Right	No	1450		
T6	Left	No	-	<i>1406</i>	-
	Right	No	-		
T7	Left	Yes	-	-	-
	Right	No	-		
T8	Left	No	2900	-	-
	Right	Yes	2530		
T9	Left	No	3625	-	-
	Right	No	3575		
T10	Left	No	2565	-	-
	Right	No	2220		

D.2 Specimen layout

All specimens are assembled from the available pipe material as listed in Table 9.4. An overview of each 20 m long specimen is presented in Figure D.1 to Figure D.10.

	H86916400B	H86916024	H86916331B
D	220 mm	220 mm	220 mm
t	5.6 mm	5.6 mm	5.5 mm
$\sigma_{y,ref}$	567 MPa	571 MPa	591 MPa
$\sigma_{u,ref}$	607 MPa	612 MPa	646 MPa

Figure D.1 Test T1: specimen assembly.

	H60415859	H60410114	H60423730
D	407 mm	407 mm	407 mm
t	7.6 mm	7.5 mm	7.5 mm
$\sigma_{y,ref}$	552 MPa	562 MPa	535 MPa
$\sigma_{u,ref}$	597 MPa	630 MPa	592 MPa

Figure D.2 Test T2: specimen assembly.

	H86916400B	H86916270B	H86916024	H86916331B
D	220 mm	220 mm	220 mm	220 mm
t	5.5 mm	5.6 mm	5.6 mm	5.5 mm
$\sigma_{y,ref}$	567 MPa	594 MPa	571 MPa	591 MPa
$\sigma_{u,ref}$	607 MPa	653 MPa	612 MPa	646 MPa

Figure D.3 Test T3: specimen assembly.

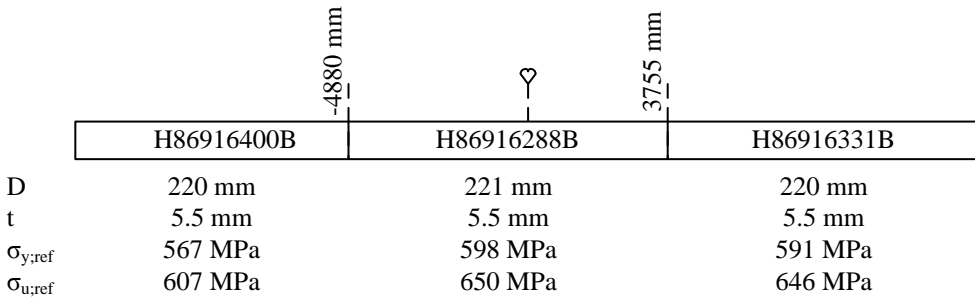


Figure D.4 Test T4: specimen assembly.

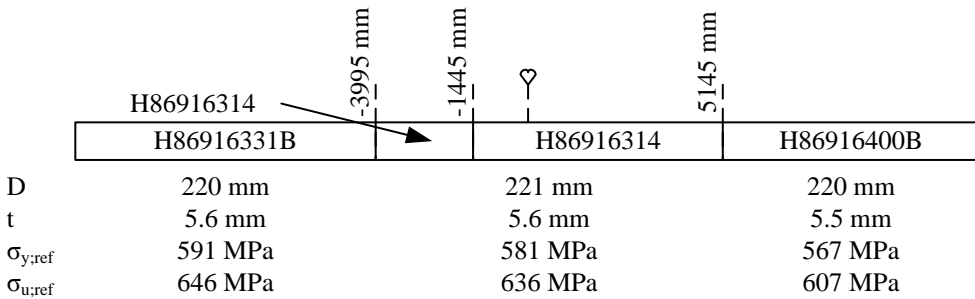


Figure D.5 Test T5: specimen assembly.

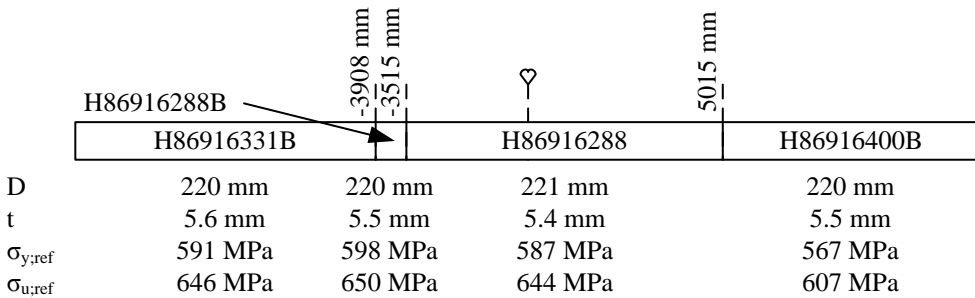


Figure D.6 Test T6: specimen assembly.

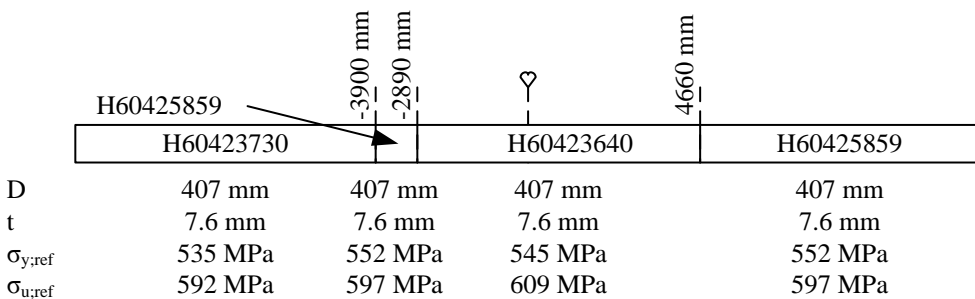


Figure D.7 Test T7: specimen assembly.

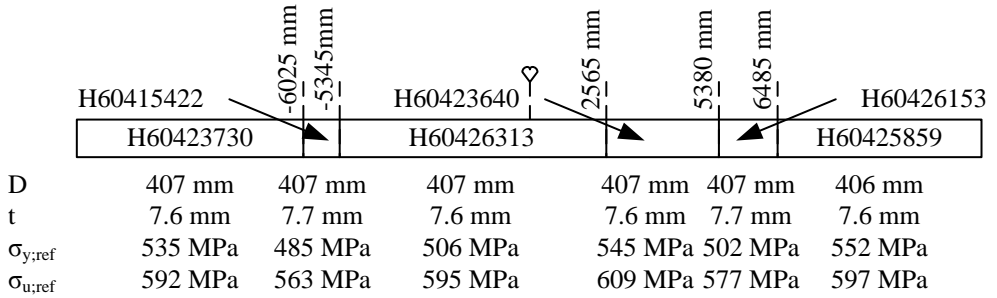


Figure D.8 Test T8: specimen assembly.

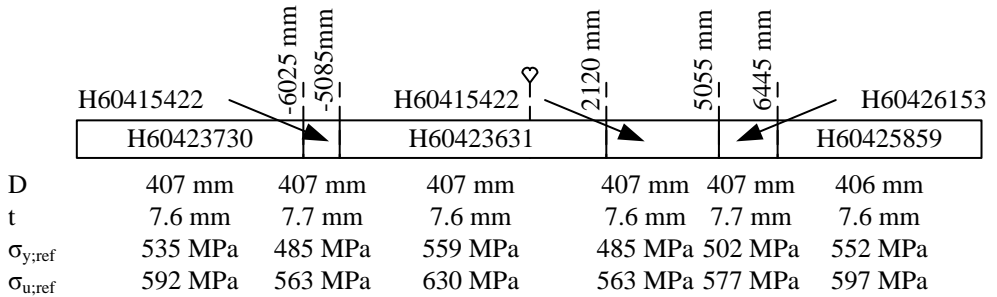


Figure D.9 Test T9: specimen assembly.

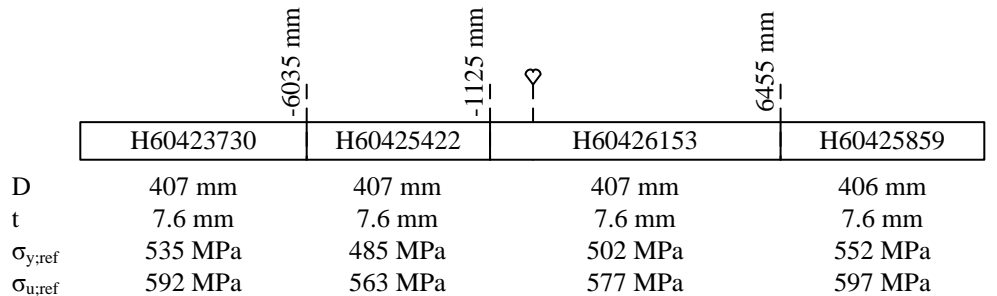


Figure D.10 Test T10: specimen assembly.

D.3 Ring-spring geometry

The location of each ring-spring (see Figure D.11) is listed in Table D.2. The force-deformation relation of each ring-spring ($F_{ring}-u_{ring}$) can be found in Van Es and Gresnigt (2016b).

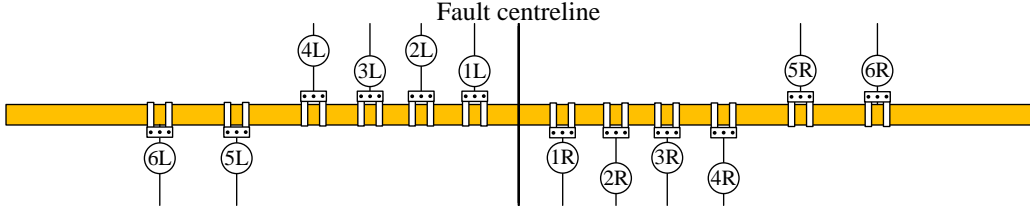


Figure D.11 Location of ring-springs in test setup for buried pipelines.

Table D.2 Location of ring-springs in test setup for buried pipelines.

Test	Distance of ring-spring to fault [mm]											
	6L	5L	4L	3L	2L	1L	1R	2R	3R	4R	5R	6R
T1	5250	4000	3000	2200	1400	700	700	1400	2200	3000	4000	5250
T2	7000	5500	4000	2900	1900	850	850	1900	2900	4000	5500	7000
T3	6000	4250	3250	2350	1550	750	750	1550	2350	3250	4250	6000
T4	4750	3500	2600	1875	1150	580	580	1150	1875	2600	3500	4750
T5	5000	3750	2900	2100	1350	600	600	1350	2100	2900	3750	5000
T6	5125	3950	2900	2100	1350	650	650	1350	2100	2900	3950	5125
T7	8000	6500	5900	4050	2700	1000	1000	2700	4050	5900	6500	8000
T8	7000	5500	4000	2900	1900	850	850	1900	2900	4000	5500	7000
T9	8000	6250	5250	3700	2200	850	850	2200	3700	5250	6250	8000
T10	6800	5250	3800	2500	1600	800	800	1600	2500	3800	5250	6800

D.4 Ring-spring response

The response of all ring-springs to the applied fault movement is presented in the figures below. The ring forces presented in the figures were transferred evenly to the pipeline specimen by two steel straps (see Figure 9.21c). In some graphs a discontinuity in ring-spring force is visible. In most cases, this is the result of shifting of the load application straps (see Table D.1). In case of test T2, this is caused by the failure of the load application straps (see Table D.1 and section 9.6.2 of the main text of this thesis).

Test T1

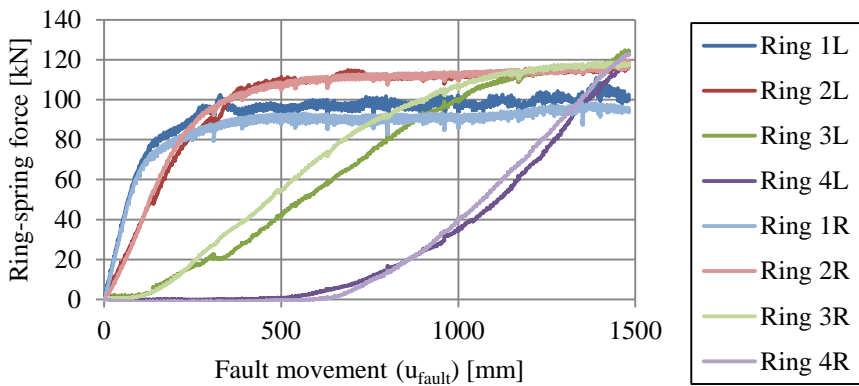


Figure D.12 Response of rings 1-4 during test T1.

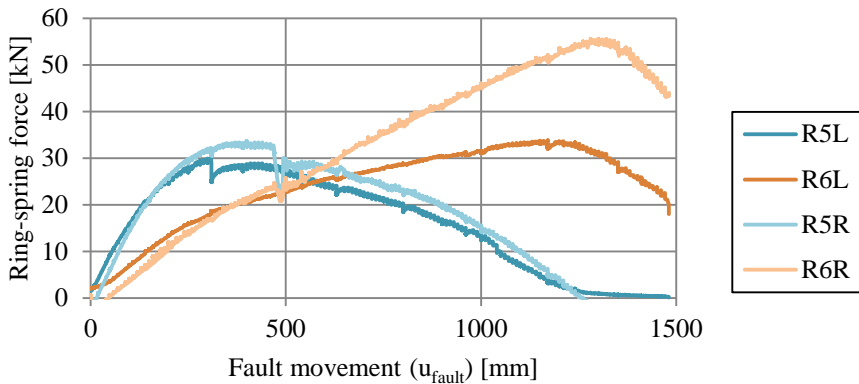


Figure D.13 Response of rings 5-6 during test T1.

Test T2

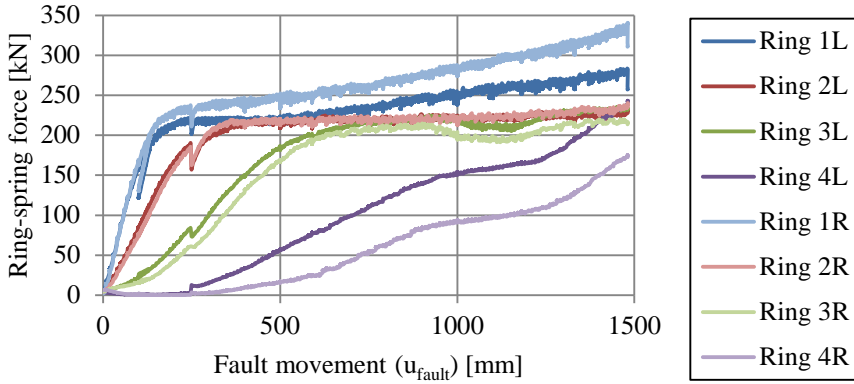


Figure D.14 Response of rings 1-4 during test T2.

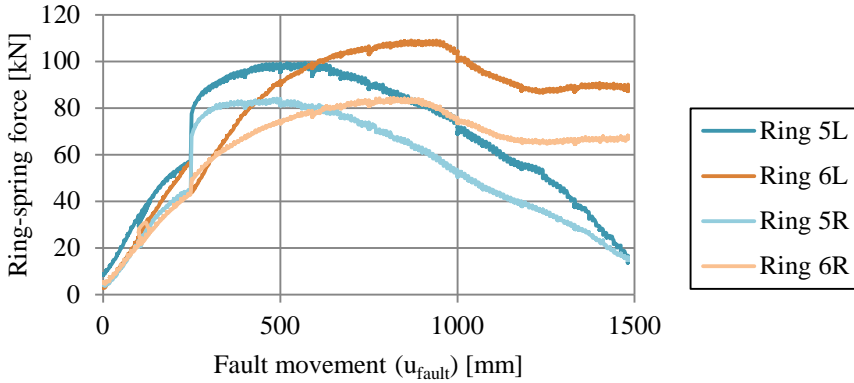


Figure D.15 Response of rings 5-6 during test T2.

Test T3

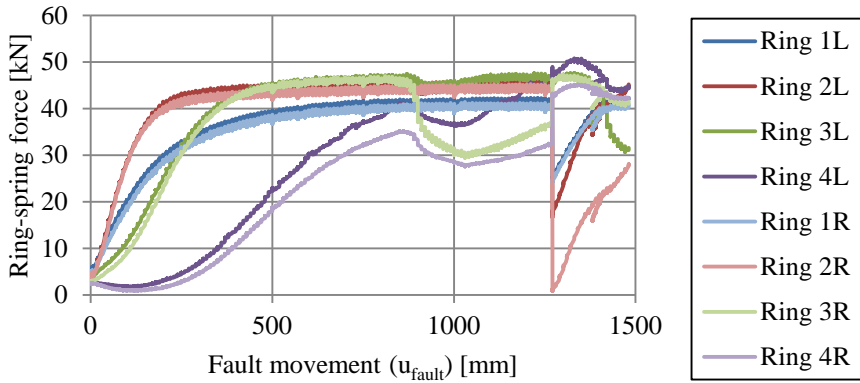


Figure D.16 Response of rings 1-4 during test T3.

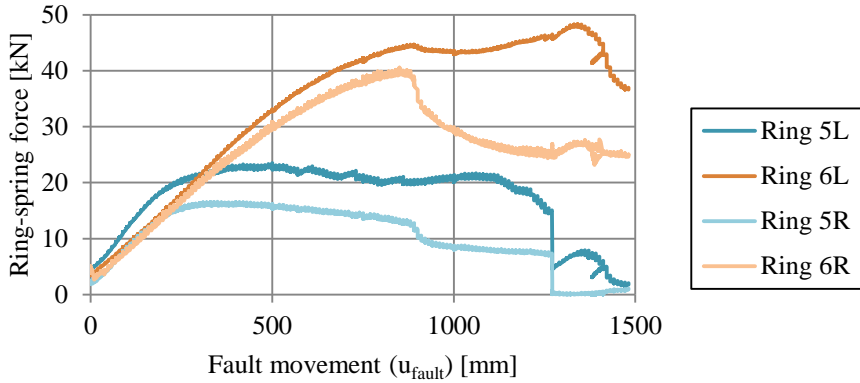


Figure D.17 Response of rings 5-6 during test T3.

Test T4

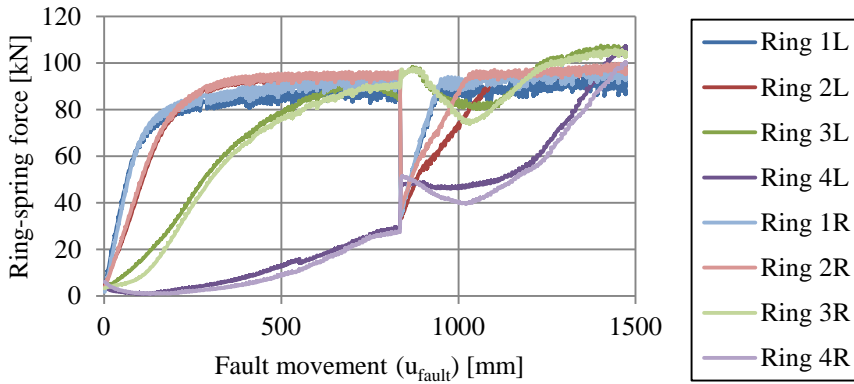


Figure D.18 Response of rings 1-4 during test T4.

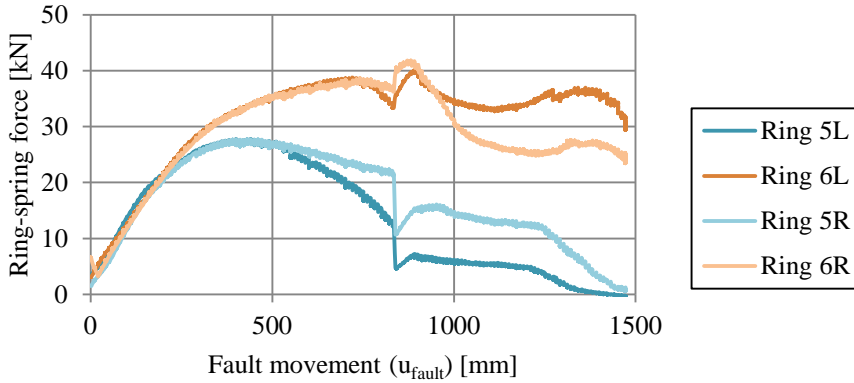


Figure D.19 Response of rings 5-6 during test T4.

Test T5

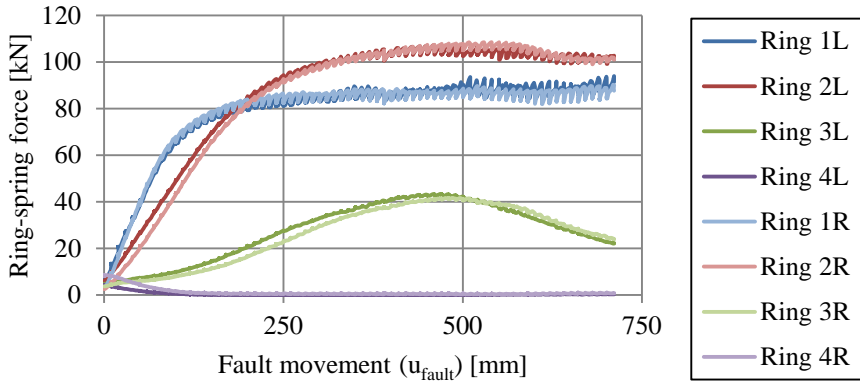


Figure D.20 Response of rings 1-4 during test T5.

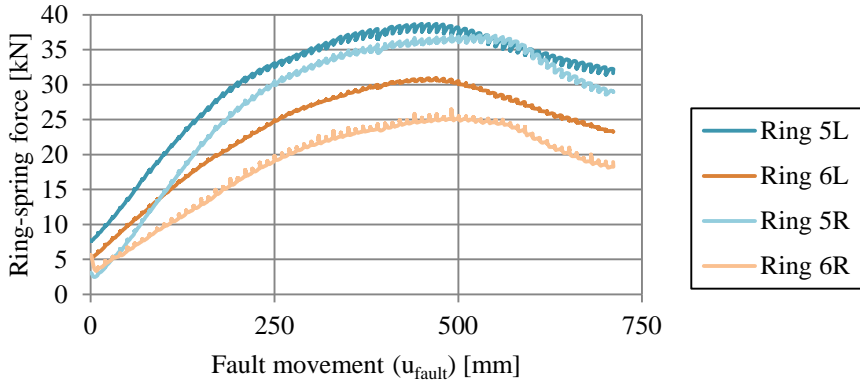


Figure D.21 Response of rings 5-6 during test T5.

Test T6

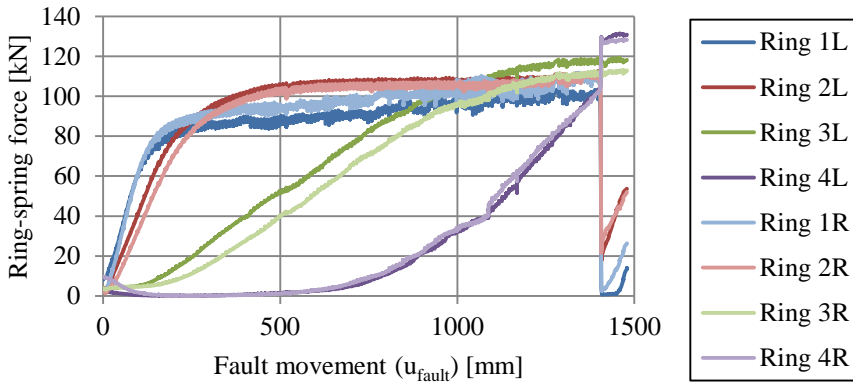


Figure D.22 Response of rings 1-4 during test T6.

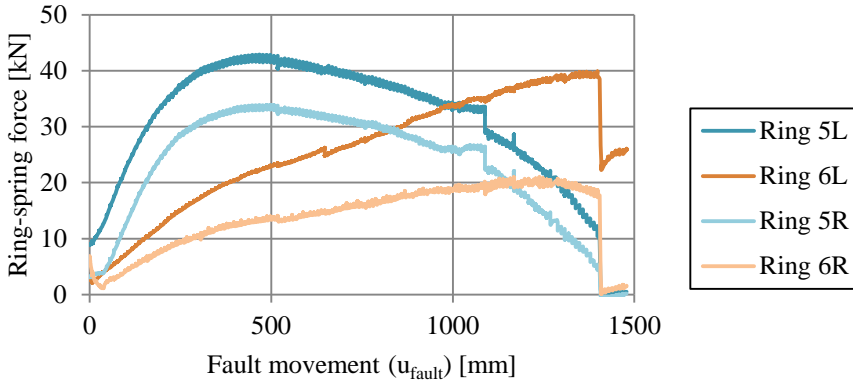


Figure D.23 Response of rings 5-6 during test T6.

Test T7

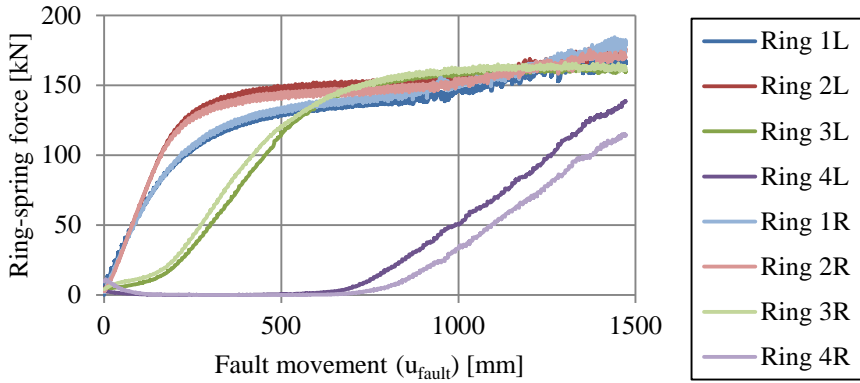


Figure D.24 Response of rings 1-4 during test T7.

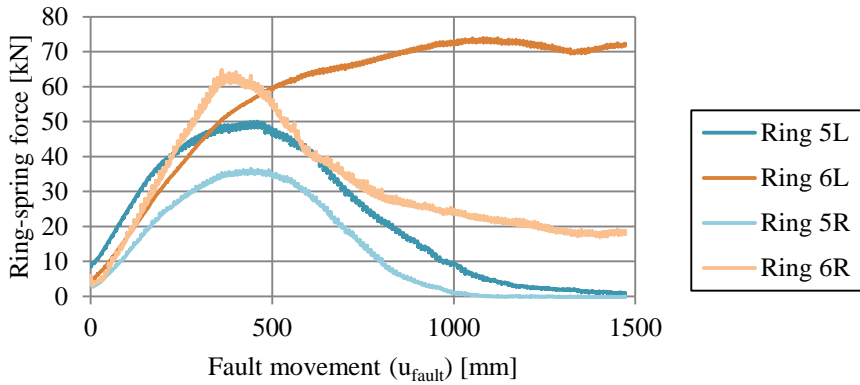


Figure D.25 Response of rings 5-6 during test T7.

Test T8

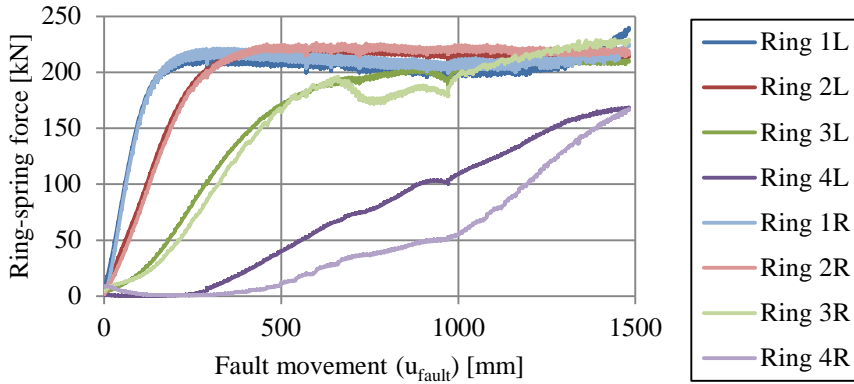


Figure D.26 Response of rings 1-4 during test T8.

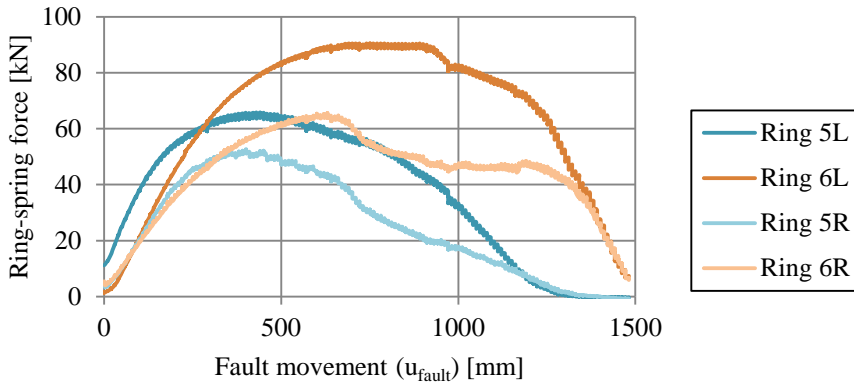


Figure D.27 Response of rings 5-6 during test T8.

Test T9

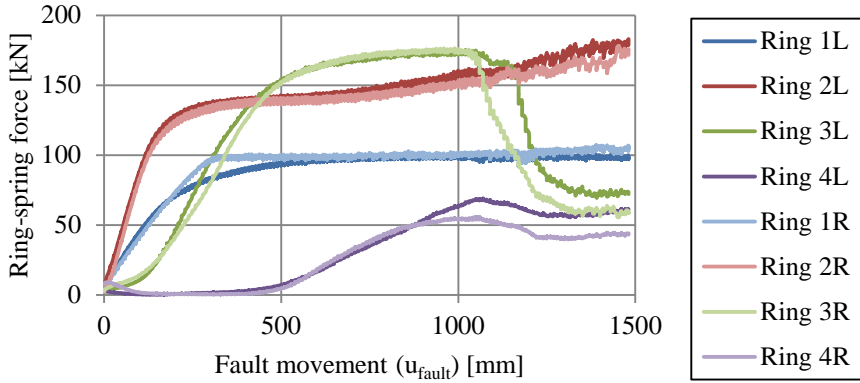


Figure D.28 Response of rings 1-4 during test T9.

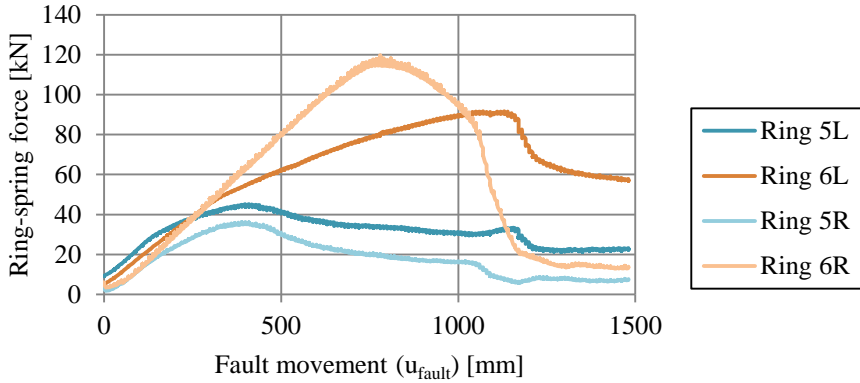


Figure D.29 Response of rings 5-6 during test T9.

Test T10

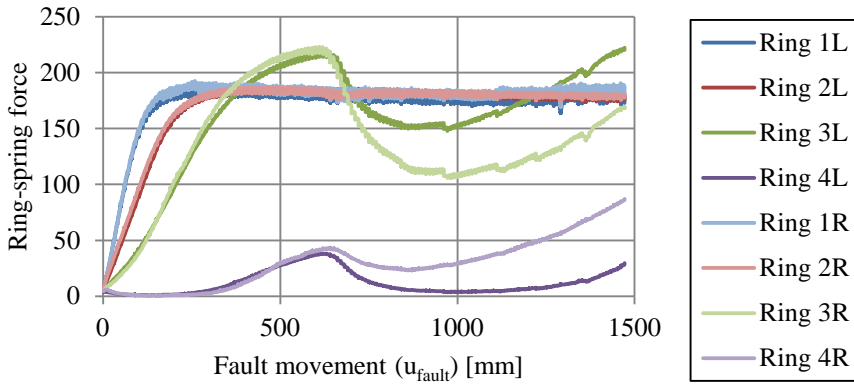


Figure D.30 Response of rings 1-4 during test T10.

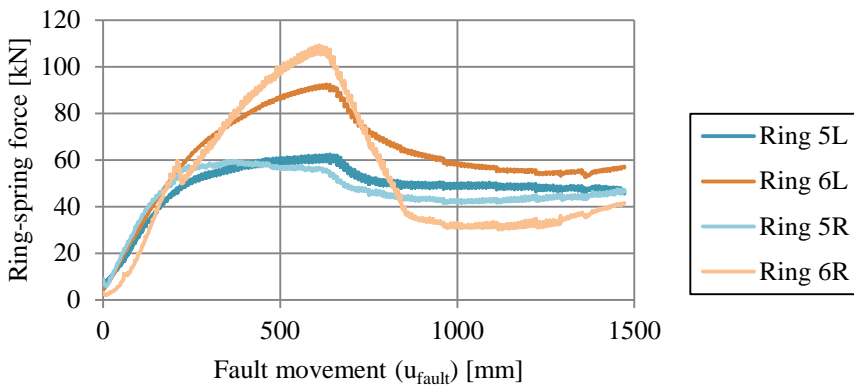
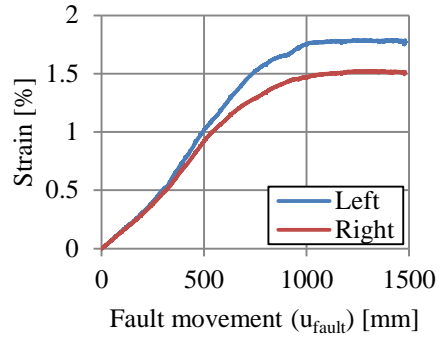
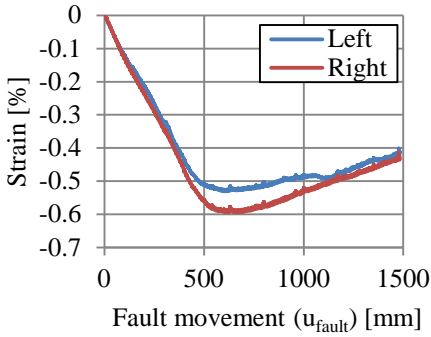


Figure D.31 Response of rings 5-6 during test T10.

D.5 Results of strain measurements

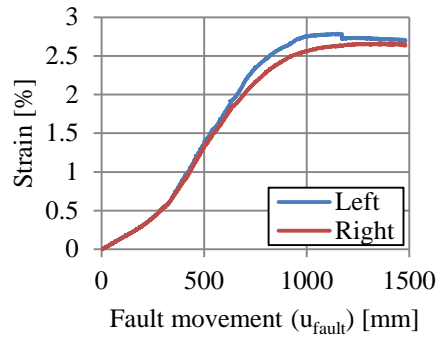
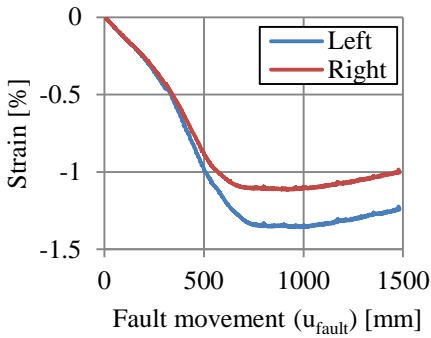
An overview of the distributions of longitudinal strain over the pipeline length is presented in section 9.6 of the main text of this thesis. Additionally, in this appendix, the development of strain during the tests is presented for a selection of measurement locations. In the figures, pairs of strain gauges in longitudinal direction at equal distances and opposite sides of the fault and pipeline are presented in one graph. For various reasons, some strain gauge measurements failed during the tests (see section 9.6 of the main text of this thesis). In the graphs, this is indicated with the label 'SG failure'.

Test T1



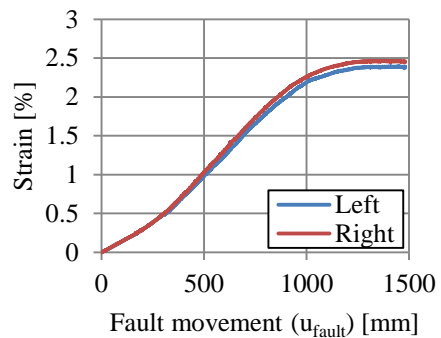
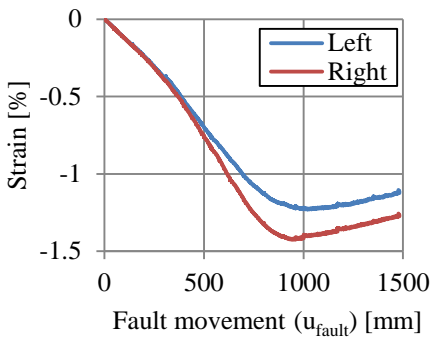
(a) Compressive strain 1250 mm from the fault

(b) Tensile strain 1250 mm from the fault



(c) Compressive strain 1500 mm from the fault

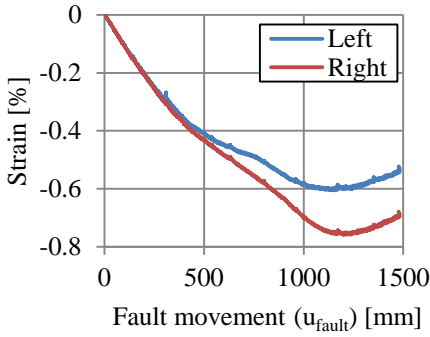
(d) Tensile strain 1500 mm from the fault



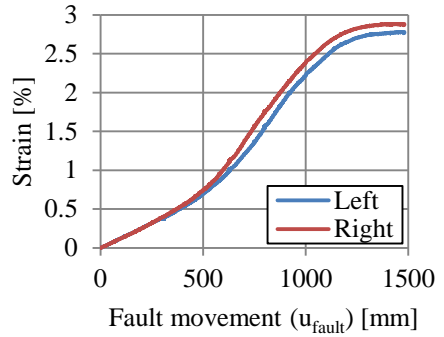
(e) Compressive strain 1750 mm from the fault

(f) Tensile strain 1750 mm from the fault

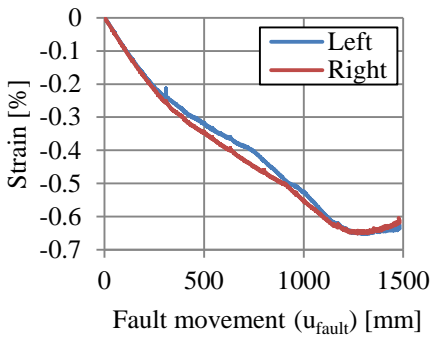
Figure D.32 Development of strain in pipeline specimen T1.



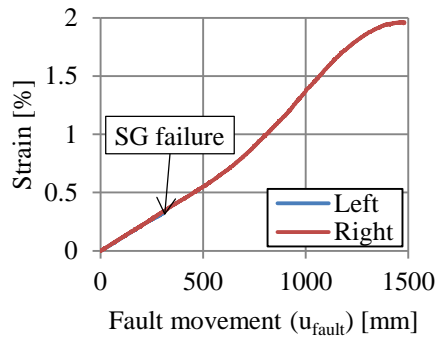
(a) Compressive strain 2000 mm from the fault



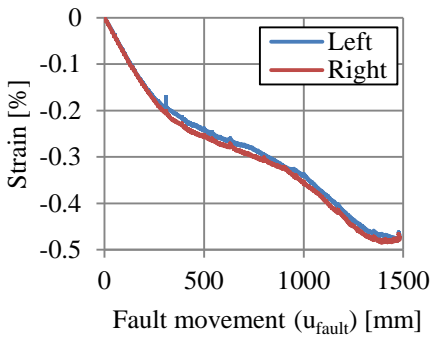
(b) Tensile strain 2000 mm from the fault



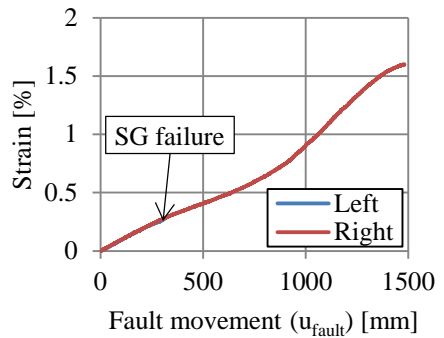
(c) Compressive strain 2250 mm from the fault



(d) Tensile strain 2250 mm from the fault



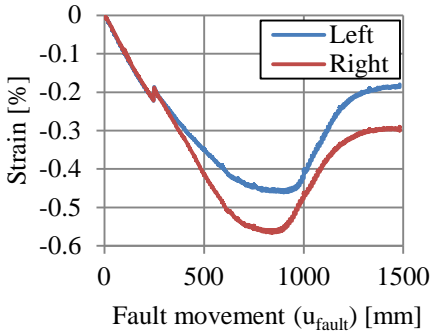
(e) Compressive strain 2500 mm from the fault



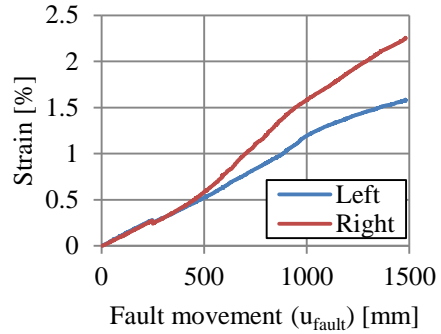
(f) Tensile strain 2500 mm from the fault

Figure D.33 Development of strain in pipeline specimen T1 (continued).

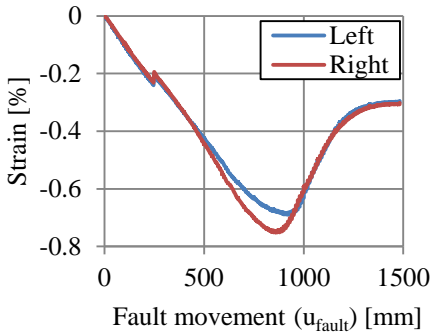
Test T2



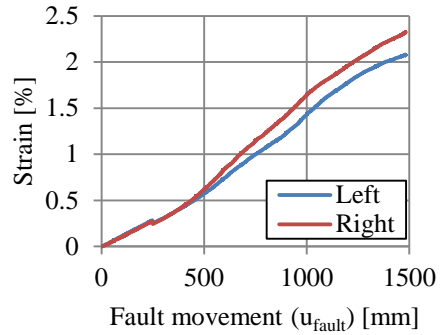
(a) Compressive strain 2000 mm from the fault



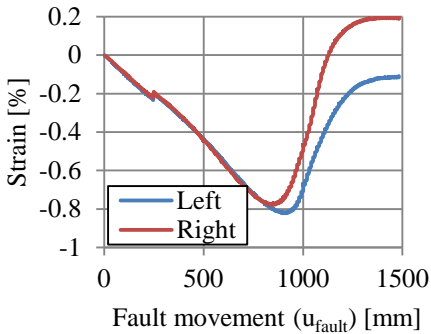
(b) Tensile strain 2000 mm from the fault



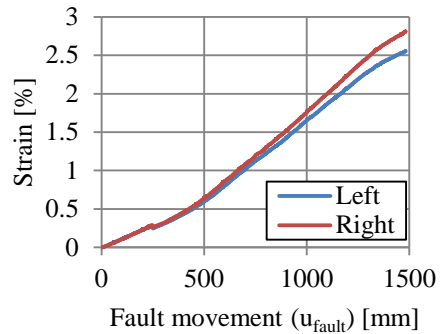
(c) Compressive strain 2250 mm from the fault



(d) Tensile strain 2250 mm from the fault

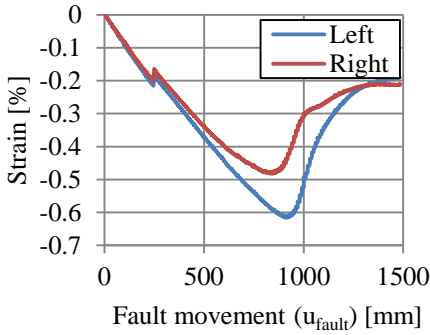


(e) Compressive strain 2500 mm from the fault

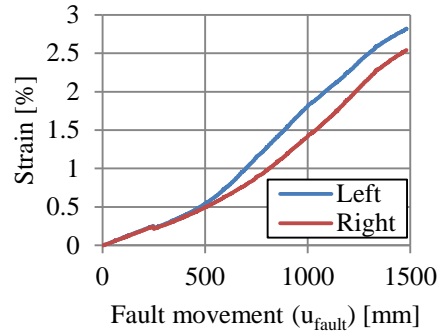


(f) Tensile strain 2500 mm from the fault

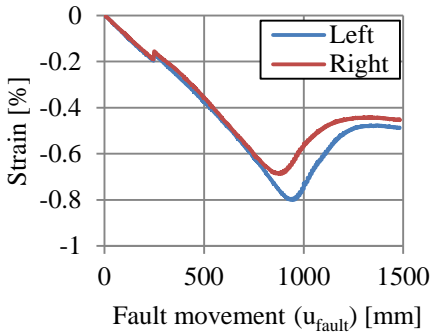
Figure D.34 Development of strain in pipeline specimen T2.



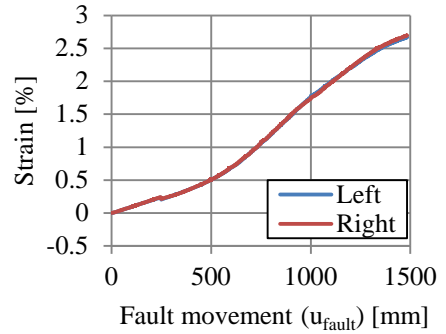
(a) Compressive strain 2750 mm from the fault



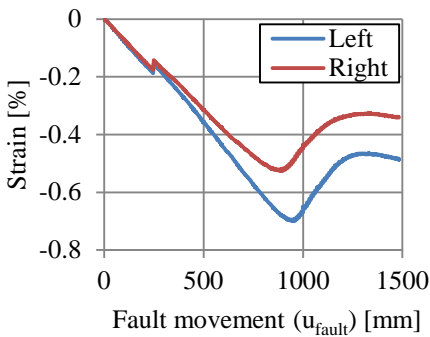
(b) Tensile strain 2750 mm from the fault



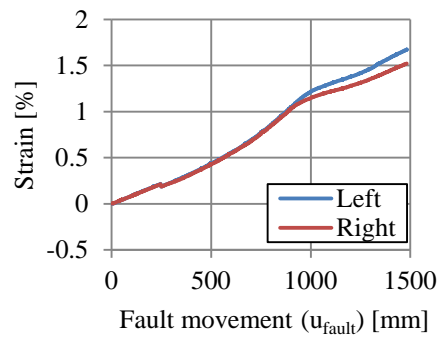
(c) Compressive strain 3000 mm from the fault



(d) Tensile strain 3000 mm from the fault



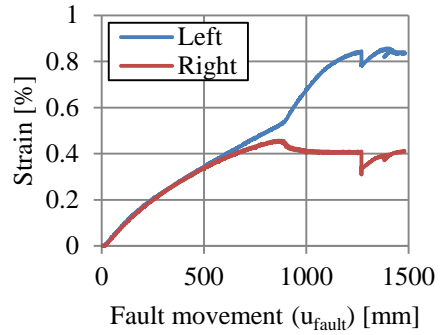
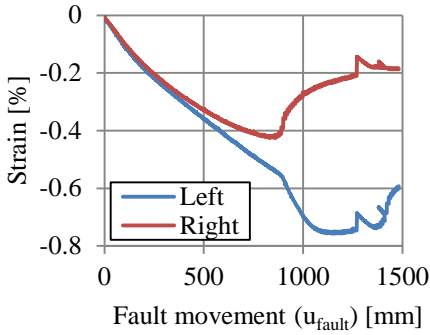
(e) Compressive strain 3250 mm from the fault



(f) Tensile strain 3250 mm from the fault

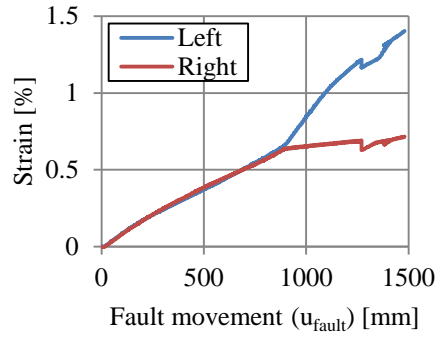
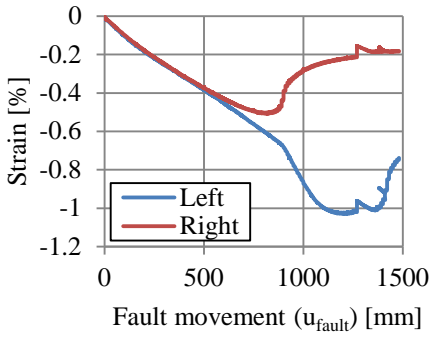
Figure D.35 Development of strain in pipeline specimen T2 (continued).

Test T3



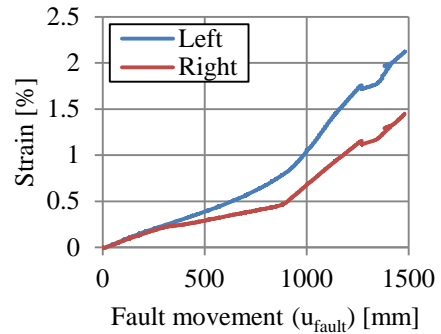
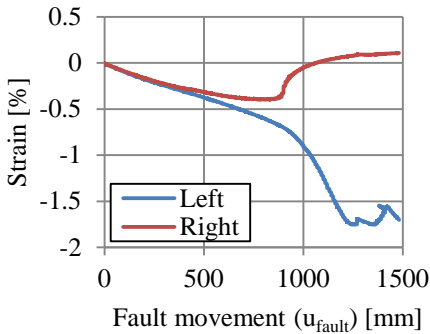
(a) Compressive strain 1675 mm from the fault

(b) Tensile strain 1675 mm from the fault



(c) Compressive strain 1950 mm from the fault

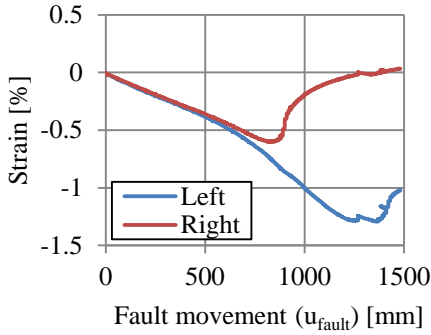
(d) Tensile strain 1950 mm from the fault



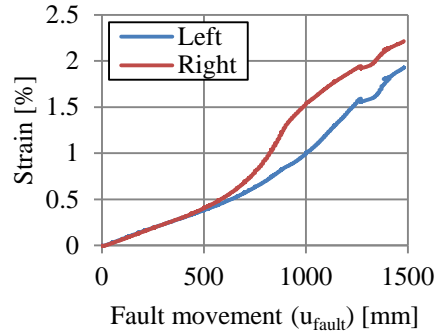
(e) Compressive strain 2225 mm from the fault

(f) Tensile strain 2225 mm from the fault

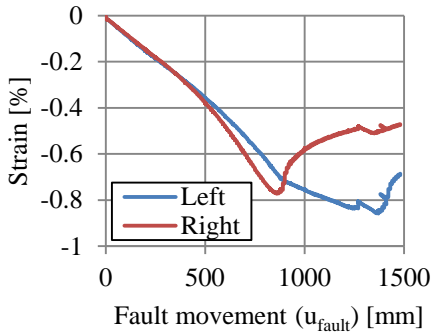
Figure D.36 Development of strain in pipeline specimen T3.



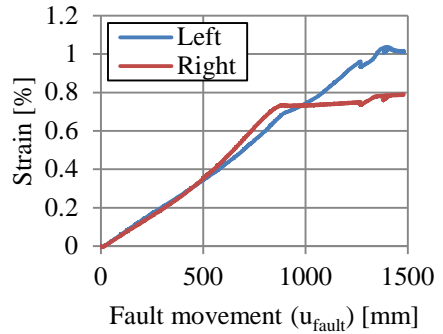
(a) Compressive strain 2500 mm from the fault



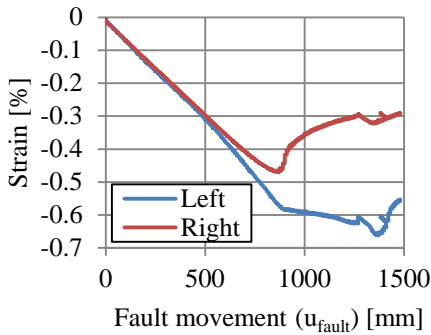
(b) Tensile strain 2500 mm from the fault



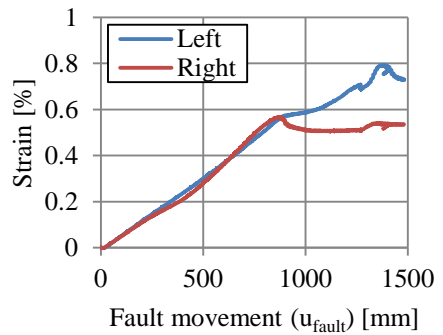
(c) Compressive strain 2775 mm from the fault



(d) Tensile strain 2775 mm from the fault



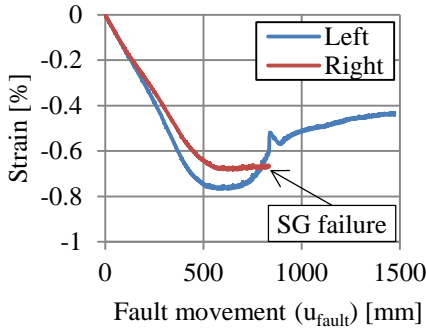
(e) Compressive strain 3050 mm from the fault



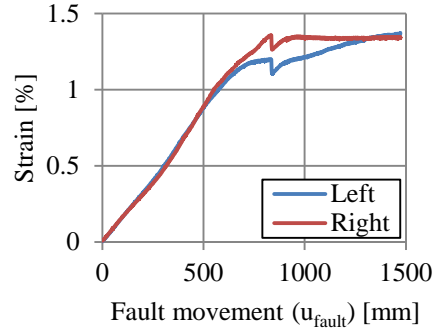
(f) Tensile strain 3050 mm from the fault

Figure D.37 Development of strain in pipeline specimen T3 (continued).

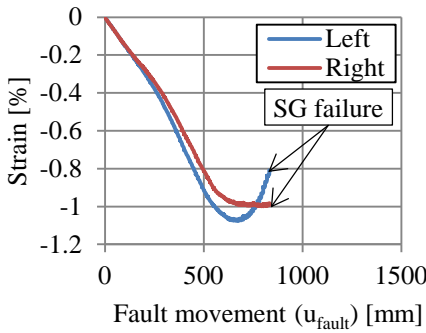
Test T4



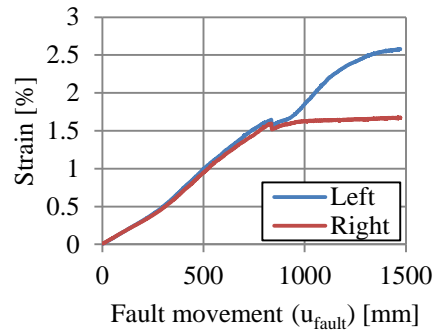
(a) Compressive strain 1200 mm from the fault



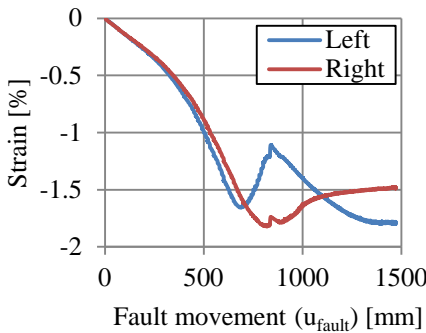
(b) Tensile strain 1200 mm from the fault



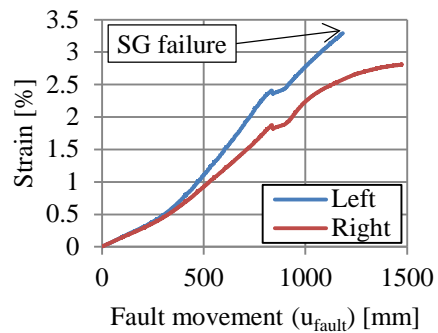
(c) Compressive strain 1400 mm from the fault



(d) Tensile strain 1400 mm from the fault

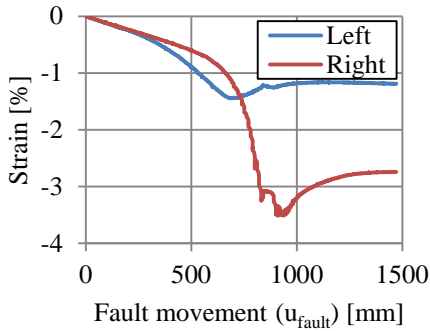


(e) Compressive strain 1600 mm from the fault

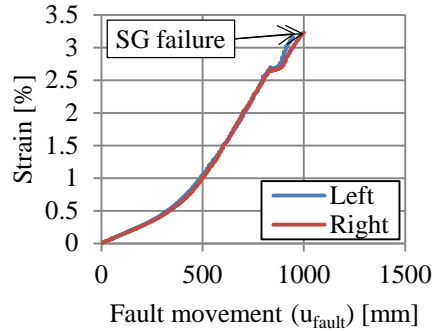


(f) Tensile strain 1600 mm from the fault

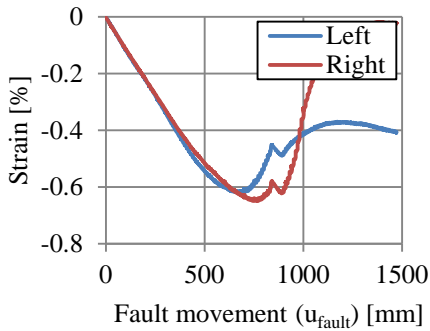
Figure D.38 Development of strain in pipeline specimen T4.



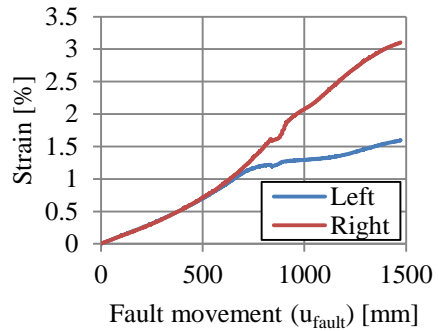
(a) Compressive strain 1800 mm from the fault



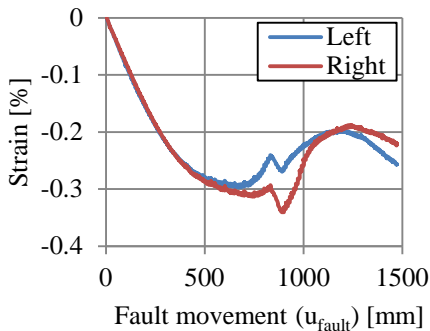
(b) Tensile strain 1800 mm from the fault



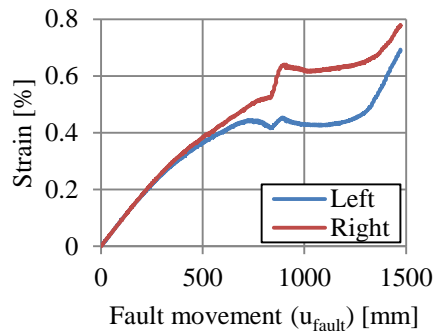
(c) Compressive strain 2000 mm from the fault



(d) Tensile strain 2000 mm from the fault



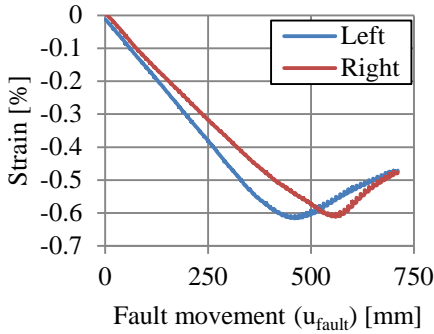
(e) Compressive strain 2500 mm from the fault



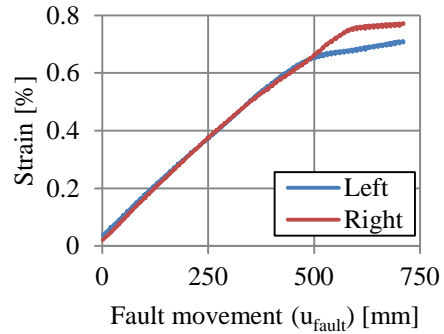
(f) Tensile strain 2500 mm from the fault

Figure D.39 Development of strain in pipeline specimen T4 (continued).

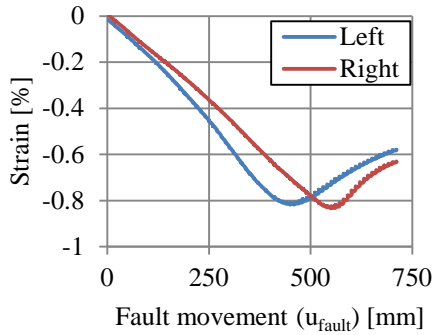
Test T5



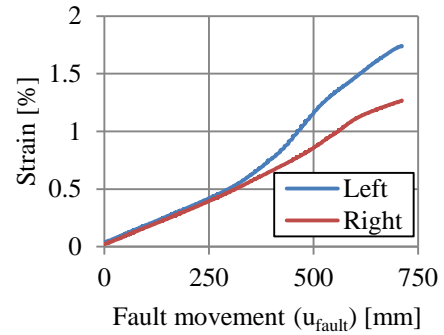
(a) Compressive strain 1100 mm from the fault



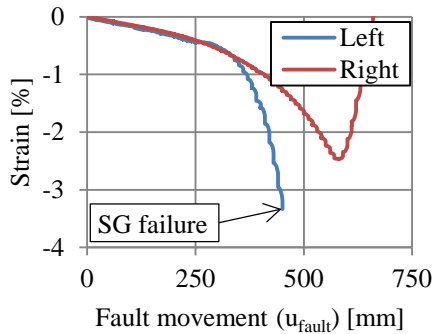
(b) Tensile strain 1100 mm from the fault



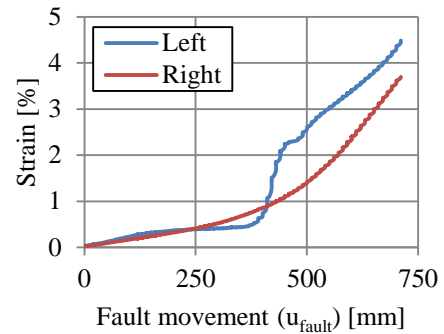
(c) Compressive strain 1250 mm from the fault



(d) Tensile strain 1250 mm from the fault

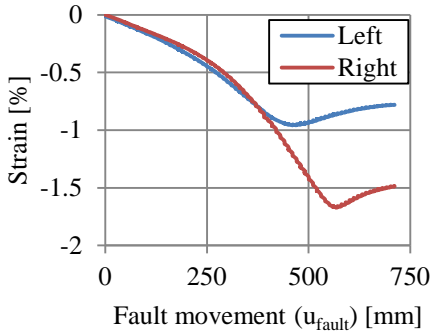


(e) Compressive strain 1450 mm from the fault

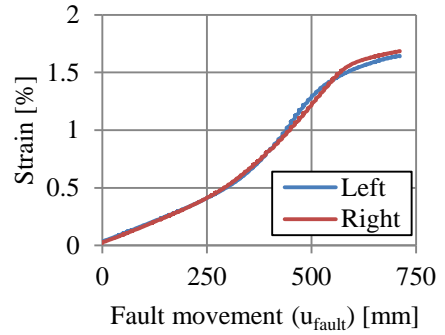


(e) Tensile strain 1450 mm from the fault

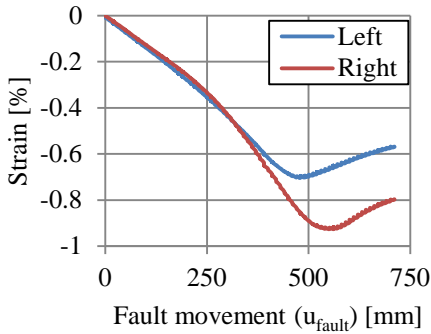
Figure D.40 Development of strain in pipeline specimen T5.



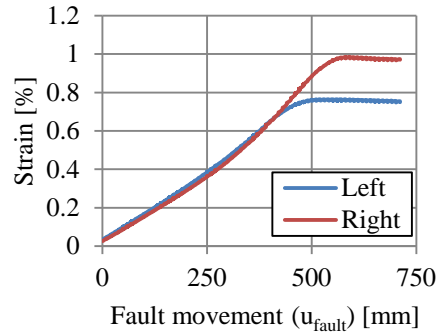
(a) Compressive strain 1650 mm from the fault



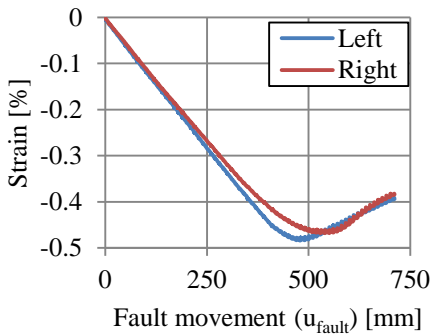
(b) Tensile strain 1650 mm from the fault



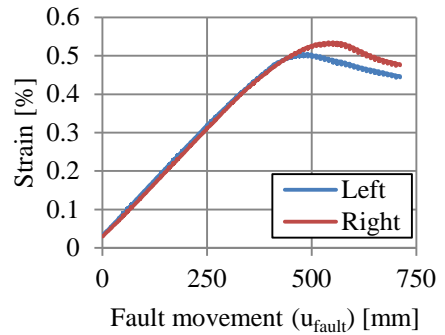
(c) Compressive strain 1850 mm from the fault



(d) Tensile strain 1850 mm from the fault



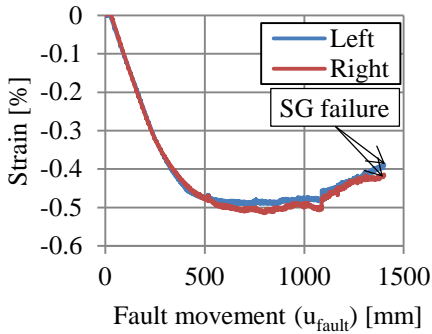
(e) Compressive strain 2150 mm from the fault



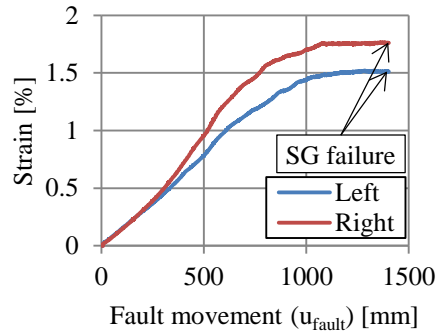
(f) Tensile strain 2150 mm from the fault

Figure D.41 Development of strain in pipeline specimen T5 (continued).

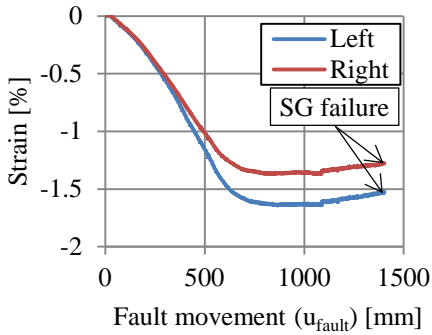
Test T6



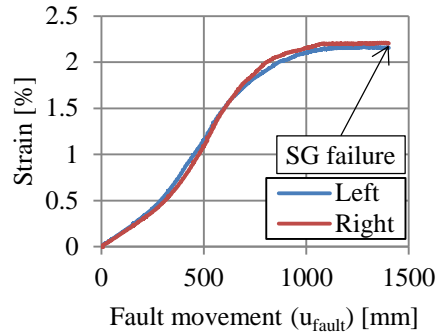
(a) Compressive strain 1160 mm from the fault



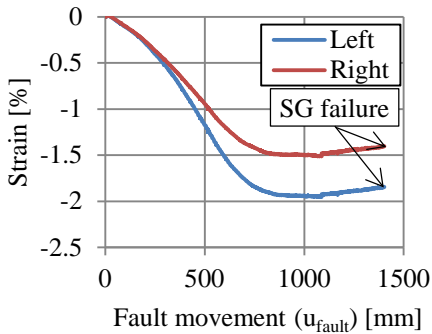
(b) Tensile strain 1160 mm from the fault



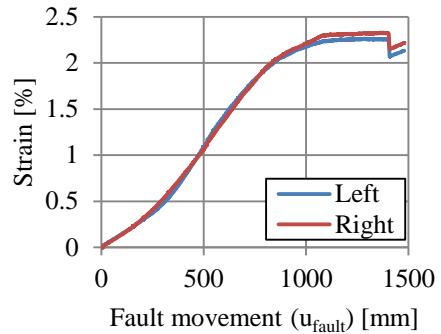
(c) Compressive strain 1420 mm from the fault



(d) Tensile strain 1420 mm from the fault

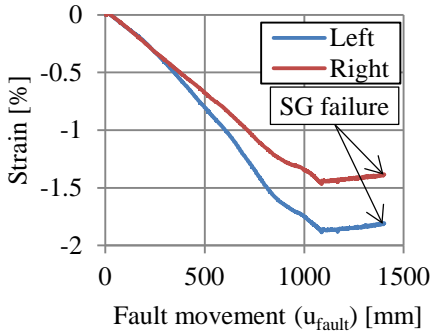


(e) Compressive strain 1630 mm from the fault

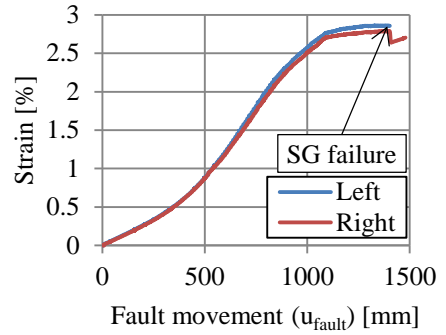


(f) Tensile strain 1630 mm from the fault

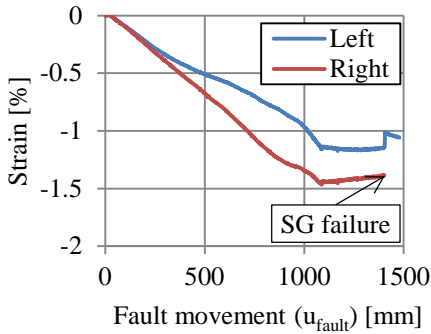
Figure D.42 Development of strain in pipeline specimen T6.



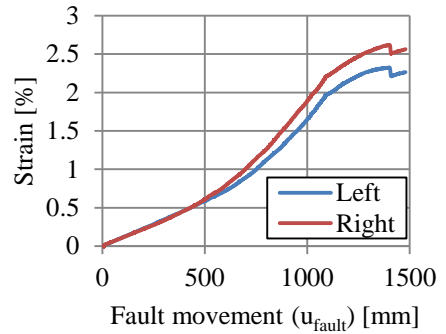
(a) Compressive strain 1840 mm from the fault



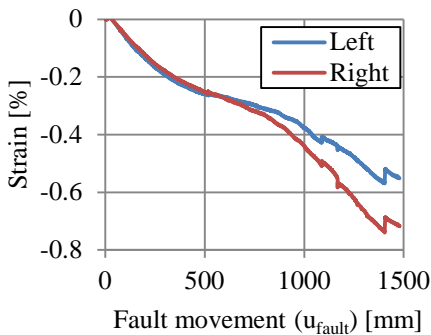
(b) Tensile strain 1840 mm from the fault



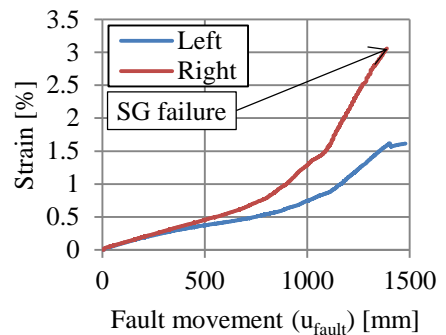
(c) Compressive strain 2125 mm from the fault



(d) Tensile strain 2125 mm from the fault



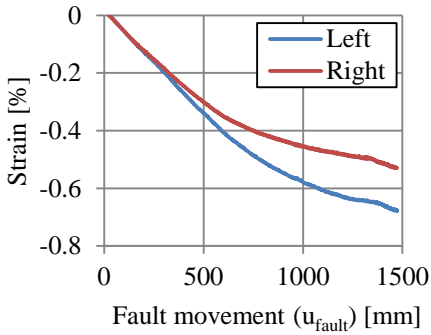
(e) Compressive strain 2550 mm from the fault



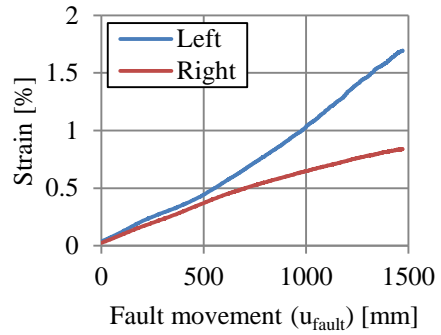
(f) Tensile strain 2550 mm from the fault

Figure D.43 Development of strain in pipeline specimen T6 (continued).

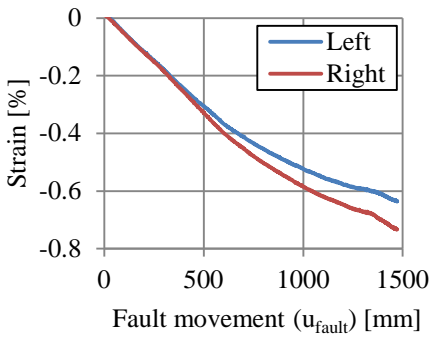
Test T7



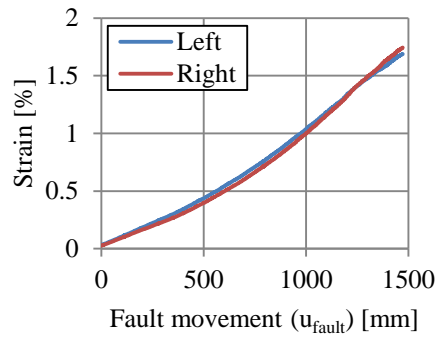
(a) Compressive strain 3000 mm from the fault



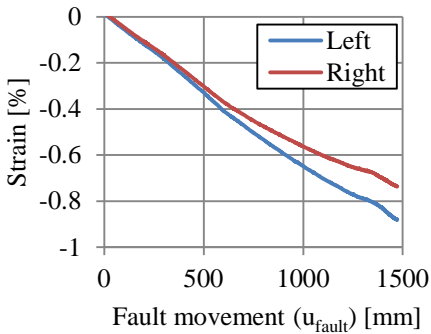
(b) Tensile strain 3000 mm from the fault



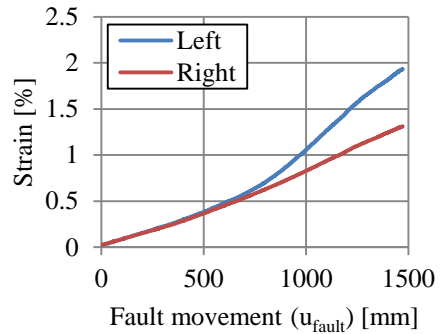
(c) Compressive strain 3375 mm from the fault



(d) Tensile strain 3375 mm from the fault

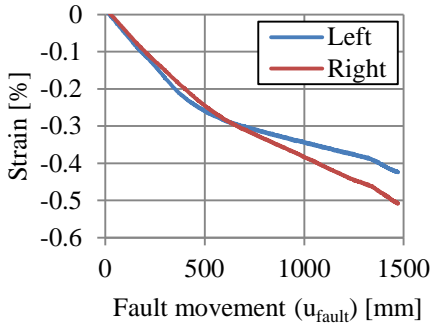


(e) Compressive strain 3625 mm from the fault

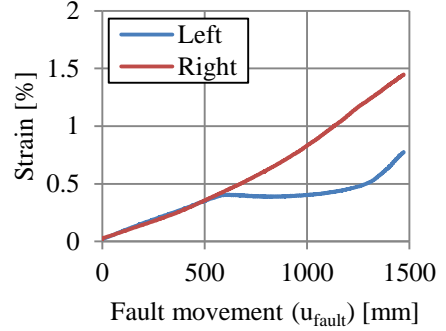


(f) Tensile strain 3625 mm from the fault

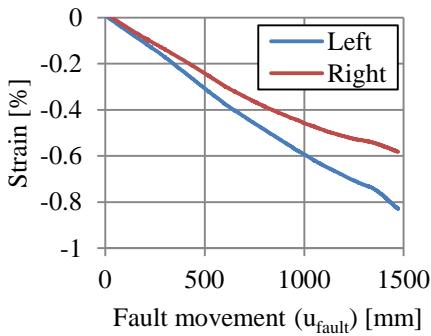
Figure D.44 Development of strain in pipeline specimen T7.



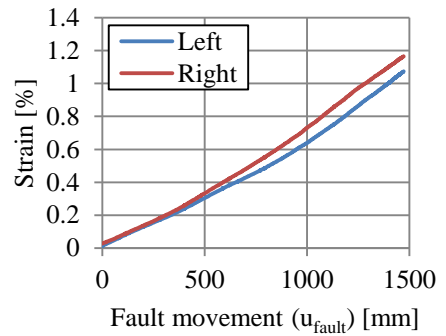
(a) Compressive strain 3875 mm from the fault



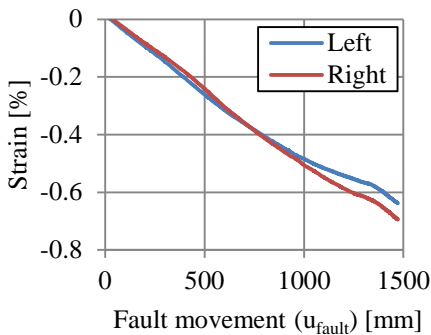
(b) Tensile strain 3875 mm from the fault



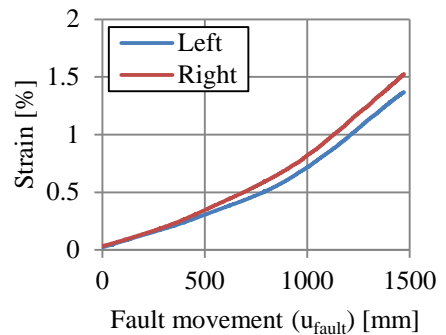
(c) Compressive strain 4125 mm from the fault



(d) Tensile strain 4125 mm from the fault



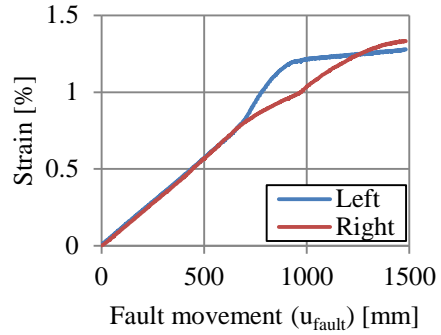
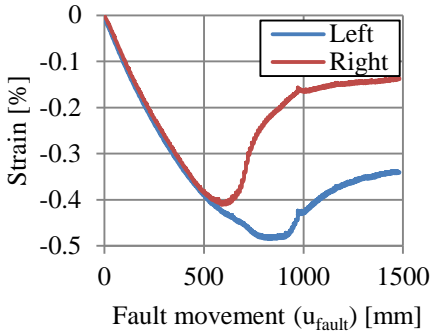
(e) Compressive strain 4375 mm from the fault



(f) Tensile strain 4375 mm from the fault

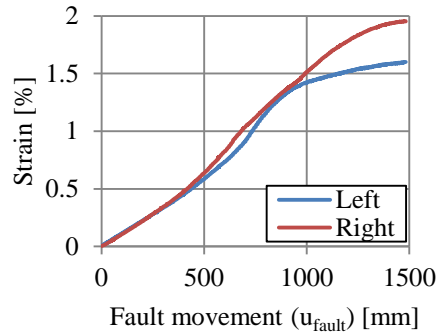
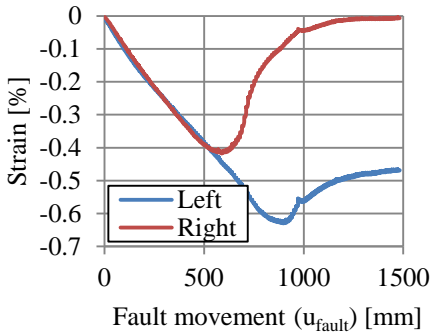
Figure D.45 Development of strain in pipeline specimen T7.

Test T8



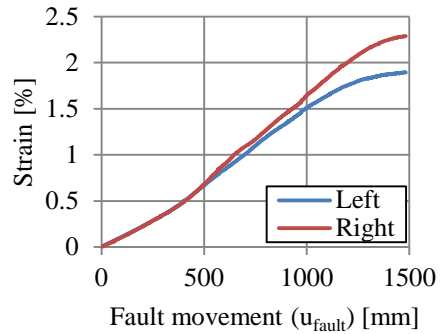
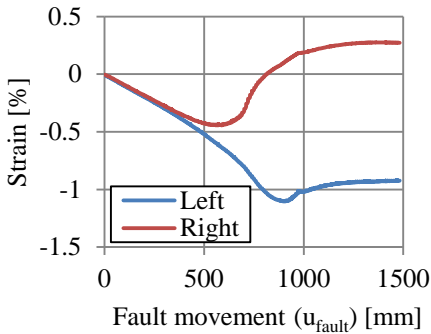
(a) Compressive strain 1900 mm from the fault

(b) Tensile strain 1900 mm from the fault



(c) Compressive strain 2175 mm from the fault

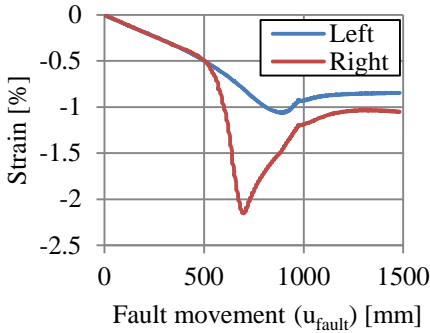
(d) Tensile strain 2175 mm from the fault



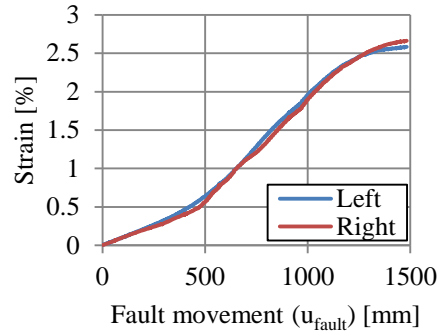
(e) Compressive strain 2400 mm from the fault

(f) Tensile strain 2400 mm from the fault

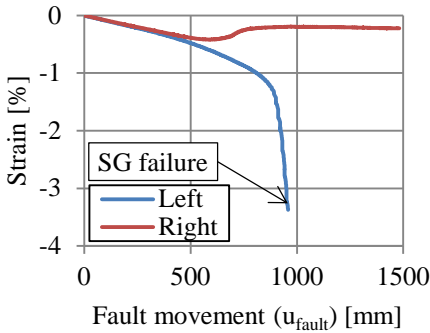
Figure D.46 Development of strain in pipeline specimen T8.



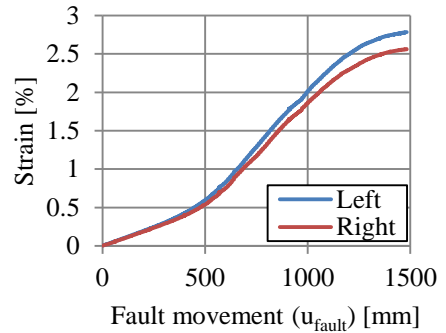
(a) Compressive strain 2625 mm from the fault



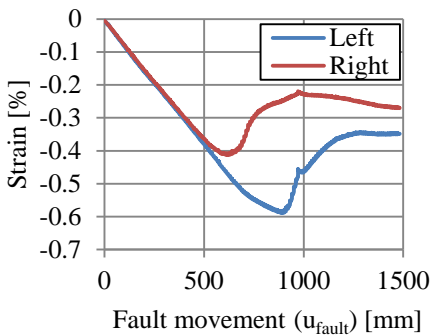
(b) Tensile strain 2625 mm from the fault



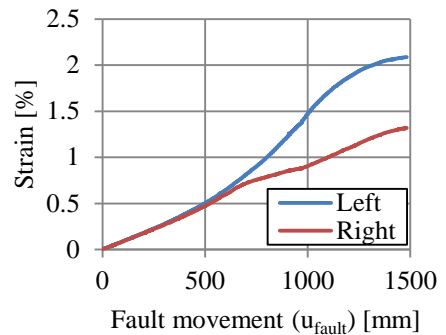
(c) Compressive strain 2900 mm from the fault



(d) Tensile strain 2900 mm from the fault



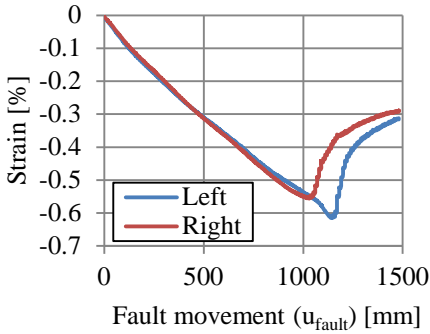
(e) Compressive strain 3175 mm from the fault



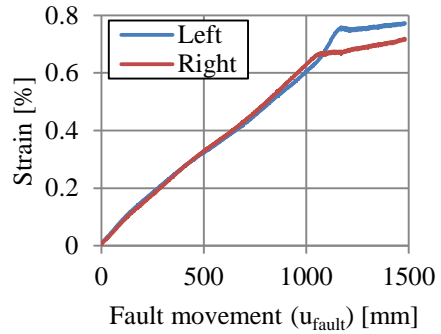
(f) Tensile strain 3175 mm from the fault

Figure D.47 Development of strain in pipeline specimen T8 (continued).

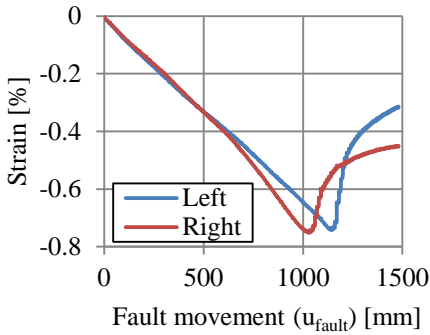
Test T9



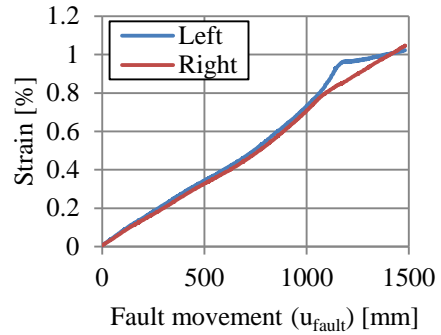
(a) Compressive strain 2850 mm from the fault



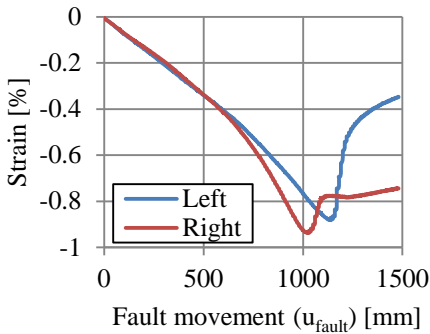
(b) Tensile strain 2850 mm from the fault



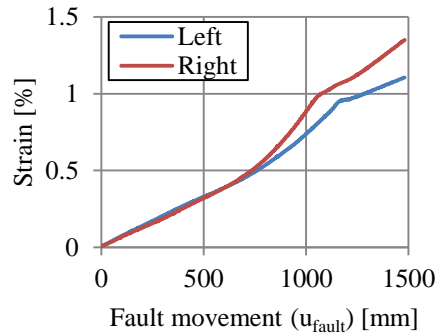
(c) Compressive strain 3150 mm from the fault



(d) Tensile strain 3150 mm from the fault

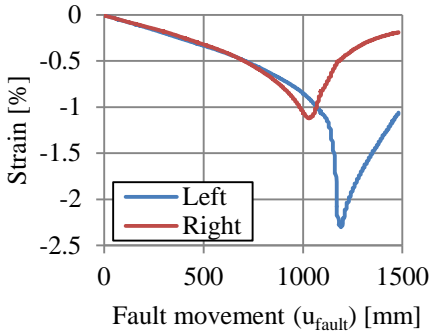


(e) Compressive strain 3425 mm from the fault

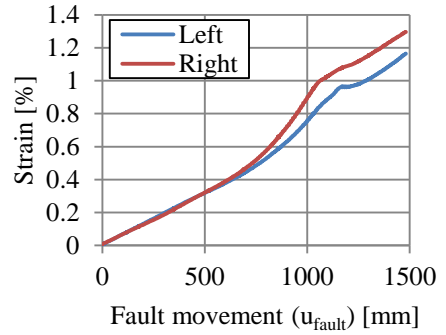


(f) Tensile strain 3425 mm from the fault

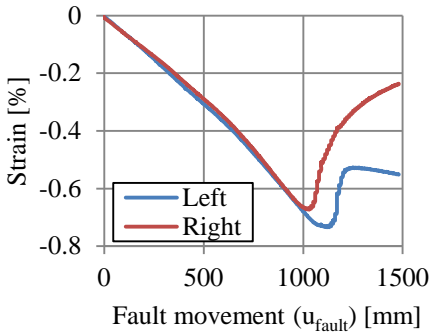
Figure D.48 Development of strain in pipeline specimen T9.



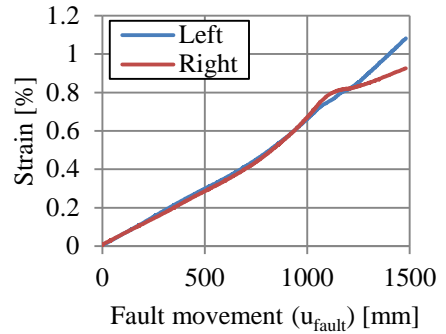
(a) Compressive strain 3750 mm from the fault



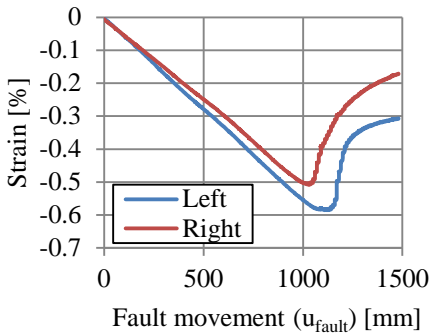
(b) Tensile strain 3750 mm from the fault



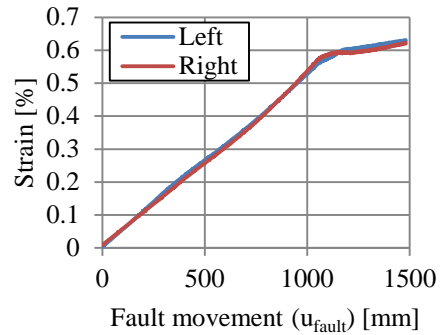
(c) Compressive strain 4050 mm from the fault



(d) Tensile strain 4050 mm from the fault



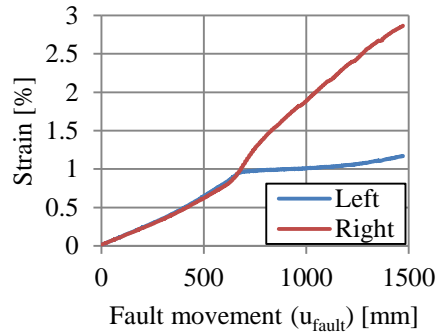
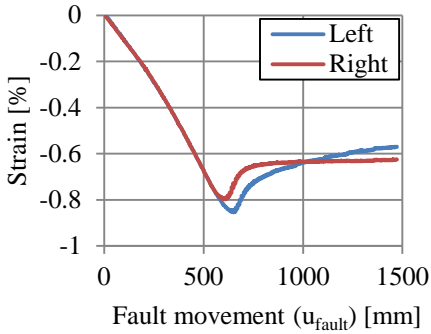
(e) Compressive strain 4350 mm from the fault



(f) Tensile strain 4350 mm from the fault

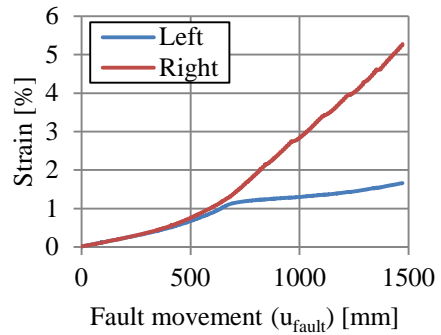
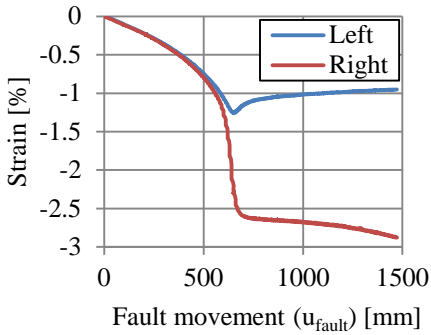
Figure D.49 Development of strain in pipeline specimen T9 (continued).

Test T10



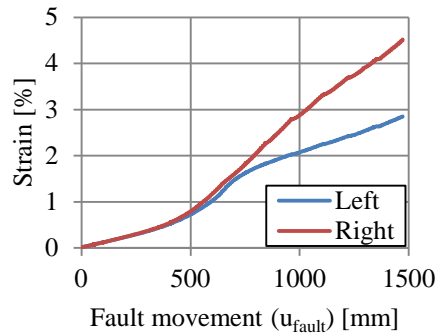
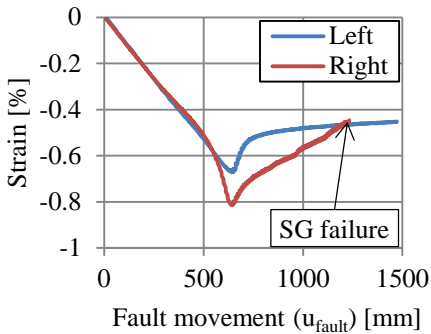
(a) Compressive strain 2000 mm from the fault

(b) Tensile strain 2000 mm from the fault



(c) Compressive strain 2150 mm from the fault

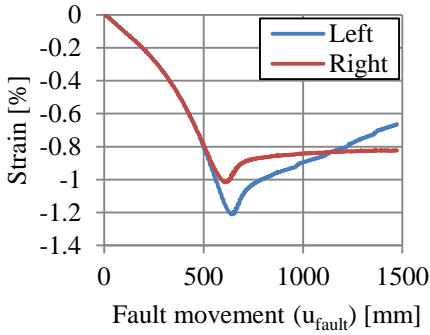
(d) Tensile strain 2150 mm from the fault



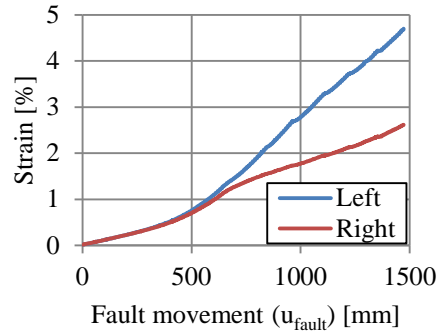
(e) Compressive strain 2300 mm from the fault

(f) Tensile strain 2300 mm from the fault

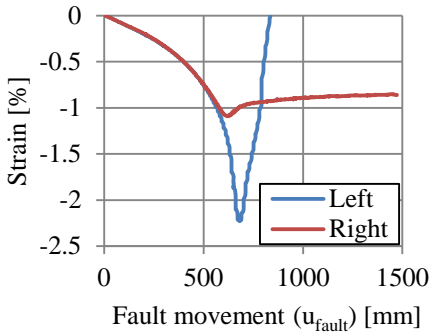
Figure D.50 Development of strain in pipeline specimen T10.



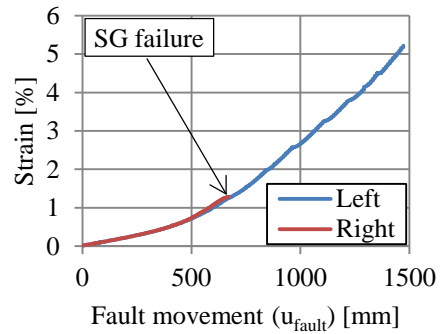
(a) Compressive strain 2450 mm from the fault



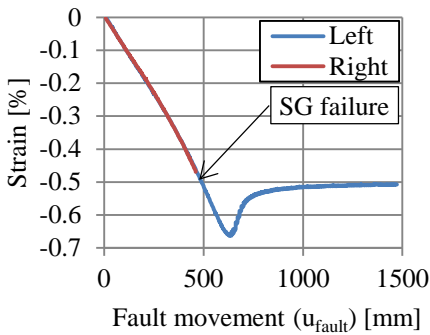
(b) Tensile strain 2450 mm from the fault



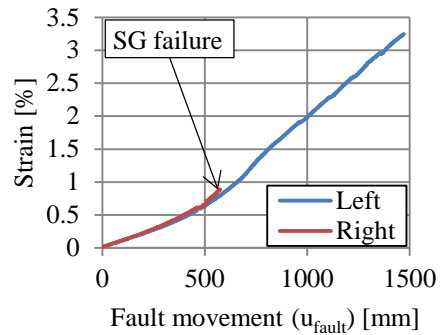
(c) Compressive strain 2575 mm from the fault



(d) Tensile strain 2575 mm from the fault



(e) Compressive strain 2775 mm from the fault



(f) Tensile strain 2775 mm from the fault

Figure D.51 Development of strain in pipeline specimen T10 (continued).

D.6 Results of ovalisation measurements

In this appendix, a general overview of the distribution of the ovalisation over the pipeline length is presented. Furthermore, the development of ovalisation during the tests is presented for a selection of measurement locations. All presented ovalisation measurements are normalized according to equation (D.1). In case of tests with internal pressure, the ovalisation measurements were set at zero after pressurizing, before starting the fault movement test. In case of failure of the measurement equipment, results were removed from the graphs, resulting in a discontinuous line.

$$\Delta D_{norm} = \frac{\Delta D}{D_n} \tag{D.1}$$

Test T1

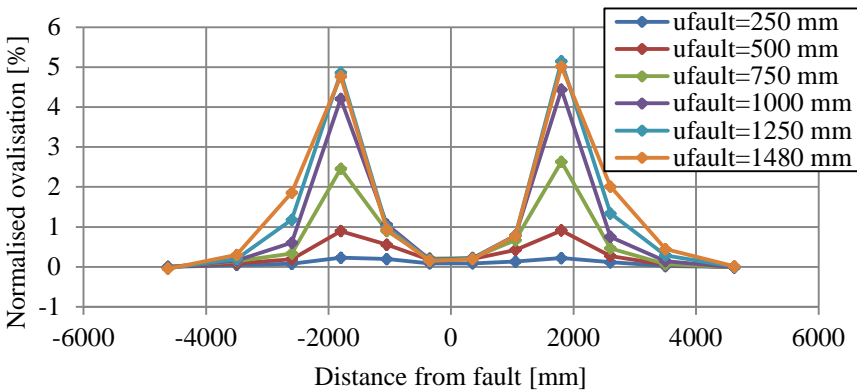
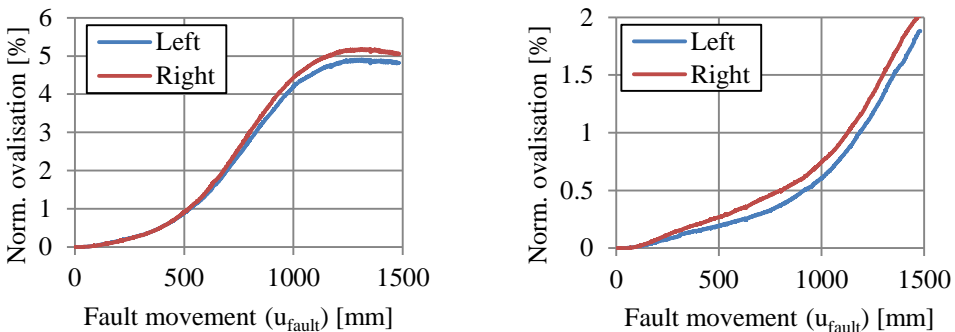


Figure D.52 Distribution of vertical ovalisation over the length of specimen T1.



(a) Ovalisation 1800 mm from the fault

(b) Ovalisation 2600 mm from the fault

Figure D.53 Development of ovalisation in specimen T1.

Test T2

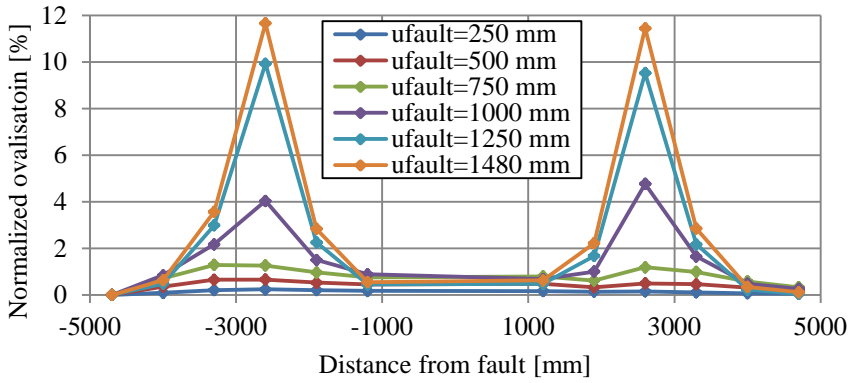
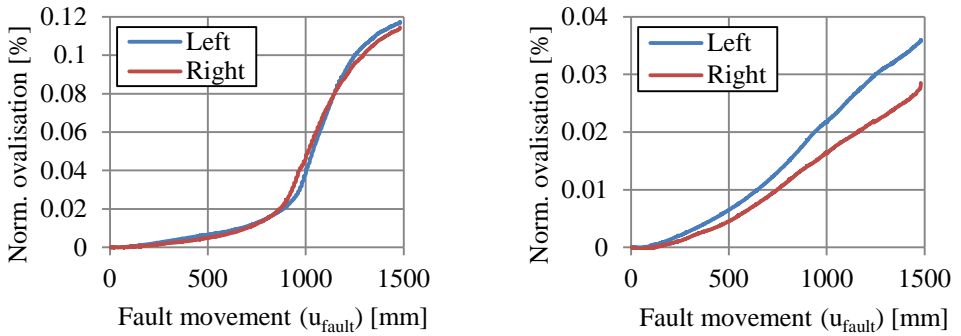


Figure D.54 Distribution of vertical ovalisation over the length of specimen T2.



(a) Ovalisation 2600 from the fault

(b) Ovalisation 3300 mm from the fault

Figure D.55 Development of vertical ovalisation in specimen T2.

Test T3

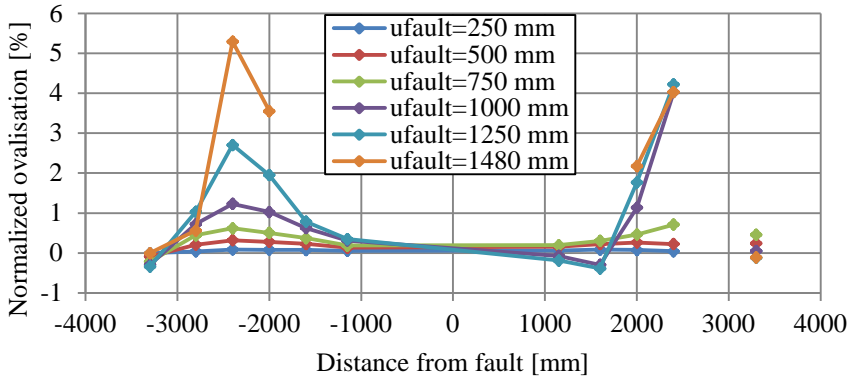
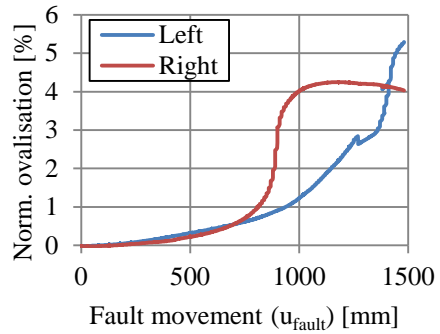
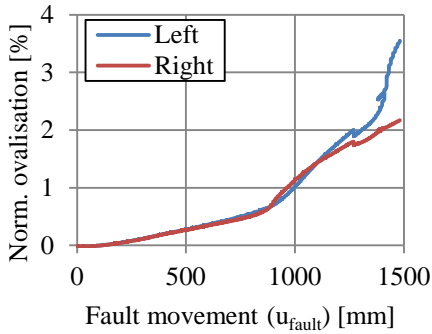


Figure D.56 Distribution of vertical ovalisation over the length of specimen T3.



(a) Ovalisation 2000 mm from the fault

(b) Ovalisation 2400 mm from the fault

Figure D.57 Development over vertical ovalisation in specimen T3.

Test T4

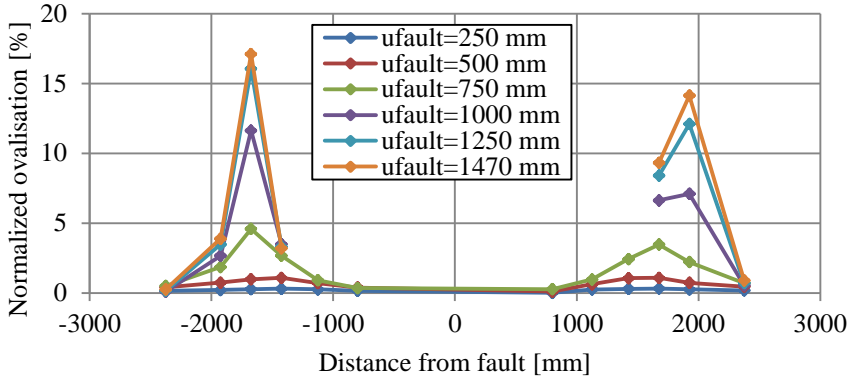
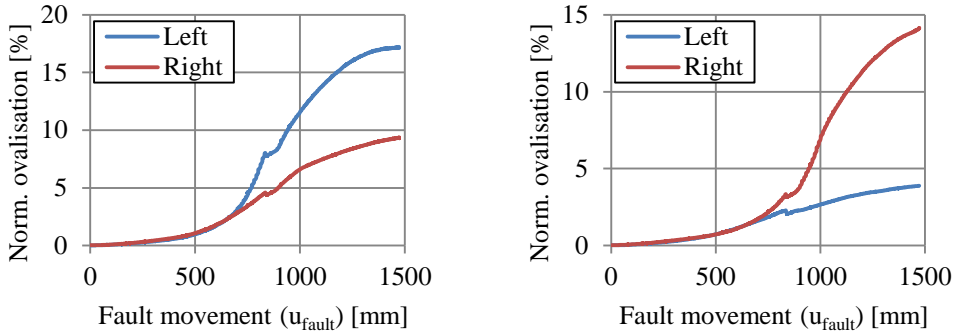


Figure D.58 Distribution of vertical ovalisation over the length of specimen T4.



(a) Ovalisation 1675 mm from the fault

(b) Ovalisation 1925 mm from the fault

Figure D.59 Development of vertical ovalisation in specimen T4.

Test T5

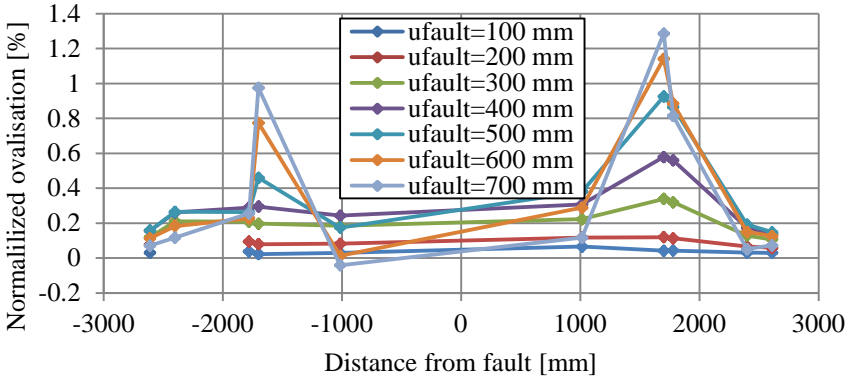


Figure D.60 Distribution of vertical ovalisation over the length of specimen T5.

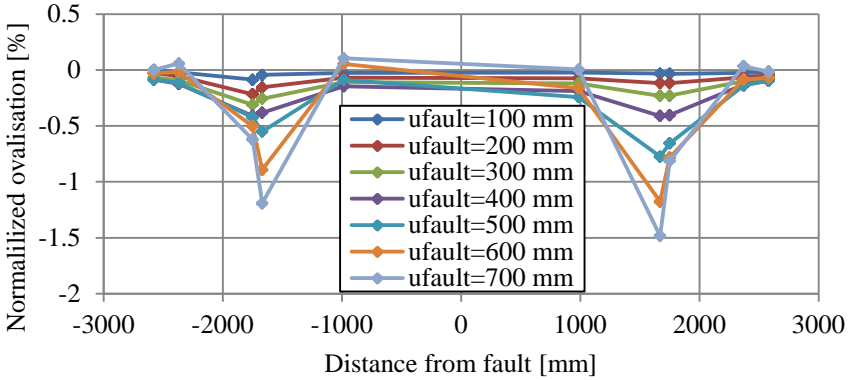
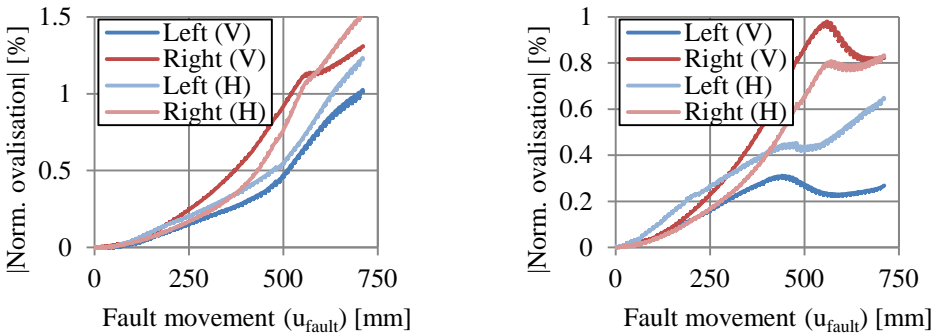


Figure D.61 Distribution of horizontal ovalisation over the length of specimen T5.



(a) Ovalisation 1685 mm from the fault

(b) Ovalisation 1765 mm from the fault

Figure D.62 Development of horizontal and vertical ovalisation in specimen T5.

Test T6

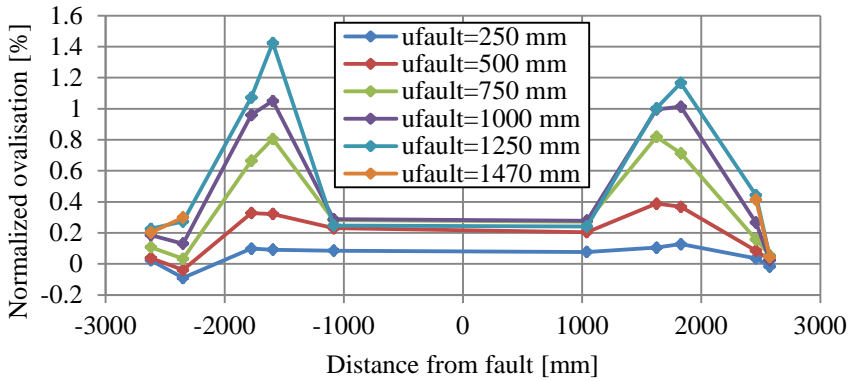


Figure D.63 Distribution of vertical ovalisation over the length of specimen T6.

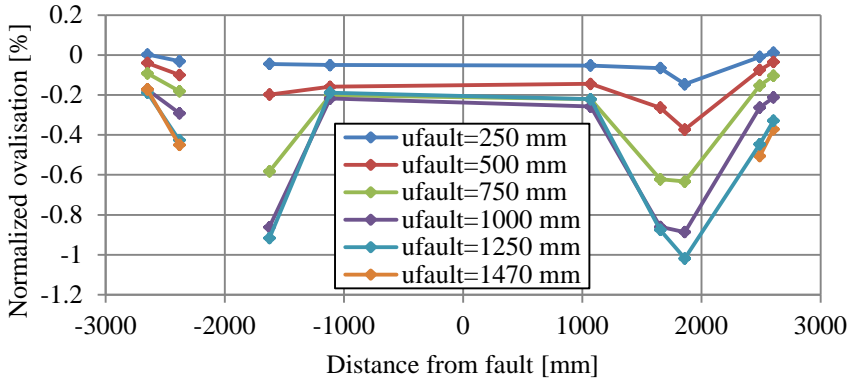
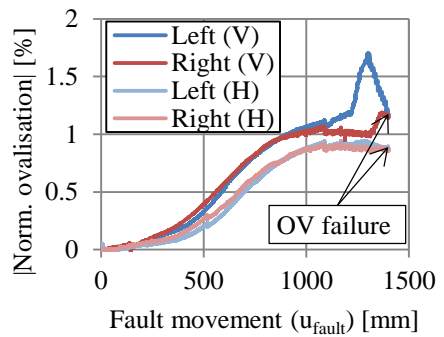
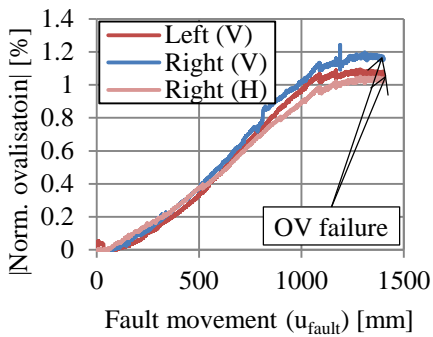


Figure D.64 Distribution of horizontal ovalisation over the length of specimen T6.



(a) Ovalisation 1810 mm from the fault

(b) Ovalisation 1625 mm from the fault

Figure D.65 Development of horizontal and vertical ovalisation in specimen T6.

Test T7

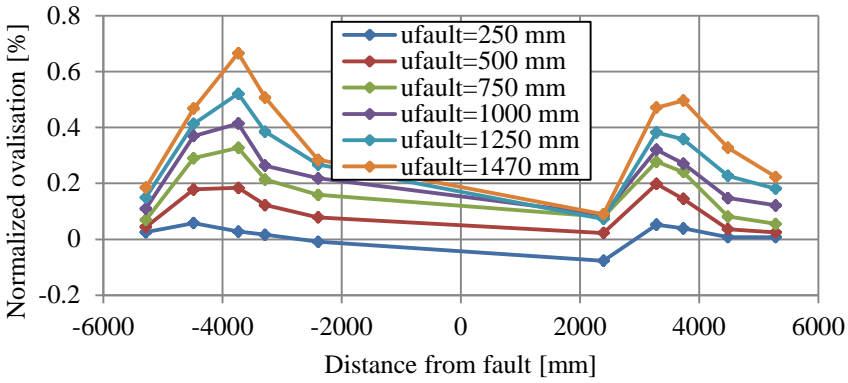


Figure D.66 Distribution of vertical ovalisation over the length of specimen T7.

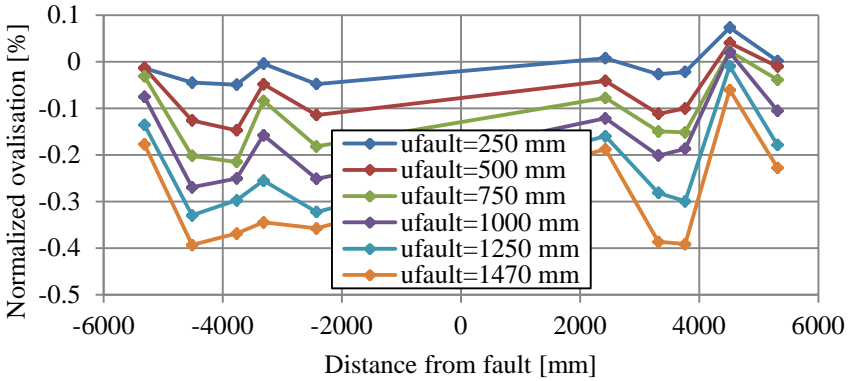
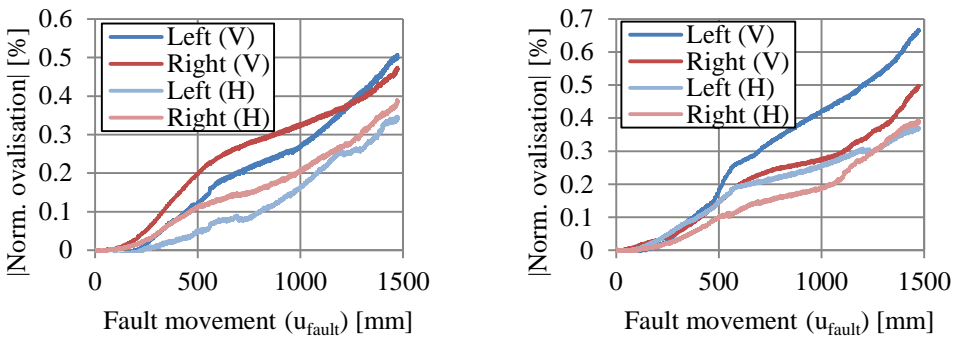


Figure D.67 Distribution of horizontal ovalisation over the length of specimen T7.



(a) Ovalisation 3300 mm from the fault

(b) Ovalisation 3750 mm from the fault

Figure D.68 Development of horizontal and vertical ovalisation in specimen T7.

Test T8

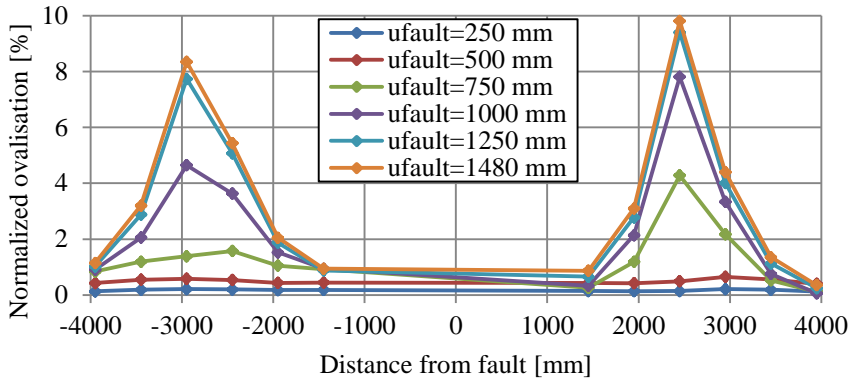
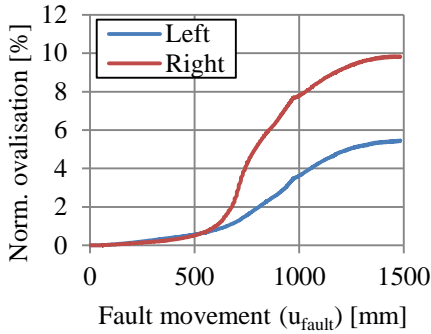
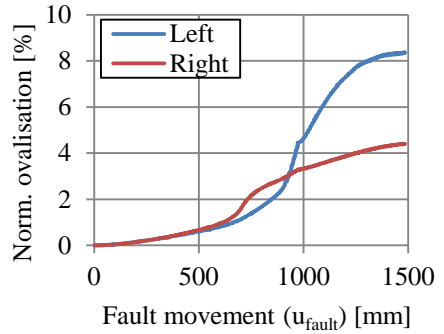


Figure D.69 Distribution of vertical ovalisation over the length of specimen T8.



(a) Ovalisation 2450 mm from the fault



(b) Ovalisation 2950 mm from the fault

Figure D.70 Development of vertical ovalisation in specimen T8.

Test T9

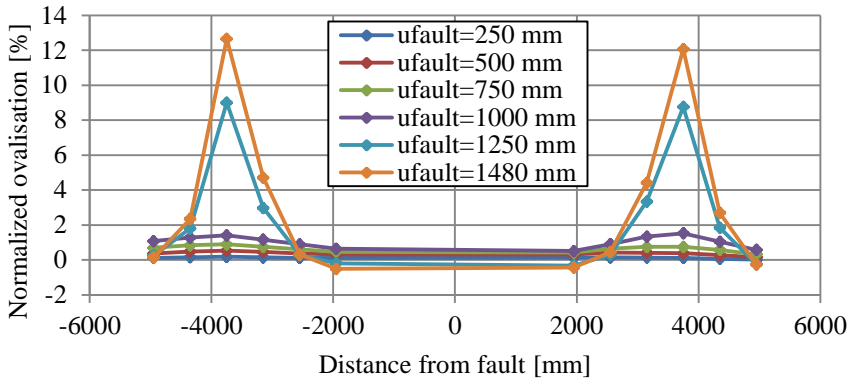
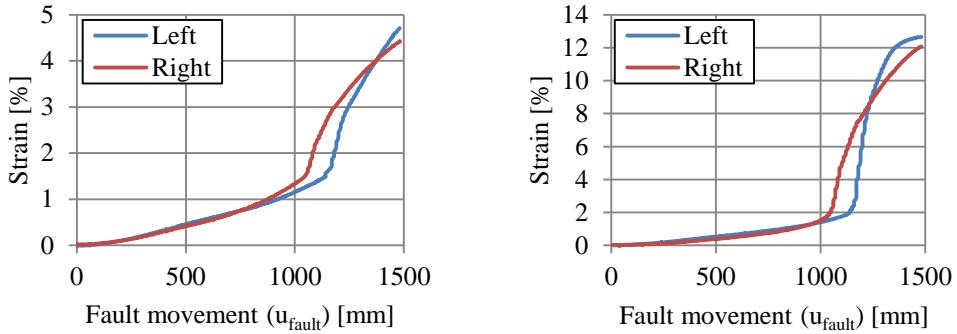


Figure D.71 Distribution of vertical ovalisation over the length of pipeline specimen T9.



(a) Ovalisation 3150 mm from the fault

(b) Ovalisation 3750 mm from the fault

Figure D.72 Development of vertical ovalisation in specimen T9.

Test T10

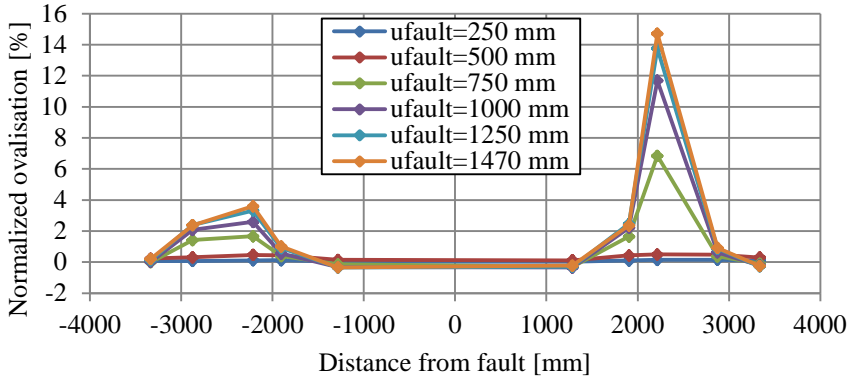


Figure D.73 Distribution of vertical ovalisation over the length of specimen T10.

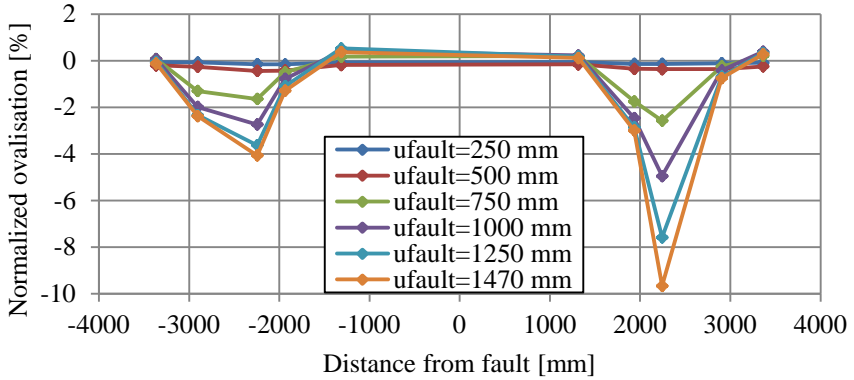
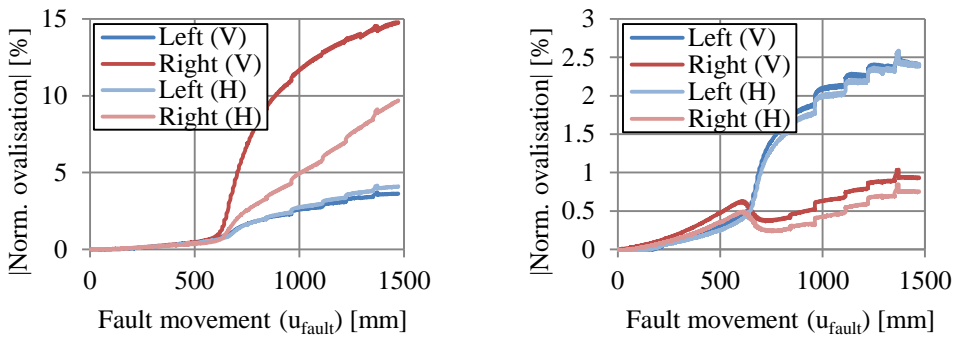


Figure D.74 Distribution of horizontal ovalisation over the length of specimen T10.



(a) Ovalisation 2230 mm from the fault

(b) Ovalisation 2890 mm from the fault

Figure D.75 Development of horizontal and vertical ovalisation in specimen T10.

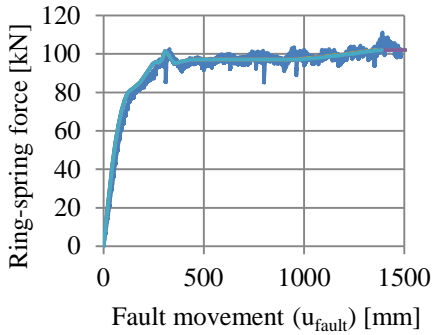
Appendix E: Results of calibration and validation of numerical model for buried pipelines

This appendix presents an overview of the results of the calculations performed for validation of the model for buried pipelines as presented in Chapter 11 of the main text of this thesis. A comparison of the response of the ring-springs to the applied fault movement is presented in Appendix E.1, followed by a comparison of the longitudinal strains in the pipeline in Appendix E.2 and a comparison of the pipeline ovalisation in Appendix E.3.

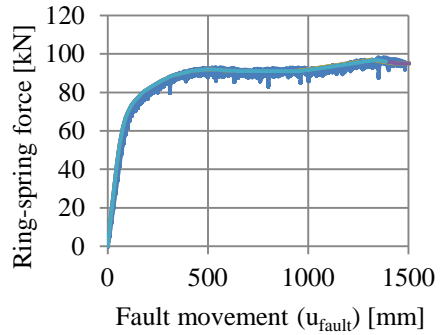
E.1 Comparison of ring-spring response

This appendix presents a comparison of the measured ring-spring response to the applied fault movement in the test and in the validation model. For each ring-spring the relation between applied fault movement and ring-spring force is presented. For calibration of the model, the imperfection amplitude was varied in the model. The results for all applied imperfection sizes are presented.

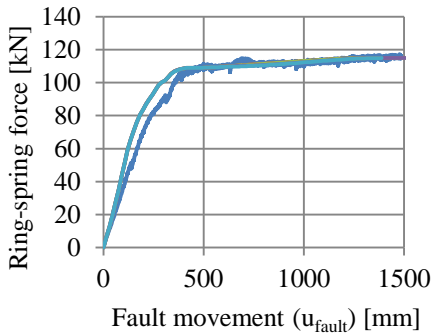
Test T1



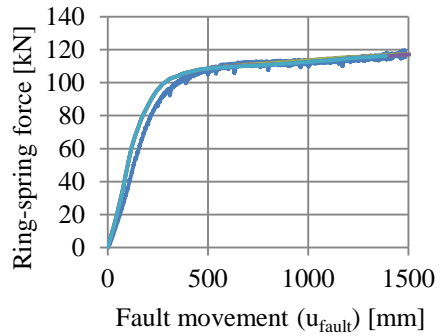
(a) Ring 1L



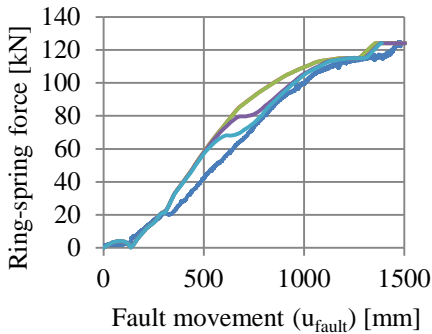
(b) Ring 1R



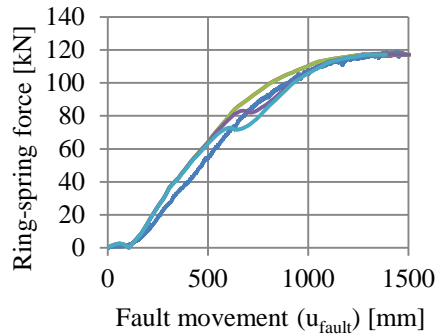
(c) Ring 2L



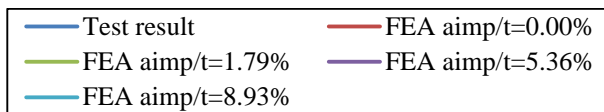
(d) Ring 2R



(e) Ring 3L

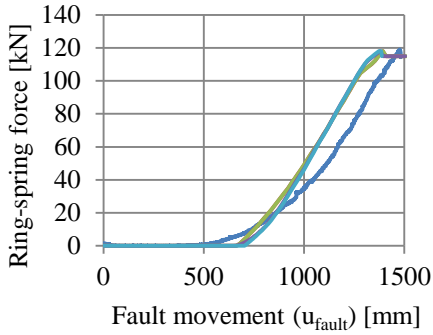


(f) Ring 3R

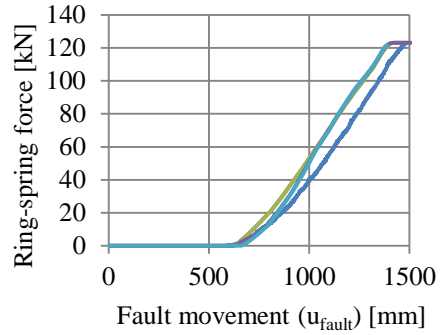


(g) Legend to graphs

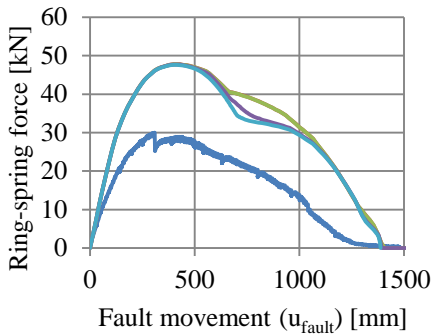
Figure E.1 Comparison of response of rings 1-3 for test T1.



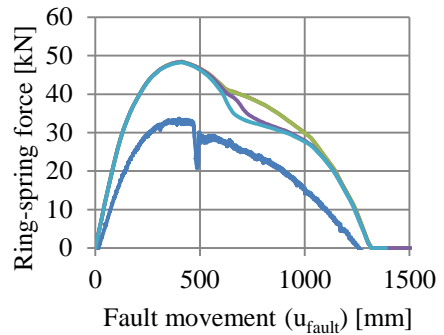
(a) Ring 4L



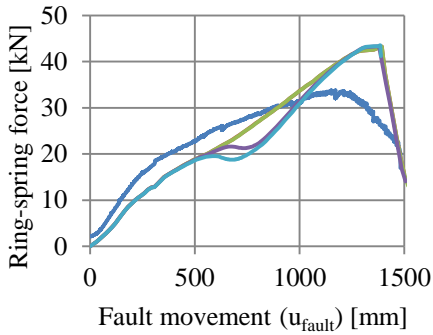
(b) Ring 4R



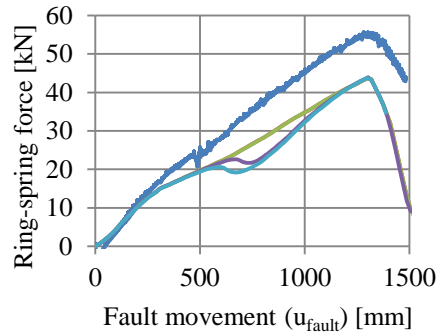
(c) Ring 5L



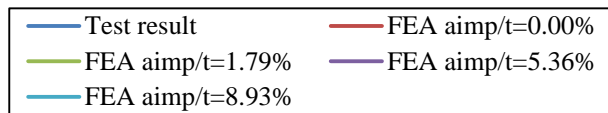
(d) Ring 5R



(e) Ring 6L



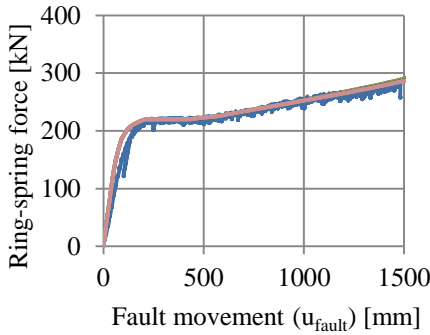
(f) Ring 6R



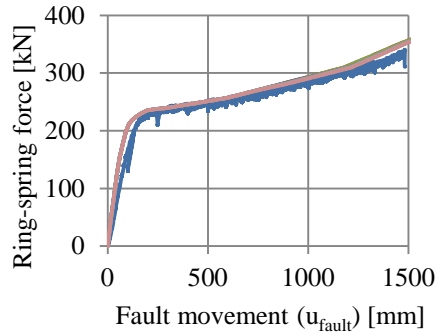
(g) Legend to graphs

Figure E.2 Comparison of response of rings 4-6 for test T1.

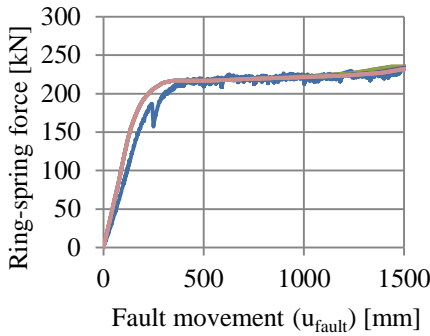
Test T2



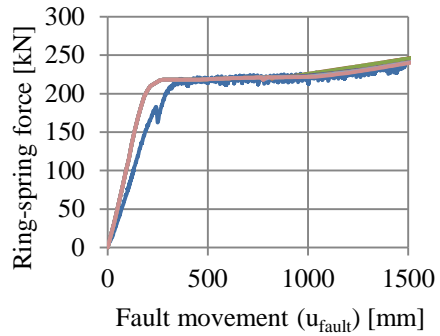
(a) Ring 1L



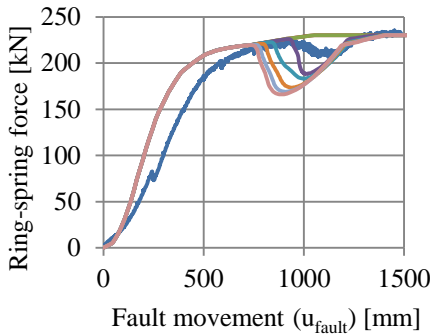
(b) Ring 1R



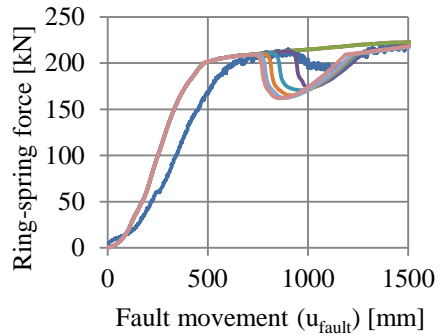
(c) Ring 2L



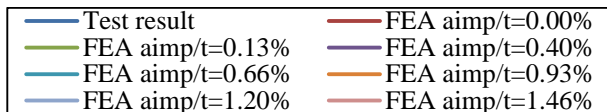
(d) Ring 2R



(e) Ring 3L

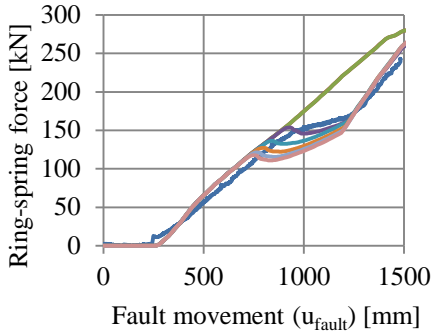


(f) Ring 3R

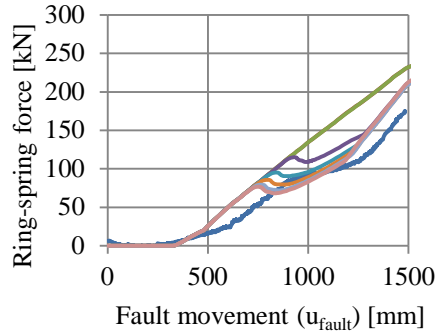


(g) Legend to graphs

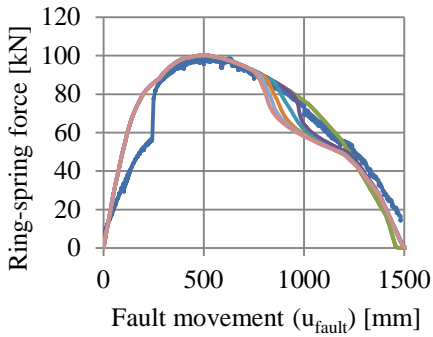
Figure E.3 Comparison of response of rings 1-3 for test T2.



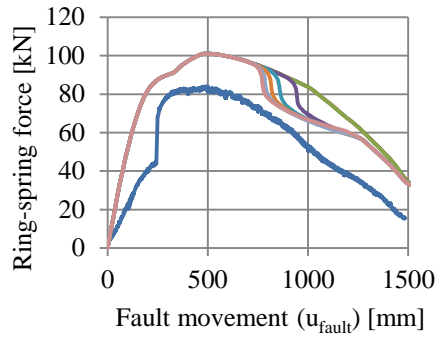
(a) Ring 4L



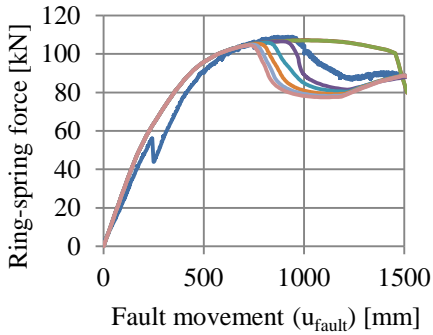
(b) Ring 4R



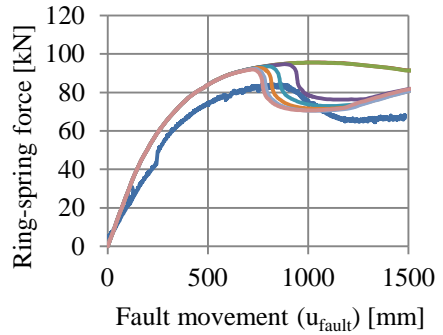
(c) Ring 5L



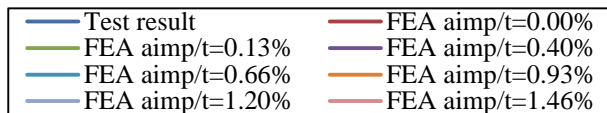
(d) Ring 5R



(e) Ring 6L



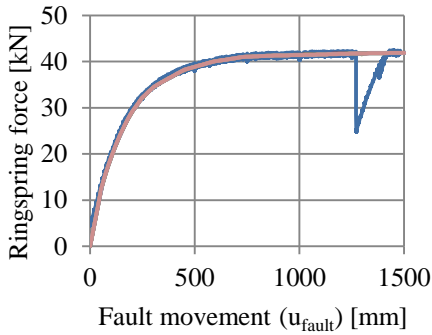
(f) Ring 6R



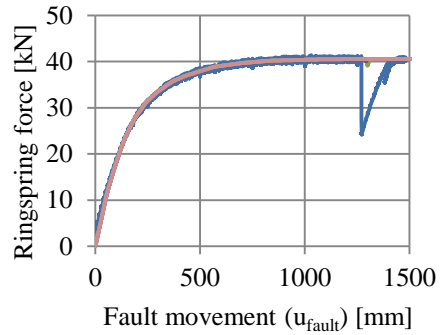
(g) Legend to graphs

Figure E.4 Comparison of response of rings 4-6 for test T2.

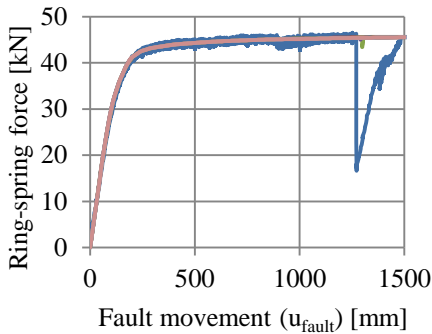
Test T3



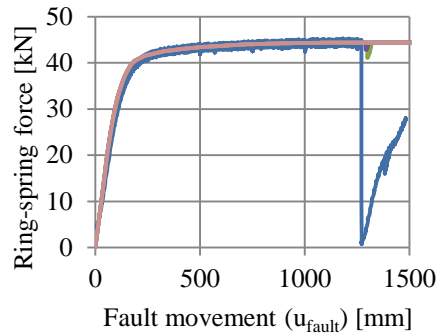
(a) Ring 1L



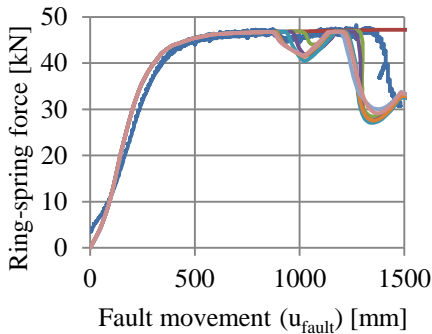
(b) Ring 1R



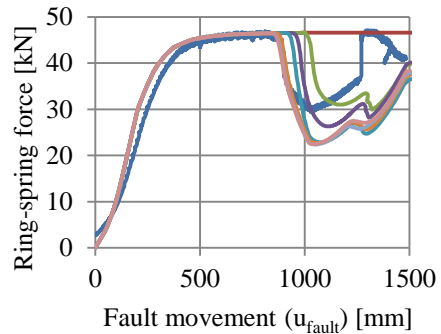
(c) Ring 2L



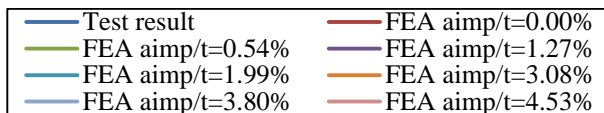
(d) Ring 2R



(e) Ring 3L

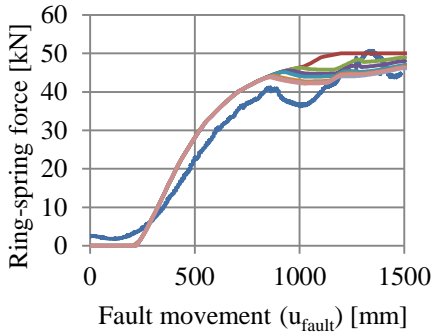


(f) Ring 3R

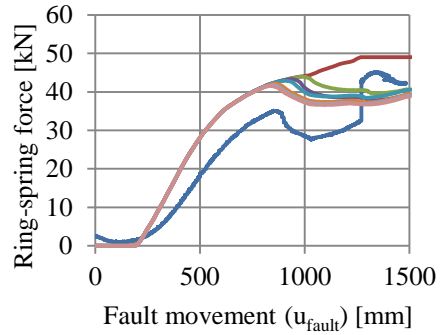


(g) Legend to graphs

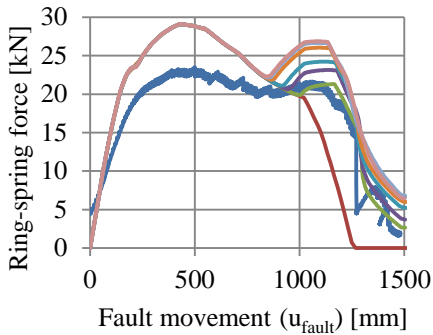
Figure E.5 Comparison of response of rings 1-3 for test T3.



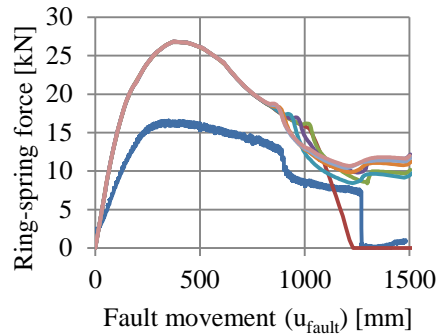
(a) Ring 4L



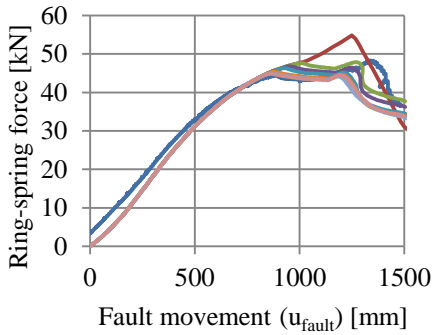
(b) Ring 4R



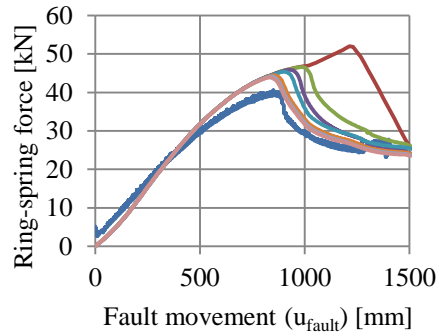
(c) Ring 5L



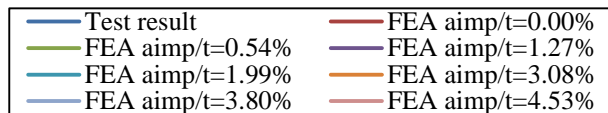
(d) Ring 5R



(e) Ring 6L



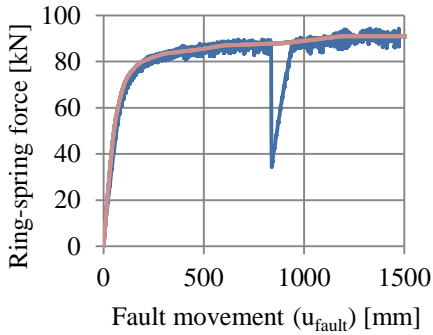
(f) Ring 6R



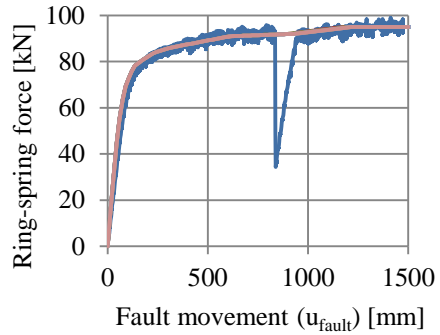
(g) Legend to graphs

Figure E.6 Comparison of response of rings 4-6 for test T3.

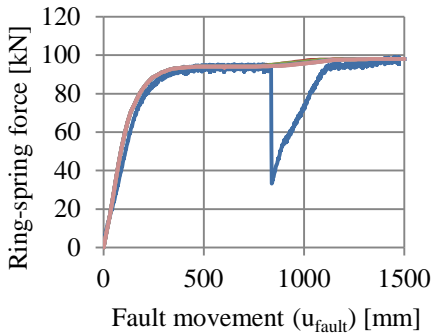
Test T4



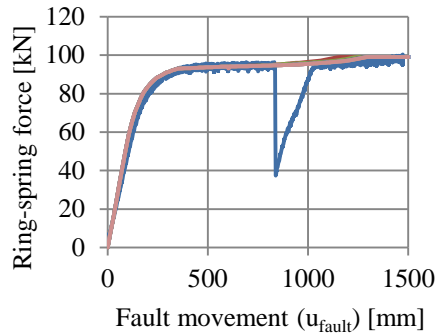
(a) Ring 1L



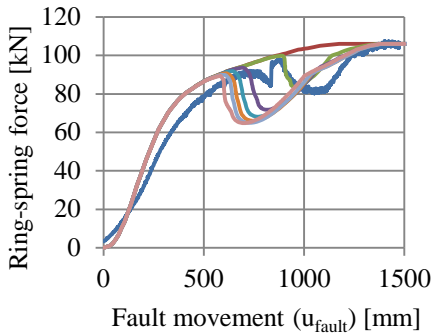
(b) Ring 1R



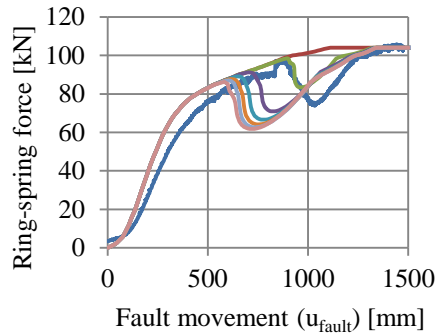
(c) Ring 2L



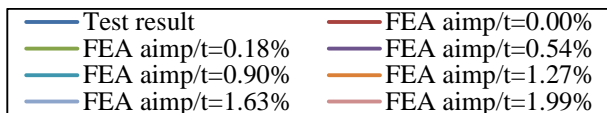
(d) Ring 2R



(e) Ring 3L

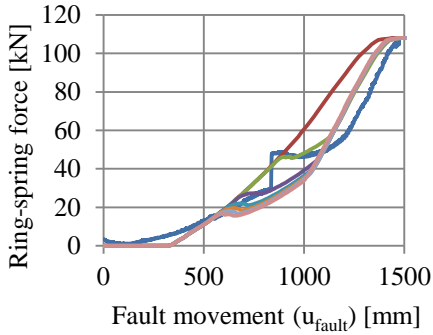


(f) Ring 3R

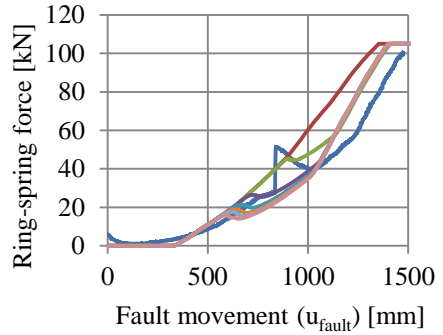


(g) Legend to graphs

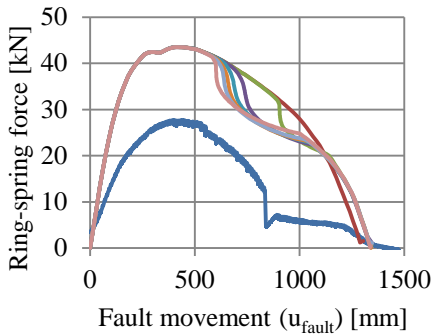
Figure E.7 Comparison of response of rings 1-3 for test T4.



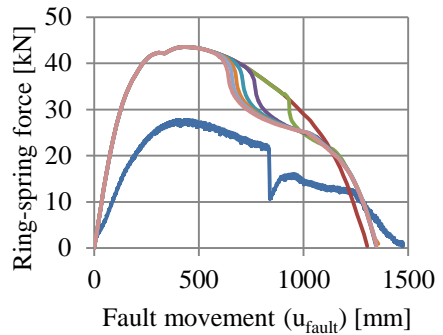
(a) Ring 4L



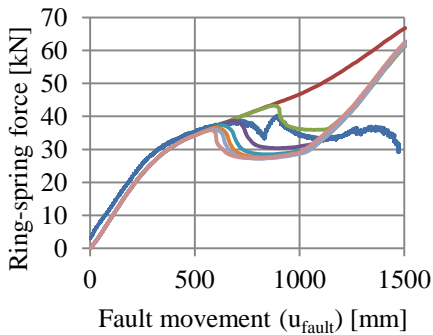
(b) Ring 4R



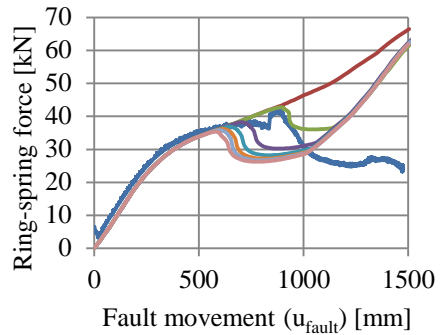
(c) Ring 5L



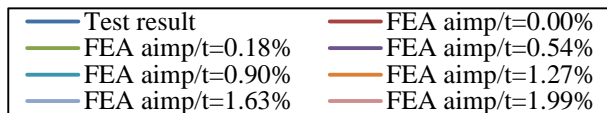
(d) Ring 5R



(e) Ring 6L



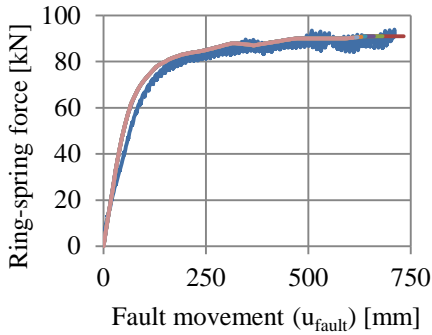
(f) Ring 6R



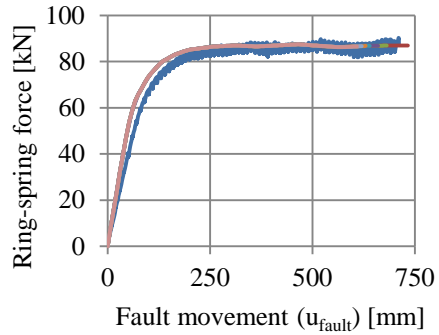
(g) Legend to graphs

Figure E.8 Comparison of response of rings 4-6 for test T4.

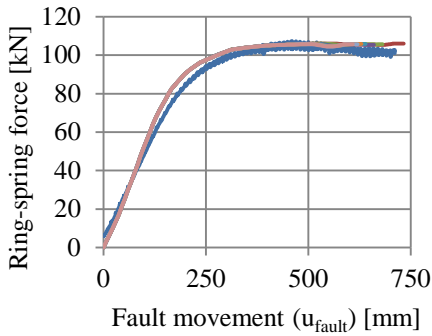
Test T5



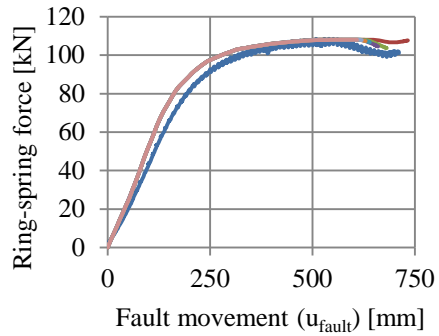
(a) Ring 1L



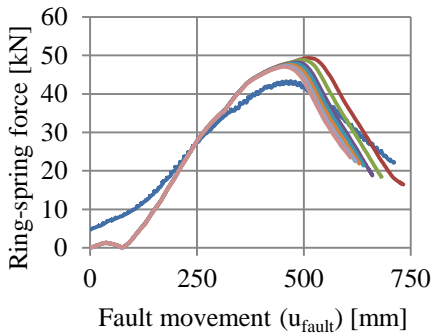
(b) Ring 1R



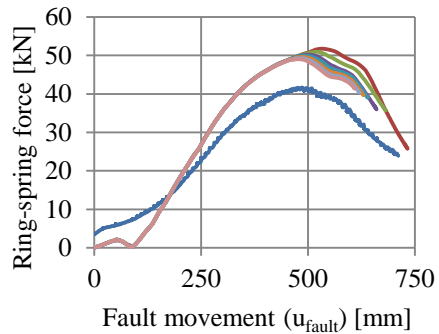
(c) Ring 2L



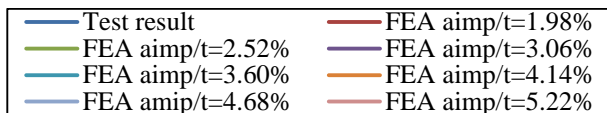
(d) Ring 2R



(e) Ring 3L

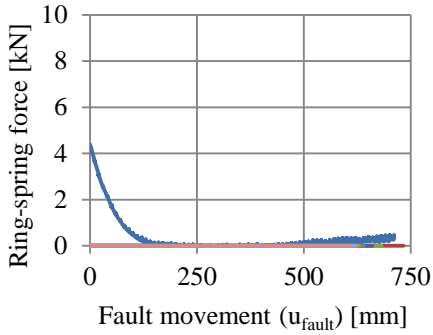


(f) Ring 3R

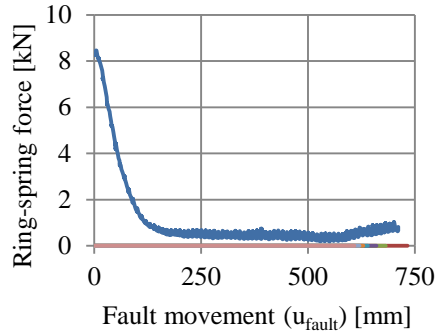


(g) Legend to graphs

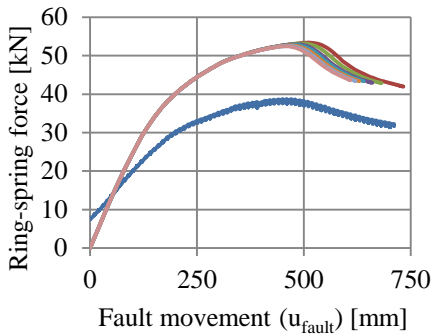
Figure E.9 Comparison of response of rings 1-3 for test T5.



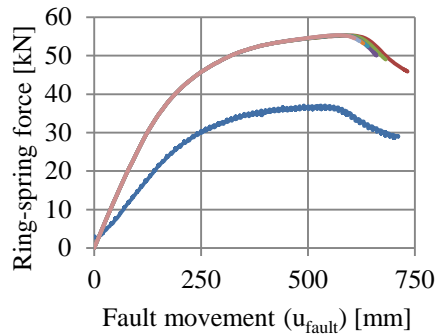
(a) Ring 4L



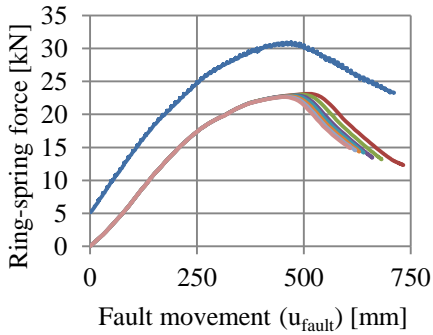
(b) Ring 4R



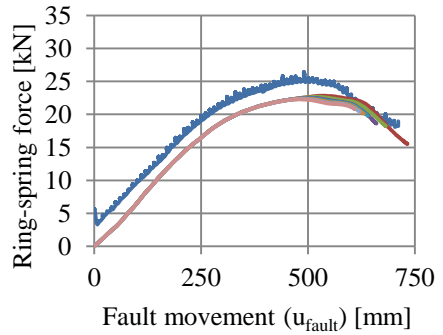
(c) Ring 5L



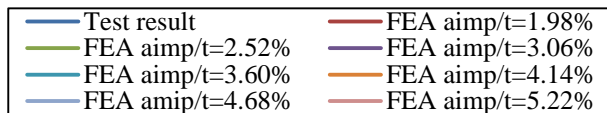
(d) Ring 5R



(e) Ring 6L



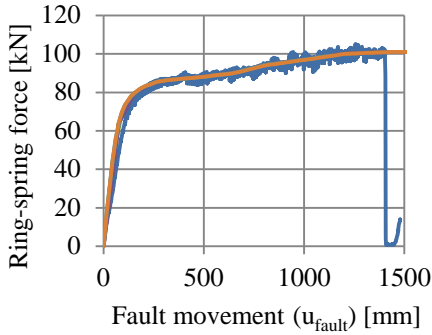
(f) Ring 6R



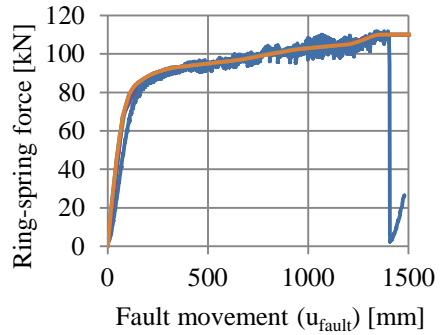
(g) Legend to graphs

Figure E.10 Comparison of response of rings 4-6 for test T5.

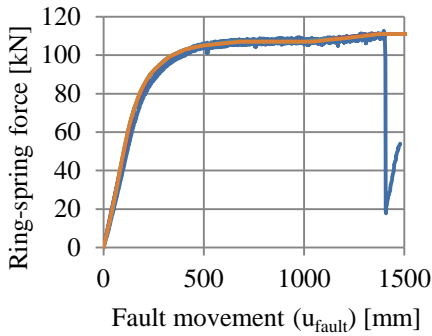
Test T6



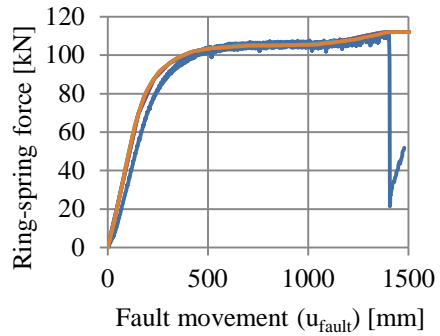
(a) Ring 1L



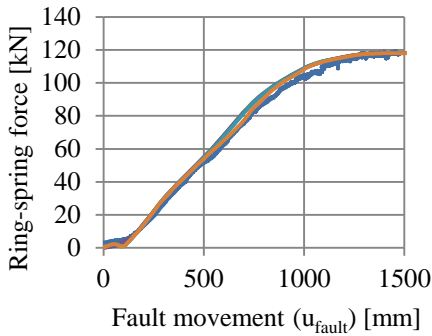
(b) Ring 1R



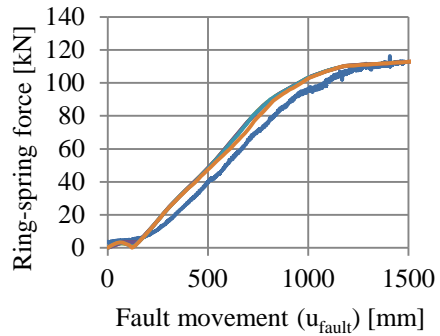
(c) Ring 2L



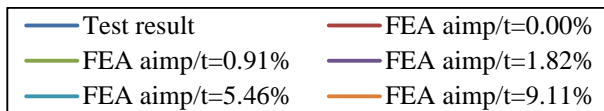
(d) Ring 2R



(e) Ring 3L

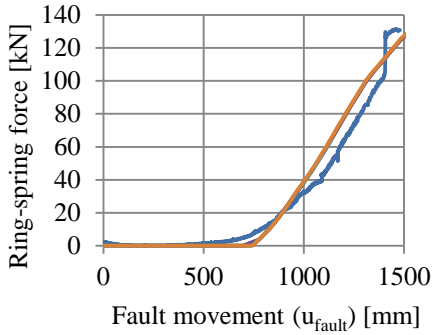


(f) Ring 3R

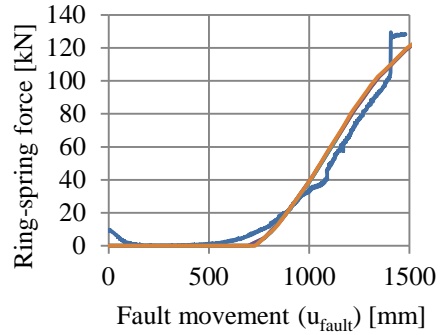


(g) Legend to graphs

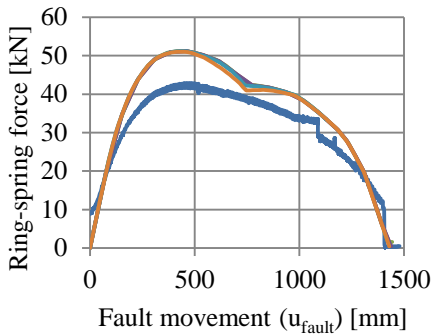
Figure E.11 Comparison of response of rings 1-3 for test T6.



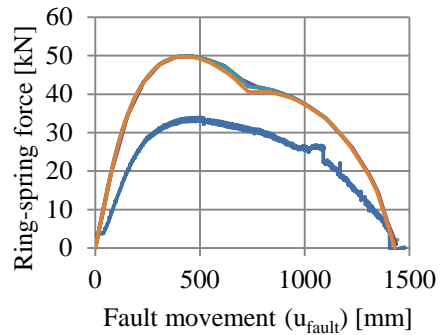
(a) Ring 4L



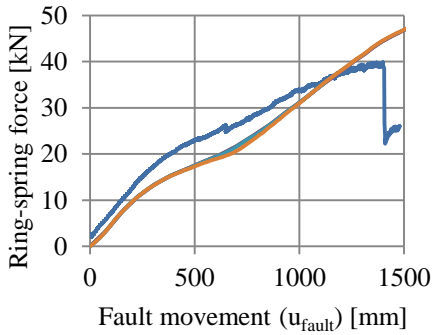
(b) Ring 4R



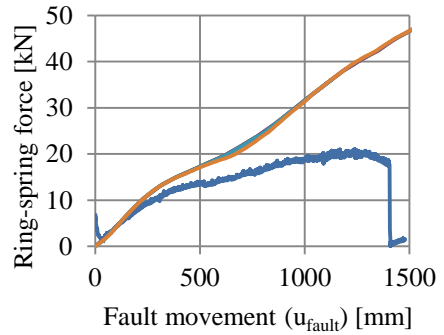
(c) Ring 5L



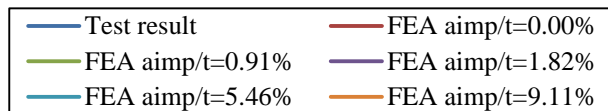
(d) Ring 5R



(e) Ring 6L



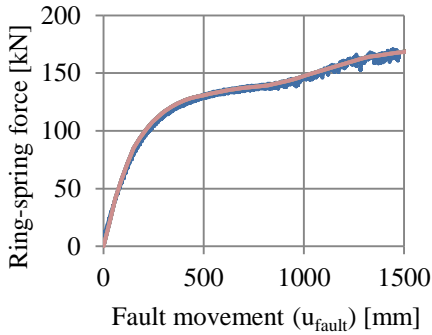
(f) Ring 6R



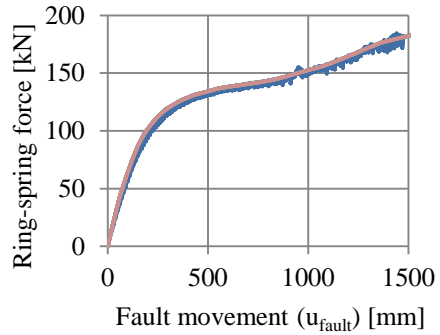
(g) Legend to graphs

Figure E.12 Comparison of response of rings 4-6 for test T6.

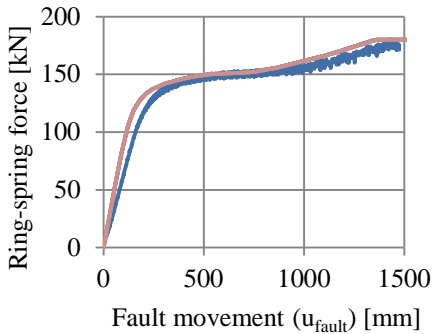
Test T7



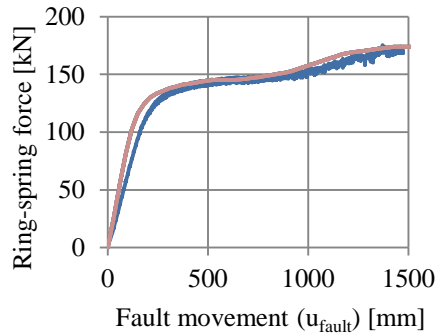
(a) Ring 1L



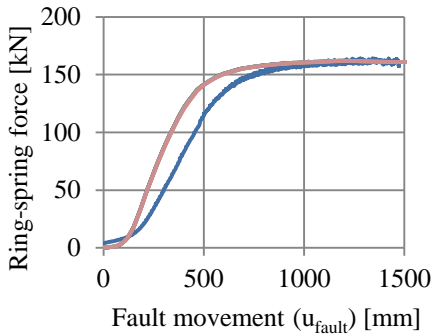
(b) Ring 1R



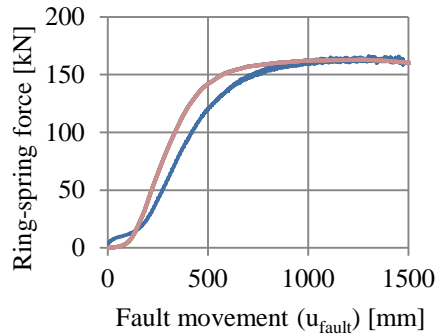
(c) Ring 2L



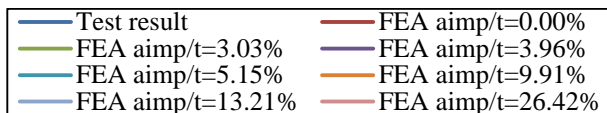
(d) Ring 2R



(e) Ring 3L

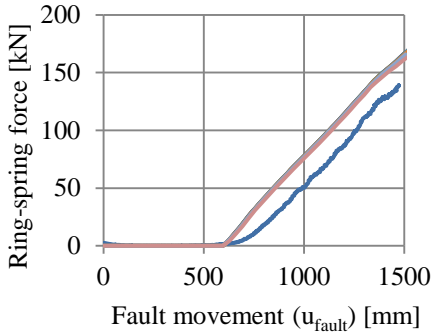


(f) Ring 3R

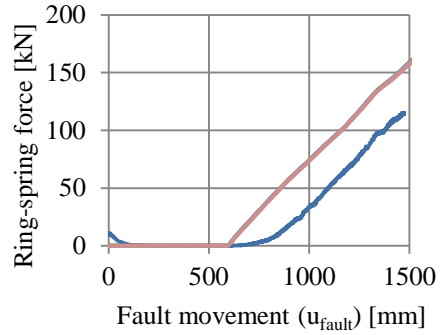


(g) Legend to graphs

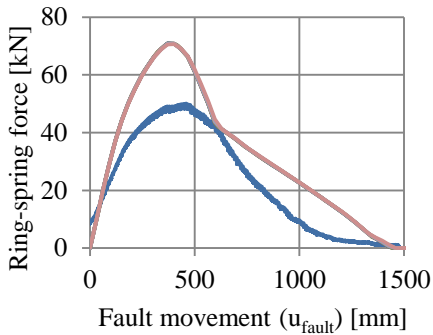
Figure E.13 Comparison of response of rings 1-3 for test T7.



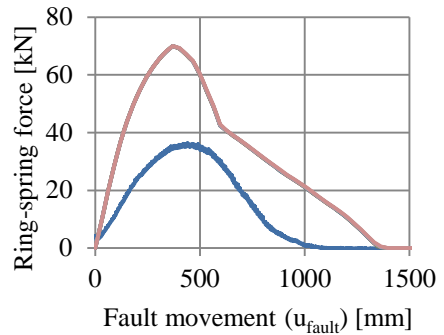
(a) Ring 4L



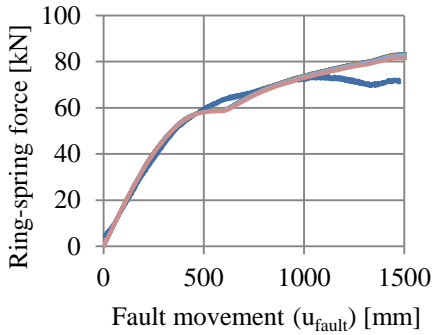
(b) Ring 4R



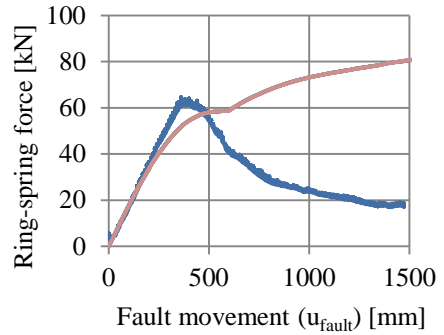
(c) Ring 5L



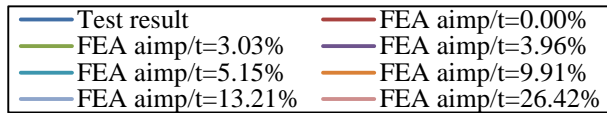
(d) Ring 5R



(e) Ring 6L



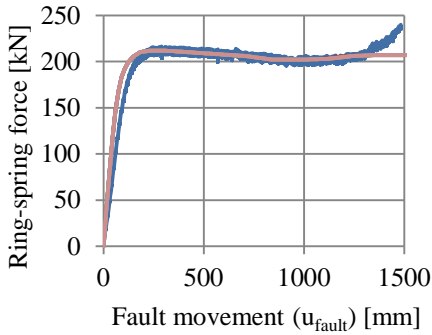
(f) Ring 6R



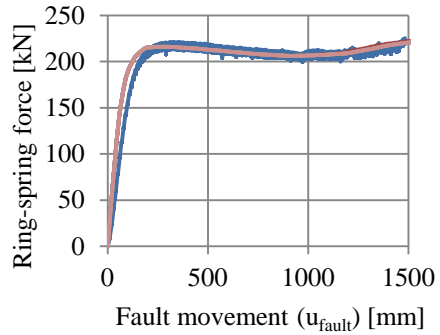
(g) Legend to graphs

Figure E.14 Comparison of response of rings 4-6 for test T7.

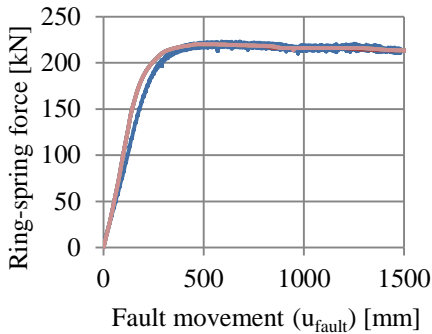
Test T8



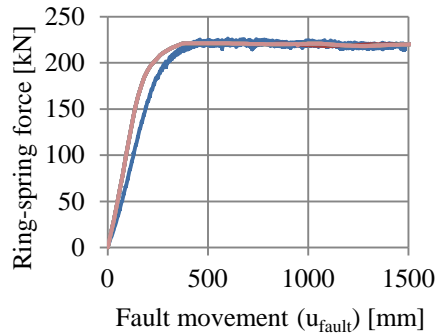
(a) Ring 1L



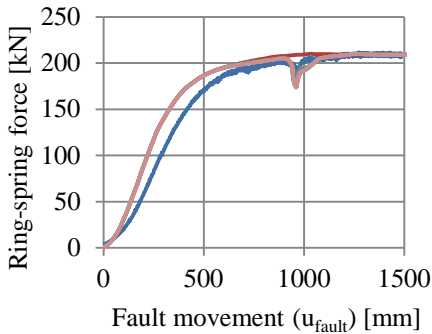
(b) Ring 1R



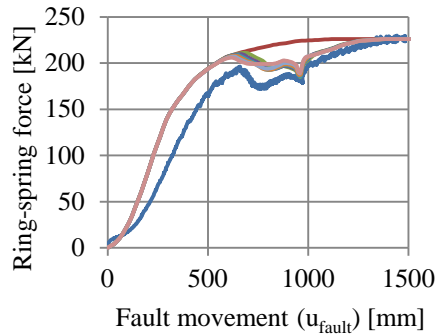
(c) Ring 2L



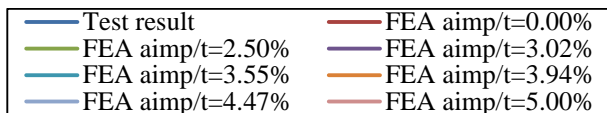
(d) Ring 2R



(e) Ring 3L



(f) Ring 3R



(g) Legend to graphs

Figure E.15 Comparison of response of rings 1-3 for test T8.

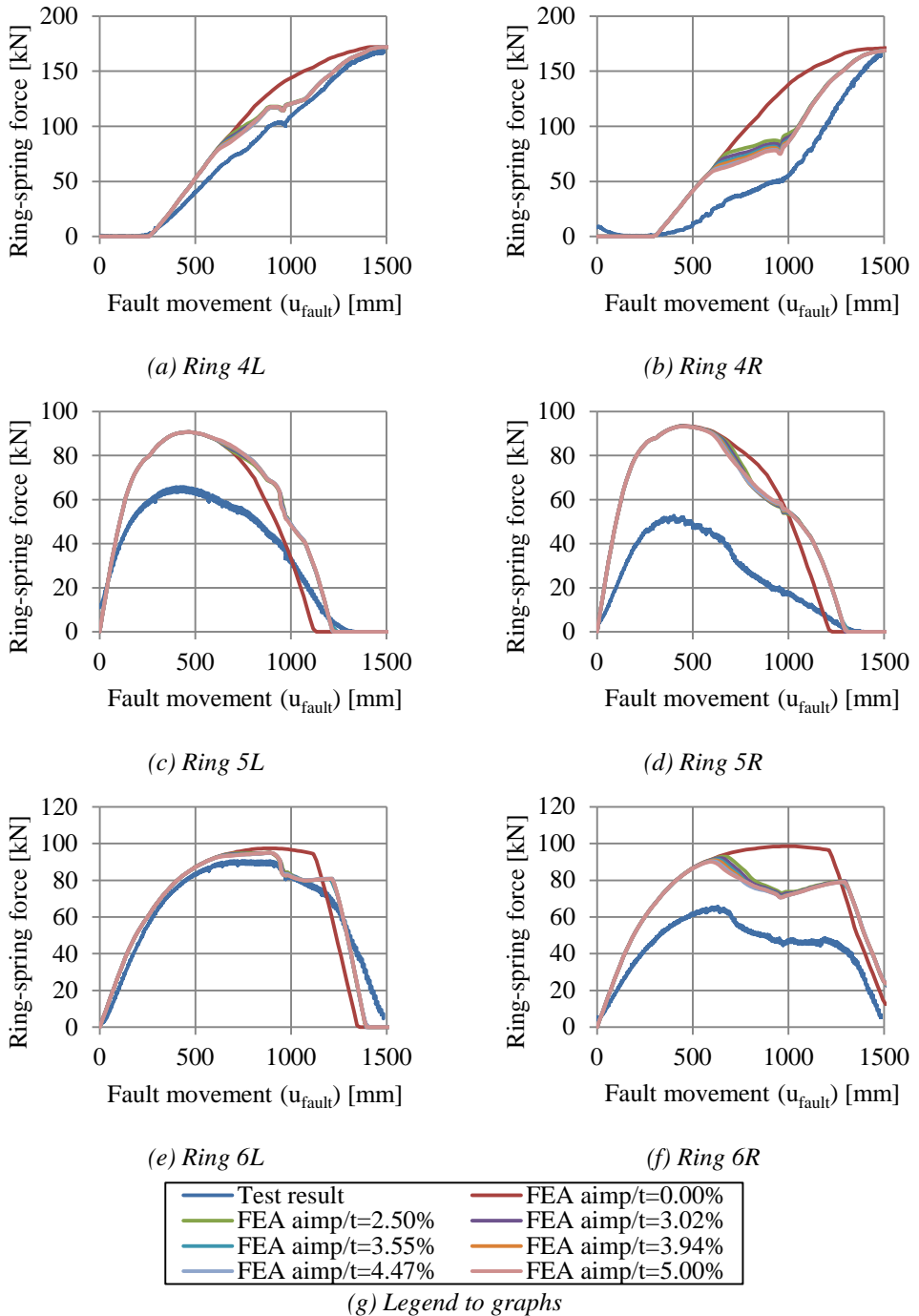
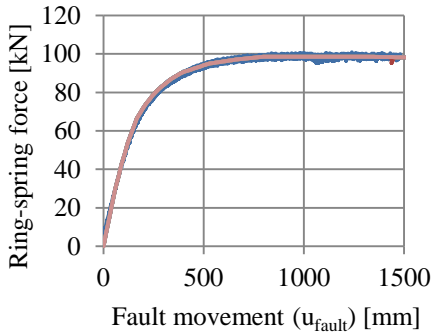
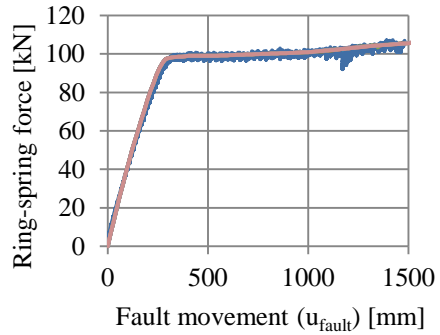


Figure E.16 Comparison of response of rings 4-6 for test T8.

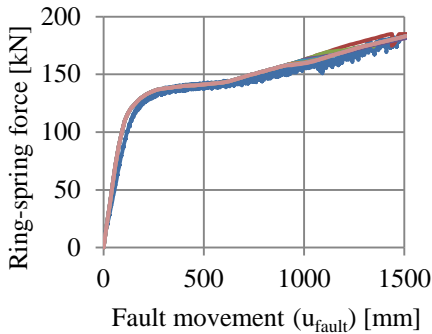
Test T9



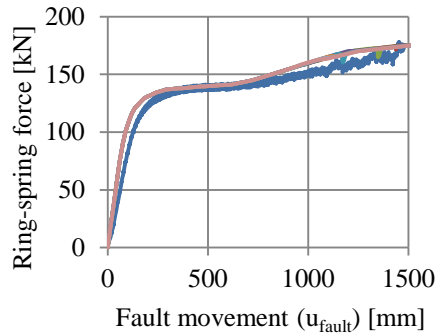
(a) Ring 1L



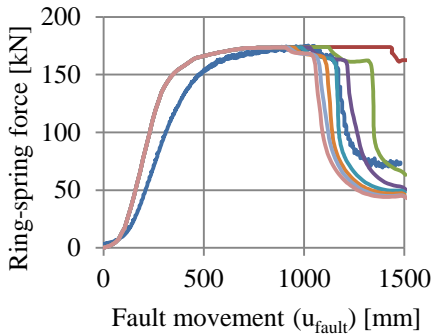
(b) Ring 1R



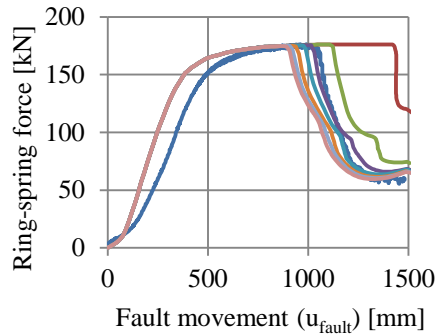
(c) Ring 2L



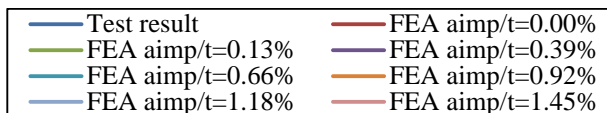
(d) Ring 2R



(e) Ring 3L

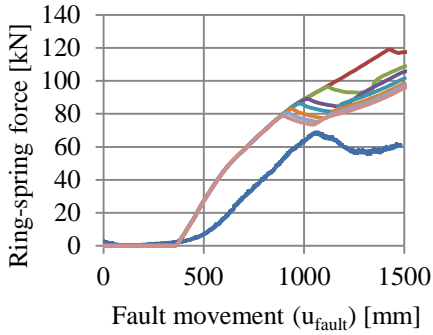


(f) Ring 3R

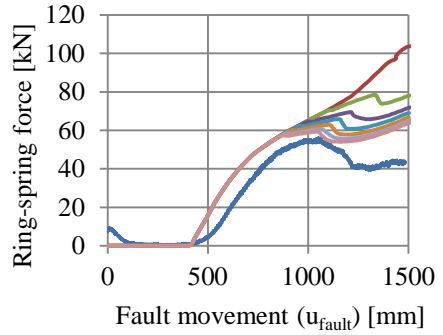


(g) Legend to graphs

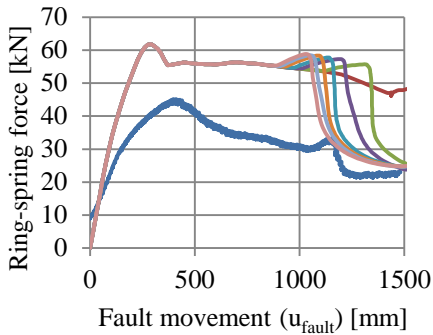
Figure E.17 Comparison of response of rings 1-3 for test T9.



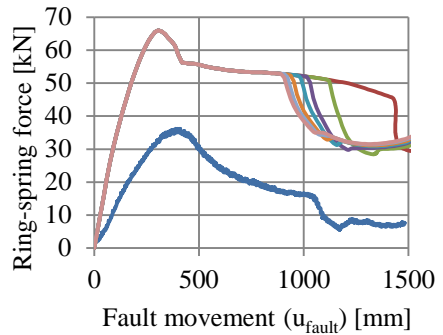
(a) Ring 4L



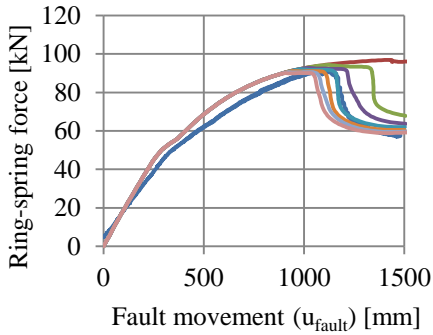
(b) Ring 4R



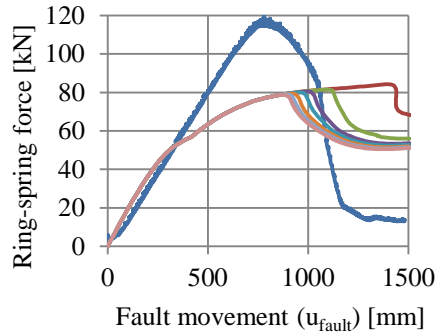
(c) Ring 5L



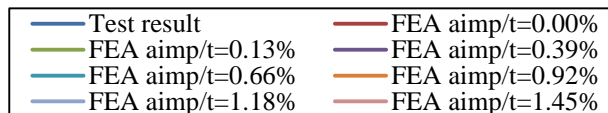
(d) Ring 5R



(e) Ring 6L



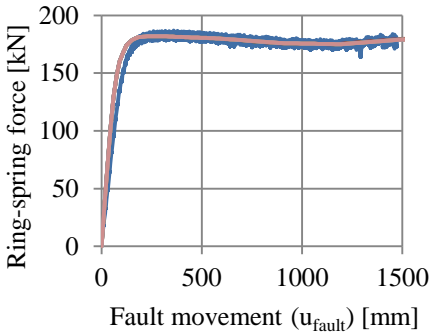
(f) Ring 6R



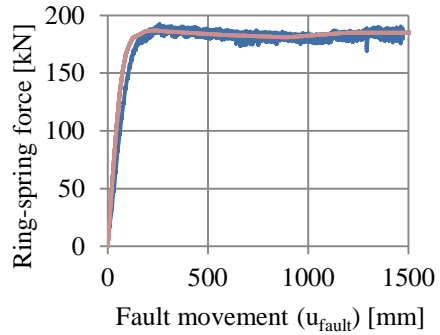
(g) Legend to graphs

Figure E.18 Comparison of response of rings 4-6 for test T9.

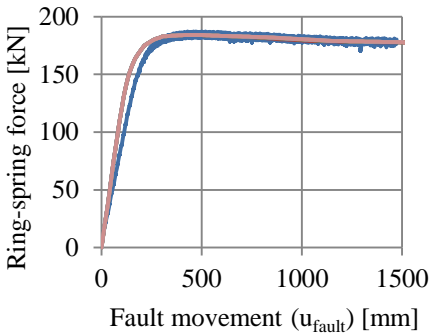
Test T10



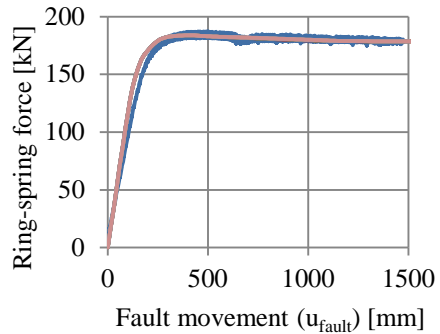
(a) Ring 1L



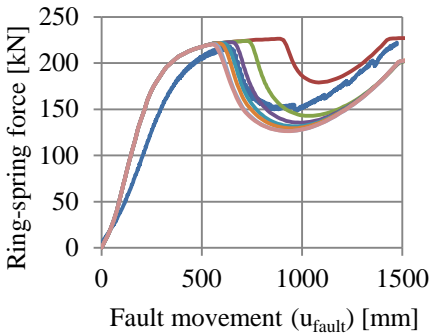
(b) Ring 1R



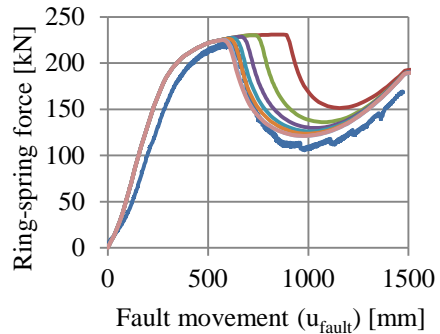
(c) Ring 2L



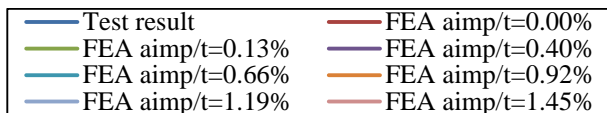
(d) Ring 2R



(e) Ring 3L

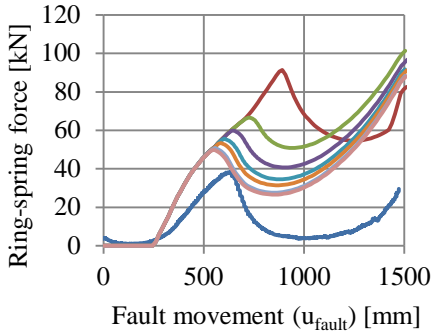


(f) Ring 3R

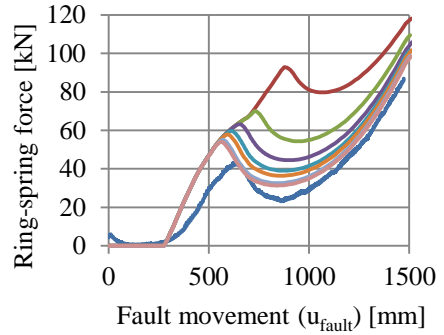


(g) Legend to graphs

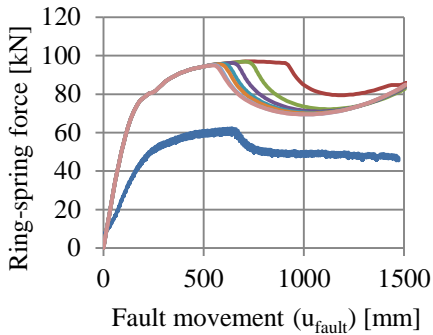
Figure E.19 Comparison of response of rings 1-3 for test T10.



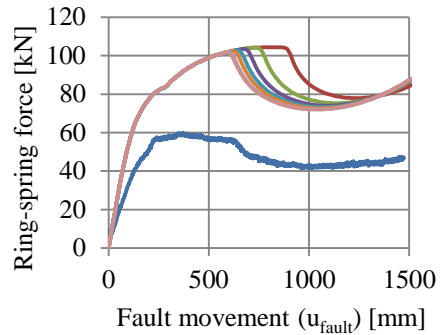
(a) Ring 4L



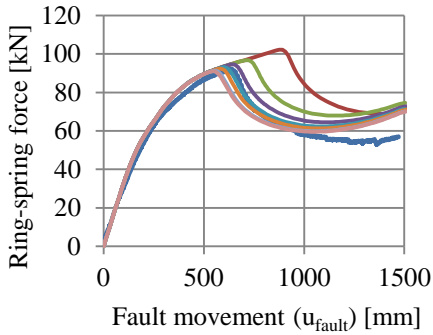
(b) Ring 4R



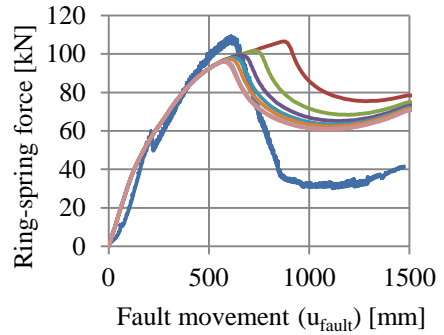
(c) Ring 5L



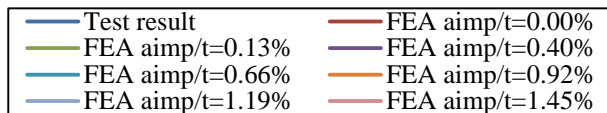
(d) Ring 5R



(e) Ring 6L



(f) Ring 6R



(g) Legend to graphs

Figure E.20 Comparison of response of rings 4-6 for test T10.

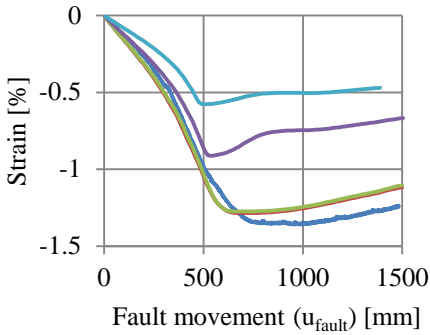
E.2 Comparison of strain

This appendix presents a comparison of the measured pipe response to the applied fault movement in the test and in the validation model. For a number of relevant strain gauges in longitudinal direction, the relation between applied fault movement and measured strain is presented. For calibration of the model, the imperfection amplitude was varied in the model. The results for all applied imperfection sizes are presented in the diagrams presenting the relation between fault movement and strain. Because the strains in the tests were measured on the outside of the pipe wall with strain gauges, the strains were also extracted from the FE-model at this location.

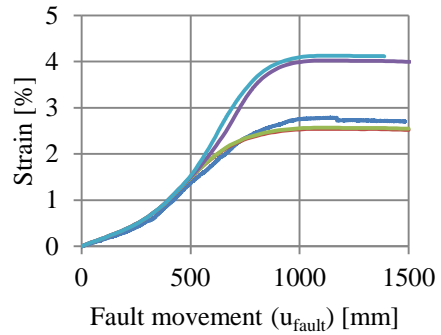
Furthermore, for each pipe, an overview of the distribution of longitudinal strain over the specimen length is presented. A comparison is made between the measured data from the test and the model. For these graphs, the result of the model with the best prediction of the critical fault movement was used. The used initial imperfection is stated in the caption of the figure. In case of a Category 2 test, only the initial imperfection at the girth weld is stated.

In the graphs, both the uncorrected and corrected test results are presented (see section 11.2 of the main text of this thesis). At the maximum fault displacement, this correction could not be applied. Therefore, in these graphs only the uncorrected results are presented.

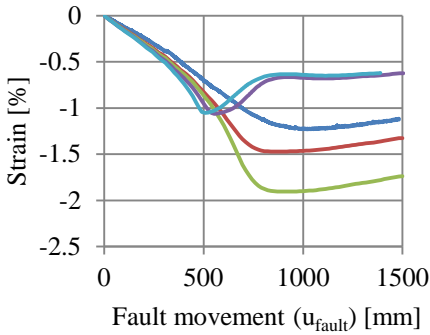
Test T1



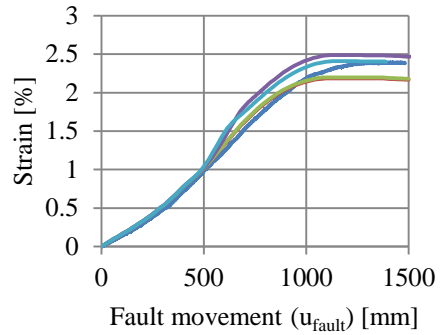
(a) Compressive strain 1500 mm from the fault



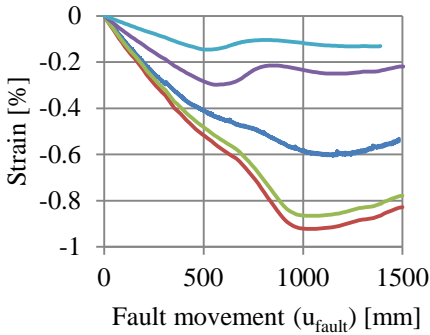
(b) Tensile strain 1500 mm from the fault



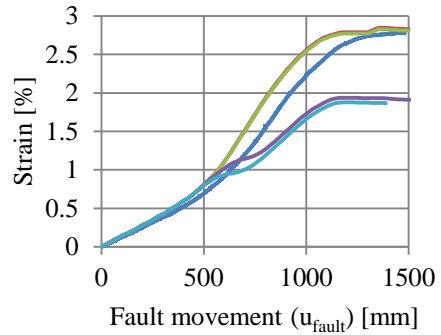
(c) Compressive strain 1750 mm from the fault



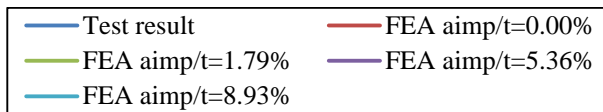
(d) Tensile strain 1750 mm from the fault



(e) Compressive strain 2000 mm from the fault

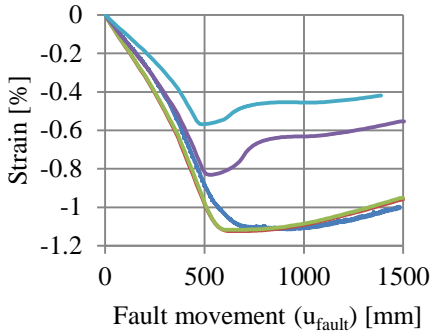


(f) Tensile strain 2000 mm from the fault

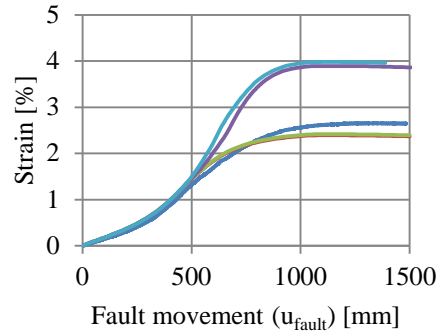


(g) Legend to graphs

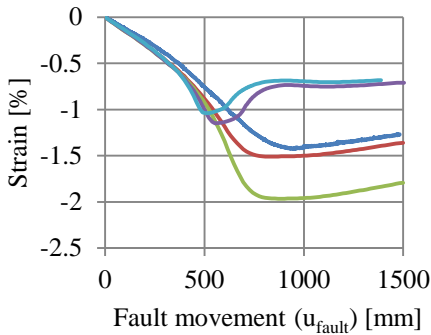
Figure E.21 Comparison of strain between test T1 and FE-model on the left side of the fault.



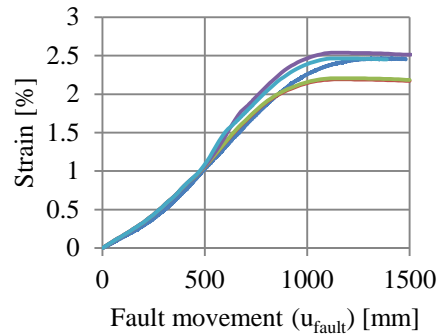
(a) Compressive strain 1500 mm from the fault



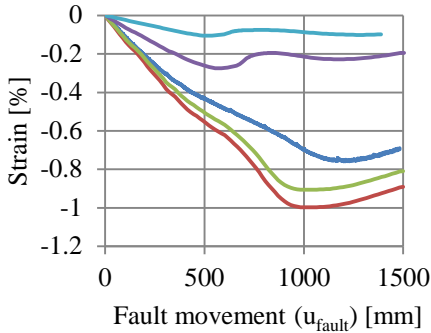
(b) Tensile strain 1500 mm from the fault



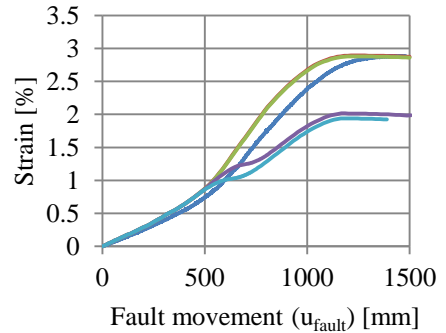
(c) Compressive strain 1750 mm from the fault



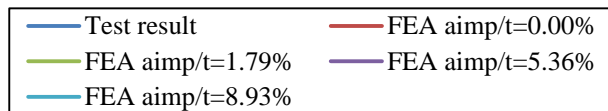
(d) Tensile strain 1750 mm from the fault



(e) Compressive strain 2000 mm from the fault

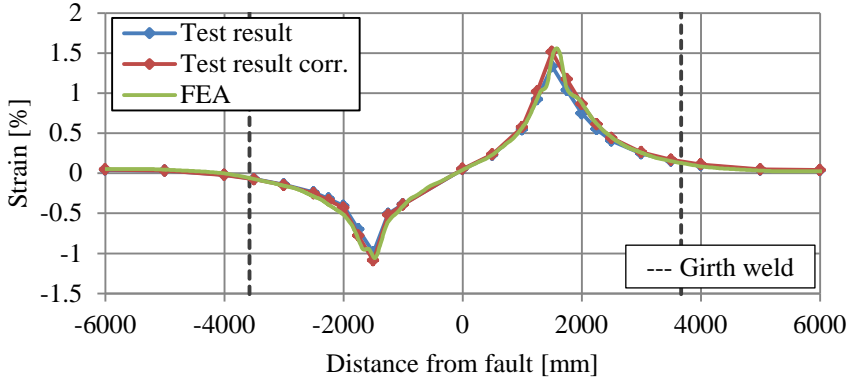


(f) Tensile strain 2000 mm from the fault

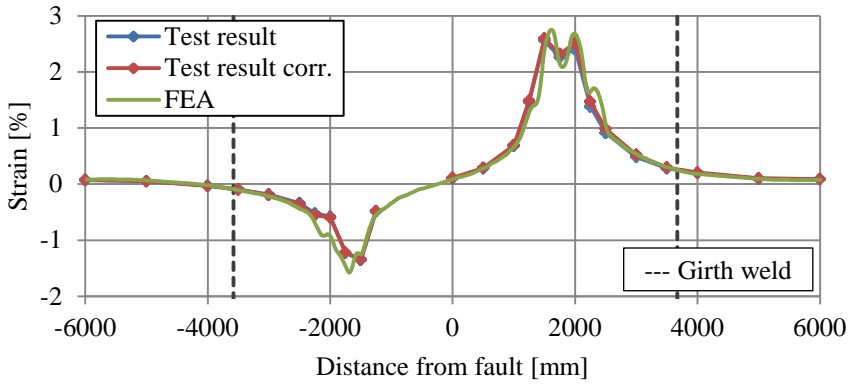


(g) Legend to graphs

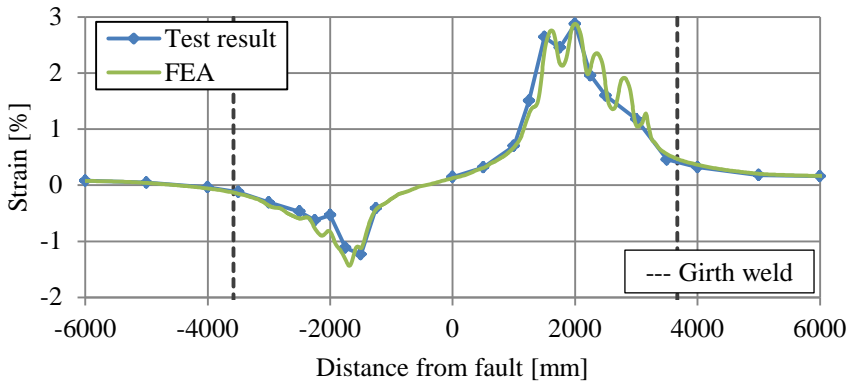
Figure E.22 Comparison of strain between test T1 and FE-model on the right side of the fault.



(a) Comparison of strains at a fault movement of 500 mm

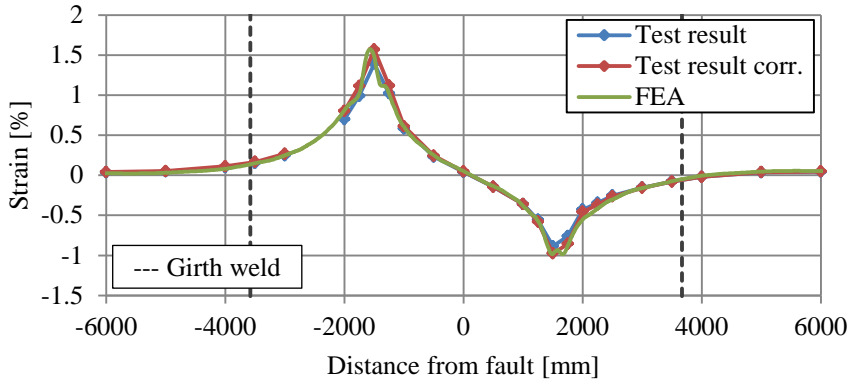


(b) Comparison of strains at a fault movement of 1000 mm

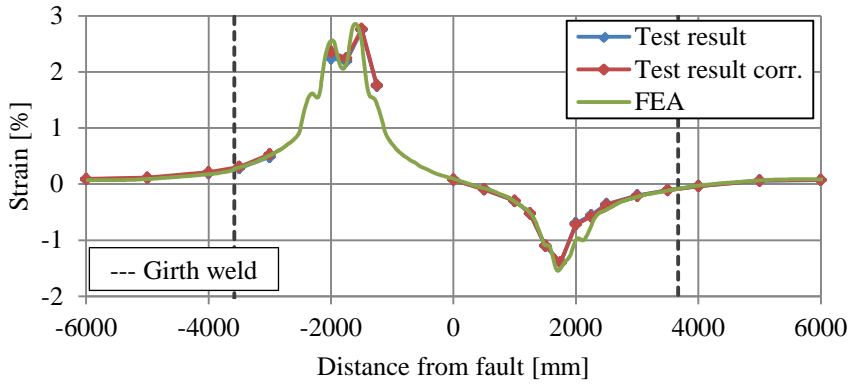


(c) Comparison of strains at a fault movement of 1480 mm

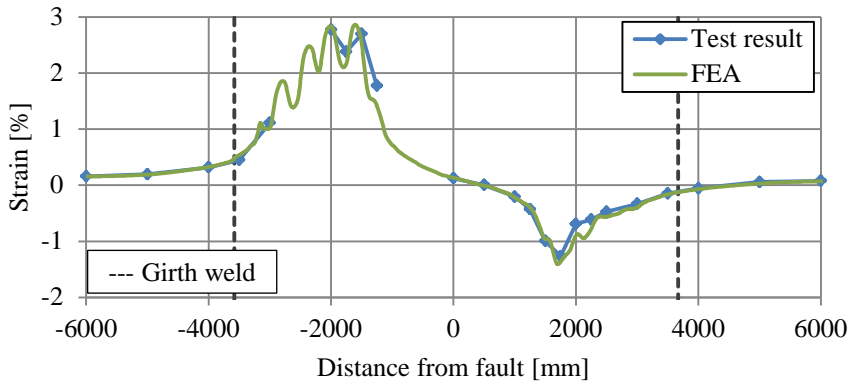
Figure E.23 Comparison of strain distributions at the front side of specimen T1 ($a_{imp}/t=0.00\%$).



(a) Comparison of strains at a fault movement of 500 mm



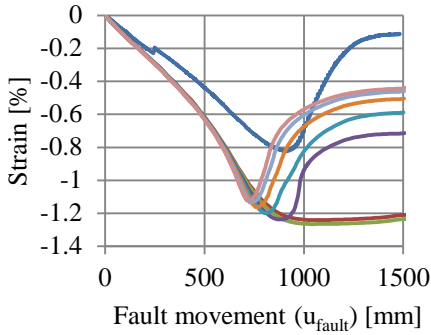
(b) Comparison of strains at a fault movement of 1000 mm



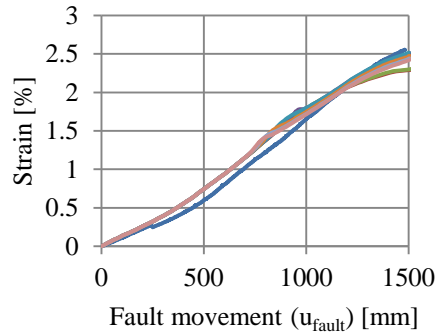
(c) Comparison of strains at a fault movement of 1480 mm

Figure E.24 Comparison of strain distributions at the back side of specimen T1 ($a_{imp}/t=0.00\%$).

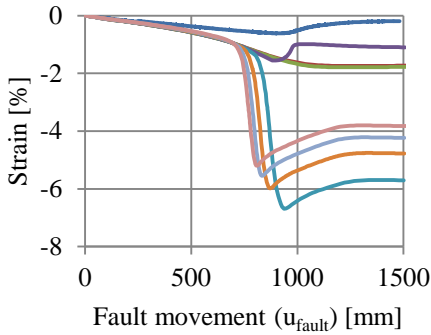
Test T2



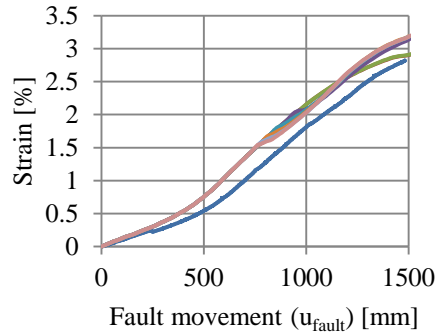
(a) Compressive strain 2500 mm from the fault



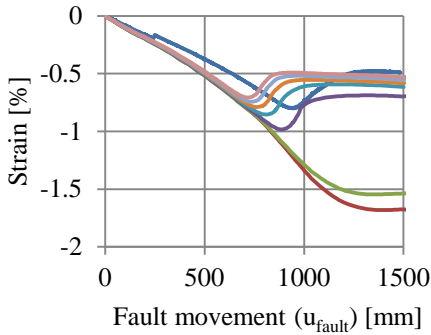
(b) Tensile strain 2500 mm from the fault



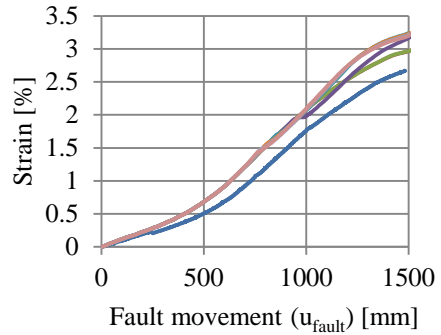
(c) Compressive strain 2750 mm from the fault



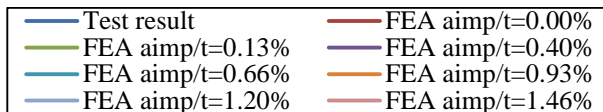
(d) Tensile strain 2750 mm from the fault



(e) Compressive strain 3000 mm from the fault

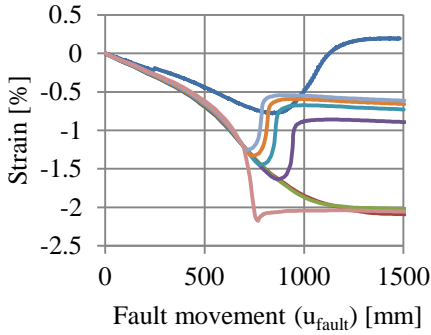


(f) Tensile strain 3000 mm from the fault

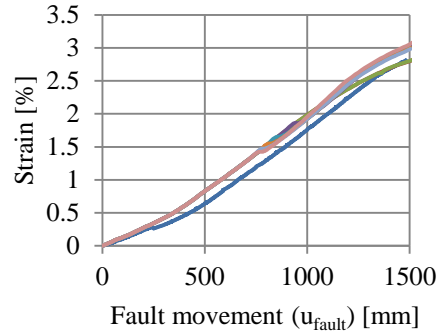


(g) Legend to graphs

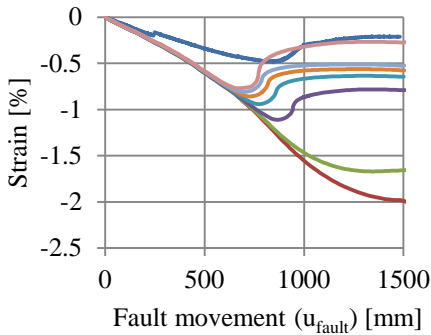
Figure E.25 Comparison of strain between test T2 and FE-model on the left side of the fault.



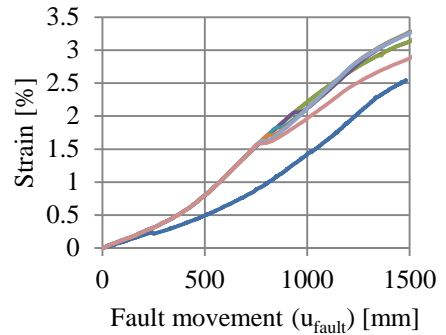
(a) Compressive strain 2500 mm from the fault



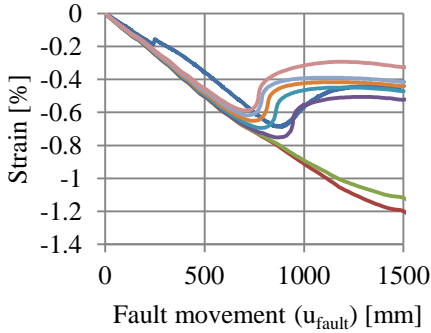
(b) Tensile strain 2500 mm from the fault



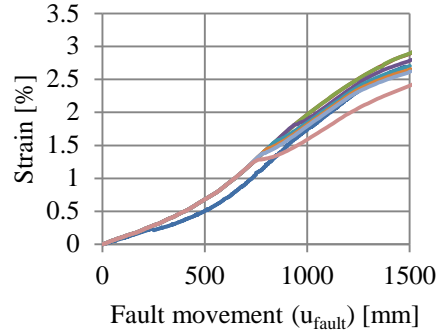
(c) Compressive strain 2750 mm from the fault



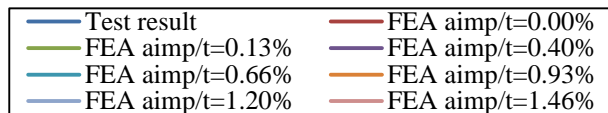
(d) Tensile strain 2750 mm from the fault



(e) Compressive strain 3000 mm from the fault

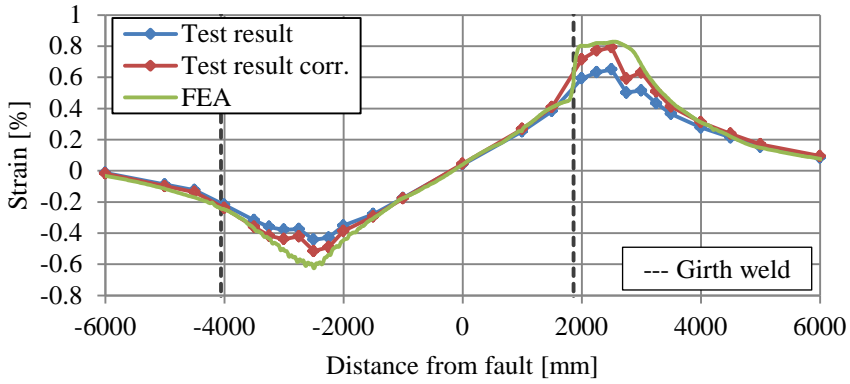


(f) Tensile strain 3000 mm from the fault

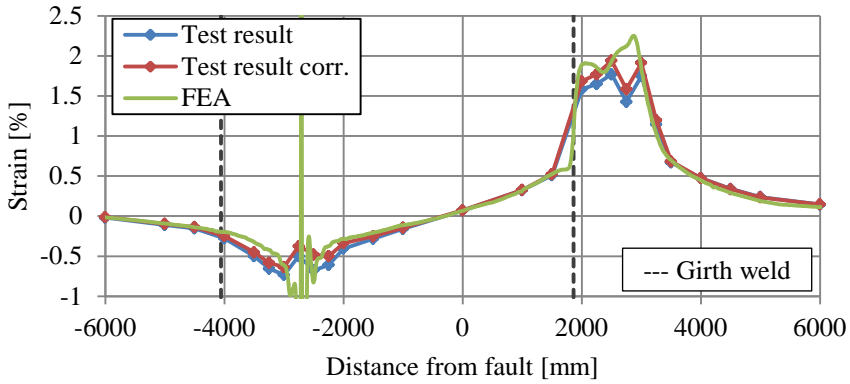


(g) Legend to graphs

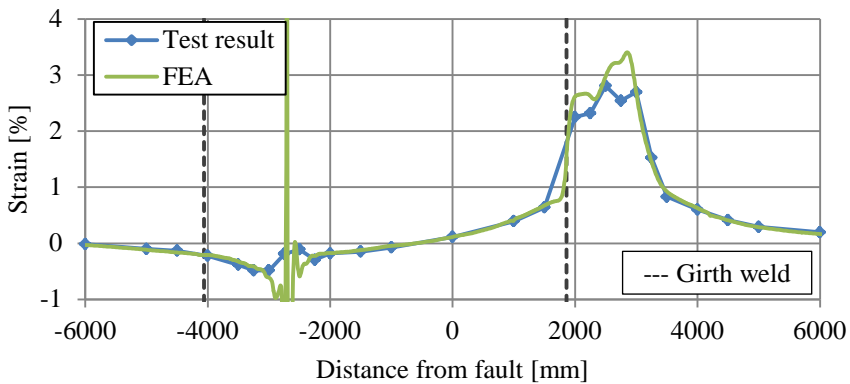
Figure E.26 Comparison of strain between test T2 and FE-model on the right side of the fault.



(a) Comparison of strains at a fault movement of 500 mm

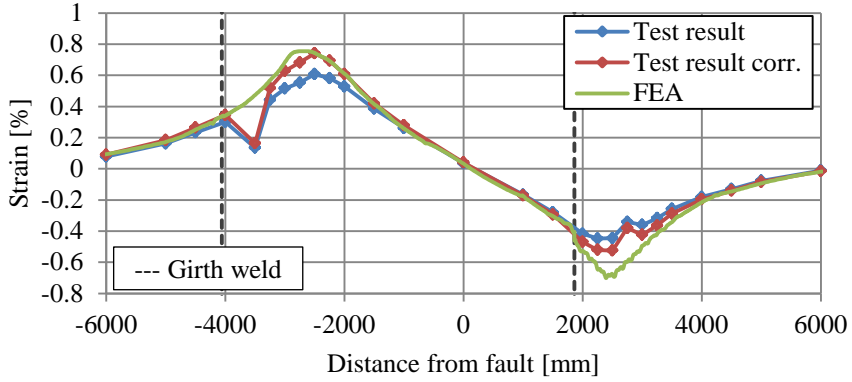


(b) Comparison of strains at a fault movement of 1000 mm

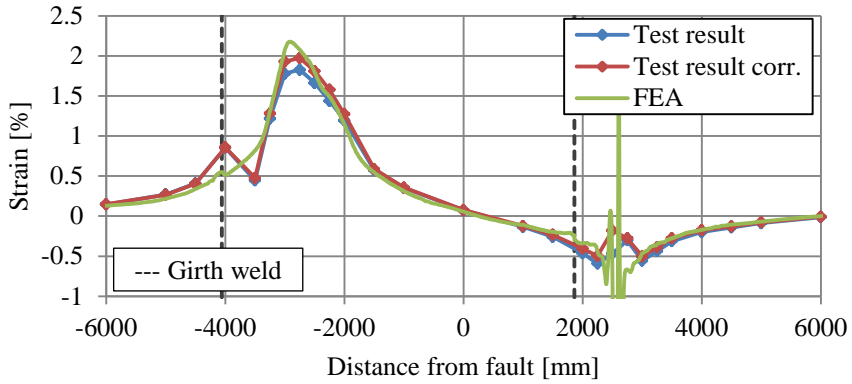


(c) Comparison of strains at a fault movement of 1480 mm

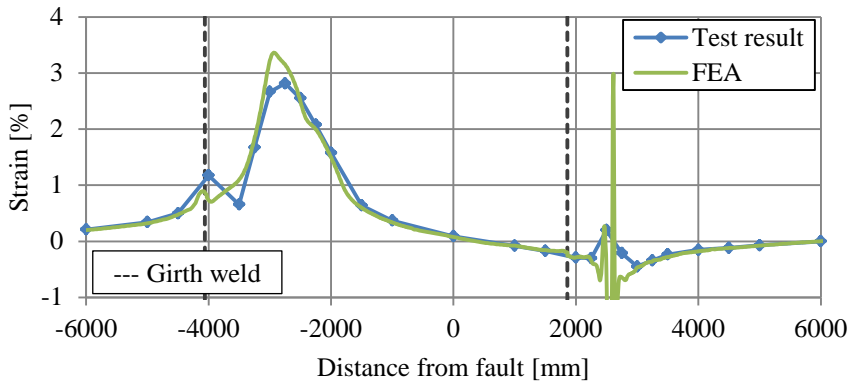
Figure E.27 Comparison of strain distributions at the front side of specimen T2 ($a_{imp}/t=0.66\%$).



(a) Comparison of strains at a fault movement of 500 mm



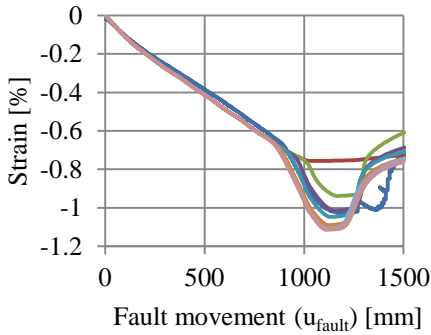
(b) Comparison of strains at a fault movement of 1000 mm



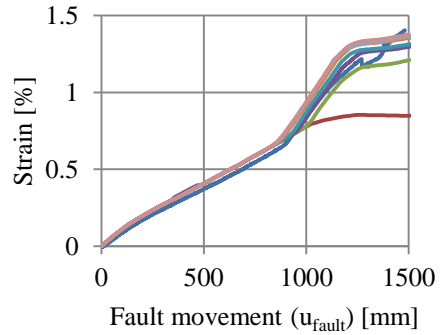
(c) Comparison of strains at a fault movement of 1480 mm

Figure E.28 Comparison of strain distributions at the back side of specimen T2 ($a_{imp}/t=0.66\%$).

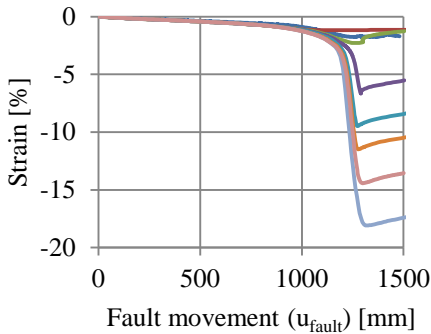
Test T3



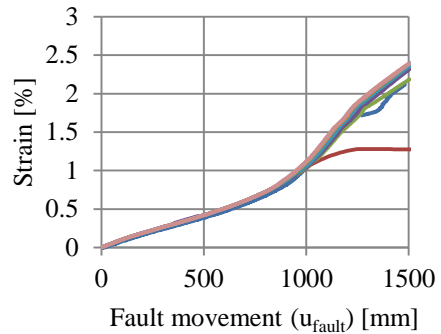
(a) Compressive strain 1950 mm from the fault



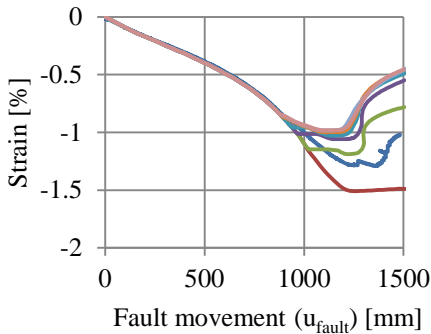
(b) Tensile strain 1950 mm from the fault



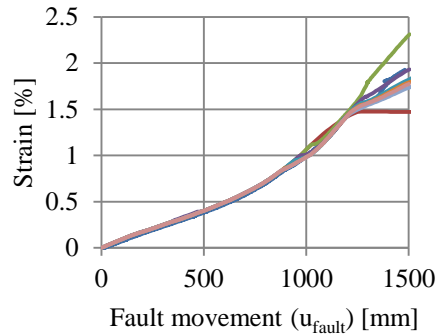
(c) Compressive strain 2250 mm from the fault



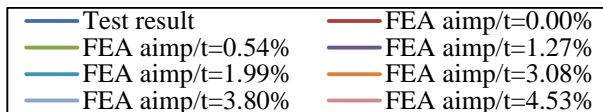
(d) Tensile strain 2250 mm from the fault



(e) Compressive strain 2500 mm from the fault

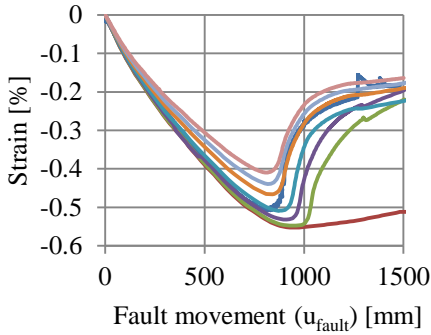


(f) Tensile strain 2500 mm from the fault

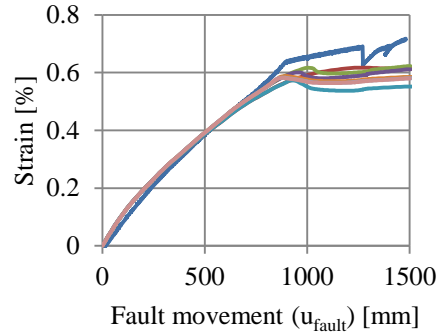


(g) Legend to graphs

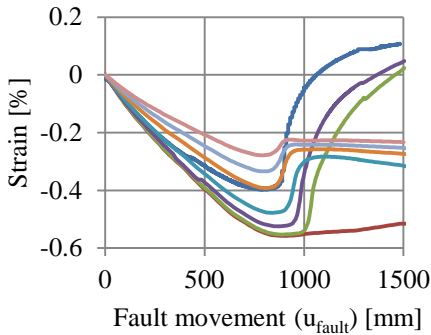
Figure E.29 Comparison of strain between test T3 and FE-model on the left side of the fault.



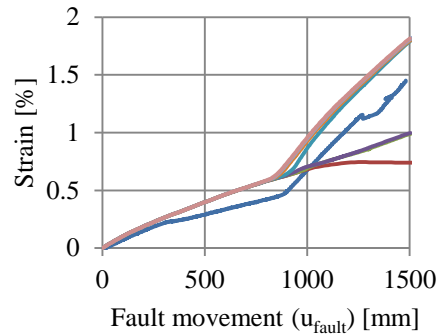
(a) Compressive strain 1950 mm from the fault



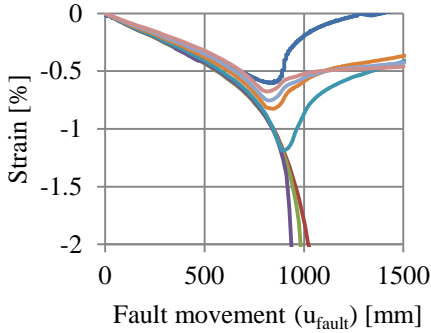
(b) Tensile strain 1950 mm from the fault



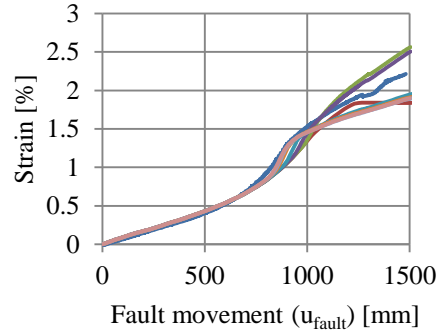
(c) Compressive strain 2250 mm from the fault



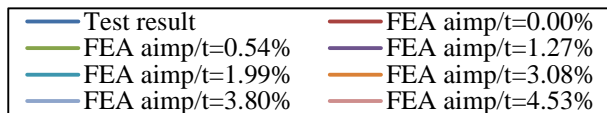
(d) Tensile strain 2250 mm from the fault



(e) Compressive strain 2500 mm from the fault

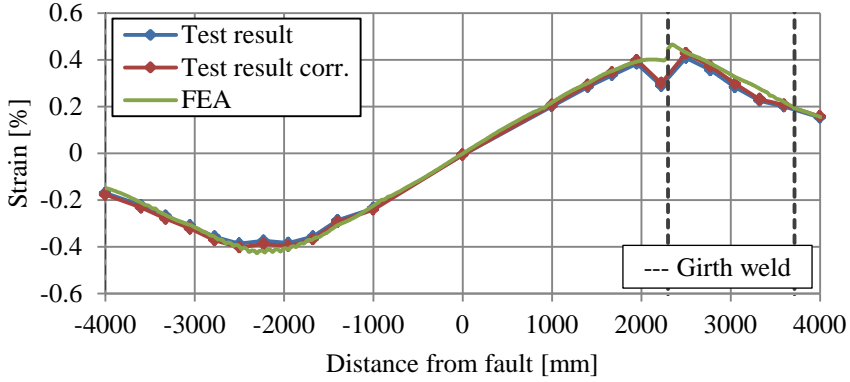


(f) Tensile strain 2500 mm from the fault

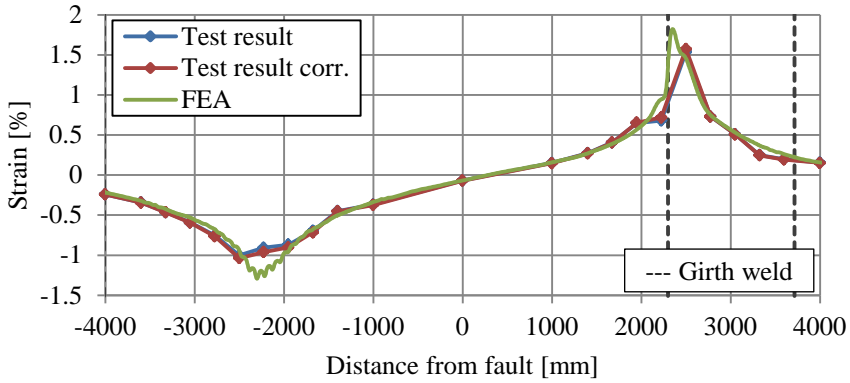


(g) Legend to graphs

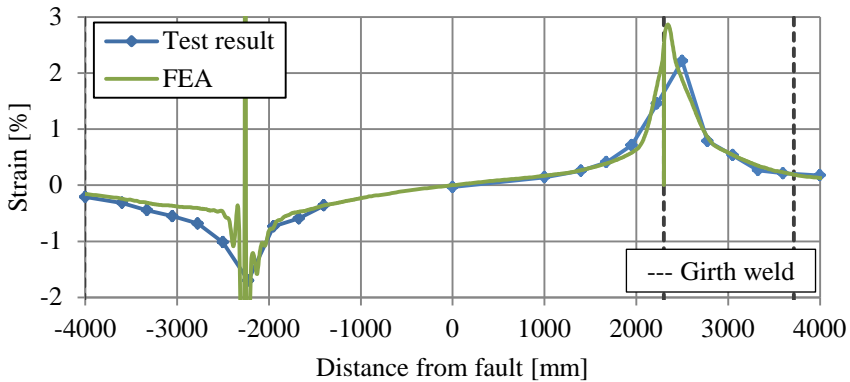
Figure E.30 Comparison of strain between test T3 and FE-model on the right side of the fault.



(a) Comparison of strains at a fault movement of 500 mm

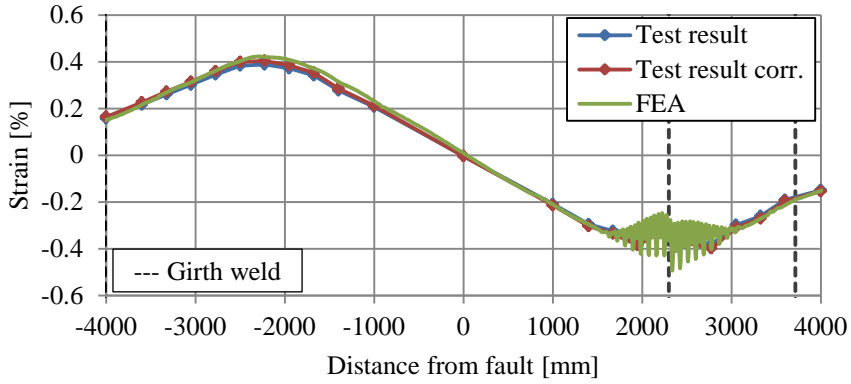


(b) Comparison of strains at a fault movement of 1000 mm

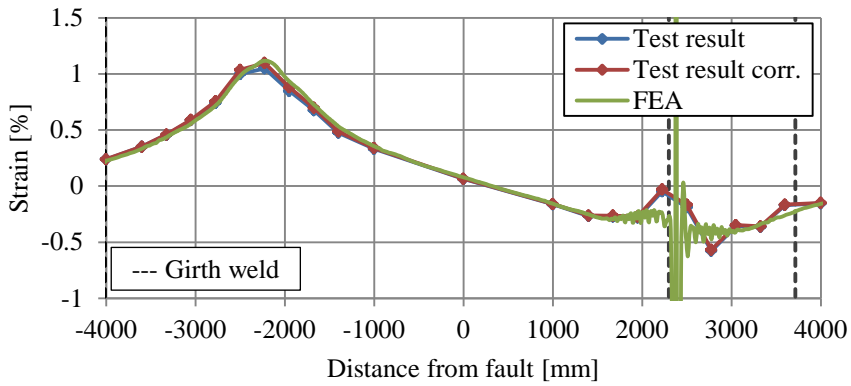


(c) Comparison of strains at a fault movement of 1480 mm

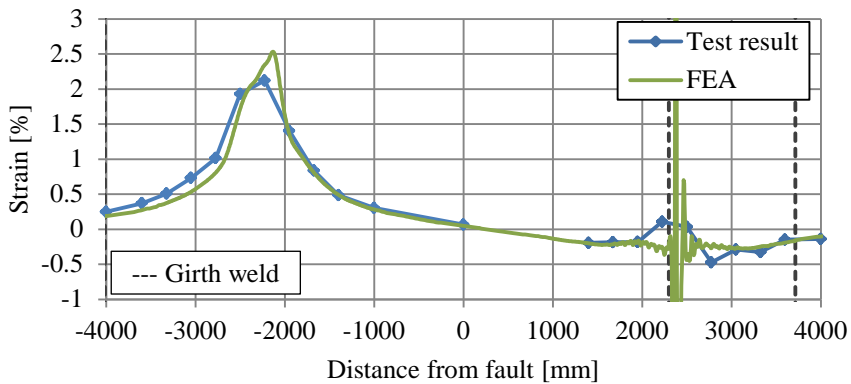
Figure E.31 Comparison of strain distributions at the front side of specimen T3 ($a_{imp}/t=3.80\%$).



(a) Comparison of strains at a fault movement of 500 mm



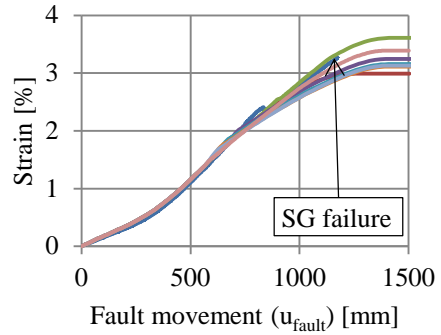
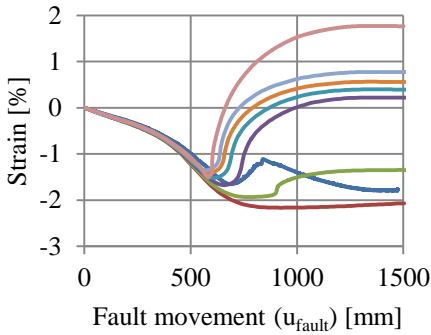
(b) Comparison of strains at a fault movement of 1000 mm



(c) Comparison of strains at a fault movement of 1480 mm

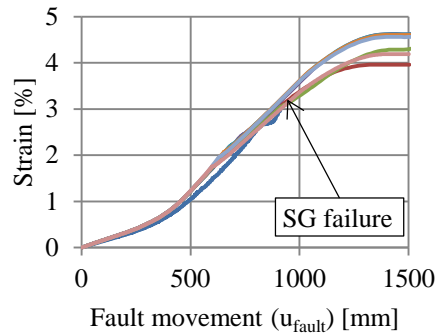
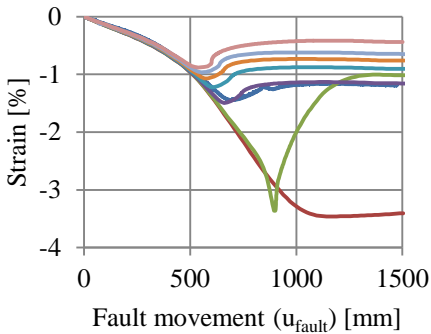
Figure E.32 Comparison of strain distributions at the back side of specimen T3 ($a_{imp}/t=3.80\%$).

Test T4



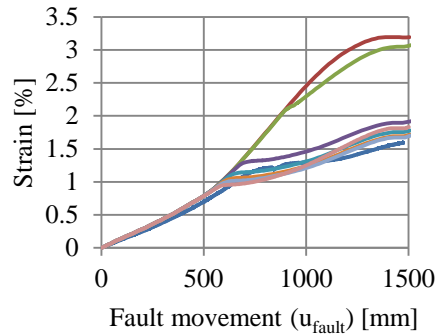
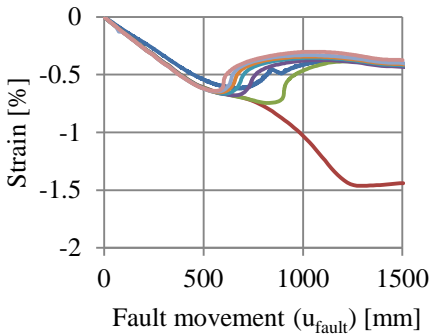
(a) Compressive strain 1600 mm from the fault

(b) Tensile strain 1600 mm from the fault



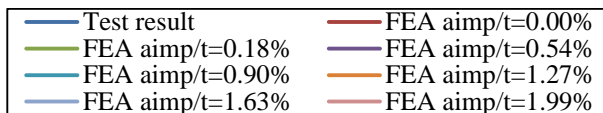
(c) Compressive strain 1800 mm from the fault

(d) Tensile strain 1800 mm from the fault



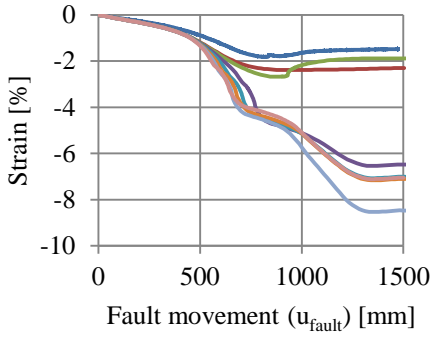
(e) Compressive strain 2000 mm from the fault

(f) Tensile strain 2000 mm from the fault

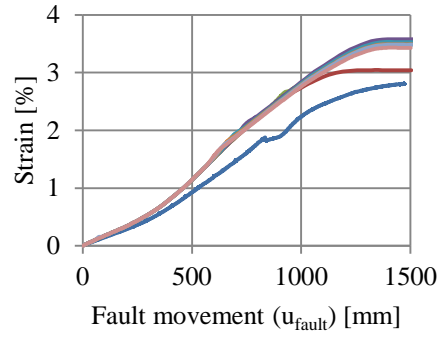


(g) Legend to graphs

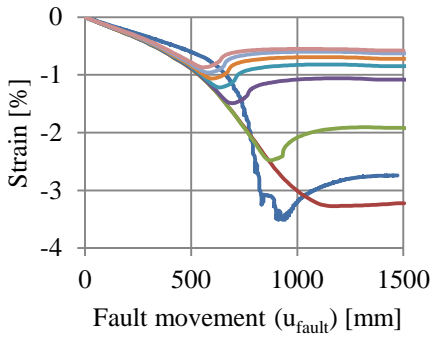
Figure E.33 Comparison of strain between test T4 and FE-model on the left side of the fault.



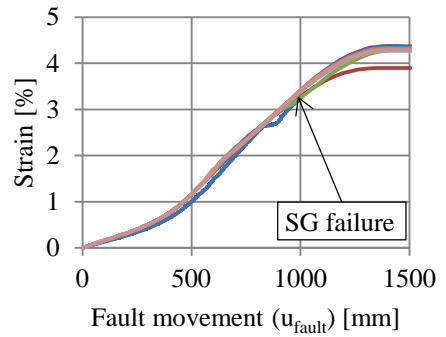
(a) Compressive strain 1600 mm from the fault



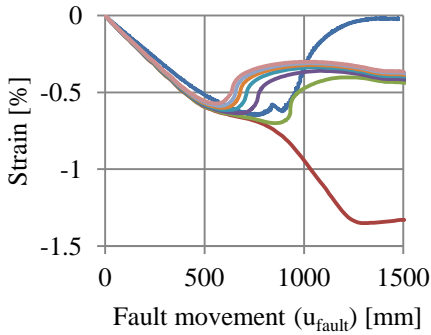
(b) Tensile strain 1600 mm from the fault



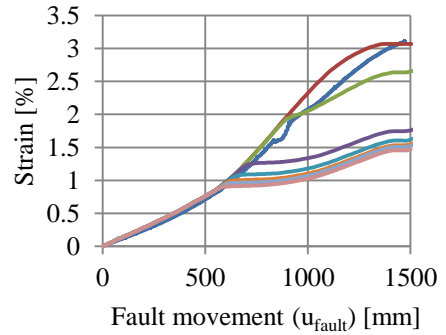
(c) Compressive strain 1800 mm from the fault



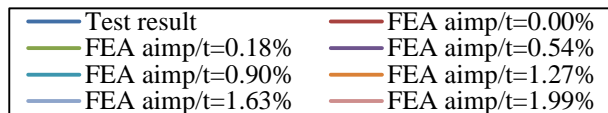
(d) Tensile strain 1800 mm from the fault



(e) Compressive strain 2000 mm from the fault

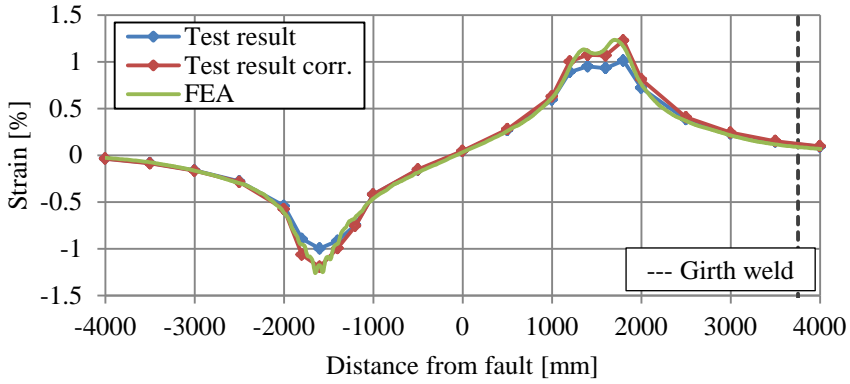


(f) Tensile strain 2000 mm from the fault

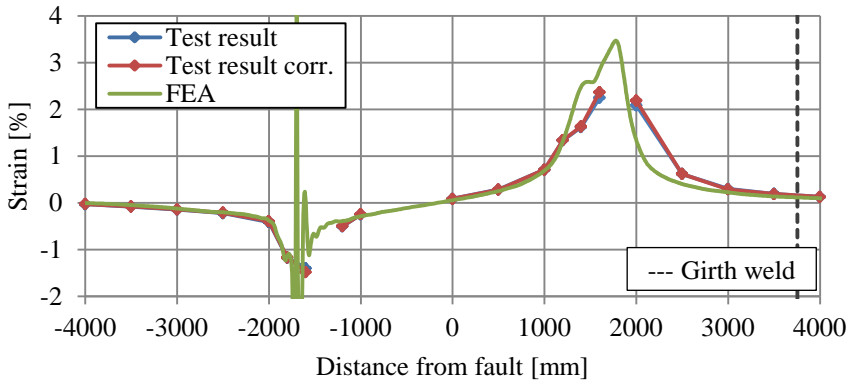


(g) Legend to graphs

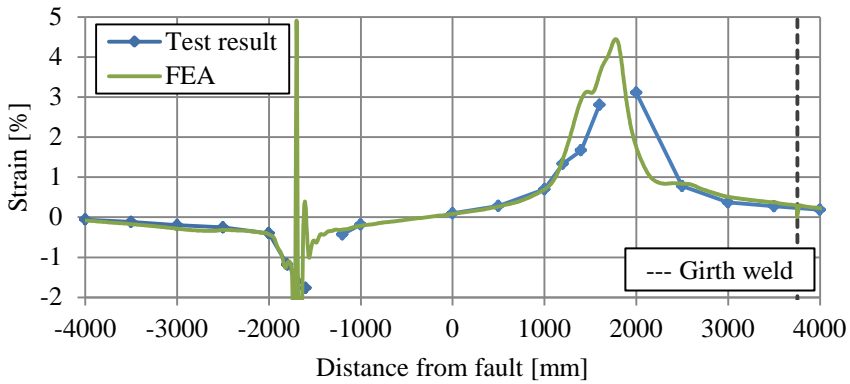
Figure E.34 Comparison of strain between test T4 and FE-model on the right side of the fault.



(a) Comparison of strains at a fault movement of 500 mm

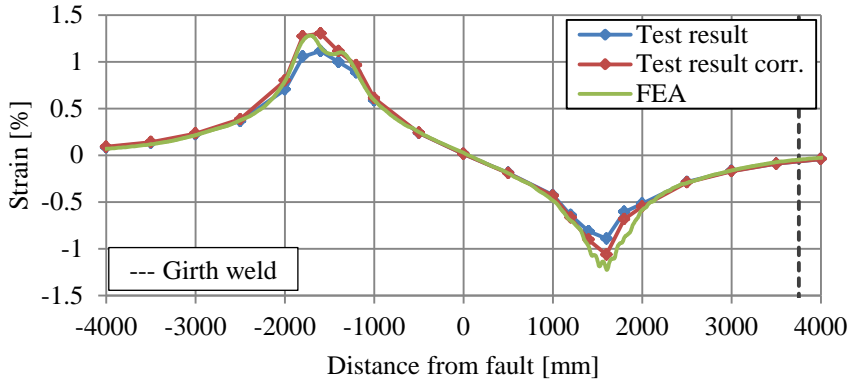


(b) Comparison of strains at a fault movement of 1000 mm

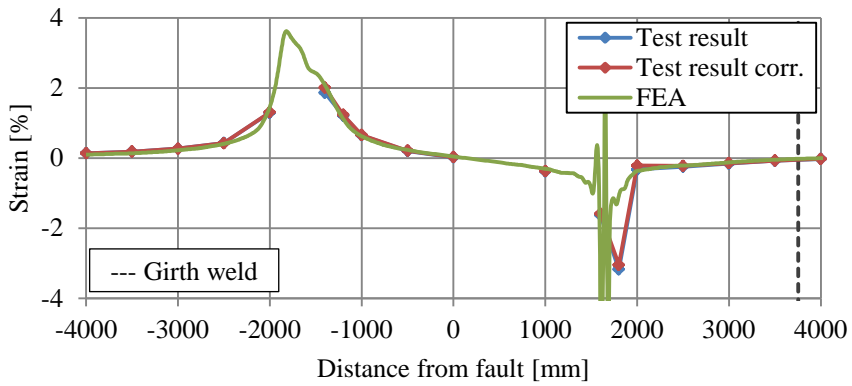


(c) Comparison of strains at a fault movement of 1470 mm

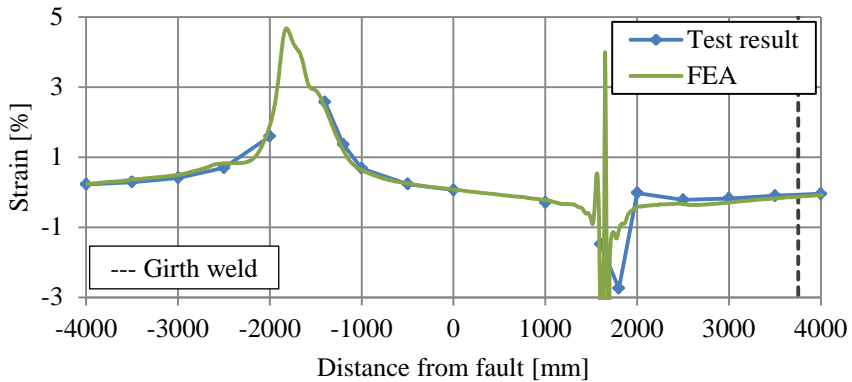
Figure E.35 Comparison of strain distributions at the front side of specimen T4 ($a_{imp}/t=0.54\%$).



(a) Comparison of strains at a fault movement of 500 mm



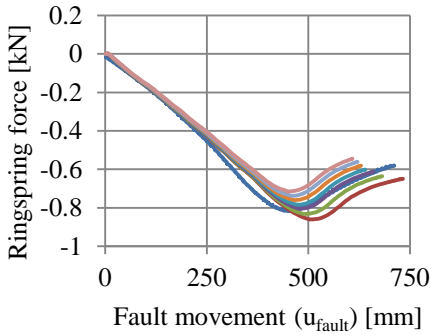
(b) Comparison of strains at a fault movement of 1000 mm



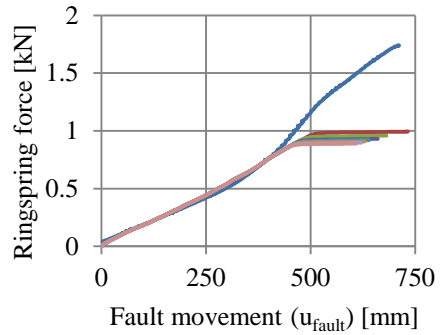
(c) Comparison of strains at a fault movement of 1470 mm

Figure E.36 Comparison of strain distributions at the back side of specimen T4 ($a_{imp}/t=0.54\%$).

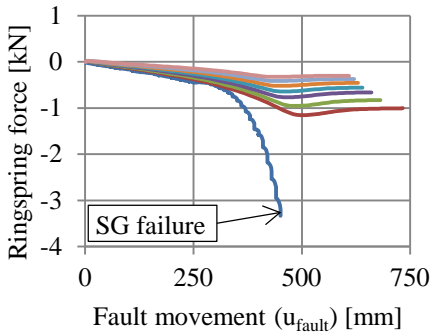
Test T5



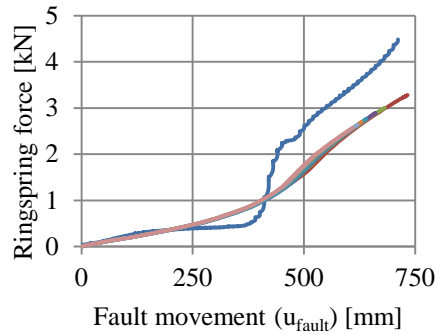
(a) Compressive strain 1250 mm from the fault



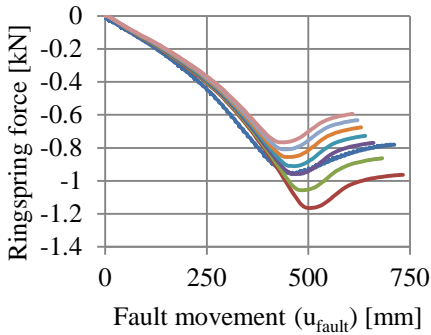
(b) Tensile strain 1250 mm from the fault



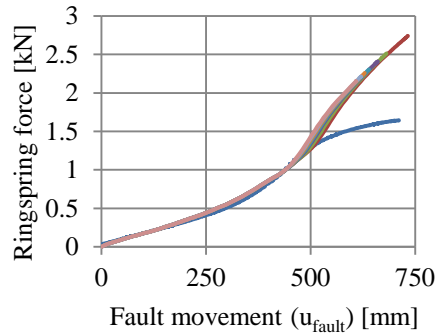
(c) Compressive strain 1450 mm from the fault



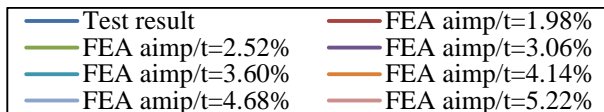
(d) Tensile strain 1450 mm from the fault



(e) Compressive strain 1650 mm from the fault

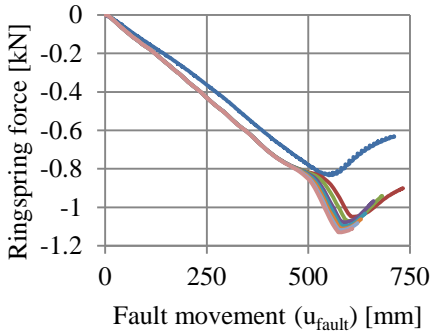


(f) Tensile strain 1650 mm from the fault

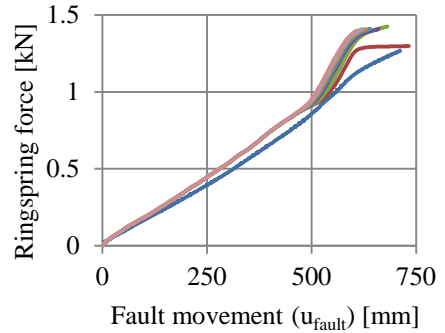


(g) Legend to graphs

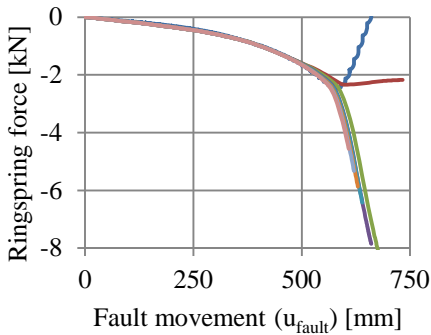
Figure E.37 Comparison of strain between test T5 and FE-model on the left side of the fault.



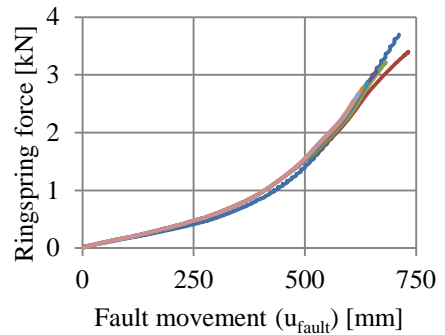
(a) Compressive strain 1250 mm from the fault



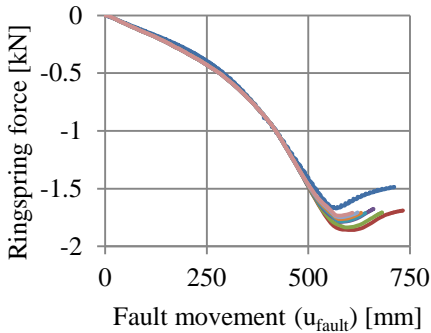
(b) Tensile strain 1250 mm from the fault



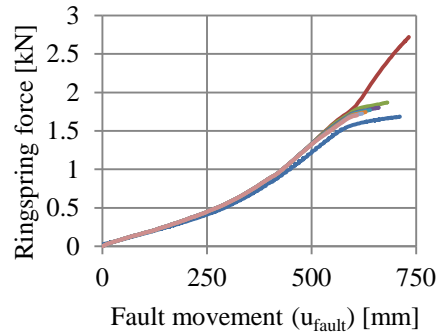
(c) Compressive strain 1450 mm from the fault



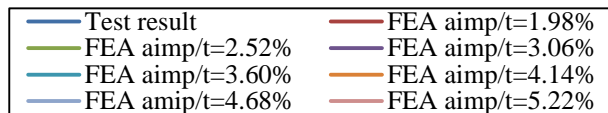
(d) Tensile strain 1450 mm from the fault



(e) Compressive strain 1650 mm from the fault

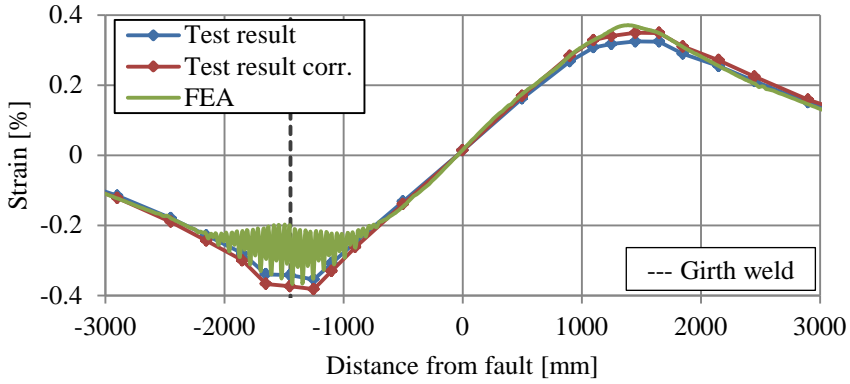


(f) Tensile strain 1650 mm from the fault

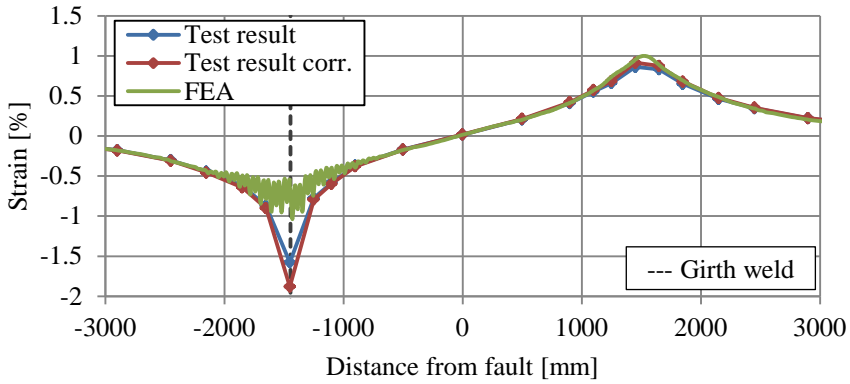


(g) Legend to graphs

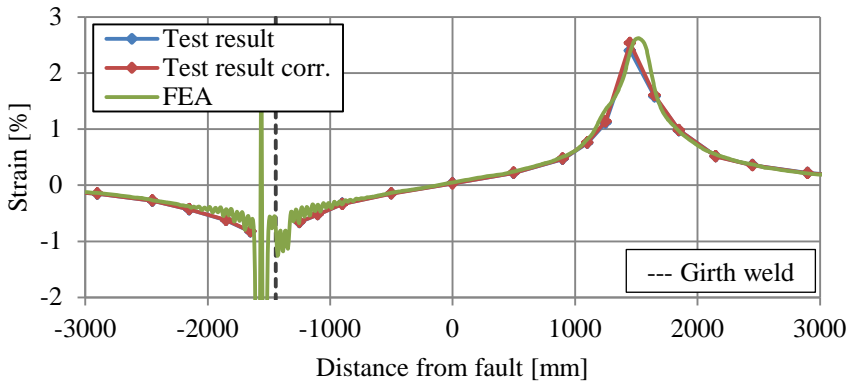
Figure E.38 Comparison of strain between test T5 and FE-model on the right side of the fault.



(a) Comparison of strains at a fault movement of 200 mm

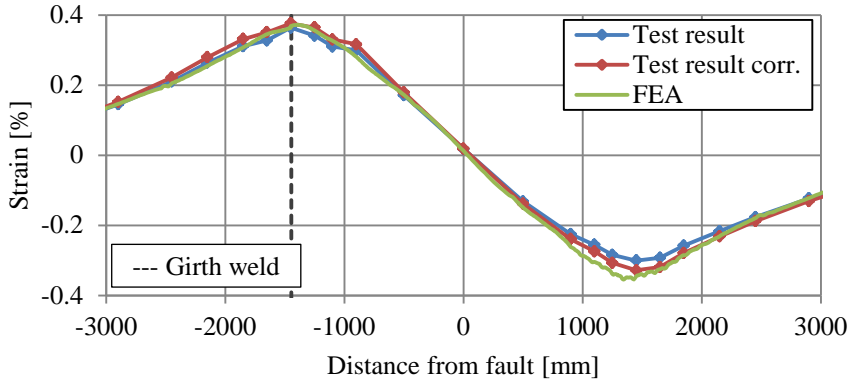


(b) Comparison of strains at a fault movement of 400 mm

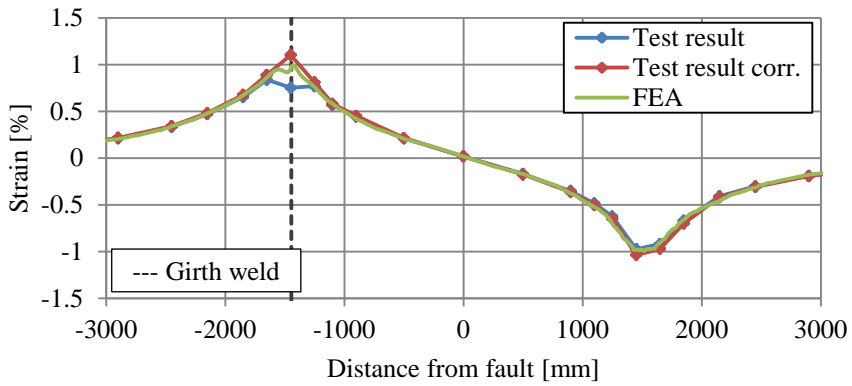


(c) Comparison of strains at a fault movement of 600 mm

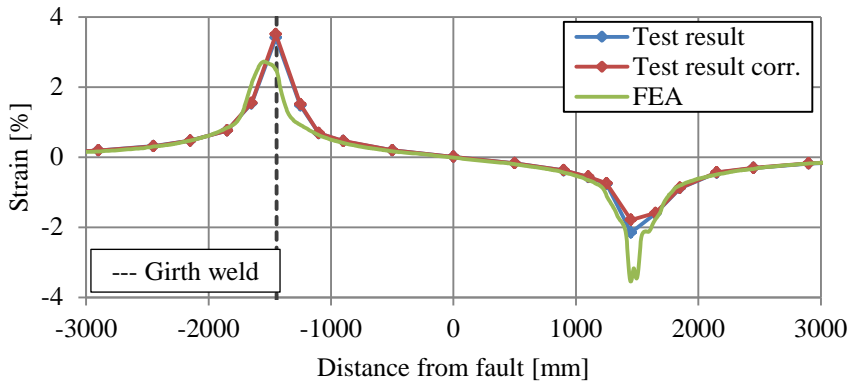
Figure E.39 Comparison of strain distributions at the front side of specimen T5 ($a_{imp}/t=3.60\%$).



(a) Comparison of strains at a fault movement of 200 mm



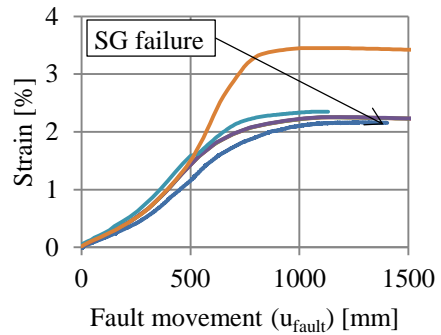
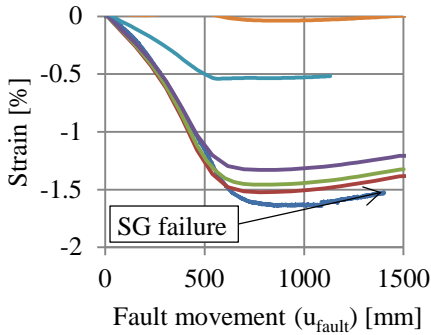
(b) Comparison of strains at a fault movement of 400 mm



(c) Comparison of strains at a fault movement of 600 mm

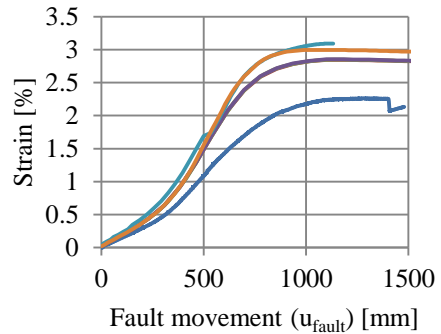
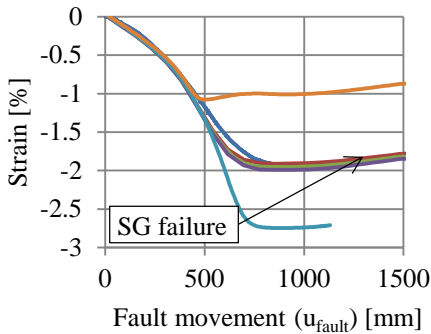
Figure E.40 Comparison of strain distributions at the back side of specimen T5 ($a_{imp}/t=3.60\%$).

Test T6



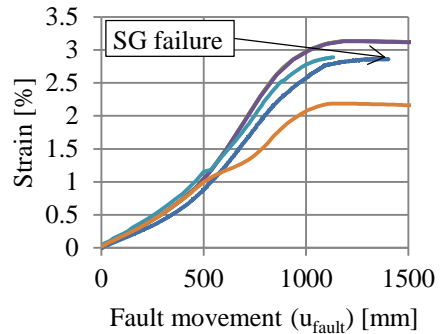
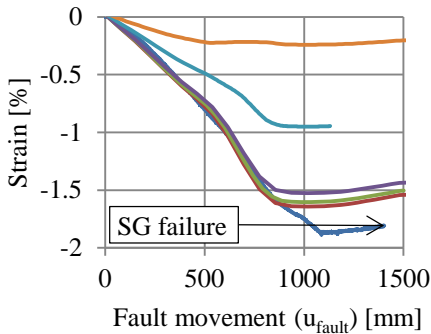
(a) Compressive strain 1420 mm from the fault

(b) Tensile strain 1420 mm from the fault



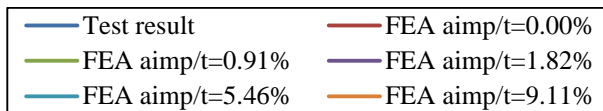
(c) Compressive strain 1630 mm from the fault

(d) Tensile strain 1630 mm from the fault



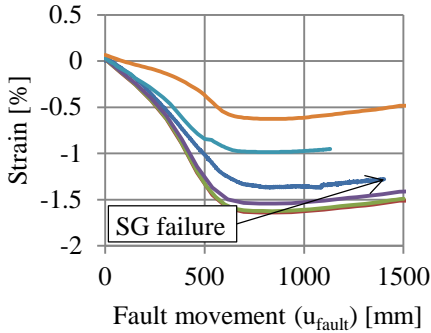
(e) Compressive strain 1840 mm from the fault

(f) Tensile strain 1840 mm from the fault

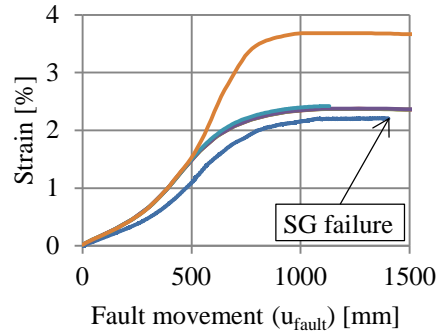


(g) Legend to graphs

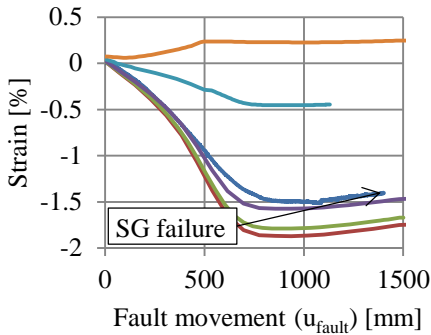
Figure E.41 Comparison of strain between test T6 and FE-model on the left side of the fault .



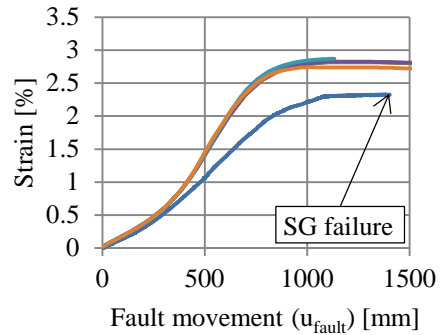
(a) Compressive strain 1420 mm from the fault



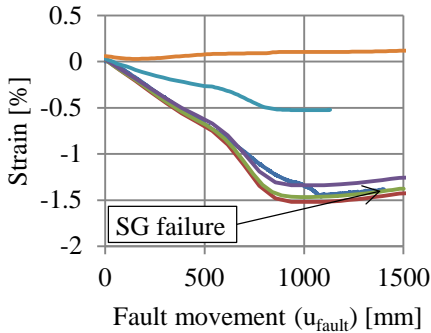
(b) Tensile strain 1420 mm from the fault



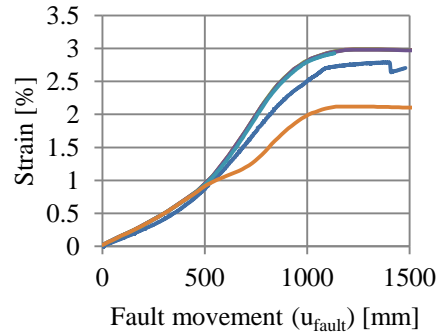
(c) Compressive strain 1630 mm from the fault



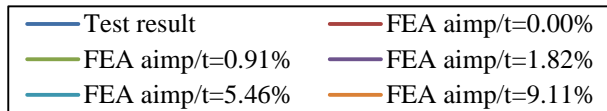
(d) Tensile strain 1630 mm from the fault



(e) Compressive strain 1840 mm from the fault

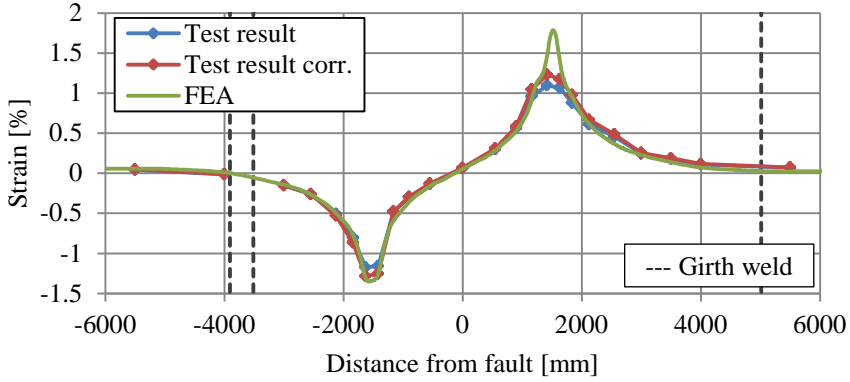


(f) Tensile strain 1840 mm from the fault

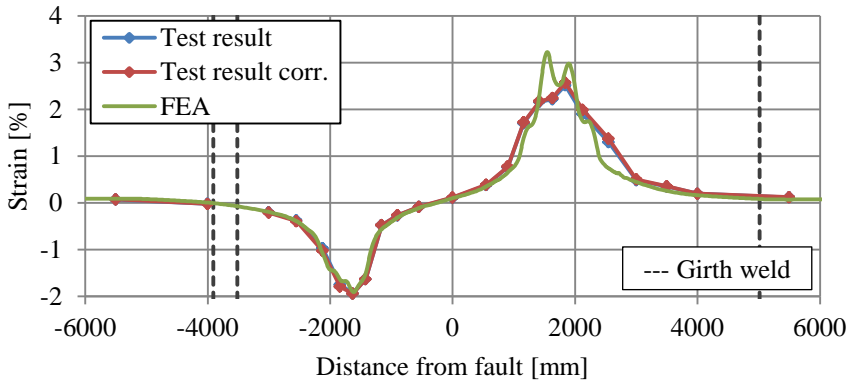


(g) Legend to graphs

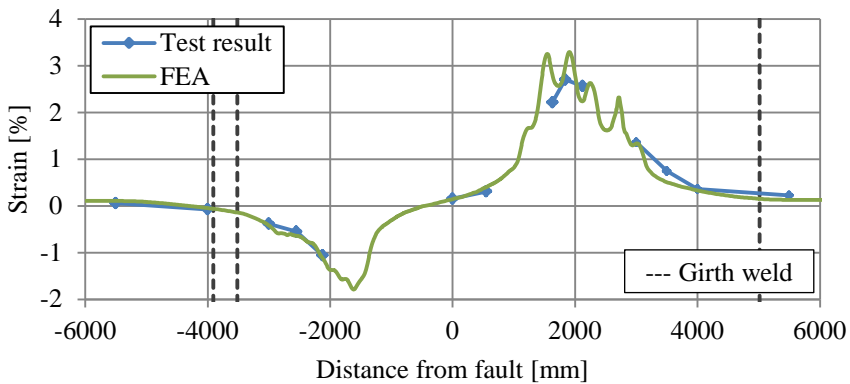
Figure E.42 Comparison of strain between test T6 and FE-model on the right side of the fault.



(a) Comparison of strains at a fault movement of 500 mm

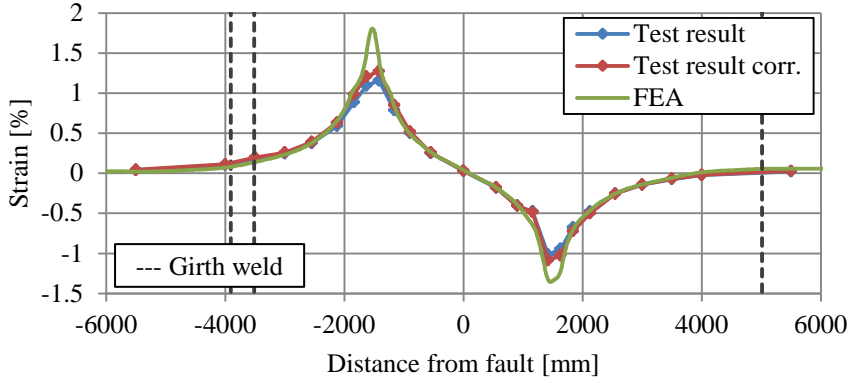


(b) Comparison of strains at a fault movement of 1000 mm

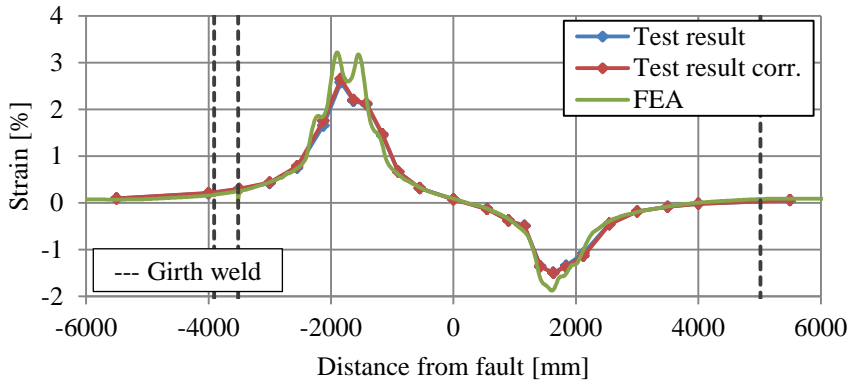


(c) Comparison of strains at a fault movement of 1480 mm

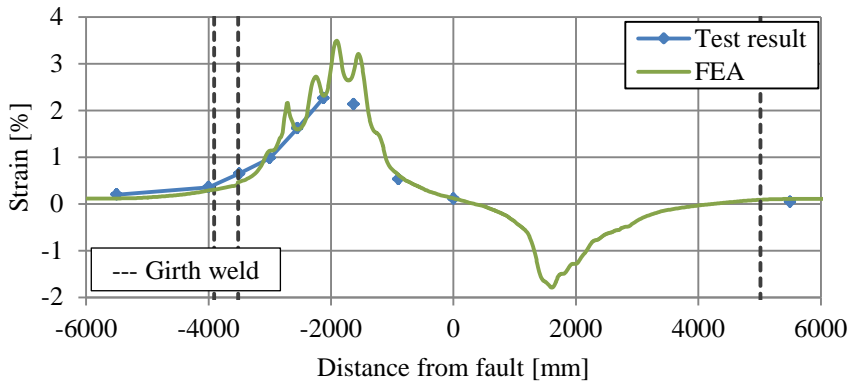
Figure E.43 Comparison of strain distributions at the front side of specimen T6 ($a_{imp}/t=0.00\%$).



(a) Comparison of strains at a fault movement of 500 mm



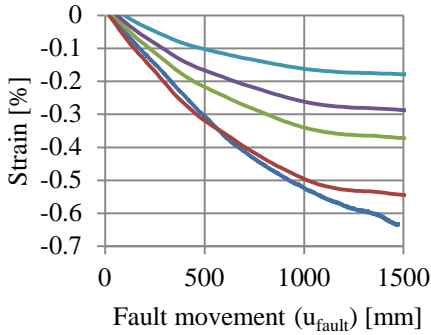
(b) Comparison of strains at a fault movement of 1000 mm



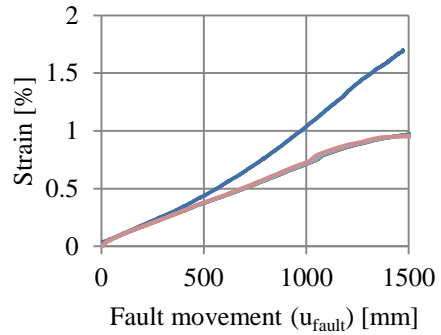
(c) Comparison of strains at a fault movement of 1480 mm

Figure E.44 Comparison of strain distributions at the back side of specimen T6 ($a_{imp}/t=0.00\%$).

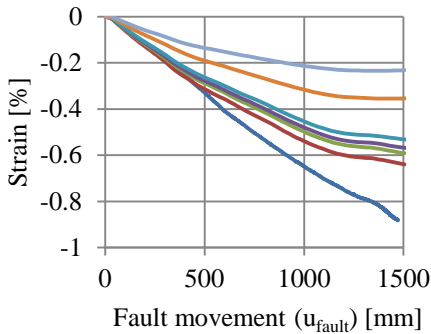
Test T7



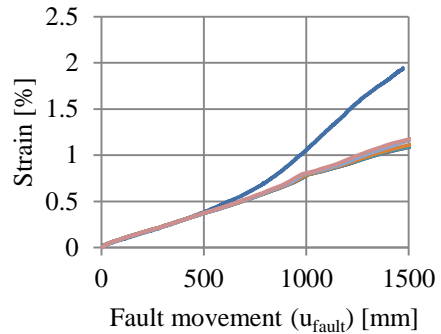
(a) Compressive strain 3375 mm from the fault



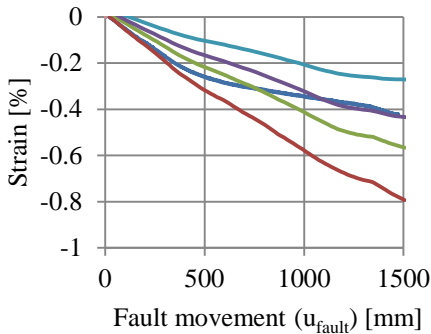
(b) Tensile strain 3375 mm from the fault



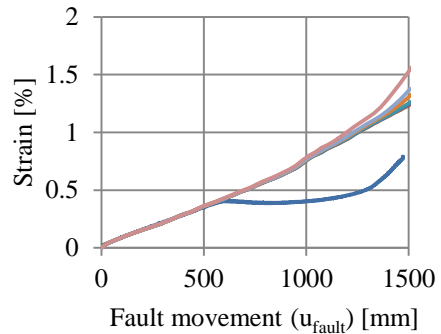
(c) Compressive strain 3625 mm from the fault



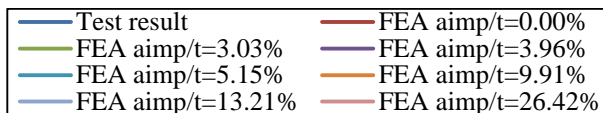
(d) Tensile strain 3625 mm from the fault



(e) Compressive strain 3875 mm from the fault

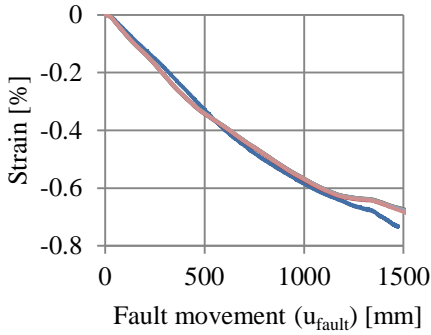


(f) Tensile strain 3875 mm from the fault

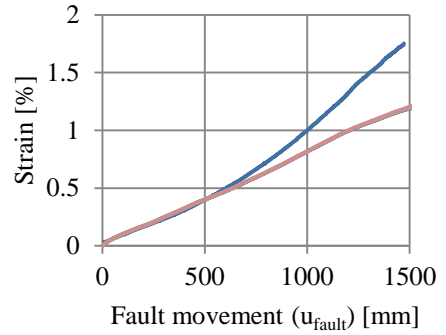


(g) Legend to graphs

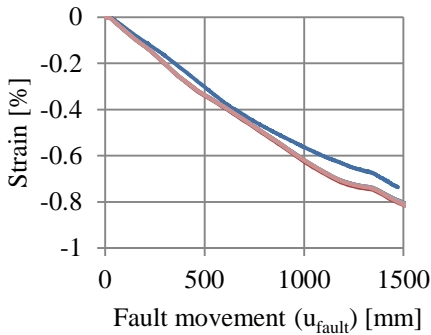
Figure E.45 Comparison of strain between test T7 and FE-model on the left side of the fault.



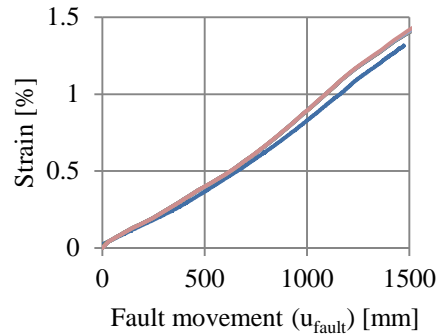
(a) Compressive strain 3375 mm from the fault



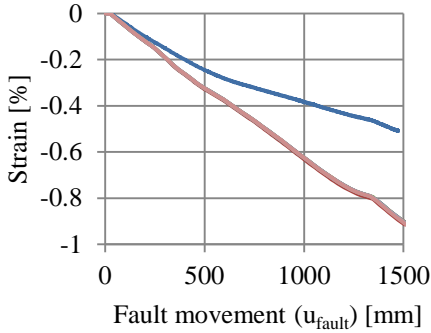
(b) Tensile strain 3375 mm from the fault



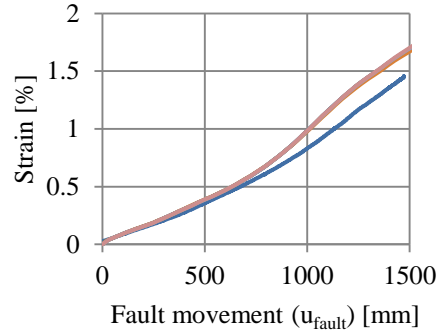
(c) Compressive strain 3625 mm from the fault



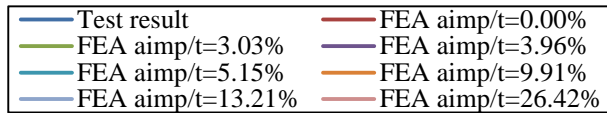
(d) Tensile strain 3625 mm from the fault



(e) Compressive strain 3875 mm from the fault

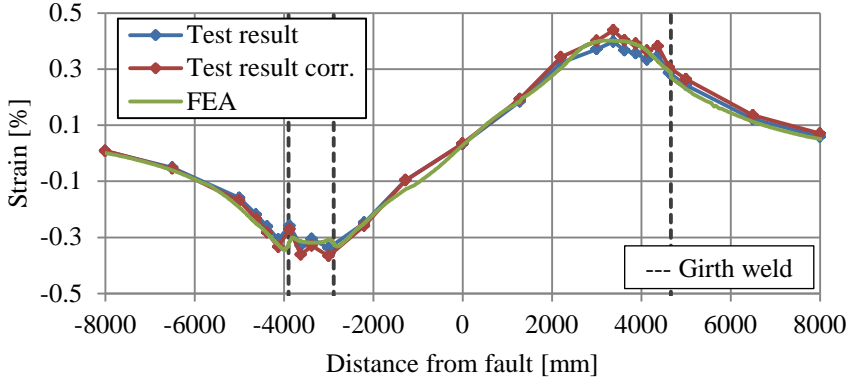


(f) Tensile strain 3875 mm from the fault

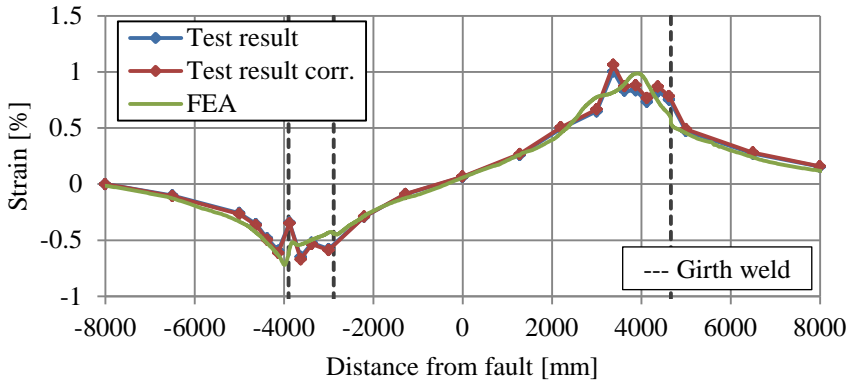


(g) Legend to graphs

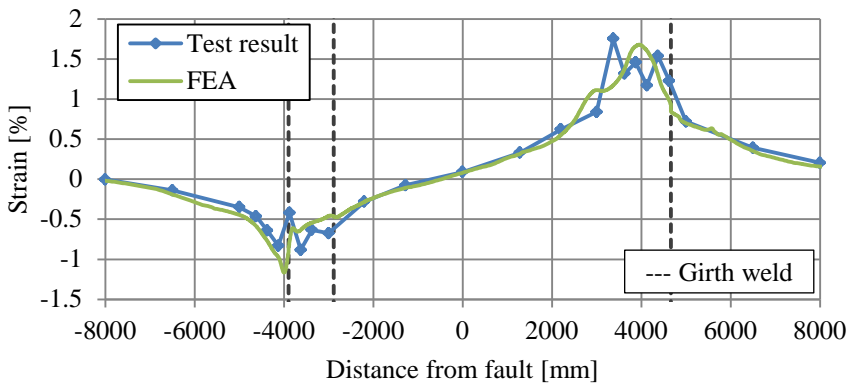
Figure E.46 Comparison of strain between test T7 and FE-model on the right side of the fault.



(a) Comparison of strains at a fault movement of 500 mm

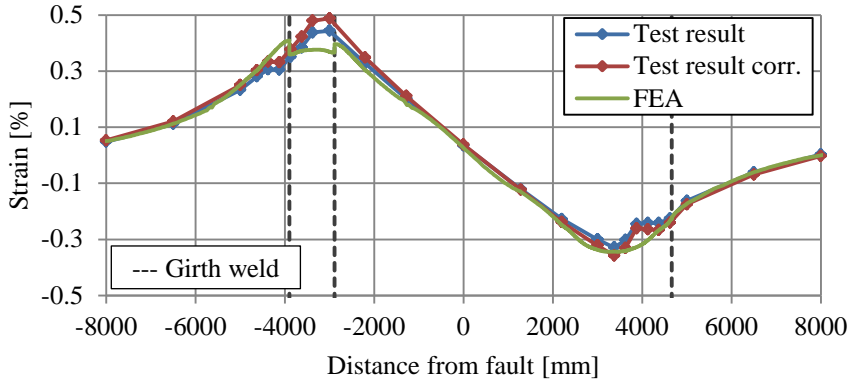


(b) Comparison of strains at a fault movement of 1000 mm

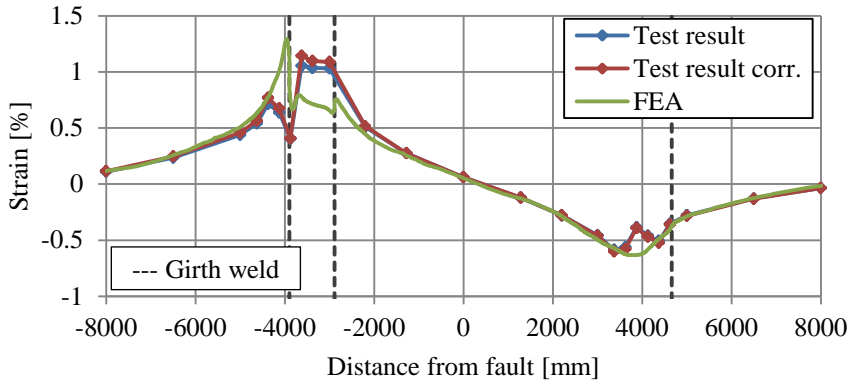


(c) Comparison of strains at a fault movement of 1470 mm

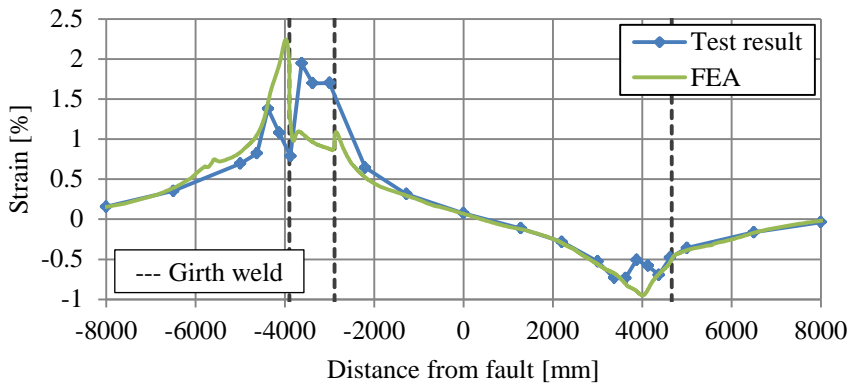
Figure E.47 Comparison of strain distributions at the front side of specimen T7 ($a_{imp}/t=0.00\%$).



(a) Comparison of strains at a fault movement of 500 mm



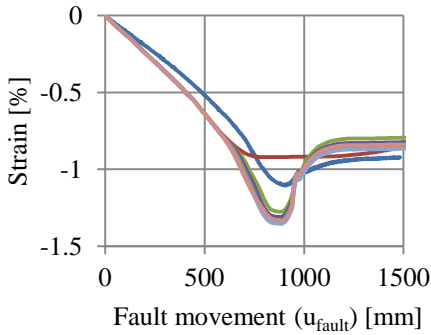
(b) Comparison of strains at a fault movement of 1000 mm



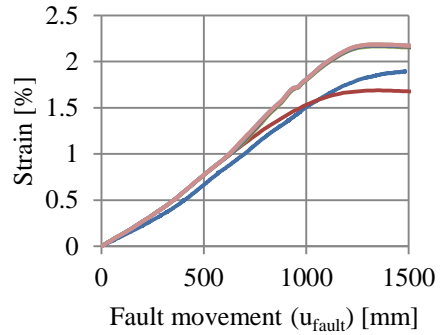
(c) Comparison of strains at a fault movement of 1470 mm

Figure E.48 Comparison of strain distributions at the back side of specimen T7 ($a_{imp}/t=0.00\%$).

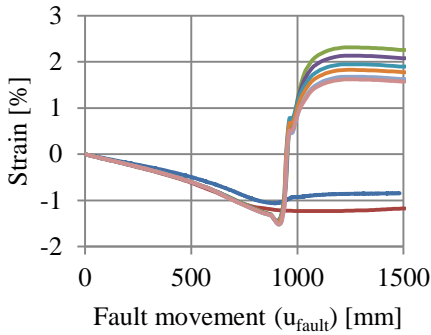
Test T8



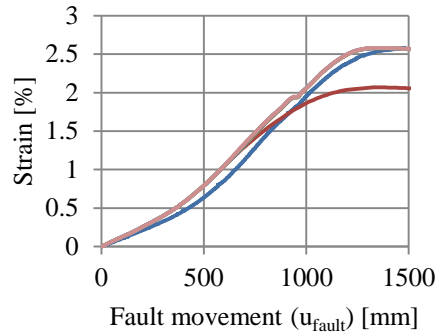
(a) Compressive strain 2400 mm from the fault



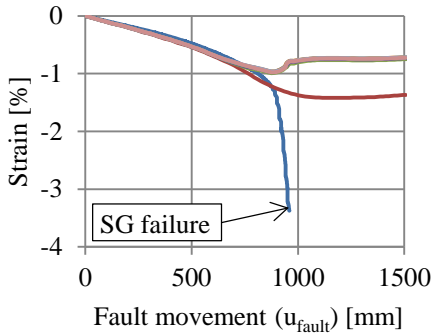
(b) Tensile strain 2400 mm from the fault



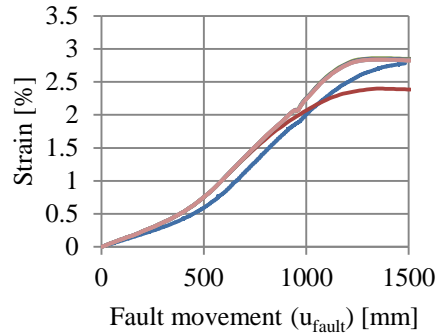
(c) Compressive strain 2625 mm from the fault



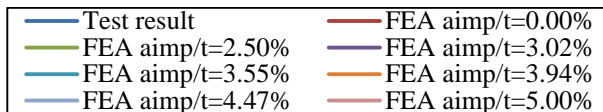
(d) Tensile strain 2625 mm from the fault



(e) Compressive strain 2900 mm from the fault

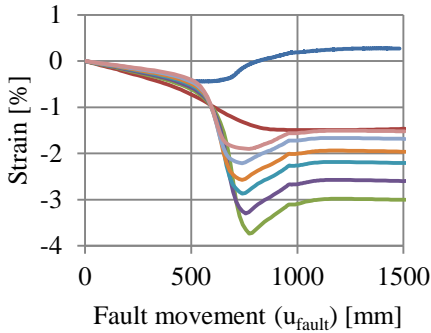


(f) Tensile strain 2900 mm from the fault

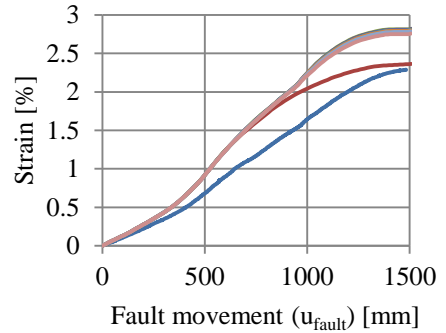


(g) Legend to graphs

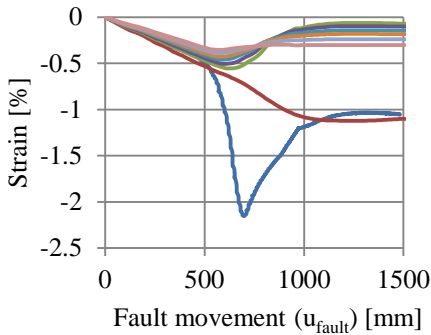
Figure E.49 Comparison of strain between test T8 and FE-model on the left side of the fault.



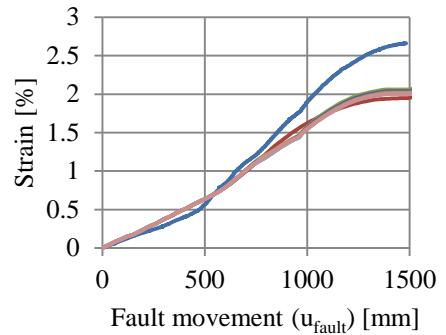
(a) Compressive strain 2400 mm from the fault



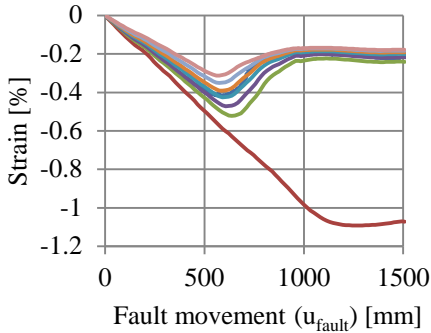
(b) Tensile strain 2400 mm from the fault



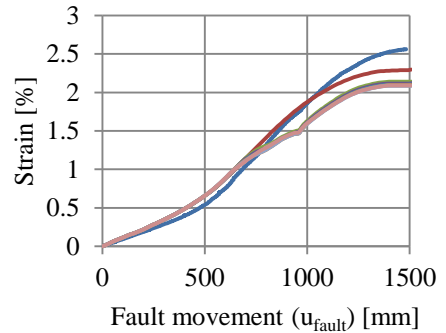
(c) Compressive strain 2625 mm from the fault



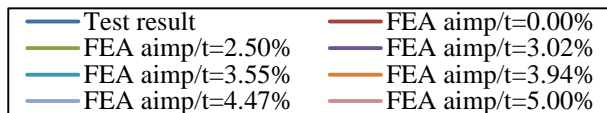
(d) Tensile strain 2625 mm from the fault



(e) Compressive strain 2900 mm from the fault

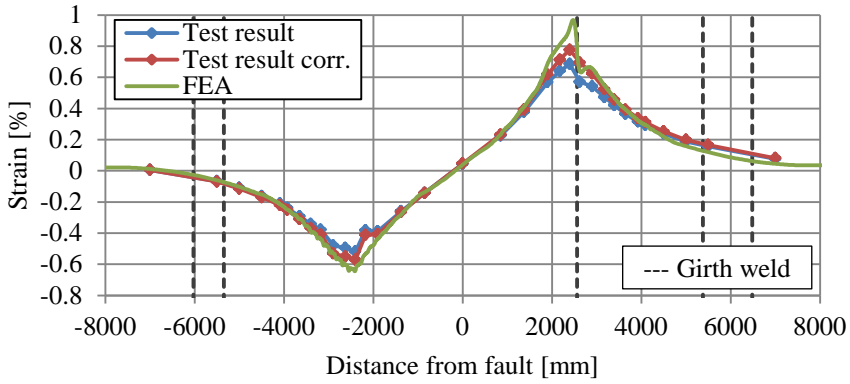


(f) Tensile strain 2900 mm from the fault

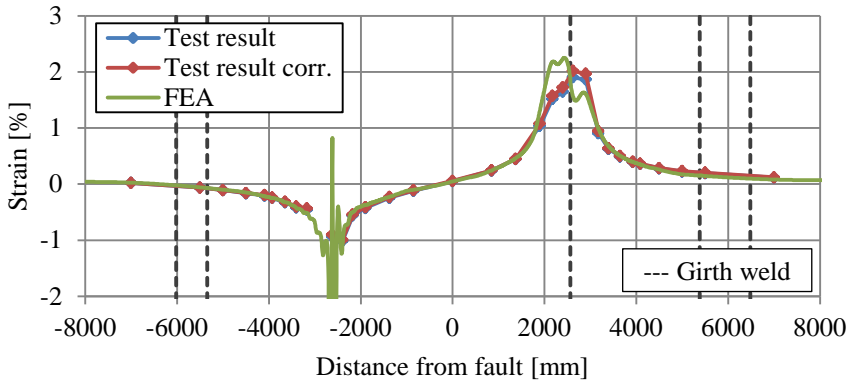


(g) Legend to graphs

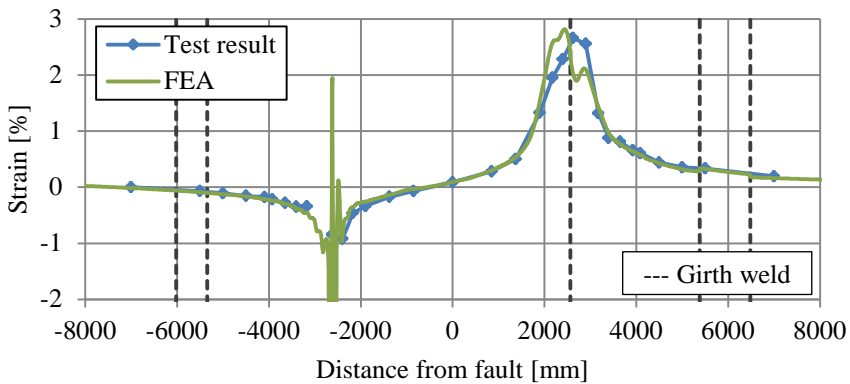
Figure E.50 Comparison of strain between test T8 and FE-model on the right side of the fault.



(a) Comparison of strains at a fault movement of 500 mm

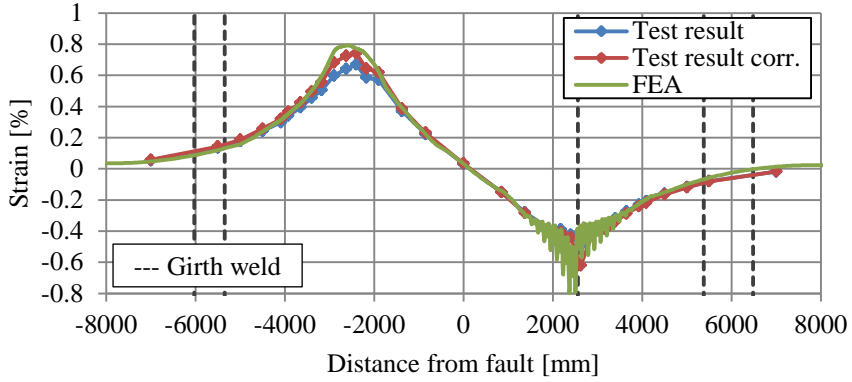


(b) Comparison of strains at a fault movement of 1000 mm

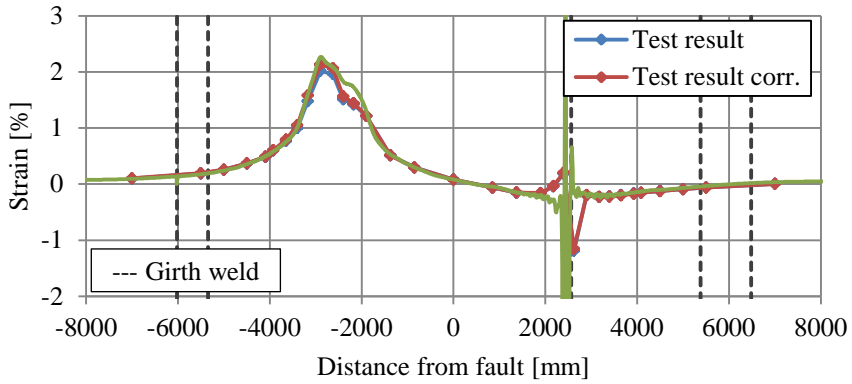


(c) Comparison of strains at a fault movement of 1480 mm

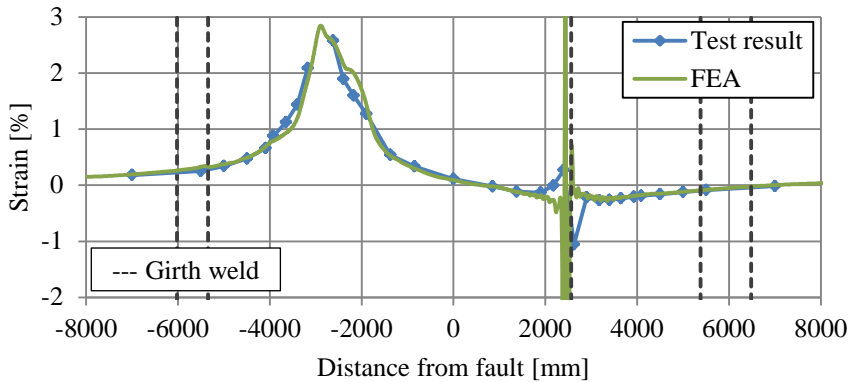
Figure E.51 Comparison of strain distributions at the front side of specimen T8 ($a_{imp}/t=3.55\%$).



(a) Comparison of strains at a fault movement of 500 mm



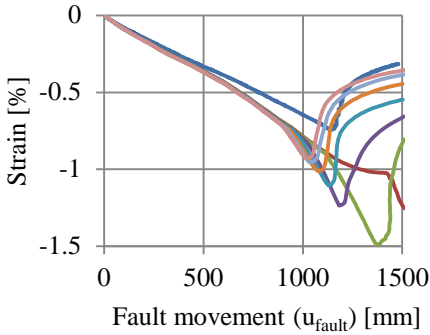
(b) Comparison of strains at a fault movement of 1000 mm



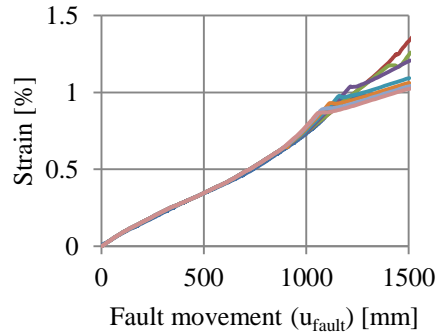
(c) Comparison of strains at a fault movement of 1480 mm

Figure E.52 Comparison of strain distributions at the back side of specimen T8 ($a_{imp}/t=3.55\%$).

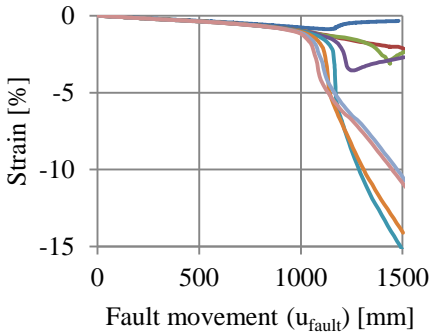
Test T9



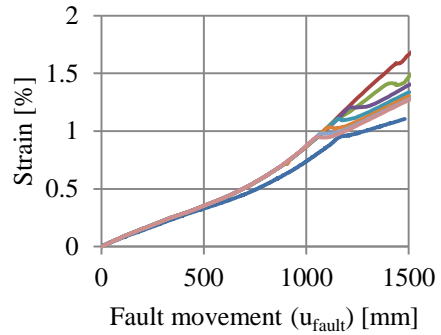
(a) Compressive strain 3150 mm from the fault



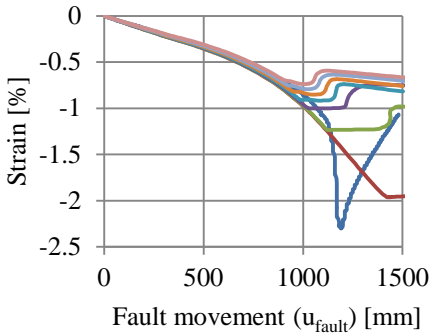
(b) Tensile strain 3150 mm from the fault



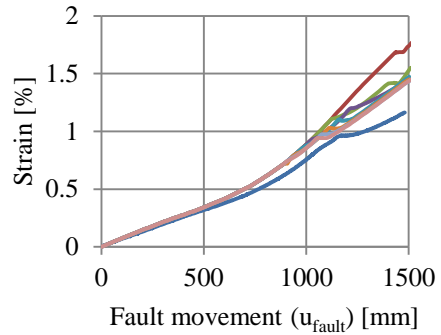
(c) Compressive strain 3425 mm from the fault



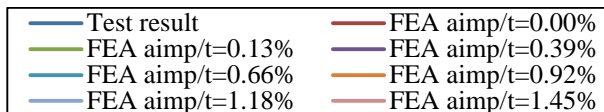
(d) Tensile strain 3425 mm from the fault



(e) Compressive strain 3750 mm from the fault

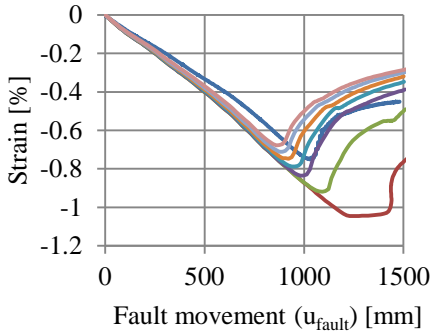


(f) Tensile strain 3750 mm from the fault

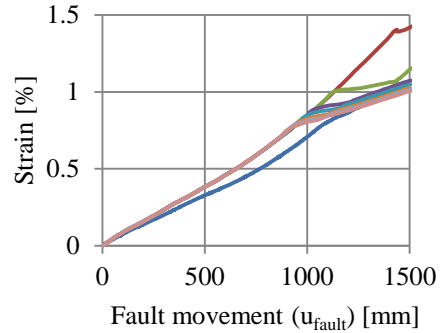


(g) Legend to graphs

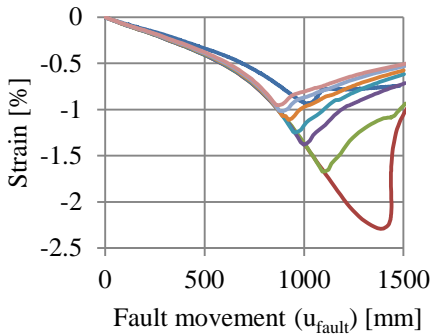
Figure E.53 Comparison of strain between test T9 and FE-model on the left side of the fault.



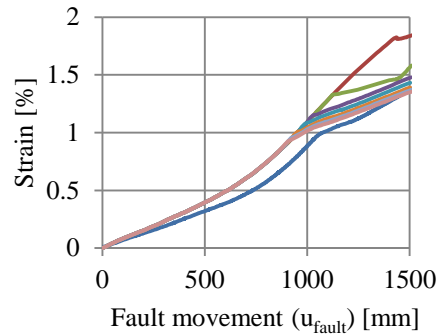
(a) Compressive strain 3150 mm from the fault



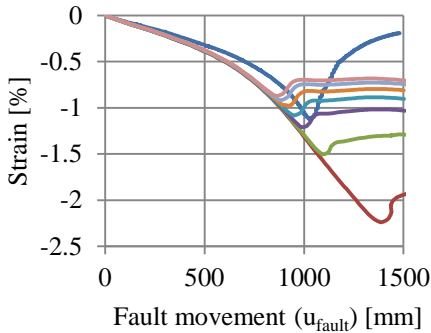
(b) Tensile strain 3150 mm from the fault



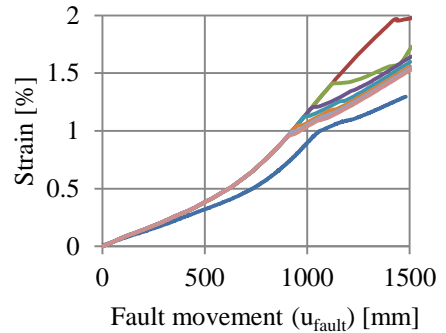
(c) Compressive strain 3425 mm from the fault



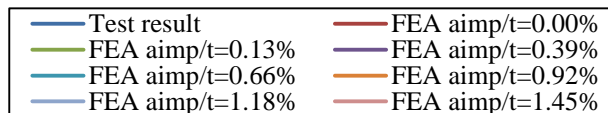
(d) Tensile strain 3425 mm from the fault



(e) Compressive strain 3750 mm from the fault

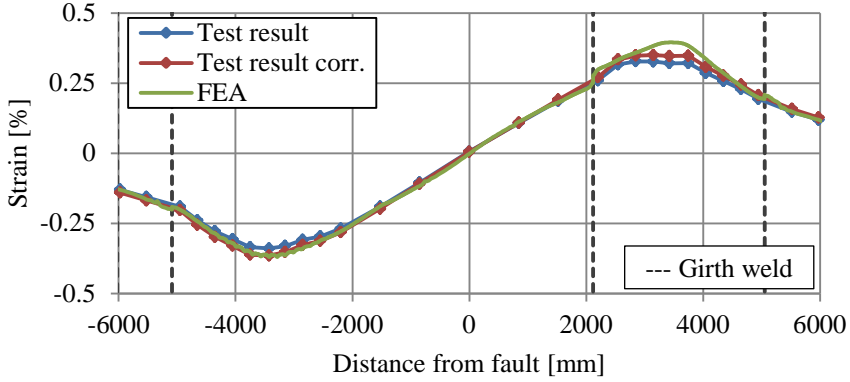


(f) Tensile strain 3750 mm from the fault

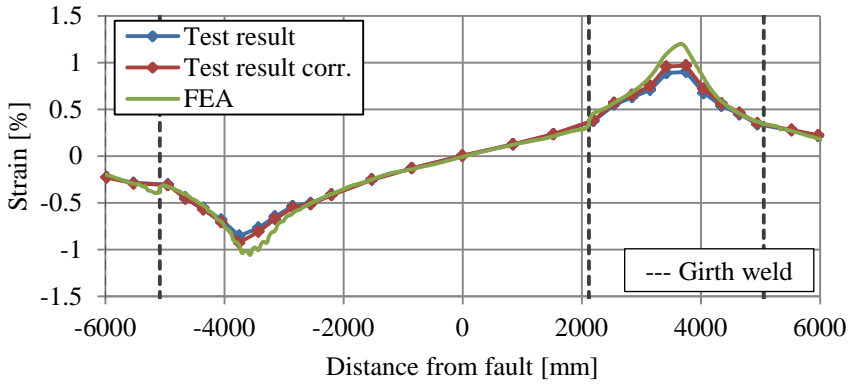


(g) Legend to graphs

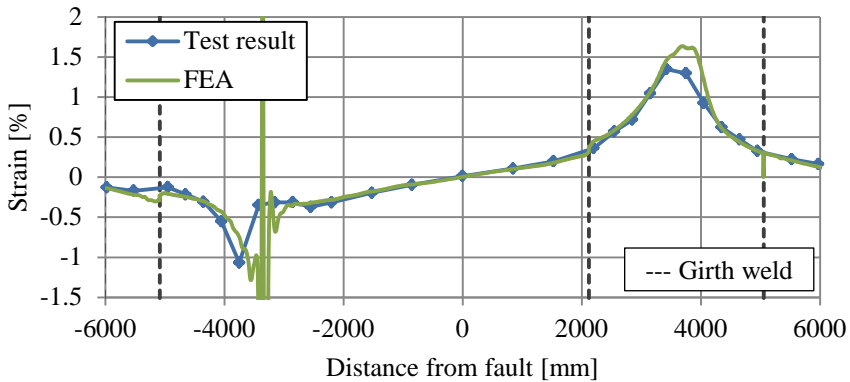
Figure E.54 Comparison of strain between test T9 and FE-model on the right side of the fault.



(a) Comparison of strains at a fault movement of 500 mm

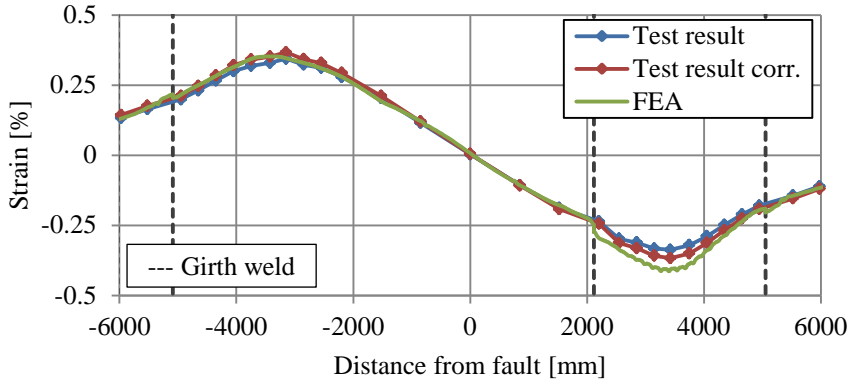


(b) Comparison of strains at a fault movement of 1000 mm

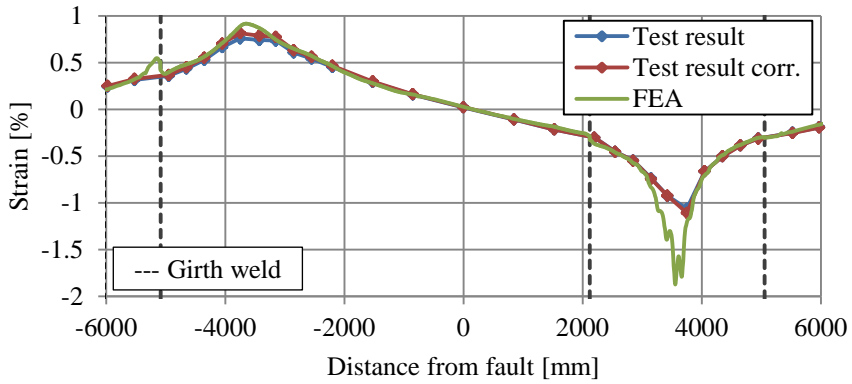


(c) Comparison of strains at a fault movement of 1480 mm

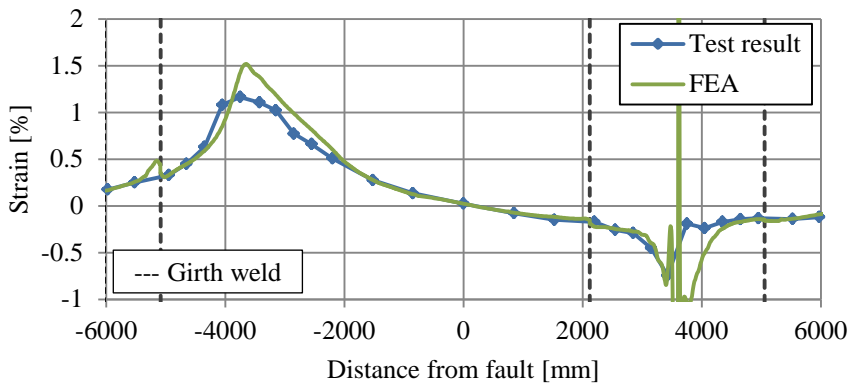
Figure E.55 Comparison of strain distributions at the front side of specimen T9 ($a_{imp}/t=0.39\%$).



(a) Comparison of strains at a fault movement of 500 mm



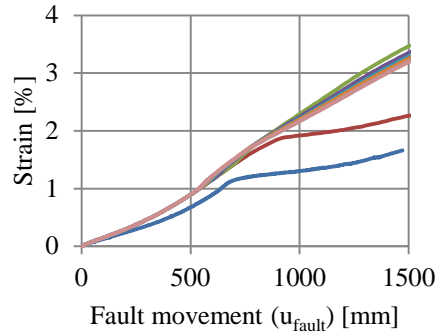
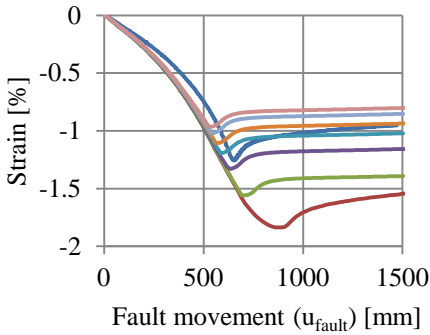
(b) Comparison of strains at a fault movement of 1000 mm



(c) Comparison of strains at a fault movement of 1480 mm

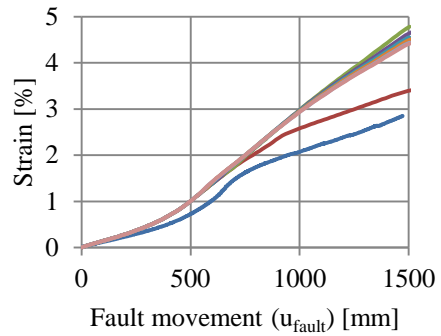
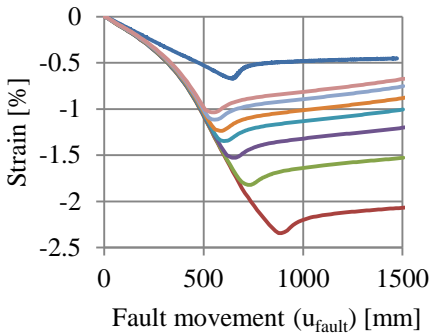
Figure E.56 Comparison of strain distributions at the back side of specimen T9 ($a_{imp}/t=0.39\%$).

Test T10



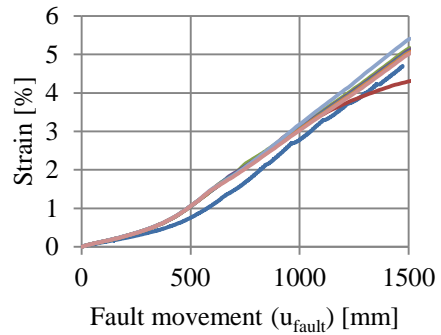
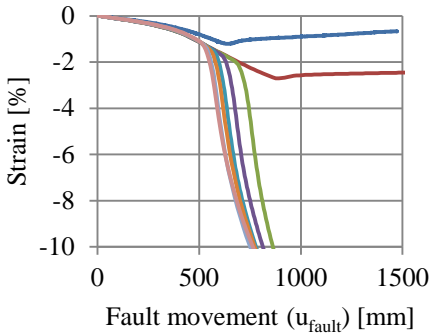
(a) Compressive strain 2150 mm from the fault

(b) Tensile strain 2150 mm from the fault.



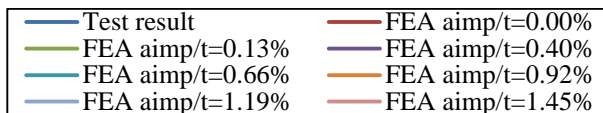
(c) Compressive strain 2300 mm from the fault

(d) Tensile strain 2300 mm from the fault



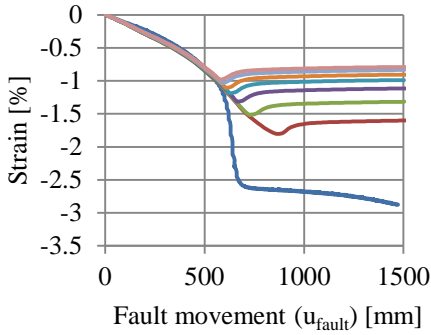
(e) Compressive strain 2450 mm from the fault

(f) Tensile strain 2450 mm from the fault

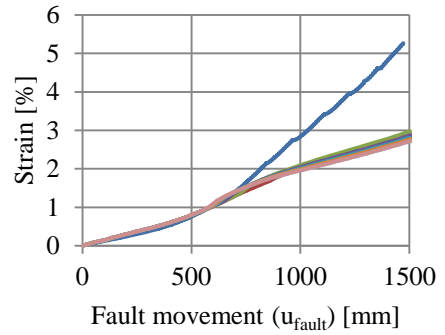


(g) Legend to graphs

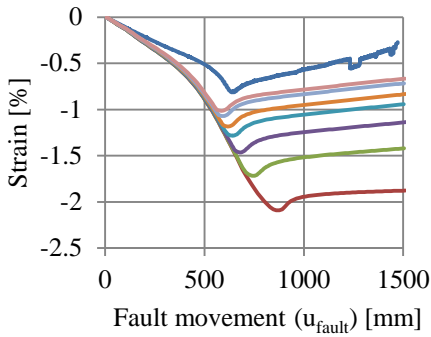
Figure E.57 Comparison of strain between test T10 and FE-model on the left side of the fault.



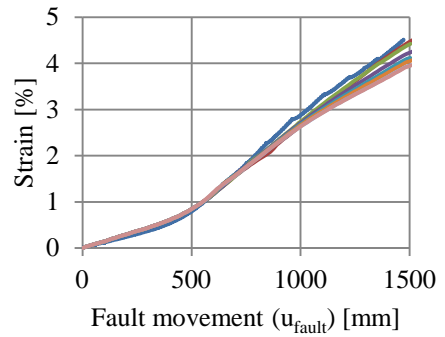
(a) Compressive strain 2150 mm from the fault



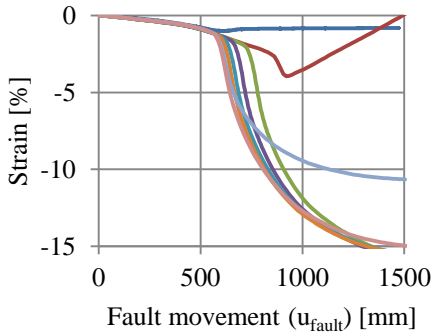
(b) Tensile strain 2150 mm from the fault



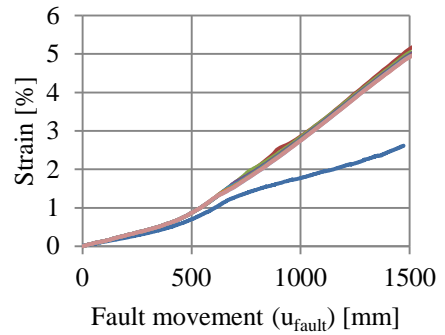
(c) Compressive strain 2300 mm from the fault



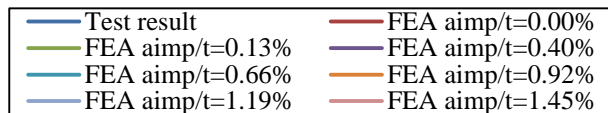
(d) Tensile strain 2300 mm from the fault



(e) Compressive strain 2450 mm from the fault

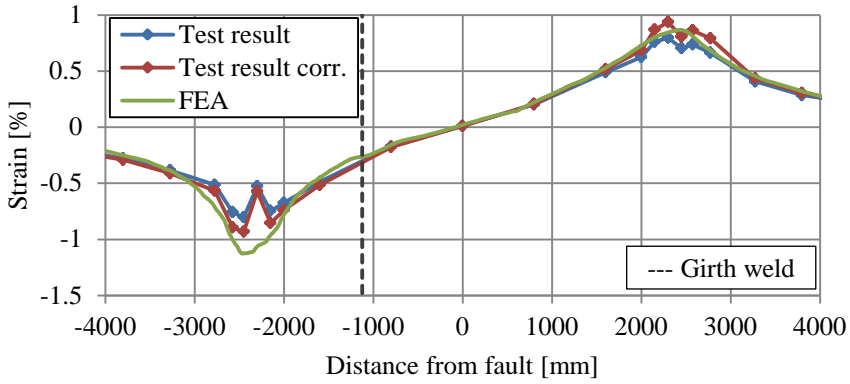


(f) Tensile strain 2450 mm from the fault

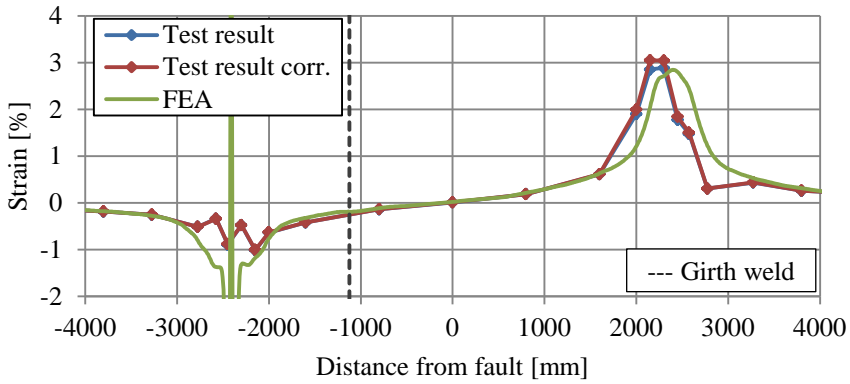


(g) Legend to graphs

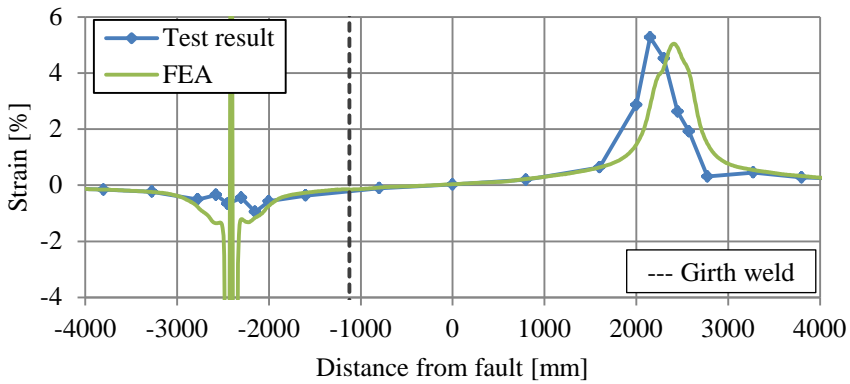
Figure E.58 Comparison of strain between test T10 and FE-model on the right side of the fault.



(a) Comparison of strains at a fault movement of 500 mm

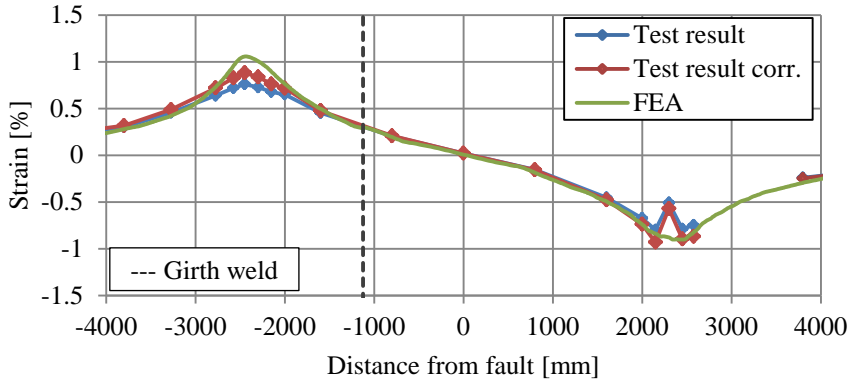


(b) Comparison of strains at a fault movement of 1000 mm

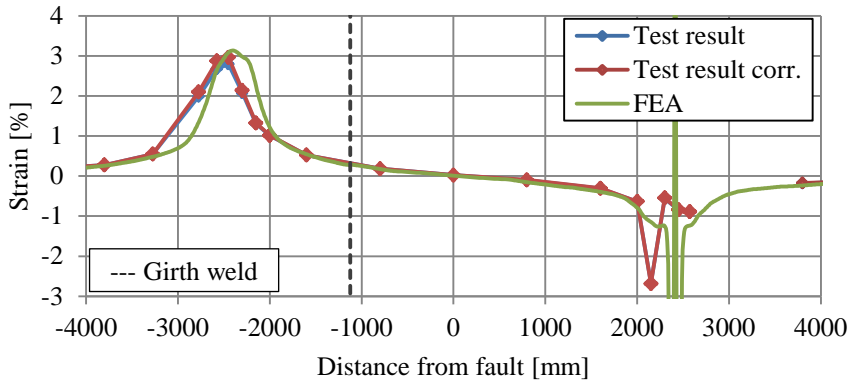


(c) Comparison of strains at a fault movement of 1470 mm

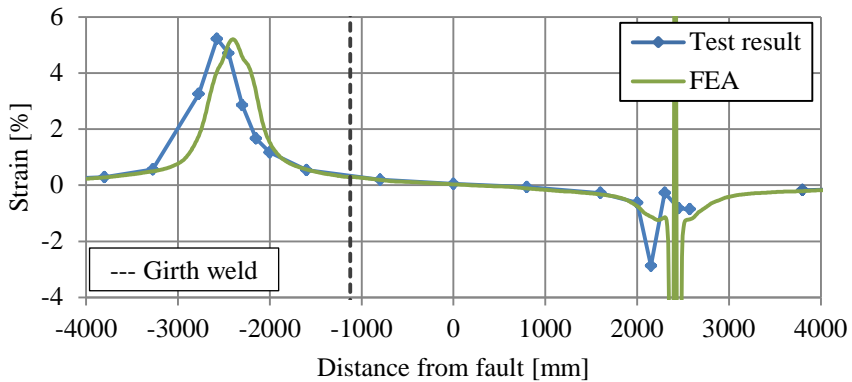
Figure E.59 Comparison of strain distributions at the front side of specimen T10 ($a_{imp}/t=0.40\%$).



(a) Comparison of strains at a fault movement of 500 mm



(b) Comparison of strains at a fault movement of 1000 mm



(c) Comparison of strains at a fault movement of 1470 mm

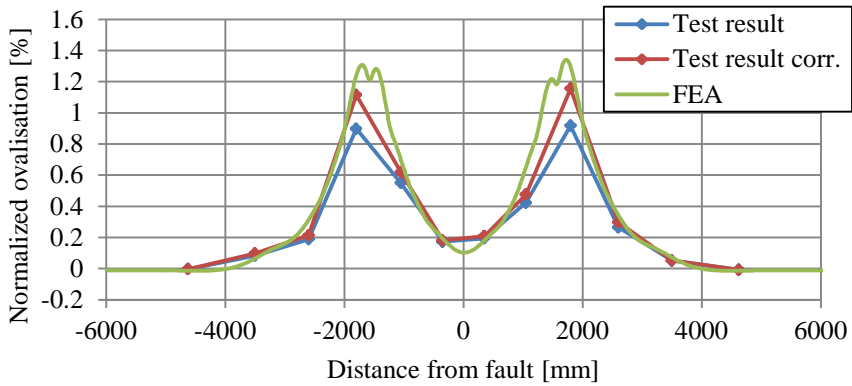
Figure E.60 Comparison of strain distributions at the back side of specimen T10 ($a_{imp}/t=0.40\%$).

E.3 Comparison of ovalisation

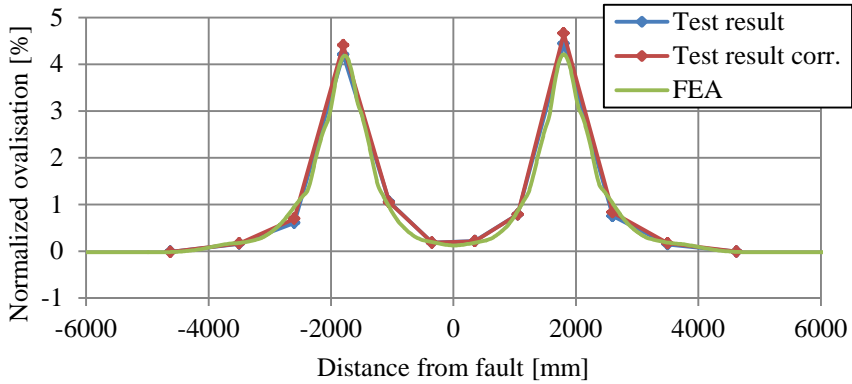
This appendix presents a comparison of the measured pipe response to the applied fault movement in the test and in the validation model. For each pipe, an overview of the distribution of vertical ovalisation over the specimen length is presented. A comparison is made between the measured data from the test and the model. For these graphs, the result of the model with the best prediction of the critical fault movement was used. The used initial imperfection is stated in the caption of the figure. In case of a Category 2 test, only the initial imperfection at the girth weld is stated.

In the graphs, both the uncorrected and corrected test results are presented (see section 11.2 of the main text of this thesis). At the maximum fault displacement, this correction could not be applied. Therefore, in these graphs only the uncorrected results are presented.

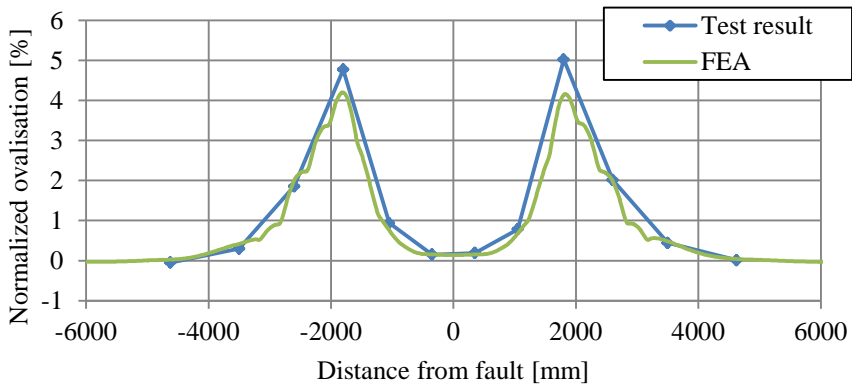
Test T1



(a) Comparison of ovalisations at a fault movement of 500 mm



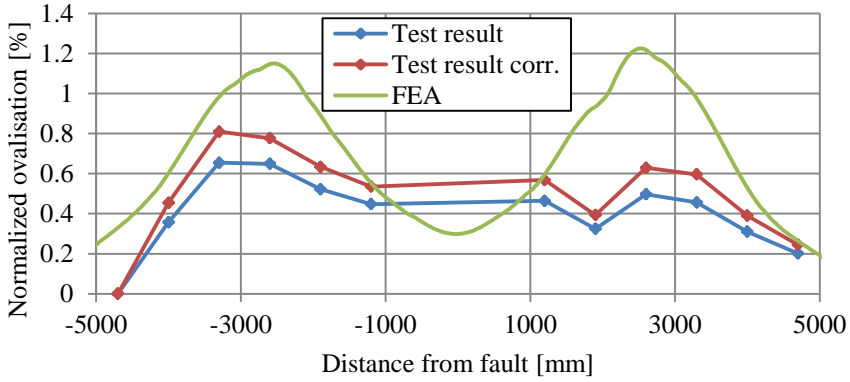
(b) Comparison of ovalisations at a fault movement of 1000 mm



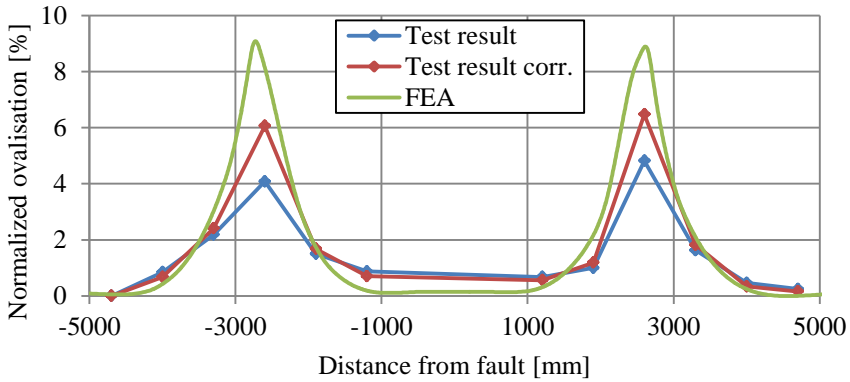
(c) Comparison of ovalisations at a fault movement of 1480 mm

Figure E.61 Comparison of distributions of vertical ovalisation due to bending ($a_{imp}/t=0.00\%$).

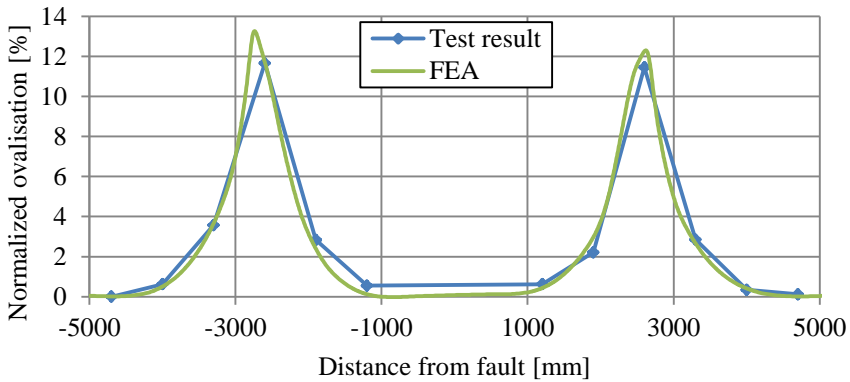
Test T2



(a) Comparison of ovalisations at a fault movement of 500 mm



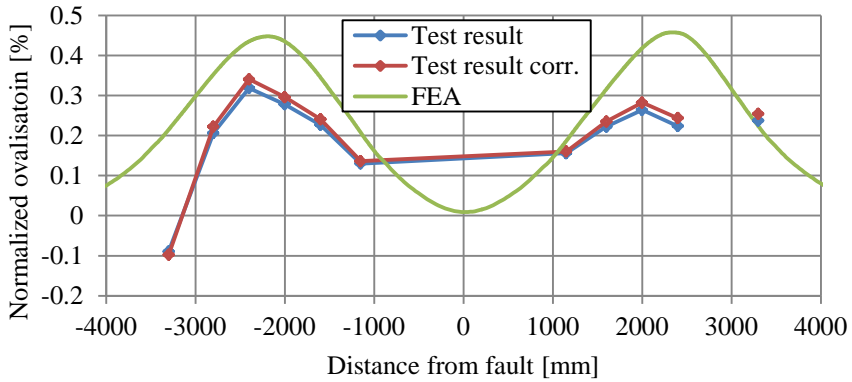
(b) Comparison of ovalisations at a fault movement of 1000 mm



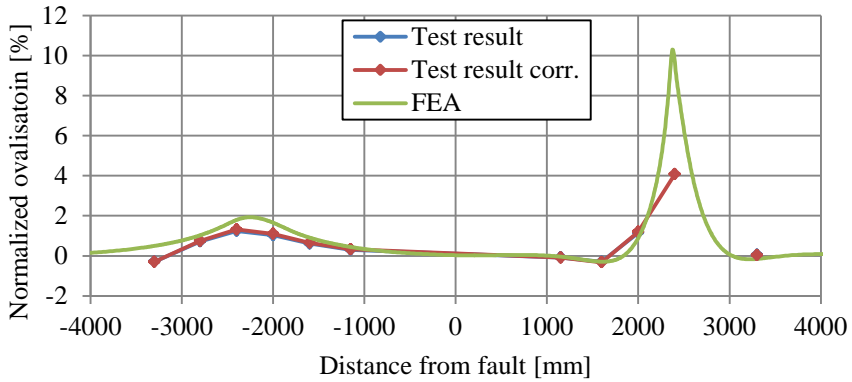
(c) Comparison of ovalisations at a fault movement of 1480 mm

Figure E.62 Comparison of distributions of vertical ovalisation due to bending ($a_{imp}/t=0.66\%$).

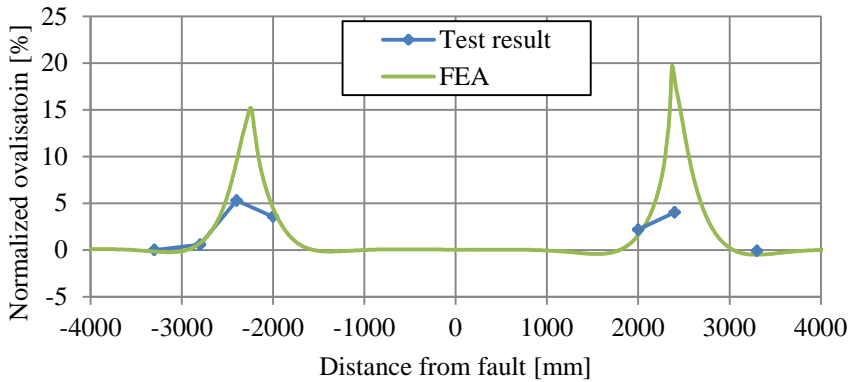
Test T3



(a) Comparison of ovalisations at a fault movement of 500 mm



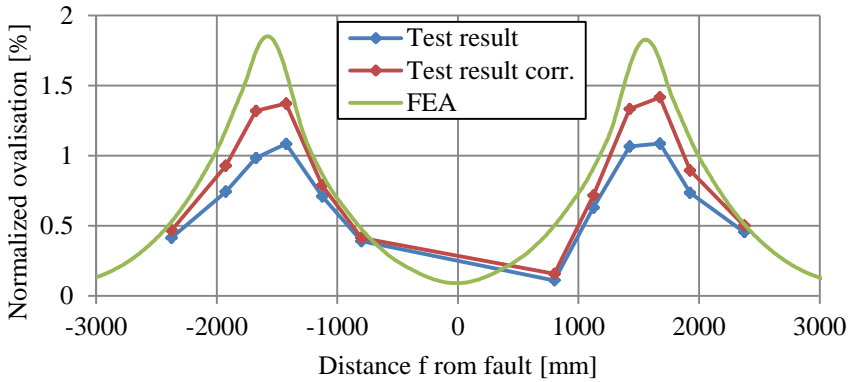
(b) Comparison of ovalisations at a fault movement of 1000 mm



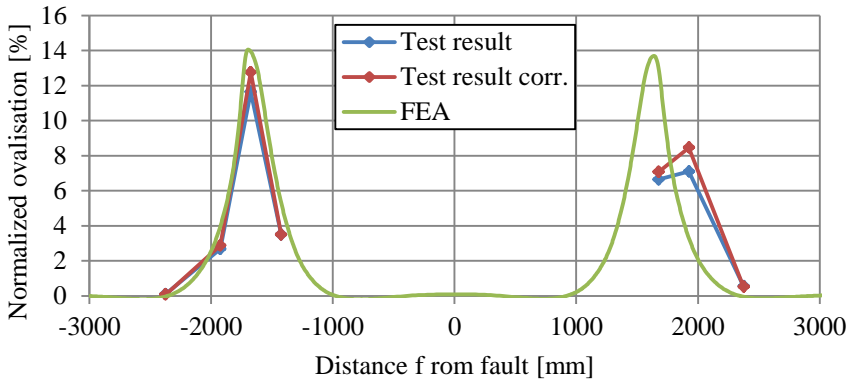
(c) Comparison of ovalisations at a fault movement of 1480 mm

Figure E.63 Comparison of distributions of vertical ovalisation due to bending ($a_{imp}/t=3.80\%$).

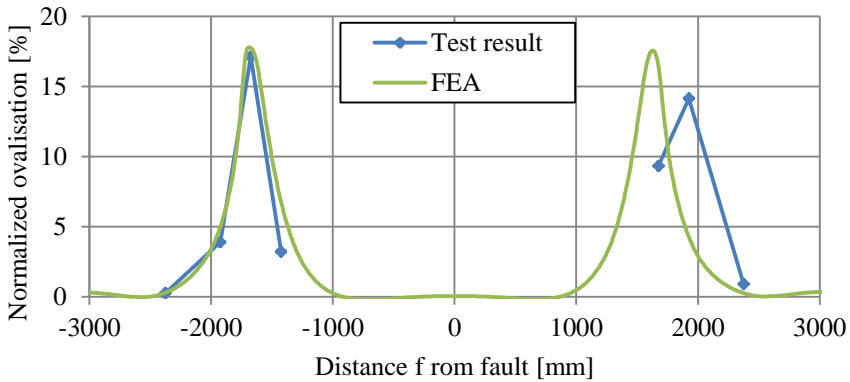
Test T4



(a) Comparison of ovalisations at a fault movement of 500 mm



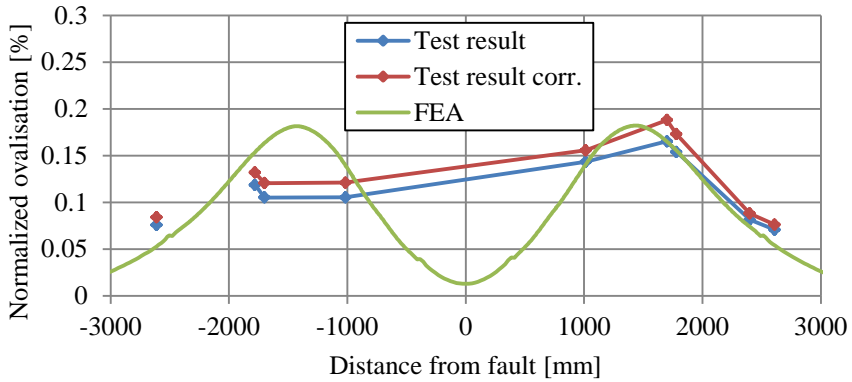
(b) Comparison of ovalisations at a fault movement of 1000 mm



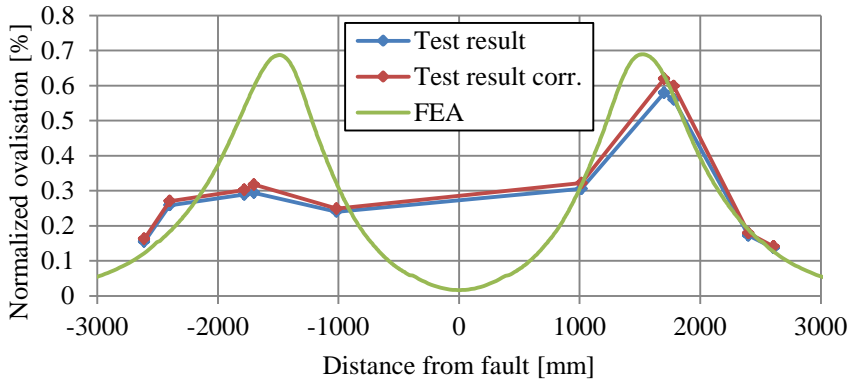
(c) Comparison of ovalisations at a fault movement of 1470 mm

Figure E.64 Comparison of distributions of vertical ovalisation due to bending ($a_{imp}/t=0.54\%$).

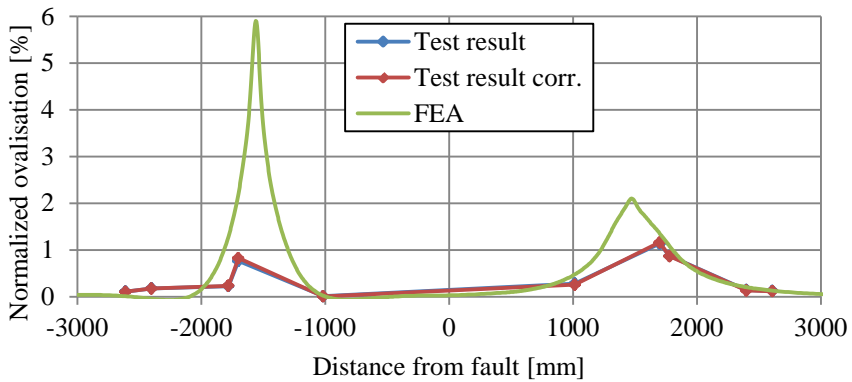
Test T5



(a) Comparison of ovalisations at a fault movement of 200 mm



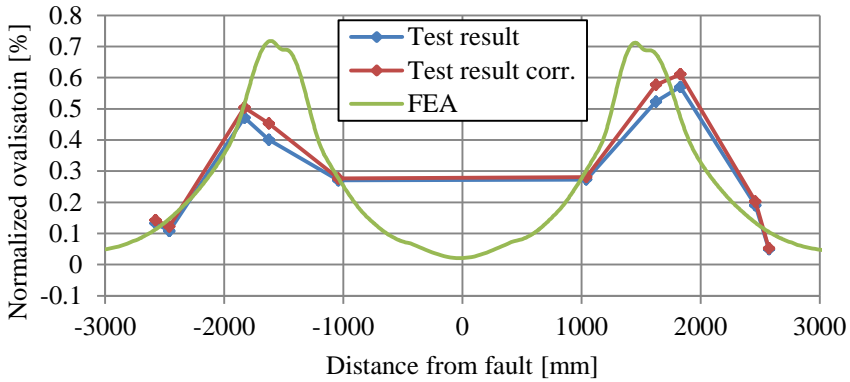
(b) Comparison of ovalisations at a fault movement of 400 mm



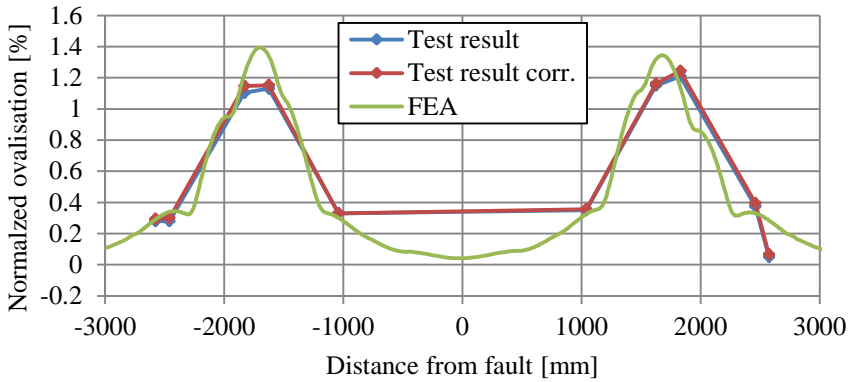
(c) Comparison of ovalisations at a fault movement of 600 mm

Figure E.65 Comparison of distributions of vertical ovalisation due to bending ($a_{imp}/t=3.60\%$).

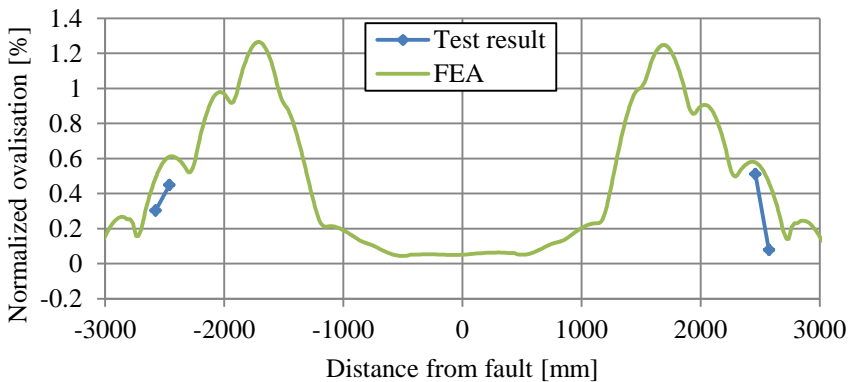
Test T6



(a) Comparison of ovalisations at a fault movement of 500 mm



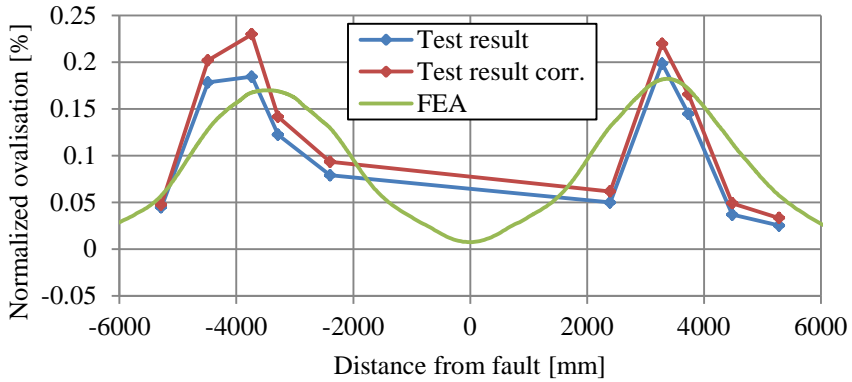
(b) Comparison of ovalisations at a fault movement of 1000 mm



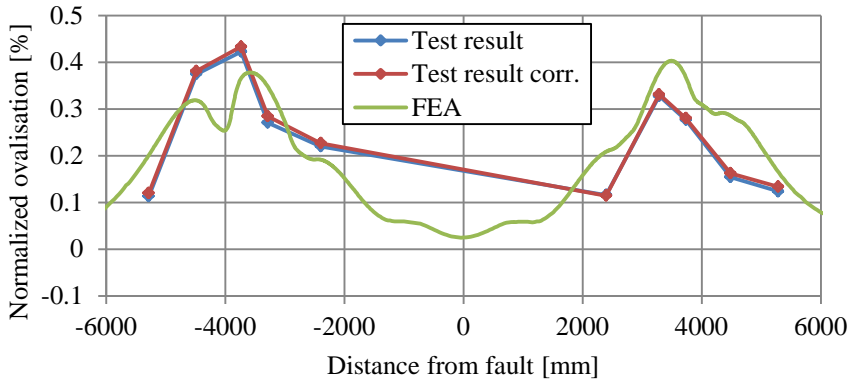
(c) Comparison of ovalisations at a fault movement of 1480 mm

Figure E.66 Comparison of distributions of vertical ovalisation due to bending ($a_{imp}/t=0.00\%$).

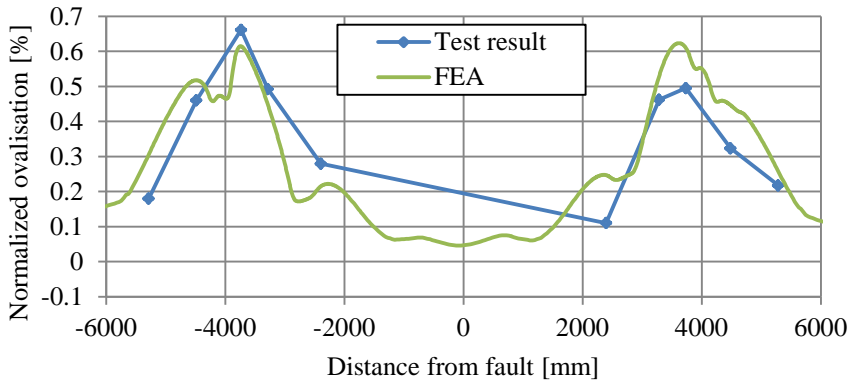
Test T7



(a) Comparison of ovalisations at a fault movement of 500 mm



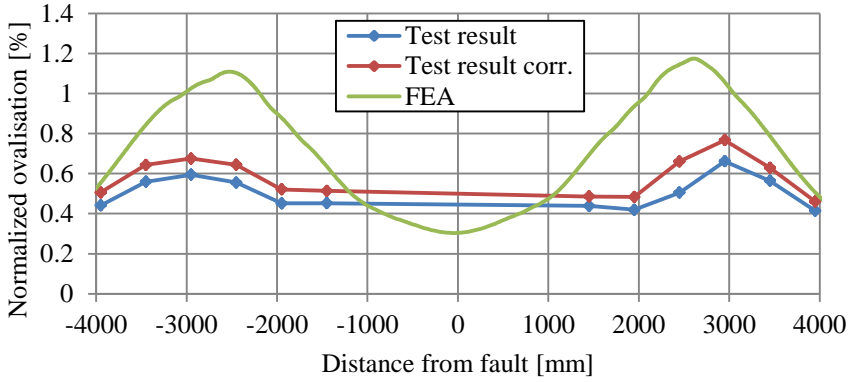
(b) Comparison of ovalisations at a fault movement of 1000 mm



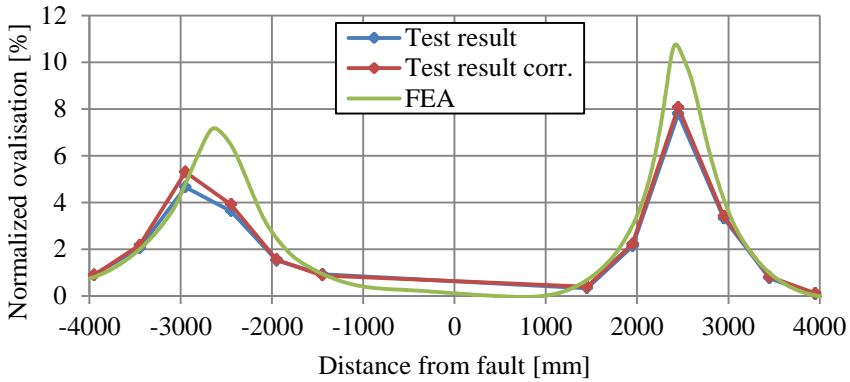
(c) Comparison of ovalisations at a fault movement of 1470 mm

Figure E.67 Comparison of distributions of vertical ovalisation due to bending ($a_{imp}/t=0.00\%$).

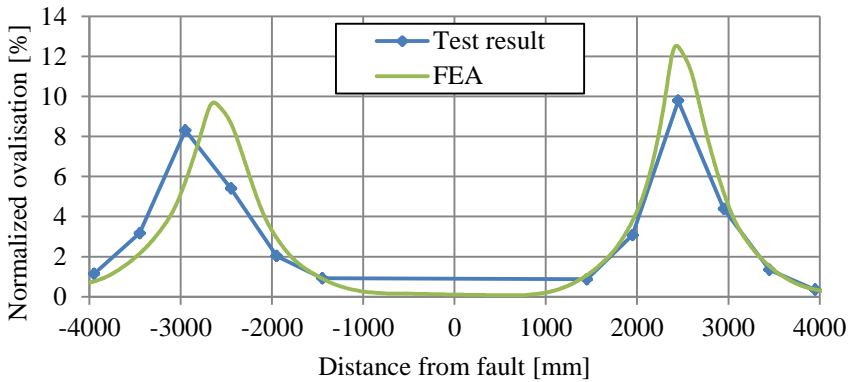
Test T8



(a) Comparison of ovalisations at a fault movement of 500 mm



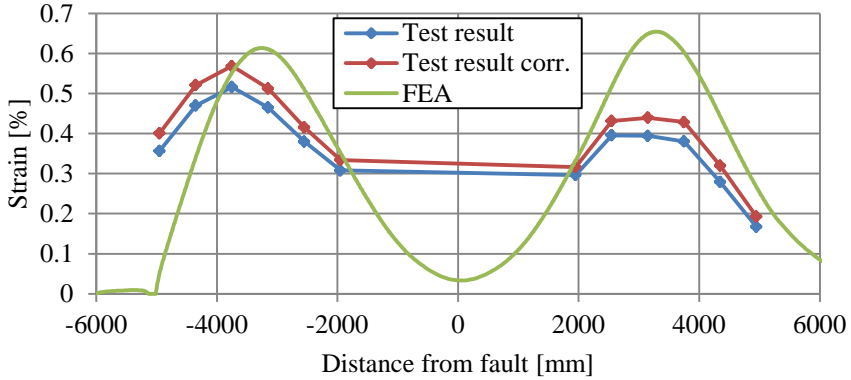
(b) Comparison of ovalisations at a fault movement of 1000 mm



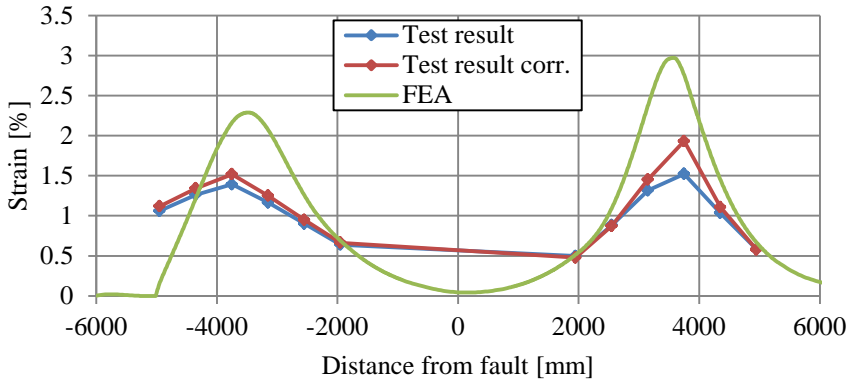
(c) Comparison of ovalisations at a fault movement of 1480 mm

Figure E.68 Comparison of distributions of vertical ovalisation due to bending ($a_{imp}/t=3.55\%$).

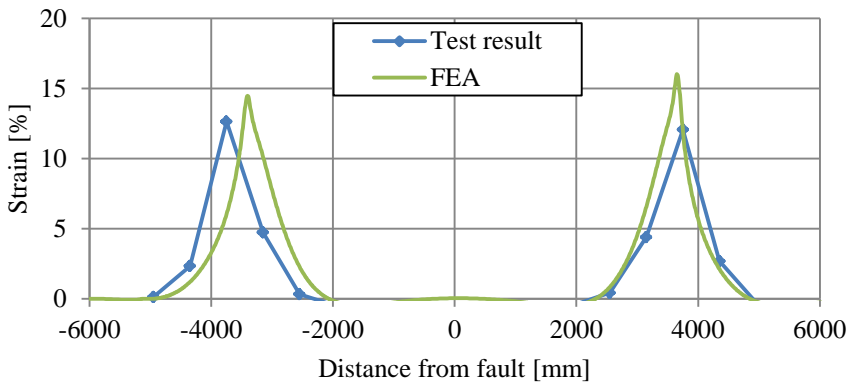
Test T9



(a) Comparison of ovalisations at a fault movement of 500 mm



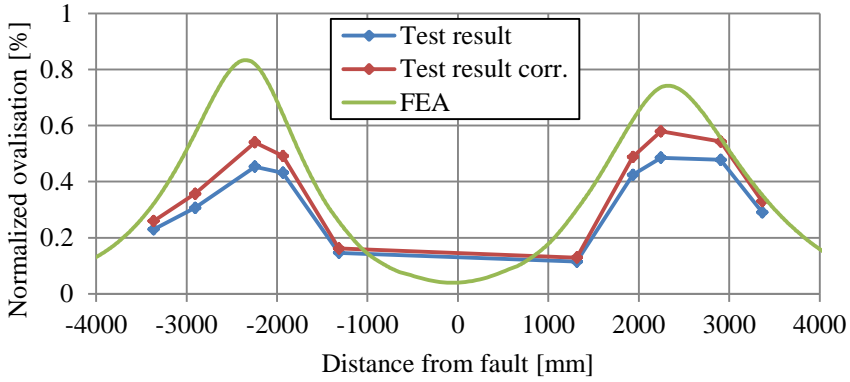
(b) Comparison of ovalisations at a fault movement of 1000 mm



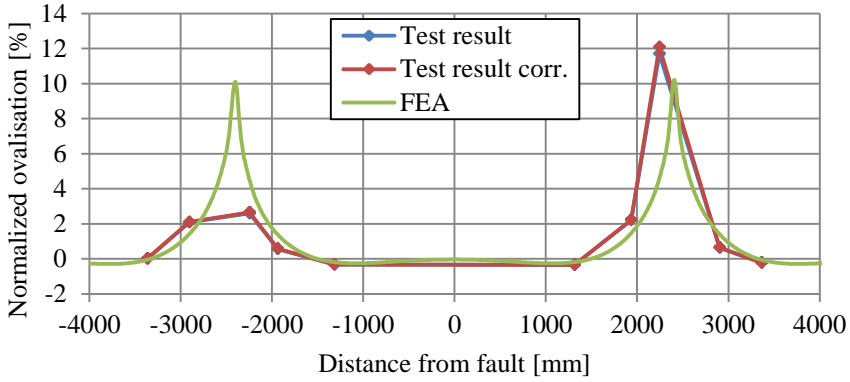
(c) Comparison of ovalisations at a fault movement of 1480 mm

Figure E.69 Comparison of distributions of vertical ovalisation due to bending ($a_{imp}/t=0.39\%$).

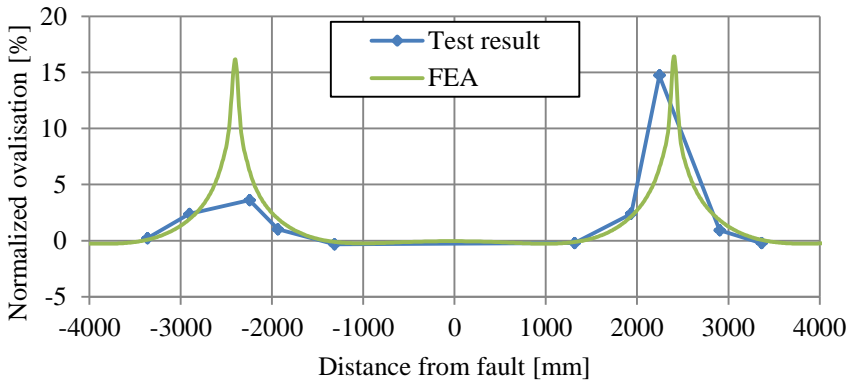
Test T10



(a) Comparison of ovalisations at a fault movement of 500 mm



(b) Comparison of ovalisations at a fault movement of 1000 mm



(c) Comparison of ovalisations at a fault movement of 1470 mm

Figure E.70 Comparison of distributions of vertical ovalisation due to bending ($a_{imp}/t=0.40\%$).

Appendix F: Stress-strain diagrams

This appendix presents the results of the tensile tests performed for the research presented in this study. Appendix F.1 presents the results of the tensile tests performed on specimens taken from the tubes considered in Part II of this study. Appendix F.2 presents the results of the tensile tests performed on specimens taken from the pipes considered in Part III of this study.

F.1 Stress-strain diagrams of tubes tested in Part II

This appendix presents the results of the tensile tests performed on specimens taken from the tubes tested in Part II of this study. As discussed in section 5.3.1 of the main text of this thesis, four tensile tests were performed per specimen part. Tensile tests were performed on test specimens taken out in axial direction of the tube on the inside and outside of the tube wall. The remaining two specimens were taken out in hoop direction of the tube on the inside and outside of the tube wall. The results of these tests are presented in Appendix F.1.1. In a similar fashion, four compressive tests were performed on a selection of tubes. The full results of these tests are included in the main text of this thesis (see Figure 5.37 and Figure 5.38). Further tensile testing was performed on specimens taken out from the weld material of the spiral welds. The results of these tests are presented in Appendix F.1.2.

F.1.1 Tensile tests on tube material

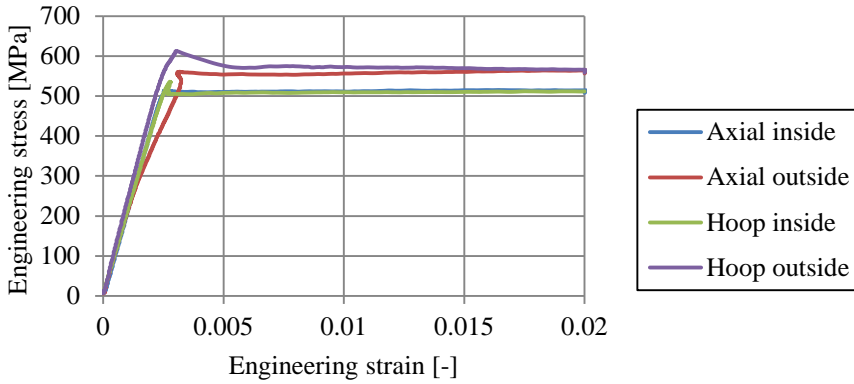


Figure F.1 Results of tensile tests performed on specimens taken from tube T1.

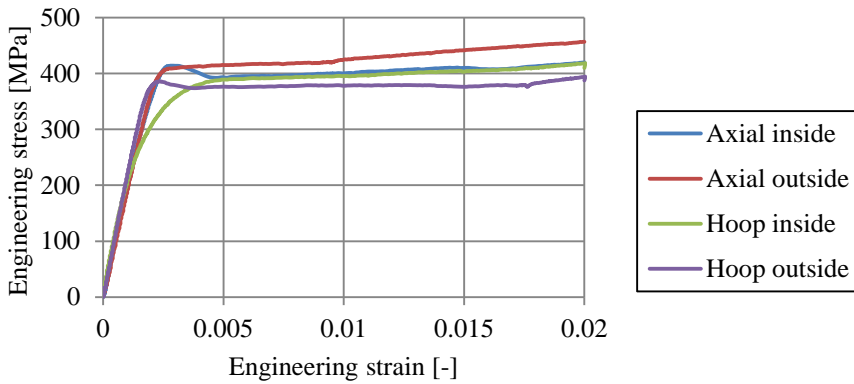


Figure F.2 Results of tensile tests performed on specimens taken from tube T2.

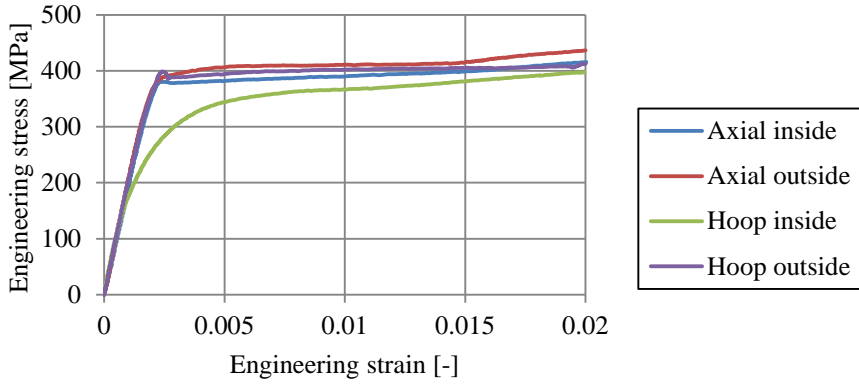


Figure F.3 Results of tensile tests performed on specimens taken from tube part T3L.

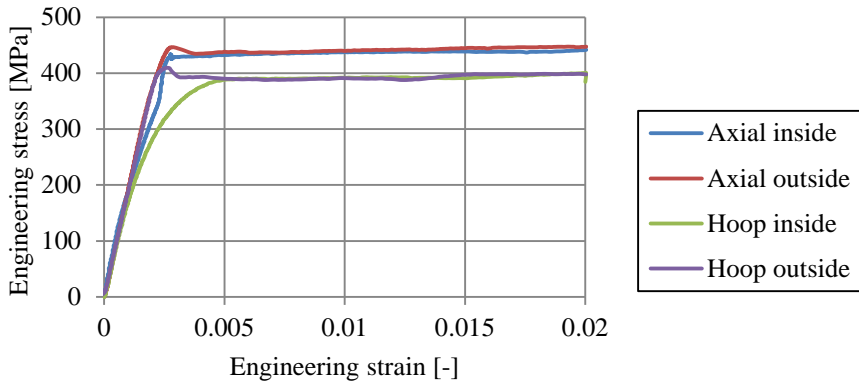


Figure F.4 Results of tensile tests performed on specimens taken from tube part T3R.

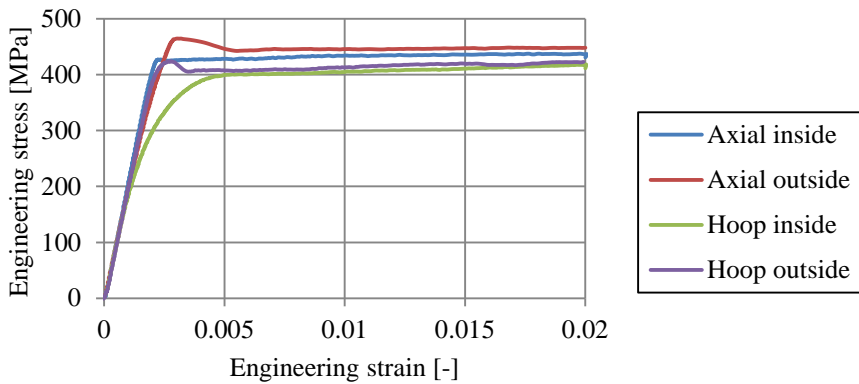


Figure F.5 Results of tensile tests performed on specimens taken from tube T4.

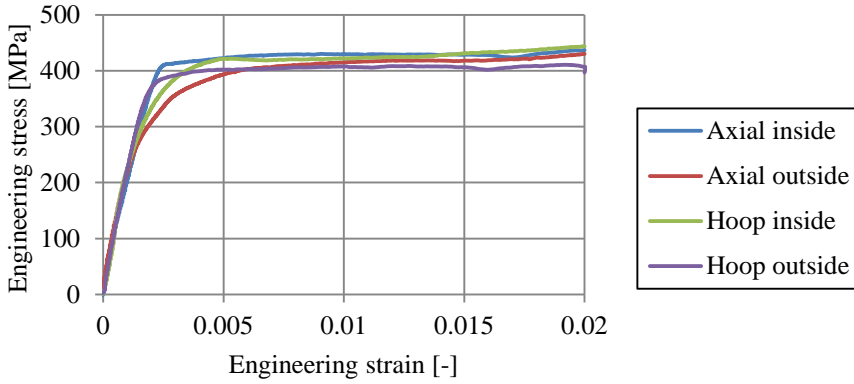


Figure F.6 Results of tensile tests performed on specimens taken from tube T5.

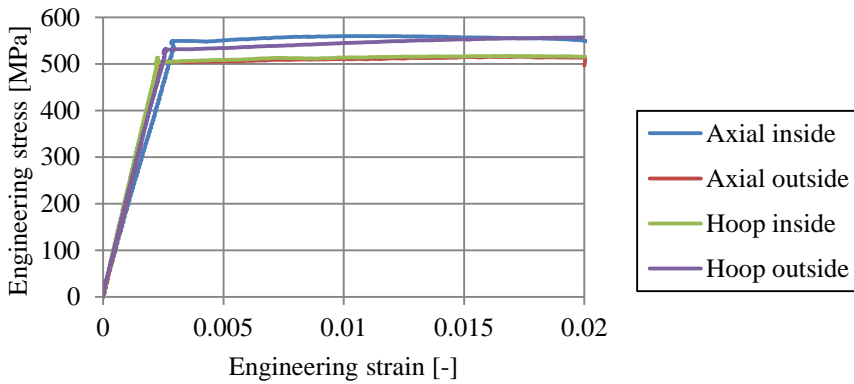


Figure F.7 Results of tensile tests performed on specimens taken from tube part T6L.

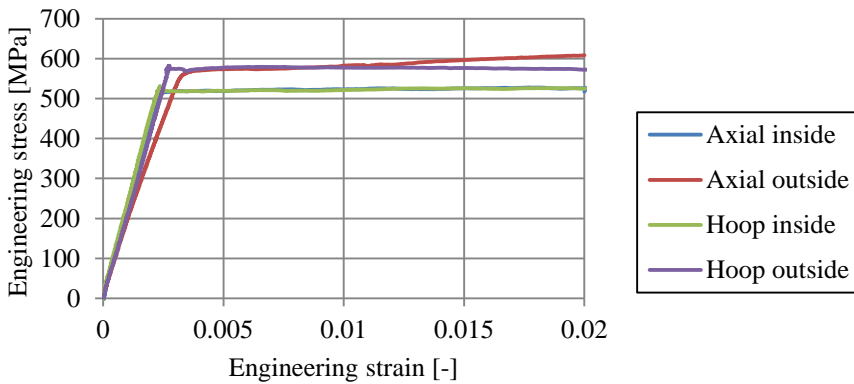


Figure F.8 Results of tensile tests performed on specimens taken from tube part T6R.

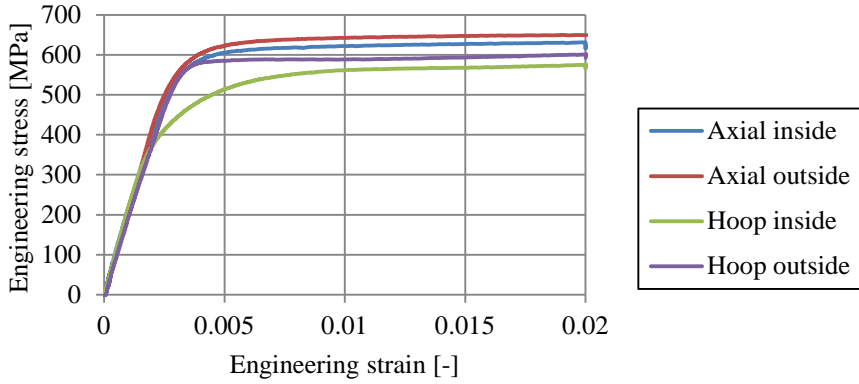


Figure F.9 Results of tensile tests performed on specimens taken from tube part T7L.

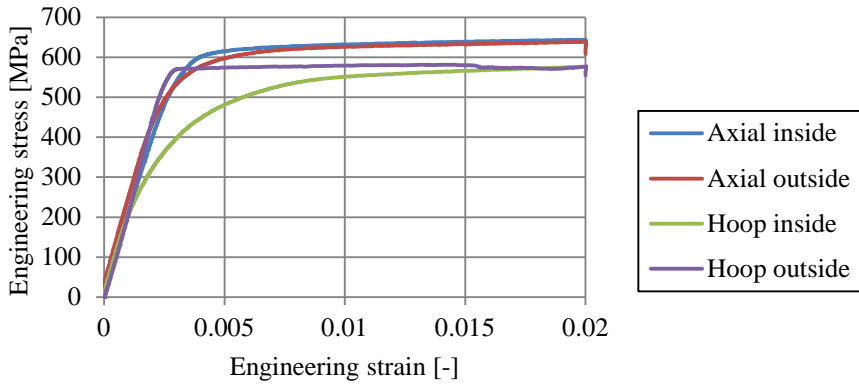


Figure F.10 Results of tensile tests performed on specimens taken from tube part T7M.

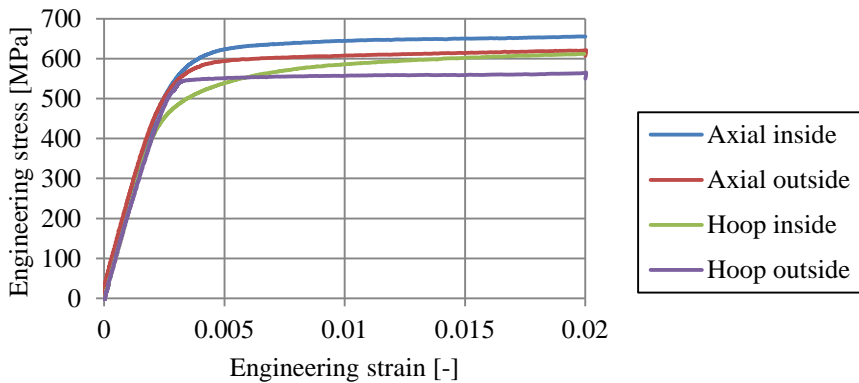


Figure F.11 Results of tensile tests performed on specimens taken from tube part T7R.

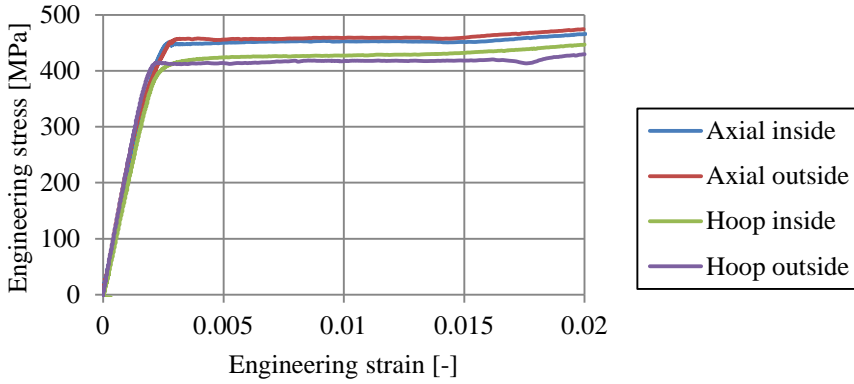


Figure F.12 Results of tensile tests performed on specimens taken from tube T8.

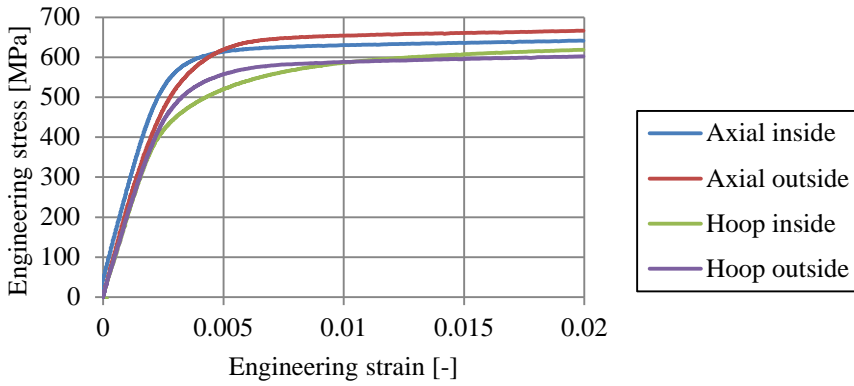


Figure F.13 Results of tensile tests performed on specimens taken from tube T9.

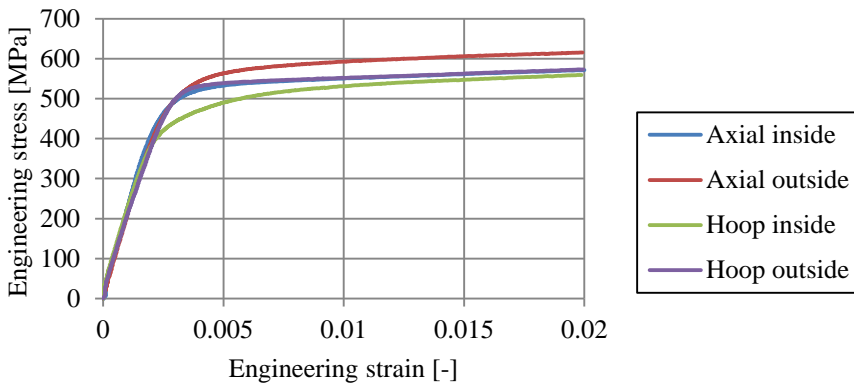


Figure F.14 Results of tensile tests performed on specimens taken from tube part T10L.

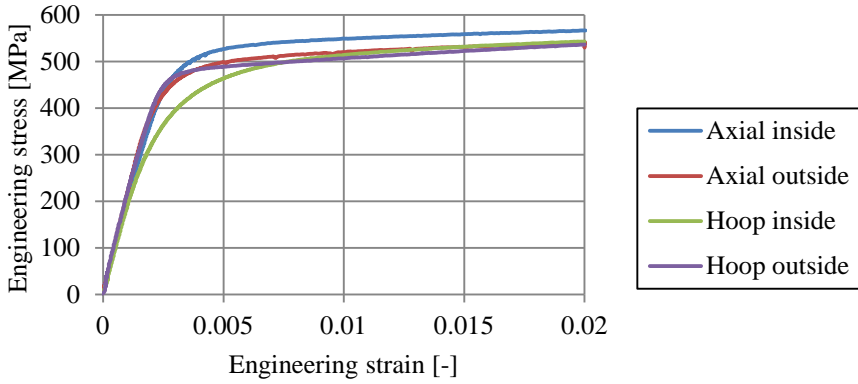


Figure F.15 Results of tensile tests performed on specimens taken from tube part T10M.

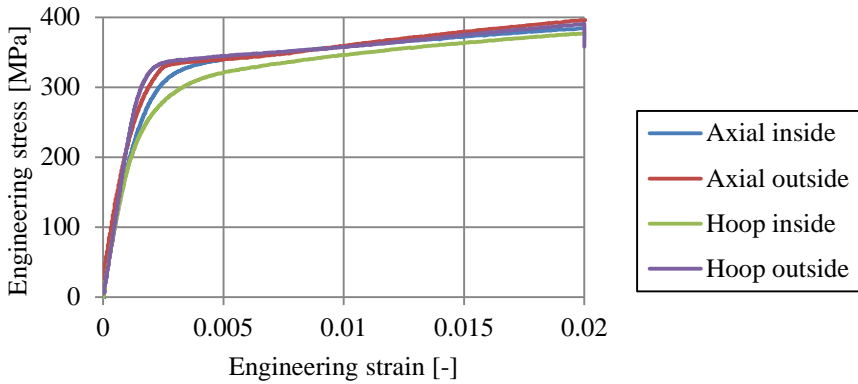


Figure F.16 Results of tensile tests performed on specimens taken from tube part T10R.

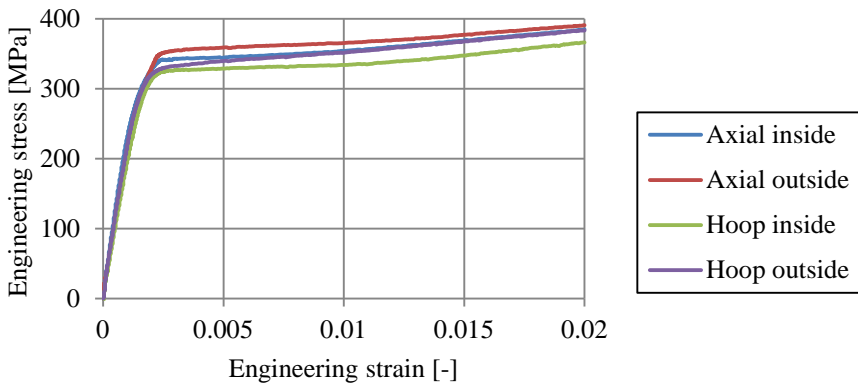


Figure F.17 Results of tensile tests performed on specimens taken from tube T11.

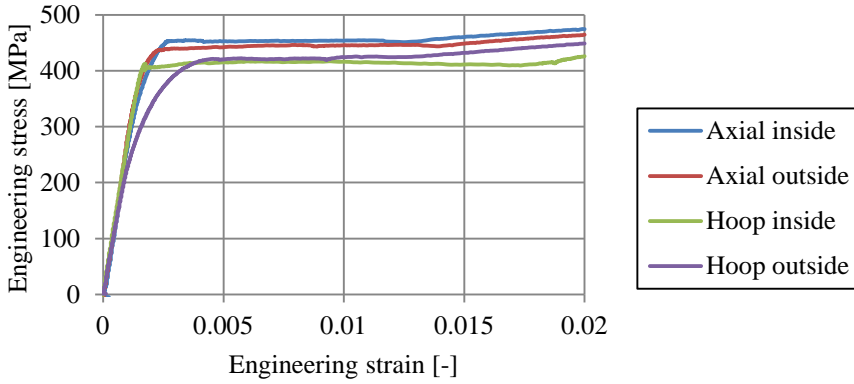


Figure F.18 Results of tensile tests performed on specimens taken from tube part T12L.

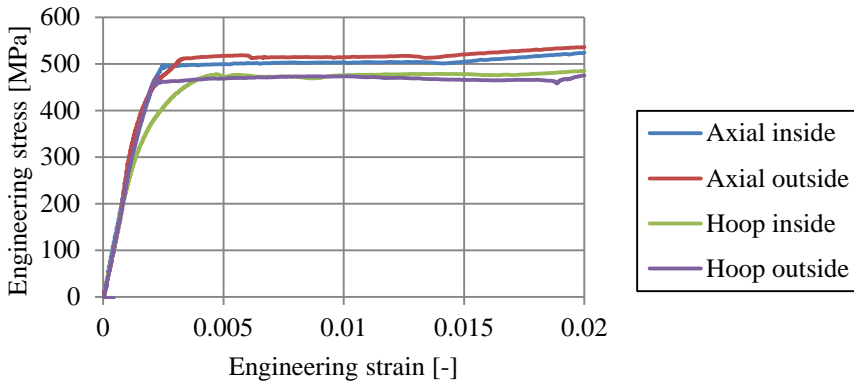


Figure F.19 Results of tensile tests performed on specimens taken from tube part T12M.

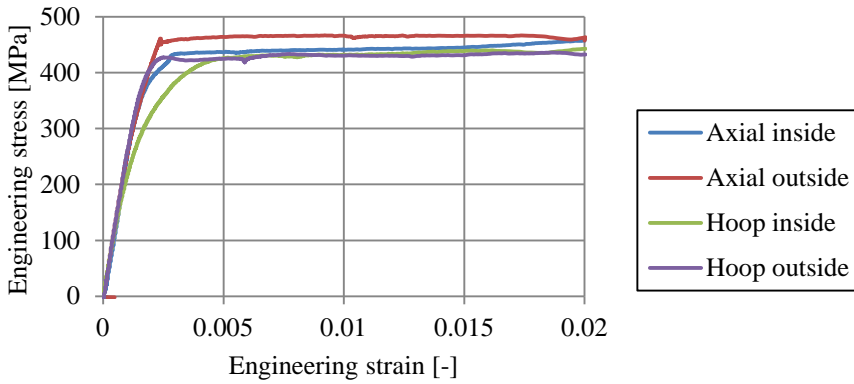


Figure F.20 Results of tensile tests performed on specimens taken from tube part T12R.

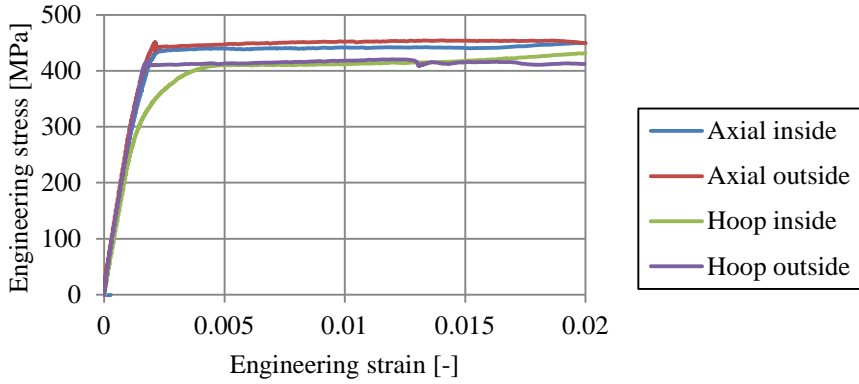


Figure F.21 Results of tensile tests performed on specimens taken from tube part T13L.

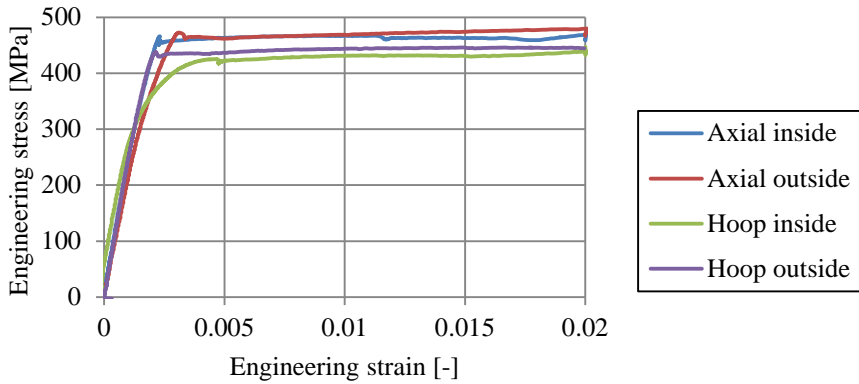


Figure F.22 Results of tensile tests performed on specimens taken from tube part T13R.

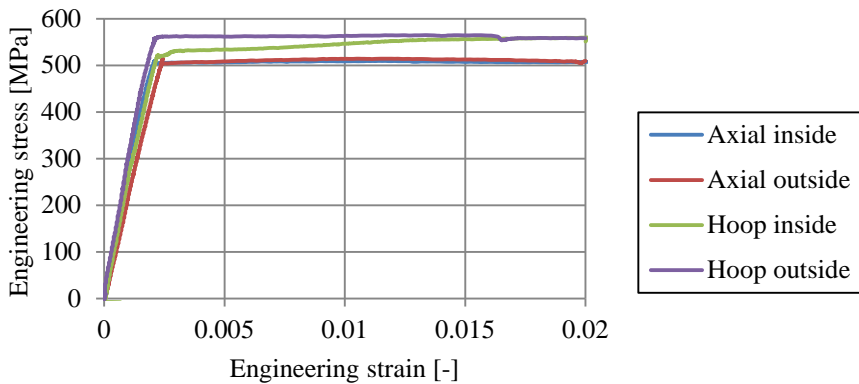


Figure F.23 Results of tensile tests performed on specimens taken from tube T14.

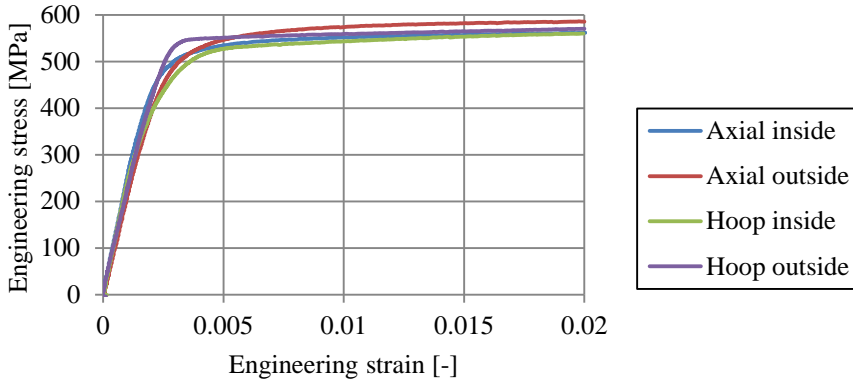


Figure F.24 Results of tensile tests performed on specimens taken from tube T15.

F.1.2 Tensile tests on spiral weld material

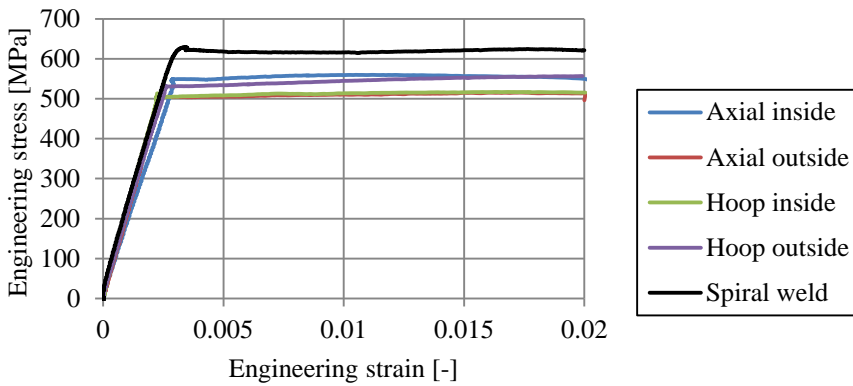


Figure F.25 Result of tensile test performed on a specimen taken from a spiral weld in specimen part T6L in comparison with the stress-strain behaviour of the parent material (see Figure F.7).

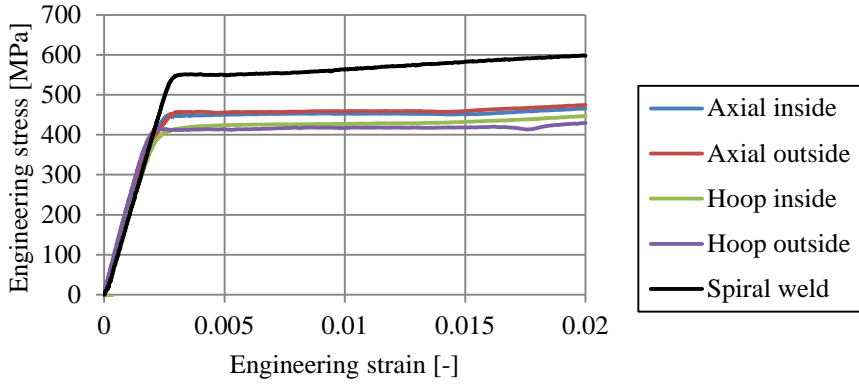


Figure F.26 Result of tensile test performed on a specimen taken from a spiral weld in specimen T8 in comparison with the stress-strain behaviour of the parent material (see Figure F.12).

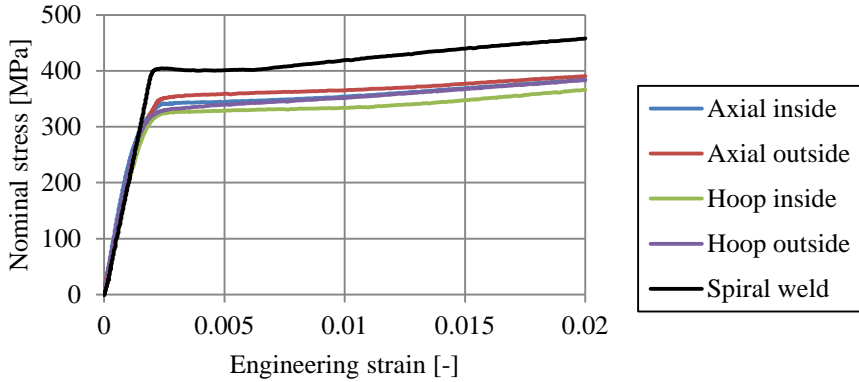


Figure F.27 Result of tensile test performed on a specimen taken from a spiral weld in specimen T11 in comparison with the stress-strain behaviour of the parent material (see Figure F.17).

F.2 Stress-strain diagrams of pipes tested in Part III

This appendix presents the results of the tensile tests performed on specimens taken from the pipes tested in Part III of this study. As discussed in section 9.3.1 of the main text of this thesis, four tensile tests were performed per available pipe. Two tests were performed on test specimens taken out in axial direction of the pipe and two tests were performed on test specimens taken out in hoop direction of the pipe. The coupons had a thickness equal to the pipe wall thickness.

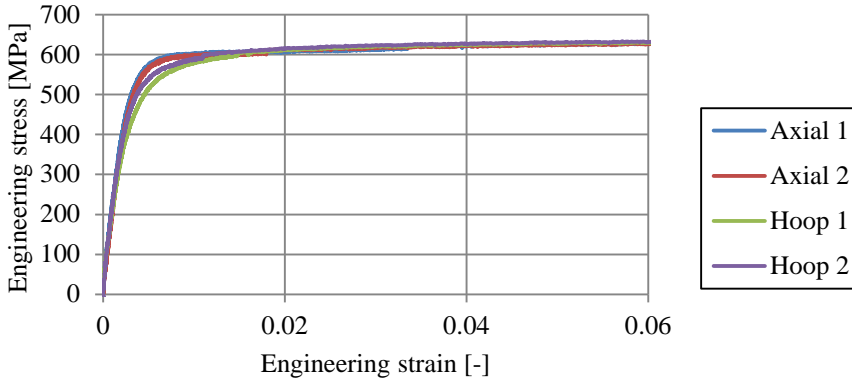


Figure F.28 Results of tensile tests performed on specimens taken from pipe H60410114.

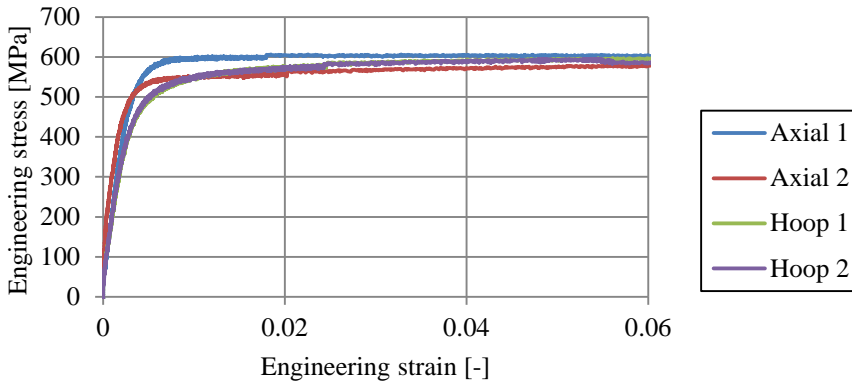


Figure F.29 Results of tensile tests performed on specimens taken from pipe H60414405.

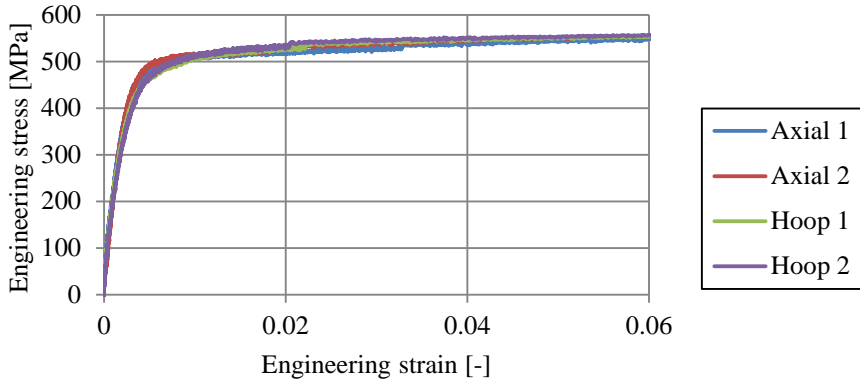


Figure F.30 Results of tensile tests performed on specimens taken from pipe H60415422.

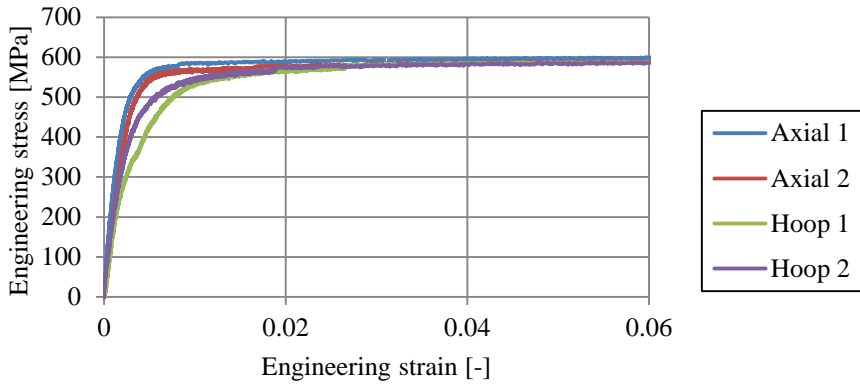


Figure F.31 Results of tensile tests performed on specimens taken from pipe H60415859.

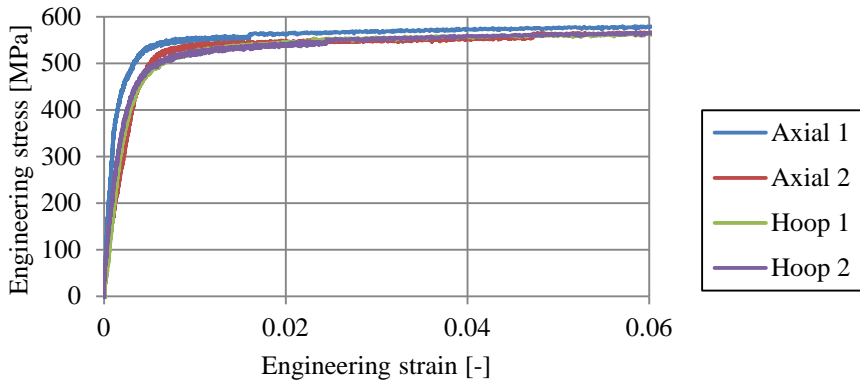


Figure F.32 Results of tensile tests performed on specimens taken from pipe H60416153.

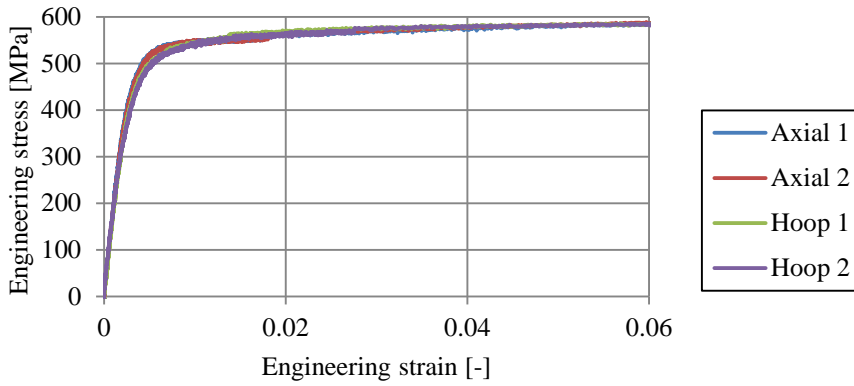


Figure F.33 Results of tensile tests performed on specimens taken from pipe H60416313.

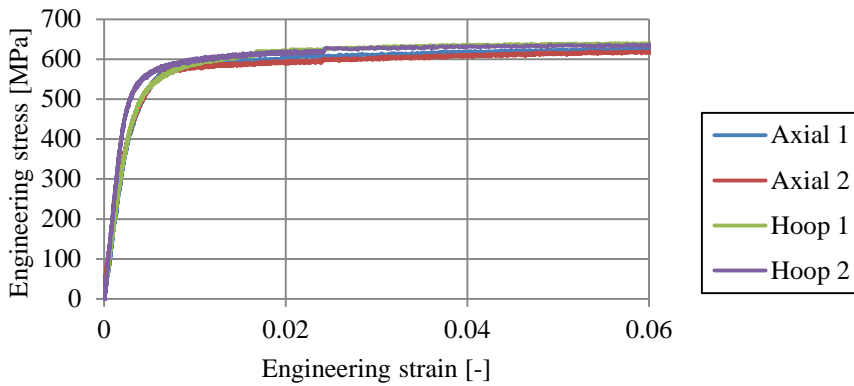


Figure F.34 Results of tensile tests performed on specimens taken from pipe H60423631.

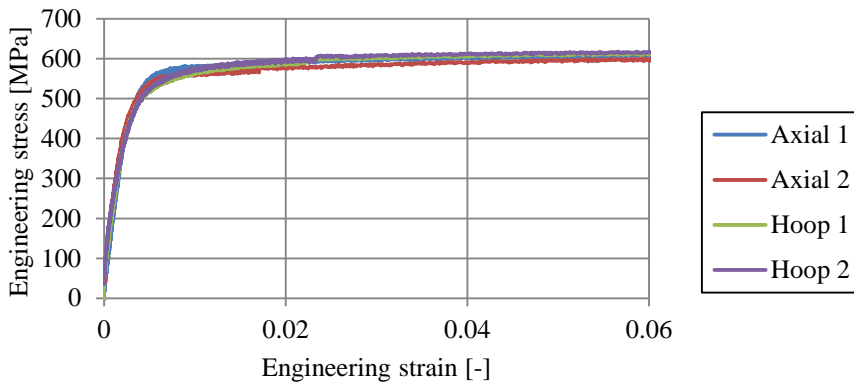


Figure F.35 Results of tensile tests performed on specimens taken from pipe H60423640.

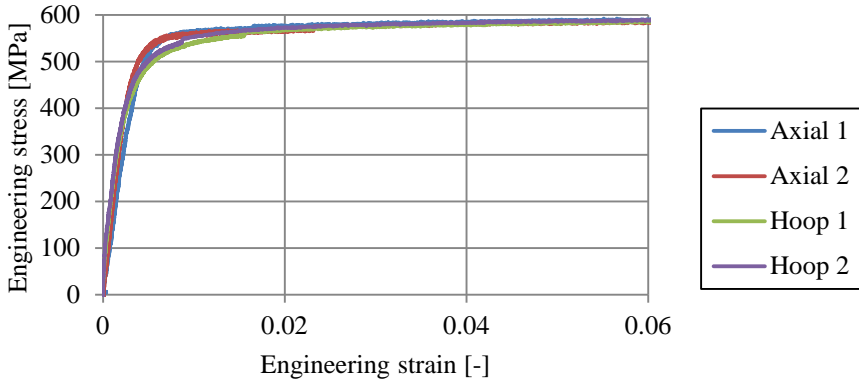


Figure F.36 Results of tensile tests performed on specimens taken from pipe H60423730.

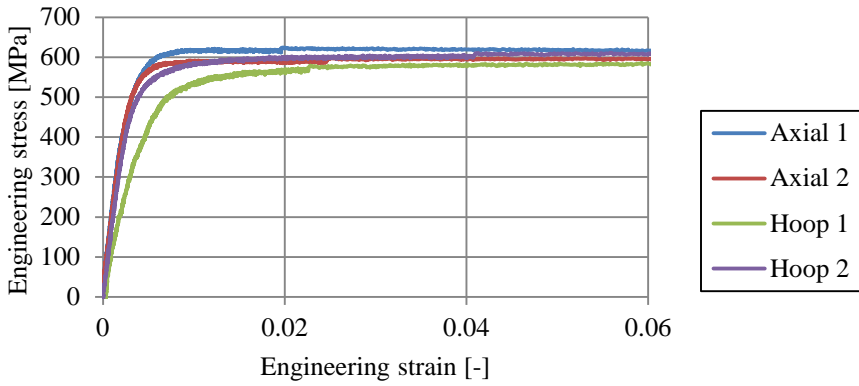


Figure F.37 Results of tensile tests performed on specimens taken from pipe H86916024.

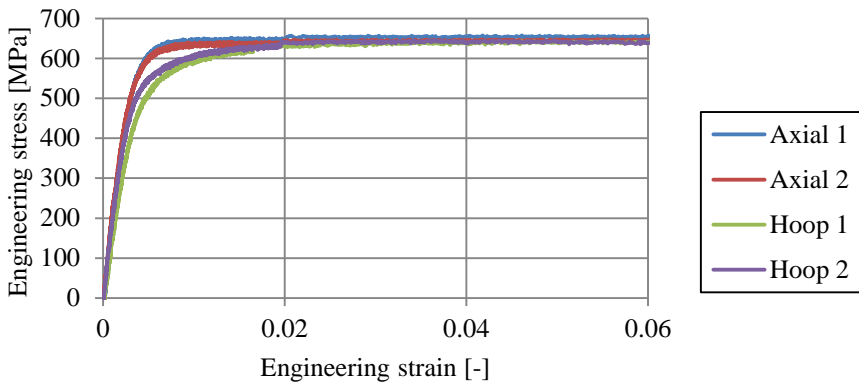


Figure F.38 Results of tensile tests performed on specimens taken from pipe H86916270B.

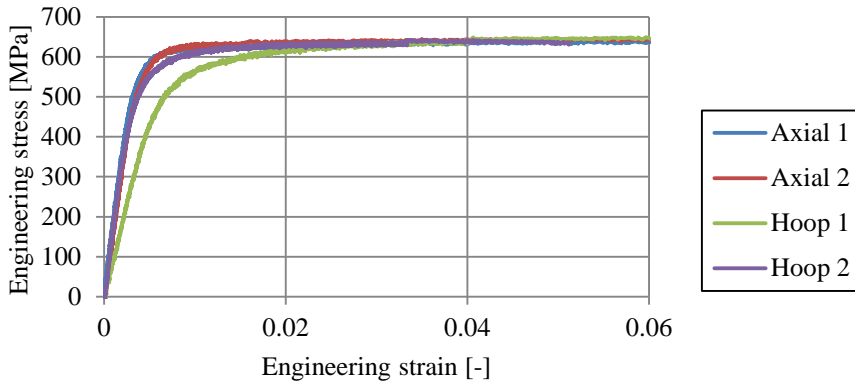


Figure F.39 Results of tensile tests performed on specimens taken from pipe H86916288.

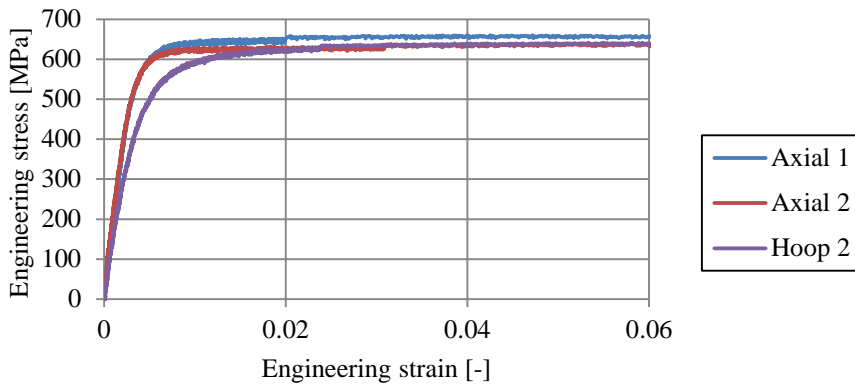


Figure F.40 Results of tensile tests performed on specimens taken from pipe H86916288B.

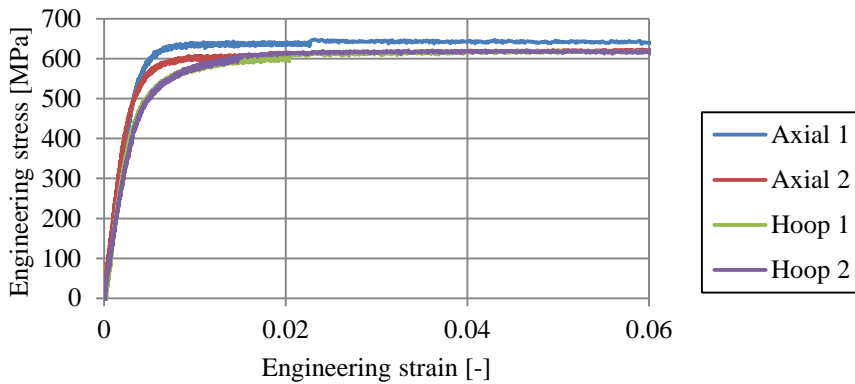


Figure F.41 Results of tensile tests performed on specimens taken from pipe H86916314.

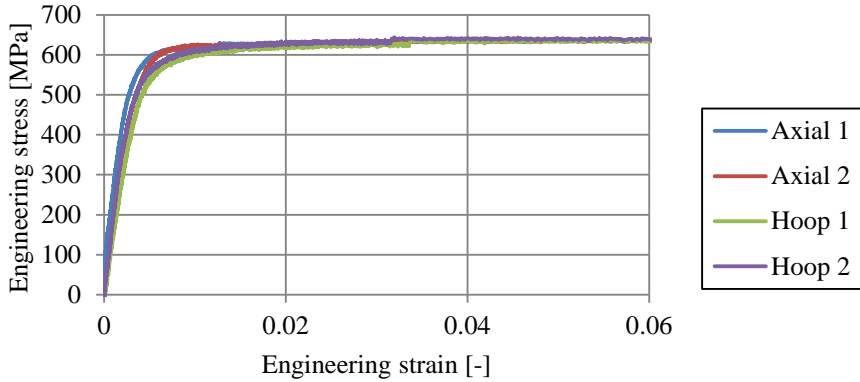


Figure F.42 Results of tensile tests performed on specimens taken from pipe H86916331B.

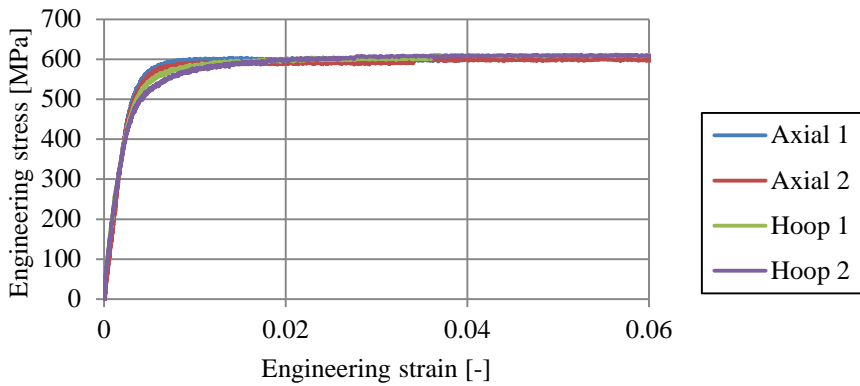


Figure F.43 Results of tensile tests performed on specimens taken from pipe H86916400B.

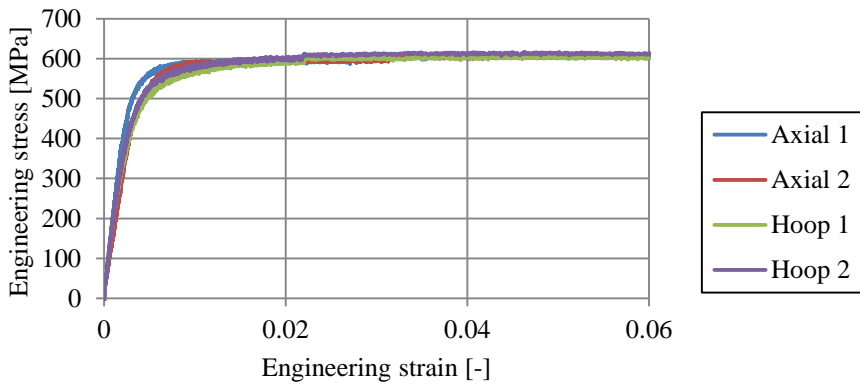


Figure F.44 Results of tensile tests performed on specimens taken from pipe H86916408.

Appendix G: Probabilistic evaluation of test results

In this appendix, the safety analysis of four prediction models is discussed in Appendices G.1 to G.4. Each of these appendices starts with an overview of the considered model, followed by an analysis of the coefficients of variation of the input variables of the prediction model. Subsequently, a comparison between the mean, characteristic and design model and the test results is presented. If necessary, the determined safety margin is analysed and revised.

The analyses in Appendices G.2 to G.4 were performed assuming a safety level corresponding to a reliability index (β) of 3.8, in accordance with Eurocode 0 (EN 1990, 2002). The analysis in Appendix G.1 was performed assuming a safety level corresponding to a reliability index (β) of 3.3 and 3.6, because this corresponds well with existing guidelines for local buckling in pipelines (see section 1.3.4 of the main text of this thesis). While calculating the design values of the considered prediction models, a sensitivity factor for the resistance equal to 0.8 was assumed. It is therefore implicitly assumed that equation C.7 in Eurocode 0, annex C holds for all analyses in this appendix.

The probabilistic evaluation of test results was performed in accordance with the recommendations made in Eurocode 0, annex D and by Bijlaard et al. (1988). Minor differences exist between the procedures described in these two documents. A larger inconsistency between these two procedures is found in the fractile factors for the characteristic and design strengths. In this study, the procedures described by Bijlaard et al. were used. The used fractile factors therefore refer to a level of confidence of 75%. More information on the background calculation methods of the fractile factors can be found in Gulvanessian et al. (2012).

The influence of the difference between the nominal value and mean value of the yield strength on the necessary safety margins was taken into account in accordance with the proposal by Bijlaard et al.. For geometric parameters such as the diameter and wall thickness it was assumed that the nominal value of these parameters is equal to the mean value of their probability density functions. A study by Alpsten (1972) shows that, for I-sections, such an assumption may be incorrect. It is therefore recommended to verify this assumption for tubular members.

In this appendix, coefficients and partial safety factors are given in more digits than in the main text, to serve reproducibility of the analyses. In the main text of this thesis, appropriately rounded numbers are presented.

G.1 Local buckling of tubes

A design model was derived from the test results that were collected in Chapter 1 of the main text of this thesis. This model is described in equations (2.8), (2.9) and (2.10) in section 2.3.5 of the main text of this thesis. A comparison between the calculation model and the collected test results is presented in Figure G.1.

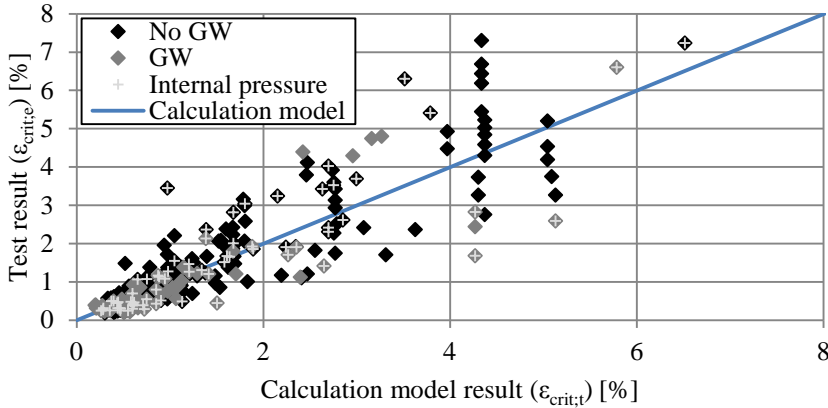


Figure G.1 Comparison of calculation model and test results.

G.1.1 Coefficient of variation of design function variables

The calculation model contains four variables: D , t , σ_y and P . The design internal pressure is considered to be deterministic. The probabilistic analysis of this parameter should be appropriately addressed when determining the corresponding partial factor for this action. The three remaining parameters are considered as a stochastic variable. To calculate the characteristic and design values of the critical compressive strain, the coefficient of variation of each of these parameters was determined.

Diameter

Since the design rule that is being developed is most applicable to pipelines, for the tube diameter, reference is made to API specification 5L for line pipe (2008). In this standard, the outside dimensions tolerances are $\pm 1\%$. The variable D was assumed to be uniformly distributed according to equation (G.1). The resulting coefficient of variation V_D is 0.0058. Alternatively, a lognormal or normal distribution can be assumed for the pipe diameter. When the tolerances stated in the API specifications are assumed to represent a 95% confidence interval of a normal distribution, the calculated coefficient of variation is very close to the value calculated from equation (G.1).

$$f(D) = \begin{cases} \frac{1}{D_{max} - D_{min}} & \text{for } D_{min} \leq D \leq D_{max} \\ 0 & \text{for } D < D_{min} \text{ or } D > D_{max} \end{cases} \quad (G.1)$$

With:

$$D_{min}: 0.99 \cdot D_m = 0.99 \cdot D_n$$

$$D_{max}: 1.01 \cdot D_m = 1.01 \cdot D_n$$

ISO 16708 (2006), which defines reliability-based limit state methods for petroleum and natural gas pipeline systems, states a coefficient of variation of less than 0.001 in a normal distribution. The larger variation according to API specifications is more conservative and is therefore taken into account in the calculation.

Wall thickness

Similarly as for the tube diameter, API specifications (2008) specify the tolerances on wall thickness in tubular members. The standard specifies the wall thickness tolerance for tubes originating from various manufacturing processes and specified wall thicknesses. Assuming that seamless pipes are only considered for thick-walled pipes and that welded pipes are only applied for wall thicknesses above 5 mm, a tolerance of $\pm 10\%$ can be used. The variable t may be assumed to be uniformly distributed according to equation (G.2). The resulting coefficient of variation V_t is 0.058.

$$f(t) = \begin{cases} \frac{1}{t_{max} - t_{min}} & \text{for } t_{min} \leq t \leq t_{max} \\ 0 & \text{for } t < t_{min} \text{ or } t > t_{max} \end{cases} \quad (G.2)$$

With:

$$t_{min}: 0.90 \cdot t_m = 0.90 \cdot t_n$$

$$t_{max}: 1.10 \cdot t_m = 1.10 \cdot t_n$$

Apart from wall thickness tolerances, API specifications also define mass tolerances. For most pipes, a +10%, -3.5% tolerance is defined on mass. Using the specified diameter and mass tolerances, the resulting tolerances on wall thickness were calculated by Van Foeken and Gresnigt (1998), resulting in a coefficient of variation of $V_t=0.035$. ISO 16708 (2006) states a coefficient of variation of 0.005 to 0.02 for the wall thickness of tubes in a normal distribution. Similarly as for the pipe diameter, a conservative value of V_t was implemented in the model. More specifically, the value of $V_t=0.035$, as calculated by Van Foeken and Gresnigt (1998), was used.

Yield strength

Commonly, the coefficient of variation for the yield strength of steel is taken as 0.07 (Bijlaard et al., 1988), (JCSS, 2000). ISO 16708 (2006) states a coefficient of variation of 0.02 to 0.06. Similar as for the wall thickness and tube diameter, a conservative value of 0.07 was selected.

G.1.2 Mean, characteristic and design model

The tests can be predicted using a calculation model that uses mean values of variables as input. In case of the collected test data, the reported actual values of the input variables of the model were substituted as mean values. The mean, characteristic and design model using mean values of the input variables are presented in equation (G.3) with appropriate coefficients given in Table G.1. The model has an acceptable correlation with the available test data ($\rho=0.88$). A comparison between the models and collected test results is presented in Figure G.2. In section 2.4 of the main text of this thesis, the design model is presented as the mean model divided by a partial safety factor.

$$\epsilon_{crit;m} = A \cdot \left(\frac{t}{D} \right)^{1.499} \cdot \alpha_{GW} \cdot \alpha_p \quad (G.3)$$

With:

A : Dimensionless coefficient, see Table G.1.

α_{GW} : Influence factor to account for the effect of the presence of a girth weld (see section 2.3.5 of the main text of this thesis)

α_p : Influence factor to account for the effect of the presence of a positive internal pressure (see section 2.3.5 of the main text of this thesis)

Table G.1 Coefficients for equation (G.3).

Model I.D.	Safety level	A
Mean	Mean value	3.808
Characteristic	5% fractile	1.839
Design ($\beta=3.3$)	$P_f=4.8 \cdot 10^{-4}$	1.238
Design ($\beta=3.6$)	$P_f=1.6 \cdot 10^{-6}$	1.126

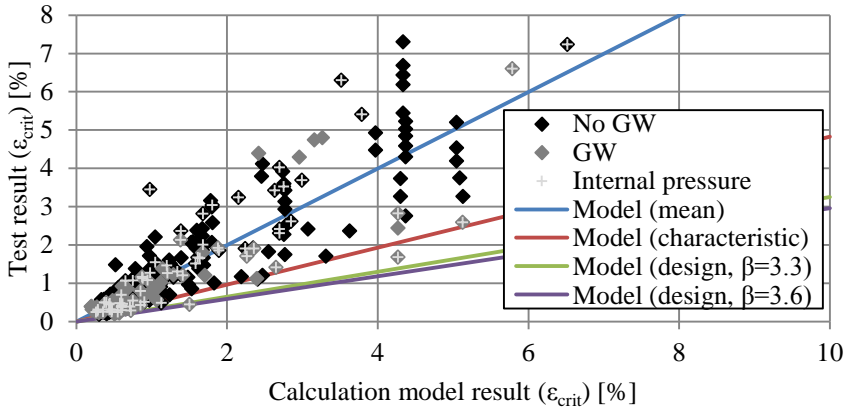


Figure G.2 Comparison of mean, characteristic and design calculation model with test results.

For application in design, an equation using nominal variables was developed. It was assumed that the nominal value of the geometrical variables of the geometrical variables (D and t) is the average value of their distribution function (see Appendix G.1.1). For the yield strength it was assumed that the nominal value is a 2.3% lower bound value of a lognormal distribution. In the model, the yield strength is only used in the influence factor for internal pressure α_p . The ratio between α_p that is predicted using nominal and mean values for the yield strength is presented in Figure G.3. Due to the average yield strength being larger than the nominal yield strength, the pressure ratio is overestimated, resulting in an overestimation of the beneficial effect of internal pressure. The adjusted influence factor α_p^* that is corrected for this phenomenon is presented in equation (G.4) and Figure G.4.

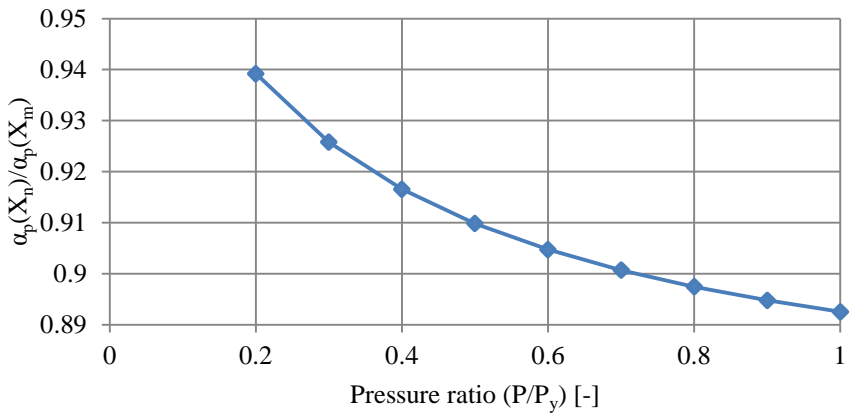


Figure G.3 Ratio between calculated value of α_p using nominal and mean values for the yield strength.

$$\begin{aligned}
 \alpha_p^*(X_n) &= 1 && \text{for } 0 \leq \frac{P_d}{P_{y;n}} \leq 0.25 \\
 \alpha_p^*(X_n) &= 1.865 \cdot \frac{P_d}{P_{y;n}} + 0.534 && \text{for } 0.25 \leq \frac{P_d}{P_{y;n}} \leq 1.0
 \end{aligned}
 \tag{G.4}$$

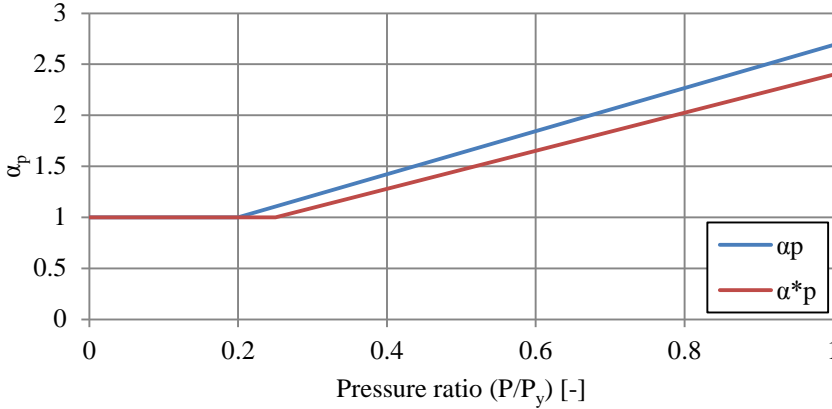


Figure G.4 Comparison between influence factors α_p and α_p^* .

G.1.3 Analysis of value of γ_M^*

The design formula stated in section 2.4 of the main text of this thesis contains a very large factor γ_M^* . This factor is mainly determined by the two considered coefficients of variation:

- Scatter of the test results around the model using the actual test specimen parameters, characterized by parameter V_δ .
- Coefficient of variation of the resistance due to the variation of the input parameters (V_r), characterized by the parameters V_t , V_D and V_{σ_y} for the coefficient of variation of wall thickness, tube diameter and yield strength respectively.

The coefficients of variation of the individual input parameters of the calculation model result in a total coefficient of variation of the resistance due to the variation of the input parameters (V_r). For design models that are a linear combination of input parameters, V_r can be directly calculated (Bijlaard et al., 1988). In case of a model that is not a linear product of the input variables, V_r is approximated on the basis of linearization of the resistance function at the mean value of each input variable for each available test result (see equation (G.5)). The maximum found value of V_r is taken into account in the calculation model. The total coefficient of variation of the resistance function V_r is calculated by vector addition of V_r and V_δ (see equation (G.6))

$$V_{rt,i} = \frac{\sum_{j=1}^k \left(\frac{\delta M_{pb}}{\delta X_j} (X_{j,m}) \cdot s_j \right)}{M_{pb}^2 (X_m)} \quad (G.5)$$

With:

$V_{rt,i}$: Value of V_{rt} for i^{th} specimen calculated by using values for X_m corresponding to that specimen.

X_m : Input variable in calculation model (mean value).

s_j : Standard deviation of j^{th} input parameter of calculation model.

$$V_r = \sqrt{V_{rt,max}^2 + V_{\delta}^2} \quad (G.6)$$

In case that all influence factors take value 1, V_{rt} and V_r could directly be calculated. For data points where this is not the case, the described process of linearization was used to determine the value of $V_{rt,i}$ and $V_{r,i}$. Figure G.5 presents the contribution of V_{rt} and V_{δ} to the total coefficient of variation of the resistance function (V_r). It is clear that the value of V_r is independent of the value of V_{rt} and is fully dominated by the scatter in the selected data (V_{δ}). Reconsideration of the coefficients of variation of the input parameters therefore will not result in a noticeable reduction in the value of γ_M^* .

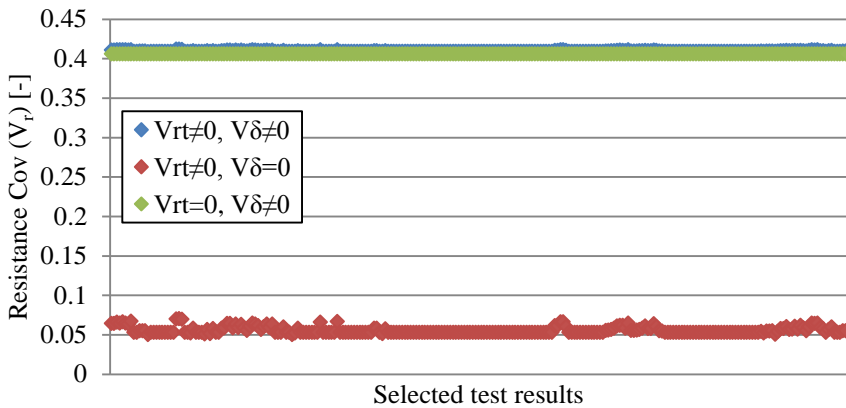


Figure G.5 Contribution of V_{rt} and V_{δ} to coefficient of variations of the resistance function (V_r).

G.2 Remaining post-buckling bending moment capacity of tubes in combined walls

In section 6.6 of the main text of this thesis it was observed that there is a correlation between the cross-sectional slenderness of a tubular member and its remaining post-buckling bending moment capacity immediately after local buckling failure. Based on linear regression, a relation between the cross-sectional slenderness and the ratio between M_{pb} and M_{pl} was found. The calculation model therefore has the form of equation (G.7), which can be rewritten to equation (G.8) so that the remaining post-buckling bending moment can be calculated directly. A comparison between the calculation model and the test results is presented in Figure G.6. An excellent correlation between the model and the test results is found ($\rho = 0.99$).

$$\frac{M_{pb}}{M_{pl}} = A \cdot \frac{D}{t \cdot \varepsilon^2} + B \tag{G.7}$$

With:

ε : Coefficient depending on the yield strength of the steel. $\varepsilon^2 = 235/\sigma_y$.

$$M_{pb} = \left(A \cdot \frac{D}{t \cdot \varepsilon^2} + B \right) \cdot \left(D^3 - (D - 2 \cdot t)^3 \right) \cdot \frac{\sigma_y}{6} \approx \left(A \cdot \frac{D}{t \cdot \varepsilon^2} + B \right) \cdot (D - t)^2 \cdot t \cdot \sigma_y \tag{G.8}$$

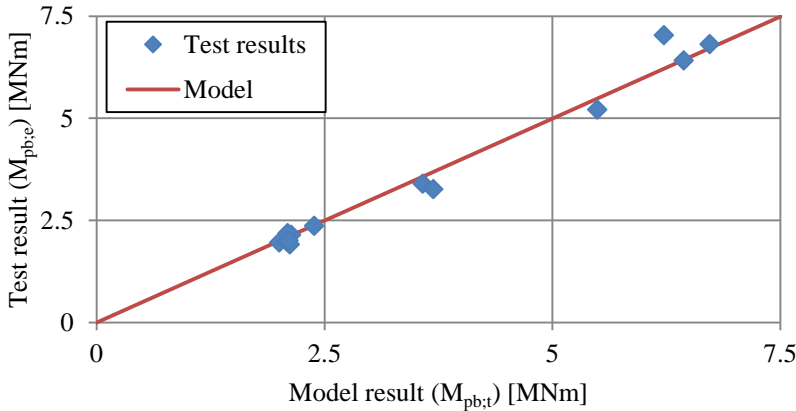


Figure G.6 Comparison of calculation model and test results.

G.2.1 Coefficient of variation of design function variables

The calculation model contains four variables: D , t , σ_y and ε . Because ε is only defined by σ_y , effectively M_{pb} is dependent on three variables. To calculate the characteristic and design resistance of the remaining post-buckling bending moment capacity, the coefficient of variation of each of these variables was determined.

Diameter

For the diameter, reference is made to EN 10219-2 (2006) which applies for the tubes under consideration in Part II of this study. In this product standard, the outside dimensions tolerances are $\pm 1\%$, with a minimum of ± 0.5 mm and a maximum of ± 10 mm. For civil engineering structures, it was assumed that this can be simplified to tolerances of 1% . The variable D was assumed to be uniformly distributed according to equation (G.9). The resulting coefficient of variation V_D is 0.0058. Alternatively, a lognormal or normal distribution can be assumed for the tube diameter. When the tolerances stated in EN 10219-2 were assumed to represent a 95% confidence interval, the calculated coefficient of variation was very close to the value calculated from equation (G.9).

$$f(D) = \begin{cases} \frac{1}{D_{max} - D_{min}} & \text{for } D_{min} \leq D \leq D_{max} \\ 0 & \text{for } D < D_{min} \text{ or } D > D_{max} \end{cases} \quad (\text{G.9})$$

With:

$$D_{min}: 0.99 \cdot D_m = 0.99 \cdot D_n$$

$$D_{max}: 1.01 \cdot D_m = 1.01 \cdot D_n$$

Wall thickness

Similarly as for the diameter, EN 10219-2 (2006) specifies the tolerances on wall thickness in tubular members. The product standard specifies the wall thickness tolerance as $\pm 10\%$ with a maximum of 2 mm. In this study, this was simplified to a tolerance of $\pm 10\%$. This implies that for elements with a wall thickness exceeding 20 mm, the analysis is conservative. The variable t was assumed to be uniformly distributed according to equation (G.10). The resulting coefficient of variation V_t is 0.058.

$$f(t) = \begin{cases} \frac{1}{t_{max} - t_{min}} & \text{for } t_{min} \leq t \leq t_{max} \\ 0 & \text{for } t < t_{min} \text{ or } t > t_{max} \end{cases} \quad (\text{G.10})$$

With:

$$t_{min}: 0.90 \cdot t_m = 0.90 \cdot t_n$$

$$t_{max}: 1.10 \cdot t_m = 1.10 \cdot t_n$$

Yield strength

Commonly, the coefficient of variation for the yield strength of steel is taken as 0.07 (Bijlaard et al., 1988), (JCSS, 2000).

G.2.2 Mean, characteristic and design model

For comparison of the developed model with test results, the measured values of the input variables of the model were substituted as mean values. The mean, characteristic and design model using mean values of the input variables is presented in equation (G.11) with appropriate coefficients in Table G.2. A comparison between the three calculation models and the test results is presented in Figure G.7.

$$M_{pb} = \left(A \cdot \frac{D_m}{t_m \cdot \varepsilon_m^2} + B \right) \cdot \left(D_m^3 - (D_m - 2 \cdot t_m)^3 \right) \cdot \frac{\sigma_{y;m}}{6} \approx \left(A \cdot \frac{D_m}{t_m \cdot \varepsilon_m^2} + B \right) \cdot (D_m - t_m)^2 \cdot t_m \cdot \sigma_{y;m} \quad (G.11)$$

With:

A: Dimensionless coefficient, see Table G.2

B: Dimensionless coefficient, see Table G.2

Table G.2 Coefficients for equation (G.11).

Model I.D.	Safety level	A	B
Mean	Mean value	$-2.646 \cdot 10^{-3}$	$1.042 \cdot 10^0$
Characteristic	5% fractile	$-2.002 \cdot 10^{-3}$	$7.883 \cdot 10^{-1}$
Design	$P_f=7 \cdot 10^{-5}$ ($\beta=3.8$)	$-1.597 \cdot 10^{-3}$	$6.289 \cdot 10^{-1}$

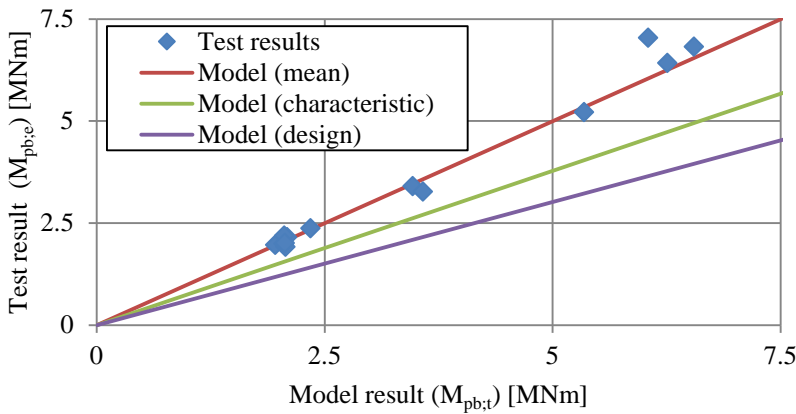


Figure G.7 Comparison of mean, characteristic and design calculation model with test results.

For application in design, an equation using nominal variables was developed, which is stated in equation (G.12). It was assumed that the nominal value of the geometrical variables (D and t) is the average value of their distribution function (see Appendix G.2.1). For the yield strength it was assumed that the nominal value is a 2.3% lower bound value of a lognormal distribution. The correction factor to the model factor ΔK (see equation G.13) is dependent of the cross-

sectional slenderness, as presented in Figure G.8. For simplicity, a slenderness-independent correction of 1.271 was applied, which is the average over the considered slenderness spectrum. The general design formula for the remaining post-buckling bending moment capacity is stated in equation (G.14). A comparison between the test results and design model is presented in Figure G.9.

$$M_{pb;d} = \frac{M_{pb;k}(X_m)}{\gamma_M} = \frac{M_{pb;m}(X_n)}{\gamma_M^*} = \frac{\left(A \cdot \frac{D_n}{t_n \cdot \varepsilon_n^2} + B\right) \cdot (D_n - t_n)^2 \cdot t_n \cdot \sigma_{y;n}}{\gamma_M^*} \quad (G.12)$$

$$\gamma_M^* = \frac{M_{pb;m}(X_n)}{M_{pb;k}(X_m)} \cdot \gamma_M = \Delta K \cdot \gamma_M \quad (G.13)$$

With:

X_n : Nominal values of the input parameters

X_m : Mean values of the input parameters

ΔK : Model factor correction factor

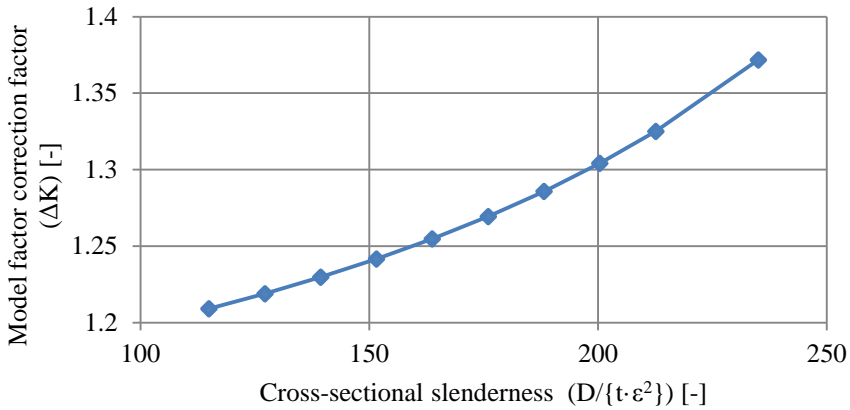


Figure G.8 Ratio between calculated post-buckling bending moment using nominal and mean values for the input parameters.

$$M_{pb;d}(X_n) = \frac{M_{pb;m}(X_n)}{\gamma_M^*} = \frac{\left(A \cdot \frac{D_n}{t_n \cdot \varepsilon_n^2} + B \right) \cdot (D_n - t_n)^2 \cdot t_n \cdot \sigma_{y;n}}{\gamma_M^*} \quad (G.14)$$

Validated for the parameter range:

$$115 \leq \frac{D}{t \cdot \varepsilon^2} \leq 235, \quad 65 \leq \frac{D}{t} \leq 125 \text{ and } 330 \leq \sigma_y \leq 620$$

With:

A: Dimensionless coefficient. $A = -2.646 \cdot 10^{-3}$.

B: Dimensionless coefficient. $B = 1.042 \cdot 10^0$.

γ_M^* : Model factor. For equation (D.6), $\gamma_M^* = 1.594$

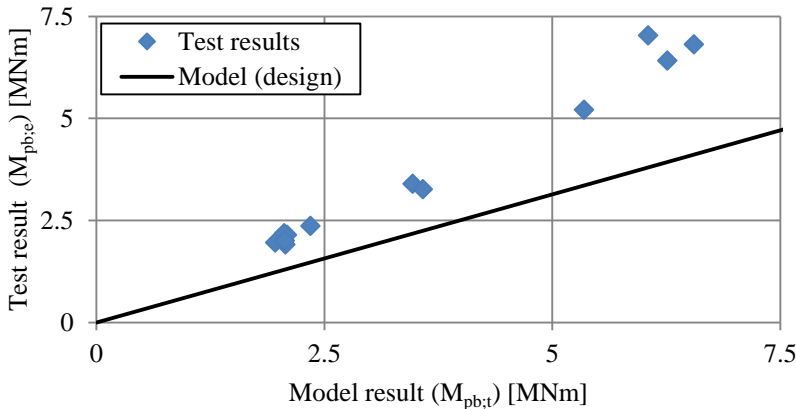


Figure G.9 Comparison between design model using nominal input values and test results.

G.2.3 Analysis of value of γ_M^*

The design formula stated in equation (G.14) contains a fairly large factor γ_M^* . This factor is mainly determined by the two considered coefficients of variation:

- Scatter of the test results around the model using the actual test specimen parameters, characterized by parameter V_δ .
- Coefficient of variation of the resistance due to variation of the input parameters (V_{rt}), characterized by the parameters V_t , V_D and V_{σ_y} for the coefficient of variation of wall thickness, tube diameter and yield strength respectively.

As the resistance function under consideration is not a linear combination of input parameters, local linearization of the design function is necessary to determine the value of V_{rt} (see Appendix G.1.3). In the considered model, the magnitude of V_δ is determined by the accuracy of the

calculation model. As the current model is a simple linear regression of the test data, some inaccuracy is expected. However, the total coefficient of variation of the resistance function (V_r) is dominated by the magnitude of V_{rt} . This is illustrated in Figure G.10, which clearly shows that even in the case of a perfect model ($V_\delta=0$), the coefficient of variation of the resistance function hardly changes. For the calculation model under consideration, reduction of factor γ_M^* is therefore most feasible by reduction of V_{rt} .

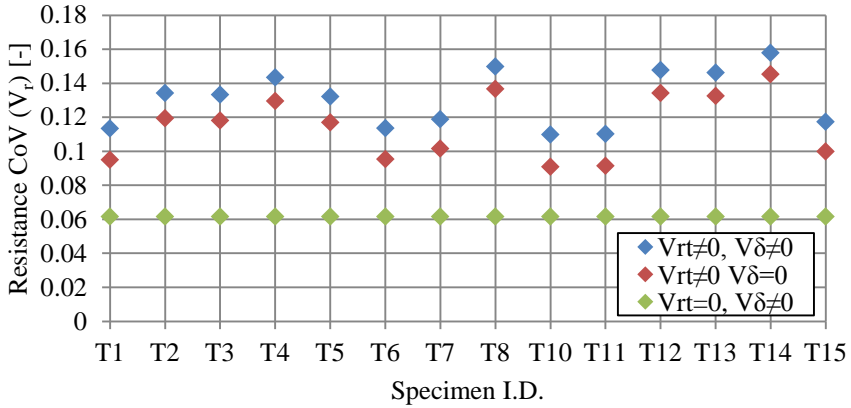


Figure G.10 Contribution of V_{rt} and V_δ to total coefficient of variation of the resistance.

An overview of the contribution of the coefficient of variation of the individual input parameters of the calculation model (V_i) on the total coefficient of variation of the input parameters (V_{rt}) is presented in Figure G.11. The figure shows that the value of V_{rt} is mainly determined by the variation in wall thickness of the tube. As a consequence, the value of γ_M^* is mainly determined by the coefficient of variation of the tube wall thickness, which is presented graphically in Figure G.12.

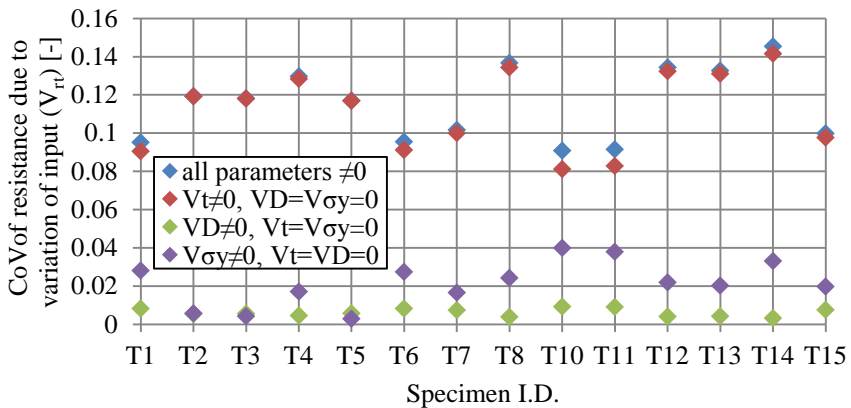


Figure G.11 Contribution of V_t , V_D and $V_{\sigma y}$ to V_{rt} .

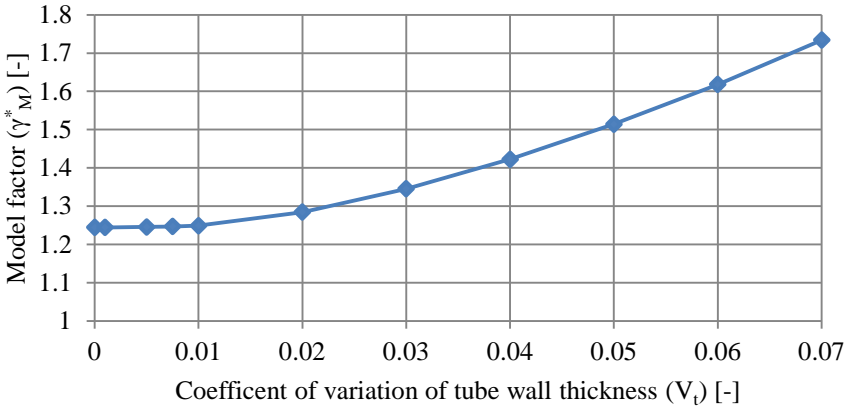


Figure G.12 Influence of V_t on γ_M^* with $V_D=0.0058$ and $V_{\sigma_y}=0.07$.

As discussed in Appendix G.2.1, the value of V_t that was taken into account in the calculations is an estimate, based on the product standard EN 10219-2. If instead of uniform, the distribution of the tube wall thickness is assumed to be lognormal, with the upper and lower limits that are stated in the standard at 2 or 3 standard deviations from the mean, V_t is reduced to 0.052 and 0.035 respectively. The latter of these results corresponds with the coefficient of variation for pipelines as found by Van Foeken and Gresnigt (1998). Another alternative value for V_t was found in ISO 16708 (2006) (see Appendix G.1.1). V_t can also be estimated by analysing the geometry of the tubes tested in Part II of this study. For each specimen, the quotient of the actual and nominal wall thickness was determined. Assuming a lognormal distribution and using the sample properties as representative for the full population, a very low value of $V_t=0.017$ was found. A summary of the various available values for V_t and the resulting model factor γ_M^* is presented in Table G.3.

Table G.3 Various values for V_t and corresponding values of γ_M^* .

Description	V_t	γ_M^*
EN 10219-2 (2006) – Uniform distribution	0.0577	1.594
EN 10219-2 (2006) – Lognormal distribution - 2σ	0.0520	1.534
EN 10219-2 (2006) – Lognormal distribution - 3σ	0.0349	1.381
ISO 16708 (2006)	0.005-0.02	1.245-1.284
Test results	0.0169	1.270

As presented in equation (G.5), the coefficient of variation V_{r_t} was determined by determining the partial derivative for each strength function input parameter. In this way, the local sensitivity of the strength function at the design point to variations of a specific input parameter was determined. In the case of the present analysis, V_{r_t} appears to be a function of the cross-sectional slenderness $D/(t \cdot \epsilon^2)$ (see Figure G.13). The values of γ_M^* that are shown in Table G.3 are based on the maximum value of V_{r_t} that was found within the considered $D/(t \cdot \epsilon^2)$ spectrum. This

resulted in a design rule that is safe, but may be too conservative in some areas of the design spectrum.

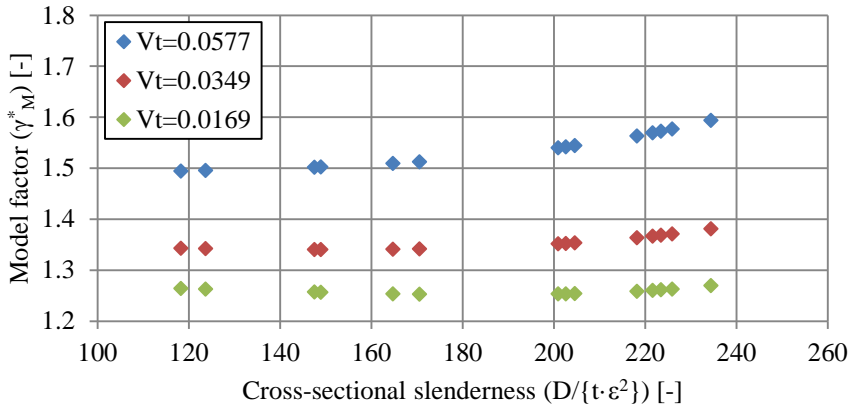


Figure G.13 Development of γ_M^* over $D/(t \cdot \epsilon^2)$ spectrum.

In conclusion, the main causes for the high value for γ_M^* are:

- A high sensitivity of the design function to the coefficient of variation of the tube wall thickness (V_t) (see Figure G.12). Choosing alternative values for V_t reduces the value of γ_M^* considerably (see Table G.3)
- Choosing the most conservative value for V_{rt} out of the individual values of $V_{rt,i}$ (see Figure G.13). This ensures sufficient safety across the full design spectrum, but may be too conservative in some areas.

If adjustments are made to mitigate the above causes, a value of γ_M^* as low as 1.245 can be obtained. However, when using this value of γ_M^* , the target safety level is met on average, but not for every individual case. Especially slender tubes (see Figure G.8 and Figure G.13) are then designed to a lower safety level. Further improvement of the design guideline may be possible by considering subsets of the data, so that different values of γ_M^* are determined for more narrow ranges of the cross-sectional slenderness.

G.2.4 Revision of mean, characteristic and design model

As shown in Appendix G.2.3, the partial safety factor γ_M^* is very sensitive to the variation coefficient of the wall thickness (V_t). The value of $V_t=0.0577$ which was initially implemented in the model may therefore need to be reconsidered. The values that ISO 16708 (2006) recommends for V_t are based on a database of pipes ranging from a diameter of about 40 mm to 1400 mm, with the majority in the range of 400 mm to 1000 mm. The upper value of V_t that is recommended corresponds well with the value that was found for the tubes used in the tests. Therefore, the model was revised, using $V_t=0.02$. Consequently, equation (G.11) is to be used with the coefficients stated in Table G.4. The partial safety factor for equation (G.14) changed to $\gamma_M^*=1.284$ in accordance to Table G.3, which is rounded to $\gamma_M^*=1.28$ in the main text of this

thesis. The comparison between the revised design model and test results is presented in Figure G.14 and Figure G.15.

Table G.4 Coefficients for equation (G.11).

Model I.D.	Safety level	A	B
Mean	Mean value	$-2.646 \cdot 10^{-3}$	$1.042 \cdot 10^0$
Characteristic	5% fractile	$-2.256 \cdot 10^{-3}$	$8.883 \cdot 10^{-1}$
Design	$P_f=7 \cdot 10^{-5}$	$-1.981 \cdot 10^{-3}$	$7.801 \cdot 10^{-1}$

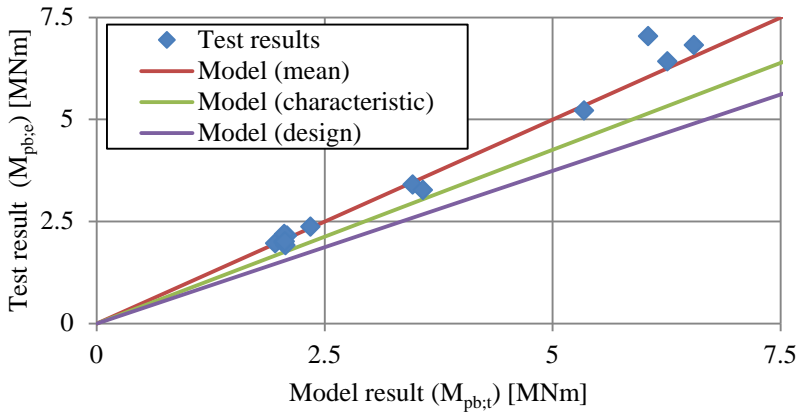


Figure G.14 Comparison of revised mean, characteristic and design model using mean input values with test results.

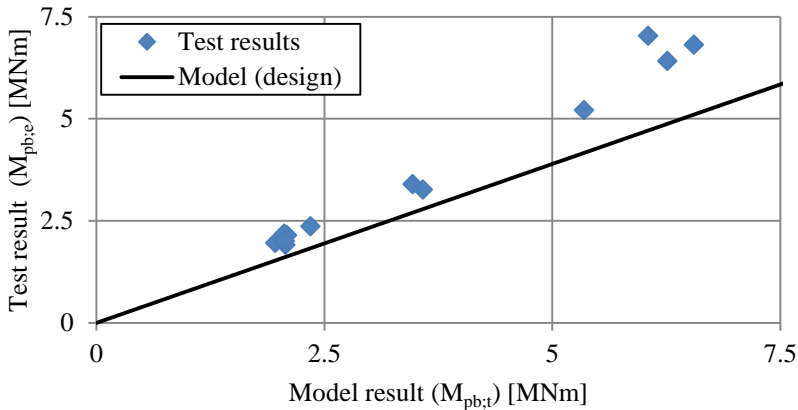


Figure G.15 Comparison between revised design model using nominal input values and test results.

G.3 Critical strain of tubes in combined walls

In section 6.9 of the main text of this thesis, a prediction model of the critical strain is compared with the results of the bending tests performed in Part II of this study. In this appendix, it is shown that this prediction model approximately corresponds to a characteristic model.

G.3.1 Coefficient of variation of design function variables

The calculation model contains two main variables: D and t . Further variables are found in the factors that take into account the effects of geometrical imperfections, local loads, strain hardening and sand fill. The prediction formula is compared with the tests presented in Part II of this study. Because these tests do not examine the effect of local loads or a sand fill, these parameters are not considered in this analysis.

Diameter

Similarly as for the remaining post-buckling bending moment capacity (see Appendix G.2.1), the coefficient of variation of the tube diameter V_D is assumed to be equal to 0.0058.

Wall thickness

Similarly as for the remaining post-buckling bending moment capacity (see Appendix G.2.4), the coefficient of variation of the tube wall thickness V_t is assumed to be equal to 0.02.

Y/T ratio

No information is available on the variation coefficient of the Y/T ratio and the mean Y/T ratio that corresponds to certain steel grades. Therefore, the Y/T ratio was assumed to be deterministic. When calculating the critical strain, the most conservative value of the Y/T ratio that is allowed in the applicable product specifications needs to be used. This approach resulted in the use of an upper bound of the value of the Y/T ratio in the formula and is therefore conservative. Alternatively, the actual Y/T ratio may be used if material certificates are available.

Geometrical imperfections

Similar to the Y/T ratio, no information is available on the variation coefficient of the geometrical imperfections in plain tubes and near girth welds and coil connection welds. Therefore, these imperfections were assumed to be deterministic. When calculating the critical strain, the most conservative value of the imperfections that are allowed in the applicable product specifications needs to be used. This approach results in the use of an upper bound of the size of the geometrical imperfections in the formula and is therefore conservative.

G.3.2 Characteristic value of critical strain

A comparison between the model proposed in Gresnigt et al. (2016) and the calculated characteristic value of that model is presented in Figure G.16. The figure shows that the proposed model and its characteristic value result in practically equal predicted values for the critical strain. The model proposed by Gresnigt et al. may therefore be used as a 5% lower bound to predict the critical strain of tubes for application in combined walls. Because for all input parameters the nominal and mean value are equal, or a conservative upper bound was selected, no distinction was made between models that use mean input values or nominal input values.

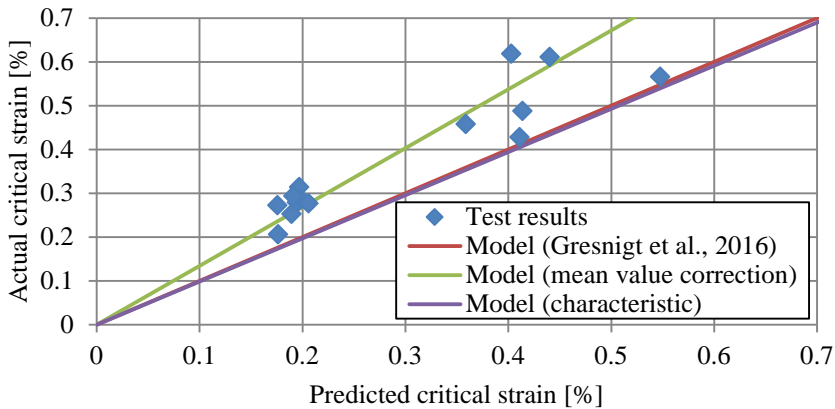


Figure G.16 Comparison of critical strain prediction model according to Gresnigt et al. (2016) and its characteristic value.

G.4 Maximum bending moment capacity of tubes in combined walls

In section 6.9 of the main text of this thesis, a prediction model of the critical strain is compared with the results of the bending tests performed in Part II of this study. In this appendix, a suitable value for the partial safety factor on the maximum bending moment capacity is derived.

G.4.1 Coefficient of variation of design function variables

The calculation model contains four variables: D , t , σ_y . Young's Modulus was assumed constant at a value of 210.000 MPa. The effect of the variation of the three remaining parameters on the variation of the predicted bending moment is difficult to determine due to the complexity of the model. Therefore, instead of using the method described in Appendix G.1.3, the effect of the

coefficients of variation of the input parameters was approximated using equation (G.15). The used coefficients of variation for each input parameter are discussed in the following sections.

$$V_{rt} = \sqrt{\sum V_i^2} \quad (\text{G.15})$$

Diameter

Similarly as for the remaining post-buckling bending moment capacity (see Appendix G.2.1), the coefficient of variation of the tube diameter V_D was assumed to be equal to 0.0058.

Wall thickness

Similarly as for the remaining post-buckling bending moment capacity (see Appendix G.2.4), the coefficient of variation of the tube wall thickness V_t was assumed to be equal to 0.02.

Yield strength

Similarly as for the remaining post-buckling bending moment capacity (see Appendix G.2.1), the coefficient of variation of the yield strength V_{σ_y} was assumed to be equal to 0.07.

G.4.2 Characteristic and design model

A comparison between the model proposed in Gresnigt et al. (2016) and the calculated characteristic and design value of the maximum bending moment is presented in Figure G.17. For the design value, a safety level corresponding to $\beta=3.8$ ($P_f=7 \cdot 10^{-5}$) was selected. In the calculation of these models, the comparison between the model and the result of test T11 was not taken into account. In this test, a relatively large difference occurred between the predicted and experimental moment-curvature diagram, while all other tests were predicted with much higher accuracy. It is assumed that the yield strength that was measured in the tensile tests on coupons taken from this tubular specimens did not represent the actual material properties of this tube with sufficient accuracy.

Figure G.17 has two remarkable features. Firstly, there is a relatively large difference between the original model and the calculated characteristic and design values, despite the good comparison of the model with the test results as shown in Appendix C. Secondly, it appears that the applied mean value correction of the model is too high for the tubes with high bending moment capacity and too small for the tubes with lower bending moment capacity. More careful examination showed that the difference in necessary mean value correction relates to the cross-sectional slenderness of the tubes. Apparently, the proposed prediction model according to Gresnigt et al. (2016) is more conservative for tubes with a higher cross-sectional slenderness.

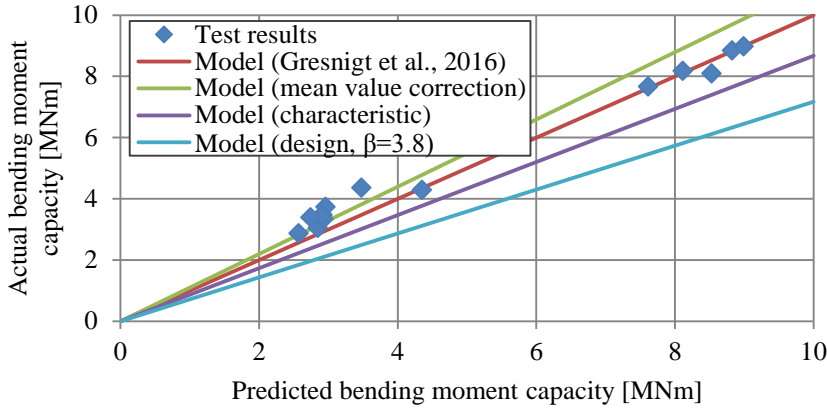


Figure G.17 Comparison of predicted bending moment capacity according to Gresnigt et al. (2016) and the corresponding characteristic and design values using mean values of the input variables.

For application in design, a model using nominal input values instead of mean values is necessary. To determine the required adjustment of the design model, the factor ΔK^* was defined as the ratio between the calculated bending moment capacity using nominal and mean values for the input parameters (see equation (G.16)). For all parameters except the yield stress it is assumed that the nominal values are equal to the mean value. For the yield stress it is assumed that the nominal value is a 2.3% lower bound value of a lognormal distribution.

$$\Delta K^* = \frac{M_{max}(X_n)}{M_{max}(X_m)} \tag{G.16}$$

The value of ΔK^* is a function of the cross-sectional slenderness $D/(\epsilon t^2)$, yield strength and the critical strain. Because the critical strain is influenced by geometrical imperfections and the strain hardening behaviour of the steel, also these parameters are of influence on the value of ΔK^* . An analysis of possible values of ΔK^* was made, using three representative yield strengths. Furthermore, two quality levels of the tube were examined: a “high-quality” tube and a “moderate-quality” tube. The selected values for the α -factors that take into account the effect of geometrical imperfections and strain hardening are presented in Table G.5.

Table G.5 Definition of α -factors for chosen tube qualities (See equation (6.4)).

Tube quality	α_{geo}	α_{sh}
Moderate	0.75	0.9
High	1	1

The resulting values for ΔK^* are presented in Figure G.18. The figure shows that for very stocky tubes, there is a considerable difference between the prediction model using nominal values and mean values of the input parameters, while there is hardly any difference for very slender tubes. This can be explained by examining the moment-curvature diagram. For very slender tubes,

local buckling occurs during the elastic phase of bending and is therefore almost independent of the yield stress, which is the only variable that has a nominal value unequal to its mean value. For very stocky tubes, local buckling occurs in the plastic plateau of the moment-curvature diagram. As a result, the prediction of M_{max} for these tubes fully benefits from the difference between the nominal and mean value of the yield stress. For the prediction of M_{max} for tubes of intermediate slenderness, some beneficial effect of the difference between nominal and mean value of the yield stress is present. For simplicity of further analysis, an approximate average value of ΔK^* was defined, as function of only the cross-sectional slenderness.

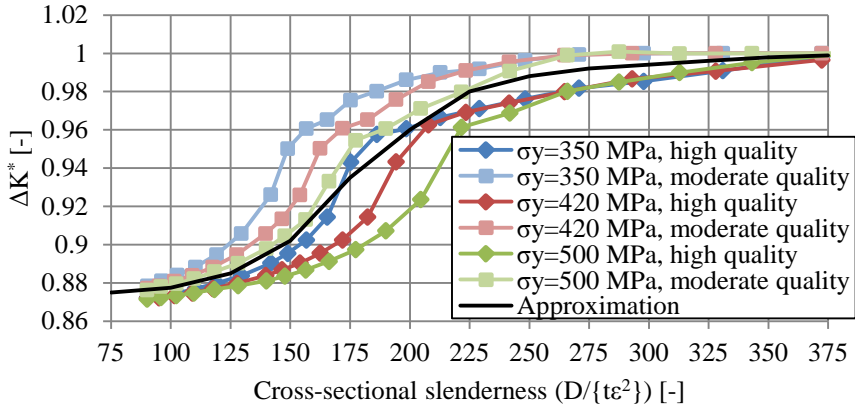


Figure G.18 Representative values of ΔK^* for combined walls.

Because the mean value correction requires a division of the data into subsets and the difference between the mean value and the nominal value of the yield stress needs to be taken into account, the characteristic and design model are revised in the following section.

G.4.3 Revision of characteristic and design model

To be able to take into account the beneficial effect of the difference between nominal and mean value of the yield stress for stocky tubes, while maintaining a sufficient safety level for more slender tubes, the data were re-analysed using two subsets of the data. The subsets were defined on the basis of the cross-sectional slenderness $D/(t\epsilon^2)$. Tubes with a cross-sectional slenderness larger than 175 were considered separately from the tubes with a lower cross-sectional slenderness. For the tubes with a cross-sectional slenderness lower than 175, the beneficial effect of the difference between the nominal and mean value of the yield strength was taken into account (see Figure G.18). For the more slender specimens, factor ΔK^* was assumed to be equal to 1. A comparison between the model proposed in Gresnigt et al. (2016) and the revised calculated characteristic and design value of the maximum bending moment is presented in Figure G.19. In this figure, the beneficial effect of the factor ΔK^* is not yet taken into account.

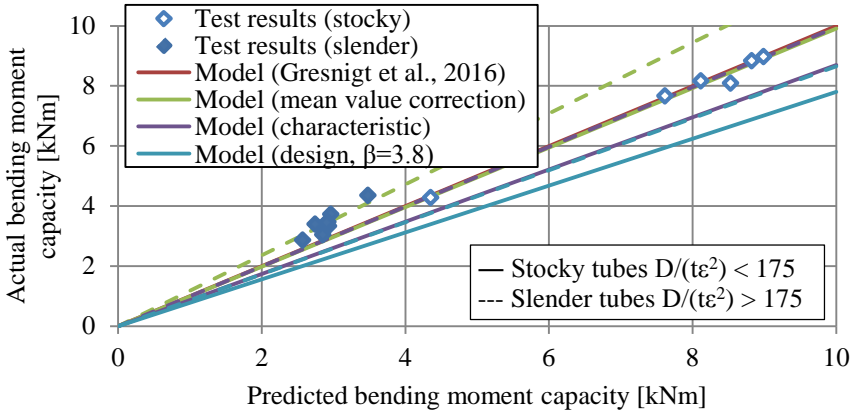


Figure G.19 Comparison of predicted bending moment capacity according to Gresnigt et al. (2016) and the corresponding revised characteristic and design values using mean values of the input variables.

To allow straightforward comparison between the various models, the model ratio was defined (see equation (G.17)) as the ratio between the calculated bending moment according to some model (mean, characteristic or design) and the bending moment predicted by the original model as published by Gresnigt et al. (2016).

$$\text{Model ratio} = \frac{\text{Model result (mean, char. or design)}}{\text{Model result according to Gresnigt et al. (2016)}} \quad (\text{G.17})$$

Using the separate model validations for the two considered subsets and taking into account the beneficial effect of the difference between the mean value and nominal value of the yield strength, it appeared that the model according to Gresnigt is approximately equal to a characteristic prediction (see Figure G.20) with exception of tubes with $100 < D/(t\epsilon^2) < 175$. In this area, the characteristic model predicts lower bending moments. However, it should be noted that in particular in the most affected slenderness range ($150 < D/(t\epsilon^2) < 175$) only two test specimens were available. Moreover, in the slenderness range $175 < D/(t\epsilon^2) < 200$ no test results were available. Further testing of tubes in these slenderness ranges may be necessary to confirm sufficient safety of the calculated design guidelines and may possibly result in improved economy.

For very stocky tubes, applying a partial safety factor of 1.11 results in a sufficiently safe design value. For very slender tubes, a partial safety factor of 1.16 is necessary. Similarly as for the characteristic value, the cross-sectional slenderness range between 100 and 175 requires a higher safety. To avoid a slenderness-dependent partial safety factor, a single partial safety factor of 1.15 is proposed, denoted in Figure G.20 as the simplified design model.

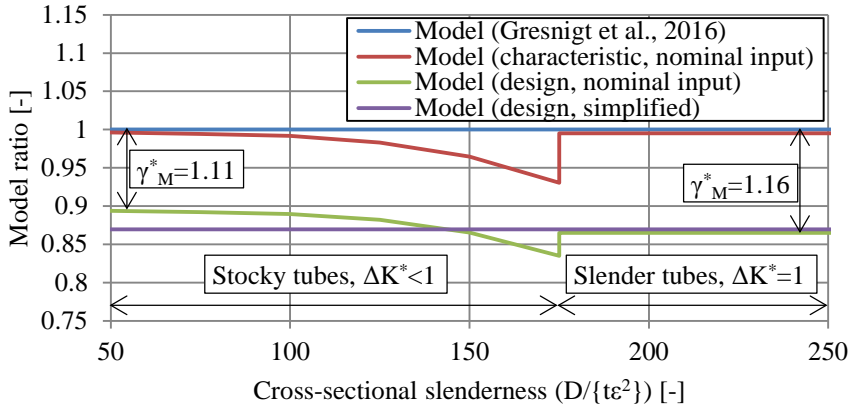


Figure G.20 Comparison of models using the model ratio.

A comparison between the simplified design model and the design model is presented in Figure G.21. The figure shows that on average the simplified design model is sufficiently safe. A slight non-conservative design situation occurs for tubes with a cross-sectional slenderness between 150 and 175. This may be prevented by increasing the partial safety factor γ_M^* to 1.2. However, in such a case, the approximated ΔK^* may also be revised to be fully conservative. This may lead to unnecessary uneconomical designs for parts of the design spectrum.

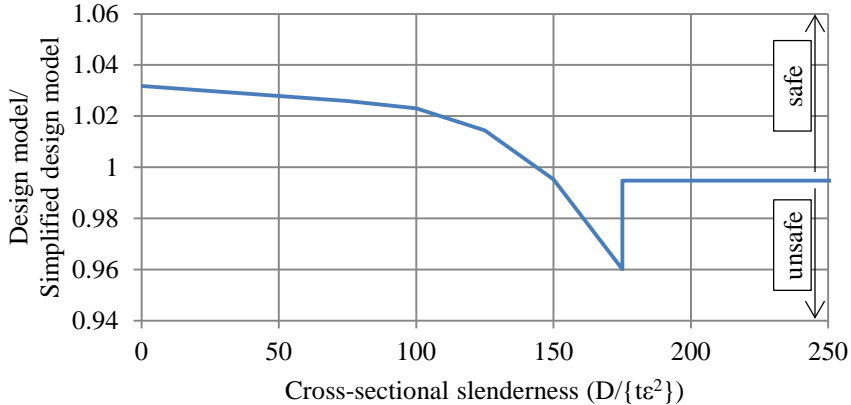


Figure G.21 Comparison of design model and simplified design model.

Curriculum Vitae

Sjors was born on February 18th, 1988 in Amersfoort, The Netherlands. Living in the nearby town Leusden, he received secondary education at the Corderius College in Amersfoort. After graduating, he moved to Delft to study Civil Engineering.

During his studies, Sjors worked as a student assistant for almost five years, which brought him in contact with education, research and experimental work. After obtaining his Master's degree, he continued research at Delft University of Technology as a PhD-candidate.

Personal information

Name: Sjors Harry Jan van Es
Date of birth: 18-02-1988
Place of birth: Amersfoort
Address: Achtmanstraat 3, 2645MD, Delfgauw
E-mail address: sjorsvanes@outlook.com

Research

2012-2016 PhD-research at Delft University of Technology, Faculty of Civil Engineering and Geosciences
Topic: Inelastic local buckling of tubes for combined walls and pipelines

Education

2009-2012 Master's programme in Civil Engineering at Delft University of Technology.
Specialisation: Steel and Timber Structures
Master thesis title: "Effect of TIG-dressing on fatigue strength and weld toe geometry of butt welded connections in high strength steel"
2006-2009 Bachelor's programme of Civil Engineering at Delft University of Technology
2000-2006 High school: Gymnasium at Corderius College in Amersfoort

Journal publications

- van Es, S.H.J., D. Vasilikis, A.M. Gresnigt and S.A. Karamanos (2016). Ultimate Bending Capacity of Spiral-Welded Steel Tubes – Part I: Experiments. *Thin-Walled Structures* 102, 286-304.
- Vasilikis, D., S.H.J. van Es, S.A. Karamanos and A.M. Gresnigt (2016). Ultimate Bending Capacity of Spiral-Welded Steel Tubes – Part II: Predictions. *Thin-Walled Structures* 102, 305-319.
- Sadowski, A.J., S.H.J. van Es, T. Reinke, J.M. Rotter, A.M. Gresnigt and T. Ummenhofer (2015). Harmonic analysis of measured initial geometric imperfections in large spiral-welded carbon steel tubes. *Engineering Structures* 85, 234-248.

Conference publications

- Gresnigt A.M., S.H.J. van Es, S.A. Karamanos and D. Vasilikis (2016). Strain-based design rules for spiral-welded tubes using analytical modelling. In *Proceedings of the 26th International Ocean and Polar Engineering Conference*, Rhodes, Greece.
- van Es, S.H.J., A.M. Gresnigt, D. Vasilikis and S.A. Karamanos (2016). Experimental and numerical investigation of the bending capacity of spiral-welded steel tubes. In *Proceedings of the International Colloquium on Stability and Ductility of Steel Structures*, Timisoara, Romania.
- Gresnigt, A.M., S.H.J. van Es, D. Vasilikis and S.A. Karamanos (2016). Strain-based design procedures for spiral-welded steel tubes in combined walls. In *Proceedings of the International Colloquium on Stability and Ductility of Steel Structures*, Timisoara, Romania.
- Peters. D.J., E.J. Broos., A.M. Gresnigt and S.H.J. van Es (2015). Local buckling resistance of sand-filled spirally welded tubes. In *Proceedings of the 25th International Offshore and Polar Engineering Conference*, Hawaii, USA.
- Vasilikis, D., S.A. Karamanos, S.H.J. van Es and A.M. Gresnigt (2014). Bending deformation capacity of large-diameter spiral-welded tubes. In *Proceedings of the 10th International Pipeline Conference*, Calgary, Canada.
- van Es, S.H.J., A.M. Gresnigt, M.H. Kolstein and F.S.K. Bijlaard (2014). Strain based design of spirally welded pipes, local buckling in 4-point bending. In *Proceedings of the 24th International Offshore and Polar Engineering Conference*, Busan, South-Korea.
- van Es, S.H.J., M.H. Kolstein, R.J.M. Pijpers and F.S.K. Bijlaard (2013). TIG-dressing of high strength steel butt welded connections – Part 2: physical testing and modelling. In *Proceedings of the 5th Fatigue Design Conference*, Senlis, France.
- van Es, S.H.J., A.M. Gresnigt, M.H. Kolstein and F.S.K. Bijlaard (2013). Local Buckling of Spirally Welded Tubes – Analysis of Imperfections and Physical Testing. In *Proceedings of the 23rd International Offshore and Polar Engineering Conference*, Anchorage, USA.